Rajesh Rajamani

Vehicle Dynamics and Control

Second Edition

Mechanical Engineering Series

Frederick F. Ling
Editor-in-Chief

The Mechanical Engineering Series features graduate texts and research monographs to address the need for information in contemporary mechanical engineering, including areas of concentration of applied mechanics, biomechanics, computational mechanics, dynamical systems and control, energetics, mechanics of materials, processing, production systems, thermal science, and tribology.

For further volumes:

Rajesh Rajamani

Vehicle Dynamics and Control

Second Edition

Dr. Rajesh Rajamani
Department of Mechanical Engineering
University of Minnesota
Minneapolis, MN 55455, USA
rajamani@me.umn.edu

For Priya

Preface

As a research advisor to graduate students working on automotive projects, I have frequently felt the need for a textbook that summarizes common vehicle control systems and the dynamic models used in the development of these control systems. While a few different textbooks on ground vehicle dynamics are already available in the market, they do not satisfy all the needs of a control systems engineer. A controls engineer needs models that are both simple enough to use for control system design but at the same time rich enough to capture all the essential features of the dynamics. This book attempts to present such models and actual automotive control systems from literature developed using these models.

The control system applications covered in the book include cruise control, adaptive cruise control, anti-lock brake systems, automated lane keeping, automated highway systems, yaw stability control, engine control, passive, active and semi-active suspensions, tire-road friction coefficient estimation, rollover prevention, and hybrid electric vehicles. A special effort has been made to explain the several different tire models commonly used in literature and to interpret them physically.

In the second edition, the topics of roll dynamics, rollover prevention and hybrid electric vehicles have been added as Chapters 15 and 16 of the book. Chapter 8 on electronic stability control has been significantly enhanced.

As the worldwide use of automobiles increases rapidly, it has become ever more important to develop vehicles that optimize the use of highway and fuel resources, provide safe and comfortable transportation and at the same time have minimal impact on the environment. To meet these diverse and often conflicting requirements, automobiles are increasingly relying on electromechanical systems that employ sensors, actuators and feedback control. It is hoped that this textbook will serve as a useful resource to researchers who work on the development of such control systems, both in

the automotive industry and at universities. The book can also serve as a textbook for a graduate level course on Vehicle Dynamics and Control.

An up-to-date errata for typographic and other errors found in the book after it has been published will be maintained at the following web-site:

http://www.menet.umn.edu/~rajamani/vdc.html

I will be grateful for reports of such errors from readers.

May 2005 and June 2011   Rajesh Rajamani
                                                                            Minneapolis, Minnesota

Acknowledgments

I am deeply grateful to Professor Karl Hedrick for introducing me to the field of Vehicle Dynamics and Control and for being my mentor when I started working in this field. My initial research with him during my doctoral studies has continued to influence my work. I am also grateful to Professor Max Donath at the University of Minnesota for his immense contribution in helping me establish a strong research program in this field.

I would also like to express my gratitude to my dear friend Professor Darbha Swaroop. The chapters on longitudinal control in this book are strongly influenced by his research results. I have had innumerable discussions with him over the years and have benefited greatly from his generosity and willingness to share his knowledge.

Several people have played a key role in making this book a reality. I am grateful to Serdar Sezen for highly improving many of my earlier drawings for this book and making them so much more clearer and professional. I would also like to thank Gridsada Phanomchoeng, Vibhor Bageshwar, Jin-Oh Hahn, Neng Piyabongkarn and Yu Wang for reviewing several chapters of this book and offering their comments. I am grateful to Lee Alexander who has worked with me on many research projects in the field of vehicle dynamics and contributed to my learning.

I would like to thank my parents Vanaja and Ramamurty Rajamani for their love and confidence in me. Finally, I would like to thank my wife Priya. But for her persistent encouragement and insistence, I might never have returned from a job in industry to a life in academics and this book would probably have never been written.

May 2005 and June 2011   Rajesh Rajamani
                                                    Minneapolis, Minnesota

Contents

Chapter 1

INTRODUCTION

The use of automobiles is increasing worldwide. In 1970, 30 million vehicles were produced and 246 million vehicles were registered worldwide (Powers and Nicastri, 2000). By 2011, approximately 72 million vehicles are expected to be produced annually and more than 800 million vehicles could be registered.

The increasing worldwide use of automobiles has motivated the need to develop vehicles that optimize the use of highway and fuel resources, provide safe and comfortable transportation and at the same time have minimal impact on the environment. It is a great challenge to develop vehicles that can satisfy these diverse and often conflicting requirements. To meet this challenge, automobiles are increasingly relying on electromechanical subsystems that employ sensors, actuators and feedback control. Advances in solid state electronics, sensors, computer technology and control systems during the last two decades have also played an enabling role in promoting this trend.

This chapter provides an overview of some of the major electromechanical feedback control systems under development in the automotive industry and in research laboratories. The following sections in the chapter describe developments related to each of the following five topics:

   a) driver assistance systems
   b) active stability control systems
   c) ride quality improvement
   d) traffic congestion solutions and
   e) fuel economy and vehicle emissions

1.1   DRIVER ASSISTANCE SYSTEMS

On average, one person dies every minute somewhere in the world due to a car crash (Powers and Nicastri, 2000). In addition to the emotional toll of car crashes, their actual costs in damages equaled 3% of the world GDP and totaled nearly one trillion dollars in 2000. Data from the National Highway Safety Transportation Safety Association (NHTSA) show that approximately 6 million accidents (with 35,000 fatalities) occur annually on US highways (NHTSA, 2010). Data also indicates that, while a variety of factors contribute to accidents, human error accounts for over 90% of all accidents (United States DOT Report, 1992).

A variety of driver assistance systems are being developed by automotive manufacturers to automate mundane driving operations, reduce driver burden and thus reduce highway accidents. Examples of such driver assistance systems under development include

   a)   collision avoidance systems which automatically detect slower moving preceding vehicles and provide warning and brake assist to the driver
   b)   adaptive cruise control (ACC) systems which are enhanced cruise control systems and enable preceding vehicles to be followed automatically at a safe distance
   c)   lane departure warning systems
   d)   lane keeping systems which automate steering on straight roads
   e)   vision enhancement/ night vision systems
   f)   driver condition monitoring systems which detect and provide warning for driver drowsiness, as well as for obstacles and pedestrians
   g)   safety event recorders and automatic collision and severity notification systems

These technologies will help reduce driver burden and make drivers less likely to be involved in accidents. This can also help reduce the resultant traffic congestion that accidents tend to cause.

Collision avoidance and adaptive cruise control systems are discussed in great depth in Chapters 5 and 6 of this book. Lane keeping systems are discussed in great detail in Chapter 3.

1.2   ACTIVE STABILITY CONTROL SYSTEMS

Vehicle stability control systems that prevent vehicles from spinning, drifting out and rolling over have been developed and recently commercialized by several automotive manufacturers. Stability control systems that prevent

vehicles from skidding and spinning out are often referred to as yaw stability control systems and are the topic of detailed description in Chapter 8 of this book. Stability control systems that prevent roll over are referred to as active rollover prevention systems and are discussed in depth in Chapter 15 of the book. An integrated stability control system can incorporate both yaw stability and roll over stability control.
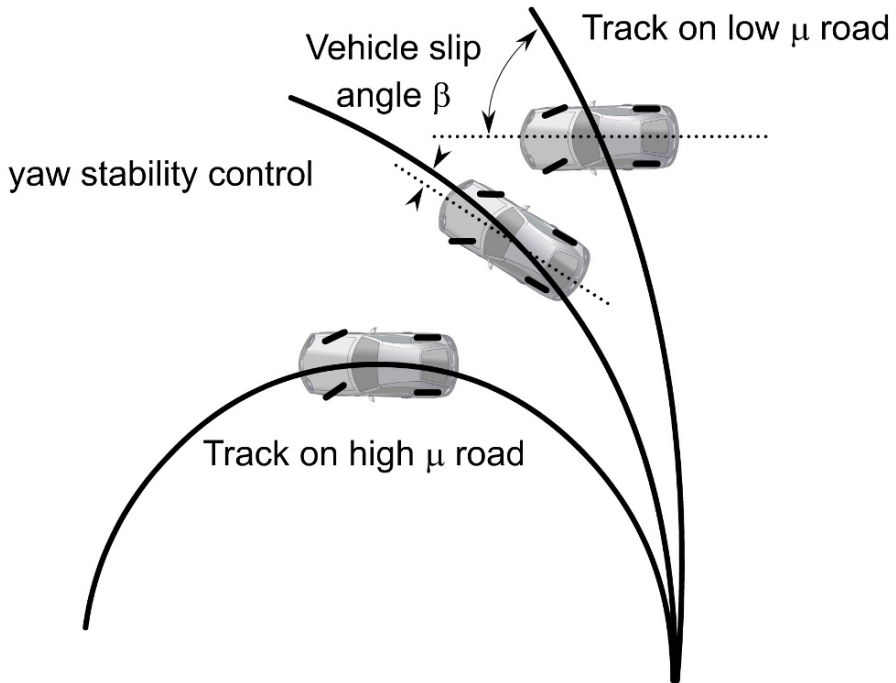
Figure 1-1. The functioning of a yaw stability control system

Figure 1-1 schematically shows the function of a yaw stability control system. In this figure, the lower curve shows the trajectory that the vehicle would follow in response to a steering input from the driver if the road were dry and had a high tire-road friction coefficient. In this case the high friction coefficient is able to provide the lateral force required by the vehicle to negotiate the curved road. If the coefficient of friction were small or if the vehicle speed were too high, then the vehicle would be unable to follow the nominal motion required by the driver – it would instead travel on a trajectory of larger radius (smaller curvature), as shown in the upper curve of Figure 1-1. The function of the yaw control system is to restore the yaw velocity of the vehicle as much as possible to the nominal motion expected by the driver. If the friction coefficient is very small, it might not be possible to entirely achieve the nominal yaw rate motion that would be achieved by

the driver on a high friction coefficient road surface. In this case, the yaw control system would partially succeed by making the vehicle's yaw rate closer to the expected nominal yaw rate, as shown by the middle curve in Figure 1-1.

Examples of yaw stability control systems that have been commercialized on production vehicles include the BMW DSC3 (Leffler, et. al., 1998) and the Mercedes ESP, which were introduced in 1995, the Cadillac Stabilitrak system (Jost, 1996) introduced in 1996 and the Chevrolet C5 Corvette Active Handling system in 1997 (Hoffman, et. al., 1998).

While most of the commercialized systems are **differential-braking** based systems, there is considerable ongoing research on two other types of yaw stability control systems: **steer-by-wire** and **active torque distribution** control. All three types of yaw stability control systems are discussed in detail in Chapter 8 of this book.

A yaw stability control system contributes to rollover stability just by helping keep the vehicle on its intended path and thus preventing the need for erratic driver steering actions. There is also considerable work being done directly on the development of active rollover prevention systems, especially for sport utility vehicles (SUVs) and trucks. Some systems such as Freightliner's Roll Stability Advisor and Volvo's Roll Stability Control systems utilize sensors on the vehicle to detect if a rollover is imminent and a corrective action is required. If corrective action is required, differential braking is used both to slow the vehicle down and to induce an understeer that contributes to reduction in the roll angle rate of the vehicle. Other types of rollover prevention technologies include Active Stabilizer Bar systems developed by Delphi and BMW (Strassberger and Guldner, 2004). In this case the forces from a stabilizer bar in the suspension are adjusted to help reduce roll while cornering.

1.3   RIDE QUALITY

The notion of using active actuators in the suspension of a vehicle to provide significantly improved ride quality, better handling and improved traction has been pursued in various forms for a long time by research engineers (Hrovat, 1997, Strassberger and Guldner, 2004). Fully active suspension systems have been implemented on Formula One racing cars, for example, the suspension system developed by Lotus Engineering (Wright and Williams, 1984). For the more regular passenger car market, semi-active suspensions are now available on some production vehicles in the market. Delphi's semi-active MagneRide system first debuted in 2002 on the Cadillac Seville STS and is now available as an option on all Corvette

models. The MagneRide system utilizes a magnetorheological fluid based shock absorber whose damping and stiffness properties can be varied rapidly in real-time. A semi-active feedback control system varies the shock absorber properties to provide enhanced ride quality and reduce the handling/ride quality trade-off.

Most semi-active and active suspension systems in the market have been designed to provide improved handling by reducing roll during cornering. Active stabilizer bar systems have been developed, for example, by BMW and Delphi and are designed to reduce roll during cornering without any deterioration in the ride quality experienced during normal travel (Strassberger and Guldner, 2004).

The **RoadMaster** system is a different type of active suspension system designed to specifically balance heavy static loads (www.activesuspension.com). It is available as an after-market option for trucks, vans and SUVs. It consists of two variable rated coil springs that fit onto the rear leaf springs and balance static forces, thus enabling vehicles to carry maximum loads without bottoming through.

The design of passive, active and semi-active suspensions is discussed in great depth in Chapters 6, 7 and 8 of this book.

1.4   TECHNOLOGIES FOR ADDRESSING TRAFFIC CONGESTION

Traffic congestion is growing in urban areas of every size and is expected to double in the next ten years. Over 5 billion hours are spent annually waiting on freeways (Texas Transportation Institute, 2010). Building adequate highways and streets to stop congestion from growing further is prohibitively expensive. A review of 68 urban areas conducted in 1999 by the Texas Transportation Institute concluded that 1800 new lane miles of freeway and 2500 new lane miles of streets would have to be added to keep congestion from growing between 1998 and 1999! This level of construction appears unlikely to happen for the foreseeable future. Data shows that the traffic volume capacity added every year by construction lags the annual increase in traffic volume demanded, thus making traffic congestion increasingly worse. The promotion of public transit systems has been difficult and ineffective. Constructing a public transit system of sufficient density so as to provide point to point access for all people remains very difficult in the USA. Personal transportation vehicles will therefore continue to be the transportation mode of choice even when traffic jams seem to compromise the apparent freedom of motion of automobiles.

While the traffic congestion issue is not being directly addressed by automotive manufacturers, there is significant vehicle-related research being conducted in various universities with the objective of alleviating highway congestion. Examples include the development of automated highway systems, the development of "traffic friendly" adaptive cruise control systems and the development of tilt controlled narrow commuter vehicles. These are discussed in the following sub-sections.

1.4.1   Automated highway systems

A significant amount of research has been conducted at California PATH on the development of automated highway systems. In an automated highway system (AHS), vehicles are fully automated and travel together in tightly packed platoons (Hedrick, Tomizuka and Varaiya, 1994, Varaiya, 1993, Rajamani, Tan, et. al., 2000). A traffic capacity that is up to three times the capacity on today's manually driven highways can be obtained. Vehicles have to be specially instrumented before they can travel on an AHS. However, once instrumented, such vehicles can travel both on regular roads as well as on an AHS. A driver with an instrumented vehicle can take a local road from home, reach an automated highway that bypasses congested downtown highway traffic, travel on the automated highway, travel on a subsequent regular highway and reach the final destination, all without leaving his/her vehicle. Thus an AHS provides point to point personal transportation suitable for the low density population in the United States.

The design of vehicle control systems for AHS is an interesting and challenging problem. Longitudinal control of vehicles for travel in platoons on an AHS is discussed in great detail in Chapter 7 of this book. Lateral control of vehicles for automated steering control on an AHS is discussed in Chapter 3.

1.4.2   "Traffic-friendly" adaptive cruise control

As discussed in section 1.1, adaptive cruise control (ACC) systems have been developed by automotive manufacturers and are an extension of the standard cruise control system. ACC systems use radar to automatically detect preceding vehicles traveling in the same lane on the highway. In the case of a slower moving preceding vehicle, an ACC system automatically switches from speed control to spacing control and follows the preceding vehicle at a safe distance using automated throttle control. Figure 1-2 shows a schematic of an adaptive cruise control system.
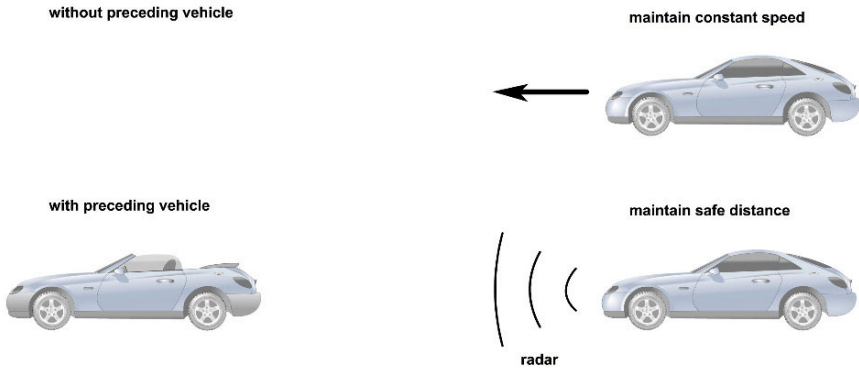
Figure 1-2. Adaptive cruise control

ACC systems are already available on production vehicles and can operate on today's highways. They have been developed by automotive manufacturers as a driver assistance tool that improves driver convenience and also contributes to safety. However, as the penetration of ACC vehicles as a percentage of total vehicles on the road increases, ACC vehicles can also significantly influence the traffic flow on a highway.

The influence of adaptive cruise control systems on highway traffic is being studied by several research groups with the objective of designing ACC systems to promote smoother and higher traffic flow (Liang and Peng, 1999, Swaroop, 1999, Swaroop 1998, Wang and Rajamani, 2001). Important issues being addressed in the research include

a) the influence of inter-vehicle spacing policies and control algorithms on traffic flow stability
b) the development of ACC algorithms to maximize traffic flow capacity while ensuring safe operation
c) the advantages of using roadside infrastructure and communication systems to help improve ACC operation.

The design of ACC systems is the focus of detailed discussion in Chapter 6 of this book.

1.4.3 Narrow tilt-controlled commuter vehicles

A different type of research activity being pursued is the development of special types of vehicles to promote higher highway traffic flow rates. A research project at the University of Minnesota focuses on the development

of a prototype commuter vehicle that is significantly narrower than a regular passenger sedan and requires the use of only a half-width lane on the highway (Gohl, et. al., 2004, Rajamani, et. al., 2003, Kidane, et. al., 2010). Adoption of such narrow vehicles for commuter travel could lead to significantly improved highway utilization.

A major challenge is to ensure that the vehicle is as easy to drive and as safe as a regular passenger sedan, in spite of being narrow. This leads to some key requirements:

The vehicle should be relatively tall in spite of being narrow. This leads to better visibility for the driver. Otherwise, in a short narrow vehicle where the vehicle height is less than the track width, the driver would ride at the height of the wheels of the many sport utility vehicles around him/her.

Since tall vehicles tend to tilt and overturn, the development of technology to assist the driver in balancing the vehicle and improving its ease of use is important.

An additional critical requirement for small vehicles is that they need significant innovations in design so as to provide improved crashworthiness, in addition to providing weather proof interiors.

A prototype commuter vehicle has been developed at the University of Minnesota with an automatic tilt control system which ensures that the vehicle has tilt stability in spite of its narrow track. The control system on the vehicle is designed to automatically estimate the radius of the path in which the driver intends the vehicle to travel and then tilt the vehicle appropriately to ensure stable tilt dynamics. Stability is maintained both while traveling straight as well as while negotiating a curve or while changing lanes. Technology is also being developed for a skid prevention system based on measurements of wheel slip and slip angle from new sensors embedded in the tires of the narrow vehicle.

The control design task for tilt control on a narrow vehicle is challenging because no single type of system can be satisfactorily used over the entire range of operating speeds. While steer-by-wire systems can be used at high speeds and direct tilt actuators can be used at medium speeds, a tilt brake system has to be used at very low speeds. Details on the tilt control system for the commuter vehicle developed at the University of Minnesota can be found in Kidane, et. al., 2010, Rajamani, et. al., 2003 and Gohl, et. al., 2004.

Intelligent Transportation Systems (ITS)

The term Intelligent Transportation Systems (ITS) is often encountered in literature on vehicle control systems. This term is used to describe a collection of concepts, devices, and services that combine control, sensing

and communication technologies to improve the safety, mobility, efficiency, and environmental impact of vehicle/highway systems. The importance of ITS lies in its potential to produce a paradigm shift (a new way of thinking) in transportation technology away from individual vehicles and reliance on building more roadways toward development of vehicles, roadways and other infrastructure which are able to cooperate effectively and efficiently in an intelligent manner.

1.5 EMISSIONS AND FUEL ECONOMY

US, European and Japanese Emission Standards continue to require significant reductions in automotive emissions, as shown in Figure 1-3 (Powers and Nicastri, 2000). The 2005 level for hydrocarbon (HC) emissions were less than 2% of the 1970 allowance. By 2005, carbon monoxide (CO) levels were only 10% of the 1970 level, while the permitted level for oxides of nitrogen (NOx) were down to 7% of the 1970 level (Powers and Nicastri, 2000). Trucks have also experienced ever-tightening emissions requirements, with emphasis placed on emissions of particulate matter (soot). Fuel economy goes hand in hand with emission reductions, and the pressure to steadily improve fuel economy also continues.

To meet the ever-tightening emissions standards, auto manufacturers and researchers are developing a number of advanced electromechanical feedback control systems. Closed-loop control of fuel injection, exhaust gas recirculation (EGR), internal EGR, camless electronically controlled engine valves, homogenous charge compression ignition (HCCI) and development of advanced emissions sensors are being pursued to address gasoline engine emissions (Ashhab, et. al., 2000, Das and Mathur, 1993, Stefanopoulou and Kolmanovsky, 1999). Variable geometry turbocharged diesel engines, electronically controlled turbo power assist systems and closed-loop control of exhaust gas recirculation play a key role in technologies being developed to address diesel engine emissions (Guzzella and Amstutz, 1998, Kolmanovsky, et. al., 1999, Stefanopoulou, et. al., 2000). Dynamic modeling and use of advanced control algorithms play a key role in the development of these emission control systems.

Emissions standards in California also require a certain percentage of vehicles sold by each automotive manufacturer to be zero emission vehicles (ZEVs) and ultra low emission vehicles (ULEVs) (http://www.arb.ca.gov/homepage.htm). This has pushed the development of hybrid electric vehicles (HEVs), plug-in hybrid vehicles and electric vehicles.

EMISSION EVOLUTION 1990 - 2000+
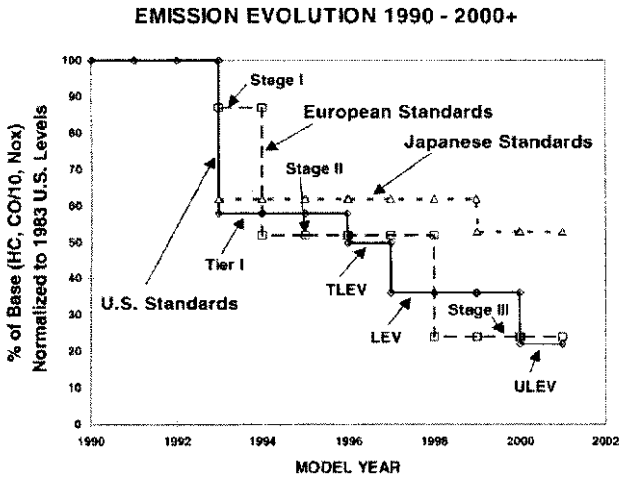
Figure 1-3. European, Japanese and US emission requirements[1]

1.5.1   Hybrid electric vehicles

A hybrid electric vehicle (HEV) includes both a conventional internal combustion engine (ICE) and an electric motor in an effort to combine the advantages of both systems. It aims to obtain significantly extended range compared to an electric vehicle, while mitigating the effect of emissions and improving fuel economy compared to a conventional ICE powertrain.

The powertrain in a HEV can be a parallel, a series, or a power-split hybrid powertrain. In a typical **parallel hybrid**, the gas engine and the electric motor both connect to the transmission independently. As a result, in a parallel hybrid, both the electric motor and the gas engine can provide propulsion power. By contrast, in a **series hybrid,** the gasoline engine turns a generator, and the generator can either charge the batteries or power an electric motor that drives the transmission. Thus, the gasoline engine never directly powers the vehicle.

HEVs have a combination of diverse components with an array of energy and power levels, as well as dissimiar dynamic properties. This results in a difficult hybrid system control problem (Bowles, et. al., 2000, Saeks, et. al., 2002, Paganelli, et. al., 2001, Schouten, et. al., 2002).

---

[1] Reprinted from Control Engineering Practice, Vol. 8, Powers and Nicastri, "Automotive Vehicle Control Challenges in the 21st Century," pp. 605-618, Copyright (2000), with permission from Elsevier.

Several hybrid cars have been available in the United States since the late 1990s, including the Honda Civic Hybrid, the Honda Insight and the Toyota Prius. Plug-in hybrid electric vehicles such as the Chevrolet Volt and purely electric vehicles such as the Nissan Leaf are being introduced in the market in 2011. Chapter 16 in the second edition of this book provides an in-depth overview of control system design for energy management in hybrid electric vehicles.

1.5.2   Fuel cell vehicles

There has been significant research conducted around the globe for the development of fuel cell vehicles. A fuel cell vehicle (FCV) has a fuel cell stack fueled by hydrogen which serves as the major source of electric power for the vehicle. Electric power is produced by a electrochemical reaction between hydrogen and oxygen, with water vapor being the only emission from the reaction.

The simplest configuration in a FCV involves supplying hydrogen directly from a hydrogen tank in which hydrogen is stored as a compressed gas or a cryogenic liquid. To avoid the difficulties of hydrogen storage and the corresponding required infrastructure, a fuel processor using methanol or gasoline as a fuel can be incorporated to produce a hydrogen-rich gas stream on board. To compensate for the slow start-up and transient responses of the fuel processor, and to take advantage of regenerative power at braking, a battery may be used at additional cost, weight and complexity. Several prototype fuel cell powered cars and buses are available in North America, Japan and Europe with and without fuel processors.

An FCV with fuel processor on board still requires several major technical advances for practical vehicle applications. Component and subsystem level technologies for FCV development have been demonstrated. The next important step for vehicle realization is integrating these into a constrained vehicle environment and developing coordinated control systems for the overall powertrain system (Pukrushpan, et. al., 2004).

REFERENCES

Ashhab, M.-S, S., Stefanopoulou, A.G., Cook, J.A., Levin, M.B., "Control-Oriented Model for Camless Intake Process (Part I)," *ASME Journal of Dynamic Systems, Measurement, and Control*, Vol 122, pp. 122-130, March 2000 .

Ashhab, M.-S, S., Stefanopoulou, A.G., Cook, J.A., Levin, M.B., "Control of Camless Intake Process (Part II)," *ASME Journal of Dynamic Systems, Measurement, and Control*, Vol 122, pp. 131-139, March 2000.

Bowles, P., Peng, H. and Zhang, X, "Energy management in a parallel hybrid electric vehicle with a continuously variable transmission," *Proceedings of the American Control Conference,* Vol. 1, IEEE, Piscataway, NJ, USA,00CB36334. p 55-59, 2000.

Das, L M. and Mathur, R., "Exhaust gas recirculation for NOx control in a multicylinder hydrogen-supplemented S.I. engine," *International Journal of Hydrogen Energy*, Vol. 18, No. 12, pp. 1013-1018, Dec 1993.

Eisele, D. D. and Peng, H., "Vehicle Dynamics Control with Rollover Prevention for Articulated Heavy Trucks," *Proceedings of AVEC 2000*, 5th International Symposium on Advanced Vehicle Control, August 22-24, Ann Arbor, Michigan, 2000.

Jones, W.D. (2002), "Building Safer Cars," *IEEE Spectrum,* January 2002, pp 82-85.

Gohl, J., Rajamani, R., Alexander, L. and Starr, P., "Active Roll Mode Control Implementation on a Narrow Tilting Vehicle," *Vehicle System Dynamics*, Vol. 42, No. 5, pp. 347-372, 2004.

Guzzella, L. Amstutz, A., "Control of diesel engines," *IEEE Control Systems Magazine,* Vol. 18, No. 5, pp. 53-71, October 1998.

Hedrick, J K. Tomizuka, M. Varaiya, P, "Control Issues in Automated Highway Systems," *IEEE Control Systems Magazine. v 14 n 6, . p 21-32 , Dec 1994*

Hibbard, R. and Karnopp, D., "Twenty-First Century Transportation System Solutions – a New Type of Small, Relatively Tall and Narrow Tilting Commuter Vehicle," *Vehicle System Dynamics*, Vol. 25, pp. 321-347, 1996.

Hrovat, D., "Survey of Advanced Suspension Developments and Related Optimal Control Applications," *Automatica*, Vol. 33, No. 10, pp. 1781-1817, October 1997.

Kidane, S., Rajamani, R., Alexander, L., Starr, P.J. and Donath, M., "Development and Experimental Evaluation of a Tilt Stability Control System for Narrow Commuter Vehicles," *IEEE Transactions on Control Systems Technology*, Vol. 18, No. 6, pp. 1266-1279, 2010.

Kolmanovsky, I. Stefanopoulou, A G. Powell, B K., "Improving turbocharged **diesel** engine operation with turbo power assist system," *Proceedings of the IEEE Conference on Control Applications*, Vol. 1, pp. 454-459, 1999.

Lewis, A.S. and El-Gindy, M., "Sliding mode control for rollover prevention of heavy vehicles based on lateral acceleration," International Journal of Heavy Vehicle Systems, Vol. 10, No. 1/2, pp. 9-34, 2003.

Liang, C.Y. and Peng, H., "Design and simulations of a traffic-friendly adaptive cruise control algorithm," *Dynamic Systems and Control Division*, American Society of Mechanical Engineers, DSC, Vol. 64*,* ASME, Fairfield, NJ, USA. Pp. 713-719, 1998.

Liang, C.Y. and Peng, H**., "**Optimal adaptive cruise control with guaranteed string stability," *Vehicle System Dynamics*, Vol. 32, No. 4, pp. 313-330, 1999.

NHTSA, "Traffic Safety Facts – Highlights of 2009 Motor Vehicle Crashes," *National Highway Traffic Safety Administration Report*, DOT HS 811 363, August 2010.

NHTSA, Fatality Analysis Reporting System, Web-Based Encyclopedia, www-fars/nhtsa.gov

Paganelli, G. Tateno, M. Brahma, A. Rizzoni, G. Guezennec, Y., "Control development for a hybrid-electric sport-utility vehicle: Strategy, implementation and field test results," *Proceedings of the American Control Conference*, Vol. 6, p 5064-5069 (IEEE cat n 01CH37148), 2001.

Powers, W.F. and Nicastri, P.R., (2000) "Automotive Vehicle Control Challenges in the 21st Century," *Control Engineering Practice*, Vol. 8, pp. 605-618.

Pukrushpan, J.T., Stefanopoulou, A.G. and Peng, H, *Control of Fuel Cell Power Systems: Principles, Modeling, Analysis, and Feedback Design*, Springer-Verlag, London, ISBN 1-85233-816, 2004.

Rajamani, R., Gohl, J., Alexander, L. and Starr, P., "Dynamics of Narrow Tilting Vehicles," *Mathematical and Computer Modeling of Dynamical Systems*, Vol. 9, No. 2, pp. 209-231, 2003.

Rajamani, R and Zhu, C., "Semi-Autonomous Adaptive Cruise Control", *IEEE Transactions on Vehicular Technology*, Vol. 51, No. 5, pp. 1186-1192, September 2002.

Rajamani, R., Tan, H.S., Law, B. and Zhang, W.B., "Demonstration of Integrated Lateral and Longitudinal Control for the Operation of Automated Vehicles in Platoons," *IEEE Transactions on Control Systems Technology*, Vol. 8, No. 4, pp. 695-708, July 2000.

Saeks, R., Cox, C.J., Neidhoefer, J., Mays, P.R. and Murray, J.J., "Adaptive Control of a Hybrid Electric Vehicle," *IEEE Transactions on Intelligent Transportation Systems,* Vol. 3, No. 4, pp. 213-234, December 2002.

Santhanakrishnan, K. and Rajamani, R., "On Spacing Policies for Highway Vehicle Automation," *IEEE Transactions on Intelligent Transportation Systems*, Vol. 4, No. 4, pp. 198-204, December 2003.

Schouten, Niels J. Salman, Mutasim A. Kheir, Naim A., "Fuzzy logic control for parallel hybrid vehicles," *IEEE Transactions on Control Systems Technology*, Vol. 10, No. 3, pp. 460-468. May 2002.

Swaroop, D. and Rajagopal, K.R., "Intelligent Cruise Control Systems and Traffic Flow Stability," *Transportation Research Part C : Emerging Technologies*, Vol. 7, No. 6, pp. 329-352, 1999.

Swaroop D. Swaroop, R. Huandra, "Design of an ICC system based on a traffic flow specification," *Vehicle System Dynamics Journal*, Vol. 30, no. 5, pp. 319-44, 1998.

Stefanopoulou, A.G., Kolmanovsky, I. and Freudenberg, J.S., "Control of variable geometry turbocharged diesel engines for reduced emissions," *IEEE Transactions on Control Systems Technology*, Vol. 8, No. 4, pp. 733-745, July 2000.

Stefanopoulou, A.G. and Kolmanovsky, I., "Analysis and Control of Transient Torque Response in Engines with Inernal Exhaust Gas Recirculation," *IEEE Transactions on Control System Technology*, Vol.7, No.5, pp.555-566, September 1999.

Strassberger, M. and Guldner, J., "BMW's Dynamic Drive: An Active Stabilizer Bar Systems," *IEEE Control Systems Magazine*, pp. 28-29, 107, August 2004.

Texas Transportation Institute, "Urban Mobility Report 2010," http://mobility.tamu.edu, December 2010.

United States Department of Transportation, NHTSA, FARS and GES, "Fatal Accident Reporting System (FARS) and General Estimates System (GES)," 1992.

Varaiya, Pravin, "Smart Cars on Smart Roads: Problems of Control," *IEEE Transactions on Automatic Control*, Vol. 38, No. 2, pp. 195-207, Feb 1993.

Wang, J. and Rajamani, R., "Should Adaptive Cruise Control Systems be Designed to Maintain a Constant Time Gap Between Vehicles?", *Proceedings of the Dynamic Systems and Control Division*, ASME International Mechanical Engineering Congress and Exposition, 2001.

Wright, P.G. and Williams, D.A., "The application of active suspension to high performance road vehicles," Microprocessors in Fluid Engineering, *Institute of Mechanical Engineers Conference*, 1984.

Chapter 2

LATERAL VEHICLE DYNAMICS

The first section in this chapter provides a review of several types of lateral control systems that are currently under development by automotive manufacturers and researchers. The subsequent sections in the chapter study kinematic and dynamic models for lateral vehicle motion. Control system design for lateral vehicle applications is studied later in Chapter 3.

2.1   LATERAL SYSTEMS UNDER COMMERCIAL DEVELOPMENT

Lane departures are the number one cause of fatal accidents in the United States, and account for more than 39% of crash-related fatalities. Reports by the National Highway Transportation Safety Administration (NHTSA) state that as many as 1,575,000 accidents annually are caused by distracted drivers - a large percentage of which can be attributed to unintended lane departures. Lane departures are also identified by NHTSA as a major cause of rollover incidents involving sport utility vehicles (SUVs) and light trucks (http://www.nhtsa.gov).

Three types of lateral systems have been developed in the automotive industry that address lane departure accidents: lane departure warning systems (LDWS), lane keeping systems (LKS) and yaw stability control systems. A significant amount of research is also being conducted by university researchers on these types of systems.

2.1.1   Lane departure warning

A lane departure warning (LDW) system is a system that monitors the vehicle's position with respect to the lane and provides warning if the vehicle is about to leave the lane. An example of a commercial LDW system under development is the AutoVue LDW system by Iteris, Inc. shown in Figure 2-1.
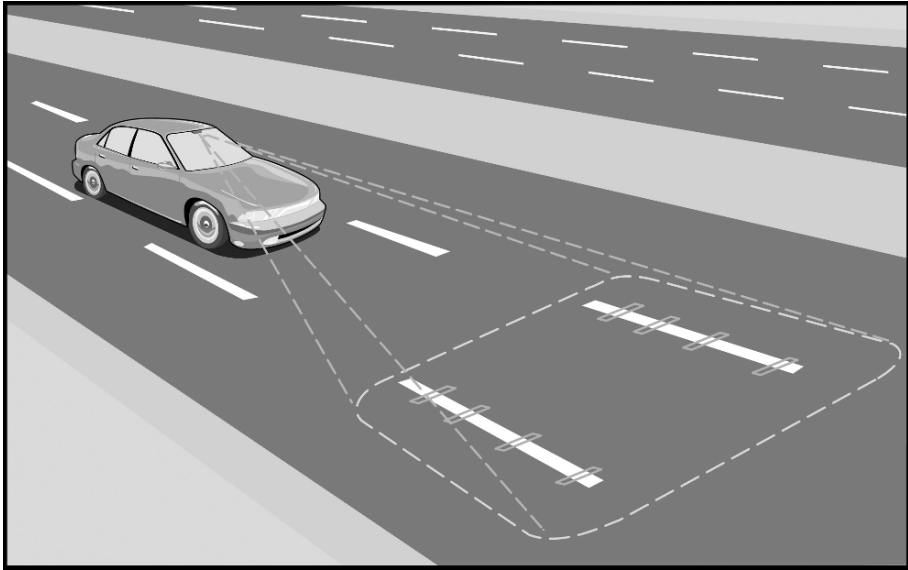
Figure 2-1. LDW system based on lane markings[1]

The AutoVue device is a small, integrated unit consisting of a camera, onboard computer and software that attaches to the windshield, dashboard or overhead. The system is programmed to recognize the difference between the road and lane markings. The unit's camera tracks visible lane markings and feeds the information into the unit's computer, which combines this data with the vehicle's speed. Using image recognition software and proprietary algorithms, the computer can predict when a vehicle begins to drift towards an unintended lane change. When this occurs, the unit automatically emits the commonly known rumble strip sound, alerting the driver to make a correction.

AutoVue is publicized as working effectively both during day and night, and in most weather conditions where the lane markings are visible. By

---

[1] Figure courtesy of Iteris, Inc.

simply using the turn signal, a driver indicates to the system that a planned lane departure is intended and the alarm does not sound.

Lane departure warning systems made by Iteris are now in use on trucks manufactured by Mercedes and Freightliner. Iteris' chief competitor, *AssistWare*, has also had success in the heavy truck market: their *SafeTrac* system is now available as a factory option on *Kenworth* trucks and via direct sales to commercial fleets (http://www.assistware.com).

2.1.2 Lane keeping systems

A lane-keeping system automatically controls the steering to keep the vehicle in its lane and also follow the lane as it curves around. Over the last ten years, several research groups at universities have developed and demonstrated lane keeping systems. Researchers at California PATH demonstrated a lane keeping system based on the use of cylindrical magnets embedded at regular intervals in the center of the highway lane. The magnetic field from the embedded permanent magnets was used for lateral position measurement of the vehicle (Guldner, et. al., 1996). Research groups at Berkeley (Taylor, et. al., 1999) and at Carnegie Mellon (Thorpe, et. al., 1998) have developed lateral position measurement systems using vision cameras and demonstrated lateral control systems using vision based measurement. Researchers at the University of Minnesota have developed lane departure warning and lane keeping systems based on the use of differential GPS for lateral position measurements (Donath, et. al., 1997).

Systems are also under development by several automotive manufacturers, including Nissan. A lane-keeping system called LKS, which has recently been introduced in Japan on Nissan's *Cima* model, offers automatic steering in parallel with the driver (http://ivsource.net). Seeking to strike a balance between system complexity and driver responsibility, the system is targeted at 'monotonous driving' situations. The system operates only on 'straight-ish' roads (a minimum radius will eventually be specified) and above a minimum defined speed. Nissan's premise is that drivers feel tired after long hours of continuous expressway driving as a result of having to constantly steer their vehicles slightly to keep them in their lane. The LKS attempts to reduce such fatigue by improving stability on the straight highway road. But the driver must remain engaged in actively steering the vehicle – if he/she does not, the LKS gradually reduces its degree of assistance. The practical result is that you can't "tune out" and expect the car to drive for you. Nissan's argument is that this approach achieves the difficult balance between providing driver assistance while maintaining driver responsibility. The low level of steering force added by the control isn't enough to interfere with the driver's maneuvers.

The system uses a single CCD camera to recognize the lane demarkation, a steering actuator to steer the front wheels, and an electronic control unit. The camera estimates the road geometry and the host vehicle's position in the lane. Based on this information, along with vehicle velocity and steering wheel angle, the control unit calculates the steering torque needed to keep within the lane.

Nissan is also developing a LDW system called its Lane Departure Avoidance (LDA) system (http://ivsource.net). The LDA system aims to reduce road departure crashes by delaying a driver's deviation from the lane in addition to providing warning through audio signals and steering wheel vibrations. Nissan's LDA creates a lateral "buffer" for the driver, and kicks into action to automatically steer if the vehicle starts to depart the lane. But, unlike a true co-pilot, the system won't continue to handle the steering job – with haptic feedback in the steering wheel, the driver is alerted to the system activation and is expected to re-assert safe control by himself or herself. The automatic steering assist is steadily reduced over a period of several seconds. So, a road departure crash is still possible, but is expected be less likely unless the driver is seriously incapacitated.

LDA is accomplished using the same basic components of LKS: a camera, a steering actuator, an electronic control unit, and a buzzer or other warning devicer.

2.1.3   Yaw stability control systems

Vehicle stability control systems that prevent vehicles from spinning and drifting out have been developed and recently commercialized by several automotive manufacturers. Such stability control systems are also often referred to as yaw control systems or electronic stability control systems.

Figure 2-2 schematically shows the function of a yaw control system. In this figure, the lower curve shows the trajectory that the vehicle would follow in response to a steering input from the driver if the road were dry and had a high tire-road friction coefficient. In this case the high friction coefficient is able to provide the lateral force required by the vehicle to negotiate the curved road. If the coefficient of friction were small or if the vehicle speed were too high, then the vehicle would be unable to follow the nominal motion required by the driver – it would instead travel on a trajectory of larger radius (smaller curvature), as shown in the upper curve of Figure 2-2. The function of the yaw control system is to restore the yaw velocity of the vehicle as much as possible to the nominal motion expected by the driver. If the friction coefficient is very small, it might not be possible to entirely achieve the nominal yaw rate motion that would be achieved by

the driver on a high friction coefficient road surface. In this case, the yaw control system would partially succeed by making the vehicle's yaw rate closer to the expected nominal yaw rate, as shown by the middle curve in Figure 2-2.
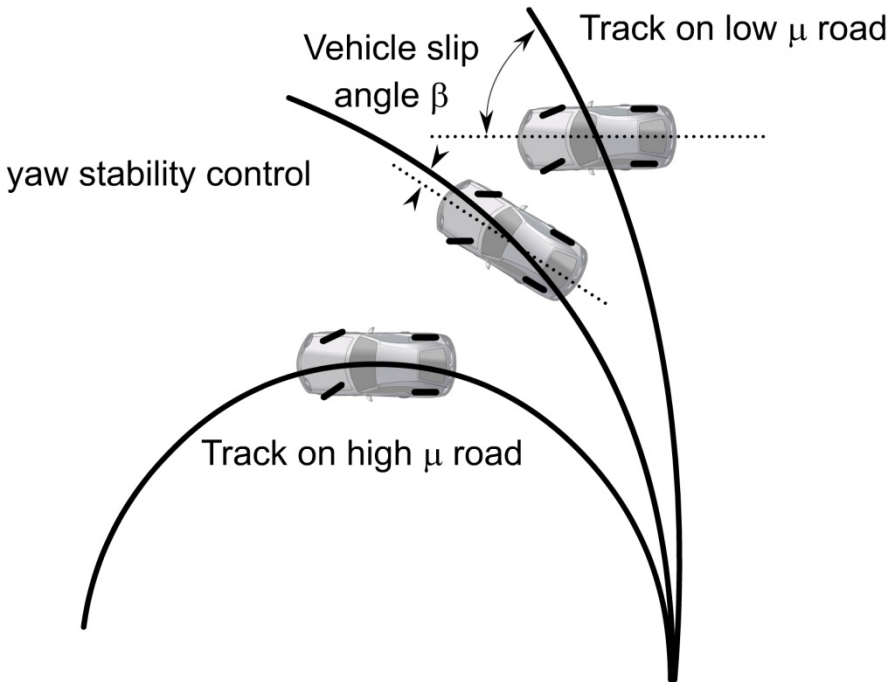
Figure 2-2. The functioning of a yaw control system

Many companies have investigated and developed yaw control systems during the last ten years through simulations and on prototype experimental vehicles. Some of these yaw control systems have also been commercialized on production vehicles. Examples include the BMW DSC3 (Leffler, et. al., 1998) and the Mercedes ESP, which were introduced in 1995, the Cadillac Stabilitrak system (Jost, 1996) introduced in 1996 and the Chevrolet C5 Corvette Active Handling system in 1997 (Hoffman, et.al., 1998).

Three types of stability control systems have been proposed and developed for yaw control:

Differential Braking systems which utilize the ABS brake system on the vehicle to apply differential braking between the right and left wheels to control yaw moment.

Steer-by-Wire systems which modify the driver's steering angle input and add a correction steering angle to the wheels

Active Torque Distribution systems which utilize active differentials and all wheel drive technology to independently control the drive torque distributed to each wheel and thus provide active control of both traction and yaw moment.

By large, the differential braking systems have received the most attention from researchers and have been implemented on several production vehicles. Steer-by-wire systems have received attention from academic researchers (Ackermann, 1994, Ackermann, 1997). Active torque distribution systems have received attention in the recent past and are likely to become available on production cars in the future.

Differential braking systems are the major focus of coverage in this book. They are discussed in section 8.2. Steer-by-wire systems are discussed in section 8.3 and active torque distribution systems are discussed in section 8.4.

2.2   KINEMATIC MODEL OF LATERAL VEHICLE MOTION

Under certain assumptions described below, a kinematic model for the lateral motion of a vehicle can be developed. Such a model provides a mathematical description of the vehicle motion without considering the forces that affect the motion. The equations of motion are based purely on geometric relationships governing the system.

Consider a bicycle model of the vehicle as shown in Figure 2-3 (Wang and Qi, 2001). In the bicycle model, the two left and right front wheels are represented by one single wheel at point A. Similarly the rear wheels are represented by one central rear wheel at point B. The steering angles for the front and rear wheels are represented by δ_f and δ_r respectively. The model is derived assuming both front and rear wheels can be steered. For front-wheel-only steering, the rear steering angle δ_r can be set to zero. The center of gravity (c.g.) of the vehicle is at point C. The distances of points A and B from the c.g. of the vehicle are ℓ_f and ℓ_r respectively. The wheelbase of the vehicle is $L = \ell_f + \ell_r$.

The vehicle is assumed to have planar motion. Three coordinates are required to describe the motion of the vehicle: X , Y and ψ . (X, Y) are inertial coordinates of the location of the c.g. of the vehicle while ψ describes the orientation of the vehicle. The velocity at the c.g. of the vehicle is denoted by V and makes an angle β with the longitudinal axis of the vehicle. The angle β is called the slip angle of the vehicle.
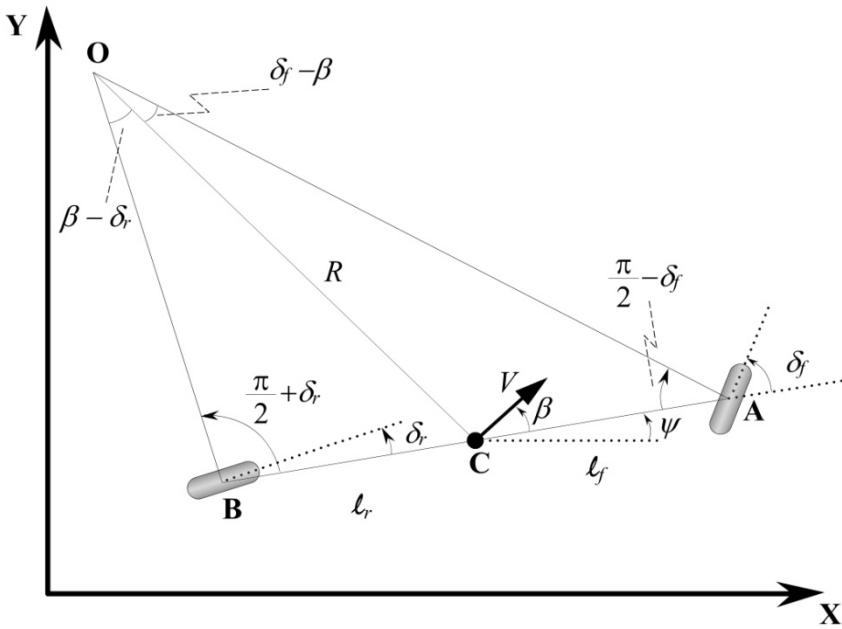
Figure 2-3. Kinematics of lateral vehicle motion

Assumptions

The major assumption used in the development of the kinematic model is that the velocity vectors at points A and B are in the direction of the orientation of the front and rear wheels respectively. In other words, the velocity vector at the front wheel makes an angle δ_f with the longitudinal axis of the vehicle. Likewise, the velocity vector at the rear wheel makes an angle δ_r with the longitudinal axis of the vehicle. This is equivalent to assuming that the "slip angles" at both wheels are zero. This is a reasonable assumption for low speed motion of the vehicle (for example, for speeds less than 5 m/s). At low speeds, the lateral force generated by the tires is small. In order to drive on any circular road of radius R, the total lateral force from both tires is

$$\frac{mV^2}{R}$$

which varies quadratically with the speed V and is small at low speeds. When the lateral forces are small, as explained later in section 2.4, it is indeed very reasonable to assume that the velocity vector at each wheel is in the direction of the wheel.

The point O is the instantaneous rolling center for the vehicle. The point O is defined by the intersection of lines AO and BO which are drawn perpendicular to the orientation of the two rolling wheels.

The radius of the vehicle's path R is defined by the length of the line OC which connects the center of gravity C to the instantaneous rolling center O. The velocity at the c.g. is perpendicular to the line OC. The direction of the velocity at the c.g. with respect to the longitudinal axis of the vehicle is called the slip angle of the vehicle β.

The angle ψ is called the heading angle of the vehicle. The course angle for the vehicle is $\gamma = \psi + \beta$.

Apply the sine rule to triangle OCA.

$$\frac{\sin(\delta_f - \beta)}{\ell_f} = \frac{\sin\left(\dfrac{\pi}{2} - \delta_f\right)}{R} \tag{2.1}$$

Apply the sine rule to triangle OCB.

$$\frac{\sin(\beta - \delta_r)}{\ell_r} = \frac{\sin\left(\dfrac{\pi}{2} + \delta_r\right)}{R} \tag{2.2}$$

From Eq. (2.1)

$$\frac{\sin(\delta_f)\cos(\beta) - \sin(\beta)\cos(\delta_f)}{\ell_f} = \frac{\cos(\delta_f)}{R} \tag{2.3}$$

From Eq. (2.2)

$$\frac{\cos(\delta_r)\sin(\beta) - \cos(\beta)\sin(\delta_r)}{\ell_r} = \frac{\cos(\delta_r)}{R} \tag{2.4}$$

Multiply both sides of Eq. (2.3) by $\dfrac{\ell_f}{\cos(\delta_f)}$. We get

$$\tan(\delta_f)\cos(\beta) - \sin(\beta) = \frac{\ell_f}{R} \tag{2.5}$$

Multiply both sides of Eq. (2.4) by $\dfrac{\ell_r}{\cos(\delta_r)}$. We get

$$\sin(\beta) - \tan(\delta_r)\cos(\beta) = \frac{\ell_r}{R} \tag{2.6}$$

Adding Eqs. (2.5) and (2.6)

$$\{\tan(\delta_f) - \tan(\delta_r)\}\cos(\beta) = \frac{\ell_f + \ell_r}{R} \tag{2.7}$$

If we assume that the radius of the vehicle path changes slowly due to low vehicle speed, then the rate of change of orientation of the vehicle (i.e. $\dot{\psi}$) must be equal to the angular velocity of the vehicle. Since the angular velocity of the vehicle is $\dfrac{V}{R}$, it follows that

$$\dot{\psi} = \frac{V}{R} \tag{2.8}$$

Using Eq. (2.8), Eq. (2.7) can be re-written as

$$\dot{\psi} = \frac{V\cos(\beta)}{\ell_f + \ell_r}\left(\tan(\delta_f) - \tan(\delta_r)\right) \tag{2.9}$$

The overall equations of motion are therefore given by

$$\dot{X} = V\cos(\psi + \beta) \tag{2.10}$$

$$\dot{Y} = V\sin(\psi + \beta) \tag{2.11}$$

$$\dot{\psi} = \frac{V\cos(\beta)}{\ell_f + \ell_r}\left(\tan(\delta_f) - \tan(\delta_r)\right) \tag{2.12}$$

In this model there are three inputs: δ_f, δ_r and V. The velocity V is an external variable and can be assumed to be a time varying function or can be obtained from a longitudinal vehicle model.

The slip angle β can be obtained by multiplying Eq. (2.5) by ℓ_r and subtracting it from Eq. (2.6) multiplied by ℓ_f :

$$\beta = \tan^{-1}\left(\frac{\ell_f \tan \delta_r + \ell_r \tan \delta_f}{\ell_f + \ell_r}\right) \tag{2.13}$$

Remark

Here it is appropriate to include a note on the "bicycle" model assumption. Both the left and right front wheels were represented by one front wheel in the bicycle model. It should be noted that the left and right steering angles in general will be approximately equal, but not exactly so. This is because the radius of the path each of these wheels travels is different. Consider a front wheel steered vehicle as shown in Figure 2-4.
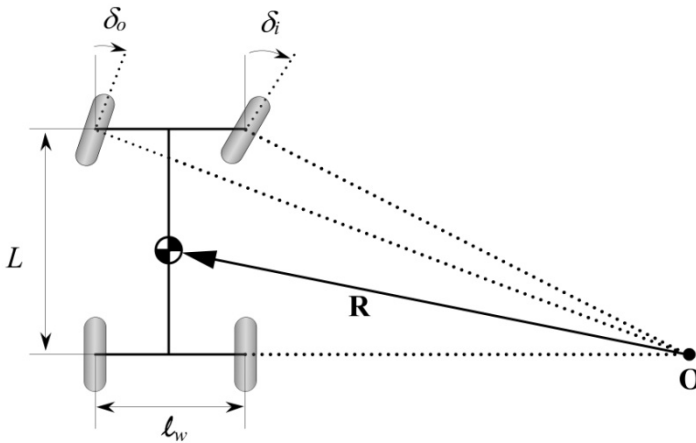
Figure 2-4. Ackerman turning geometry

Let ℓ_w be the track width of the vehicle and δ_o and δ_i be the outer and inner steering angles respectively. Let the wheelbase $L = \ell_f + \ell_r$ be small compared to the radius R. If the slip angle β is small, then Eq. (2.12) can be approximated by

$$\frac{\dot{\psi}}{V} \approx \frac{1}{R} = \frac{\delta}{L}$$

or

$$\delta = \frac{L}{R} \tag{2.14}$$

Since the radius at the inner and outer wheels are different, we have

$$\delta_o = \frac{L}{R + \dfrac{\ell_w}{2}} \tag{2.15}$$

$$\delta_i = \frac{L}{R - \dfrac{\ell_w}{2}} \tag{2.16}$$

The average front wheel steering angle is approximately given by

$$\delta = \frac{\delta_o + \delta_i}{2} \cong \frac{L}{R} \tag{2.17}$$

The difference between δ_o and δ_i is

$$\delta_i - \delta_o = \frac{L}{R^2}\ell_w = \delta^2\frac{\ell_w}{L} \tag{2.18}$$

Thus the difference in the steering angles of the two front wheels is proportional to the square of the average steering angle. Such a differential steer can be obtained from a trapezoidal tie rod arrangement, as shown in Figure 2-5. As can be seen from the figure, for both left and right turns, the inner wheel always turns a larger steering angle.
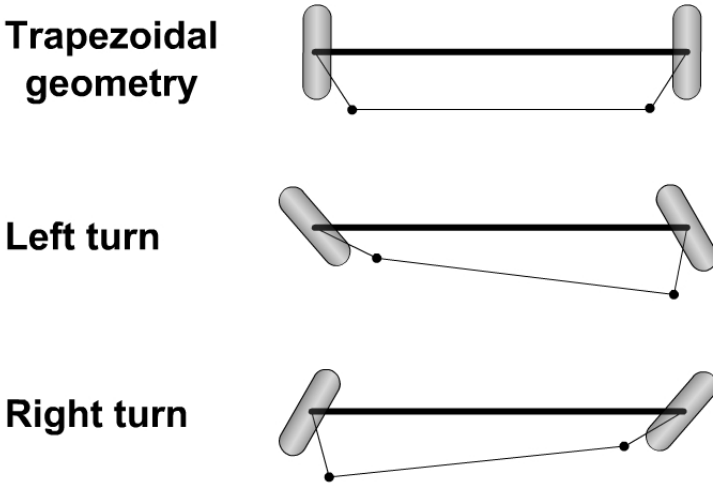
Figure 2-5. Differential steer from a trapezoidal tie-rod arrangement

Table 2.1 Summary of kinematic model equations

SUMMARY OF KINEMATIC MODEL EQUATIONS		
Symbol	Nomenclature	Equation
X	Global X axis coordinate	$\dot{X} = V\cos(\psi + \beta)$
Y	Global Y axis coordinate	$\dot{Y} = V\sin(\psi + \beta)$
ψ	Yaw angle; orientation angle of vehicle with respect to global X axis	$\dot{\psi} = \dfrac{V\cos(\beta)}{\ell_f + \ell_r}\left(\tan(\delta_f) - \tan(\delta_r)\right)$
β	Vehicle slip angle	$\beta = \tan^{-1}\left(\dfrac{\ell_f \tan\delta_r + \ell_r \tan\delta_f}{\ell_f + \ell_r}\right)$

2.3 BICYCLE MODEL OF LATERAL VEHICLE DYNAMICS

At higher vehicle speeds, the assumption that the velocity at each wheel is in the direction of the wheel can no longer be made. In this case, instead of a kinematic model, a dynamic model for lateral vehicle motion must be developed.

A "bicycle" model of the vehicle with two degrees of freedom is considered, as shown in Figure 2-6. The two degrees of freedom are represented by the vehicle lateral position y and the vehicle yaw angle ψ. The vehicle lateral position is measured along the lateral axis of the vehicle to the point O which is the center of rotation of the vehicle. The vehicle yaw angle ψ is measured with respect to the global X axis. The longitudinal velocity of the vehicle at the c.g. is denoted by V_x.
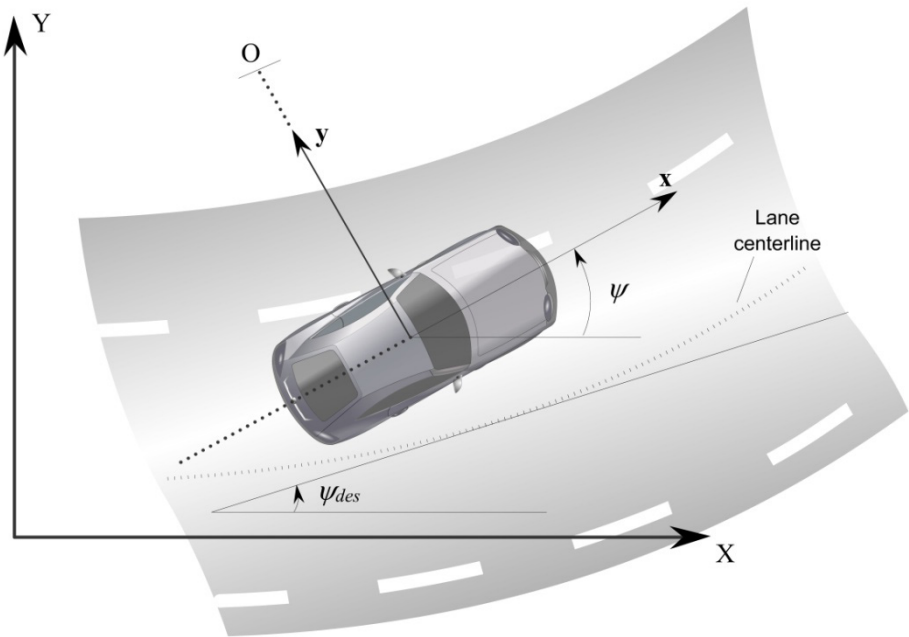
Figure 2-6. Lateral vehicle dynamics

The influence of road bank angle will be considered later. Ignoring road bank angle for now and applying Newton's second law for motion along the y axis (Guldner, et. al., 1996),

$$ma_y = F_{yf} + F_{yr} \tag{2.19}$$

where $a_y = \left(\dfrac{d^2 y}{dt^2}\right)_{inertial}$ is the inertial acceleration of the vehicle at the

c.g. in the direction of the y axis and F_{yf} and F_{yr} are the lateral tire forces of the front and rear wheels respectively. Two terms contribute to a_y: the acceleration $\ddot{y}$ which is due to motion along the y axis and the centripetal acceleration $V_x \dot{\psi}$. Hence

$$a_y = \ddot{y} + V_x \dot{\psi} \tag{2.20}$$

Substituting from Eq. (2.20) into Eq. (2.19), the equation for the lateral translational motion of the vehicle is obtained as

$$m(\ddot{y} + \dot{\psi} V_x) = F_{yf} + F_{yr} \tag{2.21}$$

Moment balance about the z axis yields the equation for the yaw dynamics as

$$I_z \ddot{\psi} = \ell_f F_{yf} - \ell_r F_{yr} \tag{2.22}$$

where ℓ_f and ℓ_r are the distances of the front tire and the rear tire respectively from the c.g. of the vehicle.

The next step is to model the lateral tire forces F_{yf} and F_{yr} that act on the vehicle. Experimental results show that the lateral tire force of a tire is proportional to the "slip-angle" for small slip-angles. The slip angle of a tire is defined as the angle between the orientation of the tire and the orientation of the velocity vector of the wheel (see Figure 2-7). In Figure 2-7, the slip angle of the front wheel is

$$\alpha_f = \delta - \theta_{Vf} \tag{2.23}$$

where θ_{vf} is the angle that the velocity vector makes with the longitudinal axis of the vehicle and δ is the front wheel steering angle. The rear slip angle is similarly given by

$$\alpha_r = -\theta_{Vr} \tag{2.24}$$

A physical explanation of why the lateral tire force is proportional to slip angle can be found in Chapter 13 (in section 13.4).
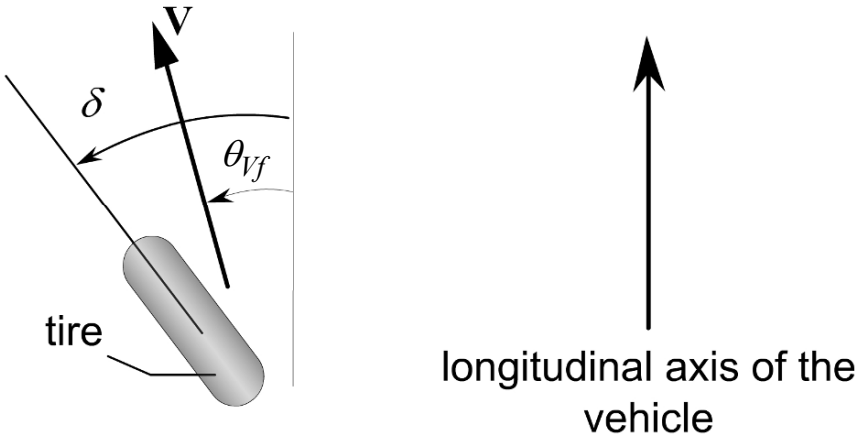
Figure 2-7. Tire slip-angle

The lateral tire force for the front wheels of the vehicle can therefore be written as

$$F_{yf} = 2C_{\alpha f}\left(\delta - \theta_{Vf}\right) \tag{2.25}$$

where the proportionality constant $C_{\alpha f}$ is called the cornering stiffness of each front tire, δ is the front wheel steering angle and θ_{Vf} is the front tire velocity angle. The factor 2 accounts for the fact that there are two front wheels.

Similarly the lateral tire for the rear wheels can be written as

$$F_{yr} = 2C_{\alpha r}\left(-\theta_{Vr}\right) \tag{2.26}$$

where $C_{\alpha r}$ is the cornering stiffness of each rear tire and θ_{Vr} is the rear tire velocity angle.

The following relations can be used to calculate θ_{Vf} and θ_{Vr}:

$$\tan\left(\theta_{Vf}\right) = \frac{V_y + \ell_f\dot{\psi}}{V_x} \tag{2.27}$$

$$\tan\left(\theta_{Vr}\right) = \frac{V_y - \ell_r\dot{\psi}}{V_x} \tag{2.28}$$

Using small angle approximations and using the notation $V_y = \dot{y}$,

$$\theta_{Vf} = \frac{\dot{y} + \ell_f \dot{\psi}}{V_x} \tag{2.29}$$

$$\theta_{Vr} = \frac{\dot{y} - \ell_r \dot{\psi}}{V_x} \tag{2.30}$$

Substituting from Eqs. (2.23), (2.24), (2.29) and (2.30) into Eqs. (2.21) and (2.22), the state space model can be written as

$$\frac{d}{dt}\begin{Bmatrix} y \\ \dot{y} \\ \psi \\ \dot{\psi} \end{Bmatrix} = \begin{bmatrix} 0 & 1 & 0 & 0 \\ 0 & -\dfrac{2C_{\alpha f} + 2C_{\alpha r}}{mV_x} & 0 & -V_x - \dfrac{2C_{\alpha f}\ell_f - 2C_{\alpha r}\ell_r}{mV_x} \\ 0 & 0 & 0 & 1 \\ 0 & -\dfrac{2\ell_f C_{\alpha f} - 2\ell_r C_{\alpha r}}{I_z V_x} & 0 & -\dfrac{2\ell_f^2 C_{\alpha f} + 2\ell_r^2 C_{\alpha r}}{I_z V_x} \end{bmatrix}$$

$$+ \begin{Bmatrix} 0 \\ \dfrac{2C_{\alpha f}}{m} \\ 0 \\ \dfrac{2\ell_f C_{\alpha f}}{I_z} \end{Bmatrix} \delta \tag{2.31}$$

Consideration of road bank angle

If the influence of road bank angles is included, then Eq. (2.21) can be rewritten as

$$m(\ddot{y} + \dot{\psi}V_x) = F_{yf} + F_{yr} + F_{bank} \tag{2.32}$$

where $F_{bank} = mg\sin(\phi)$ and ϕ is the road bank angle with sign convention as shown in .

The yaw dynamics of the vehicle are not affected by road bank angle. Hence Eq. (2.22) remains the same even in the presence of a bank angle.
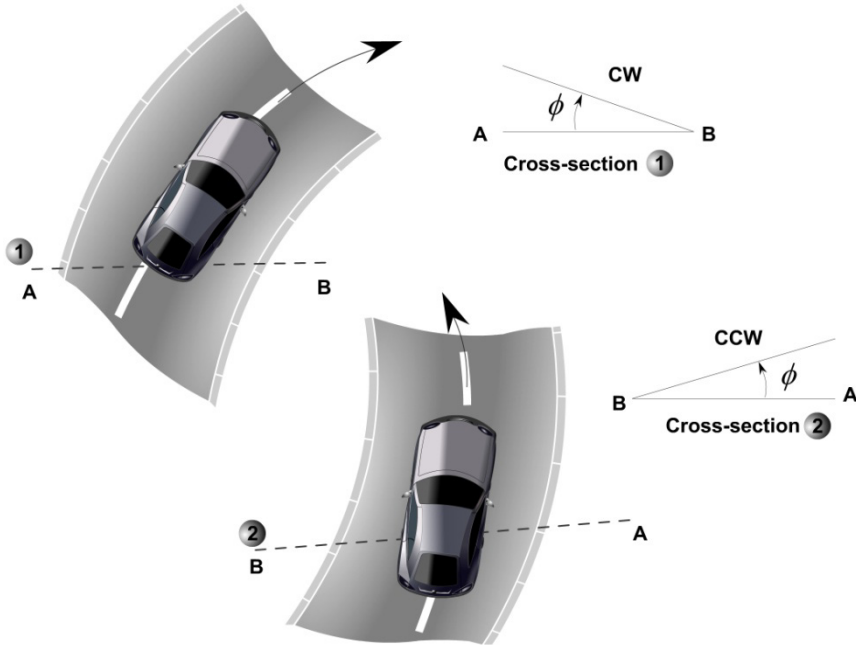
Figure 2-8. Sign convention for bank angle

Comment on lateral tire forces at larger slip angles

The assumption that the lateral tire force is proportional to slip angle will not hold at large slip angles. In such cases, the lateral tire force will depend on slip angle, the normal tire load F_z, the tire-road friction coefficient μ and also the magnitude of longitudinal tire force that is being simultaneously generated. For a more complete lateral tire model that includes the influence of all these variables, see chapter 13 of this book. At large slip angles, the tire model will no longer be linear.

2.4   MOTION OF A PARTICLE RELATIVE TO A ROTATING FRAME

This section describes the relation between acceleration in body fixed coordinates and acceleration in inertial coordinates for a general rotating rigid body. This formulation can be used to obtain inertial acceleration values of a vehicle with yaw rate, roll and pitch rotational motion. In this section, the formulation is used to obtain inertial acceleration along the lateral axis of a vehicle which has rotational yaw motion.

Consider a rotating body, as shown in Figure 2-9, described in two coordinate systems: a coordinate system fixed in inertial space (XYZ) and a coordinate system fixed to the body (xyz). At the time instant under consideration, assume that both coordinate systems have the same orientation. Let the angular speed of the body be $\vec{\Omega}$.
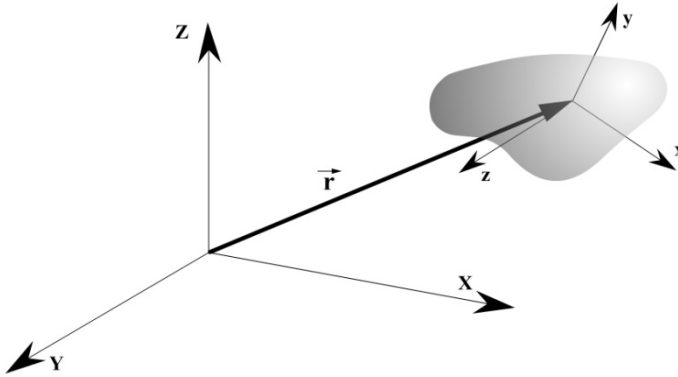
Figure 2-9. Inertial and body-fixed coordinate systems

Consider a particle P with inertial coordinates $\begin{bmatrix} X & Y & Z \end{bmatrix}^T$ and body-fixed coordinates $\begin{bmatrix} x & y & z \end{bmatrix}^T$ located on the body. Let $\vec{r}$ be the vector from the origin of the inertial coordinate system to the point P. The acceleration of this particle in inertial coordinates can be related to its acceleration in body-fixed coordinates as follows (Merriam and Kraige, 1987):

$$\frac{d^2}{dt^2}\begin{Bmatrix} X \\ Y \\ Z \end{Bmatrix} = \frac{d^2}{dt^2}\begin{Bmatrix} x \\ y \\ z \end{Bmatrix} + \vec{\Omega} \times (\vec{\Omega} \times \vec{r}) + \dot{\vec{\Omega}} \times \vec{r} + 2\vec{\Omega} \times \dot{\vec{r}} \qquad (2.33)$$

All the vectors on the right-hand side of the above equation are expressed in body-fixed coordinates.

Apply Eq. (2.33) to the case of the lateral vehicle system shown in Figure 2-10.

Let $\hat{i}, \hat{j}, \hat{k}$ be unit vectors in the direction of the x, y, z axes. We have

$$\vec{\Omega} = \dot{\psi}\,\hat{k} \qquad (2.34)$$

$$\vec{r} = -R\hat{j} \tag{2.35}$$

From Eq. (2.33)

$$\vec{a}_{inertial} = \vec{\Omega} \times (\vec{\Omega} \times \vec{r}) + \dot{\vec{\Omega}} \times \vec{r} + 2\,\vec{\Omega} \times \dot{\vec{r}} + \vec{a}_{body\_fixed}$$

or

$$\vec{a}_{inertial} = \dot{\psi}\hat{k} \times (\dot{\psi}\hat{k} \ \times \ -R\hat{j}) \ + \ \ddot{\psi}\,\hat{k} \ \times \ -R\hat{j} \ + \ 2\,\dot{\psi}\,\hat{k} \ \times \ -\dot{R}\hat{j} + \ddot{x}\,\hat{i} + \ddot{y}\,\hat{j}$$

or

$$\vec{a}_{inertial} = \dot{\psi}^2 R\,\hat{j} + (R\ddot{\psi} + 2\dot{\psi}\dot{R})\,\hat{i} + \ddot{x}\,\hat{i} + \ddot{y}\,\hat{j} \tag{2.36}$$

Hence $a_y = \dot{\psi}^2 R + \ddot{y} = V_x\dot{\psi} + \ddot{y}$.

Hence the inertial acceleration along the y axis is

$$a_y = \ddot{y} + V_x\dot{\psi} \tag{2.37}$$
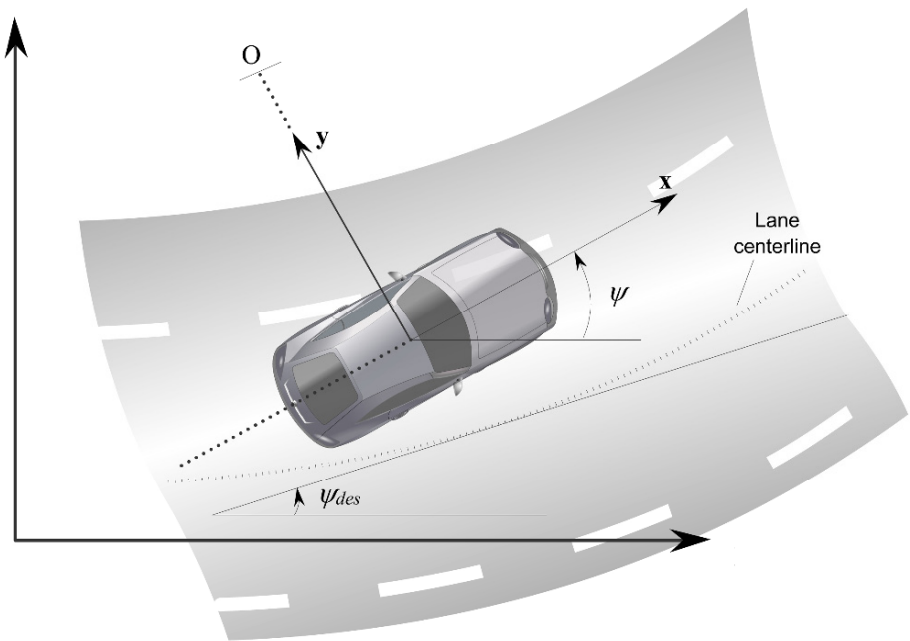
Figure 2-10. The lateral system in terms of rotating coordinates

2.5   DYNAMIC MODEL IN TERMS OF ERROR WITH RESPECT TO ROAD

When the objective is to develop a steering control system for automatic lane keeping, it is useful to utilize a dynamic model in which the state variables are in terms of position and orientation error with respect to the road.

Hence the lateral model developed in section 2.3 will be re-defined in terms of the following error variables:

e_1, the distance of the c.g. of the vehicle from the center line of the lane

e_2, the orientation error of the vehicle with respect to the road.

Consider a vehicle traveling with constant longitudinal velocity V_x on a road of constant radius R. Again, assume that the radius R is large so that the same small angle assumptions as in the previous section can be made. Define the rate of change of the desired orientation of the vehicle as

$$\dot{\psi}_{des} = \frac{V_x}{R} \tag{2.38}$$

The desired acceleration of the vehicle can then be written as

$$\frac{V_x^2}{R} = V_x \dot{\psi}_{des} \tag{2.39}$$

Define $\ddot{e}_1$ and e_2 as follows (Guldner, et. al., 1996):

$$\ddot{e}_1 = (\ddot{y} + V_x\dot{\psi}) - \frac{V_x^2}{R} = \ddot{y} + V_x(\dot{\psi} - \dot{\psi}_{des}) \tag{2.40}$$

and

$$e_2 = \psi - \psi_{des} \tag{2.41}$$

Define

$$\dot{e}_1 = \dot{y} + V_x(\psi - \psi_{des}) \tag{2.42}$$

Eq. (2.42) is consistent with Eq. (2.40) if the velocity V_x is constant. If the velocity were not constant, one would integrate Eq. (2.40) and obtain

$$\dot{e}_1 = \dot{y} + \int V_x e_2 dt$$

This would yield a model that is nonlinear and time varying and would not be useful for control system design. Hence the approach taken is to assume the longitudinal velocity is constant and obtain a LTI model. If the velocity varies, the LTI model is replaced with an LPV model in which longitudinal velocity is a time varying parameter (see section 3.4 in the next chapter).

Substituting from Eqs. (2.41) and (2.42) into (2.21) and (2.22), we find

$$
\begin{aligned}
m\ddot{e}_1 = \dot{e}_1 &\left[-\frac{2}{V_x} C_{\alpha f} - \frac{2}{V_x} C_{\alpha r} \right] + e_2 \left[2C_{\alpha f} + 2C_{\alpha r} \right] \\
&+ \dot{e}_2 \left[-\frac{2C_{\alpha f} \ell_f}{V_x} + \frac{2C_{\alpha r} \ell_r}{V_x} \right] \\
&+ \dot{\psi}_{des} \left[-\frac{2C_{\alpha f} \ell_f}{V_x} + \frac{2C_{\alpha r} \ell_r}{V_x} \right] + 2C_{\alpha f} \delta
\end{aligned}
\tag{2.43}
$$

and

$$
\begin{aligned}
I_z \ddot{e}_2 = 2C_{\alpha f} \ell_1 \delta &+ \dot{e}_1 \left[-\frac{2C_{\alpha f} \ell_f}{V_x} + \frac{2C_{\alpha r} \ell_r}{V_x} \right] \\
&+ e_2 \left[2C_{\alpha f} \ell_f - 2C_{\alpha r} \ell_r \right] + \dot{e}_2 \left[-\frac{2C_{\alpha f} \ell_f^2}{V_x} - \frac{2C_{\alpha r} \ell_r^2}{V_x} \right] \\
&- I_z \ddot{\psi}_{des} + \dot{\psi}_{des} \left[-\frac{2C_{\alpha f} \ell_f^2}{V_x} - \frac{2C_{\alpha r} \ell_r^2}{V_x} \right]
\end{aligned}
\tag{2.44}
$$

The state space model in tracking error variables is therefore given by

$$
\frac{d}{dt}
\begin{bmatrix}
e_1 \\
\dot{e}_1 \\
e_2 \\
\dot{e}_2
\end{bmatrix}
=
$$

$$
\begin{bmatrix}
0 & 1 & 0 & 0 \\
0 & -\dfrac{2C_{\alpha f} + 2C_{\alpha r}}{mV_x} & \dfrac{2C_{\alpha f} + 2C_{\alpha r}}{m} & \dfrac{-2C_{\alpha f}\ell_f + 2C_{\alpha r}\ell_r}{mV_x} \\
0 & 0 & 0 & 1 \\
0 & -\dfrac{2C_{\alpha f}\ell_f - 2C_{\alpha r}\ell_r}{I_z V_x} & \dfrac{2C_{\alpha f}\ell_f - 2C_{\alpha r}\ell_r}{I_z} & -\dfrac{2C_{\alpha f}\ell_f^2 + 2C_{\alpha r}\ell_r^2}{I_z V_x}
\end{bmatrix}
\begin{bmatrix} e_1 \\ \dot{e}_1 \\ e_2 \\ \dot{e}_2 \end{bmatrix}
$$

$$
+ \begin{bmatrix} 0 \\ \dfrac{2C_{\alpha f}}{m} \\ 0 \\ \dfrac{2C_{\alpha f}\ell_f}{I_z} \end{bmatrix} \delta
+ \begin{bmatrix} 0 \\ -\dfrac{2C_{\alpha f}\ell_f - 2C_{\alpha r}\ell_r}{mV_x} - V_x \\ 0 \\ -\dfrac{2C_{\alpha f}\ell_f^2 + 2C_{\alpha r}\ell_r^2}{I_z V_x} \end{bmatrix} \dot{\psi}_{des}
$$

$$(2.45)$$

The tracking objective of the steering control problem can therefore be expressed as a problem of stabilizing the dynamics given by Eq. (2.45). Note that the lateral dynamics model shown above is a function of the longitudinal vehicle speed V_x which has been assumed to be constant.

If the influence of road bank angle is included, then Eq. (2.45) gets rewritten as

$$
\frac{d}{dt} \begin{bmatrix} e_1 \\ \dot{e}_1 \\ e_2 \\ \dot{e}_2 \end{bmatrix}
= \begin{bmatrix} 0 \\ \dfrac{2C_{\alpha f}}{m} \\ 0 \\ \dfrac{2C_{\alpha f}\ell_f}{I_z} \end{bmatrix} \delta
+ \begin{bmatrix} 0 \\ -\dfrac{2C_{\alpha f}\ell_f - 2C_{\alpha r}\ell_r}{mV_x} - V_x \\ 0 \\ -\dfrac{2C_{\alpha f}\ell_f^2 + 2C_{\alpha r}\ell_r^2}{I_z V_x} \end{bmatrix} \dot{\psi}_{des}
+ \begin{bmatrix} 0 \\ g \\ 0 \\ 0 \end{bmatrix} \sin(\phi)
$$

$$
+ \begin{bmatrix}
0 & 1 & 0 & 0 \\
0 & -\dfrac{2C_{\alpha f} + 2C_{\alpha r}}{mV_x} & \dfrac{2C_{\alpha f} + 2C_{\alpha r}}{m} & \dfrac{-2C_{\alpha f}\ell_f + 2C_{\alpha r}\ell_r}{mV_x} \\
0 & 0 & 0 & 1 \\
0 & -\dfrac{2C_{\alpha f}\ell_f - 2C_{\alpha r}\ell_r}{I_z V_x} & \dfrac{2C_{\alpha f}\ell_f - 2C_{\alpha r}\ell_r}{I_z} & -\dfrac{2C_{\alpha f}\ell_f^2 + 2C_{\alpha r}\ell_r^2}{I_z V_x}
\end{bmatrix}
\begin{bmatrix} e_1 \\ \dot{e}_1 \\ e_2 \\ \dot{e}_2 \end{bmatrix}
$$

$$(2.46)$$

Table 2.2 Summary of dynamic model equations in terms of error with respect to road

SUMMARY OF DYNAMIC MODEL EQUATIONS		
Symbol	Nomenclature	Equation
x	State space vector	$x = \begin{bmatrix} e_1 & \dot{e}_1 & e_2 & \dot{e}_2 \end{bmatrix}^T$
		$\dot{x} = Ax + B_1\delta + B_2\dot{\psi}_{des} + B_3\sin(\phi)$
		Matrices A, B_1, B_2 and B_3 are defined in equation (2.46)
e_1	Lateral position error with respect to road	$\ddot{e}_1 = \ddot{y} + V_x\left(\dot{\psi} - \dot{\psi}_{des}\right)$
e_2	Yaw angle error with respect to road	$e_2 = \left(\psi - \psi_{des}\right)$
δ	Front wheel steering angle	
$\dot{\psi}_{des}$	Desired yaw rate determined from road radius R	$\dot{\psi}_{des} = \dfrac{V_x}{R}$
ϕ	Bank angle with sign convention as defined by Fig. 2.8	

2.6 DYNAMIC MODEL IN TERMS OF YAW RATE AND SLIP ANGLE

In Figure 2-11, vehicle sideslip angle β is defined as the angle between the longitudinal axis of the vehicle and the orientation of vehicle velocity vector, and $r \equiv \dot{\psi}$ is the yaw rate of the vehicle body. The lateral dynamics of the vehicle is controlled by the front wheel steering angle δ.
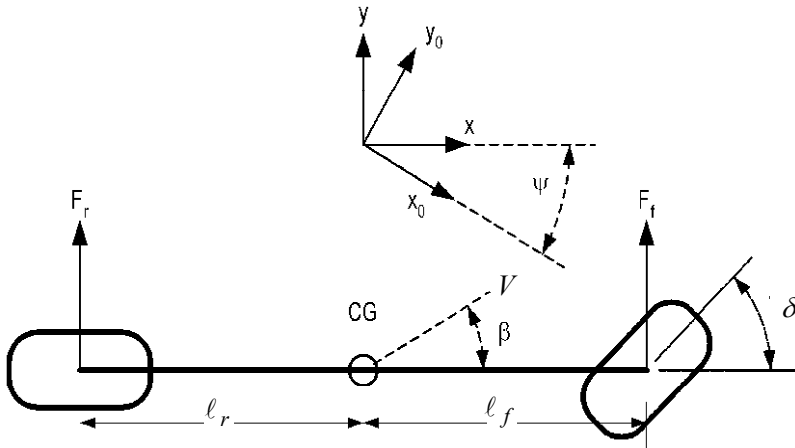
Figure 2-11. Single track model for vehicle lateral dynamics

The body side slip angle can be related to e_1 and e_2 as follows. Under small angle assumptions

$$\beta = \frac{\dot{y}}{V_x} = \frac{1}{V_x}(\dot{e}_1 - V_x e_2) = \frac{1}{V_x}\dot{e}_1 - e_2 \tag{2.47}$$

Using the body side slip angle β and the yaw rate of vehicle body $r \equiv \dot{\psi}$ as state variables, the vehicle lateral dynamics can then be described by the following differential equations (Ackerman, 1997):

$$mV_x\left(\frac{d\beta}{dt} + \dot{\psi}\right) = mV_x\left(\frac{d\beta}{dt} + r\right) = F_{yf} + F_{yr} + F_{bank} \tag{2.48}$$

$$I_z\ddot{\psi} = I_z\dot{r} = \ell_f F_{yf} - \ell_r F_{yr} \tag{2.49}$$

where m is vehicle mass, V_x is vehicle longitudinal velocity, F_{yf}, F_{yr} are front and rear tire forces, respectively, F_{bank} is the force due to road bank angle, I_z is yaw moment of inertia, and ℓ_f, ℓ_r are distances from CG (center of gravity) to front and rear tires, respectively.

For small tire slip angles, the lateral tire forces can be approximated as a linear function of tire slip angle. The front and rear tire forces and tire slip angles are defined as follows:

$$F_{yf} = C_{\alpha f} \alpha_f , \ \alpha_f = \delta - \theta_{vf} = \delta - \beta - \frac{\ell_f r}{V_x} \tag{2.50}$$

$$F_{yr} = C_{\alpha r} \alpha_r , \ \alpha_r = -\theta_{vr} = -\beta + \frac{\ell_r r}{V_x} \tag{2.51}$$

where $C_{\alpha f}$ and $C_{\alpha r}$ are the cornering stiffness of the front and rear tires respectively. Substituting (2.50) and (2.51) into (2.48) and (2.49) yields the following description for the vehicle lateral dynamics:

$$\frac{d\beta}{dt} = -r + \frac{C_{\alpha f}}{mV_x}\left(\delta - \beta - \frac{\ell_f r}{V_x}\right) + \frac{C_{\alpha r}}{mV_x}\left(-\beta + \frac{\ell_r r}{V_x}\right) + \frac{g\sin\phi}{V_x} \tag{2.52}$$

$$\frac{dr}{dt} = \frac{\ell_f C_{\alpha f}}{I_z}\left(\delta - \beta - \frac{\ell_f r}{V_x}\right) - \frac{\ell_r C_{\alpha r}}{I_z}\left(-\beta + \frac{\ell_r r}{V_x}\right) \tag{2.53}$$

2.7   FROM BODY FIXED TO GLOBAL COORDINATES

The dynamic model described in sections 2.5 is based on body fixed coordinates. It is suitable for control system design, since a lane keeping controller must utilize body fixed measurements of position error with respect to road. To obtain a global picture of the trajectory traversed by the vehicle, however, the time history of the body-fixed coordinates must be converted into trajectories in inertial space.

As shown in Figure 2-12, the lateral distance between the c.g. of the vehicle and the road centerline is e_1. The position of the vehicle in global coordinates is therefore given by

$$X = X_{des} - e_1 \sin(\psi) \tag{2.54}$$

$$Y = Y_{des} + e_1 \cos(\psi) \tag{2.55}$$
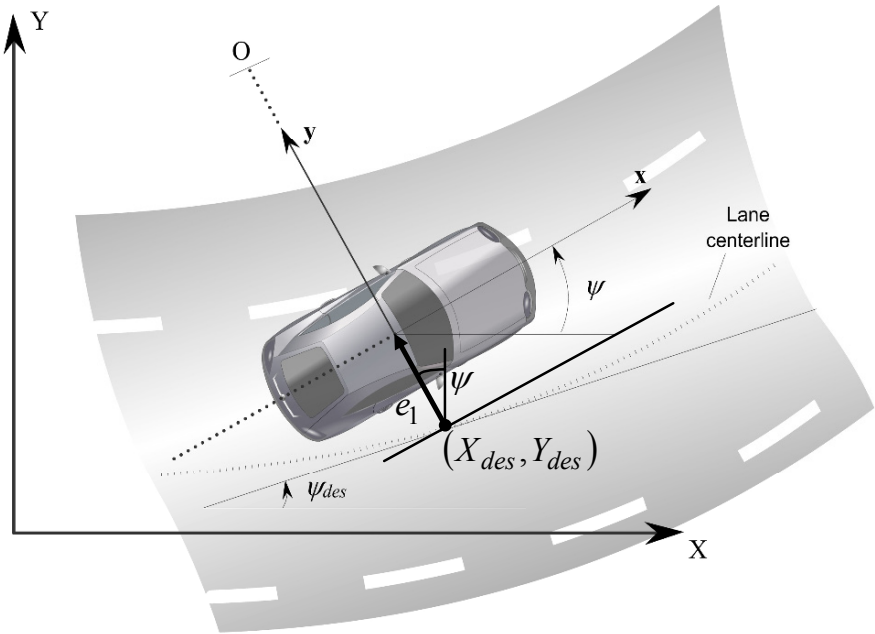
Figure 2-12. From body fixed to global coordinates

where (X_{des}, Y_{des}) are the global coordinates of the point on the road centerline which lies on a line along the lateral axis of the vehicle.

Using $X_{des} = \int_0^t V \cos(\psi_{des}) dt$, $Y_{des} = \int_0^t V \sin(\psi_{des}) dt$ and replacing ψ by $\psi = e_2 + \psi_{des}$ in equations (2.54) and (2.55), the global coordinates of the vehicle are obtained as

$$X = \int_0^t V \cos(\psi_{des}) dt - e_1 \sin(e_2 + \psi_{des}) \qquad (2.56)$$

$$Y = \int_0^t V \sin(\psi_{des}) dt + e_1 \cos(e_2 + \psi_{des}) \qquad (2.57)$$

2.8   ROAD MODEL

The curvature of a road is the inverse of the road radius i.e. $\dfrac{1}{R}$. Continuity of curvature is an important criterion that a road should satisfy in order to ensure that the lateral control system can track it. Clothoid spirals are curves that are used to transition smoothly from one curvature value to another (for example, in going from a straight road to a circular road).

A clothoid is defined to be a spiral whose curvature is a linear function of its arc length and is mathematically defined in terms of Fresnel integrals (Kiencke and Nielsen, 2000). The parametric equation of a clothoid is

$$\begin{bmatrix} x(t) \\ y(t) \end{bmatrix} = a \begin{bmatrix} C(t) \\ S(t) \end{bmatrix} \tag{2.58}$$

where the scaling factor a is positive, the parameter t is non-negative, and the Fresnel integrals are represented as

$$C(t) = \int_0^t \cos\left(\frac{\pi u^2}{2}\right) du \tag{2.59}$$

$$S(t) = \int_0^t \sin\left(\frac{\pi u^2}{2}\right) du \tag{2.60}$$

The clothoid in Eq. (2.58) (in its standard form) is in the first quadrant and starts at $t = 0$ and converges to $\left(\dfrac{a}{2}, \dfrac{a}{2}\right)$ as $t \to \infty$. Figure 2-13 shows a clothoid spiral using $a = 6000$.

The integrals of the Fresnel integrals are

$$C_I(t) = \int_0^t C(u)du = tC(t) - \frac{1}{\pi}\sin\left(\frac{\pi t^2}{2}\right) \tag{2.61}$$

$$S_I(t) = \int_0^t S(u)du = tS(t) + \frac{1}{\pi}\cos\left(\frac{\pi t^2}{2}\right) - \frac{1}{\pi} \tag{2.62}$$

The following geometric formulae for clothoids shown in Table 2.3 are often useful for designing clothoids to transition from a straight line to a circle or from one circle to a circle of different radius (Sasipalli, et. al., 1997).
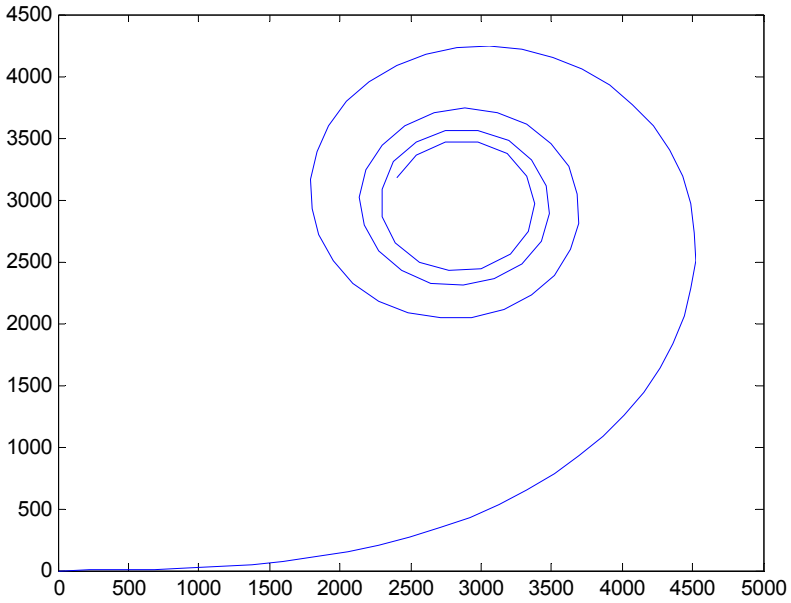
Figure 2-13. Clothoid spiral using a scaling value a= 6000

Table 2.3 Geometric Formulae of Clothoids

	Geometric Element	Parametric Expression
Geometric Formulae of Clothoids		
1	angle of tangent	$\dfrac{\pi}{2}t^2$
2	curvature	$\dfrac{\pi}{a}t$
3	arc length	$ds = a\,dt$
4	center of circle of curvature	$\left(\dfrac{a}{t}C_I(t), \dfrac{a}{t}\left\{S_I(t)+\dfrac{1}{\pi}\right\}\right)$

Calculation of the cartesian coordinates from Eqs. (2.59) and (2.60) has to be done numerically i.e. the above integrals cannot be evaluated analytically. Figure 2-14 shows a clothoid spiral used to transition from a straight line segment to a circular arc.
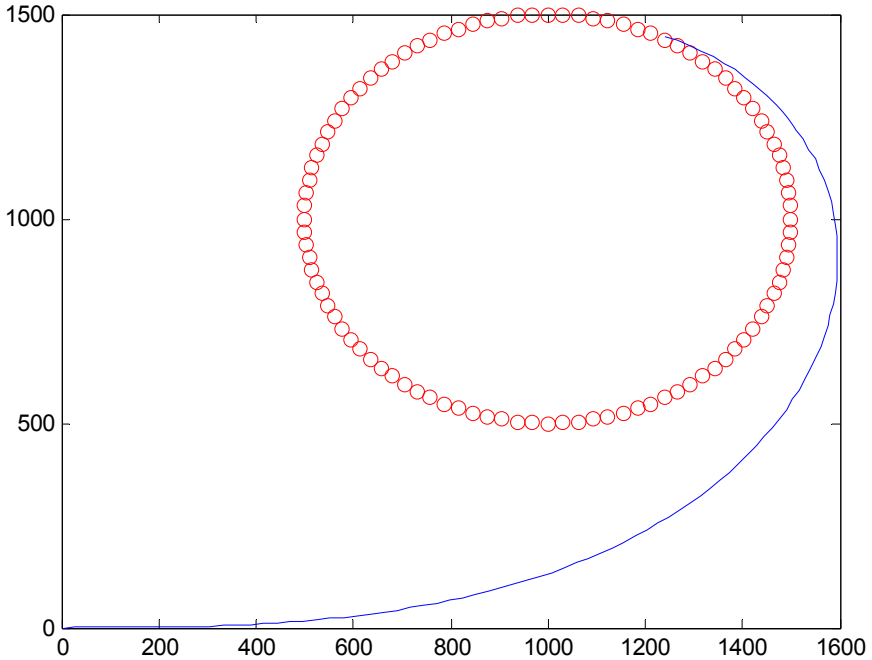
Figure 2-14. Clothoid spiral joining a straight line and a circle.

2.9   CHAPTER SUMMARY

This chapter discussed a variety of models that describe lateral vehicle motion. These models can be used to design steering control systems for lateral lane keeping. These models can also be extended for use in yaw stability control, rollover control and other vehicle control applications.

The major lateral models discussed in the chapter were

1. Kinematic vehicle model
2. Dynamic vehicle model in terms of inertial lateral position and yaw angle
3. Dynamic vehicle model in terms of road-error variables
4. Dynamic vehicle model in terms of yaw rate and vehicle slip angle

The kinematic model provides equations of motion purely in terms of geometric relationships governing the system. It is a useful model for very low speed applications, for example vehicle control for automated parking.

The dynamic models discussed in this chapter are useful for lane keeping applications and can also be extended for use in yaw stability control and rollover prevention applications. The extension and use of these models for yaw stability control is discussed in Chapter 8.

The transformation of coordinates from body-fixed to global axes was also presented. In addition road models were discussed and the use of clothoid spirals to transition smoothly from one road curvature to another was described.

NOMENCLATURE

F_y	lateral tire force
F_{yf}	lateral tire force on front tires
F_{yr}	lateral tire force on rear tires
V_x	longitudinal velocity at c.g. of vehicle
V	total velocity at c.g. of vehicle
$\dot{y}$	lateral velocity at c.g. of vehicle
V_y	lateral velocity at c.g. of vehicle (same as $\dot{y}$)
m	total mass of vehicle
I_z	yaw moment of inertia of vehicle
ℓ_f	longitudinal distance from c.g. to front tires
ℓ_r	longitudinal distance from c.g. to rear tires
L	total wheel base ($\ell_f + \ell_r$)
ψ	yaw angle of vehicle in global axes
$\dot{\psi}$	yaw rate of vehicle
r	yaw rate of vehicle (same as $\dot{\psi}$)
X, Y	global axes
δ	steering wheel angle
δ_f	front wheel steering angle

δ_r	rear wheel steering angle
δ_o	steering angle of outer wheels
δ_i	steering angle of inner wheels
ℓ_w	track width
α_f	slip angle at front tires
α_r	slip angle at rear tires
C_α	cornering stiffness of tire
F_z	normal force on tire
μ	tire-road friction coefficient
$\dot{\psi}_{des}$	desired yaw rate from road
β	slip angle at vehicle c.g. (center of gravity)
θ_V	velocity angle (angle of velocity vector with longitudinal axis)
ϕ	road bank angle
R	turn radius of vehicle or radius of road
e_1	lateral position error with respect to road
e_2	yaw angle error with respect to road
$C(t)$	Fresnel integral
$S(t)$	Fresnel integral

REFERENCES

Ackerman, J., "Robust control prevent car skidding, "*IEEE Control Systems Magazine,* Vol. 17, No. 3, June 1997, pp. 23-31.

Donath, M., Morellas, V., Morris, T. and Alexander, L., "Preview based control of a tractor trailer using DGPS for preventing road departure accidents", *Proceedings of the IEEE Conference on Intelligent Transportation Systems,* ITSC'97, Boston, MA, November, 1997.

Guldner, J., Tan, H.-S. and Patwardhan, S., "Analysis of automatic steering control for highway vehicle with look-down lateral reference systems", *Vehicle System Dynamics,* vol. 26, no. 4, pp.243-269, 1996.

Hoffman, D. and Rizzo, M., "Chevrolet C5 Corvette vehicle dynamic control system," *SAE Technical Paper Series,* SAE-980233, 1998.

Jost, K., "Cadillac stability enhancement," *Automotive Engineering,* October, 1996.

Kiencke, U. and Nielsen, L., *Automotive Control Systems for Engine, Driveline and Vehicle*, SAE International, ISBN 0-7680-0505-1, 2000.

Leffler, H., Auffhammer, R., Heyken, R. and Roth, H., "New driving stability control system with reduced technical effort for compact and medium class passenger cars," *SAE Technical Paper Series,* SAE-980234, 1998.

Meriam, J.L. and Kraige, L.G., "Engineering Mechanics: Dynamics", Fifth Edition, John Wiley & Sons, Inc., New York, ISBN 047126606X, 2003.

Peng, H. and Tomizuka, M., "Preview control for vehicle lateral guidance in highway automation," *Journal of Dynamic Systems Measurement & Control-Transactions of the Asme,* Vol. 115, No. 4, pp. 679-686, Dec 1993.

Rajamani, R., Tan, H.S., Law, B. and Zhang, W.B., "Demonstration of integrated lateral and longitudinal control for the operation of automated vehicles in platoons," *IEEE Transactions on Control Systems Technology,* Vol. 8, No. 4, pp. 695-708, July 2000.

R. Rajamani, C.Zhu and L. Alexander (2003), "Lateral control of a backward driven front-steering vehicle", *Control Engineering Practice*, Vol. 11, No. 5, pp. 531-540, 2003.

Sasipalli, V.S.R., Sasipalli, G.S. and Harada, K., "Single spiral in highway design and bounds for their scaling," *IEICE Transactions on Information and Systems,* Vol. E80-D, No. 11, November 1997.

Taylor, C.J., Kosecka, J., Blasi, R. and Malik, J., "A comparative study of vision-based lateral control strategies for autonomous highway driving," , *International Journal of Robotics Research,* Vol. 18, No. 5, pp. 442-453, May 1999.

Thorpe, C.E., Hebert, M., Kanade, T. and Shafer, S., "Vision and navigation for the Carnegie-Mellon Navlab, "*IEEE Transactions on Pattern Analysis and Machine Intelligence,* Vol. 10, No. 3, pp. 362-373, May 1998.

Wang, D. and Qi, F., "Trajectory planning for a four wheel steering vehicle," *Proceedings of the 2001 IEEE International Conference on Robotics and Automation,* Seoul, Korea, May 21-26, 2001.

Chapter 3

STEERING CONTROL FOR AUTOMATED LANE KEEPING

Kinematic and dynamic models for lateral vehicle dynamics were discussed in the previous chapter. This chapter discusses lateral control systems used to control a vehicle to stay in the center of its lane.

The chapter is organized as follows. Control design by state feedback is discussed first in section 3.1. Steady state errors and the steady state steering angle required to negotiate a curved road are analyzed in sections 3.2 and 3.3. The subsequent sections of the chapter concentrate on control design by output feedback (sections 3.5, 3.6, 3.7, 3.8, 3.9 and 3.10).

3.1   STATE FEEDBACK

As seen in the previous chapter, under the small slip angle and bicycle model assumptions, the state space model for the lateral dynamics of the vehicle is given by

$$\dot{x} = Ax + B_1\delta + B_2\dot{\psi}_{des} \tag{3.1}$$

with $x = \{e_1 \quad \dot{e}_1 \quad e_2 \quad \dot{e}_2\}^T$, where e_1 is the lateral position error of the c.g., e_2 is the yaw angle difference between the vehicle and the road, δ is the front wheel steering angle input, $\dot{\psi}_{des}$ is the desired yaw rate determined by road curvature and vehicle speed and the matrices A, B_1 and B_2 have been presented earlier in Chapter 2 (section 2.5, equation (2.45)).

The following values of vehicle parameters will be used for all the simulations in this chapter.

$m = 1573$, $I_z = 2873$, $\ell_f = 1.1$, $\ell_r = 1.58$, $C_{\alpha f} = 80000$, $C_{\alpha r} = 80000$;

These values are representative of parameters for a passenger sedan.

The open-loop matrix A has two eigenvalues at the origin and is unstable. The system has to be stabilized by feedback.

Calculations show that the pair (A, B_1) is controllable. Hence, using the state feedback law

$$\delta = -Kx = -k_1 e_1 - k_2 e_2 - k_3 e_3 - k_4 e_4 \tag{3.2}$$

the eigenvalues of the closed-loop matrix $(A - BK)$ can be placed at any desired locations. The closed-loop system using this state feedback controller is

$$\dot{x} = (A - B_1 K)x + B_2 \dot{\psi}_{des} \tag{3.3}$$

The following Matlab command can be used to place the eigenvalues of the closed-loop system.

K = place(A,B1,P)

This command yields a feedback matrix K such that the eigenvalues of the matrix $A - B_1 K$ are at the desired locations specified in the vector P.

Eigenvalues placed at $\begin{bmatrix} -5 - 3j & -5 + 3j & -7 & -10 \end{bmatrix}^T$ lead to the following simulation results shown in Figures 3-1, 3-2 and 3-3.

In these simulations a longitudinal speed of 30 m/s is used. The road is initially straight and then becomes circular with a radius of 1000 meters starting at a time of 1 second. The corresponding desired yaw rate can be calculated from $\dot{\psi}_{des} = \dfrac{V_x}{R} = 0.03 \, \text{rad/s} = 1.72 \, \text{deg/s}$. The desired yaw rate is shown in Figure 3-1 and is a step input from 0 to 1.72 deg/sec at 1 second. The time histories of the lateral error e_1 and yaw angle error e_2 are shown in Figure 3-2 and Figure 3-3 respectively.

Due to the presence of the $B_2 \dot{\psi}_{des}$ term in equation (3.3), the tracking errors need not all converge to zero, even though the matrix $(A - B_1 K)$ is stable. The steady state values of e_1 and e_2 are non-zero because the input due to road curvature $\dot{\psi}_{des}$ is non-zero. A physical interpretation of these steady state errors is provided in sections 3.2 and 3.3.
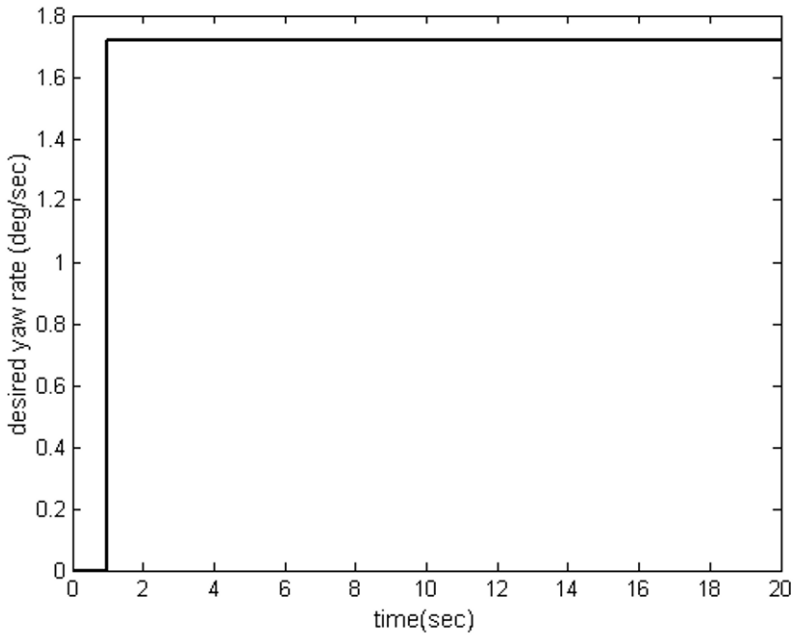
Figure 3-1. Desired yaw rate for simulations
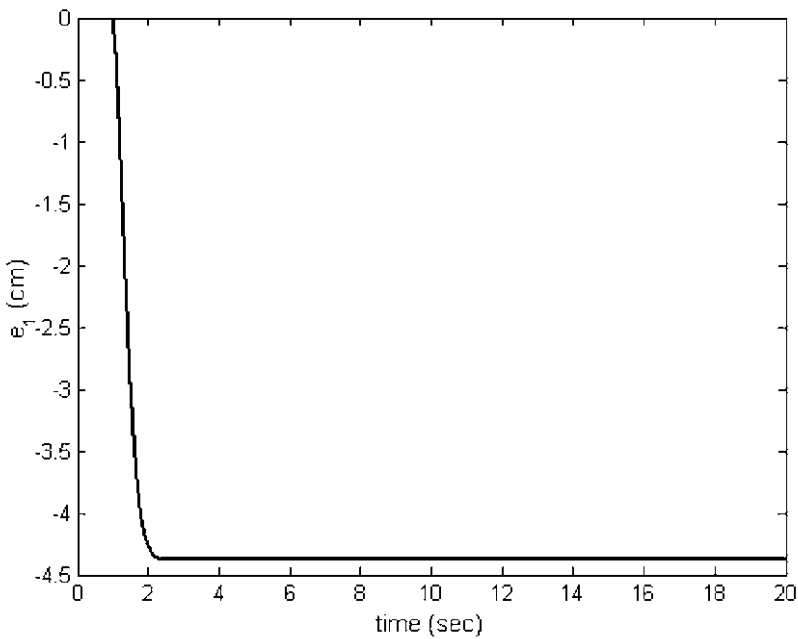
Figure 3-2. Lateral position error using state feedback
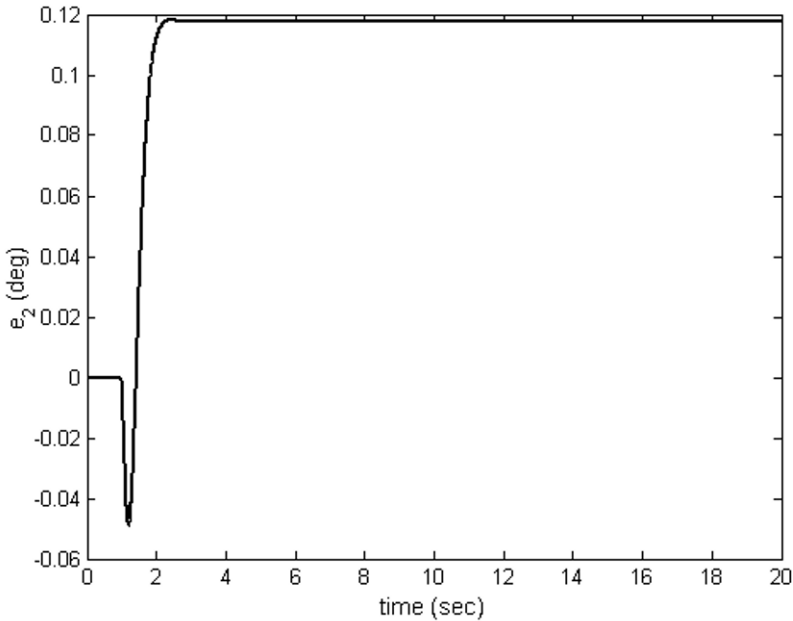
Figure 3-3. Yaw angle error using state feedback

3.2 STEADY STATE ERROR FROM DYNAMIC EQUATIONS

As before, the state space model for the closed-loop lateral system under state feedback is given by

$$\dot{x} = (A - B_1 K)x + B_2 \dot{\psi}_{des}$$

Due to the presence of the $B_2 \dot{\psi}_{des}$ term, the tracking errors will not all converge to zero when the vehicle is traveling on a curve, even though the matrix $(A - B_1 K)$ is asymptotically stable.

In this section, we will investigate whether the use of a feedforward term in addition to state feedback can ensure zero steady state errors on a curve. Assume that the steering controller is obtained by state feedback plus a feedforward term that attempts to compensate for the road curvature:

$$\delta = -Kx + \delta_{ff} \tag{3.4}$$

Then, the closed-loop system is given by

$$\dot{x} = (A - B_1 K)x + B_1 \delta_{ff} + B_2 \dot{\psi}_{des} \tag{3.5}$$

Taking Laplace transforms, assuming zero initial conditions, we find

$$X(s) = [sI - (A - B_1 K)]^{-1} \{B_1 L(\delta_{ff}) + B_2 L(\dot{\psi}_{des})\} \tag{3.6}$$

where $L(\delta_{ff})$ and $L(\dot{\psi}_{des})$ are Laplace transforms of δ_{ff} and $\dot{\psi}_{des}$ respectively.

If the vehicle travels at constant speed V_x on a road with constant radius of curvature R, then

$$\dot{\psi}_{des} = \text{constant} = \frac{V_x}{R} \tag{3.7}$$

and its Laplace transform is $\dfrac{V_x}{Rs}$. Similarly, if the feedforward term is constant, then its Laplace transform is $\dfrac{\delta_{ff}}{s}$.

Using the Final Value Theorem, the steady state tracking error is given by

$$x_{ss} = \lim_{t \to \infty} x(t) = \lim_{s \to 0} sX(s) = -(A - B_1 K)^{-1} \left\{ B_1 \delta_{ss} + B_2 \frac{V_x}{R} \right\} \tag{3.8}$$

Evaluation of equation (3.8) using the Symbolic Toolbox in Matlab yields the steady state errors

$$x_{ss} = \left\{ \begin{array}{c} \dfrac{\delta_{ff}}{k_1} \\ 0 \\ 0 \\ 0 \end{array} \right\} +$$

$$\left\{ \begin{array}{c} -\dfrac{1}{k_1} \dfrac{mV_x^2}{R(\ell_f + \ell_r)} \left[\dfrac{\ell_r}{2C_{\alpha f}} - \dfrac{\ell_f}{2C_{\alpha r}} + \dfrac{\ell_f}{2C_{\alpha r}} k_3 \right] - \dfrac{1}{k_1 R} \left[\ell_f + \ell_r - \ell_r k_3 \right] \\ 0 \\ \dfrac{1}{2RC_{\alpha r}(\ell_f + \ell_r)} \left[-2C_{\alpha r} \ell_f \ell_r - 2C_{\alpha r} \ell_r^2 + \ell_f mV_x^2 \right] \\ 0 \end{array} \right\} \tag{3.9}$$

From equation (3.9), we see that the lateral position error e_1 can be made zero by appropriate choice of δ_{ff}. However, δ_{ff} cannot influence the steady state yaw error, as seen from equation (3.9). The yaw angle error has a steady state term that cannot be corrected, no matter how the feedforward steering angle is chosen. The steady state yaw-angle error is

$$e_{2\_ss} = \frac{1}{2RC_{\alpha r}(\ell_f + \ell_r)}\left[-2C_{\alpha r}\ell_f\ell_r - 2C_{\alpha r}\ell_r^2 + \ell_f mV_x^2\right]$$

$$= -\frac{\ell_r}{R} + \frac{\ell_f}{2C_{\alpha r}(\ell_f + \ell_r)}\frac{mV_x^2}{R} \tag{3.10}$$

The steady state lateral position error can be made zero if the feedforward steering angle is chosen as

$$\delta_{ff} = \frac{mV_x^2}{RL}\left[\frac{\ell_r}{2C_{\alpha f}} - \frac{\ell_f}{2C_{\alpha r}} + \frac{\ell_f}{2C_{\alpha r}}k_3\right] + \frac{L}{R} - \frac{\ell_r}{R}k_3 \tag{3.11}$$

which upon closer inspection is seen to be

$$\delta_{ff} = \frac{L}{R} + K_V a_y - k_3\left[\frac{\ell_r}{R} - \frac{\ell_f}{2C_{\alpha r}}\frac{mV_x^2}{R\ell}\right] \tag{3.12}$$

where $K_V = \dfrac{\ell_r m}{2C_{\alpha f}(\ell_f + \ell_r)} - \dfrac{\ell_f m}{2C_{\alpha r}(\ell_f + \ell_r)}$ is called the understeer gradient and $a_y = \dfrac{V_x^2}{R}$. If we denote $m_r = m\dfrac{\ell_f}{L}$ as the portion of the vehicle mass carried on the rear axle and $m_f = m\dfrac{\ell_r}{L}$ as the portion of the vehicle mass carried on the front axle, then $K_V = \dfrac{m_f}{2C_{\alpha f}} - \dfrac{m_r}{2C_{\alpha r}}$.

Hence

$$\delta_{ff} = \frac{L}{R} + K_V a_y + k_3 e_{2\_ss} \tag{3.13}$$

The steady state steering angle for zero lateral position error is given by

$$\delta_{ss} = \delta_{ff} - Kx_{ss} \ \text{ or}$$

$$\delta_{ss} = \delta_{ff} - k_3 e_{2ss} \ \text{ or}$$

$$\delta_{ss} = \frac{L}{R} + K_V a_y \tag{3.14}$$

Table 3-1. Summary of state feedback controller with feedforward

SUMMARY OF STATE FEEDBACK CONTROLLER WITH FEEDFORWARD		
Symbol	Nomenclature	Equation
e_{2_ss}	Steady-state yaw angle error	$e_{2\_ss} = -\dfrac{\ell_r}{R} + \dfrac{\ell_f}{2C_r(\ell_f + \ell_r)} \dfrac{mV_x^2}{R}$ $= -\dfrac{\ell_r}{R} + \alpha_r$
δ_{ss}	Steady-state steering angle	$\delta_{ss} = \dfrac{L}{R} + K_V a_y$
δ_{ff}	Feedforward component of steering angle	$\delta_{ff} = \dfrac{L}{R} + K_V a_y - k_3 e_{2\_ss}$
α_f	Slip angle at front tires	$\alpha_f = \dfrac{m_f}{2C_{\alpha f}} \dfrac{V_x^2}{R}$
α_r	Slip angle at rear tires	$\alpha_r = \dfrac{m_r}{2C_{\alpha r}} \dfrac{V_x^2}{R}$
K_V	Understeer gradient	$K_V = \dfrac{m_f}{2C_{\alpha f}} - \dfrac{m_r}{2C_{\alpha r}}$

In conclusion, the lateral position error e_1 can be made zero at steady state by appropriate choice of the feedforward input δ_{ff}. However, the steady state yaw angle will be equal to $e_{2\_ss} = -\dfrac{\ell_r}{R} + \dfrac{\ell_f}{2C_{\alpha r}\left(\ell_f + \ell_r\right)}\dfrac{mV_x^2}{R}$ and cannot be changed by the feedforward steering input.

3.3   UNDERSTANDING STEADY STATE CORNERING

3.3.1   Steering angle for steady state cornering

This section uses geometric analysis to provide an answer to the question "What is the steady state steering angle required to negotiate a curve of radius R?" (Gillespie, 1992, Wong, 2001). As expected, the geometric analysis provides the same answer as the feedforward system analysis of the previous section. However, a better physical understanding of the lateral tire force requirements is obtained from the geometric analysis.

As discussed in the previous chapter, the slip angle at each wheel is the angle between the orientation of the wheel and the orientation of its velocity vector. Let the slip angle at the front wheel be denoted by α_f and that at the rear wheel be denoted by α_r, as shown in Figure 3-4. The instantaneous turn center O of the vehicle is the point at which the two lines perpendicular to the velocities of the two wheels meet.

Let $L = \ell_f + \ell_r$ be the wheelbase i.e. the distance between the centers of the front and rear wheels. Then, from the above figure, the angle subtended at the center of rotation is $\delta - \alpha_f + \alpha_r$. Under the assumption that the road radius is much larger than the wheelbase of the vehicle ($R \gg L$) (so that chord length is approximately equal to arc length), we have

$$\delta - \alpha_f + \alpha_r \approx \frac{L}{R} \tag{3.15}$$

Hence the steady state steering angle is given by

$$\delta = \frac{L}{R} + \alpha_f - \alpha_r \tag{3.16}$$
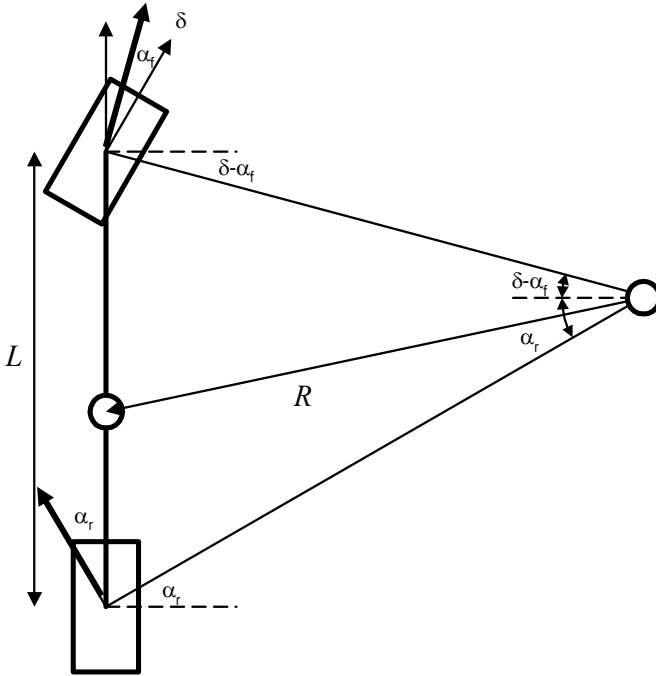
Figure 3-4. Steering angle for high speed cornering

The steady state slip angles α_f and α_r are related to the road radius as follows. Steady state force and moment equilibrium equations for the vehicle yield

$$F_{yf} + F_{yr} = m\frac{V_x^2}{R} \tag{3.17}$$

$$F_{yf}\ell_f - F_{yr}\ell_r = 0 \tag{3.18}$$

From the moment equilibrium (3.18) we have

$$F_{yf} = \frac{\ell_r}{\ell_f}F_{yr} \tag{3.19}$$

Using the relationship between front and rear tire forces of equation (3.19) in the force equilibrium equation (3.17), we have

$$F_{yr} = m \frac{\ell_f}{L} \frac{V_x^2}{R} = m_r \frac{V_x^2}{R} \tag{3.20}$$

where $m_r = m \dfrac{\ell_f}{L}$ is the portion of the vehicle mass carried on the rear axle. In words, the lateral force developed at the rear axle is m_r times the lateral acceleration. The same procedure can be used to find the front tire force :

$$F_{yf} = m \frac{\ell_r}{L} \frac{V_x^2}{R} = m_f \frac{V_x^2}{R} \tag{3.21}$$

where $m_f = m \dfrac{\ell_r}{L}$ is the portion of the vehicle mass carried on the front axle.

Assume that the slip angles are small so that the lateral tire force at each wheel is proportional to its slip angle. Denoting the cornering stiffness of each front tire by $C_{\alpha f}$ and that of each rear tire by $C_{\alpha r}$, and assuming that there are two front and two rear tires, the slip angles are

$$\alpha_f = \frac{F_{yf}}{2C_{\alpha f}} = \frac{m_f}{2C_{\alpha f}} \frac{V_x^2}{R}, \quad \alpha_r = \frac{F_{yr}}{2C_{\alpha r}} = \frac{m_r}{2C_{\alpha r}} \frac{V_x^2}{R} \tag{3.22}$$

The steady state steering angle is therefore given by

$$\delta = \frac{L}{R} + \alpha_f - \alpha_r = \frac{L}{R} + \left(\frac{m_f}{2C_{\alpha f}} - \frac{m_r}{2C_{\alpha r}} \right) \frac{V_x^2}{R}$$

or

$$\delta = \frac{L}{R} + K_V a_y \tag{3.23}$$

where the parameter K_V is called the <u>understeer gradient</u> and $a_y = \dfrac{V_x^2}{R}$.

Equation (3.23) is the formula that relates vehicle velocity and road curvature to the steering angle required for negotiating the circular road. This is the same as equation (3.14) obtained previously.

Depending on the relative values of the front and rear cornering stiffness and mass distribution values, three possibilities exist for the value of K_V:

1. Neutral steer

In this case the understeer gradient K_V is zero due to equal slip angles at the rear and front tires.

$$\frac{m_f}{C_f} = \frac{m_r}{C_r} \Rightarrow K_V = 0 \Rightarrow \alpha_f = \alpha_r$$

In the case of neutral steer, on a constant radius turn, no change in the steering angle is required as speed is varied. The steering angle depends only on the curve radius and the wheelbase.

2. Understeer

In this case the understeer gradient $K_V > 0$ due to a larger slip angle at the front tires compared to the rear tires.

$$\frac{m_f}{C_f} > \frac{m_r}{C_r} \Rightarrow K_V > 0 \Rightarrow \alpha_f > \alpha_r$$

In the case of understeer, on a constant radius turn, the steering angle will have to increase with speed in proportion to K_V times the lateral acceleration.

3. Oversteer

In this case the understeer gradient $K_V < 0$ due to a smaller slip angle at the front tires compared to the rear tires.

$$\frac{m_f}{C_f} < \frac{m_r}{C_r} \Rightarrow K_V < 0 \Rightarrow \alpha_f < \alpha_r$$

In the case of oversteer, on a constant radius turn, the steer angle will have to decrease as the speed is increased.

The steering angle as a function of vehicle longitudinal speed is shown in Figure 3-5 for the three cases of neutral steer, understeer and oversteer. Note that in the case of oversteer, the steering angle decreases with speed and could eventually reach zero at a speed called critical speed.
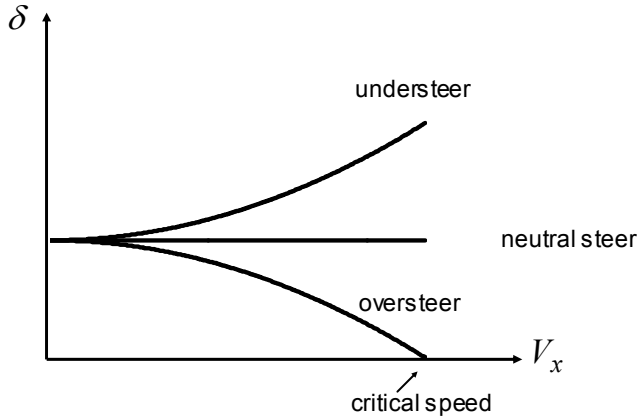
Figure 3-5. Steering angle variation with speed

3.3.2 Can the yaw-angle error be zero ?

If the parameters of the vehicle and the vehicle speed were such that

$$\frac{\ell_r}{R} = \frac{\ell_f}{2C_r\ell}\frac{mV_x^2}{R} \tag{3.24}$$

then the steady state yaw error of equation (3.10) would also be zero. This happens at one particular speed V_x at which equation (3.24) is satisfied and this speed is independent of the radius of the path.

The physical interpretation of equation (3.24) is as follows. The right hand side of the equation, as we have seen during the geometric analysis, is the slip angle at the rear tire. The left hand side of the equation is the angle γ subtended by the rear portion of the vehicle at the center of the circular path, as shown in Figure 3-6 below.
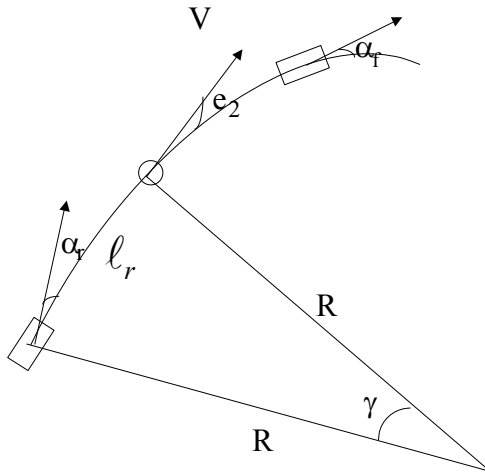
Figure 3-6. Steady state yaw angle error

Since the vehicle has a finite length, both its lateral position error and its yaw-angle error cannot always be made simultaneously zero. If the steady-state lateral position error is zero, then the steady state yaw-angle error can be zero only if the slip angle at the rear is the same as the angle γ subtended by the vehicle at the center of the circular path. This happens at one particular speed V_x at which equation (3.24) is satisfied and this speed is independent of the radius of the path.

3.3.3 Is non-zero yaw angle error a concern?

The above geometric analysis shows that no matter which control law is used, the yaw angle error e_2 will have a steady state value. This is because the slip angles at the rear and front wheels are completely determined, once the radius of the road and the vehicle speed V_x are fixed. Hence the slip angle of the vehicle β is automatically determined. The slip angle of the vehicle is

$$\beta = \frac{\dot{y}}{V_x} = \frac{1}{V_x}\left(\dot{e}_1 - V_x e_2\right) \tag{3.25}$$

Since the steady state value of $\dot{e}_1$ is zero, it follows that the steady state value of the vehicle slip angle is

$$\beta = -e_{2\_ss} \tag{3.26}$$

or

$$\beta = -\left(\psi - \psi_{des}\right)_{ss}$$

Hence

$$\left(\beta + \psi\right)_{ss} = \psi_{des} \tag{3.27}$$

The steady state error in e_2 is not a cause of concern. We don't necessarily need e_2 to converge to zero – all we need is that the heading angle $\psi + \beta$ converge to the desired angle ψ_{des}. Since the steady state error in e_2 is equal to β, from equation (3.27), it is guaranteed that $\psi + \beta$ will converge to ψ_{des}.

3.4   CONSIDERATION OF VARYING LONGITUDINAL VELOCITY

In general the longitudinal vehicle speed can vary in which case the system matrices $A(V_x)$ and $B_1(V_x)$ are time varying (or parameter varying). A constant state feedback matrix K can be used to obtain stability for varying velocity by exploiting the convex nature of the lateral dynamic system. The approach is to choose K such that $A(V_x) - B_1(V_x)K$ is simultaneously quadratically stabilized at the two extreme values of V_x. The following Theorem summarizes the design result that can be used for full state feedback control system design.

Theorem 3.1:

Let the closed-loop matrix be defined as

$$A_{CL}(V_x) = A(V_x) - B_1(V_x)K \tag{3.28}$$

Let

$$A_{\min} = A_{CL}(V_{\min}) = A(V_{\min}) - B_1(V_{\min})K \text{ and}$$

$$A_{\max} = A_{CL}(V_{\max}) = A(V_{\max}) - B_1(V_{\max})K$$

be defined as the values of $A_{CL}(V_x)$ at the extremes of the varying parameter V_x.

If a constant state feedback matrix K is chosen such that

$$A_{\min}{}^T P + P A_{\min} < 0 \tag{3.29}$$

and

$$A_{\max}{}^T P + P A_{\max} < 0 \tag{3.30}$$

for some $P > 0$, then the closed-loop system is stable for velocity varying in the range $V_{\min} \le V_x \le V_{\max}$.

Proof:

First, note that the closed-loop matrix can be rewritten as a convex combination of $A_{\min}$ and $A_{\max}$:

$$A_{CL}(V_x) = A(V_x) - B_1(V_x)K = aA_{\min} + (1-a)A_{\max} \quad \text{with} \quad 0 \le a(V_x) \le 1 \tag{3.31}$$

where $a(V_x)$ is a parameter whose value depends on the operating speed V_x.

Using the Lyapunov function candidate $V = x^T P x$, we find that its derivative is

$$\dot{V} = \dot{x}^T P x + x^T P \dot{x} = x^T (A_{CL}{}^T P + P A_{CL}) x$$

$$= a x^T (A_{\min}{}^T P + P A_{\min}) x + (1-a) x^T (A_{\max}{}^T P + P A_{\max}) x$$

$$< 0$$

Hence the proof.

3.5   OUTPUT FEEDBACK

The lateral position of the vehicle with respect to the road is usually measured at a location ahead of the vehicle, as shown in Figure 3-7. Sensor systems used for measurement of lateral position include differential GPS (Donath, et. al., 1997), vision cameras (Taylor, et. al., 1999, Thorpe, et. al., 1998) and magnetometers that measure the magnetic field from permanent magnets embedded in the roadway (Guldner, et. al., 1996).
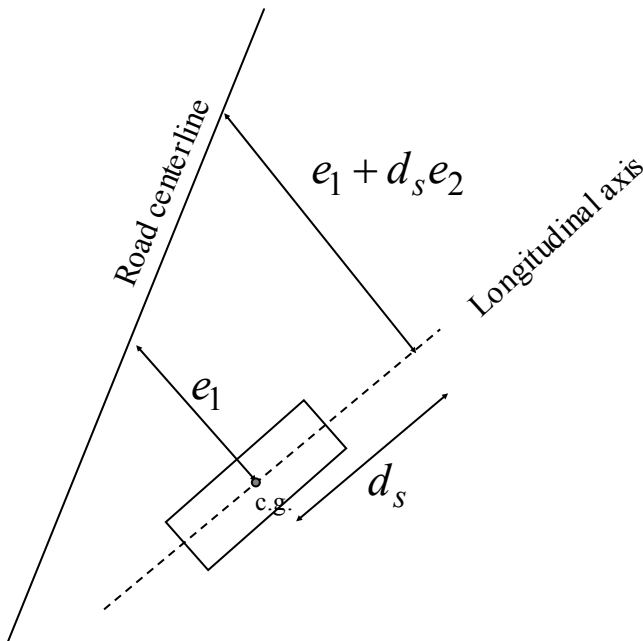
Figure 3-7. Look ahead lateral position measurement with respect to road

If we assume that the yaw angle error e_2 is small so that chord lengths can be approximated by arc lengths, then the measurement equation that relates the output to the states is as follows:

$$y = e_1 + d_s e_2 \tag{3.32}$$

where d_s is the longitudinal distance of the point ahead of the vehicle c.g. at which the sensor measurement is made.

3.6 UNITY FEEDBACK LOOP SYSTEM

Consider the following block diagram for the output feedback system shown in Figure 3-8. Here $P(s)$ is the plant transfer function between the steering angle input for the vehicle and the lateral position measurement output described in section 3.5. $C(s)$ represents the transfer function for the controller (to be determined later). The road-determined desired yaw rate $\dot{\psi}_{des}$ affects the system dynamics through a transfer function denoted in Figure 3-8 as $G(s)$. The signal $n(t)$ is the sensor noise that affects the system.
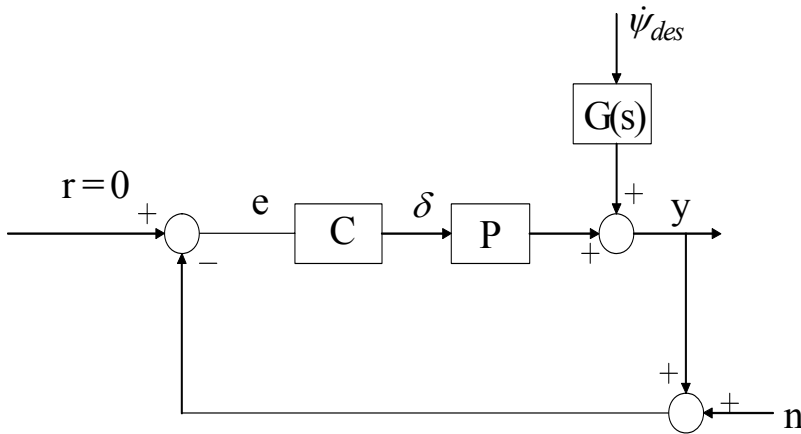
Figure 3-8. Unity feedback loop system

Figure 3-9 and Figure 3-10 shows the zeros and poles of $P(s)$ for values of $d_s = 2.0$ meters and $d_s = 7.0$ meters respectively. $P(s)$ has two poles at the origin, a pair of complex conjugate poles and a pair of complex conjugate zeros. Note that the zeros in Figure 3-10 are much better damped than the zeros in Figure 3-9. As d_s is increased, the damping increases for the complex conjugate pair of zeros. Figure 3-11 shows the magnitude and phase Bode plots for the plant transfer function $P(s)$ with $d_s = 2$ meters. A longitudinal velocity of 25m/s has been used in the model.
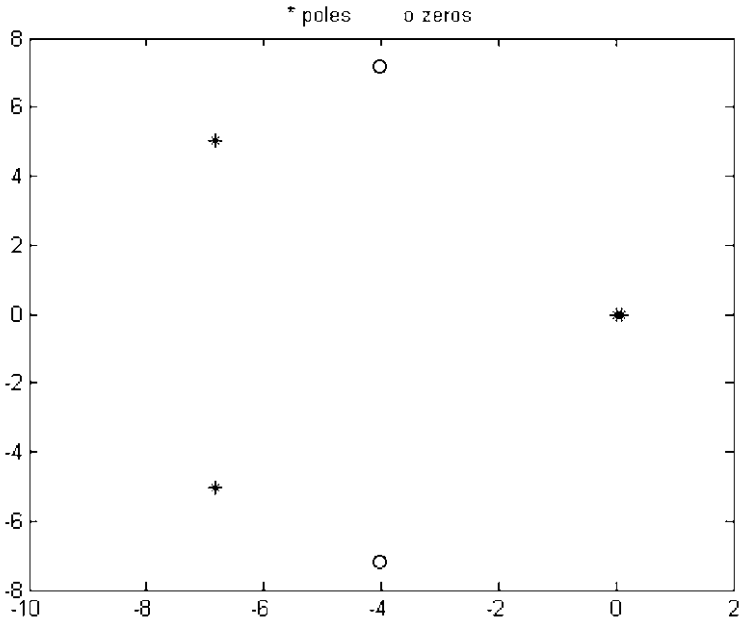
Figure 3-9. Zeros and poles of the open loop system for d_s = 2 meters
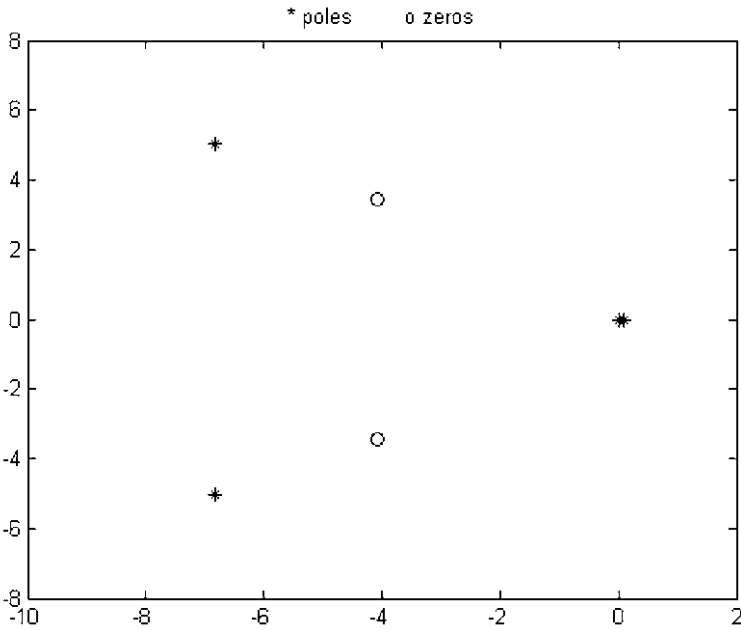
Figure 3-10. Zeros and poles of the open loop system for d_s = 7 meters
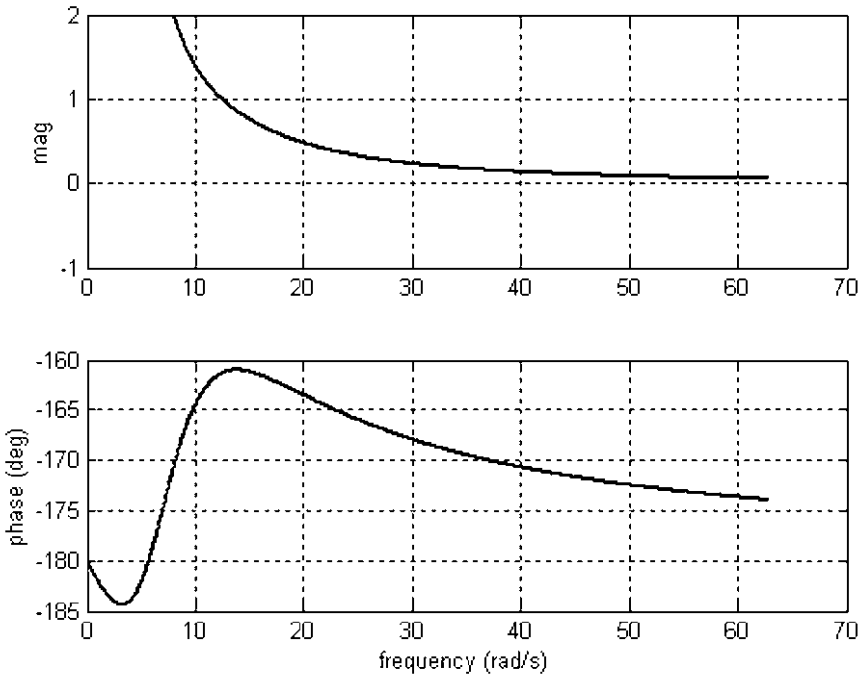
Figure 3-11. Bode plots for open-loop plant $P(s)$

3.7   LOOP ANALYSIS WITH A PROPORTIONAL CONTROLLER

An operating speed of 25 m/s and a sensor measurement location of $d_s = 2$ meters is assumed in this section for the lateral vehicle system. The open-loop transfer function $P(s)$ has two poles at the origin, an additional pair of complex conjugate poles and a pair of complex conjugate zeros. If the feedback loop were closed with a proportional controller, then $C(s) = K$ where K is the gain of the controller. The transfer function $PC(s)$ is of the type

$$PC(s) = \frac{\left(s^2 + 2\xi_n\omega_n s + \omega_n^2\right)}{s^2\left(s^2 + 2\xi_d\omega_d s + \omega_d^2\right)} \tag{3.33}$$

The contour Γ_s that s traverses in the complex plane for purposes of plotting the Nyquist plot must not pass through any poles or zeros of the open loop transfer function $PC(s)$. Hence it must not pass through the origin. Hence the following contour Γ_s as shown below in Figure 3-12 was used for the Nyquist plot. A semi-circle of radius ε is used to make a detour, so as to avoid going through the origin. By letting $\varepsilon \to 0$, the contour Γ_s will enclose the entire open right half plane.
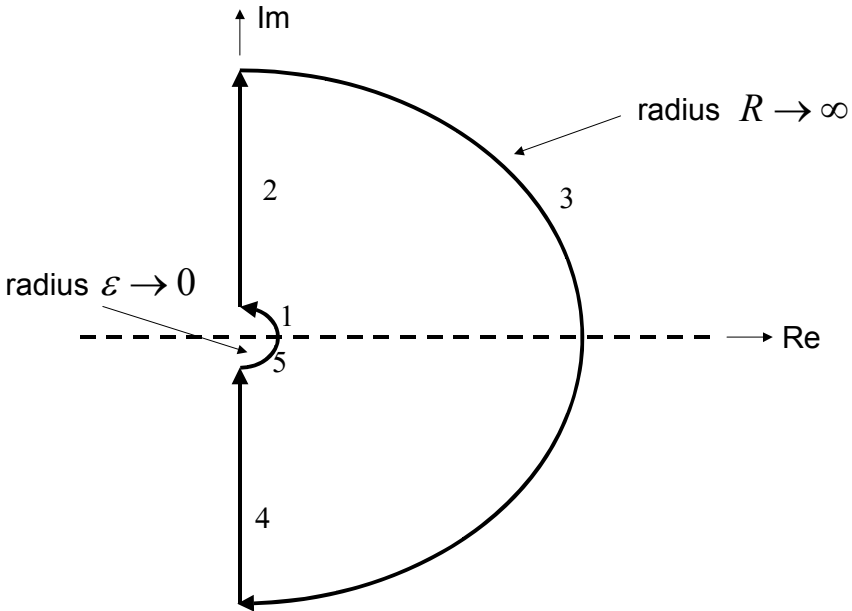
Figure 3-12. The Γ_s contour used for the Nyquist plot

Portions of the Γ_s contour have been marked as sections 1, 2, 3, 4 and 5. Section 3 consists of a semi-circle of radius R with $R \to \infty$ so as to cover the entire right half plane. The contour Γ_{PC} must be drawn for all values of s that s takes from the Γ_s contour. Section 3 of Γ_s gets mapped to the origin in the Γ_{PC} plane. It is important to draw the Γ_{PC} contour for sections 1, 2, 4 and 5 of Γ_s (see Figure 3-13) and determine how many times this contour encircles the –1 point. The Γ_{PC} contour for sections 1 and 2 is shown in the Nyquist plot in Figure 3-14.
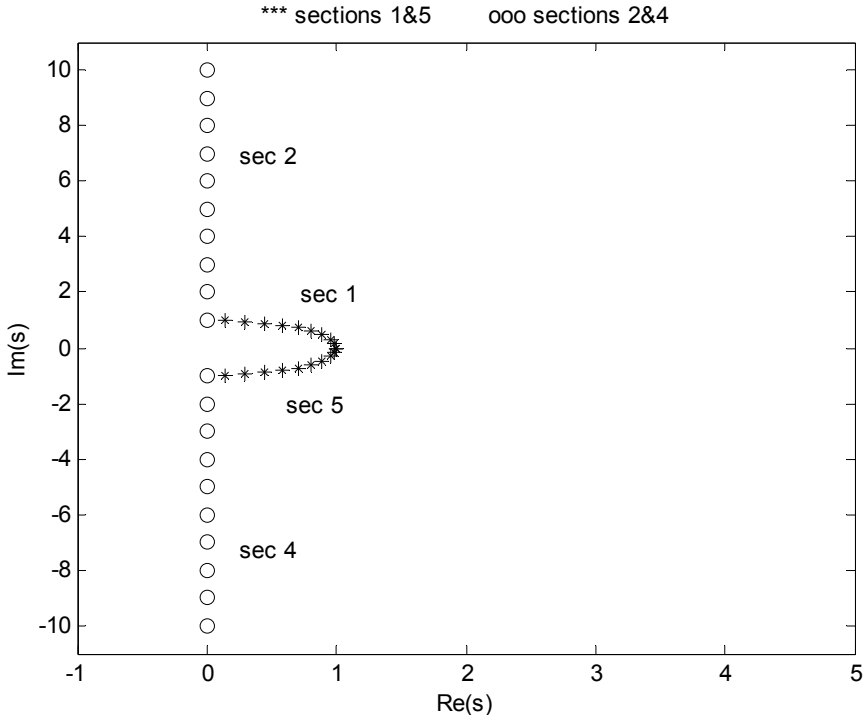
Figure 3-13. Sections 1, 2, 4 and 5 of the Γ_S contour used for the Nyquist plot
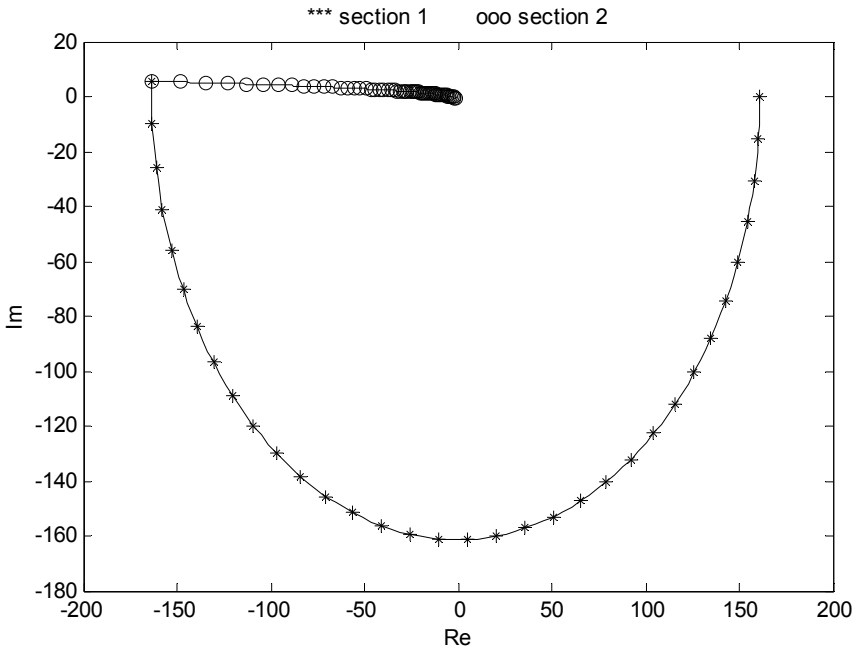
Figure 3-14. Nyquist plot (Γ_{PC} contour) obtained using sections 1 and 2 of the Γ_S contour
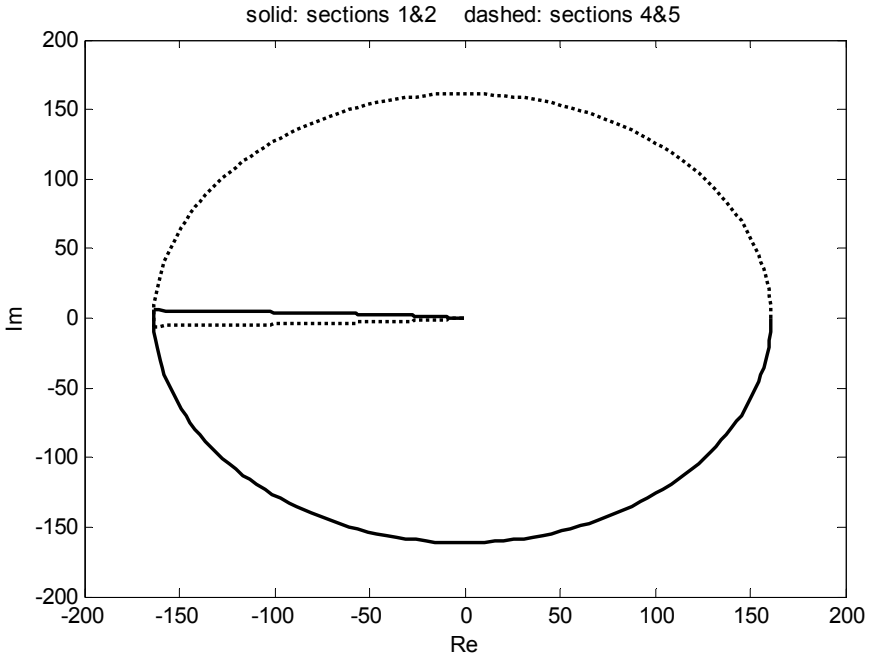
Figure 3-15. Nyquist plot obtained using sections 1, 2, 4 and 5 of the Γ_S contour

The Γ_{PC} contour corresponding to the entire Γ_S contour (sections 1, 2, 4 and 5) is shown in Figure 3-15. The solid line in this figure corresponds to sections 1 and 2 of Γ_S while the dashed line corresponds to sections 4 and 5 of Γ_S.

To determine how many times the above Γ_{PC} contour encircles the -1 point, it is necessary to zoom into the region near the -1 point, as is being done in Figure 3-16 and Figure 3-17. In Figure 3-16, a proportional gain of $K = 1$ is used. In this case, the Γ_{PC} contour encircles the -1 point twice: once clockwise and once counterclockwise. The clockwise encirclement can be easily seen in the big picture Nyquist plot of Figure 3-15. In the zoomed section of Figure 3-16, a counter clockwise encirclement can be seen. In the zoomed section of Figure 3-17, where the proportional gain is much smaller ($K = 0.01$), there is no counterclockwise encircelement of the -1 point. Thus in the case of the larger proportional gain, the total number of encircelements is $N = 1 - 1 = 0$ while in the case of the smaller proportional gain, the total number of encircelements is $N = 1$.

Figure 3-16. Zooming into the Nyquist plot: Gain = 1
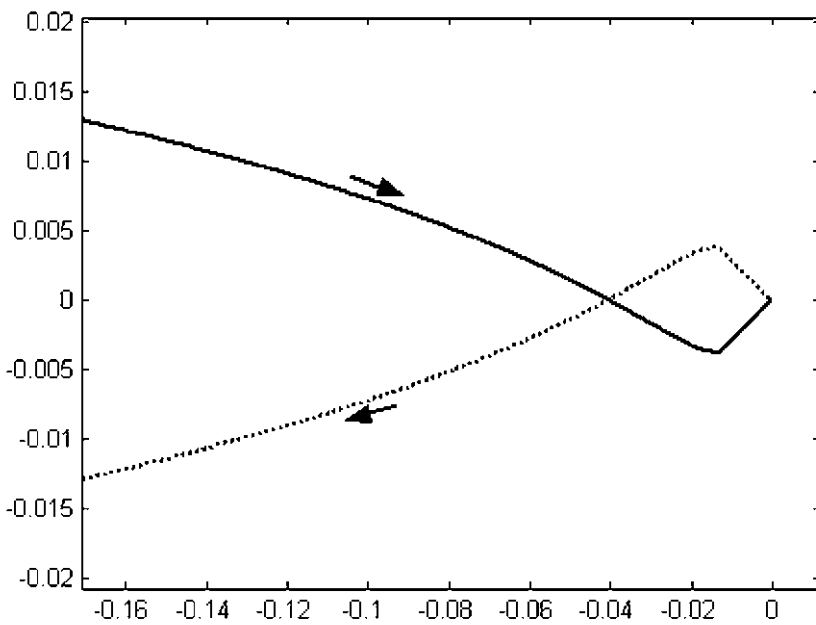
Figure 3-17. Zooming into the Nyquist plot: Gain = 0.01
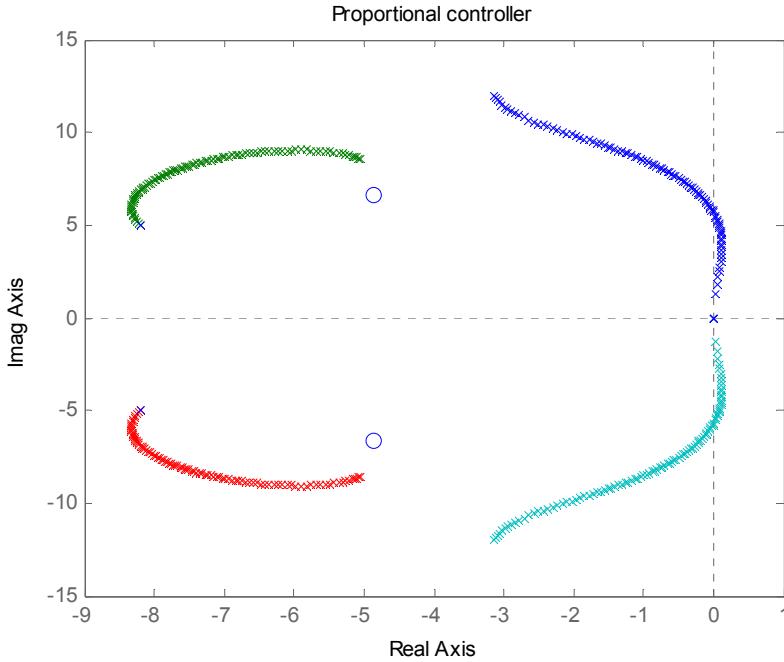
Figure 3-18. Root Locus with proportional controller

Thus the closed-loop system will be stable with proportional control if adequately large gain is used, but is unstable for small gain.

Figure 3-18 shows the root locus plot for varying feedback gain with the proportional controller. Again it can be seen that for small proportional gain, there is a pair of complex conjugate poles that are unstable. As the proportional gain is increased, these poles become stable.

It is important to note that with adequately large proportional gain, although the closed loop system gets stabilized, it still has poor phase margin. This can be seen from the Nyquist plots as well as the Bode plot showing the gain and phase margins in Figure 3-19. In Figure 3-19, with a proportional gain of 1, a phase margin of 18 degrees is obtained. It can be deduced from the plot that this is close to the best phase margin that can be obtained for this system. With a smaller gain of 0.1, the closed-loop system is unstable. With a higher proportional gain of 10, the system only has a phase margin of 8 degrees. Phase uncertainty can therefore easily change the number of encirclements of the –1 point for this system.

Gm = -12.138 dB (at 5.7257 rad/sec), Pm = 18.714 deg (at 12.523 rad/sec)
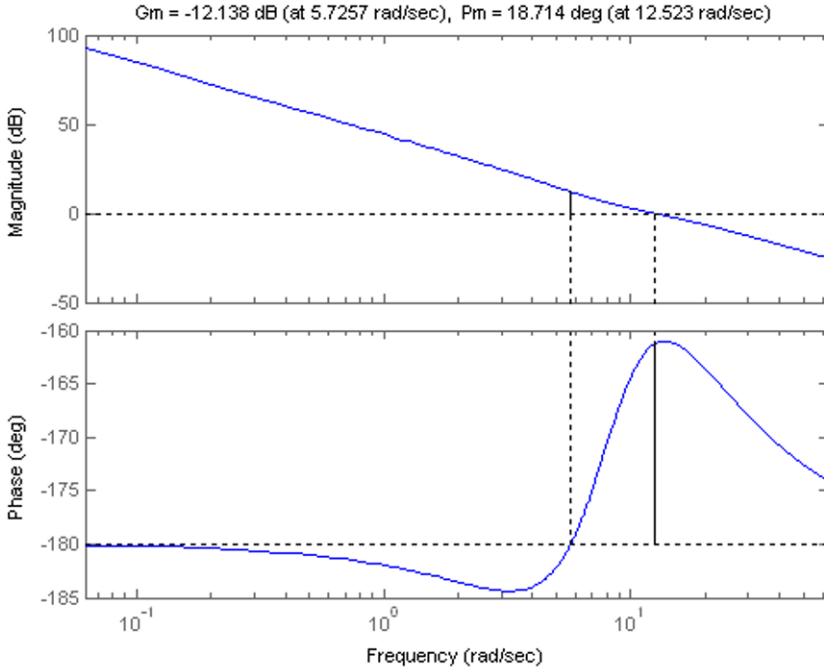
Figure 3-19. Gain margin and phase margin with a unity gain proportional controller

3.8 LOOP ANALYSIS WITH A LEAD COMPENSATOR

It is clear that robust gain and phase margin can be obtained if phase is added in the low frequency range (gain crossover range) for the system with unity feedback. Hence a lead compensator is suggested. The following transfer function can be used for the controller (compensator)

$$C(s) = K \frac{T_n s + 1}{T_d s + 1} \tag{3.34}$$

Values for T_n and T_d can be chosen so as to design the closed-loop system to have any desired value of phase margin. Values of $T_n = 0.5$ and $T_d = 0.1$ and $K = 0.01$ are used here as an illustration. In the plots shown in the next few pages, the above arbitrary values of T_n and T_d are used just to show that this compensator will increase the phase margin of the system.

Figure 3-20 shows the Bode plot for $PC(s)$ using the above lead compensator. Figure 3-23 shows the gain and phase margins of this system with a compensator gain $K = 1$. Figure 3-24 shows the gain and phase margins of this system with a compensator gain $K = 0.1$. It is clear that with the lead compensator phase has been added at the low frequencies to improve phase margin.

Figures 3-21 and 3-22 show the Nyquist plot for $PC(s)$. Figure 3-21 shows the Nyquist plot corresponding to sections 1 and 2 of Γ_s while Figure 3-22 shows the Nyquist plot corresponding to sections 1, 2, 4 and 5 of Γ_s. It is clear that the Nyquist curve does not encircle the –1 point and the closed-loop system is stable for all values of the compensator gain K.

Figure 3-25 shows the root locus plot for the system with lead compensator. Again, it is clear that the closed-loop system is stable for all values of the compensator gain K.
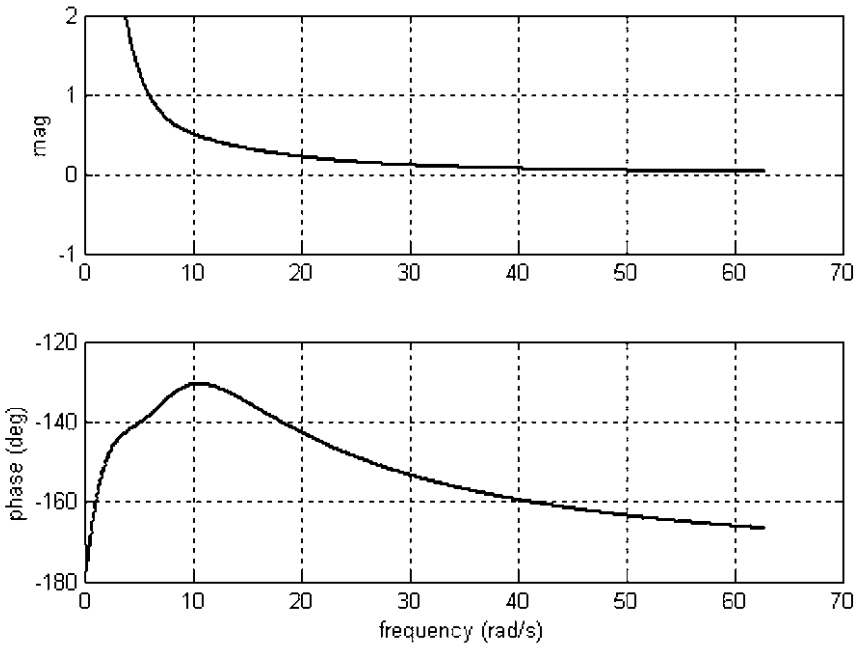
Figure 3-20. Bode plot for $PC(s)$ using a lead compensator ($K = 0.01$)
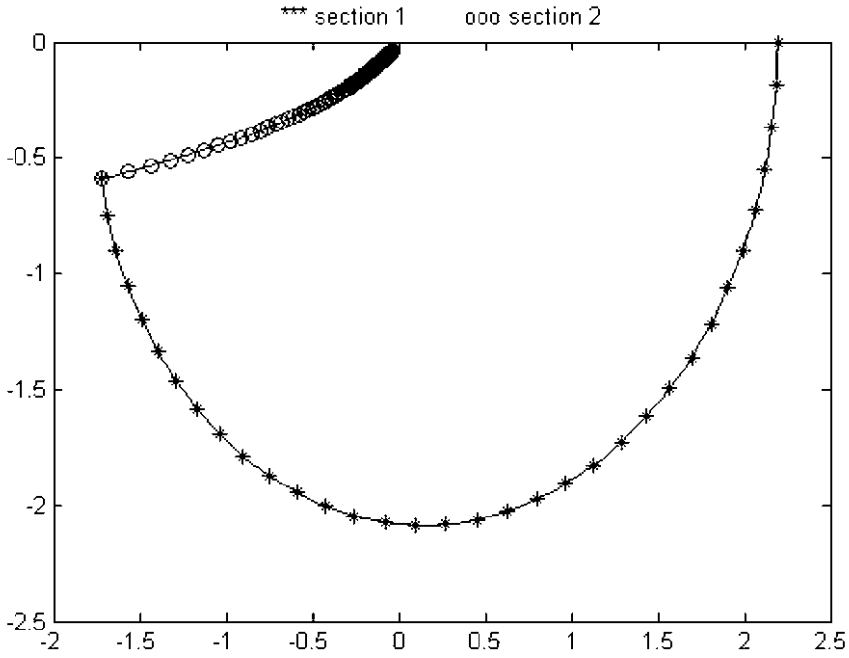
Figure 3-21. Nyquist plot corresponding to sections 1 and 2 of Γ_s (with lead compensator)
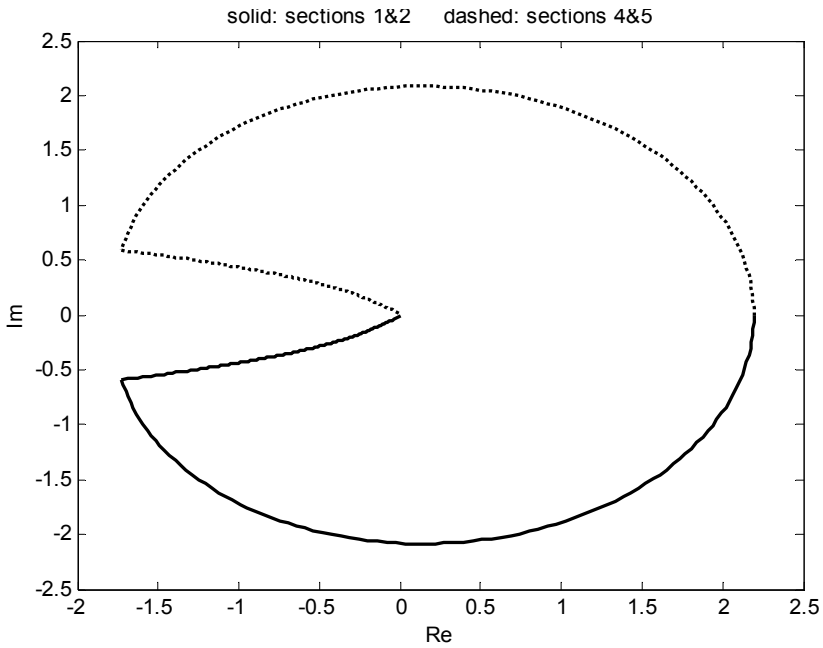
Figure 3-22. Nyquist plot corresponding to sections 1, 2, 4 and 5 of Γ_s (with lead compensator)
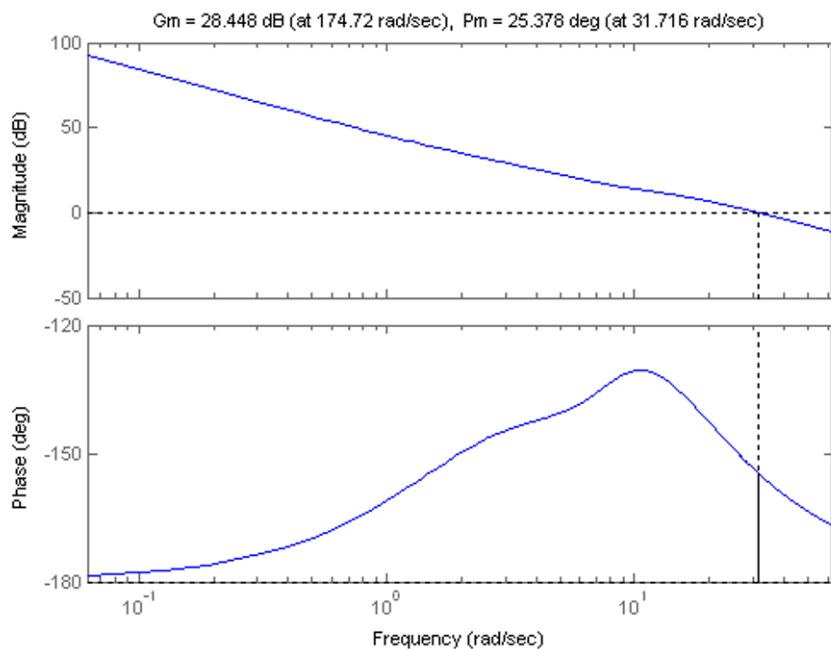
Figure 3-23. Bode plot showing gain and phase margins (with lead compensator, $K = 1$)
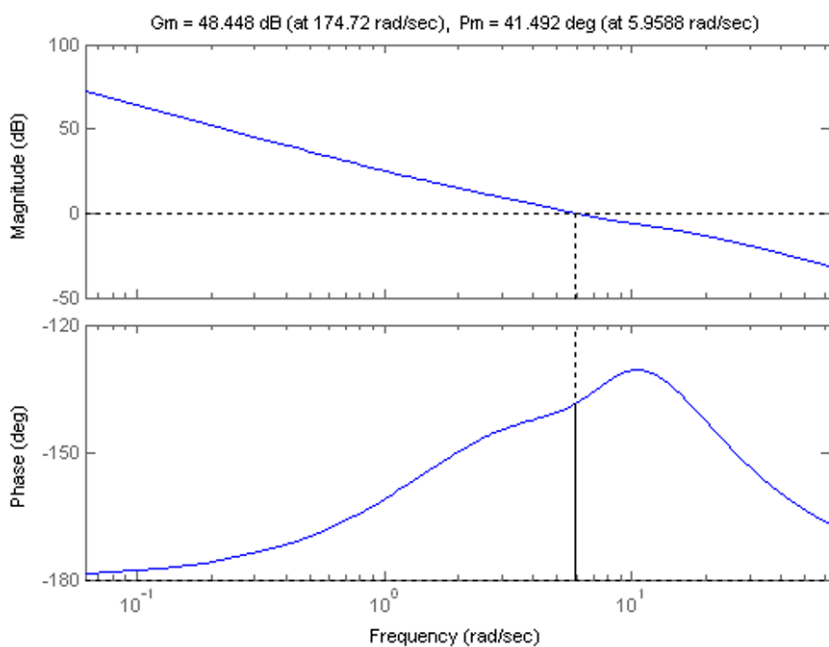
Figure 3-24. Bode plot showing gain and phase margins (with lead compensator, $K = 0.1$)
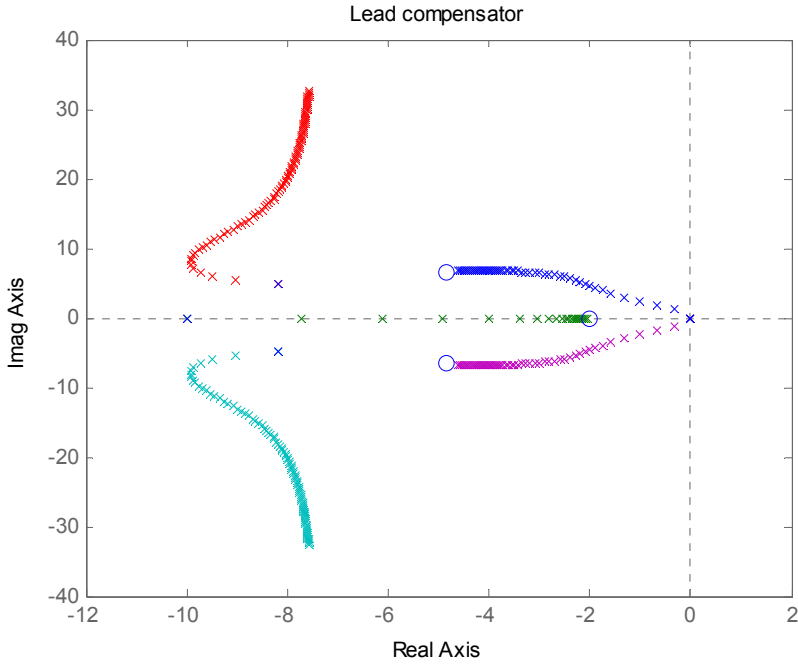
Figure 3-25. Root locus with lead compensator

3.9 SIMULATION OF PERFORMANCE WITH LEAD COMPENSATOR

To simulate the closed-loop system incorporating the lead compensator, the following state space extension can be used. The steering input is related to the sensor measurement by the following transfer function relation:

$$\delta(s) = -K \frac{T_n s + 1}{T_d s + 1} Y(s) \tag{3.35}$$

Hence, in the time domain,

$$T_d \dot{\delta} + \delta = -KT_n \dot{y} - Ky \tag{3.36}$$

Now

$$y = Cx$$

and

$$\dot{y} = CAx + CB_1\delta + CB_2\dot{\psi}_d$$

Since $CB_1 = 0$, $CB_2 = 0$, we have

$$T_d\dot{\delta} + \delta = -KT_nCAx - KCx \tag{3.37}$$

To find a state space model for the complete system including the lead compensator, define a fifth state

$$x_5 = \delta$$

Then, combining equation (3.37) and the previous linear time invariant model for the lateral system, the following extended state space representation can be used to represent the closed-loop dynamics:

$$\begin{bmatrix} \dot{x} \\ \dot{\delta} \end{bmatrix} = \begin{bmatrix} A & B_1 \\ -\dfrac{T_n}{T_d}KCA - \dfrac{1}{T_d}KC & -\dfrac{1}{T_d} \end{bmatrix} \begin{bmatrix} x \\ \delta \end{bmatrix} + \begin{bmatrix} B_2 \\ 0 \end{bmatrix} \dot{\psi}_d \tag{3.38}$$

3.10   ANALYSIS OF CLOSED-LOOP PERFORMANCE

3.10.1   Performance variation with vehicle speed

Bode plots of the transfer function of the open loop system from steering angle to yaw rate are shown in Figure 3-26 for various speeds. Speeds of 10, 20 and 30 m/s are shown, with the solid line representing 10 m/s, the dashed line respresenting 20 m/s and the solid line marked by '+'s representing 30 m/s. The plots show that the transfer function has less damping at higher speeds.
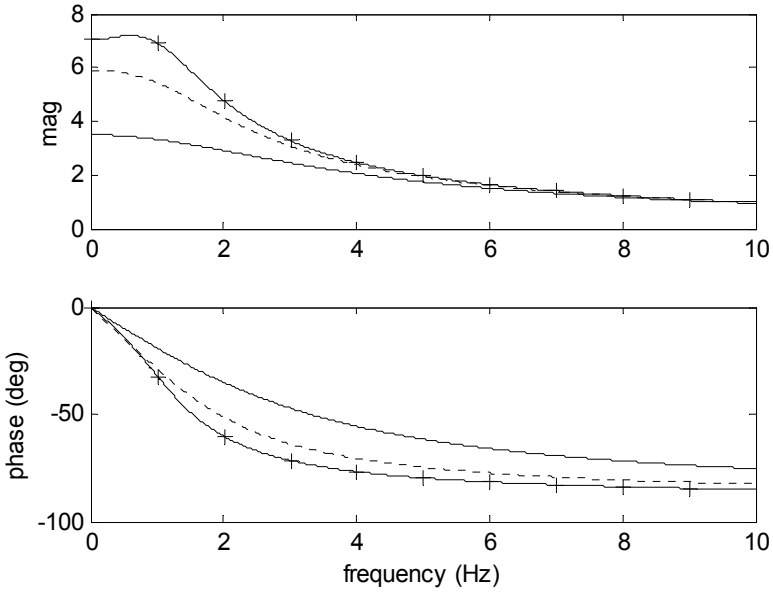
Figure 3-26. Transfer function from steering angle to yaw rate at various speeds
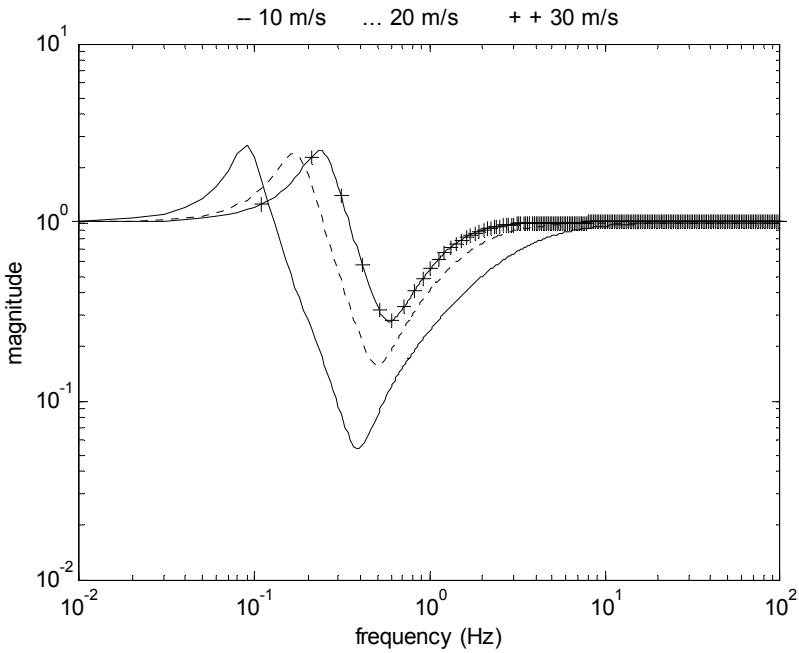
Figure 3-27. Closed-loop transfer function $\dot{\psi} / \dot{\psi}_{des}$ at different speeds (magnitude)

Using the same lead compensator discussed in section 3.7, Bode plots of the closed-loop transfer function $\dfrac{\dot{\psi}}{\dot{\psi}_d}$ are shown in Figure 3-27 and Figure 3-28. It can be seen that the closed-loop system also is better damped at lower speeds and has less damping at higher speeds. A value of $d_s = 2.0$ m was used for the sensor location.
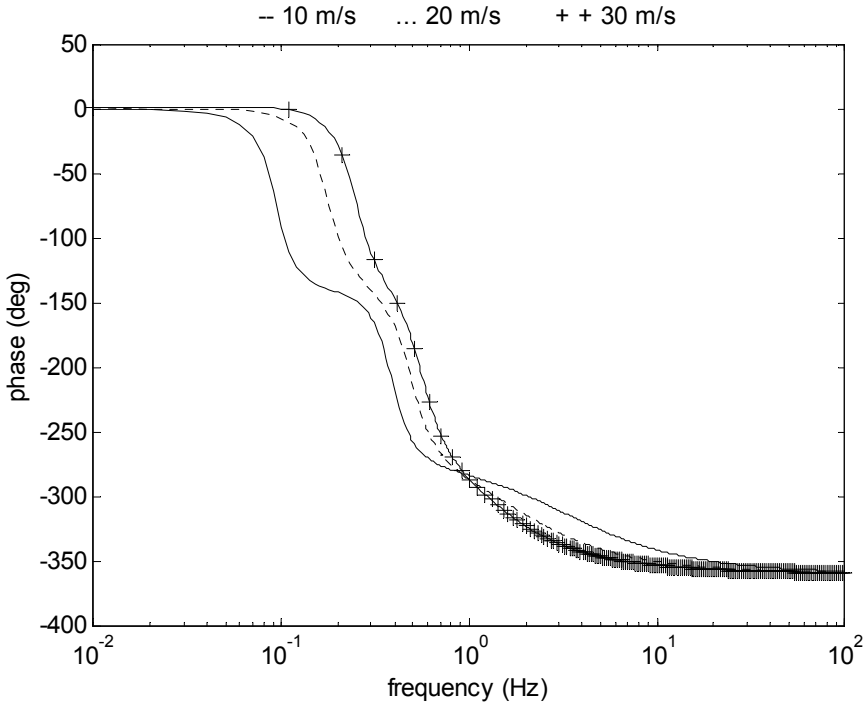
Figure 3-28. Closed-loop transfer function $\dot{\psi}/\dot{\psi}_{des}$ at different speeds (phase)

3.10.2   Performance variation with sensor location

Another important variable that influences closed-loop performance and robustness is the sensor location variable d_s. As seen in Figure 3-29 and Figure 3-30, as the variable d_s is increased, the system is better damped. This is also observed in the time response plots shown in Figure 3-31, where the higher values of d_s gives a better damped step response. A velocity of 30 m/s was used in the simulations.
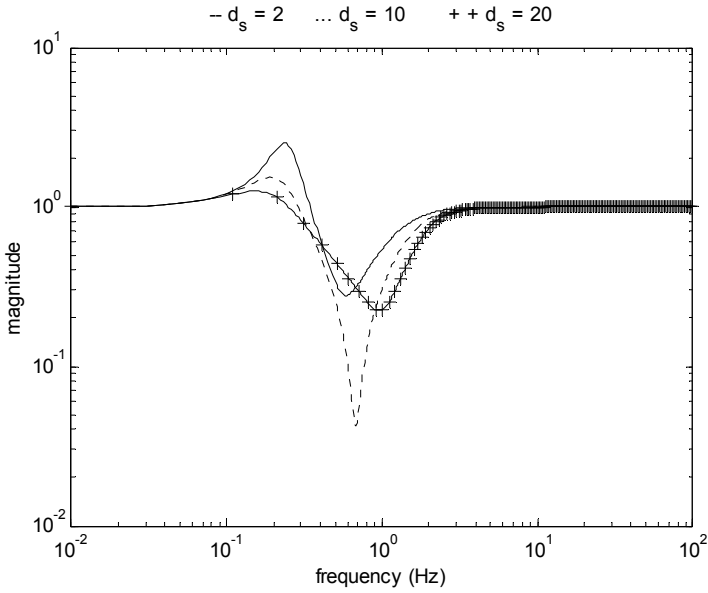
Figure 3-29. Closed-loop transfer function $\dot{\psi} / \dot{\psi}_{des}$ at different values of d_s (magnitude)
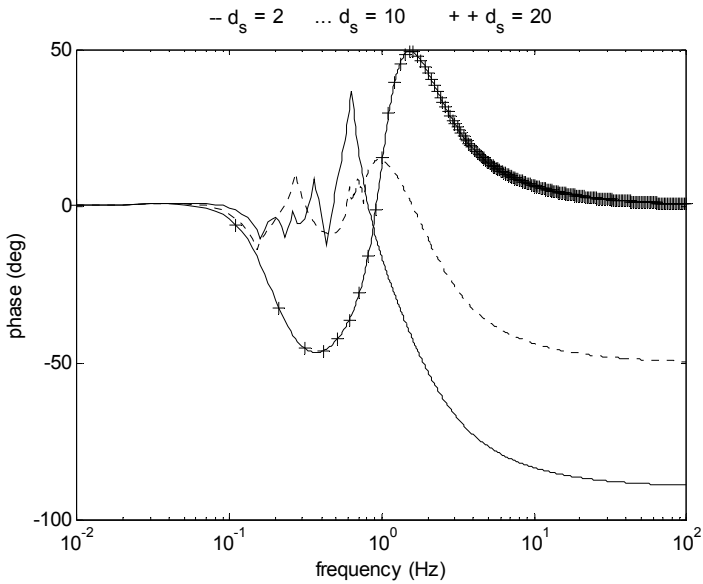
Figure 3-30. Closed-loop transfer function $\dot{\psi} / \dot{\psi}_{des}$ at different values of d_s (phase)
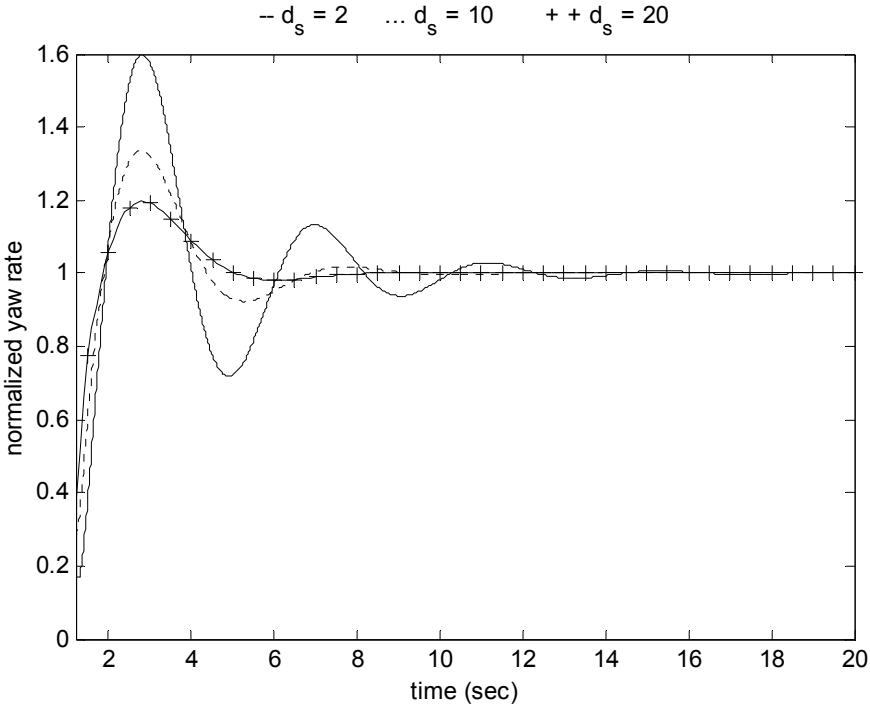
Figure 3-31. Step response of the transfer function $\dot{\psi} / \dot{\psi}_{des}$ at different values of d_s

3.11   COMPENSATOR DESIGN WITH LOOK-AHEAD SENSOR MEASUREMENT

In the previous section, it was seen that larger values of d_s provided better damping in the closed-loop transfer functions. Large values of d_s correspond to "look-ahead" measurement in which the lateral position error with respect to road is measured at a distance significantly ahead of the vehicle. Look ahead measurement is typical when a vision system is used for lateral position measurement. If magnetometers or differential GPS is used for position measurement, then look ahead sensing can be obtained by combining the on-vehicle lateral position measurement with vehicle yaw angle measurement so as to extrapolate the lateral position error to a look-ahead point. In other words, the look ahead distance d_s is artificially increased by measuring both e_1 and e_2 and then calculating $y = e_1 + d_s e_2$, instead of directly measuring $e_1 + d_s e_2$.

The open-loop transfer function $P(s) = \dfrac{y}{\delta}(s)$ is shown below in the Bode plot in Figure 3-32 for a longitudinal speed of 25 m/s, using $d_s = 15$ meters. From the Bode plot, it can be seen that this look-ahead system has much better phase characteristics than the original system discussed in section 7 which used $d_s = 2$ meters.
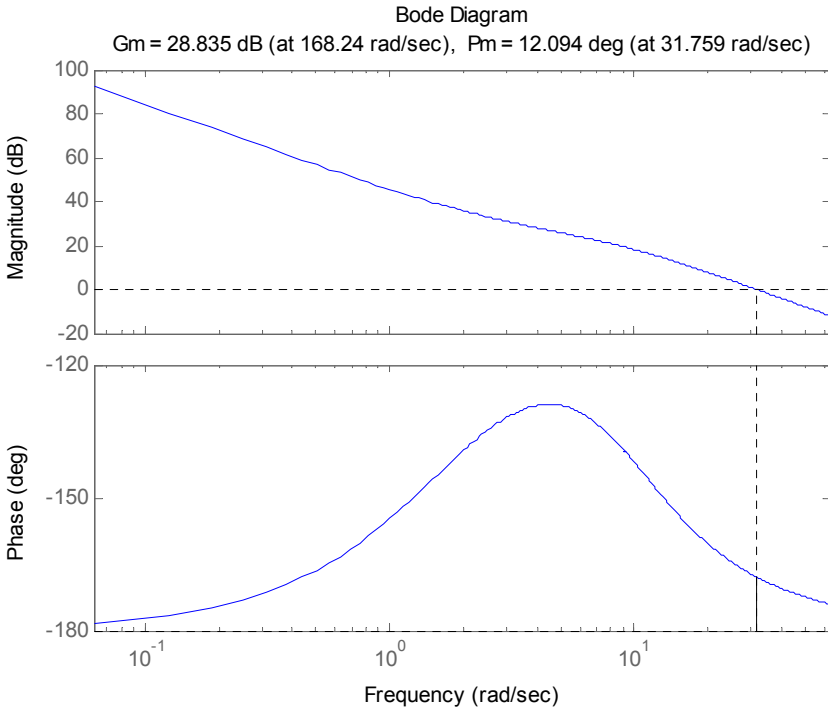
Figure 3-32. Gain & phase margins using proportional feedback with unit gain and a high value of d_s

Adequate phase margin can be obtained for this system simply by reducing the gain at intermediate frequencies appropriately so that crossover occurs at a lower frequency with adequate phase. A lag compensator would be able to adequately perform this task.

3.12   CHAPTER SUMMARY

This chapter discussed steering control system design for lateral lane keeping applications.

First, the use of full information in the form of state feedback was presented. The lateral system is controllable and can be stabilized by state feedback. On a straight road, with the use of a state feedback controller, all position and yaw errors were shown to converge to zero. On a circular road, however, these errors do not converge to zero with state feedback. The use of a feedforward term in the control system enables the position error to converge to zero. However, the yaw angle error will always have a steady state value, resulting in a steady state vehicle slip angle. Equations for the feedforward term and for the steady state slip angle were presented.

Next, control system design using output feedback was discussed. The output measurement was assumed to be lateral position measurement with respect to road center at a look-ahead point. Such a measurement is available from vision cameras and can also be obtained from other types of lateral position measurement systems. Nyquist plots were used to design a control system. It was shown that a proportional controller could stabilize the system if adequately large gains could be used. However, it would still suffer from poor phase margin. The use of a lead compensator together with proportional feedback ensures both adequate phase and gain margins and good performance. Another important result presented in the chapter was that by increasing the look-ahead distance at which lateral position measurement is made, a simple lag compensator would be adequate at providing good performance and robustness.

NOMENCLATURE

e_1 lateral position error with respect to road

e_2 yaw angle error with respect to road

A, B_1, B_2 matrices used in linear state space model for lateral dynamics

δ steering wheel angle

R turn radius of vehicle or radius of road

K feedback gain matrix for state feedback controller

δ_{ff} feedforward steering angle

δ_{ss} steady state steering angle

e_{2_ss} steady state yaw angle error

K_V understeer gradient

x_{ss}	steady state tracking errors on a curve
F_y	lateral tire force
F_{yf}	lateral tire force on front tires
F_{yr}	lateral tire force on rear tires
V_x	longitudinal velocity at c.g. of vehicle
$\dot{y}$	lateral velocity at c.g. of vehicle
m	total mass of vehicle
I_z	yaw moment of inertia of vehicle
ℓ_f	longitudinal distance from c.g. to front tires
ℓ_r	longitudinal distance from c.g. to rear tires
L	total wheel base ($\ell_f + \ell_r$)
ψ	yaw angle of vehicle in global axes
$\dot{\psi}$	yaw rate of vehicle
X, Y	global axes
α_f	slip angle at front tires
α_r	slip angle at rear tires
C_α	cornering stiffness of tire
F_z	normal force on tire
μ	tire-road friction coefficient
$\dot{\psi}_{des}$	desired yaw rate from road
β	slip angle at vehicle c.g. (center of gravity)
θ_V	velocity angle (angle of velocity vector with longitudinal axis)
θ_{Vf}	velocity angle at front wheels
θ_{Vr}	velocity angle at rear wheels
ϕ	road bank angle
γ	angle subtended by vehicle at center of circular vehicle path

$V_{\min}$ minimum longitudinal velocity

$V_{\max}$ maximum longitudinal velocity

P matrix used in Lyapunov function candidate

d_s look-ahead distance for lateral position measurement

$P(s)$, $C(s)$ plant and controller in unity feedback loop

Γ_s, Γ_{PC} contours used for Nyquist plot

REFERENCES

Ackermann, J. Guldner,J. Sienel,W. Steinhauser, R., Utkin, B.,” Linear and nonlinear controller design for robust automatic Steering”. *IEEE transactions on Control Systems Technology*, Vol. 3, No. 1, March 1995, pp132-142.

J. Ackermann, “Robust Decoupling, Ideal Steering Dynamics, and Yaw Stabilization of 4WS Cars,” *Automatica*, vol. 30, pp. 1761-1768, 1994.

Chen, C. and Tomizuka, M., “Vehicle Lateral Control on Automated Highways: A Back-stepping Approach”, *Proceedings of the IEEE Conference on Decision and Control*, December 1997.

Donath, M., Morellas, V., Morris, T. and Alexander, L., “Preview Based Control of a Tractor Trailer Using DGPS for Preventing Road Departure Accidents”, *Proceedings of the IEEE Conference on Intelligent Transportation Systems*, ITSC’97, Boston, MA, November, 1997.

Gillespie, T., *Fundamentals of Vehicle Dynamics*, Society of Automotive Engineers, 1992.

Guldner, J., Tan, H.-S. and Patwardhan, S., “Analysis of Automatic Steering Control for Highway Vehicle with Look-Down Lateral Reference Systems”, *Vehicle System Dynamics*, vol. 26, no. 4, pp.243-269, 1996.

Guldner, J., Sienel, W., Tan, H.S., Ackermann, J., Patwardhan, S. and Tilman Bunte “Robust automatic steering control for look-down reference systems with front and rear sensors”, *IEEE Transactions on Control Systems Technology*, vol.7, No.1, January 1999, pp2-11.

Hingwe, P. and Tomizuka, M., “Experimental evaluation of a chatter free sliding mode control for lateral control in AHS”, *Proceeding of the American Control Conference*, Vol. 5, p 3365-3369, 1997. IEEE, Piscataway, NJ, USA, 97CH36041.

Malik, J., “Development of Binocular Stereopsis for Vehicle Lateral Control, Longitudinal Control and Obstacle Detection, “*PATH MOU 257*, Final report.

Patwardhan, S., Tan, H.S and Guldner, J., “A General Framework for Automatic Steering Control: System Analysis,” *Proceedings of the American Control Conference*, Vol. 3, pp. 1598-1602, 1997.

Satyajit Patwardhan, Han-Shue Tan, Jurgen Guldner, “Lane Following During Backward Driving for Front Wheel Steered Vehicles”, *Proceeding of the American Control Conference*, Albuquerque, New Mexico, June 1997.

Huei Peng and Masayoshi Tomizuka, “Preview Control of Vehicle Lateral Guidance in Highway Automation”, *Journal of Dynamic Systems, Measurement, and Control*, Dec.1993, Vol,. 115 P679-685.

Kosecka, J., Blasi, R., Taylor, C.J. and Malik, J., "Vision Based Lateral Control of Vehicles," *Intelligent Transportation Systems*, November 1997, Boston.

R. Rajamani, H.S. Tan, B. Law and W.B. Zhang, "Demonstration of Integrated Lateral and Longitudinal Control for the Operation of Automated Vehicles in Platoons", *IEEE Transactions on Control Systems Technology,* Vol. 8, No. 4, pp. 695-708, July 2000.

R. Rajamani, C. Zhu and L. Alexander, "Lateral Control of a Backward Driven Front Steering Vehicle," *Control Engineering Practice*, to appear, 2003.

Tan, H.S., Guldner, J., Chen, C. and Patwardhan, S., "Lane Changing on Automated Highways with Look Down Reference Systems," *Proceedings of the IFAC Workshop on Advances in Automotive Control*, February 1998.

Taylor, C.J., Kosecka, J., Blasi, R. and Malik, J., "A Comparative Study of Vision-Based Lateral Control Strategies for Autonomous Highway Driving," *International Journal of Robotics Research*, Vol. 18, No. 5, pp. 442-453, May 1999.

Thorpe, C.E., Hebert, M., Kanade, T. and Shafer, S., "Vision and Navigation for the Carnegie-Mellon Navlab, "*IEEE Transactions on Pattern Analysis and Machine Intelligence,* Vol. 10, No. 3, pp. 362-373, May 1998.

Weber, J., Koller, D., Luong, Q.T. and Malik, J., "An Integrated Stereo Based Approach to Automatic Vehicle Guidance, "Proceedings of the International Conference on Computer Vision, Boston, June 1995.

Wong, J.Y., *Theory of Ground Vehicles*, Wiley-Interscience, ISBN 0-471-35461-9, Third Edition, 2001

W.B. Zhang and R.E. Parsons, "An Intelligent Roadway Reference System for Vehicle Lateral Guidance/Control," *Proceedings of the American Control Conference*, San Diego, CA, USA, pp. 281-286, 1990.

Chapter 4

LONGITUDINAL VEHICLE DYNAMICS

The control of longitudinal vehicle motion has been pursued at many different levels by researchers and automotive manufacturers. Common systems involving longitudinal control available on today's passenger cars include cruise control, anti-lock brake systems and traction control systems. Other advanced longitudinal control systems that have been the topic of intense research include radar-based collision avoidance systems, adaptive cruise control systems, individual wheel torque control with active differentials and longitudinal control systems for the operation of vehicles in platoons on automated highway systems.

   This chapter presents dynamic models for the longitudinal motion of the vehicle. The two major elements of the longitudinal vehicle model are the vehicle dynamics and the powertrain dynamics. The vehicle dynamics are influenced by longitudinal tire forces, aerodynamic drag forces, rolling resistance forces and gravitational forces. Models for these forces are discussed in section 4.1. The longitudinal powertrain system of the vehicle consists of the internal combustion engine, the torque converter, the transmission and the wheels. Models for these components are discussed in section 4.2.

4.1   LONGITUDINAL VEHICLE DYNAMICS

Consider a vehicle moving on an inclined road as shown in Figure 4-1. The external longitudinal forces acting on the vehicle include aerodynamic drag forces, gravitational forces, longitudinal tire forces and rolling resistance forces. These forces are described in detail in the sub-sections that follow.
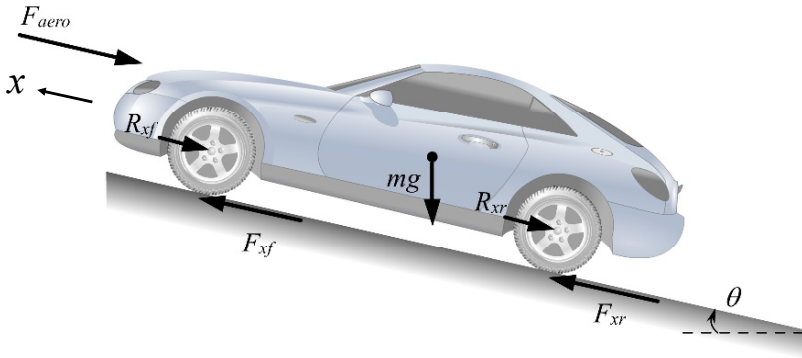
Figure 4-1. Longitudinal forces acting on a vehicle moving on an inclined road

A force balance along the vehicle longitudinal axis yields

$$m\ddot{x} = F_{xf} + F_{xr} - F_{aero} - R_{xf} - R_{xr} - mg\sin(\theta) \qquad (4.1)$$

where

F_{xf} is the longitudinal tire force at the front tires

F_{xr} is the longitudinal tire force at the rear tires

F_{aero} is the equivalent longitudinal aerodynamic drag force

R_{xf} is the force due to rolling resistance at the front tires

R_{xr} is the force due to rolling resistance at the rear tires

m is the mass of the vehicle

g is the acceleration due to gravity

θ is the angle of inclination of the road on which the vehicle is traveling

The angle θ is defined to be positive clockwise when the longitudinal direction of motion x is towards the left (as in Figure 4-1). It is defined to be positive counter clockwise when the longitudinal direction of motion x is towards the right.

4.1.1 Aerodynamic drag force

The equivalent aerodynamic drag force on a vehicle can be represented as

$$F_{aero} = \frac{1}{2}\rho C_d A_F (V_x + V_{wind})^2 \tag{4.2}$$

where ρ is the mass density of air, C_d is the aerodynamic drag coefficient, A_F is the frontal area of the vehicle, which is the projected area of the vehicle in the direction of travel, $V_x = \dot{x}$ is the longitudinal vehicle velocity, V_{wind} is the wind velocity (positive for a headwind and negative for a tailwind).

Atmospheric conditions affect air density ρ and hence can significantly affect aerodynamic drag. The commonly used standard set of conditions to which all aerodynamic test data are referred to are a temperature of 15 ^oC and a barometric pressure of 101.32 kPa (Wong, 2001). The corresponding mass density of air ρ may be taken as 1.225 kg/m^3.

The frontal area A_F is in the range of 79-84 % of the area calculated from the vehicle width and height for passenger cars (Wang, 2001). According to Wang, 2001, the following relationship between vehicle mass and frontal area can be used for passenger cars with mass in the range of 800-2000 kg:

$$A_f = 1.6 + 0.00056(m - 765) \tag{4.3}$$

The aerodynamic drag coefficient C_d can be roughly determined from a coast-down test (White and Korst, 1972). In a coast down test, the throttle angle is kept at zero and the vehicle is allowed to slow under the effects of aerodynamic drag and rolling resistance. Since there is neither braking nor throttle angle inputs, the longitudinal tire force under these conditions is small and can be assumed to be zero. The road is assumed to be level with $\theta = 0$ and the wind velocity V_{wind} is assumed to be zero.

Under these conditions, the longitudinal dynamics equation can be re-written as

$$-m\frac{dV_x}{dt} = \frac{1}{2}\rho V_x^2 A_F C_d + R_x \tag{4.4}$$

or

$$-\frac{dV_x}{\dfrac{\rho A_F C_d V_x^{\,2}}{2m} + \dfrac{R_x}{m}} = dt \qquad (4.5)$$

Integrating equation (4.5), assuming an initial longitudinal velocity of V_0, one obtains (White and Korst, 1972)

$$t = \left[\frac{2m^2}{\rho A_F C_d R_x}\right]^{1/2} \left\{ \tan^{-1}\left[V_o\left(\frac{\rho A_F C_d}{2R_x}\right)^{1/2}\right] - \tan^{-1}\left[V_x\left(\frac{\rho A_F C_d}{2R_x}\right)^{1/2}\right] \right\}$$

$$(4.6)$$

Let the total time for the vehicle to coast-down to a stop be $t = T$. Then, non-dimensionalizing using the parameter

$$\beta = V_o\left(\frac{\rho A_F C_d}{2R_x}\right)^{1/2} \qquad (4.7)$$

yields

$$\frac{V_x}{V_o} = \frac{1}{\beta}\tan\left[\left(1 - \frac{t}{T}\right)\tan^{-1}(\beta)\right] \qquad (4.8)$$

In equation (4.8), V_x and t can be measured and the initial velocity V_0 is known. Equation (4.8) represents a one-parameter family, in β, of curves in which non-dimensional velocity $\dfrac{V_x}{V_o}$ can be plotted against non-dimensional time $\dfrac{t}{T}$. From such a plot, the value of β for a particular vehicle can be obtained.

Once β has been obtained from equation (4.8), then the following algebraic expressions can be used to calculate the rolling resistance and drag coefficient (White and Korst, 1972):

$$C_d = \frac{2m\beta \tan^{-1}(\beta)}{V_o T \rho A_F} \tag{4.9}$$

$$R_x = \frac{V_o m \tan^{-1}(\beta)}{\beta T} \tag{4.10}$$

These algebraic expressions are obtained by substitution of the final and initial values of time and velocity in equation (4.6) (White and Korst, 1972).

4.1.2 Longitudinal tire force

The longitudinal tire forces F_{xf} and F_{xr} are friction forces from the ground that act on the tires.

Experimental results have established that the longitudinal tire force generated by each tire depends on

a) the slip ratio (defined below),
b) the normal load on the tire and
c) the friction coefficient of the tire-road interface.

The vertical force on a tire is called the tire normal load. The normal load on a tire

a) comes from a portion of the weight of the vehicle
b) is influenced by fore-aft location of the c.g., vehicle longitudinal acceleration, aerodynamic drag forces and grade of the road.
  Section 4.1.5 describes calculation of the tire normal loads.

Slip Ratio

The difference between the actual longitudinal velocity at the axle of the wheel V_x and the equivalent rotational velocity $r_{eff}\omega_w$ of the tire is called longitudinal slip. In other words, longitudinal slip is equal to $r_{eff}\omega_w - V_x$. *Longitudinal slip ratio* is defined as

$$\sigma_x = \frac{r_{eff}\omega_w - V_x}{V_x} \quad \text{during braking} \tag{4.11}$$

$$\sigma_x = \frac{r_{eff}\omega_w - V_x}{r_{eff}\omega_w} \quad \text{during acceleration} \tag{4.12}$$

An explanation of why longitudinal tire force depends on the slip ratio is provided in section 4.1.3. A more complete understanding of the influence of all three variables – slip ratio, normal force and tire-road friction coefficient – on tire force can be obtained by reading Chapter 13 of this book.

If the friction coefficient of the tire-road interface is assumed to be 1 and the normal force is assumed to be a constant, the typical variation of longitudinal tire force as a function of the slip ratio is shown in Figure 4-2.

As can be seen from the figure, in the case where longitudinal slip ratio is small (typically less than 0.1 on dry surface), as it is during normal driving, the longitudinal tire force is found to be proportional to the slip ratio. The tire force in this small-slip region can then be modeled as

$$F_{xf} = C_{\sigma f}\sigma_{xf} \tag{4.13}$$

$$F_{xr} = C_{\sigma r}\sigma_{xr} \tag{4.14}$$

where $C_{\sigma f}$ and $C_{\sigma r}$ are called the longitudinal tire stiffness parameters of the front and rear tires respectively.
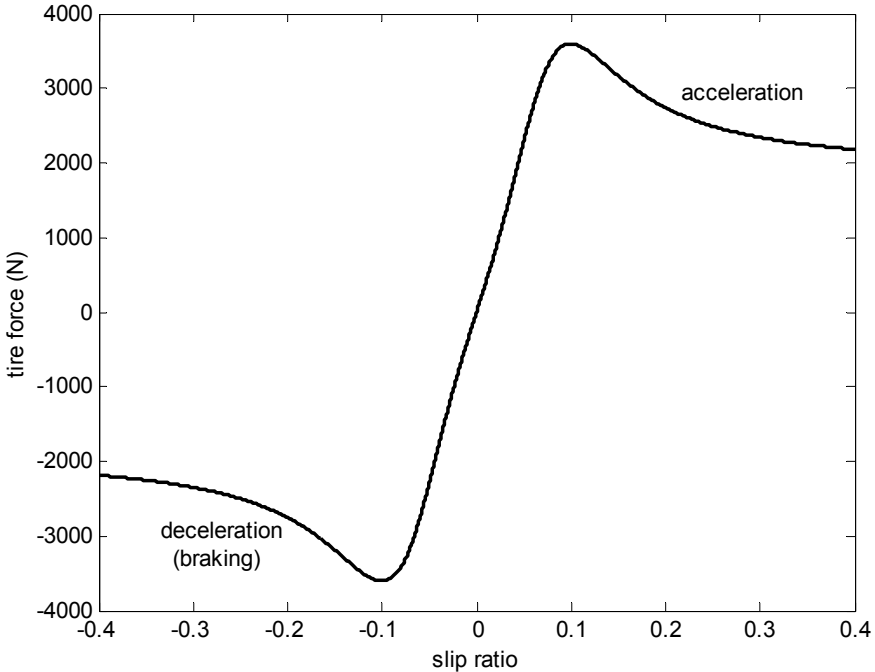
Figure 4-2. Longitudinal tire force as a function of slip ratio

If the longitudinal slip ratio is not small or if the road is slippery, then a nonlinear tire model needs to be used to calculate the longitudinal tire force. The Pacejka "Magic Formula" model or the Dugoff tire model can be used to model tire forces in this case (Pacejka and Bakker, 1993, Pacejka, 1996 and Dugoff, et. al., 1969). These models are discussed in detail in Chapter 13 of this book.

4.1.3   Why does longitudinal tire force depend on slip ?

A rough explanation of why the longitudinal tire force depends on slip ratio can be seen from Figure 4-3.

The lower portion of Figure 4-3 shows a schematic representation of deformation of the tread elements of the tire. The tread elements are modeled as a series of independent springs that undergo longitudinal deformation and resist with a constant longitudinal stiffness. Such a model of the tire is called a "brush" model or an "elastic foundation" model (Pacejka, 1991, Dixon, 1991).

Let the longitudinal velocity of the wheel be V_x and its rotational velocity be ω_w. Then the net velocity at the treads, as shown in Figure 4-3 is $r_{eff}\omega_w - V_x$.

The tire on a vehicle deforms due to the normal load on it and makes contact with the road over a non-zero footprint area called the contact patch (see Figure 13-1 of this book).

First, consider the case where the wheel is a driving wheel, for example, the front wheels in a front-wheel drive vehicle. In this case, since the wheel is a driving wheel, $r_{eff}\omega_w > V_x$. Hence the net velocity of the treads is in a direction opposite to that of the longitudinal velocity of the vehicle. Assume that the slip $r_{eff}\omega_w - V_x$ is small. Then there is a region of the contact patch where the tread elements do not slide with respect to the ground (called the "static region" in Figure 4-3). As the tire rotates and a tread element enters the contact patch, its tip which is in contact with the ground must have zero velocity. This is because there is no sliding in the static region of the contact patch. The top of the tread element moves with a velocity of $R\omega_w - V_x$. Hence the tread element will bend forward as shown in Figure 4-3 and the bending will be in the direction of the longitudinal direction of motion of the vehicle. The maximum bending deflection of the tread is proportional to the slip velocity $r_{eff}\omega_w - V_x$ and to the time duration for which the tread element remains in the contact patch. The time duration in the contact patch is inversely proportional to the rotational velocity $r_{eff}\omega_w$. Hence the maximum

deflection of the tread element is proportional to the ratio of slip to absolute velocity i.e. proportional to the slip ratio $\dfrac{r_{eff}\omega_w - V_x}{r_{eff}\omega_w}$.

Direction of longitudinal motion

$r_{eff}\,\omega_w$

V_x

$r_{eff}\,\omega_w$ - V_x

bristles in brush model for tire

Contact patch

start of contact patch

end of contact patch

static region   sliding region
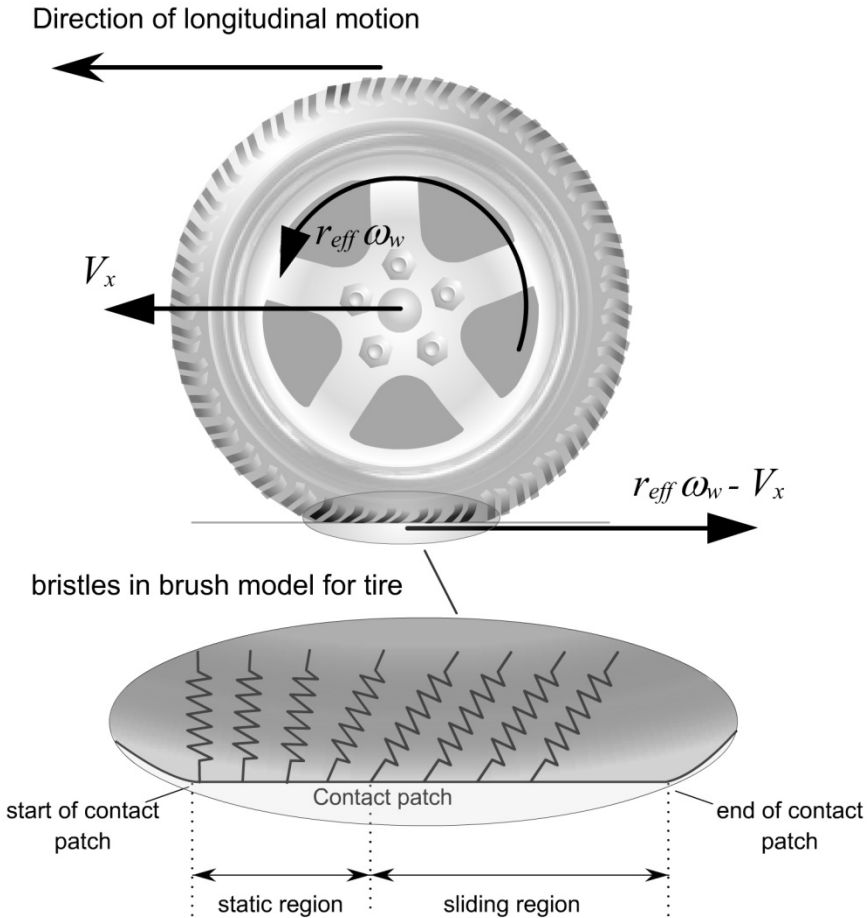
Figure 4-3. Longitudinal force in a driving wheel

Thus the net longitudinal force on the tires from the ground is in the forward direction in the case of a driving wheel and is proportional to the slip ratio of the wheel.

In the case where the tire is on a driven wheel, the longitudinal velocity is greater than the rotational velocity $(V_x > r_{eff}\omega_w)$. In this case the net velocity at the treads is in the forward direction and hence the bristles on the tire will bend backwards. Hence the tire force on the driven wheel is in a

direction opposite to that of the vehicle's longitudinal velocity. Again, for small slip ratio, the tire force will be proportional to slip ratio.

4.1.4 Rolling resistance

As the tire rotates, both the tire and the road are subject to deformation in the contact patch. The road is of course much stiffer and so its deformation can be neglected. But the tire is elastic and new material from the tire continuously enter the contact patch as the tire rotates. Due to the normal load, this material is deflected vertically as it goes through the contact patch and then springs back to its original shape after it leaves the contact patch. Due to the internal damping of the tire material, the energy spent in deforming the tire material is not completely recovered when the material returns to its original shape. This loss of energy can be represented by a force on the tires called the rolling resistance that acts to oppose the motion of the vehicle.

The loss of energy in tire deformation also results in a non-symmetric distribution of the normal tire load over the contact patch. When the tires are static (not rotating), then the distribution of the normal load F_z in the contact patch is symmetric with respect to the center of the contact patch. However, when the tires are rotating, the normal load distribution is non-symmetric, as shown in Figure 4-4.

Imagine the tire being represented by a series of independent springs which resist vertical deformation, as shown in Figure 4-4. As each spring element enters the contact patch, it undergoes vertical deformation. The vertical deformation of the spring reaches its maximum at the center of the contact patch and goes back to zero at the end of the contact patch. If these springs were purely elastic and had no viscous dissipation, then the normal load on the contact patch would be symmetric. But, due to viscous dissipation, the force required to compress the springs in the first half of the contact patch is not fully recovered in the second half of the contact patch. Hence the normal load is not symmetric but is larger in the forward half of the contact patch. This asymmetric normal load distribution is shown in Figure 4-4.

Hence, when the tires are rotating, the resultant normal load F_z moves forward by a distance Δx, as shown in Figure 4-5.
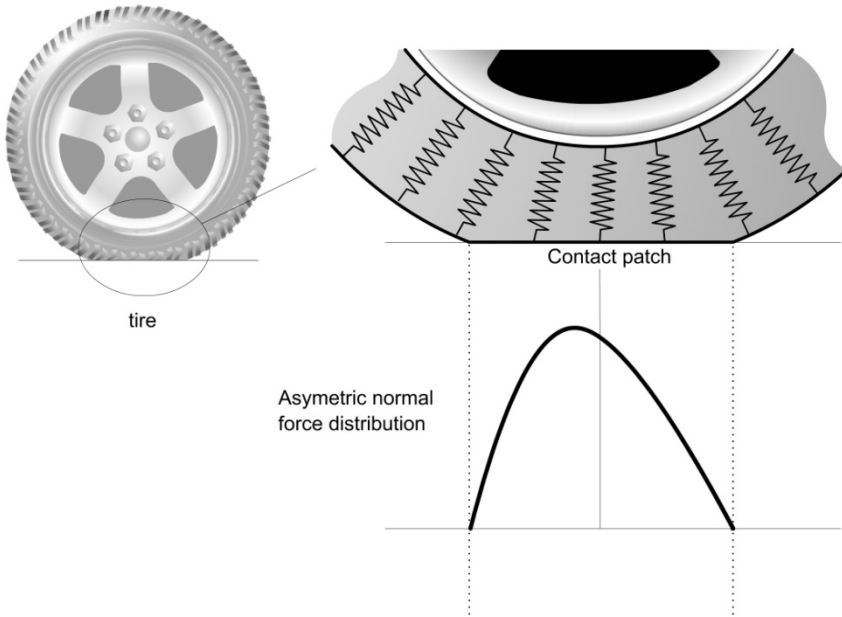
Figure 4-4. Asymmetric normal load distribution on the contact patch

Typically, the rolling resistance is modeled as being roughly proportional to the normal force on each set of tires i.e.

$$R_{xf} + R_{xr} = f(F_{zf} + F_{zr})$$ (4.15)

where f is the rolling resistance coefficient. To see why this approximation is made for the rolling resistance force, consider the action of the normal load and rolling resistance forces shown in Figure 4-5.

The moment $F_z(\Delta x)$ due to the offset normal load is balanced by the moment due to the rolling resistance force $R_x r_{stat}$, where r_{stat} is the statically loaded radius of the tire. Hence

$$R_x = \frac{F_z(\Delta x)}{r_{stat}}$$ (4.16)

The variable Δx is not easily measured and therefore R_x is simply modeled as being proportional to F_z with a proportionality constant f.
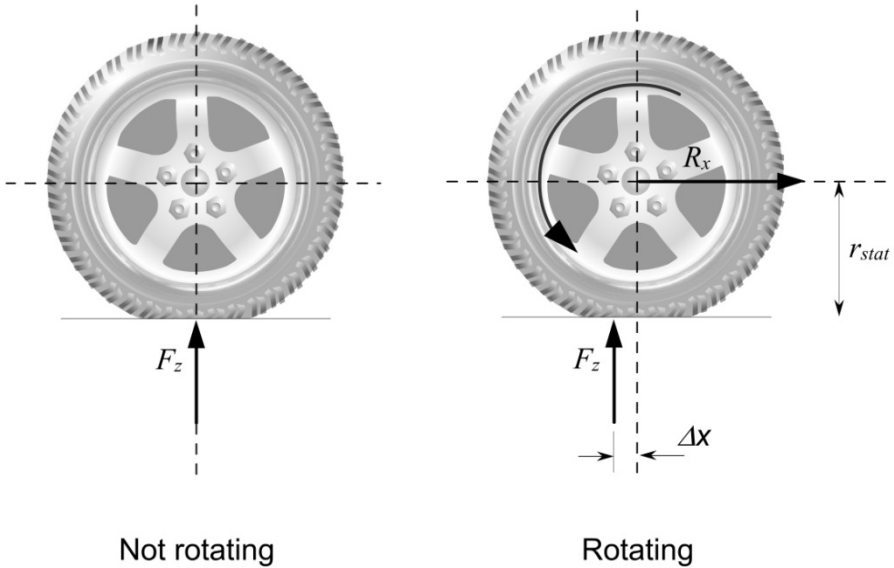
Figure 4-5. Description of rolling resistance

The value of the rolling resistance coefficient f varies in the range 0.01 to 0.04. A value of 0.015 is typical for passenger cars with radial tires (Wong, 2001).

4.1.5 Calculation of normal tire forces

In addition to the total weight of the vehicle, the normal load on the tires is influenced by

a) fore-aft location of the c.g.
b) longitudinal acceleration of the vehicle
c) aerodynamic drag forces on the vehicle
d) grade (inclination) of the road

The normal force distribution on the tires can be determined by assuming that the net pitch torque on the vehicle is zero. In other words, the pitch angle of the vehicle is assumed to have reached a steady state value. Define the following variables

h the height of the c.g. of the vehicle

h_{aero} the height of the location at which the equivalent aerodynamic force acts

ℓ_f the longitudinal distance of the front axle from the c.g. of the vehicle

ℓ_r the longitudinal distance of the rear axle from the c.g. of the vehicle

r_{eff} the effective radius of the tires
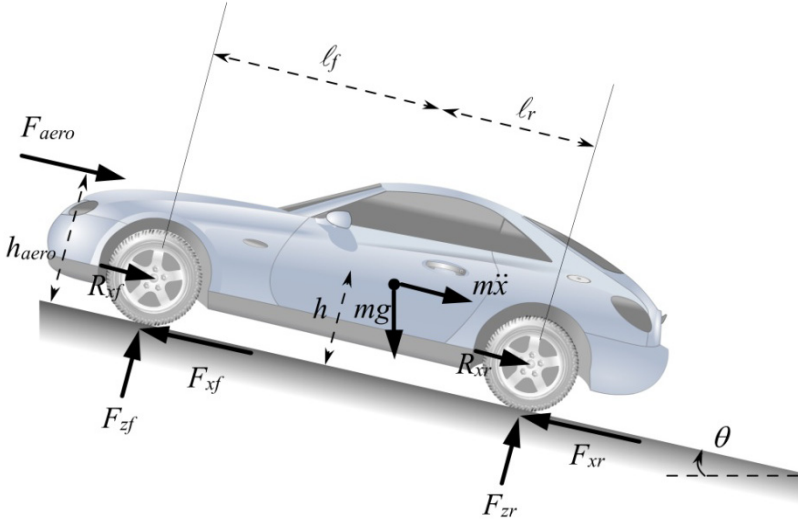
Figure 4-6. Calculation of normal tire loads

Taking moments about the contact point of the rear tire in Figure 4-6

$$F_{zf}(\ell_f + \ell_r) + F_{aero}h_{aero} + m\ddot{x}h + mgh\sin(\theta) - mg\ell_r\cos(\theta) = 0$$

Solving for F_{zf} yields

$$F_{zf} = \frac{-F_{aero}h_{aero} - m\ddot{x}h - mgh\sin(\theta) + mg\ell_r\cos(\theta)}{\ell_f + \ell_r} \qquad (4.17)$$

Taking moments about the contact point of the front tire

$$F_{zr}(\ell_f + \ell_r) - F_{aero}h_{aero} - m\ddot{x}h - mgh\sin(\theta) - mg\ell_f\cos(\theta) = 0$$

Solving for F_{zr} yields

$$F_{zr} = \frac{F_{aero}h_{aero} + m\ddot{x}h + mgh\sin(\theta) + mg\ell_f\cos(\theta)}{\ell_f + \ell_r} \qquad (4.18)$$

Hence, as the vehicle accelerates, the normal load on the front tires decreases whereas the normal load on the rear tires increases.

4.1.6   Calculation of effective tire radius

The effective tire radius r_{eff} is the value of the radius which relates the rotational angular velocity of the wheel ω_w to the linear longitudinal velocity of the wheel V_{eff} as it moves through the contact patch of the tire with the ground.
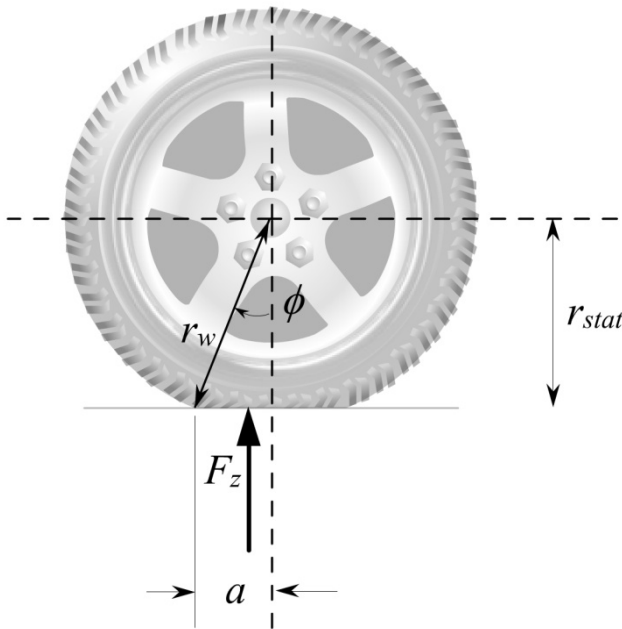
Figure 4-7. Calculation of effective tire radius

If the rotational speed of the wheel is ω_w, the linear equivalent of the rotational speed of the tire is $V_{eff} = r_{eff}\omega_w$ (Kiencke and Nielsen, 2000).

As shown in Figure 4-7, let $2a$ be the longitudinal length of the contact patch and ϕ be the angle made by the radial line joining the center of the wheel to the end of the contact patch. Let t be the duration of time taken by an element of the tire to move through half the contact patch. Then (Kiencke and Nielsen, 2000)

$$V_{eff} = r_{eff}\omega_w = \frac{a}{t} \tag{4.19}$$

At the same time, the rotational speed of the wheel is

$$\omega_w = \frac{\phi}{t} \qquad (4.20)$$

Hence

$$r_{eff} = \frac{a}{\phi} \qquad (4.21)$$

The static tire radius is the difference between the undeformed radius of the tire r_w and the static vertical deflection of the tire:

$$r_{stat} = r_w - \frac{F_z}{k_t} \qquad (4.22)$$

where k_t is the vertical tire stiffness.

From the geometric relationships seen in Figure 4-7

$$r_{stat} = r_w \cos(\phi) \qquad (4.23)$$

$$a = r_w \sin(\phi) \qquad (4.24)$$

Hence the effective tire radius is given by

$$r_{eff} = \frac{\sin\left\{\cos^{-1}\left(\dfrac{r_{stat}}{r_w}\right)\right\}}{\cos^{-1}\left(\dfrac{r_{stat}}{r_w}\right)} r_w \qquad (4.25)$$

Note that since $r_{eff} = \dfrac{\sin(\phi)}{\phi} r_w$, $r_{eff} < r_w$ and that since $r_{eff} = \dfrac{\tan(\phi)}{\phi} r_{stat}$, $r_{eff} > r_{stat}$. Thus

$$r_{stat} < r_{eff} < r_w \tag{4.26}$$

4.2 DRIVELINE DYNAMICS

In the previous section, we saw that the longitudinal motion equation for the vehicle is of the type

$$m\ddot{x} = F_{xf} + F_{xr} - R_{xf} - R_{xr} - F_{aero} - mg\sin(\theta) \tag{4.27}$$

where F_{xf} and F_{xr} are the longitudinal tire forces. The longitudinal tire forces on the driving wheels are the primary forces that help the vehicle move forward. These forces depend on the difference between the rotational wheel velocity $r_{eff}\omega_w$ and the vehicle longitudinal velocity $\dot{x}$. The wheel rotational velocity ω_w is highly influenced by the driveline dynamics of the vehicle. The major components of a driveline are shown in Figure 4-8 below. The flow of power and the direction of loads on the components is shown in Figure 4-9.
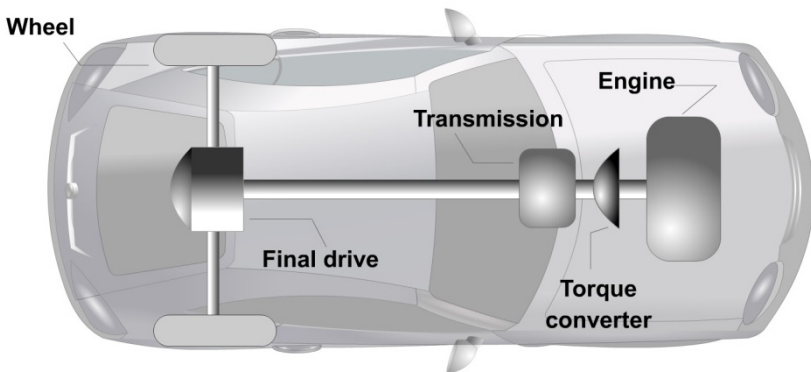
Figure 4-8. Components of a front-wheel drive vehicle powertrain
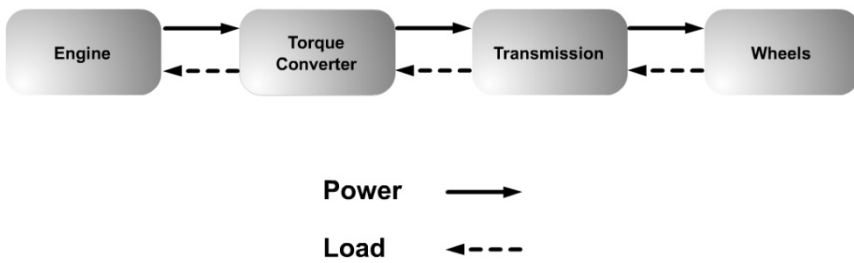
Figure 4-9. Power flow and loads in vehicle drivetrain

4.2.1   Torque converter

The torque converter is a type of fluid coupling that connects the engine to the transmission. If the engine is turning slowly, such as when the car is idling at a stoplight, the amount of torque passed through the torque converter is very small, so keeping the car still requires only a light pressure on the brake pedal.

In addition to allowing the car come to a complete stop without stalling the engine, the torque converter gives the car more torque when it accelerates out of a stop. Modern torque converters can multiply the torque of the engine by two to three times. This effect only happens when the engine is turning much faster than the transmission. At higher speeds, the transmission catches up to the engine, eventually moving at *almost* the same speed. Ideally, though, the transmission should move at exactly the same speed as the engine, because the difference in speed wastes power. To counter this effect, many cars have a torque converter with a lockup clutch. When the two halves of the torque converter get up to speed, this clutch locks them together, eliminating the slippage and improving efficiency.

The torque converter is typically unlocked as soon as the driver removes his/her foot from the accelerator pedal and steps on the brakes. This allows the engine to keep running even if the driver brakes to slow the wheels down.

The major components of the torque converter are a pump, a turbine and the transmission fluid. The fins that make up the pump of the torque converter are attached to the flywheel of the engine. The pump therefore turns at the same speed as the engine. The turbine is connected to the transmission and causes the transmission to spin at the same speed as the turbine, this basically moves the car. The coupling between the turbine and the pump is through the transmission fluid. Torque is transmitted from the pump to the turbine of the torque converter.

Torque converter modeling (both physically based and input-output data based) has been studied by various researchers (see, for example, Kotwicki, 1982, Tugcu, et. al., 1986, Runde, 1986). The static model of Kotwicki (1982) is desirable for control because of its simplicity. It has a reasonable agreement with experimental data for a fairly wide range of operating conditions. This model is a quadratic regression fit of the data from a simple experiment, which involves measuring only the input and output speeds and torques of the torque converter. For the torque converter in Kotwicki (1982), the model expressions are as outlined below.

Let T_p and T_t be pump and turbine torques and $\omega_p (= \omega_e)$ and ω_t be pump and turbine speeds. For converter mode (i.e. $\omega_t / \omega_p < 0.9$), the pump and turbine torques are given by

$$T_p = 3.4325es - 3\omega_p^2 + 2.2210\text{x}10^{-3}\omega_p\omega_t - 4.6041\text{x}10^{-3}\omega_t^2$$

(4.28)

$$T_t = 5.7656\text{x}10^{-3}\omega_p^2 + 0.3107\text{x}10^{-3}\omega_p\omega_t - 5.4323\text{x}10^{-3}\omega_t^2$$

(4.29)

For fluid coupling mode (i.e. $\omega_t / \omega_p \geq 0.9$), the pump and turbine torques are given by

$$T_p = T_t$$
$$= -6.7644\text{x}10^{-3}\omega_p^2 + 32.0024\text{x}10^{-3}\omega_p\omega_t - 25.2441\text{x}10^{-3}\omega_t^2$$

(4.30)

The above equations assume SI units.

The input-output schematic of the torque converter model is shown below in Figure 4-10.

Figure 4-10. Schematic of torque converter model

When the torque converter is locked, as in the third or higher gears, the pump torque is equal to the turbine torque. The pump torque can be calculated in this case by calculating the load on the engine from the wheels and the transmission. This calculation is shown in section 5.5.1.

4.2.2   Transmission dynamics

Let R be the gear ratio of the transmission. The value of R depends on the operating gear and includes the final gear reduction in the differential. In general, $R < 1$ and increases as the gear shifts upwards.

The schematic of the transmission model is shown in Figure 4-11. The turbine torque T_t is the input torque to the transmission. Let the torque transmitted to the wheels be T_{wheels}. At steady state operation under the first, second or higher gears of the transmission, the torque transmitted to the wheels is

$$T_{wheels} = \frac{1}{R} T_t \qquad\qquad (4.31)$$

The relation between the transmission and wheel speeds is

$$\omega_t = \frac{1}{R} \omega_w \qquad\qquad (4.32)$$
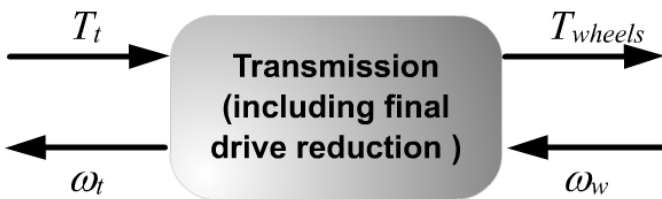
Figure 4-11. Schematic of transmission model

The steady state gear ratio R depends on the operating gear. The operating gear is determined by a gear shift schedule that depends on both the transmission shaft speed and the throttle opening (with fully open throttle angle being counted as 90 degrees). Figure 4-12 shows example up shift and down shift schedules for a 5-speed automatic transmission. Note that the up-shift for each gear change occurs at higher speeds as the throttle angle input from the driver is higher (i.e. the driver is demanding higher torque).
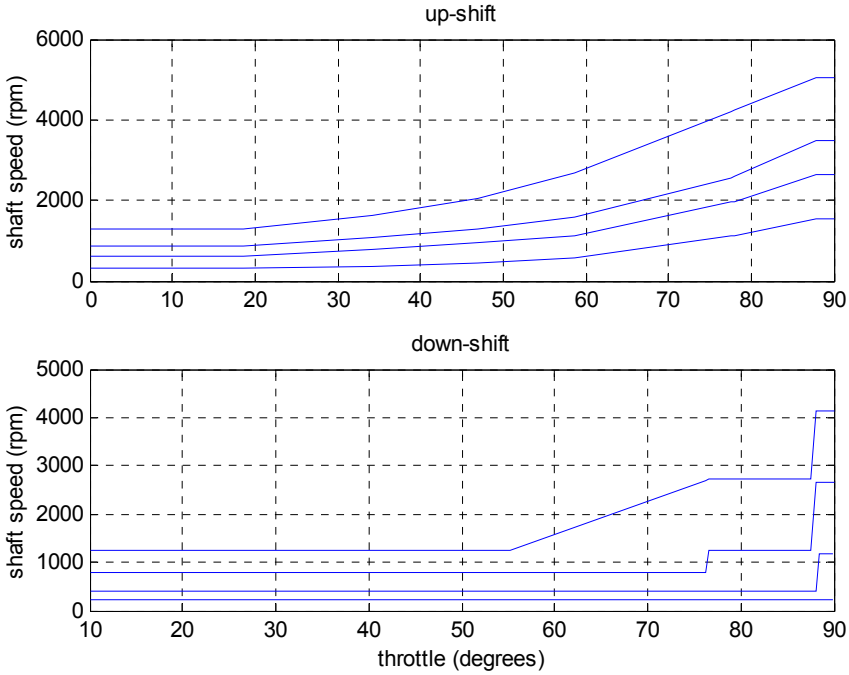
Figure 4-12. Example up shift and down shift schedules for an automatic transmission

Equations describing the dynamics *during* a gear change are complex and can be found in Cho and Hedrick, 1989. An alternative is to replace equations (4.31) and (4.32) by the following 1st order equations *during* a gear change:

$$\tau \dot{T}_{wheel} + T_{wheel} = \frac{1}{R} T_t \tag{4.33}$$

$$\tau \dot{\omega}_t + \omega_t = \frac{\omega_w}{R} \tag{4.34}$$

Equations (4.33) is initialized with $T_{wheel} = 0$ at the instant that the gear change is initiated. R is the gear ratio at the new gear into which the transmission shifts. ω_t is initialized at $\frac{1}{R_{old}} \omega_w$ where R_{old} is the old gear ratio.

The gear change is assumed to be complete when T_{wheel} and ω_t converge to $\dfrac{1}{R}T_t$ and $\dfrac{\omega_w}{R}$ within a threshold value. Once the gear change is complete, equations (4.31) and (4.32) can be used again to represent the transmission.

4.2.3   Engine dynamics

The engine rotational speed dynamics can be described by the equation

$$I_e \dot{\omega}_e = T_i - T_f - T_a - T_p \tag{4.35}$$

where T_i is the engine combustion torque, T_f are the torque frictional losses, T_a is the accessory torque and T_p is the pump torque and represents the load on the engine from the torque converter.

Using the notation

$$T_e = T_i - T_f - T_a \tag{4.36}$$

to represent the net engine torque after losses, we have

$$I_e \dot{\omega}_e = T_e - T_p \tag{4.37}$$

The net engine torque T_e depends on the dynamics in the intake and exhaust manifold of the engine and on the accelerator input from the driver. Engine models are discussed in Chapter 9 for both SI and diesel engines and describe how T_e can be calculated. T_p is pump torque and is obtained from equations (4.28) and (4.30) of the torque converter.

The input-output schematic of the engine inertia model is shown in Figure 4-13.
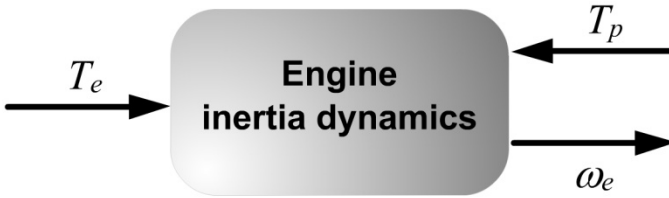
Figure 4-13. Schematic of engine inertia model

4.2.4 Wheel Dynamics

For the driving wheels (for example, the front wheels in a front-wheel driven car), the dynamic equation for the wheel rotational dynamics is

$$I_w \dot{\omega}_{wf} = T_{wheel} - r_{eff} F_{xf} \tag{4.38}$$

where ω_{wf}, T_{wheel} and r_{eff} have been defined earlier and F_{xf} is the longitudinal tire force from the front wheels.

For the non-driven wheels

$$I_w \dot{\omega}_{wr} = -r_{eff} F_{xr} \tag{4.39}$$

where F_{xr} is the longitudinal tire force from the rear wheels.

Figure 4-14. Schematic of wheel dynamics

The total longitudinal tire force is given by

$$F_x = F_{xf} + F_{xr} \tag{4.40}$$

Each of the two tire force terms F_{xf} and F_{xr} is a function of the slip ratio at the front and rear wheels respectively (see section 4.1.2). For

calculation of the slip ratio at the front wheels, ω_{wf} should be used, while for the calculation of the slip ratio at the rear wheels ω_{wr} should be used.

Table 4-1. Summary of longitudinal vehicle dynamic equations

Summary of longitudinal vehicle dynamic equations		
Primary Vehicle Dynamic Equation $$m\ddot{x} = F_{xf} + F_{xr} - F_{aero} - R_{xf} - R_{xr} - mg\sin(\theta)$$		
1	Front longitudinal tire force	$F_{xf} = C_{\sigma f}\sigma_{xf}$ where $$\sigma_{xf} = \frac{r_{eff}\omega_{wf} - \dot{x}}{\dot{x}} \quad \text{during braking}$$ $$\sigma_{xf} = \frac{r_{eff}\omega_{wf} - \dot{x}}{r_{eff}\omega_{wf}} \quad \text{during acceleration}$$
2	Rear longitudinal tire force	$F_{xr} = C_{\sigma r}\sigma_{xr}$ where $$\sigma_{xr} = \frac{r_{eff}\omega_{wr} - \dot{x}}{\dot{x}} \quad \text{during braking}$$ $$\sigma_{xr} = \frac{r_{eff}\omega_{wr} - \dot{x}}{r_{eff}\omega_{wr}} \quad \text{during acceleration}$$
3	Rolling resistance	$R_{xf} + R_{xr} = f(F_{zf} + F_{zr})$ where the front normal tire force is $$F_{zf} = \frac{-F_{aero}h_{aero} - m\ddot{x}h - mgh\sin(\theta) + mg\ell_r\cos(\theta)}{\ell_f + \ell_r}$$ and the rear normal tire force is $$F_{zr} = \frac{F_{aero}h_{aero} + m\ddot{x}h + mgh\sin(\theta) + mg\ell_f\cos(\theta)}{\ell_f + \ell_r}$$
4	Aerodynamic drag force	$$F_{aero} = \frac{1}{2}\rho C_d A_F(\dot{x} + V_{wind})^2$$

4.3   CHAPTER SUMMARY

This chapter presented dynamic equations for the longitudinal motion of the vehicle. The two major elements of the longitudinal dynamic model were the vehicle dynamics and the driveline dynamics.

The vehicle dynamic equations were strongly influenced by longitudinal tire forces, aerodynamic drag forces, rolling resistance forces and gravitational forces. These forces were discussed in detail and mathematical models for each of these forces were described.

The longitudinal driveline system of the vehicle consisted of the internal combustion engine, the torque converter, the transmission and the wheels. Dynamic models for these components were discussed.

NOMENCLATURE

F_{xf}	longitudinal tire force at the front tires
F_{xr}	longitudinal tire force at the rear tires
F_{aero}	equivalent longitudinal aerodynamic drag force
R_{xf}	force due to rolling resistance at the front tires
R_{xr}	force due to rolling resistance at the rear tires
m	mass of the vehicle
g	acceleration due to gravity
θ	angle of inclination of the road on which the vehicle is traveling
ω_w	angular velocity of wheel
r_{eff}	effective radius of rotating tire
r_{stat}	static radius of tire
r_w	radius of undeformed tire
F_z	normal load on tire
Δx	longitudinal distance from center of contact patch at which equivalent normal load acts
a	half-length of contact patch
ϕ	subtended half-angle of contact patch

V_x	longitudinal vehicle velocity
V_{wind}	wind velocity
V_{eff}	effective linear velocity of rotating tire $(=r_{eff}\,\omega_w)$
ρ	mass density of air
C_d	aerodynamic drag coefficient
A_F	frontal area of the vehicle
β	parameter related to aerodynamic drag coefficient calculation
σ_x	slip ratio
h	height of c.g. of vehicle
h_{aero}	height at which equivalent aerodynamic drag force acts
ℓ_f	the longitudinal distance of the front axle from the c.g. of the vehicle
ℓ_r	the longitudinal distance of the rear axle from the c.g. of the vehicle
ω_e	rotational engine speed
ω_t	angular speed of turbine on torque converter
T_p	pump torque
T_t	turbine torque
T_{wheels}	torque transmitted to the wheels
ω_w	angular speed of wheel
τ	time constant in gear change dynamics
R	gear ratio
I_e	engine inertia
T_e	net engine torque after losses
ω_{wf} , ω_{wr}	angular speed of front and rear wheels respectively

REFERENCES

Cho, D. and Hedrick, J.K., "Automotive Powertrain Modeling for Control," *ASME Journal of Dynamic Systems, Measurement and Control*, Vol. 111, pp. 568-576, December 1989.

Dugoff, H., Fancher, P.S. and Segal, L., "Tyre performance charecteristics affecting vehicle response to steering and braking control inputs," *Final Report, Contract CST-460*, Office of Vehicle Systems Research, US National Bureau of Standards, 1969.

Kiencke, U. and Nielsen, L., *Automotive Control Systems for Engine, Driveline and Vehicle*, SAE International, ISBN 0-7680-0505-1, 2000.

Kotwicki, A.J., "Dynamic Models for Torque Converter Equipped Vehicles," *SAE Technical Paper Series*, Paper No. 82039, 1982.

Pacejka, H.B. and Bakker, E., "The Magic Formula Tyre Model," *Vehicle System Dynamics*, v 21, Supplement, Tyre Models for Vehicle Dynamics Analysis, p 1-18, 1993

Pacejka, H.B., "The Tyre as a Vehicle Component," *XXVI FISITA Congress*, Prague, June 16-23, 1996.

Tugcu, A.K., Hebbale, K.V., Alexandridis, A.A., and Karmel, A.M., "Modeling and Simulation of the Powertrain Dynamics of Vehicles Equipped with Automatic Tarnsmission," *Proceedings of the Symposium on Simulation of Ground Vehicles and Transportation Systems*, ASME Winter Annual Meeting, Anaheim, December 1986.

Runde, J., "Modeling and Control of an Automatic Transmission," *S.M.M.E. Thesis*, Department of Mechanical Engineering, M.I.T., January 1986.

White, R.A. and Korst, H.H., "The Determination of Vehicle Drag Contributions from Coastdown Tests," *SAE Transactions*, Vol. 81, paper 720099, 1972.

Wong, J.Y., *Theory of Ground Vehicles*, Wiley-Interscience, ISBN 0-471-35461-9, Third Edition, 2001.

Chapter 5

INTRODUCTION TO LONGITUDINAL CONTROL

5.1 INTRODUCTION

The term "longitudinal controller" is typically used in referring to any control system that controls the longitudinal motion of the vehicle, for example, its longitudinal velocity, acceleration or its longitudinal distance from another preceding vehicle in the same lane on the highway. The throttle and brakes are the actuators used to implement longitudinal control.

A very familiar example of longitudinal control is the standard cruise control system available on most vehicles today. With a standard cruise control system, the driver sets a constant desired speed at which he/she would like the vehicle to travel. The cruise control system then automatically controls the throttle to maintain the desired speed. It is the driver's responsibility to ensure that the vehicle can indeed safely travel at that speed on the highway. If there happens to appear a preceding vehicle on the highway that is traveling at a slower speed or is too close to the ego vehicle, the driver must take action and if necessary apply brakes. Application of the brakes automatically disengages the cruise control system and returns control of the throttle to the driver.

The following examples describe other types of advanced longitudinal control systems.

5.1.1   Adaptive cruise control

An adaptive cruise control (ACC) system is an extension of the standard cruise control system. An ACC equipped vehicle has a radar or other sensor that measures the distance to other preceding vehicles (downstream vehicles) on the highway. In the absence of preceding vehicles, the ACC vehicle travels at a user-set speed, much like a standard cruise controlled vehicle. However, if a preceding vehicle is detected on the highway by the vehicle's radar, the ACC system determines whether or not the vehicle can continue to travel safely at the desired speed. If the preceding vehicle is too close or traveling too slowly, then the ACC system switches from speed control to spacing control (see Figure 5-1). In spacing control, the ACC vehicle controls the throttle and/ or brakes so as to maintain a desired spacing from the preceding vehicle.
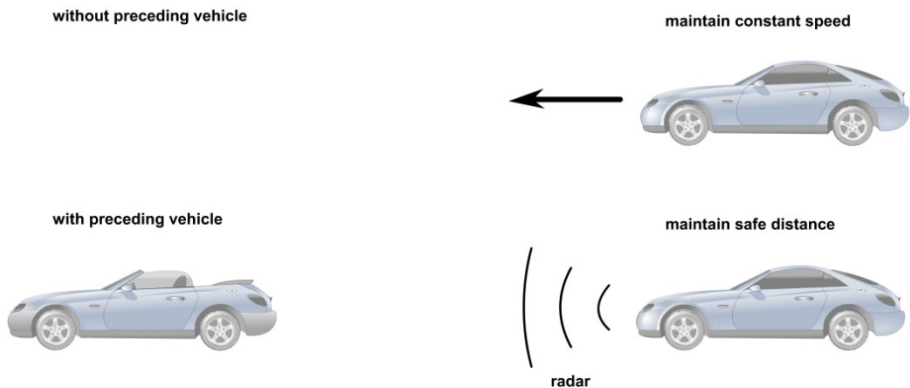
Figure 5-1. Adaptive cruise control

An ACC systems is "autonomous" - it only uses on-board sensors such as radar to accomplish the task of maintaining the desired spacing. It does not depend on wireless communication or on cooperation from other vehicles on the highway. ACC systems were first introduced in Japan (Watanabe, et. al., 1997) and Europe and are now available in the North American market (Fancher, et. al., 1997, Reichart, et. al., 1996 and Woll, 1997). The 2003 Mercedes S-class and E-class passenger sedans come with the option of a radar based Distronic adaptive cruise control system. The 2003 Lexus LS340 comes with an optional laser based adaptive cruise control system.

The design of ACC systems is discussed in detail in Chapter 6.

5.1.2 Collision avoidance

Instead of an ACC system, some vehicles come equipped with a "collision avoidance" (CA) system. A collision avoidance system also operates like a standard cruise control system in the absence of preceding vehicles and maintains a constant desired speed. If a preceding vehicle appears and the CA system determines that the desired speed can no longer be safely maintained, then the CA system reduces the throttle and/or applies brakes so as to slow the vehicle down. In addition, a warning is provided to the driver indicating the presence of other vehicles which necessitate that he or she should take over longitudinal control.

5.1.3 Automated highway systems

A completely different paradigm of longitudinal control is the control of vehicles to travel together in a tightly spaced platoon in automated highway systems (AHS). Automated highway systems have been the subject of intense research and development by several research groups, most notably by the California PATH program at the University of California, Berkeley.

Figure 5-2. Platoon of Buicks used in the NAHSC Demonstration

In an AHS, the objective is to dramatically improve the traffic flow capacity on a highway by enabling vehicles to travel together in tightly spaced platoons. The system requires that only adequately instrumented fully automated vehicles be allowed on this special highway. Manually driven vehicles cannot be allowed to operate on such a highway. Figure 5-2 below shows a photograph of eight fully automated cars traveling together in a tightly spaced platoon during a demonstration conducted by California PATH in August 1997. More details on this experimental demonstration are described in section 7.9. Automated highway systems are the focus of detailed discussion in chapter 7.

5.2   BENEFITS OF LONGITUDINAL AUTOMATION

The development of the longitudinal vehicle control systems described in the previous section has been fueled by a number of motivations, including the desire to enhance driver comfort and convenience, the desire to improve highway safety and the desire to develop solutions to alleviate the traffic congestion on highways.
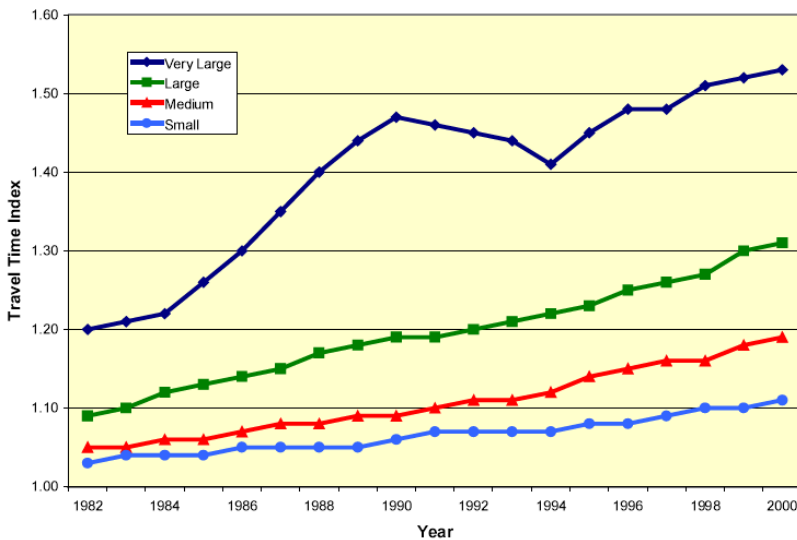
Figure 5-3. Growth in peak period travel time, 1982 to 2000
(Source: Texas Transportation Institute Report, 2002)

An ACC system provides enhanced driver comfort and convenience by allowing extended operation of the cruise control option even in the presence

of other traffic. ACC systems and other automated systems in general are also expected to contribute towards increased safety on the highways. This is because statistics of highway accidents show that over 90% of accidents are caused by human error (United States DOT Report, 1992). Only a very small percentage of accidents are the result of vehicle equipment failure or even due to environmental conditions (like, for example, slippery roads). Since automated systems reduce driver burden and provide driver assistance, it is expected that the use of well-designed automated systems will certainly lead to reduced accidents.
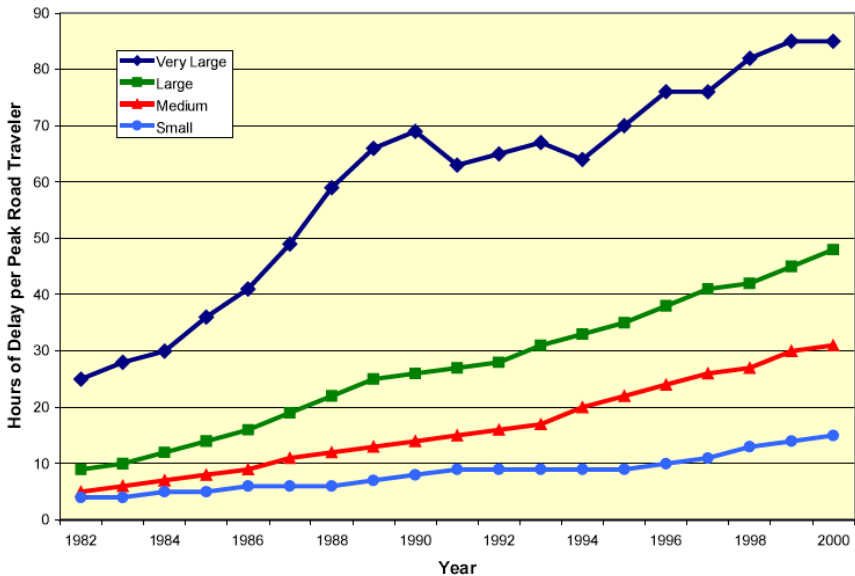
Figure 5-4. Growth in annual delay per peak road traveler, 1982 to 2000
(Source: Texas Transportation Institute Report, 2002)

The development of automated highway systems has been the direct result of the motivation to address traffic congestion on highways. Congestion has been increasing steadily in the country's major metropolitan areas to an extent where two-thirds of all highway travel today is congested travel. Using both the Travel Time Index (Figure 5-3) and annual delay per peak traveler (Figure 5-4), congestion appears to be increasing in cities of all sizes (Texas Transportation Institute Report, 2002). It appears unlikely that the congestion problem will be solved in the foreseeable future by highway expansion. The increase in traffic every year outpaces the increase in capacity due to additional highway construction (Texas Transportation Institute Report, 2002). Thus highway congestion is only expected to worsen every year. The development of AHS is an attempt to use technology to

address the traffic congestion issue. An AHS in which vehicles travel in closely packed platoons can provide a highway capacity that is three times the capacity of a typical highway (Varaiya, 1993).

Having introduced the types of longitudinal control systems under development by various automotive researchers, we next move on to studying the technical details of designing longitudinal control systems.

5.3   CRUISE CONTROL

In a standard cruise control system, the speed of the vehicle is controlled to a desired value using the throttle control input. The longitudinal control system architecture for the cruise control vehicle will be designed to be hierarchical, with an upper level controller and a lower level controller as shown in Figure 5-5.
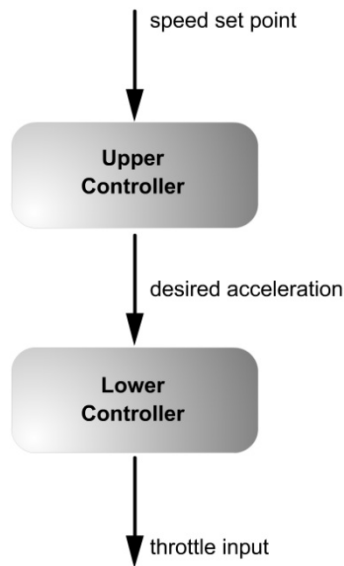
Figure 5-5. Structure of cruise control system

The upper level controller determines the desired acceleration for the vehicle. The lower level controller determines the throttle input required to track the desired acceleration. Vehicle dynamic models, engine maps and nonlinear control synthesis techniques (Choi and Devlin, 1995a and 1995b, Hedrick et al, 1991, Hedrick, et. al., 1993) are used by the lower controller in calculating the real-time throttle input required to track the desired acceleration.

    In performance specifications for the design of the upper controller, it is necessary to specify that the steady state tracking error of the controller should be zero. In other words, the speed of the vehicle should converge to the desired speed set by the driver. Other desirable performance specifications might include zero overshoot and adequately fast rise time.

    As far as the upper level controller is concerned, the plant model used for control design is

$$\ddot{x} = \frac{1}{\tau s + 1} \ddot{x}_{des} \tag{5.1}$$

or

$$\tau \dddot{x} + \ddot{x} = \ddot{x}_{des} \tag{5.2}$$

where x is the longitudinal position of the vehicle measured from an inertial reference. This means that the upper controller uses desired acceleration as the control input. The actual acceleration of the vehicle is assumed to track the desired acceleration with a time constant τ.

    As far as the lower level controller is concerned, the driveline dynamics discussed in chapter 4 and the engine dynamics discussed in chapter 9 constitute the actual longitudinal vehicle model that must be utilized in control design. The lower level controller must ensure that the vehicle acceleration tracks the desired acceleration determined by the upper controller.

    Due to the finite bandwidth associated with the lower controller, the vehicle is expected to track its desired acceleration imperfectly. Thus there is a first order lag in the lower level controller performance and hence the use of the model equation (5.1) for the upper controller which incorporates a lag in tracking desired acceleration.

    This chapter assumes a lag of $\tau = 0.5$ for analysis and simulation.

5.4 UPPER LEVEL CONTROLLER FOR CRUISE CONTROL

A typical algorithm used for the upper controller is PI control using error in speed as the feedback signal:

$$\ddot{x}_{des}(t) = -k_p\left(V_x - V_{ref}\right) - k_I \int_0^t \left(V_x - V_{ref}\right)dt \tag{5.3}$$

where V_{ref} is the desired vehicle speed set by the user.

Define the following reference position

$$x_{des} = \int_0^t V_{ref}d\tau \tag{5.4}$$

Here $x_{des}(t)$ is the position of an imagined reference vehicle that is traveling at the reference or desired speed. Then the upper controller can be rewritten as

$$\ddot{x}_{des} = -k_p\left(\dot{x} - \dot{x}_{des}\right) - k_I\left(x - x_{des}\right) \tag{5.5}$$

This is equivalent to inter-vehicle spacing control with $x - x_{des}$ being the spacing from a fictitious vehicle traveling at the desired reference speed.

The unity feedback loop denoting this closed-loop system is shown below in Figure 5-6.
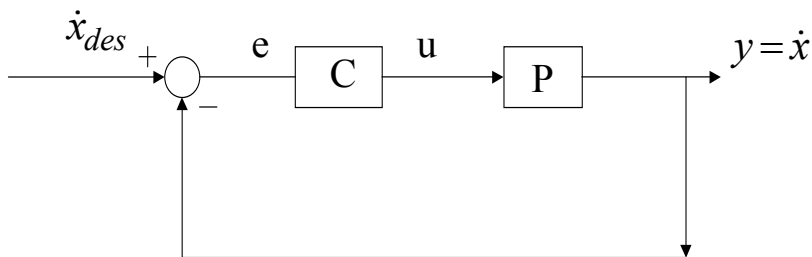
Figure 5-6. Unity feedback loop for upper controller for cruise control

As discussed previously, the plant model for the upper controller is the transfer function between desired acceleration and actual vehicle speed and is given by

$$P(s) = \frac{1}{s(\tau s + 1)} \tag{5.6}$$

The PI controller is

$$C(s) = k_p + \frac{k_i}{s} \tag{5.7}$$

Hence the closed-loop transfer function is

$$\frac{V_x}{V_{ref}} = \frac{PC}{1 + PC} = \frac{k_p s + k_i}{\tau s^3 + s^2 + k_p s + k_i} \tag{5.8}$$

A root locus of the feedback system is shown in Figure 5-7 for varying k_p with the ratio $\frac{k_p}{k_i}$ fixed at 4. A value of $\tau = 0.5$ was assumed for the system lag. Values of k_p varying from 0 to 0.75 were used. It can be seen from Figure 5-7 that the closed system is stable for all non-zero k_p. There is one closed-loop real pole and a pair of complex conjugate poles. For a value of $k_p = 0.75$, the complex poles have a damping ratio of 0.87. If the value of k_p is increased further beyond 0.75, the damping ratio of the complex poles decreases and the system becomes less damped.
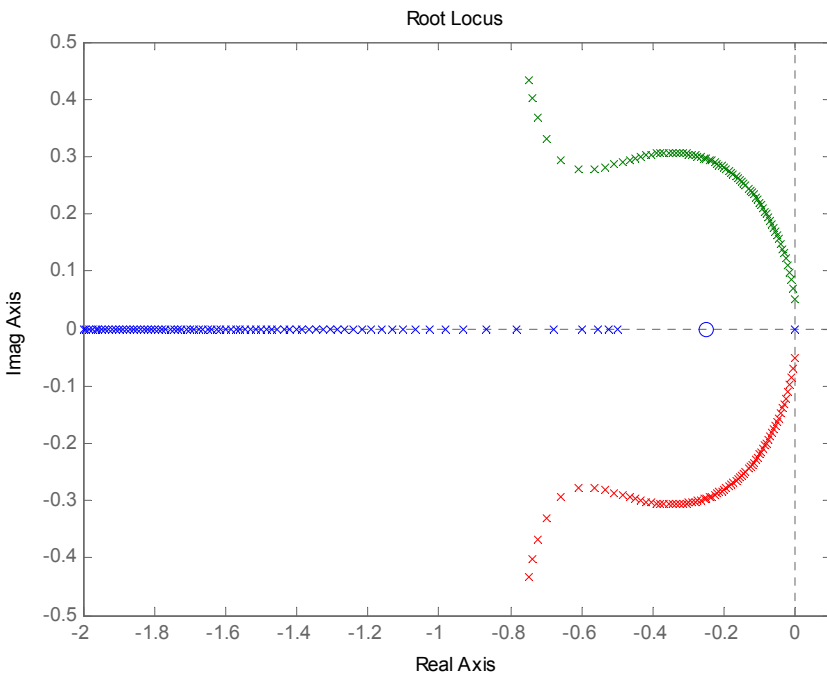
Figure 5-7. Root locus for PI controller

The Bode magnitude plot of the closed-loop transfer function is shown in Figure 5-8 for a value of $k_p = 0.75$. As seen in the figure, the resulting bandwidth of the closed-loop system is 0.2 Hz.
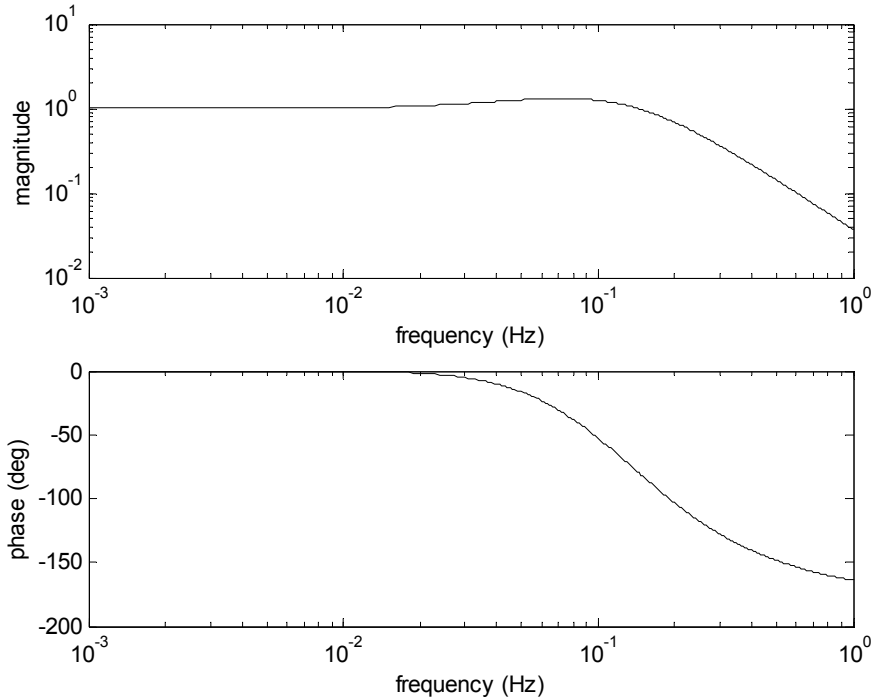
Figure 5-8. Closed-loop transfer function with PI controller

5.5   LOWER LEVEL CONTROLLER FOR CRUISE CONTROL

In the lower controller, the throttle input is calculated so as to track the desired acceleration determined by the upper controller. A simplified model of longitudinal vehicle dynamics can be used in the design of the lower level controller. This simplified model is typically based on the assumptions that the torque converter in the vehicle is locked and that there is zero-slip between the tires and the road (Hedrick, et. al., 1991). These are very reasonable assumptions during cruise control because

a)   The cruise control system is typically engaged in gears 3 and higher where the torque converter is indeed locked.

b)   The tire slip is small since the longitudinal maneuvers involved in cruise control are very gentle.

Using the above assumptions, the engine torque required to track the desired acceleration command is first calculated. This calculation is described in section 5.5.1. Once the required engine torque has been obtained, engine maps and nonlinear control techniques are used to calculate the throttle input that will provide this required torque.

5.5.1   Engine Torque Calculation for Desired Acceleration

A model of the driveline dynamics was discussed in section 4.2 of this book and should be reviewed by the reader. Consider the case where the torque converter is locked $(T_t = T_p)$, the transmission is in steady state (it is not undergoing a gear shift) and the longitudinal tire slip is negligible. In this case, the wheel speed ω_w is proportional to the engine speed ω_e and related through the gear ratio R as follows

$$\omega_w = R\omega_e \qquad (5.9)$$

and the transmission shaft speed is equal to the engine speed

$$\omega_t = \omega_e \qquad (5.10)$$

The longitudinal vehicle velocity is approximated by $\dot{x} = r_{eff}\omega_w$ where r_{eff} is the effective tire radius and hence the longitudinal acceleration is

$$\ddot{x} = r_{eff} R\dot{\omega}_e \qquad (5.11)$$

The longitudinal vehicle equation is

$$m\ddot{x} = F_x - R_x - F_{aero}$$

where F_x is the total longitudinal tire force from all tires, R_x is the rolling resistance force and F_{aero} is the aerodynamic drag force. Using equation (5.11), this can be rewritten as

$$mRr_{eff}\dot{\omega}_e = F_x - R_x - F_{aero} \qquad (5.12)$$

Hence

$$F_x = mRr_{eff}\dot{\omega}_e + R_x + F_{aero} \tag{5.13}$$

Substituting from equation (5.13) into the equation for the wheel rotational dynamics (4.38)

$$I_w\dot{\omega}_w = T_{wheel} - r_{eff}(F_x) = T_{wheel} - mRr_{eff}^2\dot{\omega}_e - r_{eff}R_x - r_{eff}F_{aero} \tag{5.14}$$

Hence, the torque at the wheels required to produce the desired acceleration is

$$T_{wheel} = I_w R\dot{\omega}_e + mRr_{eff}^2\dot{\omega}_e + r_{eff}F_{aero} + r_{eff}R_x \tag{5.15}$$

Substituting from equation (5.15) into the equation for the transmission dynamics

$$I_t\dot{\omega}_t = T_t - RT_{wheel} = T_t - I_w R^2\dot{\omega}_e - mR^2 r_{eff}^2\dot{\omega}_e - Rr_{eff}F_{aero} - Rr_{eff}R_x$$

Since $\omega_t = \omega_e$ and $T_t = T_p$, we have

$$I_t\dot{\omega}_e = T_p - I_w R^2\dot{\omega}_e - mR^2 r_{eff}^2\dot{\omega}_e - Rr_{eff}F_{aero} - Rr_{eff}R_x$$

Hence the pump torque load on the engine is

$$T_p = (I_t + I_w R^2 + mR^2 r_{eff}^2)\dot{\omega}_e + Rr_{eff}F_{aero} + Rr_{eff}R_x \tag{5.16}$$

Substituting from equation (5.16) into the engine rotational dynamics equation (4.35)

$$I_e\dot{\omega}_e = T_{net} - T_p$$
$$= T_{net} - (I_t + I_w R^2 + mR^2 r_{eff}^2)\dot{\omega}_e - Rr_{eff}F_{aero} - Rr_{eff}R_x$$

Hence

$$I_e\dot{\omega}_e = T_{net} - (I_t + I_w R^2 + mR^2 r_{eff}^2)\dot{\omega}_e - Rr_{eff}F_{aero} - Rr_{eff}R_x$$

or

$$J_e \dot{\omega}_e = T_{net} - R r_{eff} F_{aero} - R r_{eff} R_x \qquad (5.17)$$

where

$$J_e = I_e + I_t + R^2 I_w + m R^2 r_{eff}^2 \qquad (5.18)$$

Since F_{aero} is a quadratic function of vehicle velocity and can also be expressed in terms of a quadratic in ω_e, equation (5.16) represents a single first order o.d.e. that describes the vehicle dynamics in the case where the torque converter is locked and the slip is assumed to be negligible.

Substituting for F_{aero} as $F_{aero} = c_a \left(r_{eff} R \omega_e \right)^2$, the dynamics relating engine speed ω_e to the pseudo-input "net combustion torque" T_{net} can be modeled by the single first-order ode

$$\dot{\omega}_e = \frac{T_{net} - c_a R^3 r_{eff}^3 \omega_e^2 - R(r_{eff} R_x)}{J_e} \qquad (5.19)$$

where $J_e = I_e + I_t + (m r_{eff}^2 + I_\omega) R^2$ is the effective inertia reflected on the engine side.

From equation (5.19), it is clear that if the net combustion torque is chosen as

$$(T_{net}) = \frac{J_e}{R\, r_{eff}} \ddot{x}_{des} + [c_a R^3 r_{eff}^3 \omega_e^2 + R(r_{eff} R_x)] \qquad (5.20)$$

then the acceleration of the car is equal to the desired acceleration defined by the upper level controller i.e. $\ddot{x} = \ddot{x}_{des}$.

5.5.2   Engine Control

Once the required combustion torque is obtained from (5.20), the control law to calculate the throttle angle to provide this torque can be obtained by using engine dynamic models and applying nonlinear control synthesis techniques. Engine dynamic models for both SI and diesel engines and nonlinear control design to provide a desired engine torque are discussed in Chapter 9 of this book.

5.6   ANTI-LOCK BRAKE SYSTEMS

5.6.1   Motivation

Anti-lock brake systems (ABS) were originally developed to prevent wheels from locking up during hard braking. Modern ABS systems not only try to prevent wheels from locking but also try to maximize the braking forces generated by the tires by preventing the longitudinal slip ratio from exceeding an optimum value.

First, note that locking of the wheels reduces the braking forces generated by the tires and results in the vehicle taking a longer time to come to a stop. Further, locking of the front wheels prevents the driver from being able to steer the vehicle while it is coming to a stop.

To understand the influence of longitudinal slip ratio on braking forces, consider the tire force characteristics shown in Figure 5-9. As seen in Figure 5-9, the magnitude of the tire longitudinal force typically increases linearly with slip ratio for small slip ratios. It reaches a maximum (peak) value typically at a slip ratio value between 0.1 and 0.15. At slip ratios beyond this value, the magnitude of tire force decreases and levels out to a constant value.
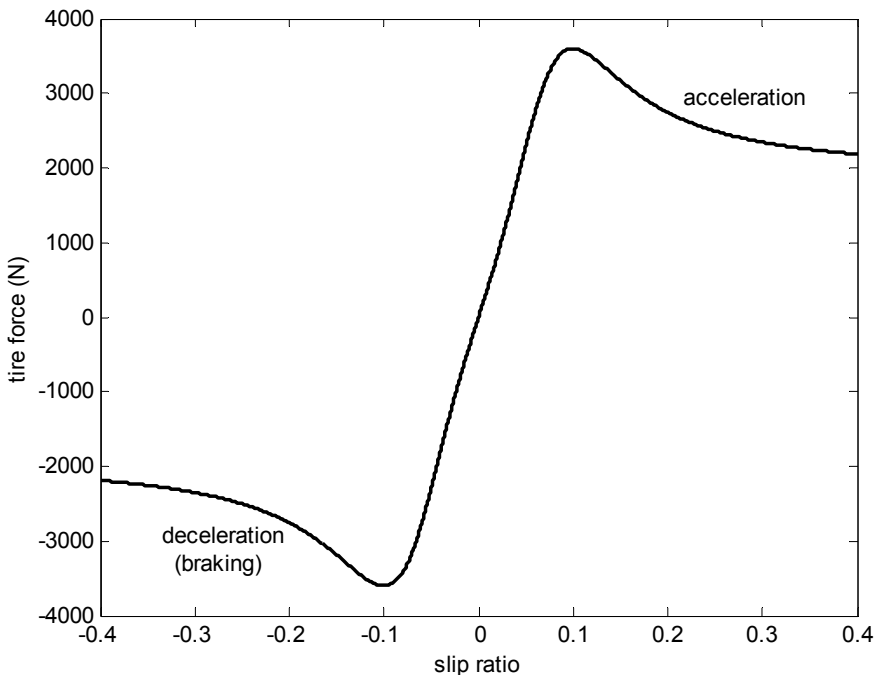
Figure 5-9. Tire longitudinal force as a function of longitudinal slip ratio

If the driver presses hard on the brakes, the wheels will slow down considerably faster than the vehicle slows down, resulting in a big slip ratio value. However, as described above, slip ratios higher than an optimum value actually result in reduced braking forces. The vehicle would take longer to come to a stop if the slip ratio exceeded the optimum value. The ABS solution then is to prevent excessive brake torque from being applied on the wheels, so that the slip ratio doesn't exceed the optimum value. This would also prevent or delay the wheels from locking up and increase steerability of the vehicle during braking.

The following simulation plots demonstrate the negative consequences of very hard braking. Figures 5-10 and 5-11 show vehicle speed and slip ratio respectively during hard braking. As seen in Figure 5-11, the wheels lock during braking and result in a slip value of −1 within 1 second of the initiation of braking. As seen in Figure 5-10, while the wheels come to a stop in 1 second, the vehicle itself does not come to a stop and only reduces in speed from 30 m/s to 13 m/s in 12 seconds.
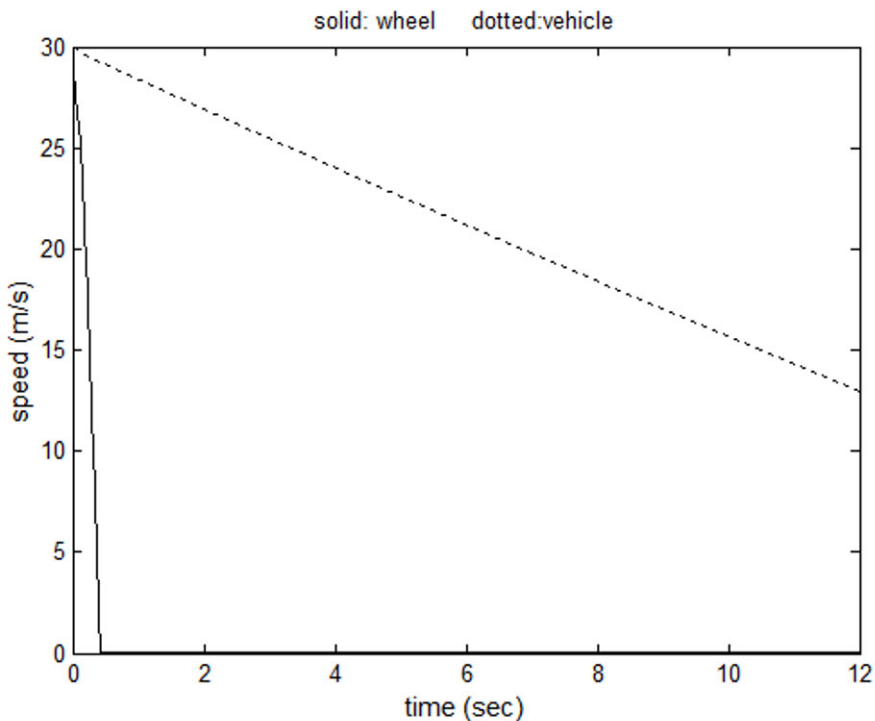
Figure 5-10. Vehicle speed during hard braking (No ABS)
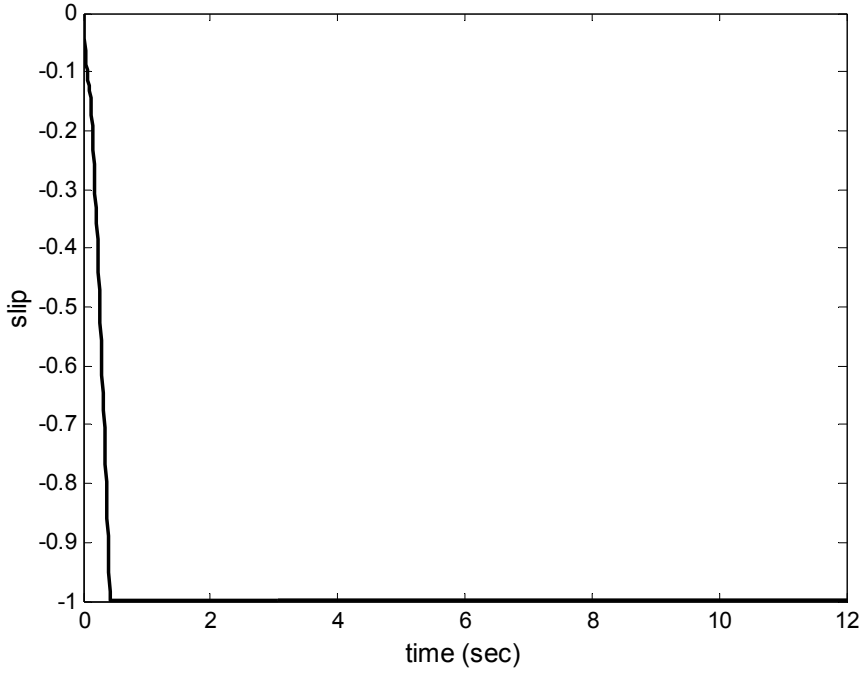
Figure 5-11. Slip Ratio during hard braking (No ABS)
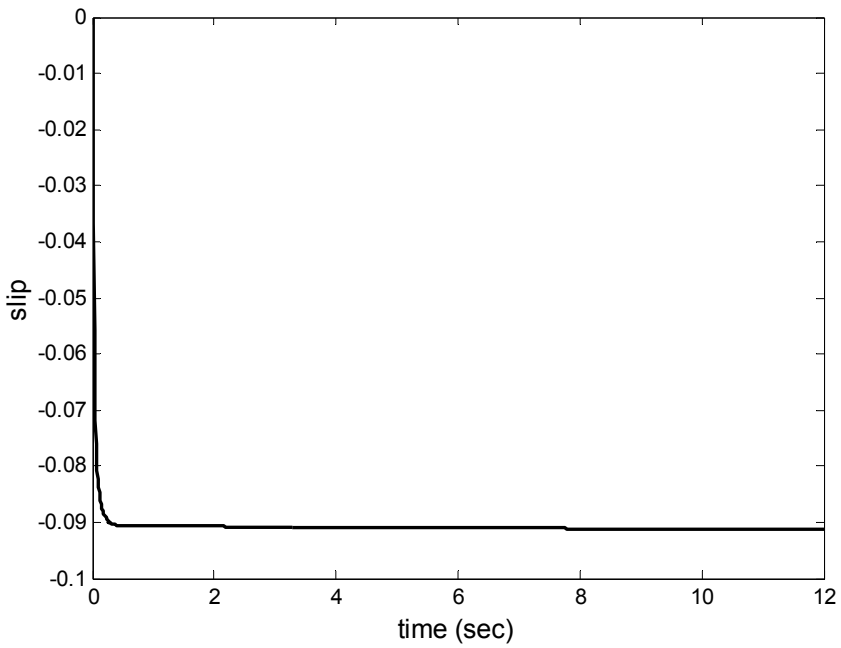
Figure 5-12. Slip Ratio with reduced braking (ABS)
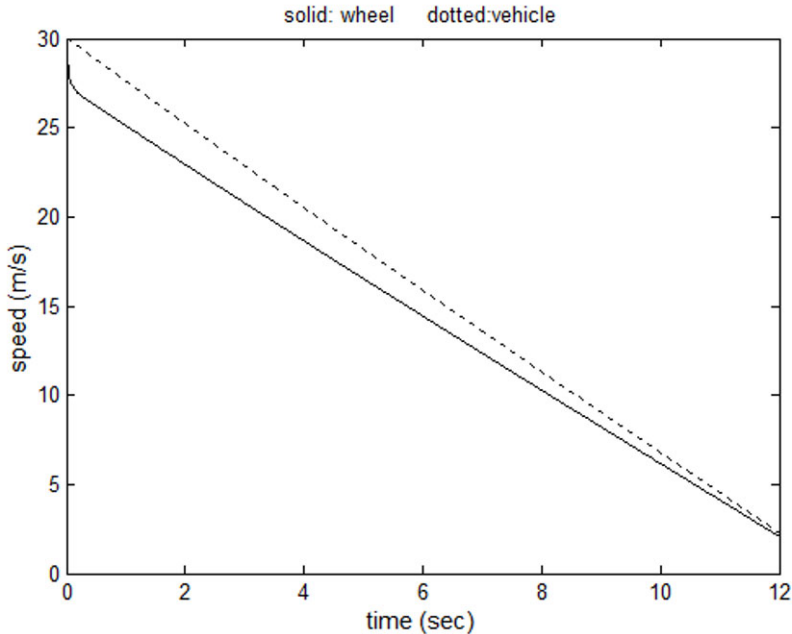
Figure 5-13. Vehicle speed with reduced braking (ABS)

Figures 5-12 and 5-13 show slip ratio and vehicle speed during *reduced braking* designed to just prevent the wheels from locking up. As seen in Figure 5-12, the slip ratio is maintained at 0.09 which is close to the optimum value of 0.1. The wheels don't lock, as seen in Figure 5-13, thus allowing the vehicle to be steered. Further, the speed of the vehicle is reduced from 30 m/s to 2 m/s in 12 seconds. Thus a significantly greater reduction in vehicle speed is obtained by limiting the amount of braking torque applied to the wheels.

5.6.2 ABS Functions

The basic objective of the ABS is to either hold or release the braking pressure on the wheels if there is a danger of the wheels locking. At the same time, the ABS needs to re-permit application of the brakes again once the danger of locking has been averted. The ABS system could also hold or release the braking pressure in order to keep the slip ratio at the wheel from exceeding an optimum value.

Depending on the number of wheels the ABS controls, ABS can be four channel four sensor, three channel three sensor or one channel one sensor. Each channel controlled by the ABS has a valve. Depending on the position of the valve, brake pressure on the wheel is held, released or controlled by the driver:

When the valve is open, pressure from the master cylinder is passed right through to the brake. This allows the brake to be controlled by the driver, allowing the amount of brake pressure desired by the driver to be applied to the brake.

When the valve is closed or blocked, that brake is isolated from the master cylinder. This holds the brake pressure and prevents it from increasing even if the driver pushes the brake pedal harder.

When the valve is in the release position, the pressure from the brake is released. In this position, not only is the brake isolated from any further braking actions of the driver, but the amount of braking pressure on the wheel is actively reduced.

A major practical problem in ABS systems is that wheel slip cannot be measured with inexpensive sensors on a passenger vehicle. Often the only measurements available to the ABS system are measurements of the individual wheel speeds at the four wheels. Algorithms that utilize these wheel speed measurements to predict if the wheels will lock and to predict if the danger of locking has been averted have to be used.

The process of determining whether or not the wheel is going to lock is called *prediction*. Prediction point slip is defined as the wheel slip at the instant the control unit predicts for the first time in a brake cycle that the wheel is going to lock.

The process of determining whether or not the danger of locking has been averted is called *reselection*. Reselection point slip is defined as the wheel slip at the instant it is predicted for the first time in a brake cycle that the danger of locking is averted.

5.6.3   Deceleration Threshold Based Algorithms

One of the most common ABS algorithms is the deceleration threshold based algorithm (Bosch Automotive Handbook, 2000). The wheel deceleration signal is used to predict if the wheel is about to lock. Here wheel deceleration is defined as angular deceleration multiplied by effective tire radius.

A common version of the deceleration threshold algorithm is summarized in Figures 5-14, 5-15, 5-16 and 5-17 (Kiencke and Nielsen, 2000 and Bosch Automotive Handbook, 2000).

Let $\dot{V}_R$ be the wheel deceleration defined as

$$\dot{V}_R = r_{eff}\dot{\omega}_w \qquad (5.21)$$

where r_{eff} is the effective tire radius and ω_w is the angular wheel speed. Let a_1, a_2, a_3 and a_4 be acceleration threshold values, all defined to be positive with $a_2 > a_1$ and $a_4 > a_3$.
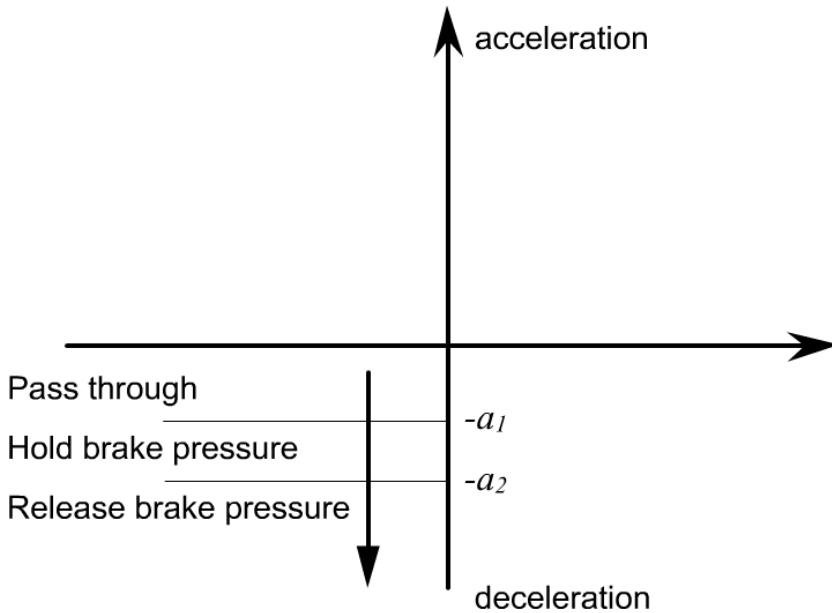
Figure 5-14. Deceleration in the first cycle

When the driver presses on the brake pedal, if the deceleration is less than a_1 (i.e. if $\dot{v}_R > -a_1$), then the driver's braking action is directly passed through to the brakes. When the deceleration exceeds a_1 for the first time (i.e $\dot{v}_R < -a_1$), the driver's braking action is no longer directly passed through to the brakes. Instead the braking pressure is held constant at the pressure value achieved when the deceleration first exceeded a_1. If the wheel deceleration continues to increase further and exceeds the value a_2 (i.e. $\dot{v}_R < -a_2$), then the braking pressure at the wheel is decreased. This will prevent the wheel from decelerating any further and could eventually result in the wheel gaining speed or accelerating. If the wheel deceleration reduces to the value a_2 (i.e. $\dot{v}_R > -a_2$), then the pressure drop is stopped. If the wheel deceleration drops below the value a_1 (i.e. $\dot{v}_R > -a_1$), then the driver's braking action is once again directly passed through to the brakes. If

the wheel actually starts accelerating, and the acceleration exceeds the relatively high threshold a_4, then the braking pressure is actually increased beyond that dictated by the driver's actions, so as to prevent the wheel from over acceleration. In this case, when the wheel's acceleration drops to the value below a_3 (i.e. $\dot{v}_R < a_3$), the driver's braking action are again passed through to the brakes. When the wheel deceleration goes below a_1 ($\dot{v}_R < -a_1$) again the second cycle starts. Running through such cycles, the wheels are prevented from locking and the wheel rotational speed is kept in an area where wheel slip is close to that of the maximum friction coefficient. Note that a_4 is a relatively high deceleration level. (much larger than a_3).

During the second braking cycle, the braking pressure is reduced right away when the deceleration first exceeds a_1 (i.e. the phase of holding brake pressure constant between a_1 and a_2 is no longer done during the second braking cycle). In the first cycle, the short pressure holding phase is used for the filtering of disturbances.

Figure 5-14 and Figure 5-15 summarize the deceleration threshold based algorithm during wheel deceleration. Figure 5-16 and Figure 5-17 summarize the algorithm during wheel acceleration.
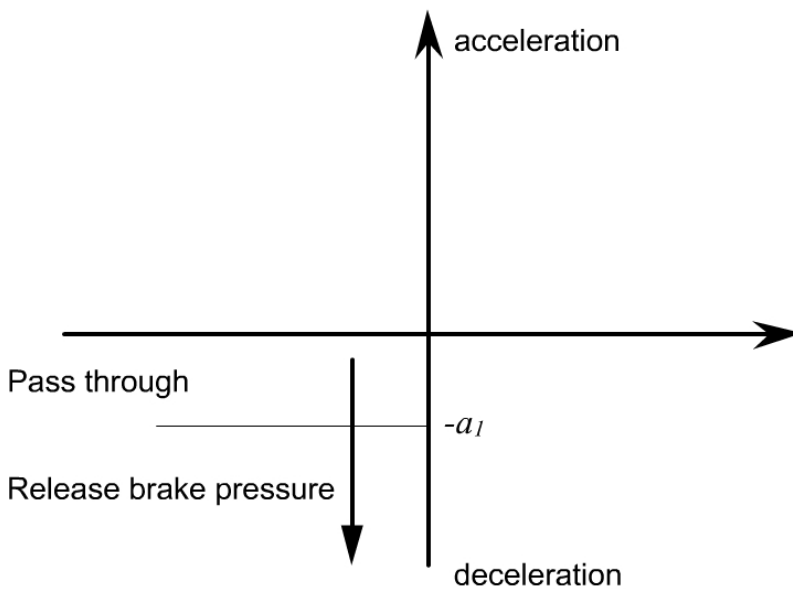
Figure 5-15. Deceleration in the second and subsequent cycles
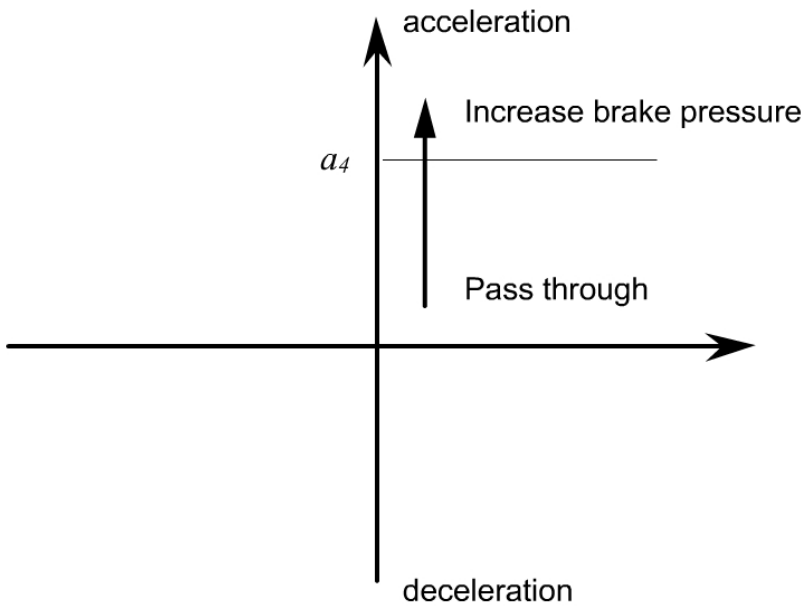
Figure 5-16. Increasing acceleration
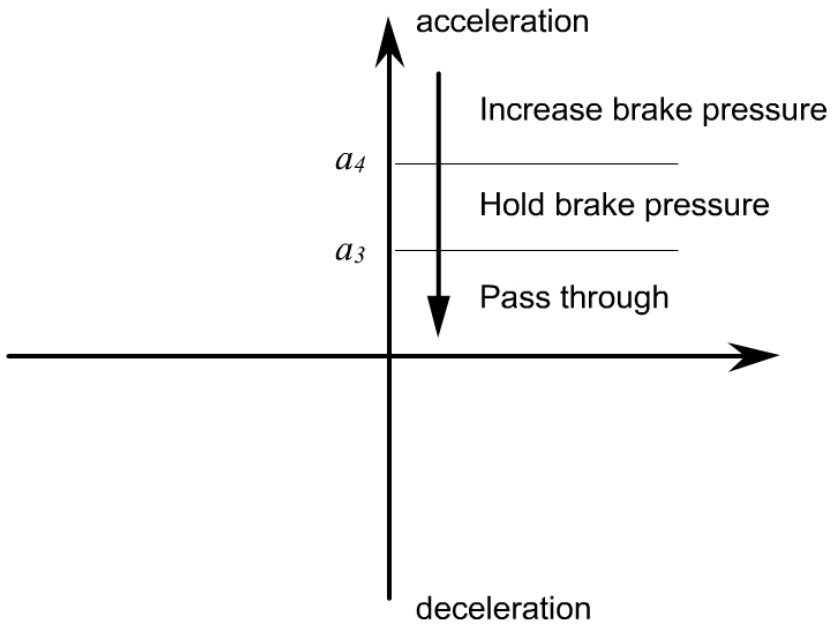
Figure 5-17. Decreasing acceleration

In a modified version of this algorithm, during the first cycle, if the deceleration exceeds a_1 and the wheel speed falls below a slip-switching threshold (determined based on the initial speed when braking first started), then the braking pressure is reduced. Thus the deceleration threshold a_2 is not used in this modified algorithm. From the second braking cycle onwards, pressure is reduced right away when the deceleration first exceeds a_1 (Bosch Automotive Handbook, 2000).

5.6.4   Other Logic Based ABS Control Systems

A number of factors influence the working of the ABS system. These include

The value of the tire-road friction coefficient, since it influences the range within which the wheel slip ratio should be maintained.

The rate of application of the brake torque (brake dynamics). During the first cycle, this depends on how the driver of the vehicle presses the brake pedal. In the subsequent cycles, it depends on the pressure build characteristics of the modulator.

Initial longitudinal velocity of the vehicle is also important, since it determines how quickly the vehicle can come to a stop.

The brake effort distribution from front to rear is also important

The performance of the ABS system for variations in the above parameters is an important consideration in ABS system design. Many logic based ABS control systems have been developed and reported in literature to address performance in the presence of the above variations.

The work by Guntur and Ouwerkerk, 1972 contains a good discussion of logic based ABS system design. It compares different logic controllers by evaluating their performance in simulations based on a mathematical vehicle model. In the simulations the authors vary three important parameters: rate of application of the brake, tire-road friction coefficients (i.e. different road conditions) and initial velocity of the vehicle. Different logic controllers are compared on the basis that, for variations in these parameters, the control unit should

1. Not fail to indicate locking of the wheel
2. Not make false predictions about locking of the wheel
3. Maintain the wheel slip within the desired range

Four different algorithms are evaluated in terms of their prediction of wheel lock. Based on their simulations results, the authors conclude that a compound condition consisting of two algorithms A_p and B_p results in the best performance (Guntur and Ouwerkerk, 1972). Method A_p sets a

maximum threshold deceleration on the wheel speed, while method B_p sets another maximum threshold on the ratio of the deceleration of the wheel speed to the angular wheel speed. In the proposed compound condition, provision is made for an adaptive feature that changes the threshold values for initial velocities exceeding 35 m/s. For initial velocities lower than 35 m/s, a static threshold algorithm is found to be adequate. In considering the suitability of methods for the prediction point, the authors allow locking of the rear wheels as long as it does not cause instability of the vehicle.

Eight different algorithms are evaluated in the same paper in terms of their identification of the reselection point (Guntur and Ouwerkerk, 1972). The authors found that a compound condition consisting of methods A_r, D_r and F_r gives a good estimation of the reselection point. Method A_r is a fixed time delay condition which ensures the reapplication of the brake after a certain fixed time lapse after each time the brake is released. Method D_r is a variable condition on the desired angular velocity. The angular velocity of the wheel at the point of initial braking in the first cycle, or the corresponding signal at the point of reapplication in a subsequent cycle, is stored and the desired angular velocity is assumed to be proportional to this value. This method is used to ensure that the driver of the vehicle can conveniently influence the performance of the anti-skid system by interrupting a given braking maneuver. Method F_r reapplies the brakes whenever a threshold on the ratio of the deceleration of the wheel speed to the angular wheel speed is exceeded. It is added to improve the braking effectiveness at low vehicle speed, and also render the anti-skid system inoperative at very low speed. The compound reselection condition devised by the authors does not incorporate an adaptive feature like the one used for the prediction point condition.

5.6.5   Recent Research Publications on ABS

The development of ABS algorithms continues be an active area of research. Many research papers have concentrated on the development of algorithms that can ensure that a desired wheel slip ratio is tracked at the wheels. Detailed dynamic models of the wheel, tire, vehicle and the hydraulic system are used and the resulting system model is nonlinear. Nonlinear control system techniques are often used to ensure tracking of a desired wheel slip ratio. The measurable states of the system are the hydraulic pressure and the wheel speed. The fact that the vehicle absolute velocity cannot be measured

means that the slip ratio itself cannot be measured. It must be estimated from a observer and this constitutes a very challenging problem. Accounting for changes in road surface conditions in the dynamic tire model (e.g. low friction coefficient on a slippery road) is an additional difficulty. Interesting research papers in this area include Unsal and Kachroo (1999) and Drakunov, et. al. (1995).

5.7   CHAPTER SUMMARY

This chapter provided an introduction to several longitudinal control systems, including standard cruise control, adaptive cruise control, collision avoidance, longitudinal control for operation of vehicles in platoons and anti lock brake systems. Control system design for standard cruise control and anti lock brake systems were discussed in detail. Chapter 6 will next provide a detailed discussion of adaptive cruise control while Chapter 7 will discuss longitudinal control for operation of vehicles in platoons.

NOMENCLATURE

x	longitudinal position of the vehicle from an inertial reference
$\dot{x}$ or V_x	longitudinal velocity of the vehicle
x_{des}	imaginary longitudinal position of a vehicle traveling with the reference speed
$\dot{x}_{ref}$ or V_{ref}	desired vehicle speed set by the driver
k_p, k_i	gains used in PI controller for cruise control
τ	time constant for lag in tracking desired acceleration
T_{net}	net combustion torque of the engine
T_{br}	brake torque
T_{wheel}	torque to the drive wheels
T_p	pump torque
ω_e	engine angular speed
ω_w	wheel angular speed

ω_t	turbine angular speed
c_a	aerodynamic drag coefficient
R	gear ratio
r_{eff}	effective tire radius
R_x	rolling resistance of the tires
F_x	total longitudinal tire force
F_{aero}	aerodynamic drag force
I_e	engine moment of inertia
I_t	transmission shaft moment of inertia
I_w	wheel moment of inertia
I_e	engine moment of inertia
J_e	effective inertia reflected on the engine side
m	vehicle mass
V_R	equivalent linear velocity of rotating wheel

a_1, a_2, a_3, a_4 acceleration thresholds used in ABS algorithm

REFERENCES

Austin, L. and Morrey, D., "Recent Advances in Antilock Braking Systems and Traction Control Systems," *Proceedings of the Institution of Mechanical Engineers,* Vol. 214, pp. 625-638, 2000.

Bosch Automotive Handbook, 5th Edition, ISBN 0-8376-0614-4, Robert Bosch GmbH, 2000.

Chandler, K.N., "Theoretical Studies in Braking," *Proceedings of the Institution of Mechanical Engineers* , 1960-61, No. 4, 147.

Cho, D. and Hedrick, J.K., "Automotive powertrain modeling for control," *ASME Journal of Dynamic Systems, Measurement and Control, Transactions*, v 111, n 4, p 568-576, Dec, 1989.

Choi, S.B. and Hedrick, J.K., "Vehicle Longitudinal Control Using an Adaptive Observer for Automated Highway Systems", *Proceedings of American Control Conference*, Seattle, Washington, 1995.

Choi, S.B. and Devlin, P., "Throttle and Brake Combined Control for Intelligent Vehicle Highway Systems", *SAE 951897*, 1995.

Decker, H., Emig, R. and Goebels, H., "Antilock Brake Systems for Commercial Vehicles," *Proceedings – Society of Automotive Engineers*, 1990, P-233, pp. 515-523.

Drakunov, S., Ozguner, U, Dix, P and Ashrafi, B., "ABS Control using Optimum Search via Sliding Modes," *IEEE Transactions on Control Systems Technology*, Vol. 3, No. 1, pp. 79-85, March 1995.

Fancher, P., Ervin, R., Sayer, J., Hagan, M., Bogard, S., Bareket, Z., Mefford, M. and Haugen, J., 1997, "Intelligent Cruise Control Field Operational test (Interim Report)", *University of Michigan Transportation Research Institute Report,* No. UMTRI-97-11, August 1997.

Guntur, R.R., Ouwerkerk, H., "Adaptive Brake Control System," *Ph.D. Thesis*, Delft University of Technology, The Netherlands, June 1975.

Guntur, R.R. and Wong, J.Y., "Some Design Aspects of Anti-Lock Brake Systems for Commercial Vehicles," *Vehicle System Dynamics*, Vol. 9, pp. 149-180, 1980.

Guntur, R.R. and Ouwerkerk, H., "Adaptive Brake Control System," *Proceedings of the Institution of Mechanical Engineers*, Vol. 186, 68/72, pp. 855-880, 1972.

Hedrick, J.K., McMahon, D., Narendran, V.K. and Swaroop, D., "Longitudinal Vehicle Controller Design for IVHS Systems", *Proceedings of the 1991 American Control Conference*, Vol. 3, pp. 3107-3112, June 1991.

Hedrick, J.K., McMahon, D. and Swaroop, D., "Vehicle Modeling and Control for Automated Highway Systems", *PATH Research Report*, UCB-ITS-PRR-93-24, 1993.

Hedrick, J K. Tomizuka, M. Varaiya, P, "Control Issues in Automated Highway Systems," *IEEE Control Systems Magazine. v 14 n 6, . p 21-32 , Dec 1994*

Ioannou, P.A. and Chien, C.C., 1993, "Autonomous Intelligent Cruise Control", *IEEE Transactions on Vehicular Technology*, Vol. 42, No. 4, pp. 657-672.

Kiencke, U. and Nielsen, L., *Automotive Control Systems for Engine, Driveline and Vehicle*, SAE International, ISBN 0-7680-0505-1, 2000.

Miyasaki, N., Fukumoto, M., Sogo, Y. and Tsukinoki, H., "Antilock Brake System (M-ABS) Based on the Friction Coefficient Between the Wheel and the Road Surface," *SAE Special Publications*, Feb 1990, pp. 101-110.

Nouillant, C., Assadian, F., Moreau, X. and Oustaloup, A., "Feedforward and Crone Feedback Control Strategies for Automobile ABS," *Vehicle System Dynamics*, 2002, Vol. 38, No. 4, pp. 293-315.

Rajamani, R., Tan, H.S., Law, B. and Zhang, W.B., "Demonstration of Integrated Lateral and Longitudinal Control for the Operation of Automated Vehicles in Platoons," *IEEE Transactions on Control Systems Technology*, Vol. 8, No. 4, pp. 695-708, July 2000.

Reichart, G., Haller, G. and Naab, K, 1996, "Driver Assistance : BMW Solutions for the Future of Individual Mobility", *Proceedings of ITS World Congress*, Orlando, October 1996.

Slotine, J.J.E. and Li, W., "Applied Nonlinear Control", Prentice Hall, 1991.

Sugai, M., Yamaguchi, H., Miyashita, M., Umeno, T. and Asano, K., "New Control Technique for Maximizing Braking Force on Antilock Brake System," *Vehicle System Dynamics*, 1999, Vol. 32, pp. 299-312.

Swaroop, D., Hedrick, J.K., Chien, C.C. and Ioannou, P. "A Comparison of Spacing and Headway Control Laws for Automatically Controlled Vehicles", *Vehicle System Dynamics Journal*, Nov. 1994, vol. 23, (no.8):597-625.

Swaroop, D. and Hedrick, J.K., "String Stability of Interconnected Dynamic Systems", *IEEE Transactions on Automatic Control*, March 1996.

Swaroop, D., 1995, "String Stability of Interconnected Systems: An Application to Platooning in Automated Highway Systems", *Ph.D. Dissertation*, University of California, Berkeley, 1995.

Swaroop, D. and Rajagopal, K.R., "Intelligent Cruise Control Systems and Traffic Flow Stability," *Transportation Research Part C : Emerging Technologies*, Vol. 7, No. 6, pp. 329-352, 1999.

Swaroop D. Swaroop, R. Huandra, "Design of an ICC system based on a traffic flow specification," *Vehicle System Dynamics Journal*, Vol. 30, no. 5, pp. 319-44, 1998.

Swaroop, D. and Bhattacharya, S.P., "Controller Synthesis for Sign Invariant Impulse Response," *IEEE Transactions on Automatic Control*, Vol. 47, No. 8, pp. 1346-1351, August, 2002.

Swaroop, D., "On the Synthesis of Controllers for Continuous Time LTI Systems that Achieve a Non-Negative Impulse Response," *Automatica*, Feb 2003.

Texas Transportation Institute Report, "2002 Urban Mobility Study," URL: mobility.tamu.edu

Tomizuka, M. and Hedrick, J.K., "Automated Vehicle Control for IVHS Systems", *Proceedings of the IFAC Conference*, Sydney, 1993.

Unsal, C. and Kachroo, P., "Sliding Mode Measurement Feedback Control for Antilock Braking Systems," *IEEE Transactions on Control Systems Technology*, March 1999, Vol. 7, No. 2, pp. 271-281.

Varaiya, Pravin, "Smart Cars on Smart Roads: Problems of Control," *IEEE Transactions on Automatic Control*, v 38 n 2, p 195-207, Feb 1993.

Watanabe, T., Kishimoto, N., Hayafune, K., Yamada, K. and Maede, N., 1997, "Development of an Intelligent Cruise Control System", *Mitsubishi Motors Corporation Report*, Japan.

Woll, J., 1997, "Radar Based Adaptive Cruise Control for Truck Applications", *SAE Paper No. 973184*, Presented at SAE International Truck and Bus Meting and Exposition, Cleveland, Ohio, November 1997.

United States Department of Transportation, *NHTSA, FARS and GES*, "Fatal Accident Reporting System (FARS) and General Estimates System (GES)," 1992.

Yanakiev, D. and Kanellakopoulos, I., 1995, "Variable time Headway for String Stability of Automated Heavy-Duty Vehicles", *Proceedings of the 34th IEEE Conference on Decision and Control*, New Orleans, LA, December 1995, pp. 4077-4081.

Yi, J., Alvarez, L., Claeys, X. and Horowitz, R., "Emergency Braking Control with an Observer Based Dynamic Tire Road Friction Model and Wheel Angular Velocity Measurement," *Vehicle System Dynamics*, 2003, Vol. 39, No. 2, pp. 81-97.

Yu, J.S., "A Robust Adaptive Wheel-Slip Controller for Antilock Brake System," *Proceedings of the 36th IEEE Conference on Decision and Control*, Dec 1997, pp. 2545-2546.

Chapter 6

ADAPTIVE CRUISE CONTROL

6.1   INTRODUCTION

An adaptive cruise control (ACC) system is an extension of the standard cruise control system. An ACC equipped vehicle has a radar or other sensor that measures the distance to other preceding vehicles (downstream vehicles) on the highway. In the absence of preceding vehicles, the ACC vehicle travels at a user-set speed, much like a vehicle with a standard cruise control system (see Figure 6-1). However, if a preceding vehicle is detected on the highway by the vehicle's radar, the ACC system determines whether or not the vehicle can continue to travel safely at the desired speed. If the preceding vehicle is too close or traveling too slowly, then the ACC system switches from speed control to spacing control. In spacing control, the ACC vehicle controls both the throttle and brakes so as to maintain a desired spacing from the preceding vehicle.

An ACC system is "autonomous" - it does not depend on wireless communication or on cooperation from other vehicles on the highway. It only uses on-board sensors such as radar to accomplish the task of maintaining the desired spacing from the preceding vehicle. The first-generation ACC systems were first introduced in Japan (Watanabe, et. al., 1997) and Europe and are now available in the North American market (Fancher, et. al., 1997, Reichart, et. al., 1996 and Woll, 1997). The 2003 Mercedes S-class and E-class passenger sedans come with the option of a radar based Distronic adaptive cruise control system. The 2003 Lexus LS340 comes with an optional laser based adaptive cruise control system.

without preceding vehicle   maintain constant speed

with preceding vehicle   maintain safe distance

radar
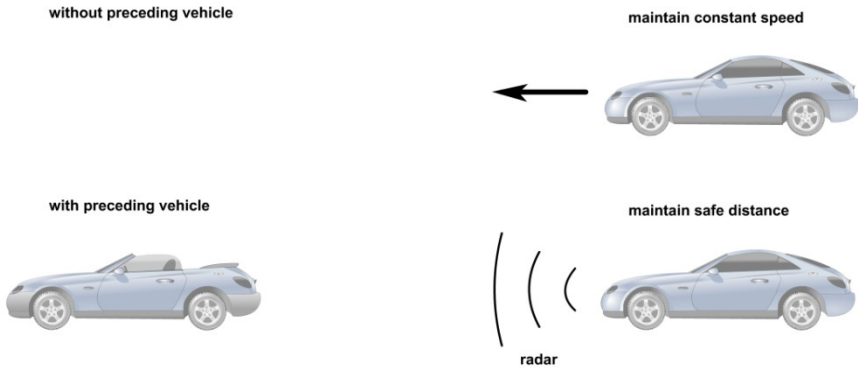
Figure 6-1. Adaptive cruise control

An ACC system provides enhanced driver comfort and convenience by allowing extended operation of the cruise control option even in the presence of other traffic. ACC systems can also possibly contribute towards increased safety on the highways. This is because statistics of highway accidents show that over 90% of accidents are caused by human error (US Department of Transportation, 1992). Only a very small percentage of accidents are the result of equipment failure or even due to environmental conditions (like slippery roads). Since an ACC system potentially reduces driver burden and partially replaces driver operation with automated operation, it is expected that the adoption of ACC systems will potentially lead to reduced accidents.

From the discussion above, it is clear that the ACC system will have two modes of steady state operation:

1) speed control
2) vehicle following (i.e. spacing control)

Vehicle following is the topic of discussion in sections 6.2, 6.3, 6.4, 6.5 and 6.6 in this chapter. Speed control has been discussed earlier in section 5.3 of Chapter 5.

The ACC system must also decide which type of steady state operation is to be used i.e. whether the vehicle should use speed control or vehicle following, based on real-time radar measurements of distance and relative velocity from any preceding vehicle. In addition, the controller must perform a number of transitional maneuvers, including

1. ensuring smooth transition from speed control to vehicle following and vice-versa

2. determining transition trajectories to ensure the vehicle reaches its desired steady state spacing or speed each time a new preceding vehicle is encountered, the current preceding vehicle makes an exit or a lane change, etc.

These transitional maneuvers and transitional control algorithms are discussed in section 6.7 of this chapter.

6.2 VEHICLE FOLLOWING SPECIFICATIONS

Vehicle following is one of the two modes of steady state operation of the ACC system. In the vehicle following mode of operation, the ACC vehicle maintains a desired spacing from the preceding vehicle. The two important specifications that the vehicle following control system must satisfy are individual vehicle stability and string stability.

a) Individual vehicle stability

The vehicle following control law is said to provide individual vehicle stability if the spacing error of the ACC vehicle converges to zero when the preceding vehicle is operating at constant speed. If the preceding vehicle is accelerating or decelerating, then the spacing error is expected to be non-zero. Spacing error in this definition refers to the difference between the actual spacing from the preceding vehicle and the desired inter-vehicle spacing.

Consider a string of vehicles on the highway using a longitudinal control system for vehicle following, as shown in Figure 6-2. Let x_i be the location of the i th vehicle measured from an inertial reference, as shown in Figure 6-2. The spacing error for the i th vehicle (the ACC vehicle under consideration) is then defined as $\delta_i = x_i - x_{i-1} + L_{des}$. Here L_{des} is the desired spacing and includes the preceding vehicle length ℓ_{i-1}. The desired spacing L_{des} could be chosen as a function of variables such as the vehicle speed $\dot{x}_i$. The ACC control law is said to provide individual vehicle stability if the following condition is satisfied

$$\ddot{x}_{i-1} \to 0 \quad \Rightarrow \quad \delta_i \to 0 \tag{6.1}$$
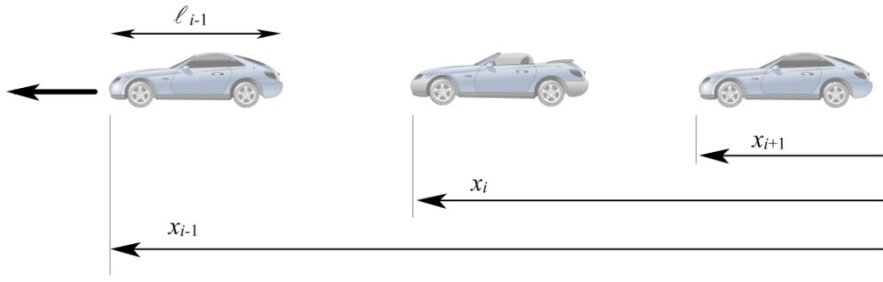
Figure 6-2. String of adaptive cruise control vehicles

b) <u>String stability</u>

If the vehicle following control law ensures individual vehicle stability, the spacing error should converge to zero when the preceding vehicle moves at constant speed. However, the spacing error is expected to be non-zero during acceleration or deceleration of the preceding vehicle. It is important then to describe how the spacing error would propagate from vehicle to vehicle in a string of ACC vehicles that use the same spacing policy and control law. The string stability of a string of ACC vehicles refers to a property in which spacing errors are guaranteed not to amplify as they propagate towards the tail of the string (Swaroop, 1995, Swaroop and Hedrick, 1996). For example, string stability ensures that any errors in spacing between the 2nd and 3rd cars does not amplify into an extremely large spacing error between cars 7 and 8 further up in the string of vehicles.

   A rigorous definition for string stability will be provided in section 6.4.

6.3   CONTROL ARCHITECTURE

The longitudinal control system architecture for an ACC vehicle is typically designed to be hierarchical, with an upper level controller and a lower level controller as shown in Figure 6-3. The upper level controller determines the desired acceleration for each vehicle. The lower level controller determines the throttle and/or brake commands required to track the desired acceleration. Vehicle dynamic models, engine maps and nonlinear control synthesis techniques (Choi and Devlin, 1995a and 1995b, Hedrick et al, 1991, Hedrick, et. al., 1993) are used by the lower controller in calculating the real-time brake and throttle inputs required to track the desired acceleration.
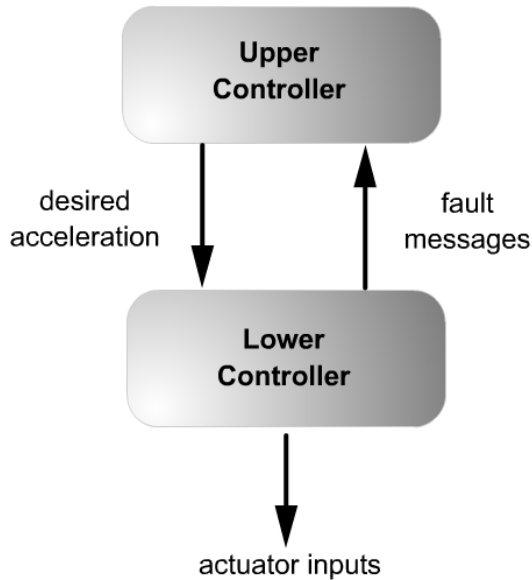
Figure 6-3. Structure of longitudinal control system

The objective of the upper controller is to determine desired acceleration such that two performance specifications are met. As discussed in section 6.2, the first specification is the individual stability of the vehicle so that it can asymptotically achieve and maintain a desired spacing with respect to the preceding vehicle on the highway. The second specification is to ensure that when many ACC vehicles on the highway operate under automatic control using the same vehicle following control law, the "string stability" of a string of vehicles can be guaranteed (Swaroop, 1995, Swaroop and Hedrick, 1996).

As far as the upper level controller is concerned, the plant model used for control design is

$$\ddot{x}_i = u \tag{6.2}$$

where the subscript i denotes the i th car in the string. The acceleration of the car is thus assumed to be the control input. However, due to the finite bandwidth associated with the lower level controller, each car is actually expected to track its desired acceleration imperfectly. The objective of the upper level controller design is therefore stated as that of meeting performance specifications 1 and 2 robustly in the presence of a first-order lag in the lower level controller performance:

$$\ddot{x}_i = \frac{1}{\tau s + 1} \ddot{x}_{i\_des} = \frac{1}{\tau s + 1} u_i \tag{6.3}$$

Equation (6.2) is thus assumed to be the nominal plant model while the performance specifications have to be met even if the actual plant model were given by equation (6.3).

This chapter assumes a lag of $\tau = 0.5$ sec for analysis and simulation. The maximum acceleration and deceleration possible are assumed to be 0.25g and -0.5g respectively.

6.4   STRING STABILITY

As described briefly earlier, the string stability of a string of ACC vehicles refers to a property in which spacing errors are guaranteed not to amplify as they propagate towards the tail of the string. In this section, mathematical conditions that ensure (and define) string stability will be provided

Let δ_i and δ_{i-1} be the spacing errors of consecutive ACC vehicles in a string. Let $\hat{H}(s)$ be the transfer function relating the spacing errors of consecutive vehicles

$$\hat{H}(s) = \frac{\delta_i}{\delta_{i-1}} \tag{6.4}$$

The system is string stable if the following two conditions are satisfied:

a) The transfer function $\hat{H}(s)$ should satisfy

$$\| \hat{H}(s) \|_\infty \leq 1 \tag{6.5}$$

b) The impulse response function $h(t)$ corresponding to $\hat{H}(s)$ should not change sign (Swaroop, 1995), i.e.

$$h(t) > 0 \quad \forall t \geq 0 \tag{6.6}$$

The reasons for these two requirements to be satisfied can be understood by reading sections 7.5 and 7.6 in Chapter 7. Roughly speaking, equation (6.5) ensures that $\| \delta_i \|_2 \leq \| \delta_{i-1} \|_2$ which means that the energy in the spacing error signal decreases as the spacing error propagates towards the

tail of the string. Equation (6.6) ensures that the steady state spacing errors of the vehicles in the string have the same sign. This is important because a positive spacing error implies that a vehicle is closer than desired while a negative spacing error implies that it is further apart than desired. If the steady state value of δ_i is positive while the steady state value of δ_{i-1} is negative, then this might be dangerous even though in terms of magnitude δ_i might be smaller than δ_{i-1}. The condition that the impulse response be positive ensures that steady state values of δ_i and δ_{i-1} have the same sign.

When conditions (6.5) and (6.6) are both satisfied, then, $\| \delta_i \|_\infty \leq \| \delta_{i-1} \|_\infty$, as discussed in section 7.5.

More details on string stability can be found in sections 7.5 and 7.6 in Chapter 7.

6.5　AUTONOMOUS CONTROL WITH CONSTANT SPACING

As discussed in section 6.1, an autonomous controller (like the ACC system) only utilizes on board sensors like radar and does not depend on inter-vehicle communication or any other form of cooperation from other vehicles on the highway. This implies that the only variables available as feedback measurements for the upper controller are inter-vehicle spacing, relative velocity and the ACC vehicle's own velocity. This section demonstrates that such an autonomous controller cannot use a constant spacing policy i.e. *the constant spacing policy is unsuitable for autonomous control applications.*

Define the measured inter-vehicle spacing as

$$\varepsilon_i = x_i - x_{i-1} + \ell_{i-1} \tag{6.7}$$

where ℓ_{i-1} is the length of the preceding vehicle. Under the constant spacing policy, the spacing error of the i th vehicle is then defined as

$$\delta_i = x_i - x_{i-1} + L_{des} \tag{6.8}$$

where L_{des} is the desired constant value of inter-vehicle spacing and includes the preceding vehicle length.

If we assume that the acceleration of the vehicle can be instantaneously controlled, then a linear control system of the type

$$\ddot{x}_i = -k_p \delta_i - k_v \dot{\delta}_i \qquad (6.9)$$

yields

$$\ddot{\delta}_i = \ddot{x}_i - \ddot{x}_{i-1} = -k_p \delta_i - k_v \dot{\delta}_i + k_p \delta_{i-1} + k_v \dot{\delta}_{i-1}$$

which leads to the following closed-loop error dynamics

$$\ddot{\delta}_i + k_v \dot{\delta}_i + k_p \delta_i = k_p \delta_{i-1} + k_v \dot{\delta}_{i-1} \qquad (6.10)$$

The transfer function

$$G(s) = \frac{\delta_i}{\delta_{i-1}}(s) = \frac{k_p + k_v s}{s^2 + k_v s + k_p} \qquad (6.11)$$

describes the propagation of spacing errors along the vehicle string. The Bode magnitude plot in Figure 6-4 is shown for $k_p = 1$, $k_v = 0.3$. The maximum magnitude of this transfer function is greater than 1 so that the autonomous control law of equation (6.9) is not string stable.
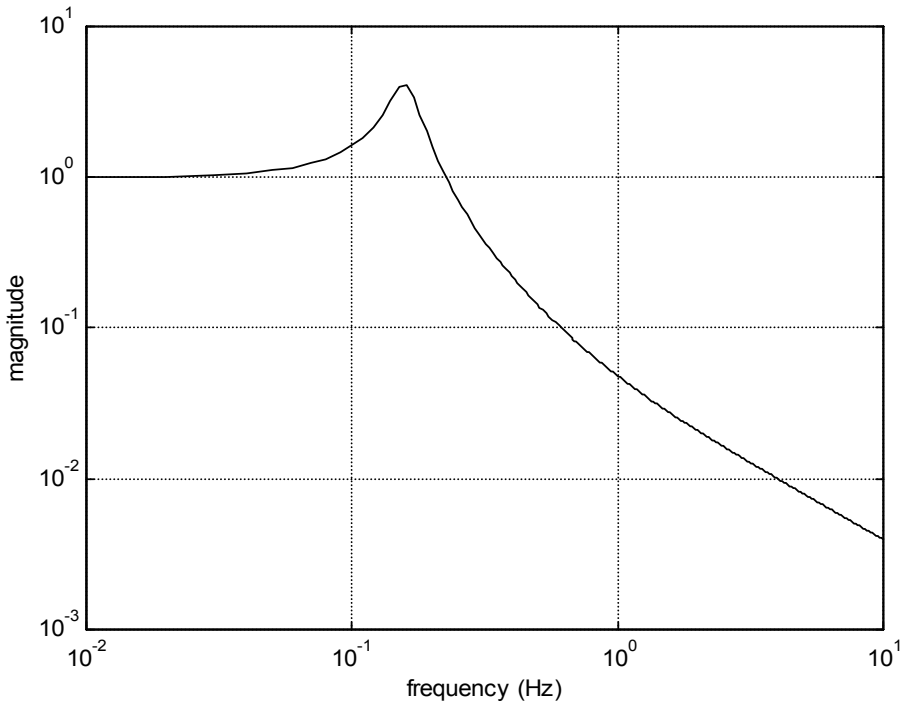
Figure 6-4. Magnitude of G(s) from equation (6.11)

All positive values of k_p and k_v guarantee that the spacing error of the i th vehicle converges to zero when the spacing error of the $i-1$ th vehicle is zero. Thus individual vehicle stability is ensured. However, there are no positive values of k_p and k_v and for which the magnitude of the transfer function $G(s)$ can be guaranteed to be less than unity. To see why this is the case, rewrite $G(s)$ as

$$G(s) = \frac{k_p}{s^2 + k_v s + k_p}\left(\frac{k_v}{k_p}s + 1\right) \tag{6.12}$$

or

$$G(s) = G_1(s)G_2(s) \tag{6.13}$$

For the magnitude of $G_1(j\omega)$ to be less than 1, one needs the damping ratio $\xi \geq 0.707$ or $\dfrac{k_v}{2\sqrt{k_p}} \geq 0.707$ i.e.

$$k_v \geq 1.414\sqrt{k_p} \tag{6.14}$$

For the magnitude of $G_2(j\omega)$ to not exceed 1 at frequencies up to the resonant frequency $\sqrt{k_p}$, one needs the frequency $\dfrac{k_p}{k_v}$ to be bigger than $\sqrt{k_p}$. Hence, one needs $\dfrac{k_p}{k_v} > \sqrt{k_p}$ or

$$\sqrt{k_p} > k_v \tag{6.15}$$

It is not possible to find gains that satisfy both equations (6.14) and (6.15). Hence the magnitude of $G(s)$ will always exceed 1.

The constant spacing policy is therefore not suitable for use on autonomous systems such as the ACC system (Swaroop, 1995).

6.6   AUTONOMOUS CONTROL WITH THE
CONSTANT TIME-GAP POLICY

Since the constant spacing policy is unsuitable for autonomous control, a
better spacing policy that can ensure both individual vehicle stability and
string stability must be used. The constant time-gap (CTG) spacing policy is
such a spacing policy. In the CTG spacing policy, the desired inter-vehicle
spacing is not constant but varies linearly with velocity:

$$L_{des} = \ell_{i-1} + h\dot{x}_i \qquad\qquad\qquad (6.16)$$

The constant parameter h is referred to as the time-gap. The spacing
error varies with the velocity and is defined as

$$\delta_i = \varepsilon_i + h\dot{x}_i \qquad\qquad\qquad (6.17)$$

where $\varepsilon_i = x_i - x_{i-1} + \ell_{i-1}$, as defined earlier in equation (6.7).

The following controller based on the CTG spacing policy was
developed by Ioannou and Chien (1993). The control law is autonomous and
can be represented as

$$\ddot{x}_{i\_des} = -\frac{1}{h}(\dot{\varepsilon}_i + \lambda\delta_i) \qquad\qquad\qquad (6.18)$$

With this control law, it can be shown that the spacing errors of
successive vehicle δ_i and δ_{i-1} are independent of each other. Differentiate
equation (6.17) to obtain

$$\dot{\delta}_i = \dot{\varepsilon}_i + h\ddot{x}_i \qquad\qquad\qquad (6.19)$$

Substituting for $\ddot{x}_i$ from equation (6.18) into equation (6.19) and
assuming $\ddot{x}_i = \ddot{x}_{i\_des}$, the error dynamics for δ_i are obtained as

$$\dot{\delta}_i = -\lambda\delta_i \qquad\qquad\qquad (6.20)$$

Thus δ_i is independent of δ_{i-1} and is expected to converge to zero as long as $\lambda > 0$. Note, however, that this result is only true if any desired acceleration can be instantaneously obtained by the vehicle i.e. if the time constant τ associated with the lower level controller performance is assumed zero.

6.6.1   String stability of the CTG spacing policy

In the presence of the lower controller and actuator dynamics, the desired acceleration is not obtained instantaneously but instead satisfies the dynamics approximated by equation (6.3):

$$\tau \dddot{x}_i + \ddot{x}_i = \ddot{x}_{i\_des}$$

Substituting for $\ddot{x}_{i\_des}$ from equation (6.18), we obtain

$$\tau \dddot{x}_i + \ddot{x}_i = -\frac{1}{h}(\dot{\varepsilon}_i + \lambda \delta_i) \tag{6.21}$$

Also, differentiating δ_i twice from equation (6.17), we obtain

$$\ddot{\delta}_i = \ddot{\varepsilon}_i + h\dddot{x}_i \tag{6.22}$$

Substituting for $\dddot{x}_i$ from equation (6.21), we find that the relation between ε_i and δ_i is given by

$$\ddot{\varepsilon}_i = \ddot{\delta}_i + \frac{1}{\tau}\left[\dot{\varepsilon}_i + h\ddot{x}_i + \lambda\delta_i\right] \text{ or}$$

$$\ddot{\varepsilon}_i = \ddot{\delta}_i + \frac{1}{\tau}\left(\dot{\delta}_i + \lambda\delta_i\right) \tag{6.23}$$

The difference between errors of successive vehicles can be written as

$$\delta_i - \delta_{i-1} = \varepsilon_i - \varepsilon_{i-1} + h(\dot{x}_i - \dot{x}_{i-1})$$

or

$$\delta_i - \delta_{i-1} = \varepsilon_i - \varepsilon_{i-1} + h\dot{\varepsilon}_i \qquad (6.24)$$

Using equation (6.23) to substitute in equation (6.24) for ε_i in terms of δ_i and for ε_{i-1} in terms of δ_{i-1}, a dynamic relation between δ_i and δ_{i-1} can be obtained. In the transfer function domain, this relation is

$$\frac{\delta_i}{\delta_{i-1}} = \frac{s + \lambda}{h\tau s^3 + hs^2 + (1 + \lambda h)s + \lambda} \qquad (6.25)$$

The string stability of this system can be analyzed by looking at the above transfer function and checking if its magnitude is always less than 1. Substituting $s = j\omega$ and evaluating the magnitude of the above transfer function, it can be shown (see Appendix 6.A) that the magnitude is always less than or equal to unity at all frequencies only if

$$h \geq 2\tau \qquad (6.26)$$

Further if equation (6.26) is satisfied, then it is guaranteed that one can find a value of λ such that $\| \hat{H}(s) \|_\infty \leq 1$. Thus the condition (6.26) is both necessary and sufficient. The above result was obtained by Swaroop (1995). In effect, this means that string stability can be maintained only if the time-gap is larger than the variable 2τ.

below shows the impulse response of the transfer function in equation (6.23) for values of $\lambda = 0.4$, $\tau = 0.5$ and $h = 1.8$ seconds. It can be seen that the impulse response of the system is non-negative for these values of the transfer function parameters. Thus, both $\left\| \hat{H}(s) \right\|_\infty \leq 1$ and $h(t) > 0$ can be ensured by this choice of controller parameters.
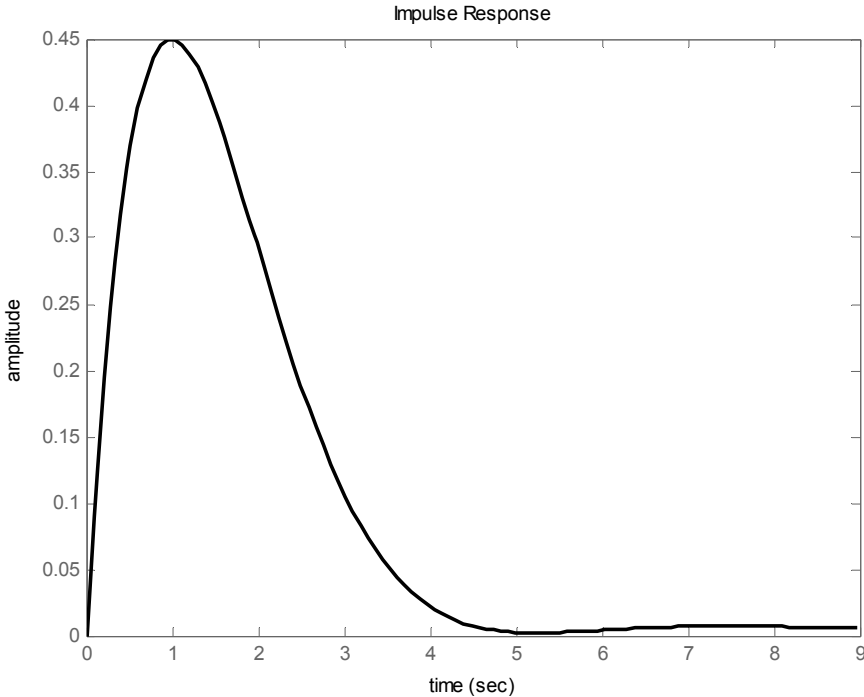
Figure 6-5. Impulse response of the constant time-gap autonomous controller

The specification $\left\| \hat{H}(s) \right\|_\infty \leq 1$ can always be met by choosing h to be sufficiently big so that equation (6.26) is satisfied. However, there are no results available that provide a direct design procedure for ensuring that the impulse response $h(t)$ is non-negative. The results in Swaroop (2003) provide indirect design tips for the same. Two necessary conditions that must be satisfied by the transfer function $\hat{H}(s)$ in order for the impulse response to be non-negative are

1) The dominant poles of the system should not be a complex conjugate pair.
2) There should not be any zeros of the system that are completely to the right of all poles of the closed-loop system.

6.6.2   Typical delay values

This section discusses what would be a typical value to expect for the constant τ which is the time constant of the lag in tracking any desired acceleration command. From equation (6.26), it is clear that the value of τ

limits the time gap h. A smaller time gap would lead to higher density of traffic and thus increased traffic capacity on the highway. However, from equation (6.26), the time gap cannot be made smaller than 2τ, since the system would then no longer be string stable.

The lag in the performance of the lower controller comes from several sources, accumulating brake or engine actuation lags and sensor signal processing lags.

(brake pressure (psi) vs time (sec))
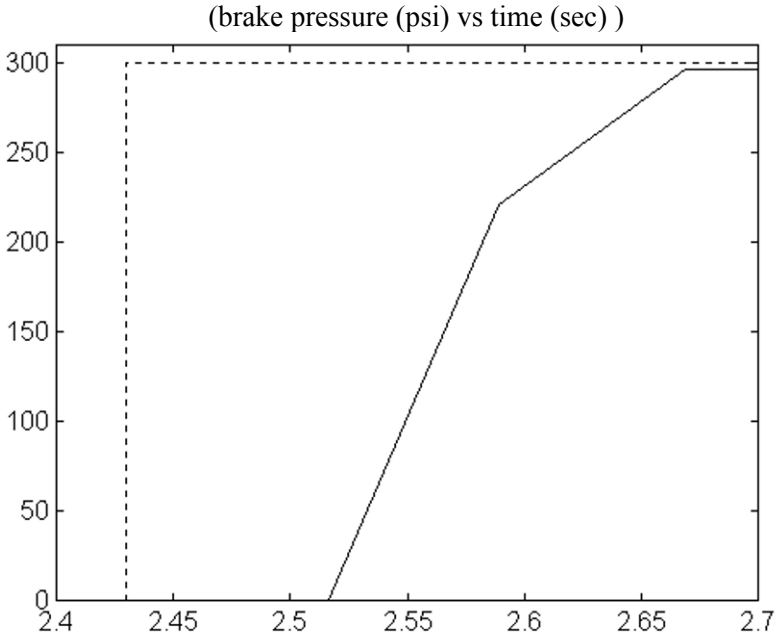
Figure 6-6. Pure-time delay and lag in an ABS-modified brake system

Figure 6-6 shows the measured performance of a brake actuator designed by a modification of the ABS system. When required to track a step input of 300 psi brake pressure, the actuator has a pure time delay of 70 milliseconds in addition to a first order time constant of 80 milliseconds. Figure 6-7 shows the measured performance of a constant-flow valve brake actuator designed at PATH. This actuator has a pure time delay of 70 milliseconds and a first order time constant of 70 milliseconds (Rajamani and Shladover, 2001).
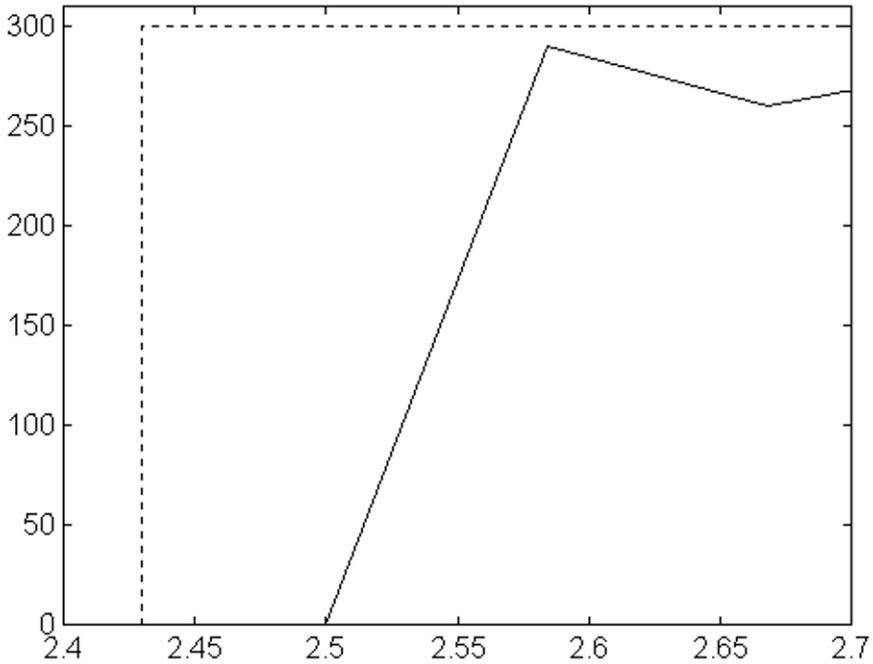
Figure 6-7. Pure time delay and lag in a constant flow brake actuator developed at PATH

If we include

1) the pure time delay in the engine response (60 milliseconds at 2000 rpm),
2) the bandwidth of the lower level multiple-sliding-surface controller that tracks acceleration
3) the bandwidth of low pass filters used for other sensors such as engine manifold pressure sensor, wheel speed sensor, etc
4) the bandwidth of the throttle actuator
5) the lag due to discrete sampling at 50 Hz (20 ms sampling)
6) the 200 ms lag due to the radar filter
7) when braking, the brake actuator lag instead of engine time delay.

it is clear that the overall time constant of the lower level controller could be as much as 500 milliseconds.

Thus, from equation (6.26), in order to ensure string stability, the smallest time-gap that can be used by the upper level controller is 1 second. This is equivalent to a steady-state spacing of 30 meters between vehicles at a speed of 30 m/s. The theoretical maximum traffic flow rate that can be achieved is therefore less than 3100 vehicles/ hour, assuming that the vehicles are 5 meters long.

An alternative nonlinear autonomous controller with a variable time gap has been proposed by Yanakiev and Kanellakopoulos (1995). Results in Yanakiev and Kanellakopoulos (1995) indicate improvements in performance and response compared to the standard constant-time-gap autonomous controller. While nonlinear controllers have the potential to overcome the minimum time-gap constraint of the standard linear controller, they are considerably more difficult to analyze. This is because linear systems tools such as frequency response and Bode plots can no longer be used in the analysis. The variable-time-gap algorithm in Yanakiev and Kanellakopoulos (1995) has not been analyzed for its robustness to the presence of the lower controller dynamics.

6.7   TRANSITIONAL TRAJECTORIES

All of the control laws presented in sections 6.2 – 6.6 were designed for steady state vehicle following. An ACC vehicle must not only execute steady-state vehicle following but also other maneuvers like speed control and transitional maneuvers like "vehicle join" for closing in on a slower moving preceding vehicle.

6.7.1   The need for a transitional controller

An ACC vehicle operates under speed control when there is no preceding target vehicle detected in its lane. While under speed control, the ACC vehicle might suddenly encounter a new vehicle in its lane. The new vehicle might be encountered because it cuts in from another lane or because it might be a slower moving vehicle in the same lane. In each case the ACC vehicle must decide whether to continue to operate under the speed control mode or transition to the vehicle following mode. If a transition to vehicle following is required, a transitional trajectory that will bring the ACC vehicle to its steady state following distance needs to be designed. Similarly, an ACC vehicle under the vehicle following mode might lose its target vehicle due to the target vehicle being faster or the target vehicle making a lane change. In such a case, the ACC vehicle must decide whether to switch to speed control or to initiate a transitional maneuver to follow a different target vehicle further downstream.

The regular constant time-gap (CTG) control law from section 6.6 cannot directly be used to follow a newly encountered vehicle. A transitional trajectory needs to be designed before the CTG control law can be used. The need for a transitional trajectory can be understood from the following example:

Example:

Consider the scenario shown in Figure 6-8 where the ACC vehicle which was operating under speed control encounters a stalled vehicle in its lane. Assume that the initial speed of the ACC vehicle is 30 m/s and that the CTG control law parameters are $\lambda = 1$, $h = 1$ sec and $L = 5$ meters.
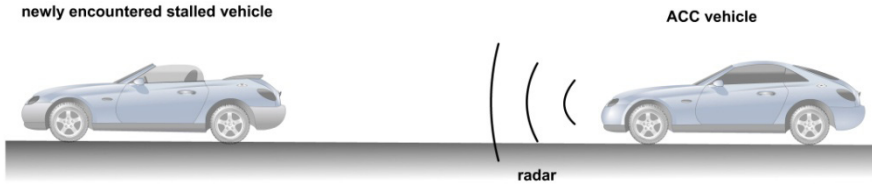
Figure 6-8. ACC vehicle encounters stalled vehicle

The final steady state desired spacing of the vehicle is $L = 5$ meters. The initial desired spacing of the vehicle is $L + h\dot{x}_i = 5 + 30 = 35$ meters. The initial spacing error is $\delta_i = x_i - x_{i-1} + L + h\dot{x}_i = -100 + 5 + 30 = -65$ and the initial relative velocity is $\dot{\varepsilon}_i = \dot{x}_i - \dot{x}_{i-1} = 30$.

If the ACC vehicle were to directly use the CTG control law $\ddot{x}_{des} = -\dfrac{1}{h}(\dot{\varepsilon}_i + \lambda \delta_i)$, then the initial desired acceleration command would turn out to be $\ddot{x}_{des} = -1(30 - 65) = 35 \, m/s^2$!

Thus the initial desired acceleration would be a huge positive value ! This is because the vehicle has a huge spacing error in which it calculates that it is too far behind the target vehicle, even though the target vehicle is moving much more slowly (is stalled).

Since the initial distance is only 100 meters, there is a danger of the ACC vehicle crashing into the stalled vehicle. The distance required for the ACC vehicle to brake to a stop starting from a speed of 30 m/s and assuming a maximum braking deceleration of 5 m/s^2 is

$$X = \frac{30^2}{2(5)} = 90 \text{ meters.}$$

Thus starting from an initial distance of 100 meters, the vehicle has barely enough distance to avoid a collision if it started braking right away. If the vehicle initially accelerated using the CTG control law, it would not have enough distance to stop and would eventually collide with the stalled vehicle!

End of example

The regular steady state vehicle following control law (without use of a transitional trajectory) does not take into account the following considerations

a) Preventing a collision is the highest priority i.e. it is not allowable to have the ACC vehicle speed up when it encounters a new target vehicle only to collide with the vehicle later.
b) The brake and engine actuators on a vehicle have limited maximum allowable values and saturate
c) A newly encountered preceding vehicle need not always be a target vehicle for vehicle following.

A transitional controller is therefore required that takes the above considerations into account.

6.7.2   Transitional controller design through $R - \dot{R}$ diagrams

When a new target vehicle is encountered by the ACC vehicle, a range-range rate diagram can be used (Fancher and Bareket, 1994) to decide whether

a) The vehicle should use speed control.
b) The vehicle should use spacing control (with a defined transition trajectory in which desired spacing varies slowly with time)
c) The vehicle should brake as hard as possible in order to avoid a crash.

The range – range rate ($R - \dot{R}$) diagram is developed as follows. Define range R and range rate $\dot{R}$ as shown in Figure 6-9 where

$$\dot{R} = \dot{x}_p - \dot{x} = V_p - V \tag{6.27}$$

$$R = x_p - x \tag{6.28}$$

and x_p, x, V_p and V are inertial positions and velocities of the preceding vehicle and ACC vehicle respectively.

$$\frac{dR}{dt} = V_p - V$$
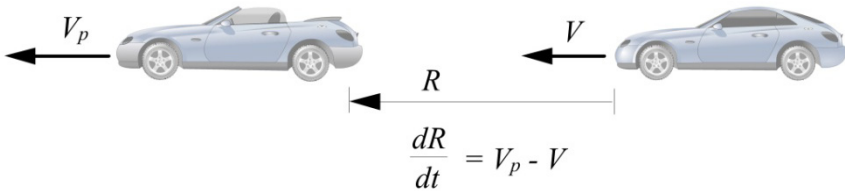
Figure 6-9. Definition of range and range rate

A typical $R - \dot{R}$ diagram, as developed by Fancher and Bareket (1994), is shown in Figure 6-10 below.
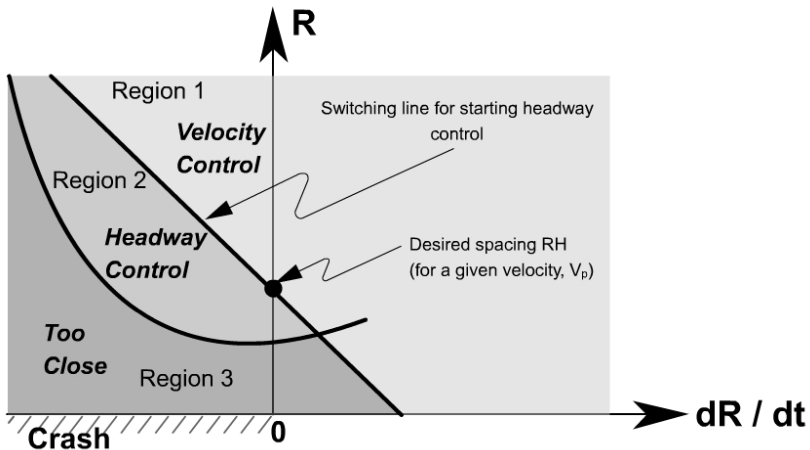
Figure 6-10. Range vs. range-rate diagram

Depending on the measured real-time values of R and $\dot{R}$ and the $R - \dot{R}$ diagram in Figure 6-10, the ACC system determines the mode of longitudinal control in which the ACC vehicle should operate. For instance, in region 1, the vehicle continues to operate under speed control. In region 2, the vehicle operates under spacing control. In region 3, the vehicle decelerates at the maximum allowable deceleration so as to try and avoid a crash.

The $R - \dot{R}$ diagram has the following properties (Fancher and Bareket, 1994):

1) <u>Possible directions of motion</u>
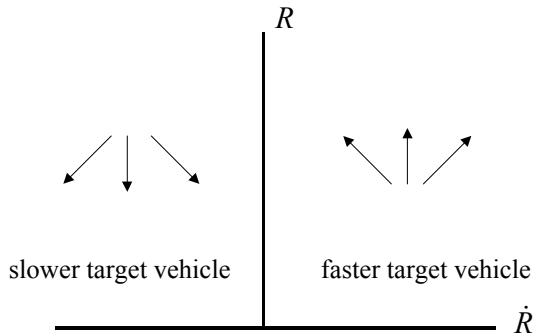
Figure 6-11. Possible directions of motion

When $\dot{R}$ is negative, R can only decrease. When $\dot{R}$ is positive, R can only increase. Hence in the right half of the $R - \dot{R}$ diagram, R can only increase. In the left half of the $R - \dot{R}$ diagram, R can only decrease. This is illustrated in Figure 6-11.
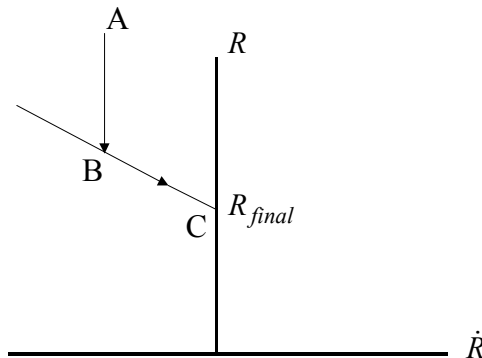
Figure 6-12. Switching line for spacing control

2) <u>Switching line for starting spacing control</u>

The switching line from speed to spacing control is given by

$$R = -T\dot{R} + R_{final} \tag{6.29}$$

where T is the slope of the switching line. When a slower vehicle is encountered at a distance larger than the desired final distance R_{final}, the switching line shown in Figure 6-12 can be used to determine when and whether the vehicle should switch to spacing control. If the distance R is greater than that given by the line, speed control should be used.

The overall strategy (shown by trajectory ABC) is to first reduce gap at constant $\dot{R}$, and then follow the desired spacing given by the switching line

$$R = -T\dot{R} + R_{final}$$

Note $\dot{R}$ is negative and hence R is always bigger than R_{final} during this trajectory.

Note that a number of alternate trajectories are also possible from point A to C. For example, a straight line path from A to C could also be used. One of the advantages of the trajectory in Figure 6-12 is that the vehicle doesn't start braking right away, as soon as a new vehicle is encountered. Instead the ACC vehicle continues at its initial speed and starts braking only after the switching line is reached. Abrupt maneuvers as soon as a new vehicle is encountered are avoided.

The control law during spacing control on this transitional trajectory is as follows. Depending on the value of $\dot{R}$, determine R from equation (6.29). Then use R as the desired inter-vehicle spacing in the PD control law

$$\ddot{x}_{des} = -k_p(x - R) - k_d(\dot{x} - \dot{R}) \tag{6.30}$$

3) Trajectory during constant deceleration

The trajectory of the ACC vehicle during constant deceleration is a parabola on the $R - \dot{R}$ diagram. In Figure 6-13, note that the larger deceleration leads to the lower parabola. This can be understood from the fact that for each value of R, $\dot{R}$ is smaller for the lower parabola.
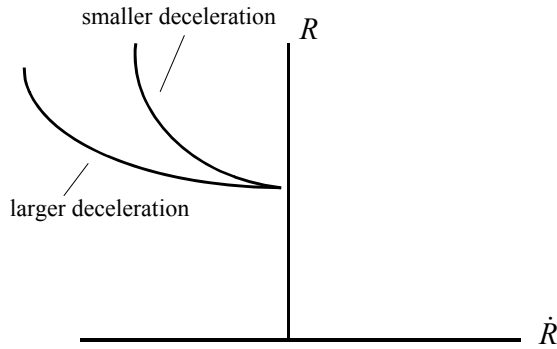
Figure 6-13. Parabolic trajectory during constant deceleration
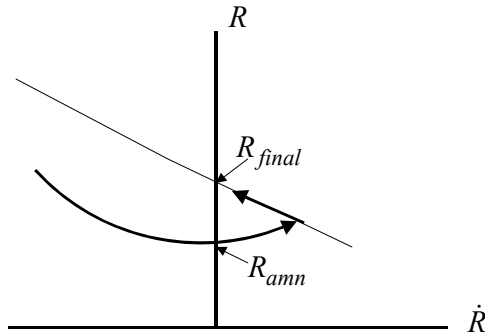
Figure 6-14. Constant deceleration followed by acceleration

As the vehicle decelerates $\dot{R}$ will increase (become less negative initially). Eventually $\dot{R}$ will become zero as the ACC vehicle slows down to the target vehicle speed. Then $\dot{R}$ will start becoming positive, as shown in Figure 6-14. When $\dot{R} > 0$, the distance between the vehicles will start increasing. Let R_{amn} be the minimum value of R achieved in the parabolic trajectory of constant deceleration. Then the equation of the parabolic trajectory is

$$R = R_{amn} + \frac{\dot{R}^2}{2D} \tag{6.31}$$

where D is the deceleration value of the vehicle. The same switching line discussed in Figure 6-12 can be used to eventually accelerate the vehicle and come to the final desired spacing R_{final}. This is shown in Figure 6-14.

4) What slope should the switching line have ?

The switching line should be such that travel along the line is comfortable and does not constitute high deceleration. The deceleration during coasting (zero throttle and zero braking) can be used to determine the slope of the switching line. Let $D = 0.4m/s^2$ be the deceleration during coasting. Construct a parabola with deceleration D that passes through R_{final} as shown in Figure 6-15. Then the trajectory of the parabola is

$$R = R_{final} + \frac{\dot{R}^2}{2D} \qquad (6.32)$$

The value of this parabola at the maximum measurable range A of the sensor e.g. 300 feet is calculated. The line passing through A and R_{final} can be used to determine the slope. Alternately, the maximum allowable $\dot{R}$ can be used in equation (6.32) to determine the point A of the switching line.
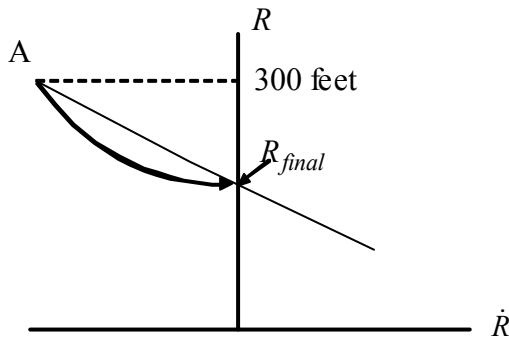
Figure 6-15. Trajectory during coasting

String stability in transitional maneuvers

Do we have to worry about string stability during these transitional maneuvers ? No. This is because only the lead car in any string of vehicles

will execute these transitional maneuvers. The other cars in the string do not execute a transitional trajectory. They only follow the lead vehicle using a steady state controller like the constant time-gap controller. Hence string stability is maintained in the string of vehicles.

6.8   LOWER LEVEL CONTROLLER

In the lower level controller, the throttle and brake actuator inputs are determined so as to track the desired acceleration determined by the upper controller. The following simplified model of vehicle dynamics is used in the development of the lower level controller. This simplified model is based on the assumptions that the torque converter in the vehicle is locked and that there is zero-slip between the tires and the road, as described in chapter 5. These assumptions relate the vehicle speed $\dot{x}_i$ directly to the engine speed ω_e:

$$\dot{x}_i = v_i = (\mathsf{R} r_{eff} \omega_e)_i \tag{6.33}$$

where R is the gear ratio and r_{eff} is the effective tire radius.

Under these assumptions, as described in section 5.5.1 of Chapter 5, the dynamics relating engine speed ω_e to the pseudo-inputs "net combustion torque" T_{net} and brake torque T_{br} can be modeled by

$$\dot{\omega}_e = \frac{T_{net} - c_a \mathsf{R}^3 r_{eff}^{\,3} \omega_e^{\,2} - \mathsf{R}(r_{eff} R_x + T_{br})}{J_e} \tag{6.34}$$

where $J_e = I_e + (m r_{eff}^{\,2} + I_\omega) \mathsf{R}^2$ is the effective inertia reflected on the engine side, R is the gear ratio and r_{eff} the tire radius.

Note that R is used in this chapter to denote the transmission gear ratio (not to be confused with R which is used in the $R - \dot{R}$ diagrams).

If the net combustion torque is chosen as

$$(T_{net})_i = \frac{J_e}{\mathsf{R} \, r_{eff}} \ddot{x}_{ides} + [c_a \mathsf{R}^3 r_{eff}^{\,3} \omega_e^{\,2} + \mathsf{R}(r_{eff} R_x + T_{br})]_i \tag{6.35}$$

then, from equation (6.34), the acceleration of the ACC vehicle is equal to the desired acceleration defined by the upper level controller : $\ddot{x}_i = \ddot{x}_{ides}$.

Once the required combustion torque is obtained from (6.35), the control law to calculate the throttle angle to provide this torque can be obtained by using engine dynamic models and applying nonlinear control synthesis techniques. Engine dynamic models for both SI and diesel engines and control design to provide a desired torque are discussed in Chapter 9 of this book.

6.9   CHAPTER SUMMARY

The longitudinal controller in an ACC system has two modes of steady state operation:

1) speed control
2) spacing control

Steady state spacing control is called vehicle following. In the vehicle following mode, the longitudinal controller must ensure that the following two properties are satisfied:

1) Individual vehicle stability, in which spacing error converges to zero if the preceding vehicle travels at constant velocity
2) String stability, in which spacing error does not amplify as it propagates towards the tail of a string of vehicles.

An ACC system is "autonomous" - it does not depend on wireless communication or on cooperation from other vehicles on the highway. It only uses on-board sensors to accomplish its control system tasks. In the case of an autonomous controller, a constant inter-vehicle spacing policy cannot be used. This is because an autonomous controller can ensure individual vehicle stability but cannot ensure string stability in the case of the constant spacing policy. Instead the constant time-gap spacing policy in which the desired spacing is proportional to speed should be used. With the constant time-gap spacing policy, both string stability and individual vehicle stability can be ensured in an autonomous manner.

In addition to executing steady-state vehicle following, the longitudinal controller must also decide which type of steady state operation is to be used i.e. whether the vehicle should use speed control or vehicle following, based on real-time radar measurements of range and range rate. In addition, the controller must perform a number of transitional maneuvers, including transitioning from spacing control to speed control when the preceding vehicle makes a lane change, executing a "vehicle join" for closing in on a slower moving preceding vehicle, etc. These transitional maneuvers can be

executed based on controllers designed using $R - \dot{R}$ diagrams. $R - \dot{R}$ diagrams were discussed in section 6.7 of the chapter.

NOMENCLATURE

x_i	longitudinal position of ACC vehicle or of the i th vehicle in a string
$\dot{x}_i$ or V_i or V	longitudinal velocity of the i th vehicle
$\varepsilon_i = x_i - x_{i-1} + \ell_{i-1}$	measured inter-vehicle spacing with ℓ_{i-1} being the length of the preceding vehicle
$\delta_i = x_i - x_{i-1} + L_{des}$	spacing error of the i th vehicle
h	value of time gap used in constant time gap controller
R	range
$\dot{R}$	range rate
V_p	velocity of preceding vehicle
R_{final}, T, D	constants used in the $R - \dot{R}$ diagrams
T_{net}	net combustion torque of the engine
T_{br}	brake torque
ω_e	engine angular speed
c_a	aerodynamic drag coefficient
R	gear ratio
r_{eff}	effective tire radius
R_x	rolling resistance of the tires
J_e	effective inertia reflected on the engine side
m	vehicle mass

REFERENCES

Choi, S.B. and Hedrick, J.K., "Vehicle Longitudinal Control Using an Adaptive Observer for Automated Highway Systems", *Proceedings of American Control Conference*, Seattle, Washington, 1995.

Choi, S.B. and Devlin, P., "Throttle and Brake Combined Control for Intelligent Vehicle Highway Systems", *SAE 951897*, 1995.

Fancher, P., Ervin, R., Sayer, J., Hagan, M., Bogard, S., Bareket, Z., Mefford, M. and Haugen, J., 1997, "Intelligent Cruise Control Field Operational test (Interim Report)", *University of Michigan Transportation Research Institute Report,* No. UMTRI-97-11, August 1997.

Fancher, P. and Bareket, Z., 1994, "Evaluating Headway Control Using Range Versus Range-Rate Relationships", *Vehicle System Dynamics*, Vol. 23, No. 8, pp. 575-596.

Hedrick, J.K., McMahon, D., Narendran, V.K. and Swaroop, D., "Longitudinal Vehicle Controller Design for IVHS Systems", *Proceedings of the 1991 American Control Conference*, Vol. 3, pp. 3107-3112, June 1991.

Hedrick, J.K., McMahon, D. and Swaroop, D., "Vehicle Modeling and Control for Automated Highway Systems", *PATH Research Report*, UCB-ITS-PRR-93-24, 1993.

Ioannou, P.A. and Chien, C.C., 1993, "Autonomous Intelligent Cruise Control", *IEEE Transactions on Vehicular Technology*, Vol. 42, No. 4, pp. 657-672.

Rajamani, R., Hedrick, J.K. and Howell, A., "A Complete Fault Diagnostic System for Longitudinal Control of Automated Vehicles", *Proceedings of the Symposium on Advanced Automotive Control*, ASME International Congress, November 1997.

Rajamani, R. and Zhu, C., 1999, "Semi-Autonomous Adaptive Cruise Control Systems", *Proceedings of the American Control Conference*, June 1999.

Rajamani, R., Tan, H.S., Law, B. and Zhang, W.B., "Demonstration of Integrated Lateral and Longitudinal Control for the Operation of Automated Vehicles in Platoons," *IEEE Transactions on Control Systems Technology*, Vol. 8, No. 4, pp. 695-708, July 2000.

R. Rajamani and S.E. Shladover, "An Experimental Comparative Study of Autonomous and Cooperative Vehicle-Follower Control Systems", *Journal of Transportation Research, Part C – Emerging Technologies*, Vol. 9 No. 1, pp. 15-31, February 2001.

Reichart, G., Haller, G. and Naab, K, 1996, "Driver Assistance: BMW Solutions for the Future of Individual Mobility", *Proceedings of ITS World Congress*, Orlando, October 1996.

Slotine, J.J.E. and Li, W., "Applied Nonlinear Control", Prentice Hall, 1991.

Swaroop, D., Hedrick, J.K., Chien, C.C. and Ioannou, P. "A Comparison of Spacing and Headway Control Laws for Automatically Controlled Vehicles", *Vehicle System Dynamics Journal*, Nov. 1994, vol. 23, (no.8):597-625.

Swaroop, D. and Hedrick, J.K., "String Stability of Interconnected Dynamic Systems", *IEEE Transactions on Automatic Control*, March 1996.

Swaroop, D., 1995, "String Stability of Interconnected Systems: An Application to Platooning in Automated Highway Systems", *Ph.D. Dissertation*, University of California, Berkeley, 1995.

Swaroop, D. and Rajagopal, K.R., "Intelligent Cruise Control Systems and Traffic Flow Stability," *Transportation Research Part C: Emerging Technologies*, Vol. 7, No. 6, pp. 329-352, 1999.

Swaroop, D. and Bhattacharya, S.P., "Controller Synthesis for Sign Invariant Impulse Response," *IEEE Transactions on Automatic Control*, Vol. 47, No. 8, pp. 1346-1351, August, 2002.

Swaroop, D., "On the Synthesis of Controllers for Continuous Time LTI Systems that Achieve a Non-Negative Impulse Response," *Automatica*, Feb 2003.

Texas Transportation Institute Report, "2001 Urban Mobility Study," URL: mobility.tamu.edu

United States Department of Transportation, *NHTSA, FARS and GES*, ''Fatal Accident Reporting System (FARS) and General Estimates System (GES),'' 1992.

Watanabe, T., Kishimoto, N., Hayafune, K., Yamada, K. and Maede, N., 1997, "Development of an Intelligent Cruise Control System", *Mitsubishi Motors Corporation Report*, Japan.

Woll, J., 1997, "Radar Based Adaptive Cruise Control for Truck Applications", *SAE Paper No. 973184*, Presented at SAE International Truck and Bus Meting and Exposition, Cleveland, Ohio, November 1997.

Yanakiev, D. and Kanellakopoulos, I., 1995, "Variable time Headway for String Stability of Automated Heavy-Duty Vehicles", *Proceedings of the 34ᵗʰ IEEE Conference on Decision and Control*, New Orleans, LA, December 1995, pp. 4077-4081.

APPENDIX 6.A

This Appendix contains a proof of the result stated in section 6.6.1, namely that the magnitude of the transfer function

$$\hat{H}(s) = \frac{\delta_i}{\delta_{i-1}} = \frac{s + \lambda}{h\tau s^3 + hs^2 + (1 + \lambda h)s + \lambda} \tag{6.36}$$

is always less than or equal to 1 at all frequencies if and only if $h \geq 2\tau$. This Appendix is adapted from the original proof presented by Swaroop (1995).

Background Result:

Consider the following quadratic inequality in ω^2:

$$a\omega^4 + b\omega^2 + c > 0 \tag{6.37}$$

We present the conditions on a, b, c under which the above inequality holds for all values of ω^2.

$$a\omega^4 + b\omega^2 + c = a\left(\omega^4 + 2\frac{b}{2a}\omega^2 + \frac{c}{a}\right)$$

$$= a\left[\left(\omega^2 + \frac{b}{2a}\right)^2 + \frac{4ac - b^2}{4a^2}\right]$$

Hence

$$a\omega^4 + b\omega^2 + c > 0$$

if either

   1) $a, b, c > 0$ (6.38)

or

   2) $b < 0$, $a > 0$, $c > 0$ and $4ac - b^2 > 0$ i.e. $b^2 - 4ac < 0$ (6.39)

Calculations:

Consider the transfer function

$$H(s) = \frac{\hat{\delta}_i}{\hat{\delta}_{i-1}} = \frac{s + \lambda}{\tau h s^3 + h s^2 + (1 + \lambda h)s + \lambda}$$

Substituting $s = j\omega$,

$$H(j\omega) = \frac{j\omega + \lambda}{(\lambda - h\omega^2) + j\omega(1 + \lambda h - \tau h\omega^2)}$$ (6.40)

$$|H(j\omega)|^2 = \frac{\omega^2 + \lambda^2}{(\lambda - h\omega^2)^2 + \omega^2(1 + \lambda h - \tau h\omega^2)^2}$$

$$|H(j\omega)| \le 1$$

$$\Leftrightarrow$$

$$\omega^2 + \lambda^2 \le (\lambda - h\omega^2)^2 + \omega^2(1 + \lambda h - \tau h\omega^2)^2$$

$$\Leftrightarrow$$

$$\tau^2 h^2 \omega^4 + \left(h^2 - 2\tau h - 2\tau\lambda h^2\right)\omega^2 + \lambda^2 h^2 \ge 0$$ (6.41)

Comparing with the background result in equations (6.38) and (6.39)

1) If $b > 0$

$$h^2 - 2\tau h - 2\lambda\tau h^2 > 0$$

Hence

$$h > \frac{2\tau}{1 - 2\lambda\tau}$$

This is possible for small λ if and only if $h > 2\tau$

2) If $b < 0$ and $b^2 - 4ac < 0$

$$(h^2 - 2\tau h - 2\lambda\tau h^2)^2 - 4\tau^2 h^2 \lambda^2 h^2 < 0$$

After simplifying

$$\lambda < \frac{4\tau h - h^2 - 4\tau^2}{8\tau^2 h - 4\tau h^2}$$

$$\lambda < \frac{-(2\tau - h)^2}{4\tau h(2\tau - h)}$$

Since λ must be positive, this implies $h > 2\tau$

Replacing the strict inequality in equation (6.37) with a simple inequality, it follows that $h \geq 2\tau$. From (1) and (2), $h \geq 2\tau$ is a necessary condition. It also follows that if $h \geq 2\tau$ is satisfied, then one can find a $\lambda > 0$ such that $|H(j\omega)| \leq 1$. Thus $h \geq 2\tau$ is both a necessary and sufficient condition for ensuring that the transfer function $\hat{H}(s)$ has a magnitude less than or equal to 1 at all frequencies.

Chapter 7

LONGITUDINAL CONTROL FOR VEHICLE PLATOONS

7.1 AUTOMATED HIGHWAY SYSTEMS

Automated highway systems are the subject of intense research and development by several research groups, most notably by the California PATH program at the University of California, Berkeley. In an automated highway system (AHS), the objective is to dramatically improve the traffic flow capacity on a highway by enabling vehicles to travel together in tightly spaced platoons. The system requires that only adequately instrumented fully automated vehicles be allowed on this special highway. Manually driven vehicles cannot be allowed to operate on such a highway. Figure 5-2 in chapter 5 shows a photograph of eight fully automated cars traveling together in a tightly spaced platoon during a demonstration conducted by California PATH in August 1997. More details on this experimental demonstration are described in section 7.9 of this chapter.

While the primary motivation for the development of AHS is to obtain significant improvements in highway traffic flow capacity, an AHS will also provide significant safety benefits. This is because over 90% of accidents on today's highways are caused by human error (US Department of Transportation, 1992). Since automated systems reduce driver burden and replace driver operation with automated operation, it is expected that an AHS will provide significantly improved safety compared to driving on today's highways.

An important feature to be noted is that an AHS is *a dual mode form of transportation*. A vehicle instrumented to travel on AHS can also travel on regular highways (driven manually). Thus an AHS vehicle is a personal vehicle that provides point to point service from any origin to any destination. The driver can drive on regular highways from home until he or she arrives at an AHS, travel under automated control on AHS, take an exit, and then travel again under manual control on a regular highway or local road to get to the final destination point. Thus, unlike a railway or other public transit system, an AHS provides point to point travel by leveraging the existing infrastructure of regular highways and roads.

7.2   VEHICLE CONTROL ON AUTOMATED HIGHWAY SYSTEMS

A popular control architecture proposed for an automated highway system (Varaiya, 1993) is hierarchical and has the 4 layers shown in Figure 7-1. The 4 layers are

a)   The network layer
b)   The link layer
c)   The coordination layer
d)   The regulation layer

The network layer controls entering traffic over the entire network and assigns a route to each vehicle as it enters the system.

The link layer is a roadside layer for a section of a highway. It broadcasts target values for speed and platoon size for that road section. These target values are based on information about the aggregate traffic state (density, speed, flow). The link layer estimates proportion of vehicles destined for various exits and advises vehicles where to change lanes in order to reach exits. It receives information about incidents or congestion downstream and accordingly reassigns vehicle paths.

The coordination layer resides on each vehicle. It determines which maneuver to initiate at any time so as to conform to the assigned path; it also coordinates that maneuver with neighboring vehicles so that the maneuver can be executed safely. It commands the regulation layer to execute the feedback law that executes the maneuver.

The regulation layer executes maneuvers. These maneuvers include

a)   Steady state maneuvers of lane keeping and either speed control or vehicle following.
b)   Transient maneuvers of lane change, highway exit, highway entry, longitudinal split from a platoon and join a platoon.
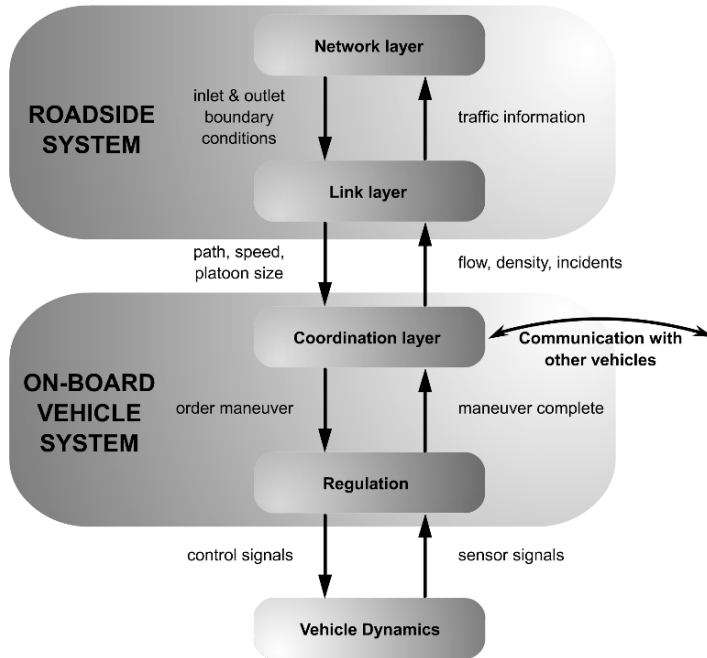
Figure 7-1. Control Architecture

The longitudinal control task discussed in this chapter is the responsibility of the regulation layer. So also is the lateral control task, discussed in chapter 3.

7.3 LONGITUDINAL CONTROL ARCHITECTURE

In the regulation layer, the longitudinal control system is responsible for executing steady state and transient longitudinal maneuvers. This longitudinal control system will also be designed to be hierarchical, with an upper level controller and a lower level controller as shown in Figure 7-2. The upper level controller determines the desired longitudinal acceleration for each vehicle. The lower level controller determines the throttle and/or brake commands required to track the desired acceleration. Vehicle dynamic models, engine maps and nonlinear control synthesis techniques (Choi and Devlin, 1995a and 1995b, Hedrick et al, 1991, Hedrick, et. al., 1993) are used by the lower controller in calculating the real-time brake and throttle inputs required to track the desired acceleration.
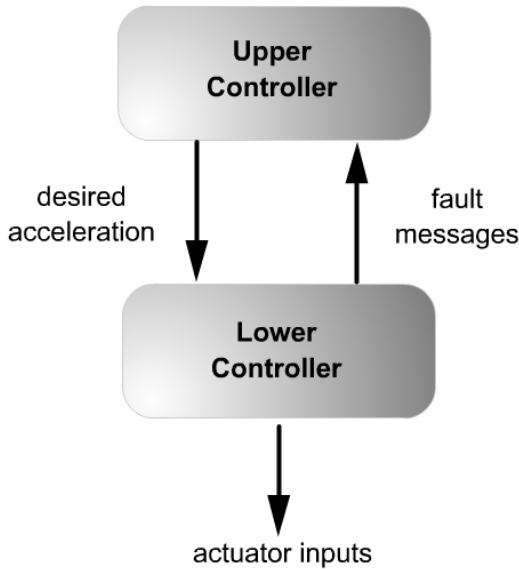
Figure 7-2. Structure of longitudinal control system

As far as the upper level controller is concerned, the plant model used for control design is

$$\ddot{x}_i = u \tag{7.1}$$

where the subscript i denotes the i th car in the platoon. The acceleration of the car is thus assumed to be the control input. However, due to the finite bandwidth associated with the lower level controller, each car is actually expected to track its desired acceleration imperfectly. The specification on the upper level controller is therefore stated as that of meeting its performance objectives robustly in the presence of a first-order lag in the lower level controller performance :

$$\ddot{x}_i = \frac{1}{\tau s + 1} \ddot{x}_{i\_des} = \frac{1}{\tau s + 1} u_i \tag{7.2}$$

Equation (7.1) is thus assumed to be the nominal plant model while the performance specifications have to be met even if the actual plant model were given by equation (7.2).

This chapter assumes a lag of $\tau = 0.5$ sec for analysis and simulation. The maximum acceleration and deceleration possible are assumed to be 0.25g and -0.5g respectively.

The longitudinal control system in the regulation layer executes two types of maneuvers

a) Steady state maneuvers of either speed control or vehicle following.
b) Transient maneuvers of splitting from a platoon and joining a platoon.

Vehicle following is the topic of discussion in sections 7.4, 7.5, 7.6, 7.7, 7.8 in this chapter. Speed control has been discussed earlier in section 5.3 of Chapter 5.

A good discussion of longitudinal transitional control algorithms for automated highway systems can be found in Li, et. al. (1997), Connoly and Hedrick (1999) and Rajamani, et. al.(2000).

7.4 VEHICLE FOLLOWING SPECIFICATIONS

In the vehicle-following mode of operation, the automated vehicle maintains a desired spacing from the preceding vehicle in the platoon. The two important specifications that the vehicle following control system must satisfy are individual vehicle stability and string stability.

a) Individual vehicle stability

Consider a platoon of vehicles using a longitudinal control system for vehicle following, as shown in Figure 7-3. Let x_i be the location of the i th vehicle measured from an inertial reference, as shown in Figure 7-2. The spacing error for the i th vehicle (the vehicle under consideration) is then defined as $\varepsilon_i = x_i - x_{i-1} + L_i$. Here L_i is the desired spacing and includes the preceding vehicle length ℓ_{i-1}. In a control system for platoon operation, the desired spacing L_i is a constant (independent of the vehicle speed $\dot{x}_i$). The control law is said to provide individual vehicle stability if the following condition is satisfied

$$\ddot{x}_{i-1} \to 0 \quad \Rightarrow \quad \varepsilon_i \to 0 \tag{7.3}$$

In other words, the spacing error of the vehicle should converge to zero if the preceding vehicle is operating at constant velocity. If the preceding vehicle is accelerating or decelerating, then the spacing error is expected to be non-zero.
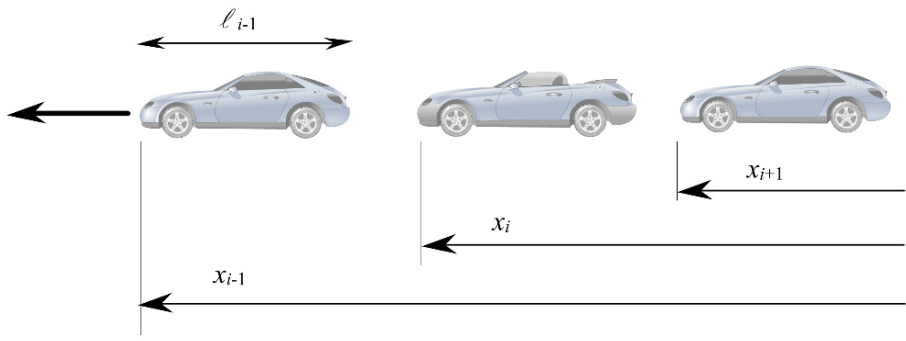
Figure 7-3. String of vehicles in a platoon

b) String stability

Since the spacing error is expected to be non-zero during acceleration/ deceleration of the preceding vehicle, it is important to describe how the spacing error would propagate from vehicle to vehicle in a string of vehicles in the platoon that use the same spacing policy and control law. The string stability of a string of vehicles refers to a property in which spacing errors are guaranteed not to amplify as they propagate towards the tail of the string (Swaroop, 1995, Swaroop and Hedrick, 1996). For example, string stability ensures that any errors in spacing between the 2nd and 3rd cars does not amplify into an extremely large spacing error between cars 7 and 8 further up in the string of vehicles.

   A rigorous definition for string stability will be provided in section 7.6, after reviewing the mathematical background on norms of signals and systems in section 7.5.

7.5   BACKGROUND ON NORMS OF SIGNALS
AND SYSTEMS

7.5.1   Norms of signals

We consider signals mapping $[0,\infty)$ to R. They are assumed to be piecewise continuous. The following signal norms can be defined (Doyle, et. al., 1992):

1. ∞-**Norm:** The ∞ norm of a signal is the least upper bound of its absolute value.

$$\| x \|_\infty = \sup_t | x(t) | \qquad (7.4)$$

2. **1-Norm:** The 1-norm of a signal $x(t)$ is the integral of its absolute value.

$$\| x \|_1 = \int_0^\infty | x(t) | \, dt \qquad (7.5)$$

3. **2-Norm:** The 2-norm of $x(t)$ is

$$\| x \|_2 = \left[\int_0^\infty | x(t) |^2 \, dt \right]^{1/2} \qquad (7.6)$$

4. p-**Norm:** The p-norm of $x(t)$ is

$$\| x \|_p = \left[\int_0^\infty | x(t) |^p \, dt \right]^{1/p} \qquad (7.7)$$

7.5.2   System norms

Consider a linear time invariant system with an input-output model which is represented in the time domain as a convolution equation:

$$y(t) = g(t) * x(t)$$

or

$$y(t) = \int_0^t g(t - \tau) x(\tau) d\tau \qquad (7.8)$$

Let $G(s)$ be the Laplace transform of $g(t)$. Then in the s-domain

$$Y(s) = G(s)X(s) \qquad (7.9)$$

where

$g(t) = L^{-1}\{G(s)\}$ is the impulse response of the system.

Define the ∞-norm of the transfer function $G(s)$ as follows:

$$\| G(s) \|_\infty = \sup_\omega | G(j\omega) |$$
(7.10)

Define the 1-norm of the impulse response as follows:

$$\| g \|_1 = \int_0^\infty | g(t) | \, dt$$
(7.11)

The ∞-norm of $G(s)$ and the 1-norm of $g(t)$ can be used to relate the size of the output of the system to the size of the input (Doyle, Francis and Tannenbaum, 1992). Specifically,

$$\| g \|_1 = \sup_{x \in L_\infty} \frac{\| y \|_\infty}{\| x \|_\infty}$$
(7.12)

$$\| G(s) \|_\infty = \sup_{x \in L_2} \frac{\| y \|_2}{\| x \|_2}$$
(7.13)

7.5.3   Use of induced norms to study signal amplification

In the study of string stability, a desirable characteristic for attenuation of propagating spacing errors is often specified as

$$\| y \|_\infty \leq \| x \|_\infty$$
(7.14)

where $y = \varepsilon_i$ is the spacing error of the ith vehicle and $x = \varepsilon_{i-1}$ is the spacing error of the $i-1$th vehicle.

Let $\hat{H}(s)$ be the transfer function relating the spacing errors of consecutive cars in the platoon.

$$\hat{H}(s) = \frac{y}{x} \tag{7.15}$$

The following condition

$$\left\|\hat{H}(s)\right\|_{\infty} \quad \leq \quad 1 \tag{7.16}$$

ensures

$$\| y \|_2 \leq \| x \|_2 \tag{7.17}$$

i.e. it ensures that the energy in the signal $y(t)$ is less than the energy in the signal $x(t)$. However, the desirable characteristic we would like to ensure is the stronger condition $\| y \|_{\infty} \leq \| x \|_{\infty}$

The norms $\| y \|_{\infty}$ and $\| x \|_{\infty}$ are related through the 1-norm of the impulse response $h(t)$

$$\| h \|_1 = \sup_{x \in L_{\infty}} \frac{\| y \|_{\infty}}{\| x \|_{\infty}} \tag{7.18}$$

The condition $\| y \|_{\infty} \leq \| x \|_{\infty}$ requires that

$$\| h \|_1 \leq 1 \tag{7.19}$$

It is much easier to design the control system to ensure that equation (7.16) is satisfied rather than to design the system to ensure that equation (7.19) is satisfied. The following Lemma shows that the condition $\| h \|_1 \leq 1$ can be replaced by the two conditions

$$\left\|\hat{H}(s)\right\|_{\infty} \leq 1 \text{ and } h(t) > 0 \tag{7.20}$$

Lemma 1 (Swaroop, 1995):

If $h(t) > 0$, then all the input output induced norms are equal

Proof:

Let γ_p be the p th induced norm i.e.

$$\gamma_p = \sup_{x \in L_p} \frac{\| y \|_p}{\| x \|_p} \tag{7.21}$$

Then, from linear systems theory (see Appendix 7.A)

$$| \hat{H}(0) | \leq \| \hat{H}(j\omega) \|_\infty \leq \gamma_p \leq \| h \|_1 \tag{7.22}$$

If $h(t) > 0$ then $| \hat{H}(0) | = \| h \|_1$, as shown below.

$$| \hat{H}(0) | = \left| \int_0^\infty h(t) dt \right| \leq \int_0^\infty | h(t) | \, dt = \int_0^\infty | h(t) | \, dt \quad \text{if and only if } h(t) \text{ does}$$

not change sign (Swaroop, 1995).

QED.

The following relation between $\| h \|_1$ and $\| H \|_\infty$ should also be considered (Boyd and Doyle, 1987):

Lemma 2 (Boyd and Doyle, 1987):

Consider a transfer matrix that is rational, proper and stable. For such a system

$$\| h \|_1 \leq (2n + 1) \| H(s) \|_\infty \tag{7.23}$$

where n is the Mcmillan degree of the system.

This relation implies that if $\| H \|_\infty$ is designed to be less than 1, then $\| h \|_1$ is also guaranteed to be correspondingly bounded.

Table 7-1. Summary of Signal Amplification Result

SUMMARY OF RESULT
Let $y(t) = \int_0^t h(t-\tau)x(\tau)d\tau$
Then $H(s) = \dfrac{Y(s)}{X(s)}$
If $H(s)$ is designed such that $\| H(s) \|_\infty \leq 1$, then $\| y \|_2 \leq \| x \|_2$
If $H(s)$ is designed such that $\| H(s) \|_\infty \leq 1$ and $h(t) > 0$, then $\| y \|_\infty \leq \| x \|_\infty$

7.6 DESIGN APPROACH FOR ENSURING STRING STABILITY

The following condition will be used to determine if the system is string stable :

$$\left\| \hat{H}(s) \right\|_\infty \quad \leq \quad 1 \qquad (7.24)$$

where $\hat{H}(s)$ is the transfer function relating the spacing errors of consecutive vehicles

$$\hat{H}(s) = \frac{\varepsilon_i}{\varepsilon_{i-1}} \qquad (7.25)$$

In addition to (7.24), a condition that the impulse response function $h(t)$ corresponding to $\hat{H}(s)$ does not change sign will be considered desirable (Swaroop, D., 1995). This can be understood, first of all, from the results in section 7.5 where it was demonstrated that the impulse response had to be positive to ensure that the two system norms $\| H \|_\infty$ and $\| h \|_1$ were equal.

An additional reason for the requirement that the impulse response be positive is as follows:

Satisfying the condition

$$\| \varepsilon_i \|_\infty \leq \| \varepsilon_{i-1} \|_\infty \tag{7.26}$$

only ensures that the maximum absolute value of the maximum spacing error decreases upstream. In the case of (sinusoidal) oscillations in error, this is adequate. However, in the case of steady state or ramp type errors, this is inadequate. In equation (7.26), no specifications are made on the sign of the spacing error. A positive spacing error implies that the vehicle is closer than desired while a negative spacing error implies that it is further apart than desired. If the steady state value of ε_i is positive while the steady state value of ε_{i-1} is negative, then this might be dangerous even though in terms of magnitude ε_i might be smaller than ε_{i-1}. The condition that the impulse response be positive ensures that steady state values of ε_i and ε_{i-1} have the same sign. Consider

$$\varepsilon_i = \int_0^t h(t-\tau)\varepsilon_{i-1}(\tau)\, d\tau \tag{7.27}$$

Thus the impulse response being positive ensures that the steady state values of ε_i and ε_{i-1} have the same sign.

Results on designing a compensator to ensure that the impulse response of a continuous time LTI system is non negative can be found in Swaroop, 2003. Such a synthesis is possible if and only if the open loop system has no real non minimum phase zeros (Swaroop, 2003).

7.7   CONSTANT SPACING WITH AUTONOMOUS CONTROL

An autonomous controller (like the adaptive cruise control system described in chapter 6) only utilizes on board sensors and does not depend on inter-vehicle communication or any other form of cooperation from other vehicles on the highway. An on-board forward looking doppler based FMCW radar can measure distance, relative velocity and azimuth angle to other vehicles in its field of view. In this section, we show that an autonomous controller cannot ensure string stability when the constant spacing policy is used.

Hence an automated highway system requires inter-vehicle communication, if the constant spacing policy is to be used.

In the constant spacing policy, the desired spacing between successive vehicles is defined by

$$x_{i\_des} = x_{i-1} - L_i \tag{7.28}$$

where L_i is a constant and includes the length ℓ_{i-1} of the preceding vehicle. The spacing error of the i th vehicle is defined as

$$\varepsilon_i = x_i - x_{i-1} + L_i \tag{7.29}$$

If we assume that the acceleration of the vehicle can be instantaneously controlled, then a linear control system of the type

$$\ddot{x}_i = -k_p \varepsilon_i - k_v \dot{\varepsilon}_i \tag{7.30}$$

yields

$$\ddot{\varepsilon}_i = \ddot{x}_i - \ddot{x}_{i-1} = -k_p \varepsilon_i - k_v \dot{\varepsilon}_i + k_p \varepsilon_{i-1} + k_v \dot{\varepsilon}_{i-1}$$

which leads to the following closed-loop error dynamics

$$\ddot{\varepsilon}_i + k_v \dot{\varepsilon}_i + k_p \varepsilon_i = k_p \varepsilon_{i-1} + k_v \dot{\varepsilon}_{i-1} \tag{7.31}$$

The transfer function

$$G(s) = \frac{\varepsilon_i}{\varepsilon_{i-1}}(s) = \frac{k_v s + k_p}{s^2 + k_v s + k_p} \tag{7.32}$$

describes the propagation of spacing errors in the platoon of vehicles. The Bode magnitude plot in Figure 7-4 is shown for $k_p = 1$, $k_v = 0.3$. The maximum magnitude of this transfer function is greater than 1 so that the autonomous control law of eqn. (7.30) is not string stable.
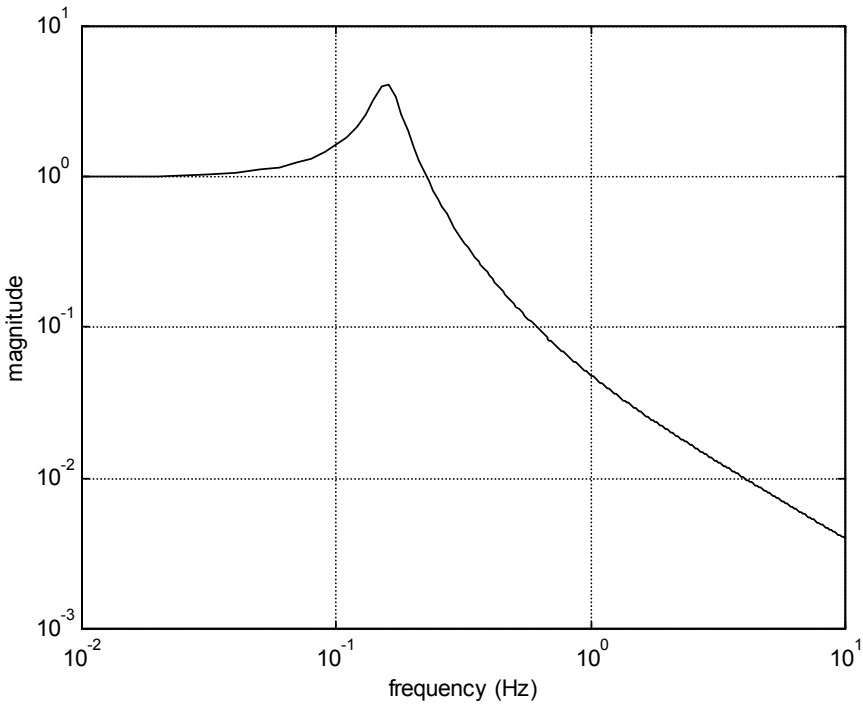
Figure 7-4. Magnitude of G(s) from Eqn. (7.32)

All positive values of k_p and k_v guarantee that the spacing error of the i th vehicle converges to zero when the spacing error of the $i-1$ th vehicle is zero. However, there are no positive values of k_p and k_v for which the magnitude of the transfer function $G(s)$ can be guaranteed to be less than unity. To see why this is the case, rewrite $G(s)$ as

$$G(s) = \frac{k_p}{s^2 + k_v s + k_p} \left(\frac{k_v}{k_p} s + 1 \right) \tag{7.33}$$

or

$$G(s) = G_1(s)G_2(s) \tag{7.34}$$

For the magnitude of $G_1(j\omega)$ to be less than 1, one needs the damping ratio $\xi \geq 0.707$ or $\dfrac{k_v}{2\sqrt{k_p}} \geq 0.707$ i.e.

$$k_v \geq 1.414\sqrt{k_p} \tag{7.35}$$

For the magnitude of $G_2(j\omega)$ to not exceed 1 at frequencies up to the resonant frequency $\sqrt{k_p}$, one needs the frequency $\dfrac{k_p}{k_v}$ to be bigger than $\sqrt{k_p}$. Hence, one needs $\dfrac{k_p}{k_v} \geq \sqrt{k_p}$ or

$$\sqrt{k_p} \geq k_v \tag{7.36}$$

It is not possible to find gains that satisfy both equations (7.35) and (7.36). Hence the magnitude of $G(s)$ will always exceed 1.

Thus, in the case of the constant spacing policy, string stability cannot be ensured by autonomous control. This has two implications

1) For platoon operation, since we need small inter-vehicle spacing and so must use the constant spacing policy, autonomous control is not possible.
2) When autonomous control is required (due to wireless communication not being feasible as in the case of ACC vehicles discussed in Chapter 6), the constant spacing policy cannot be used. Instead, a variable spacing policy like the constant time-gap policy must be used.

7.8   CONSTANT SPACING WITH WIRELESS COMMUNICATION

Instead of an autonomous controller, an alternate control system can be developed to ensure string stability with the constant spacing policy. The sliding surface method of controller design (Slotine and Li, 1991) is used. Define the following sliding surface

$$S_i = \dot{\varepsilon}_i + \frac{\omega_n}{\xi + \sqrt{\xi^2 - 1}} \frac{1}{1 - C_1} \varepsilon_i + \frac{C_1}{1 - C_1}(V_i - V_\ell) \tag{7.37}$$

where V_i and V_ℓ refer to the longitudinal velocity of the i th vehicle and lead vehicle respectively.

Setting

$$\dot{S}_i = -\lambda S_i \text{ with } \lambda = \omega_n(\xi + \sqrt{\xi^2 - 1}) \tag{7.38}$$

we find that the desired acceleration of the car is given by

$$\ddot{x}_{i\_des} = (1 - C_1)\ddot{x}_{i-1} + C_1\ddot{x}_\ell - (2\xi - C_1(\xi + \sqrt{\xi^2 - 1}))\omega_n\dot{\varepsilon}_i \tag{7.39}$$
$$- (\xi + \sqrt{\xi^2 - 1})\omega_n C_1(V_i - V_\ell) - \omega_n^2\varepsilon_i$$

The control gains to be tuned are C_1, ξ and ω_n. The gain C_1 takes on values $0 < C_1 < 1$ and can be viewed as a weighting of the lead vehicle's speed and acceleration. The gain ξ can be viewed as the damping ratio and can be set to 1 for critical damping. The gain ω_n is the bandwidth of the controller.

Equation (7.38) ensures that the sliding surface converges to zero. If all the cars in the platoon use this control law, then the cars in the platoon will be able to track the preceding car with a constant spacing i.e. the spacing error will converge to zero in the absence of lead vehicle acceleration. Mathematically, if $S_i \rightarrow 0$, then $\varepsilon_i \rightarrow 0$.

To see why this is true, note that

$$S_i - S_{i-1} = \frac{1}{1 - C_1}\dot{\varepsilon}_i - \dot{\varepsilon}_{i-1} + \frac{\omega_n}{\left(\xi + \sqrt{\xi^2 - 1}\right)\left(1 - C_1\right)}(\varepsilon_i - \varepsilon_{i-1})$$

The sliding surface law ensures that the left hand side of the above equation is zero.

If $i = 2$, then $\dot{\varepsilon}_i = V_i - V_\ell$ and $\varepsilon_{i-1} = 0$. Hence it is obvious that $\varepsilon_2 \rightarrow 0$.

It can be shown that if S_{i-1}, $S_i \to 0$ and $\varepsilon_{i-1} \to 0$, then $\varepsilon_i \to 0$. Using the principle of induction, it follows that the spacing error converges to zero for all vehicles.

Further the system is string stable, i.e. the spacing errors never amplify down the platoon even when the lead car has non-zero acceleration. To see why this is the case, consider the equation

$$S_i - S_{i-1} = \frac{1}{1-C_1}\dot{\varepsilon}_i - \dot{\varepsilon}_{i-1} + \frac{\omega_n}{\left(\xi + \sqrt{\xi^2 - 1}\right)(1-C_1)}(\varepsilon_i - \varepsilon_{i-1}) \quad (7.40)$$

Taking Laplace transforms of (7.40)

$$\hat{\varepsilon}_i(s) = \frac{s + \dfrac{\omega_n}{\left(\xi + \sqrt{\xi^2 - 1}\right)(1-C_1)}}{\dfrac{1}{1-C_1}s + \dfrac{\omega_n}{\left(\xi + \sqrt{\xi^2 - 1}\right)(1-C_1)}}\hat{\varepsilon}_{i-1}(s)$$

$$+ \frac{S_i - S_{i-1} + \dfrac{1}{1-C_1}\varepsilon_i(0) - \varepsilon_{i-1}(0)}{\dfrac{1}{1-C_1}s + \dfrac{\omega_n}{\left(\xi + \sqrt{\xi^2 - 1}\right)(1-C_1)}} \quad (7.41)$$

The conditions $\xi \geq 1$ and $C_1 < 1$ ensure that the magnitude of the transfer function in equation (7.41) is less than 1 and that the system is string stable.

Results on the robustness of the above controller, especially to lags induced by the performance of the lower level controller, can also be found in Swaroop, 1995.

Need for wireless communication

From the longitudinal control law of equation (7.39), it is clear that a wireless radio communication system is required between the cars to obtain access to all of the required signals. Each car thus obtains communicated speed and acceleration information from two other cars in the platoon - the lead car and the preceding car.

Setting $C_1 = 0$ for a two car platoon, we obtain the following classical second-order system :

$$\ddot{x}_{i\_des} = \ddot{x}_{i-1} - 2\xi\omega_n\dot{\varepsilon}_i - \omega_n^2\varepsilon_i$$

7.9   EXPERIMENTAL RESULTS

The National Automated Highway Systems Consortium (NAHSC) conducted a public demonstration in August 1997 of eight fully automated cars traveling together with small inter-vehicle spacing as a platoon. The demonstration was held in San Diego using a 7.6 mile segment of Interstate-15 HOV (carpool) lanes. This section of the two-lane highway had been equipped with magnets installed in the centers of both lanes. The magnets served as reference markers that were used by the automated steering control system to keep each car centered in its lane. Over a thousand visitors were given passenger rides in the platoon vehicles which operated continuously for several hours a day for three weeks. The maneuvers demonstrated in San Diego included starting the automated vehicles from complete rest, accelerating to cruising speed, automated steering for lane keeping, allowing any vehicle to exit from the platoon with an automated lane change, allowing new vehicles to join the platoon and bringing the platoon to a complete stop at the end of the highway (Rajamani, et. al., 2000).

The sliding surface based control law using inter-vehicle communication described above was used in the NAHSC demonstration. The performance of the control algorithm is shown in Figure 7-5 (Rajamani, et. al., 2000). The spacing accuracy of cars 6, 7 and 8 in the eight-car platoon is shown. During the entire 7.6 mile run, the spacing error between these tail vehicles of the platoon remains within $\pm$ 0.2 meters. This includes the spacing performance while the lead car accelerates, cruises, and decelerates to a complete stop and other cars in the platoon accelerate and decelerate while splitting and joining. The scenario also includes uphill and downhill grades of up to 3%, during which the maximum spacing errors occur. The acceleration profile of the car 8 corresponding to this test data is shown in Figure 7-6. The long-period peaks and valleys of Figure 7-6 correspond to changes of grade on the test track and to intentional acceleration and deceleration maneuvers built into the test and demonstration scenario. The spacing performance and ride quality that can be achieved by a fully cooperative platoon system are superior to that achieved by the most highly skilled human drivers who have driven the test vehicles.
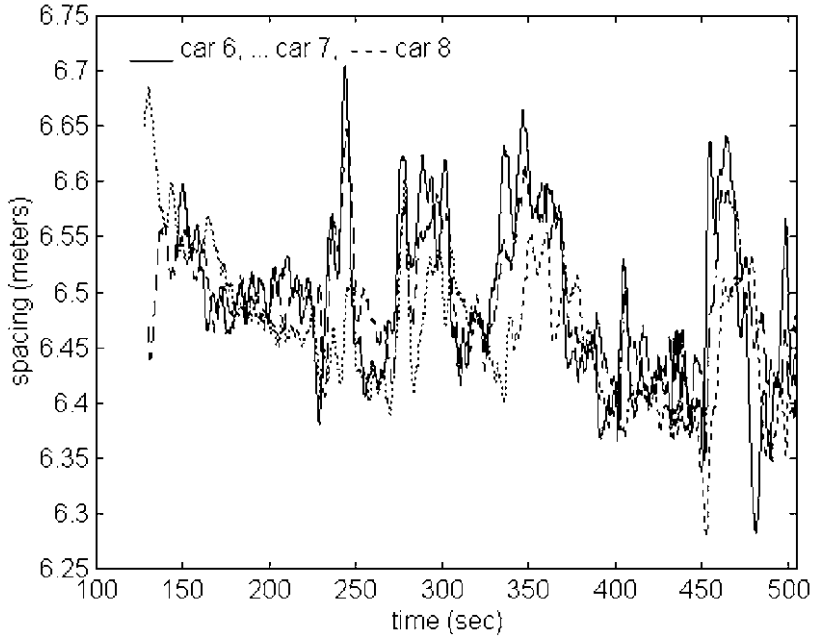
Figure 7-5. Spacing performance of cars 6,7 and 8 of an eight-car platoon
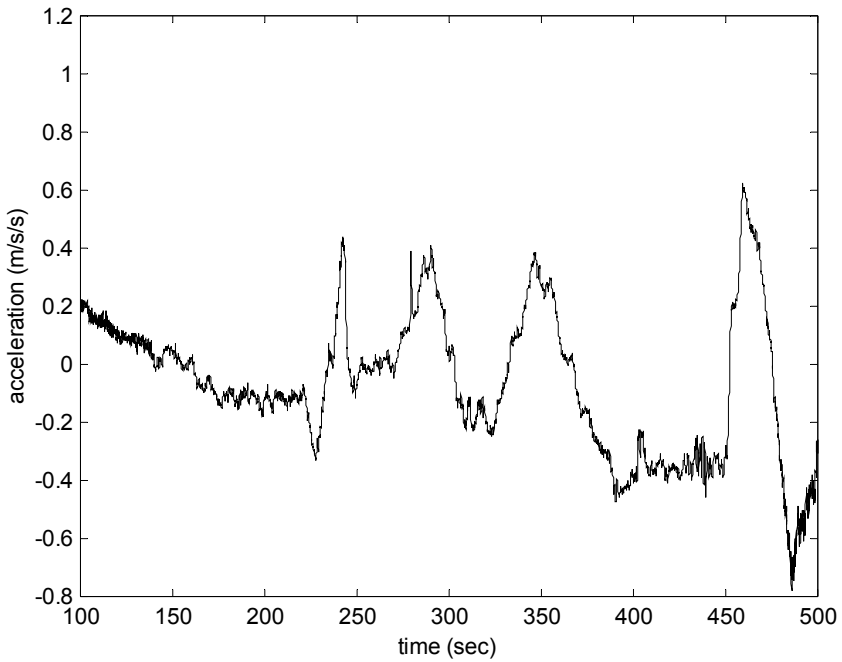
Figure 7-6. Acceleration profile for tail car of 8-car platoon

7.10   LOWER LEVEL CONTROLLER

In the lower controller, the throttle and brake actuator inputs are determined so as to track the desired acceleration determined by the upper controller. The following simplified model of vehicle dynamics is used in the development of the lower level controller. This simplified model is based on the assumptions that the torque converter in the vehicle is locked and that there is zero-slip between the tires and the road, as described in chapter 5. These assumptions relate the vehicle speed directly to the engine speed

$$\dot{x}_i = v_i = (R r_{eff} \omega_e)_i \tag{7.42}$$

Under these assumptions, as described in Chapter 5, section 5.5.1, the dynamics relating engine speed ω_e to the pseudo-inputs "net combustion torque" T_{net} and brake torque T_{br} can be modeled by

$$\dot{\omega}_e = \frac{T_{net} - c_a R^3 r_{eff}^3 \omega_e^2 - R(r_{eff} R_x + T_{br})}{J_e} \tag{7.43}$$

where $J_e = I_e + (m r_{eff}^2 + I_\omega) R^2$ is the effective inertia reflected on the engine side, R is the gear ratio and r_{eff} the tire radius.

If the net combustion torque is chosen as

$$(T_{net})_i = \frac{J_e}{R h} \ddot{x}_{ides} + [c_a R^3 r_{eff}^3 \omega_e^2 + R(r_{eff} R_x + T_{br})]_j \tag{7.44}$$

then, from equation (7.43), the acceleration of the car is equal to the desired acceleration defined by the upper level controller : $\ddot{x}_i = \ddot{x}_{ides}$.

Once the required combustion torque is obtained from (7.44), the control law to calculate the throttle angle to provide this torque can be obtained by using engine dynamic models and applying nonlinear control synthesis techniques. Engine dynamic models for both SI and diesel engines and control design to provide a desired torque are discussed in Chapter 9.

If the desired net torque defined by (7.44) is negative, the brake actuator is used to provide the desired torque. An algorithm for smooth switching between the throttle and brake actuators is presented in Choi and Devlin, 1995, and can be used by the longitudinal control system.

7.11 ADAPTIVE CONTROL FOR UNKNOWN VEHICLE PARAMETERS

In the design of the lower controller (7.44) in the previous section, it was assumed that the vehicle mass, aerodynamic drag coefficient and the rolling resistance values were exactly known. This section presents a direct adaptive controller which adapts on all three parameters and utilizes estimated values of these parameters in the control law. This adaptive controller has been implemented experimentally and its performance documented (Swaroop, 1995).

7.11.1 Redefined notation

Recall the definition of the sliding surface used to design the upper level controller

$$S_i = \dot{\varepsilon}_i + \frac{\omega_n}{\xi + \sqrt{\xi^2 - 1}} \frac{1}{1 - C_1} \varepsilon_i + \frac{C_1}{1 - C_1}(v_i - v_\ell)$$

To simplify notation, let $q_1 = \dfrac{\omega_n}{\xi + \sqrt{\xi^2 - 1}} \dfrac{1}{1 - C_1}$, $q_3 = \dfrac{C_1}{1 - C_1}$ and

$q_4 = (\xi + \sqrt{\xi^2 - 1})\omega_n C_1$. Then

$$S_i = \dot{\varepsilon}_i + q_1 \varepsilon_i + q_3(v_i - v_\ell) \tag{7.45}$$

The upper level control law is then (Swaroop, 1995)

$$\ddot{x}_{i\_des} = \frac{1}{1 + q_3}\left[\ddot{x}_{i-1} + q_3\ddot{x}_\ell + -q_1\dot{\varepsilon}_i - q_4(\dot{x}_i - \dot{x}_\ell) - \lambda S_i\right] \tag{7.46}$$

From the previous section, under the assumption of locked torque converter and negligible longitudinal slip at the tires, the engine dynamic equation under throttle control can be roughly written as

$$\dot{\omega}_e = \frac{T_{net} - c_a R^3 r_{eff}^3 \omega_e^2 - R r_{eff} R_x}{J_e} \tag{7.47}$$

Since $\dot{x}_i = Rr_{eff}\omega_e$, this equation can be rewritten as

$$M_i\ddot{x}_i = -c_i\dot{x}_i^2 - f_i + u_i \tag{7.48}$$

where $M_i = J_e Rr_{eff}$, $f_i = R^2 r_{eff}^2 R_x$ and $c_i = R^2 r_{eff}^2 c_a$ are unknown parameters and $u_i = Rr_{eff}T_{net}$ is the control torque.

In order to obtain a desired acceleration $\ddot{x}_{des}$, the control input u_i can be chosen as

$$u_i = f_i + c_i\dot{x}_i^2 + M_i\ddot{x}_{des} \tag{7.49}$$

This equation is essentially the same as equation (7.44) of the previous section. The only difference between equations (7.44) and (7.49) is the notation.

7.11.2   Adaptive controller

The objective is to find an adaptive version of the control law of equation (7.49) when the parameters c_i, f_i and M_i are unknown. The adaptive controller described in this section was developed in Swaroop (1995). Let

$$u_i = \hat{f}_i + \hat{c}_i\dot{x}_i^2 + \hat{M}_i\ddot{x}_{des} \tag{7.50}$$

where $\hat{f}_i$, $\hat{c}_i$ and $\hat{M}_i$ are estimated values of the unknown parameters f_i, c_i and M_i. Let $\tilde{f}_i = f_i - \hat{f}_i$, $\tilde{M}_i = M_i - \hat{M}_i$ and $\tilde{c}_i = c_i - \hat{c}_i$ be the errors in the estimates of the parameters.

Then, as shown in Swaroop (1995), instead of the closed loop dynamics $\dot{S}_i = -\lambda S_i$, the sliding surface dynamics are instead given by

$$\dot{S}_i + \lambda S_i = \frac{1+q_3}{M_i}\left[\tilde{M}_i\ddot{x}_{des} + \tilde{c}_i\dot{x}_i^2 + \tilde{f}_i\right] \tag{7.51}$$

Define a Lyapunov function candidate

$$V_i = \frac{M_i}{1+q_3}\frac{S_i^2}{2} + \frac{\gamma_1}{2}\tilde{M}_i^2 + \frac{\gamma_2}{2}\tilde{c}_i^2 + \frac{\gamma_3}{2}\tilde{f}_i^2 \tag{7.52}$$

Its time derivative is

$$\dot{V}_i = \frac{M_i}{1+q_3} S_i \dot{S}_i + \gamma_1 \tilde{M}_i \dot{\tilde{M}}_i + \gamma_2 \tilde{c}_i \dot{\tilde{c}}_i + \gamma_3 \tilde{f}_i \dot{\tilde{f}}_i \qquad (7.53)$$

or

$$\dot{V}_i = -\frac{\lambda M_i}{1+q_3} S_i^2 + \tilde{M}_i \left[\ddot{x}_{des} S_i + \gamma_1 \dot{\tilde{M}}_i \right] + \tilde{c}_i \left[\dot{x}_i^2 S_i + \gamma_2 \dot{\tilde{c}}_i \right] + \tilde{f}_i \left[S_i + \gamma_3 \dot{\tilde{f}}_i \right] \qquad (7.54)$$

Choose the parameter adaptation laws as (Swaroop, 1995)

$$\dot{\hat{M}}_i = -\dot{\tilde{M}}_i = \frac{1}{\gamma_1} S_i \ddot{x}_{des} \qquad (7.55)$$

$$\dot{\hat{c}}_i = -\dot{\tilde{c}}_i = \frac{1}{\gamma_2} S_i \dot{x}_i^2 \qquad (7.56)$$

$$\dot{\hat{f}}_i = -\dot{\tilde{f}}_i = \frac{1}{\gamma_3} S_i \qquad (7.57)$$

With the above adaptation laws

$$\dot{V}_i = -\frac{\lambda M_i}{1+q_3} S_i^2 \qquad (7.58)$$

Hence $\dot{V}_i$ is negative semi-definite, ensuring that S_i, $\tilde{M}_i$, $\tilde{f}_i$ and $\tilde{c}_i$ are bounded i.e. S_i, $\tilde{M}_i$, $\tilde{f}_i$, $\tilde{c}_i \in L_\infty$.

Note here that the notation L_∞ is used to refer the space of all functions that have a finite well defined ∞-norm. Likewise, L_2 is used to refer the space of all functions that have a finite well defined 2-norm.

Use of Barbalat's Lemma to show asymptotic convergence of S_i

A corollary to Barbalat's Lemma states that a function $f(t) \to 0$ as $t \to \infty$ if $f \in L_2 \cap L_\infty$ and $\dfrac{df}{dt} \in L_\infty$ (Narendra and Annaswamy, 1989). This Lemma can be used to show that $S_i \to 0$ as $t \to \infty$.

From (7.58), it follows that

$$\int_0^T S_i^2 dt = V_i(0) - V_i(T) \tag{7.59}$$

Taking the limit as $T \to \infty$ in equation (7.59), it follows that $S_i \in L_2$.

It remains to show that $\dot{S}_i \in L_\infty$.

From equation (7.48)

$$M_i \ddot{x}_i = -c_i \dot{x}_i^2 + \hat{c}_i \dot{x}_i^2 + \hat{M}_i \ddot{x}_{des} - f_i + \hat{f}_i$$

or

$$M_i \ddot{x}_i = -\tilde{c}_i \dot{x}_i^2 - \tilde{f}_i + \frac{\hat{M}_i}{1 + q_3} \left[\ddot{x}_{i-1} + q_3 \ddot{x}_\ell + -q_1 \dot{\varepsilon}_i - q_4 (\dot{x}_i - \dot{x}_\ell) - \lambda S_i \right] \tag{7.60}$$

From the above equation it follows that $\dot{x}_i$ and $\ddot{x}_i$ are bounded if $\ddot{x}_{i-1}$, $\ddot{x}_\ell$ and $\dot{x}_\ell$ are bounded. Using the principle of induction, since $\dot{x}_i$ and $\ddot{x}_i$ are bounded for $i = 1$, it can be shown that $\dot{x}_i$ and $\ddot{x}_i$ are bounded for all i. From equation (7.48) it then follows that $\ddot{x}_{ides}$ is bounded.

Since $\dot{x}_i$ and $\ddot{x}_{i\_des}$ are bounded, it follows from equation (7.51) that $\dot{S}_i \in L_\infty$.

Hence, by Barbalat's Lemma, it follows that $S_i \to 0$ as $t \to \infty$.

7.12   CHAPTER SUMMARY

It is desirable that the vehicle following control system in a platoon should be designed to satisfy the following two performance specifications:

1) Individual vehicle stability, in which spacing errors of all vehicles converge to zero if the lead vehicle of the platoon travels at constant velocity

2) String stability, in which spacing error does not amplify as it propagates towards the tail of the string of vehicles.

The mathematical conditions that ensure string stable design were analyzed. Let $H(s) = \dfrac{\varepsilon_i}{\varepsilon_{i-1}}$ be the transfer function relating the spacing error of consecutive vehicles. The string stability condition $\| \varepsilon_i \|_\infty \leq \| \varepsilon_{i-1} \|_\infty$ can be ensured by designing the longitudinal controller such that the following two conditions are met:

a) $\| H(s) \|_\infty \leq 1$

b) $h(t) > 0$

where $h(t)$ is the imulse response or the Laplace inverse of $H(s)$.

Spacing policies and control algorithms for both autonomous control as well as cooperative control utilizing inter-vehicle communication were discussed in this chapter. In the case of a constant spacing policy, an autonomous controller cannot ensure string stability, although it can ensure individual vehicle stability.

String stability can be ensured with a constant spacing policy if inter-vehicle communication is used. A well known communication architecture is one in which the lead vehicle communicates its velocity and acceleration to all the vehicles in the string. String stability is ensured by using communication from the lead and preceding vehicles by each vehicle in the platoon. A major experimental demonstration of vehicles operating in platoons using such a communication system was the NAHSC demonstration conducted in August 1997. Experimental results from the NAHSC demonstration were presented.

Finally, an adaptive controller was presented which compensates for unknown values of vehicle mass, aerodynamic drag coefficient and rolling resistance by using on line adaptation of these parameters.

NOMENCLATURE

x_i	longitudinal position of the i th vehicle
$\dot{x}_i$ or V_i	longitudinal velocity of the i th vehicle
$\varepsilon_i = x_i - x_{i-1} + L_i$	longitudinal spacing error of the i th vehicle, with L_i being the desired spacing
L_i	desired inter-vehicle spacing for the i th vehicle (includes preceding vehicle length)
V_ℓ	longitudinal velocity of the lead vehicle of the platoon
$\ddot{x}_\ell$	longitudinal acceleration of the lead vehicle of the platoon
$\ddot{x}_{des}$ or u_i	desired acceleration of the i th vehicle
C_1	control gain used in upper longitudinal controller (relative weight for lead car signal feedback compared to preceding car signal feedback).
ω_n	control gain used in upper longitudinal controller (bandwidth)
$\hat{H}(s)$	transfer function relating spacing errors of consecutive vehicles
$h(t)$	impulse response function corresponding to $\hat{H}(s)$
S_i	sliding surface used in upper controller design
η_1, η_2	sliding surface control gains
T_{net}	net combustion torque of the engine
T_{br}	brake torque
ω_e	engine angular speed
c_a	aerodynamic drag coefficient
R	gear ratio
r_{eff}	tire radius

R_x	rolling resistance of the tires
J_e	effective inertia reflected on the engine side
$\dot{m}_{ai}$	rate of mass flow into engine manifold
$\dot{m}_{a0}$	rate of mass outflow from engine manifold
$\dot{m}_a$	rate of air mass flow in engine manifold
P_m	pressure of air in engine manifold
m	vehicle mass
L_∞	space of functions that have a well defined finite ∞-norm
L_2	space of functions that have a well defined finite 2-norm
f_i, $\hat{f}_i$	actual and estimated values of a parameter related to vehicle rolling resistance
c_i, $\hat{c}_i$	actual and estimated values of a parameter related to aerodynamic drag coefficient
M_i, $\hat{M}_i$	actual and estimated values of a parameter related to vehicle mass

REFERENCES

Boyd, S. and Doyle, J., "Comparison of Peak and RMS Gains for Discrete Time Systems, *Systems and Control Letters*, Vol. 9, pp. 1-6, 1987.

Choi, S.B. and Hedrick, J.K., "Vehicle Longitudinal Control Using an Adaptive Observer for Automated Highway Systems", *Proceedings of American Control Conference*, Seattle, Washington, 1995.

Choi, S.B. and Devlin, P., "Throttle and Brake Combined Control for Intelligent Vehicle Highway Systems", *SAE 951897*, 1995.

Connoly, T.R. and Hedrick, J.K., "Longitudinal Transition Maneuvers in an Automated Higwhay System," *ASME Journal of Dynamic Systems, Measurement and Control*, Vol. 121, pp. 471-478, 1999.

Desoer, C.A. and Vidyasagar, M., *Feedback Systems: Input-Output Properties*, Academic Press, ISBN 0-12-212050-7, New York, 1975.

Doyle, J.C., Francis, B.A. and Tannenbaum, A.R., *Feedback Control Theory*, Macmillan Publishing company, NY, USA, ISBN 0-02-330011-6, 1992.

Hedrick, J.K., McMahon, D., Narendran, V.K. and Swaroop, D., "Longitudinal Vehicle Controller Design for IVHS Systems", *Proceedings of the 1991 American Control Conference*, Vol. 3, pp. 3107-3112, June 1991.

Hedrick, J.K., McMahon, D. and Swaroop, D., "Vehicle Modeling and Control for Automated Highway Systems", *PATH Research Report*, UCB-ITS-PRR-93-24, 1993.

Hedrick, J K. Tomizuka, M. Varaiya, P, "Control Issues in Automated Highway Systems," *IEEE Control Systems Magazine,* Vol. 14, No. 6, .p 21-32 , Dec 1994.

Li, P.Y., Alvarez, L., et., al., "AHS Safe Control Laws for Platoon Leaders," *IEEE Transactions on Control Systems Technology*, Vol. 5, No. 6, November, 1997.

Narendra, K.S. and Annaswamy, A.M., *Stable Adaptive Systems*, Prentice Hall, ISBN 0-13-839994-8, 1989.

Rajamani, R. and Zhu, C., 1999, "Semi-Autonomous Adaptive Cruise Control Systems", *Proceedings of the American Control Conference*, June 1999.

Rajamani, R., Tan, H.S., Law, B. and Zhang, W.B., "Demonstration of Integrated Lateral and Longitudinal Control for the Operation of Automated Vehicles in Platoons," *IEEE Transactions on Control Systems Technology*, Vol. 8, No. 4, pp. 695-708, July 2000.

Slotine, J.J.E. and Li, W., "Applied Nonlinear Control", Prentice Hall, 1991.

Swaroop, D., Hedrick, J.K., Chien, C.C. and Ioannou, P. "A Comparison of Spacing and Headway Control Laws for Automatically Controlled Vehicles", *Vehicle System Dynamics Journal*, Nov. 1994, vol. 23, (no.8):597-625.

Swaroop, D. and Hedrick, J.K., "String Stability of Interconnected Dynamic Systems", *IEEE Transactions on Automatic Control*, March 1996.

Swaroop, D., 1995, "String Stability of Interconnected Systems : An Application to Platooning in Automated Highway Systems", *Ph.D. Dissertation*, University of California, Berkeley, 1995.

Swaroop, D. and Rajagopal, K.R., "Intelligent Cruise Control Systems and Traffic Flow Stability," *Transportation Research Part C: Emerging Technologies*, Vol. 7, No. 6, pp. 329-352, 1999.

Swaroop D. Swaroop, R. Huandra, "Design of an ICC system based on a traffic flow specification," *Vehicle System Dynamics Journal*, Vol. 30, no. 5, pp. 319-44, 1998.

Swaroop, D. and Bhattacharya, S.P., "Controller Synthesis for Sign Invariant Impulse Response," *IEEE Transactions on Automatic Control*, Vol. 47, No. 8, pp. 1346-1351, August, 2002.

Swaroop, D., "On the Synthesis of Controllers for Continuous Time LTI Systems that Achieve a Non-Negative Impulse Response," *Automatica*, Feb 2003.

Texas Transportation Institute Report, "2001 Urban Mobility Study," URL : mobility.tamu.edu

Varaiya, Pravin, "Smart Cars on Smart Roads: Problems of Control," *IEEE Transactions on Automatic Control. v 38 n 2, p 195-207, Feb 1993.*

Tomizuka, M. and Hedrick, J.K., "Automated Vehicle Control for IVHS Systems", *Proceedings of the IFAC Conference*, Sydney, 1993.

United States Department of Transportation, *NHTSA, FARS and GES*, 1992, "Fatal Accident Reporting System (FARS) and General Estimates System (GES)."

Yanakiev, D. and Kanellakopoulos, I., 1995, "Variable time Headway for String Stability of Automated Heavy-Duty Vehicles", *Proceedings of the 34th IEEE Conference on Decision and Control*, New Orleans, LA, December 1995, pp. 4077-4081.

APPENDIX 7.A

Background results useful for the analysis in sections 7.5 and 7.6 are presented in this Appendix. For more details, the reader is referred to Desoer and Vidyasagar (1975).

7.A.1. Holder's Inequality

Let $f, g : R \rightarrow R$. Let p, q be non negative extended real numbers (i.e. $p \geq 1$, $p < \infty$, $q \geq 1$, $q < \infty$) with $\dfrac{1}{p} + \dfrac{1}{q} = 1$.

If $f \in L_p$ and $g \in L_q$, then

$$fg \in L_1$$

$$\| fg \|_1 \leq \| f \|_p \| g \|_q$$

When $p = 2$, $q = 2$, the Holders' inequality becomes the Schwartz Inequality.

7.A.2. Minkowski's Inequality

$$\| f + g \|_p \leq \| f \|_p + \| g \|_q$$

7.A.3. Theorem

Let $y(t) = \displaystyle\int_0^t g(t - \tau)x(\tau)d\tau$

If $x(t) \in L_p$ and $g(t) \in L_1$, then

$$\| y \|_p \leq \| g \|_1 \| x \|_p$$

Interpretation:

$$\frac{\|y\|_p}{\|x\|_p} \le \|g\|_1$$

For $p = 2$,

$$\frac{\|y\|_2}{\|x\|_2} \le \|g\|_1$$

This means that the ∞-norm of the system is always less than the 1-norm, or

$$\|G\|_\infty \le \|g\|_1$$

Chapter 8

ELECTRONIC STABILITY CONTROL

8.1 INTRODUCTION

8.1.1 The functioning of a stability control system

Vehicle stability control systems that prevent vehicles from spinning and drifting out have been developed and recently commercialized by several automotive manufacturers. Such stability control systems are also often referred to as yaw stability control systems or electronic stability control systems.

Figure 8-1 schematically shows the function of a yaw stability control system. In this figure, the lower curve shows the trajectory that the vehicle would follow in response to a steering input from the driver if the road were dry and had a high tire-road friction coefficient. In this case the high friction coefficient is able to provide the lateral force required by the vehicle to negotiate the curved road. If the coefficient of friction were small or if the vehicle speed were too high, then the vehicle would not follow the nominal motion expected by the driver – it would instead travel on a trajectory of larger radius (smaller curvature), as shown in the upper curve of Figure 8-1. The function of the yaw control system is to restore the yaw velocity of the vehicle as much as possible to the nominal motion expected by the driver. If the friction coefficient is very small, it might not be possible to entirely achieve the nominal yaw rate motion that would be achieved by the driver on a high friction coefficient road surface. In this case, the yaw control system might only partially succeed by making the vehicle's yaw rate closer to the expected nominal yaw rate, as shown by the middle curve in Figure 8-1.
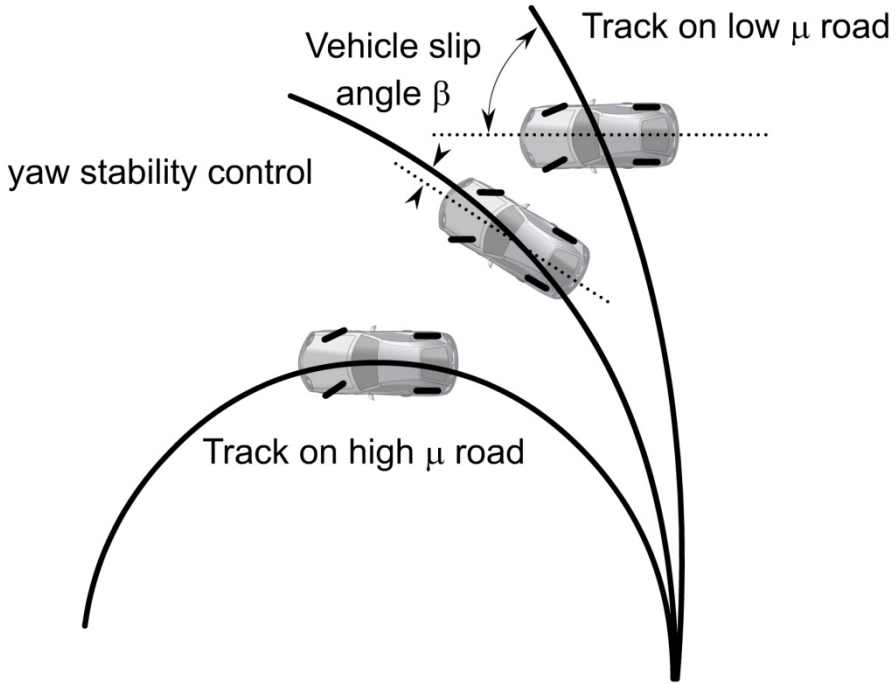
Figure 8-1. The functioning of a yaw control system

The motivation for the development of yaw control systems comes from the fact that the behavior of the vehicle at the limits of adhesion is quite different from its nominal behavior. At the limits of adhesion, the slip angle is high and the sensitivity of yaw moment to changes in steering angle becomes highly reduced. At large slip angles, changing the steering angle produces very little change in the yaw rate of the vehicle. This is very different from the yaw rate behavior at low frequencies. On dry roads, vehicle maneuverability is lost at vehicle slip angles greater than ten degrees, while on packed snow, vehicle maneuverability is lost at slip angles as low as 4 degrees (Van Zanten, et. al., 1996).

Due to the above change of vehicle behavior, drivers find it difficult to drive at the limits of physical adhesion between the tires and the road (Forster, 1991, Van Zanten, et. al., 1996). First, the driver is often not able to recognize the friction coefficient change and has no idea of the vehicle's stability margin. Further, if the limit of adhesion is reached and the vehicle skids, the driver is caught by surprise and very often reacts in a wrong way and usually steers too much. Third, due to other traffic on the road, it is important to minimize the need for the driver to act thoughtfully. The yaw control system addresses these issues by reducing the deviation of the

vehicle behavior from its normal behavior on dry roads and by preventing the vehicle slip angle from becoming large.

8.1.2 Systems developed by automotive manufacturers

Many companies have investigated and developed yaw control systems during the last ten years through simulations and on prototype experimental vehicles. Some of these yaw control systems have also been commercialized on production vehicles. Examples include the BMW DSC3 (Leffler, et. al., 1998) and the Mercedes ESP, which were introduced in 1995, the Cadillac Stabilitrak system (Jost, 1996) introduced in 1996 and the Chevrolet C5 Corvette Active Handling system in 1997 (Hoffman, et. al., 1998).

Automotive manufacturers have used a variety of different names for yaw stability control systems. These names include VSA (vehicle stability assist), VDC (vehicle dynamics control), VSC (vehicle stability control), ESP (electronic stability program), ESC (electronic stability control) and DYC (direct yaw control).

8.1.3 Types of stability control systems

Three types of stability control systems have been proposed and developed for yaw control:

1) **Differential Braking** systems which utilize the ABS brake system on the vehicle to apply differential braking between the right and left wheels to control yaw moment.
2) **Steer-by-Wire** systems which modify the driver's steering angle input and add a correction steering angle to the wheels
3) **Active Torque Distribution** systems which utilize active differentials and all wheel drive technology to independently control the drive torque distributed to each wheel and thus provide active control of both traction and yaw moment.

By large, the differential braking systems have received the most attention from researchers and have been implemented on several production vehicles. Steer-by-wire systems have received attention from academic researchers (Ackermann, 1994, Ackermann, 1997). Active torque distribution systems have received attention in the recent past and are likely to become available on production cars in the future.

Differential braking systems are the major focus of coverage in this book. They are discussed in section 8.2. Steer-by-wire systems are discussed in section 8.3 and active torque distribution systems are discussed in section 8.4.

8.2   DIFFERENTIAL BRAKING SYSTEMS

Differential braking systems typically utilize solenoid based hydraulic modulators to change the brake pressures at the four wheels. Creating differential braking by increasing the brake pressure at the left wheels compared to the right wheels, a counter-clockwise yaw moment is generated. Likewise, increasing the brake pressure at the right wheels compared to the left wheels creates a clockwise yaw moment. The sensor set used by a differential braking system typically consists of four wheel speeds, a yaw rate sensor, a steering angle sensor, a lateral accelerometer and brake pressure sensors.

8.2.1   Vehicle model

The vehicle model used to study a differential braking based yaw stability control system will typically have seven degrees of freedom. The lateral and longitudinal velocities of the vehicle ($\dot{x}$ and $\dot{y}$ respectively) and the yaw rate $\dot{\psi}$ constitute three degrees of freedom related to the vehicle body. The wheel velocities of the four wheels ($\omega_{f\ell}$, ω_{fr}, $\omega_{r\ell}$ and ω_{rr}) constitute the other four degrees of freedom. Note that the first subscript in the symbols for the wheel velocities is used to denote front or rear wheel and the second subscript is used to denote left or right wheel. Figure 8-2 shows the seven degrees of freedom of the vehicle model.
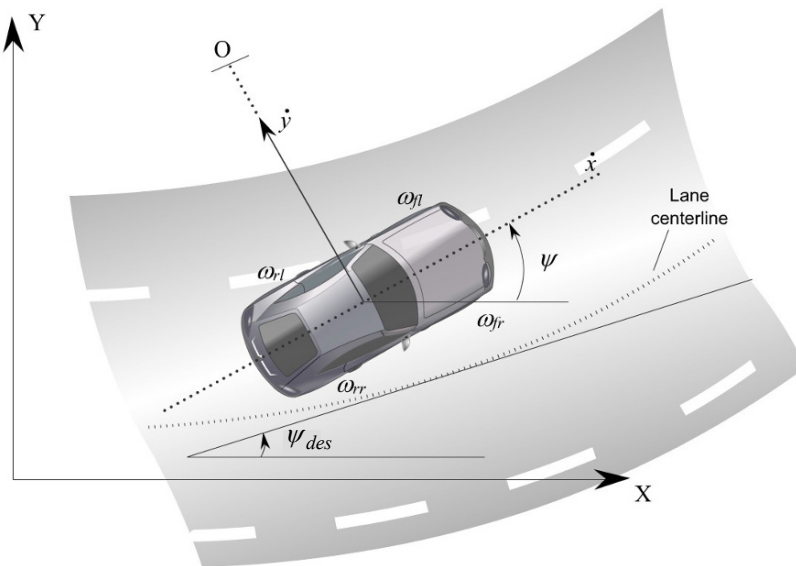
Figure 8-2. Degrees of freedom for vehicle model for differential braking based system

Vehicle Body Equations

Let the front wheel steering angle be denoted by δ. Let the longitudinal tire forces at the front left, front right, rear left and rear right tires be given by $F_{xf\ell}$, F_{xfr}, $F_{xr\ell}$ and F_{xrr} respectively. Let the lateral forces at the front left, front right, rear left and rear right tires be denoted by $F_{yf\ell}$, F_{yfr}, $F_{yr\ell}$ and F_{yrr} respectively.

Then the equations of motion of the vehicle body are

$$m\ddot{x} = \left(F_{xf\ell} + F_{xfr}\right)\cos(\delta) + F_{xr\ell} + F_{xrr} - \left(F_{yf\ell} + F_{yfr}\right)\sin(\delta) + m\dot{\psi}\dot{y}$$
(8.1)

$$m\ddot{y} = F_{yr\ell} + F_{yrr} + \left(F_{xf\ell} + F_{xfr}\right)\sin(\delta) + \left(F_{yf\ell} + F_{yfr}\right)\cos(\delta) - m\dot{\psi}\dot{x}$$
(8.2)

$$I_z\ddot{\psi} = \ell_f\left(F_{xf\ell} + F_{xfr}\right)\sin(\delta) + \ell_f\left(F_{yf\ell} + F_{yfr}\right)\cos(\delta) - \ell_r\left(F_{yr\ell} + F_{yrr}\right)$$
$$+ \frac{\ell_w}{2}\left(F_{xfr} - F_{xf\ell}\right)\cos(\delta) + \frac{\ell_w}{2}\left(F_{xrr} - F_{xr\ell}\right) + \frac{\ell_w}{2}\left(F_{yf\ell} - F_{yfr}\right)\sin(\delta)$$
(8.3)

Here the lengths ℓ_f, ℓ_r and ℓ_w refer to the longitudinal distance from the c.g. to the front wheels, longitudinal distance from the c.g. to the rear wheels and the lateral distance between left and right wheels (track width) respectively.

Slip Angle and Slip Ratio

Define the slip angles at the front and rear tires as follows

$$\alpha_f = \delta - \frac{\dot{y} + \ell_f\dot{\psi}}{\dot{x}}$$
(8.4)

$$\alpha_r = -\frac{\dot{y} - \ell_r\dot{\psi}}{\dot{x}}$$
(8.5)

Define the longitudinal slip ratios at each of the 4 wheels using the following equations

$$\sigma_x = \frac{r_{eff}\,\omega_w - \dot{x}}{\dot{x}} \quad \text{during braking} \tag{8.6}$$

$$\sigma_x = \frac{r_{eff}\,\omega_w - \dot{x}}{r_{eff}\,\omega_w} \quad \text{during acceleration} \tag{8.7}$$

Let the slip ratios at the front left, front right, rear left and rear right be denoted by $\sigma_{f\ell}$, σ_{fr}, $\sigma_{r\ell}$ and σ_{rr} respectively.

Combined Lateral-Longitudinal Tire Model Equations

The Dugoff tire model discussed in section 13.10 of this book can be utilized for calculation of tire forces. Let the cornering stiffness of each tire be given by C_α and the longitudinal tire stiffness by C_σ. Then the longitudinal tire force of each tire is given by (Dugoff, et. al., 1969)

$$F_x = C_\sigma \frac{\sigma}{1+\sigma} f(\lambda) \tag{8.8}$$

and the lateral tire force is given by

$$F_y = C_\alpha \frac{\tan(\alpha)}{1+\sigma} f(\lambda) \tag{8.9}$$

where λ is given by

$$\lambda = \frac{\mu F_z (1+\sigma)}{2\left\{ (C_\sigma \sigma)^2 + (C_\alpha \tan(\alpha))^2 \right\}^{1/2}} \tag{8.10}$$

and

$$f(\lambda) = (2 - \lambda)\lambda \ \text{if} \ \lambda < 1 \tag{8.11}$$

$$f(\lambda) = 1 \ \text{if} \ \lambda \geq 1 \tag{8.12}$$

F_z is the vertical force on the tire while μ is the tire-road friction coefficient.

Using equations (8.8), (8.9), (8.10), (8.11) and (8.12), the longitudinal tire forces $F_{xf\ell}$, F_{xfr}, $F_{xr\ell}$ and F_{xrr} and the lateral tire forces $F_{yf\ell}$, F_{yfr}, $F_{yr\ell}$ and F_{yrr} can be calculated. Note that the slip angle and slip ratio of each corresponding wheel must be used in the calculation of the lateral and longitudinal tire forces for that wheel.

Wheel dynamics

The rotational dynamics of the 4 wheels are given by the following torque balance equations:

$$J_w \dot{\omega}_{f\ell} = T_{df\ell} - T_{bf\ell} - r_{eff} F_{xf\ell} \tag{8.13}$$

$$J_w \dot{\omega}_{fr} = T_{dfr} - T_{bfr} - r_{eff} F_{xfr} \tag{8.14}$$

$$J_w \dot{\omega}_{r\ell} = T_{dr\ell} - T_{br\ell} - r_{eff} F_{xr\ell} \tag{8.15}$$

$$J_w \dot{\omega}_{rr} = T_{drr} - T_{brr} - r_{eff} F_{xrr} \tag{8.16}$$

Here $T_{df\ell}$, T_{dfr}, $T_{dr\ell}$ and T_{drr} refer to the drive torque transmitted to the front left, front right, rear left and rear right wheels respectively and $T_{bf\ell}$, T_{bfr}, $T_{br\ell}$ and T_{brr} refer to the brake torque on the front left, front right, rear left and rear right wheels respectively.

In general, the brake torque at each wheel is a function of the brake pressure at that wheel, the brake area of the wheel A_w, the brake friction coefficient μ_b and the brake radius R_b. For instance, the brake torque at the front left wheel $T_{bf\ell}$ is related to the brake pressure at the front left wheel $P_{f\ell}$ through the equation

$$T_{bf\ell} = A_w \mu_b R_b P_{bf\ell} \tag{8.17}$$

Similar equations can be written for the brake pressures P_{bfr}, $P_{br\ell}$ and P_{brr} at the front right, rear left and rear right wheels respectively.

8.2.2   Control architecture

wheel speeds
lateral acceleration
yaw rate
steering angle

sensors

Objective: Yaw stability control

Upper
Controller

desired yaw torque

Lower
Controller

Brake pressure inputs $P_{bf\ell}$, P_{bfr}, $P_{br\ell}$, P_{brr}
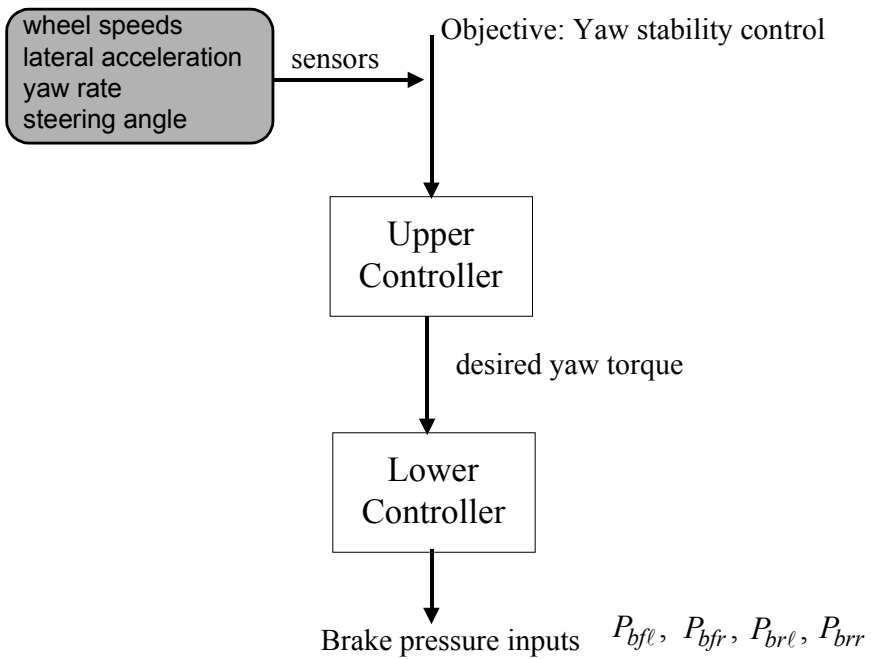
Figure 8-3. Structure of electronic stability control system

The control architecture for the yaw stability control system is hier-archical and is shown in Figure 8-3. The upper controller has the objective of ensuring yaw stability control and assumes that it can command any desired value of yaw torque. It uses measurements from wheel speed sensors, a yaw rate sensor, a lateral accelerometer and a steering angle sensor. Using these measurements and a control law to be discussed in the following sub-sections, it computes the desired value of yaw torque. The lower controller ensures that the desired value of yaw torque commanded by the upper controller is indeed obtained from the differential braking system. The lower controller utilizes the wheel rotational dynamics and controls the braking pressure at each of the 4 wheels to provide the desired yaw torque for the vehicle. The inherent assumption is that the rotational wheel dynamics are faster than the vehicle dynamics.

8.2.3 Desired yaw rate

In Chapter 3 (section 3.3), we saw that the steady state steering angle for negotiating a circular road of radius R is given by

$$\delta_{ss} = \frac{\ell_f + \ell_r}{R} + K_V a_y \tag{8.18}$$

where K_V is the understeer gradient and is given by

$$K_V = \frac{\ell_r m}{2C_{\alpha f}\left(\ell_f + \ell_r\right)} - \frac{\ell_f m}{2C_{\alpha r}\left(\ell_f + \ell_r\right)}$$

where $C_{\alpha f}$ and $C_{\alpha r}$ are the cornering stiffness for each front and rear tire respectively.

Hence, the steady state relation between steering angle and the radius of the vehicle's trajectory is

$$\delta_{ss} = \frac{\ell_f + \ell_r}{R} + \left(\frac{m\ell_r C_{\alpha r} - m\ell_f C_{\alpha f}}{2C_{\alpha f}C_{\alpha r}(\ell_f + \ell_r)}\right)\frac{V^2}{R} \tag{8.19}$$

and the radius can be expressed in terms of steering angle as

$$\frac{1}{R} = \frac{\delta_{ss}}{\ell_f + \ell_r + \dfrac{mV^2(\ell_r C_{\alpha r} - \ell_f C_{\alpha f})}{2C_{\alpha f}C_{\alpha r}L}} \tag{8.20}$$

Here $L = \ell_f + \ell_r$ is used to denote the wheelbase of the vehicle.

The desired yaw rate for the vehicle can therefore be obtained from steering angle, vehicle speed and vehicle parameters as follows

$$\dot{\psi}_{des} = \frac{\dot{x}}{R} = \frac{\dot{x}}{\ell_f + \ell_r + \dfrac{m\dot{x}^2(\ell_r C_{\alpha r} - \ell_f C_{\alpha f})}{2C_{\alpha f}C_{\alpha r}L}}\,\delta \tag{8.21}$$

Note that in the above equation, $C_{\alpha f}$ and $C_{\alpha r}$ stand for the cornering stiffness of *each* front and rear tire and it is assumed that there are two tires in the front and two tires in the rear. If the cornering stiffness of the front and rear tires are equal, then $C_{\alpha f} = C_{\alpha r} = C_\alpha$.

8.2.4   Desired side-slip angle

In Chapter 3, we found that the steady state yaw angle error during cornering is

$$e_{2\_ss} = -\frac{\ell_r}{R} + \frac{\ell_f}{2C_{\alpha r}\left(\ell_f + \ell_r\right)}\frac{mV^2}{R} = -\frac{\ell_r}{R} + \alpha_r \tag{8.22}$$

and the steady state slip angle of the vehicle is

$$\beta = -e_{2\_ss}$$

or

$$\beta = \frac{\ell_r}{R} - \frac{\ell_f}{2C_{\alpha r}\left(\ell_f + \ell_r\right)}\frac{mV^2}{R} \tag{8.23}$$

The above expression for steady state slip angle is in terms of velocity and road radius. This expression can be rewritten so that the steady state slip angle is expressed in terms of the steady state steering angle.

The steady –state steering angle, from equation (8.19) is

$$\delta_{ss} = \frac{\ell_f + \ell_r}{R} + \left(\frac{m\ell_r C_{\alpha r} - m\ell_{\alpha f}C_f}{2C_{\alpha f}C_{\alpha r}(\ell_f + \ell_r)}\right)\frac{V^2}{R}$$

Hence, the curvature of the road can be expressed as

$$\frac{1}{R} = \frac{\delta_{ss}}{\ell_f + \ell_r + \dfrac{mV^2(\ell_r C_{\alpha r} - \ell_f C_{\alpha f})}{2C_{\alpha f}C_{\alpha r}L}}$$

Combining equations (8.23) and (8.20), the steady state slip angle is

$$\beta = \frac{1}{R}\left(\ell_r - \frac{\ell_f}{2C_{\alpha r}\left(\ell_f + \ell_r\right)}mV^2 \right)$$

or

$$\beta = \frac{\delta_{ss}}{\ell_f + \ell_r + \dfrac{mV^2(\ell_r C_{\alpha r} - \ell_f C_{\alpha f})}{2C_{\alpha f}C_{\alpha r}L}}\left(\ell_r - \frac{\ell_f}{2C_{\alpha r}\left(\ell_f + \ell_r\right)}mV^2 \right)$$

which after simplification turns out to be

$$\beta_{des} = \frac{\ell_r - \dfrac{\ell_f mV^2}{2C_{\alpha r}\left(\ell_f + \ell_r\right)}}{\left(\ell_f + \ell_r\right) + \dfrac{mV^2\left(\ell_r C_{\alpha r} - \ell_f C_{\alpha f}\right)}{2C_{\alpha f}C_{\alpha r}\left(\ell_f + \ell_r\right)}}\ \delta_{ss} \tag{8.24}$$

Note: The above expression assumed that the cornering stiffness of *each* front tire is $C_{\alpha f}$ and of each rear tire is $C_{\alpha r}$.

Equation (8.24) describes the desired slip angle as a function of the driver's steering angle input, the vehicle's longitudinal velocity and vehicle parameters.

8.2.5   Upper bounded values of target yaw rate and slip angle

The desired yaw rate and the desired slip angle described in sections 8.2.3 and 8.2.4 cannot always be obtained. It is not safe, for example, to try and obtain the above desired yaw rate if the friction coefficient of the road is unable to provide tire forces to support a high yaw rate. Hence the desired yaw rate must be bounded by a function of the tire-road friction coefficient.

The lateral acceleration at the center of gravity (c.g.) of the vehicle is given by

$$a_{y\_cg} = \dot{x}\dot{\psi} + \ddot{y} \tag{8.25}$$

Since $\dot{y} = \dot{x}\tan(\beta)$, the lateral acceleration can be related to the yaw rate and the vehicle slip angle by the equation

$$a_{y\_cg} = \dot{x}\dot{\psi} + \tan(\beta)\ddot{x} + \frac{\dot{x}\dot{\beta}}{\sqrt{1 + \tan^2 \beta}} \tag{8.26}$$

The lateral acceleration must be bounded by the tire-road friction coefficient μ as follows

$$a_{y\_cg} \leq \mu g \tag{8.27}$$

The first term in the calculation of the lateral acceleration in equation (8.26) dominates. If the slip angle of the vehicle and its derivative are both assumed to be small, the second and third terms contribute only a small fraction of the total lateral acceleration. Hence, combining equations (8.26) and (8.27), the following upper bound can be used for the yaw rate

$$\dot{\psi}_{upper\_bound} = 0.85\frac{\mu g}{\dot{x}} \tag{8.28}$$

The factor 0.85 allows the second and third terms of equation (8.26) to contribute 15% to the total lateral acceleration.

The target yaw rate of the vehicle is therefore taken to be the nominal desired yaw rate defined by equation (8.21) as long as it does not exceed the upper bound defined by equation (8.28):

$$\dot{\psi}_{t\arg et} = \dot{\psi}_{des} \text{ if } \left|\dot{\psi}_{des}\right| \leq \dot{\psi}_{upper\_bound} \tag{8.29}$$

$$\dot{\psi}_{t\arg et} = \dot{\psi}_{upperbound} \text{ sgn}(\dot{\psi}_{des}) \text{ if } \left|\dot{\psi}_{des}\right| > \dot{\psi}_{upper\_bound} \tag{8.30}$$

The desired slip angle, for a given steering angle and vehicle speed, can be obtained from equation (8.24). The target slip angle must again be upper bounded so as to ensure that the slip angle does not become too large. At high slip angles, the tires lose their linear behavior and approach the limit of adhesion. Hence, it is important to limit the slip angle.

The following empirical relation on an upper bound for the slip angle is suggested

$$\beta_{upper\_bound} = \tan^{-1}(0.02\mu g) \tag{8.31}$$

This relation yields an upper bound of 10 degrees at a friction coefficient of $\mu = 0.9$ and an upper bound of 4 degrees at a friction coefficient of $\mu = 0.35$. This roughly corresponds to the desirable limits on slip angle on dry road and on packed snow respectively.

The target slip angle of the vehicle is therefore taken to be the nominal desired slip angle defined by equation (8.24) as long as it does not exceed the upper bound defined by equation (8.31):

$$\beta_{t\arg et} = \beta_{des} \text{ if } |\beta_{des}| \le \beta_{upper\_bound} \tag{8.32}$$

$$\beta_{t\arg et} = \beta_{upperbound} \text{ sgn}(\beta_{des}) \text{ if } |\beta_{des}| > \beta_{upper\_bound} \tag{8.33}$$

Several researchers in literature have simply assumed the desired slip angle to be zero and assumed that the upper bound on the yaw rate is given by $\dot{\psi}_{upper\_bound} = \dfrac{\mu g}{\dot{x}}$. However, the equations in (8.28) – (8.33) yield a better approximation to the driver-desired target values for both yaw rate and slip angle.

8.2.6 Upper controller design

The objective of the upper controller is to determine the desired yaw torque for the vehicle so as to track the target yaw rate and target slip angle discussed in section 8.2.5.

The sliding mode control design methodology has been used by several researchers to achieve the objectives of tracking yaw rate and slip angle (Drakunov, et. al., 2000, Uematsu and Gerdes, 2002, Yi, et. al., 2003 and Yoshioka, et. al., 1998). A good introduction to the general theory of sliding surface control can be found in the text by Slotine and Li (1991).

The sliding surface is chosen so as to achieve either yaw rate tracking or slip angle tracking or a combination of both. Examples of sliding surfaces that have been used by researchers include the following three

$$s = \dot{\beta} + \xi\beta \tag{8.34}$$

$$s = \dot{\psi} - \dot{\psi}_{t\arg et} \tag{8.35}$$

$$s = \dot{\psi} - \dot{\psi}_{t \arg et} + \xi \beta \qquad (8.36)$$

By ensuring that the vehicle response converges to the surface $s = 0$, one ensures that the desired yaw rate and/or slip angle are obtained. A good comparison of the performance obtained with the 3 types of sliding surfaces described above can be found in Uematsu and Gerdes (2002).

This book suggests that the following sliding surface be used for control design:

$$s = \dot{\psi} - \dot{\psi}_{t \arg et} + \xi \left(\beta - \beta_{t \arg et} \right) \qquad (8.37)$$

This surface is defined as a weighted combination of yaw rate and slip angle errors and takes the target values for yaw rate and slip angle discussed in sections 8.2.3 – 8.2.5 into consideration.

Differentiating equation (8.37)

$$\dot{s} = \ddot{\psi} - \ddot{\psi}_{t \arg et} + \xi \left(\dot{\beta} - \dot{\beta}_{t \arg et} \right) \qquad (8.38)$$

The equation for $\ddot{\psi}$ can be obtained by rewriting equation (8.3) as

$$I_z \ddot{\psi} = \ell_f \left(F_{xf\ell} + F_{xfr} \right) \sin(\delta) + \ell_f \left(F_{yf\ell} + F_{yfr} \right) \cos(\delta) - \ell_r \left(F_{yr\ell} + F_{yrr} \right)$$
$$+ \frac{\ell_w}{2} \left(F_{xfr} - F_{xf\ell} \right) \cos(\delta) + \frac{\ell_w}{2} \left(F_{xrr} - F_{xr\ell} \right) + \frac{\ell_w}{2} \left(F_{yf\ell} - F_{yfr} \right) \sin(\delta)$$
$$(8.39)$$

Ignore the terms $\ell_f \left(F_{xf\ell} + F_{xfr} \right) \sin(\delta)$ and $\dfrac{\ell_w}{2} \left(F_{yf\ell} - F_{yfr} \right) \sin(\delta)$ in equation (8.39), assuming that the steering angle is small. Next, assume that the ratio of front-to-back distribution of brake torques is fixed. Set

$$F_{xr\ell} = \rho F_{xf\ell} \qquad (8.40)$$

and

$$F_{xrr} = \rho F_{xfr} \qquad (8.41)$$

where ρ is determined by the front-to-back brake proportioning. The front-to-back brake proportioning is determined by a pressure proportioning valve

in the hydraulic system. Many pressure proportioning valves provide equal pressure to both front and rear brakes up to a certain pressure level, and then subsequently reduce the rate of pressure increase to the rear brakes (see Gillespie, 1992).

$$I_z \ddot{\psi} = \ell_f \left(F_{yf\ell} + F_{yfr}\right)\cos(\delta) - \ell_r \left(F_{yr\ell} + F_{yrr}\right)$$
$$+ \frac{\ell_w}{2}\left(F_{xfr} - F_{xf\ell}\right)\cos(\delta) + \rho \frac{\ell_w}{2}\left(F_{xfr} - F_{xf\ell}\right) \tag{8.42}$$

Denote

$$M_{\psi b} = \frac{\ell_w}{2}\left(F_{xfr} - F_{xf\ell}\right) \tag{8.43}$$

$M_{\psi b}$ is the yaw torque from differential braking and constitutes the control input for the upper controller.

Then

$$\ddot{\psi} = \frac{1}{I_z}\left[\ell_f \left(F_{yf\ell} + F_{yfr}\right)\cos(\delta) - \ell_r \left(F_{yr\ell} + F_{yrr}\right) + \left(\cos(\delta) + \rho\right)M_{\psi b}\right] \tag{8.44}$$

Substituting for $\ddot{\psi}$ in equation (8.38)

$$\dot{s} = \frac{1}{I_z}\left[\ell_f \left(F_{yf\ell} + F_{yfr}\right)\cos(\delta) - \ell_r \left(F_{yr\ell} + F_{yrr}\right) + \left(\cos(\delta) + \rho\right)M_{\psi b}\right]$$
$$- \ddot{\psi}_{target} + \xi\left(\dot{\beta} - \dot{\beta}_{target}\right) \tag{8.45}$$

Setting $\dot{s} = -\eta s$ yields the control law

$$\frac{\rho + \cos(\delta)}{I_z} M_{\psi b} =$$

$$\begin{bmatrix} -\dfrac{\ell_f}{I_z}\left(F_{yf\ell} + F_{yfr}\right)\cos(\delta) + \dfrac{\ell_r}{I_z}\left(F_{yr\ell} + F_{yrr}\right) \\[2mm] -\eta s + \ddot{\psi}_{t\,\arg et} - \xi\left(\dot{\beta} - \dot{\beta}_{t\,\arg et}\right) \end{bmatrix} \qquad (8.46)$$

The control law described in equation (8.46) above requires feedback of slip angle, slip angle derivative, and front and rear lateral tire forces. These variables cannot be easily measured but must be estimated and used for feedback. Estimation methods in literature use a combination of algorithms based on integration of inertial sensors and dynamic model based observers (Tseng, et. al., 1999, Van Zanten, et. al., 1996, Fukada, 1999, Ghoeneim, 2000, and Piyabongkarn, et. al., 2009). The use of GPS for estimation of slip ratio and slip angle has also been investigated (Daily and Bevly, 2004, Bevly, et. al., 2001).

The term $-\dfrac{\ell_f}{I_z}\left(F_{yf\ell} + F_{yfr}\right)\cos(\delta) + \dfrac{\ell_r}{I_z}\left(F_{yr\ell} + F_{yrr}\right)$ in the upper control law (8.46) is the yaw moment contribution due to lateral tire forces (steering). In other words, the yaw moment contribution from lateral forces is taken into account in determining the required yaw torque from differential braking or other ESC system. The target yaw acceleration $\ddot{\psi}_{t\,\arg et}$ is a feedforward term while the terms $-\eta s$ and $-\xi(\dot{\beta} - \dot{\beta}_{t\,\arg et})$ are feedback corrections.

The lateral force yaw moment contribution $-\dfrac{\ell_f}{I_z}\left(F_{yf\ell} + F_{yfr}\right)\cos(\delta) +$

$\dfrac{\ell_r}{I_z}\left(F_{yr\ell} + F_{yrr}\right)$ can be replaced in eqn (8.46) with an integral error feedback

term such as $-k_i \int s \, dt$:

$$\frac{\rho + \cos\delta}{I_z} M_{\psi b} = \left[-k_i \int s \, dt - \eta s + \ddot{\psi}_{t\,\arg et} - \xi(\dot{\beta} - \dot{\beta}_{traget}) \right] \qquad (8.47)$$

This simplifies the measurement and estimation requirements for the upper control law. However, control law (8.46) can provide better transient

performance than the simplified control law (8.47) based on the integral error feedback term.

8.2.7   Lower controller design

The lower controller determines the brake pressure at each wheel, so as to provide a net yaw torque that tracks the desired value for yaw torque determined by the upper controller.

By definition, $M_{\psi b} = \dfrac{\ell_w}{2}\left(F_{xfr} - F_{xf\ell}\right)$. Hence, the *extra* differential longitudinal tire force needed to produce the desired yaw torque can be obtained as

$$\Delta F_{xf} = \frac{2M_{\psi b}}{\ell_w} \tag{8.48}$$

Consider the dynamics of the front left and front right wheels

$$J_w \dot{\omega}_{f\ell} = T_{df\ell} - A_w \mu_b R_b P_{bf\ell} - r_{eff} F_{xf\ell} \tag{8.49}$$

$$J_w \dot{\omega}_{fr} = T_{dfr} - A_w \mu_b R_b P_{bfr} - r_{eff} F_{xfr} \tag{8.50}$$

The drive torque variables $T_{df\ell}$ and T_{dfr} are determined by the driver throttle input or by a combination of the driver throttle input and a traction control system. The brake pressures $P_{bf\ell}$ and P_{bfr} are determined from the braking input of the driver and the additional brake required to provide the differential braking torque for vehicle yaw control.

By inspection of equations (8.49) and (8.50), it can be seen that the desired differential longitudinal tire force ΔF_{xf} at the front tires can be obtained by choosing the brake pressures at the front left and right tires as follows:

$$P_{bf\ell} = P_0 - a\frac{\Delta F_{xf} r_{eff}}{A_w \mu_b R_b} \tag{8.51}$$

$$P_{bfr} = P_0 + (1-a)\frac{\Delta F_{xf} r_{eff}}{A_w \mu_b R_b} \tag{8.52}$$

where P_0 is the measured brake pressure at the wheel at the time that differential braking is first initiated and the constant a has to be chosen such that $0 \leq a \leq 1$ and $P_{bf\ell}$ and P_{bfr} are both positive. The brake pressure at each wheel should be zero or positive. Hence, in the case where the driver is not braking, ΔF_{xf} is positive, and $P_0 = 0$, then a has to be chosen to be zero. On the other hand, if the driver is braking and P_0 is adequately large, then a could be chosen to be 0.5. This would mean that the differential braking torque is obtained by increasing the brake pressure at one wheel and decreasing the brake pressure at the other wheel compared to the driver applied values. Thus a must be chosen in real-time based on the measured value of P_0.

8.3   STEER-BY-WIRE SYSTEMS

8.3.1   Introduction

In the use of a steer-by-wire system for yaw stability control, the front wheel steering angle is determined as a sum of two components. One component is determined directly by the driver from his/her steering wheel angle input. The other component is decided by the steer-by-wire controller, as shown in Figure 8-4. In other words, the steer-by-wire controller modifies the driver's steering command so as to ensure "skid prevention" or "skid control". This must be done in such a way that it does not interfere with the vehicle's response in following the path desired by the driver.

Significant work on the design of steer-by-wire systems for vehicle stability control has been documented by Ackermann and co-workers (Ackermann, 1997, Ackermann, 1994). The following sub-sections summarize the steer-by-wire control system for front-wheel steered vehicles designed by Ackermann (1997).
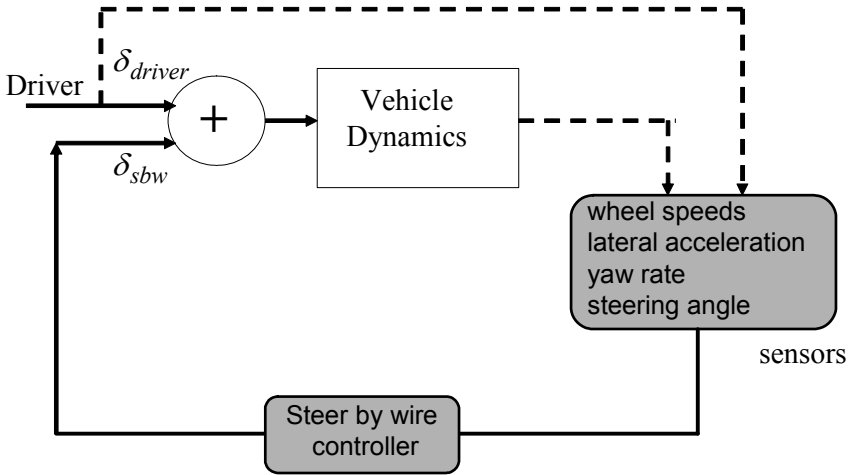
Figure 8-4. Structure of steer-by-wire stability control system

8.3.2 Choice of output for decoupling

As described in Ackermann (1997), the driver's primary task is "path following". In path following the driver keeps the car – considered as a single point mass m - on her desired path, as shown in Figure 8-5. She does this by applying a desired lateral acceleration a_{yP} to the mass m in order to re-orient the velocity vector of the vehicle so that it remains tangential to her desired path.
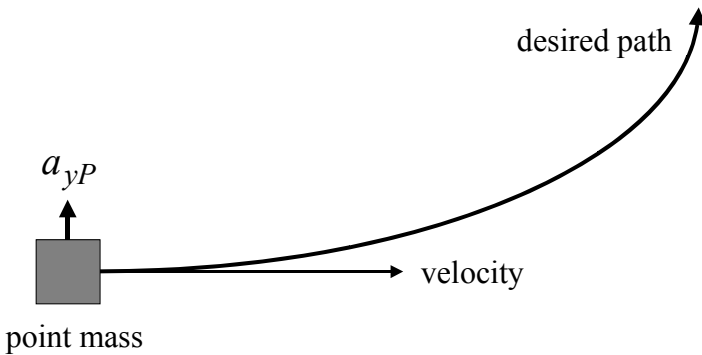
Figure 8-5. The path following task of the driver

The driver has a secondary task of "disturbance attenuation." This task results from the fact that the vehicle is not really a point mass but has a second degree of freedom which is the yaw motion of the vehicle. Let the yaw moment of inertia of the vehicle be I_z. The yaw rate of the car is excited not only by the driver desired lateral acceleration a_{yP} but also by a disturbance torque M_{zD}. The yaw rate excited by the lateral acceleration a_{yP} is expected by the driver and she is used to this yaw rate. However, disturbances such as a flat tire and asymmetric friction coefficients at the left and right wheels induce a disturbance torque M_{zD} which excite a yaw motion that the driver does not expect.

Usually, the driver has to compensate for the disturbance torque by using the steering wheel. This is a difficult task for the driver due to the fact that she is not used to counteracting for such disturbances and also due to the fact that she does not have a measure of the disturbances that cause the unexpected yaw and therefore her reaction is likely to be delayed. It often takes time for the driver to recognize the situation and the need for her special intervention.

In Ackermann (1997), the steer-by-wire electronic stability control (ESC) system is designed to perform this task of disturbance attenuation so that the driver can concentrate on her primary task of path following. For this it is necessary to decouple the secondary disturbance attenuation dynamics such that they do not influence the primary path following dynamics. The automatic control system for the yaw rate $\dot{\psi}$ should not interfere with the path following task of the driver. In control system terms, this means the yaw rate $\dot{\psi}$ should be unobservable from the lateral acceleration a_{yP}. The yaw rate dynamics will continue to depend on the lateral acceleration a_{yP}. Only then can the driver control the car to follow a path, since the vehicle must have a yaw rate to follow a path. However, the yaw rate is commanded only indirectly by the driver via a_{yP}. Nominally the driver is concerned directly only with a_{yP}. But any yaw rate induced by the disturbance attenuation automatic steering control system should be such that it does not affect the lateral acceleration a_{yP}. This decoupling has to be done in a robust manner. In particular, it must be robust with respect to vehicle velocity and road surface conditions.

From the above discussion, the motivation for removing the influence of yaw rate on lateral acceleration is clear. The next question to be answered is "At which point of the vehicle should the lateral acceleration be used as the output ?" The lateral acceleration at any point P on the vehicle is given by

$$a_{yP} = a_{y\_cg} + \ell_P \ddot{\psi} \tag{8.53}$$

where a_{y_cg} is the lateral acceleration at the c.g. of the vehicle and ℓ_P is the longitudinal distance of the point P ahead of the c.g. of the vehicle. Since $a_{y\_cg} = \dfrac{F_{yf} + F_{yr}}{m}$, we have

$$a_{yP} = \frac{1}{m}\left(F_{yf} + F_{yr}\right) + \ell_P \ddot{\psi}$$

or

$$a_{yP} = \frac{1}{m}\left(F_{yf} + F_{yr}\right) + \ell_P \frac{1}{I_z}\left(\ell_f F_{yf} - \ell_r F_{yr}\right)$$

or

$$a_{yP} = F_{yf}\left(\frac{1}{m} + \frac{\ell_P \ell_f}{I_z}\right) + F_{yr}\left(\frac{1}{m} - \frac{\ell_P \ell_r}{I_z}\right) \tag{8.54}$$

Choose the output position as

$$\ell_P = \frac{I_z}{m\ell_r} \tag{8.55}$$

This choice of the lateral acceleration output position ensures that the acceleration is independent of the rear lateral tire force F_{yr}. Thus the uncertainities associated with some of the tire forces on decoupling are removed and more robust decoupling can be achieved.

Substituting from equation (8.55) into equation (8.54)

$$a_{yP} = F_{yf}\left(\frac{1}{m} + \frac{\ell_f}{m\ell_r}\right)$$

$$a_{yP} = F_{yf}\left(\frac{\ell_r + \ell_f}{m\ell_r}\right) = \frac{L}{m\ell_r}F_{yf} \tag{8.56}$$

8.3.3   Controller Design

The total steering angle is given by

$$\delta = \delta_{driver} + \delta_{sbw} \tag{8.57}$$

where δ_{driver} is the steering angle input of the driver and δ_{sbw} is the steering angle input of the disturbance attenuation control system.

First, note that the lateral force at the front tire depends on the slip angle at the front wheels. Hence

$$a_{yP}(\alpha_f) = \frac{L}{m\ell_r} F_{yf}(\alpha_f) \tag{8.58}$$

Hence the yaw rate $\dot{\psi}$ does not influence a_{yP} if and only if $\dot{\psi}$ does not influence α_f. Hence the controller should be designed such that the front tire slip angle does not depend on the yaw rate.

Let the vehicle velocity angle at the front tires be θ_{vf}. This is the angle between the longitudinal axis of the vehicle and the velocity vector at the front wheels. Then

$$\alpha_f = \delta_{driver} + \delta_{sbw} - \theta_{vf} \tag{8.59}$$

There is no easy way to measure θ_{vf}. Otherwise the control law could be chosen as $\delta_{sbw} = \theta_{vf}$. That would ensure that the slip angle did not depend on the yaw rate. It would depend only on the driver commanded front wheel steering angle and would not depend on any other state variables.

The state equation for θ_{vf} is (Ackermann, 1994)

$$\dot{\theta}_{vf} = -\dot{\psi} + \frac{\cos^2(\theta_{vf})}{V_x} a_{yP}(\alpha_f) + g(\dot{\psi}) \tag{8.60}$$

where

$$g(\dot{\psi}) = \frac{\cos(\theta_{vf})}{V_x}\left[\left(\ell_f - \ell_P\right)\ddot{\psi}\cos(\theta_{vf}) + \left(\ell_f\dot{\psi}^2 - a_x\right)\sin(\theta_{vf})\right]$$

(8.61)

where a_x is longitudinal acceleration and could be measured by an accelerometer.

Differentiating equation (8.59)

$$\dot{\alpha}_f = \dot{\delta}_{driver} + \dot{\delta}_{sbw} - \dot{\theta}_{vf}$$

(8.62)

Substituting from equation (8.60) into equation (8.62), it is clear that if the control law is chosen as

$$\dot{\delta}_{sbw} = -\dot{\psi} + g(\dot{\psi}) + F(\delta_{driver})$$

(8.63)

then the slip angle dynamics at the front tires would be

$$\dot{\alpha}_f = -\frac{\cos^2(\theta_{vf})}{V_x}a_{yP}(\alpha_f) + \dot{\delta}_{driver} + F(\delta_{driver})$$

(8.64)

Here $F(\delta_{driver})$ is chosen as a function of the driver input only and can be interpreted as the desired yaw rate corresponding to the driver's steering angle input δ_{driver}. Thus the error in yaw rate $F(\delta_{driver}) - \dot{\psi}$ is used as a feedback term in the calculation of the steer-by-wire correction δ_{sbw} in equation (8.63).

The assumption of a small velocity angle at the front tire leads to

$$\dot{\alpha}_f = -\frac{L}{m\ell_r V_x}F_{yf}(\alpha_f) + \dot{\delta}_{driver} + F(\delta_{driver})$$

(8.65)

Thus the front wheel slip angle dynamics depend only on the external driver commanded steering input δ_{driver} and do not depend on the yaw rate $\dot{\psi}$. As we have seen, this also implies that the lateral acceleration a_{yP} does not depend on the yaw rate $\dot{\psi}$.

One question that remains to be addressed is stability of the overall system. Decoupling does not automatically ensure stability. However, using the Lyapunov function $V = \alpha_f{}^2$ and the fact that

$$\alpha_f F_{yf}(\alpha_f) > 0 \qquad\qquad\qquad\qquad (8.66)$$

it can be shown that the α_f sub-system is stable when $\delta_{driver} = 0$. It also turns out that the decoupled yaw sub-system is stable (Ackermann, 1994).

Further practical implementation issues and simplifications of the controller are discussed in Ackermann (1997). Experimental results are presented in Ackermann (1994) and Ackermann (1997).

8.4   INDEPENDENT ALL WHEEL DRIVE TORQUE DISTRIBUTION

8.4.1   Traditional four wheel drive systems

If the differential braking based yaw stability control system is used during vehicle acceleration, it reduces the acceleration of the vehicle and therefore may not provide the longitudinal response the driver needs. A solution to this problem that is being actively investigated and developed in the automotive industry is the use of independent drive torque control with all wheel drive technology to enhance both traction and handling (Sawase and Sano, 1999, Osborn and Shim, 2004).

The terms "four wheel drive" and "all wheel drive" will be quickly summarized here for the reader's benefit. In a 4-wheel drive system the drive torque is transmitted to all four wheels (as opposed, for example, to a front wheel drive vehicle where the torque is transmitted only to the two front wheels).

The advantage of a 4-wheel drive (4WD) system is that longitudinal tire traction forces are generated at all 4 wheels to help the forward motion of the vehicle. This is very helpful in situations where loss of traction is a problem, for example in snow, off-road terrain and in climbing slippery hills. Four-wheel drive systems provide no advantage, however, in stopping on a slippery surface. This is determined entirely by the brakes and not by the type of drive system.

The major components that enable 4-wheel drive operation are the differentials at the front and rear axles and the transfer case. The differential at the front (or the rear) allows the left and right wheels to spin at different

speeds. This is necessary during a turn where the outer wheel moves on a circle of larger radius and must turn faster. The transfer case routes torque from the transmission to both the front and rear axles. Depending on the design, the transfer case may provide equal amounts of torque to the front and rear axles, or it may proportion torque to the front and rear axles. The transfer case routes torque to the front and rear using a differential called the *center differential*.

In a 4-wheel drive system, when 4-wheel drive is engaged, the front and rear drive shafts are locked together so that the two axles must spin at the same speed. Four-wheel drive systems can be full-time or part-time systems. In a part-time 4-wheel drive system, the driver can select 4-wheel or 2-wheel drive operation using a lever or a switch. The driver can "shift on the fly" (switch between 2WD and 4WD while driving). This allows the use of 2 wheel drive on regular dry roads and 4-wheel drive on slippery surfaces where more traction is needed.

A full-time 4WD system, on the other hand, lets the vehicle operate in 2WD (either front or rear) until the system judges that 4WD is needed. It then automatically routes power to all four wheels, varying the ratio between front and rear axles as necessary. Usually the detection of the fact that one of the wheels of the vehicle is slipping is used to activate a system. However, some of the more recent and sophisticated systems use software that switches the system to 4WD during specific driving conditions, even before a wheel begins to slip. A full-time 4-wheel drive system is also called an *all-wheel drive* (AWD) system.

8.4.2 Torque transfer between left and right wheels using a differential

As described above in section 8.4.1, a traditional differential allows the left and right wheels of a drive axle to spin at different speeds. This is necessary in order to allow the vehicle to turn. A traditional differential is also called an "open" differential.

An open differential splits the torque evenly between each of the two wheels to which it is connected. If one of those two wheels comes off the ground, or is on a very slippery surface, very little torque is required to drive that wheel. Because the torque is split evenly, this means that the other wheel also receives very little torque. So even if the other wheel has plenty of traction, no torque is transferred to it. This is a major disadvantage of an open differential.

An improvement on the open differential is a locking differential. In a locking differential, the driver can operate a switch to lock the left and right wheels together. This ensures that both wheels together receive the total

torque. If one of the two wheels is on a slippery surface, the other wheel could still receive adequate torque and provide the longitudinal traction force. Thus a locking differential provides better traction on slippery surfaces and can be used when required by the driver.

Yet another type of differential is the limited slip differential (LSD). In a limited slip differential, a clutch progressively locks the left and right wheels together but initially allows some slip between them. This allows the inner and outer wheels to spin at different speeds during a turn but automatically locks the two wheels together when the speed difference is big so as to provide traction help on slippery surfaces.

From the above discussion on differentials it is clear that the ratio of torque transmitted to the left and right wheels is determined by the type of differential. In an open differential, the torque transmitted to both wheels is always equal. In a locked differential, the speed of both wheels is equal and both wheels receive the total torque together as one integrated system. In a limited slip differential (LSD), more torque can be transferred to the slower wheel. This increase in torque to the slower wheel is equal to the torque required to overpower the clutch used in the LSD.

8.4.3   Active Control of Torque Transfer To All Wheels

The ultimate all-wheel drive system is one in which torque transfer to each of the 4 wheels can be independently controlled. Twin clutch torque biasing differentials have recently been developed in the automotive industry in which torque can be transferred to the inner or outer wheels in a variety of different ratios as required by an active control system (Sawase and Sano, 1999). The torque transfer between front and rear wheels can be similarly controlled actively using the center differential in the transfer case. By independently controlling the drive torque transferred to each of the 4 wheels, both traction and yaw stability control can be achieved. Yaw stability control can thus be achieved during the acceleration of a vehicle without requiring differential activation of the brakes which could have resulted in a net decrease in acceleration.

Differential Braking

Causes vehicle to slow down
and may not provide
driver desired longitudinal
response if used during
vehicle acceleration

**Controlled
Limited Slip
Differential**

Capable of increasing torque
to inside wheel but not
outside wheel as it
only transfers torque
from faster running
wheel to slower one

**Twin-Clutch
Torque Transfer
Differential**

Capable of transferring torque
to either wheel without a
reduction in net vehicle
acceleration

Figure 8-6. Types of yaw stability control systems and their characteristics during vehicle acceleration

Figure 8-6 shows three different types of yaw stability control systems that can be used during vehicle acceleration and their respective characteristics.

A twin-clutch limited slip differential described in Sawase and Sano (1999) allows any ratio of drive torques between the left and right wheels. The following equations can be used to model the torque transferred to each wheel with such a twin-clutch active differential:

When the right clutch is engaged with a clutch torque T_{clutch}, the drive torque transmitted to the left wheel is

$$T_{d\ell} = \frac{1}{2}T_d - qT_{clutch} \tag{8.67}$$

while the drive torque transmitted to the right wheel is

$$T_{dr} = \frac{1}{2}T_d + qT_{clutch} \tag{8.68}$$

where q is a ratio determined by the gearing system in the twin-clutch differential and T_d is the total torque transmitted to the axle under consideration.

Similarly, when the left clutch is engaged with a clutch torque T_{clutch}, the drive torque transmitted to the left wheel is

$$T_{d\ell} = \frac{1}{2}T_d + qT_{clutch} \qquad\qquad (8.69)$$

while the drive torque transmitted to the right wheel is

$$T_{dr} = \frac{1}{2}T_d - qT_{clutch} \qquad\qquad (8.70)$$

Thus, by controlling the clutch torque, the ratio of drive torque transmitted to the left and right wheels can be controlled.

Dynamic models that include transient and steady response in torque transfer during clutch engagement in a limited slip differential or in a twin clutch differential can be found in Piyabongkarn, et. al., 2007 and Piyabongkarn, et. al., 2010.

The best configuration for independently controlling the torque to each wheel would be a system consisting of a twin-clutch torque transfer differential each at both front and rear wheels and an all wheel drive transfer case equipped with a central differential. However, weight and price considerations could make this configuration an unattractive option. An alternative is to use a central differential and just one twin-clutch torque transfer differential. Analysis in Swase and Sano (1999) and Piyabongkarn, et. al. (2010) show that a torque transfer differential at the rear wheels, in addition to a central differential, is an attractive option.

Results in Sawase and Sano (1999) show performance when a stability control system that utilizes both differential braking and torque transfer is used. The upper control system to be used for such a stability control system would be similar to the one discussed in section 8.2.6. The upper controller would determine the desired yaw moment for the vehicle. The difference would be in the lower controller. In the lower controller, the active drive torque transfer would be utilized during vehicle acceleration and differential braking would be utilized during vehicle deceleration.

8.5   NEED FOR SLIP ANGLE CONTROL

If the objective of the ESC system were to track only a desired yaw rate, the system would be simpler to implement. If both yaw rate and slip angle need to be controlled to desired values, a robust estimator is required and the ESC

system is more complex to implement. This is because slip angle cannot be easily measured and needs to be estimated.

This section explains through simulation studies the benefits of controlling both slip angle and yaw rate, as opposed to controlling only yaw rate.

Figure 8-7 shows the planar trajectory executed by a vehicle in response to an approximate step steering input on a dry road with a friction coefficient of 1. Figure 8-8 shows the slip angle of the vehicle for the same case.

Figure 8-9 shows the trajectory of the same vehicle for the same step steering input on a road with a friction coefficient of only 0.6. The system in this case uses ESC with only yaw rate being controlled. In other words, the value of ξ is assumed to be zero, so that slip angle feedback is not utilized. As seen in Figure 8-9, the vehicle has a smaller yaw rate than desired on this low friction road surface, in spite of yaw rate ESC. Furthermore, the slip angle as seen in Figure 8-10 is seen to keep increasing and reach a value of approximately -14 degrees in the duration of the simulation. With this high value of slip angle, the driver is likely to perceive the vehicle as skidding and being out of control.

On the other hand, with an ESC system that utilizes both slip angle and yaw rate control, the slip angle is limited to -4 degrees, as seen in Figure 8-12. The planar trajectory of the vehicle is approximately the same as that achieved by the ESC system with only yaw rate control, as seen in Figure 8-11.

Thus, the benefit of using combined slip angle and yaw rate control is clear from these simulations.

Next, consider a comparison of two controllers described as follows: Controller 1, developed using a sliding surface defined by

$$s = \dot{\psi} - \dot{\psi}_{t \arg et} + \xi \beta \tag{8.71}$$

and controller 2, developed using a sliding surface defined by

$$s = \dot{\psi} - \dot{\psi}_{t \arg et} + \xi (\beta - \beta_{t \arg et}) \tag{8.72}$$

A comparison of these two controllers is presented here to show that desired yaw rate and desired slip angle can both be simultaneously obtained when the friction coefficient is adequate. Figure 8-13 shows the planar trajectory of the vehicle with controller 1 on a road with friction coefficient 0.8. It can be seen that the desired trajectory and desired yaw rate are not obtained with controller 1. The slip angle in this case is lower than the slip angle on a road of friction coefficient 1 and no ESC activation, as seen in Figure 8-14.
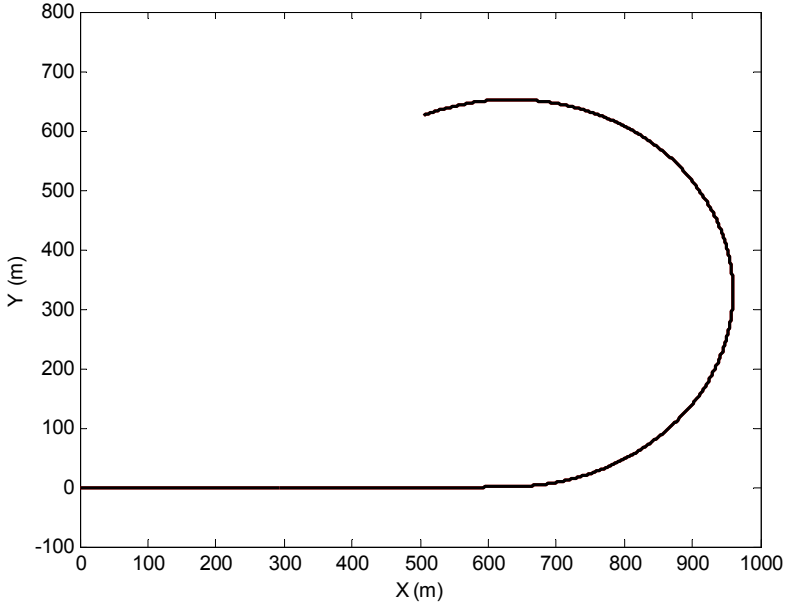
Figure 8-7. Vehicle trajectory for a step steering input
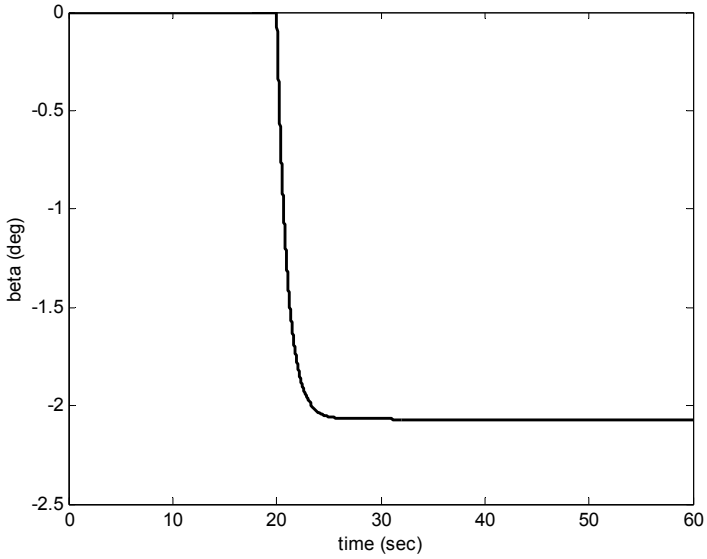
Figure 8-8. Slip angle on a dry road with a friction coefficient of 1.0
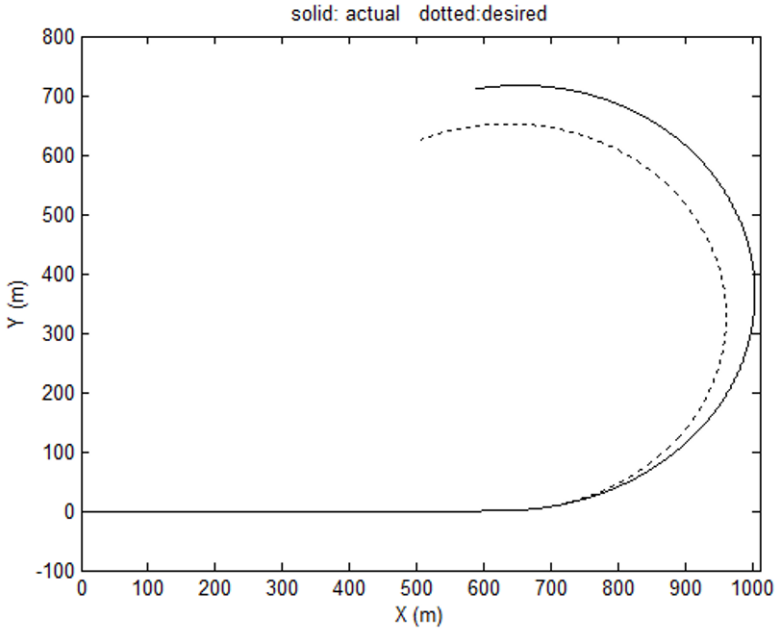
Figure 8-9. Vehicle trajectory on a road with friction coefficient of 0.6 and yaw rate control
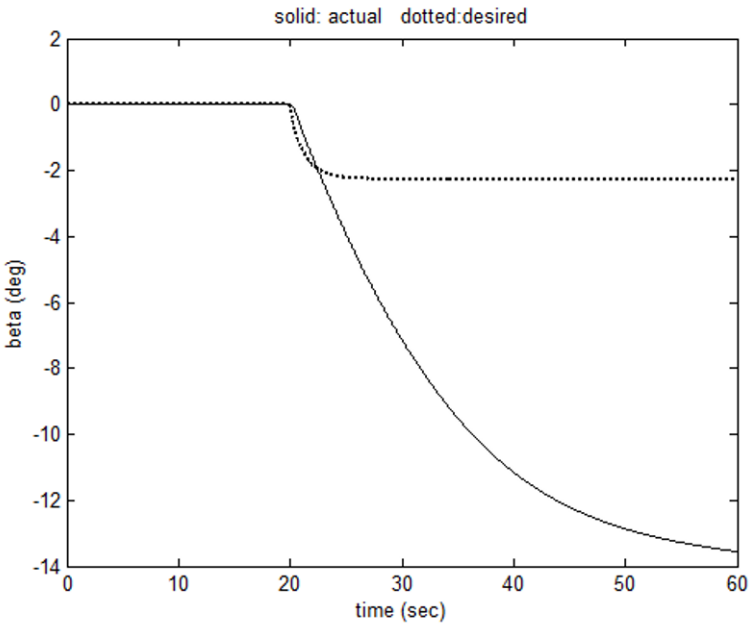
Figure 8-10. Slip angle with yaw rate control only

solid: actual   dotted:desired
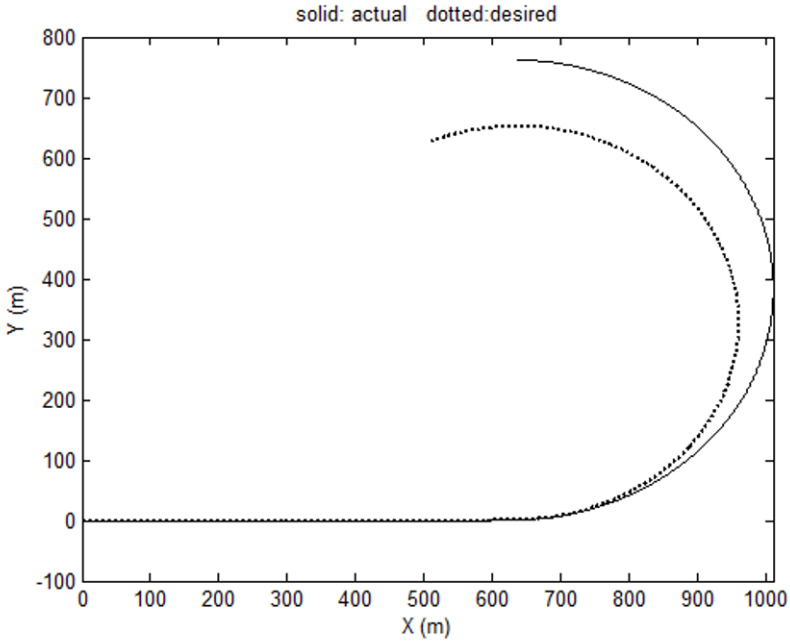
Figure 8-11. Trajectory with friction coefficient 0.6 and yaw rate + slip angle control

solid: actual   dotted:desired
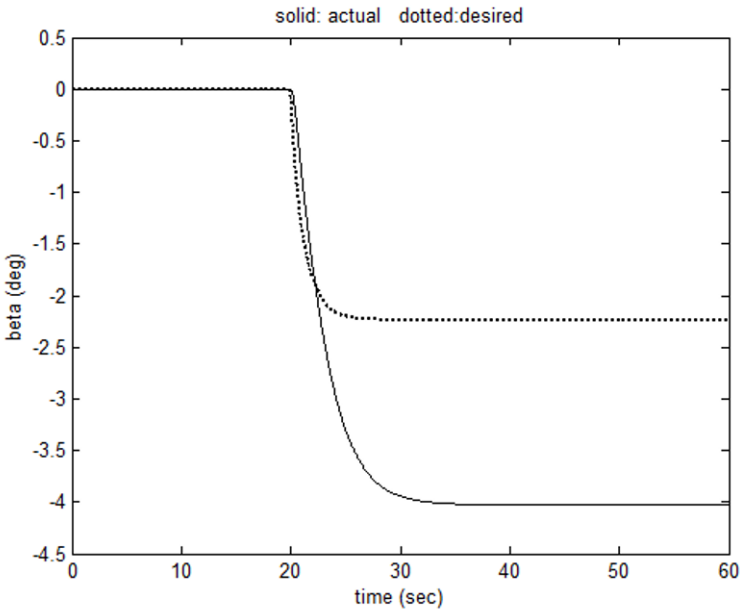
Figure 8-12. Slip angle with friction coefficient 0.6 and yaw rate + slip angle control
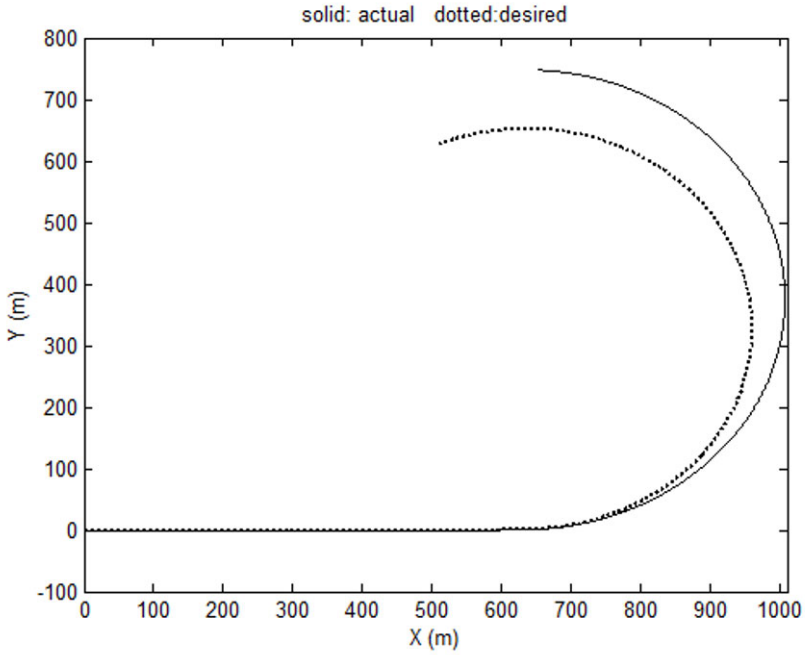
Figure 8-13. Vehicle trajectory with controller 1 on a road with friction coefficient 0.8
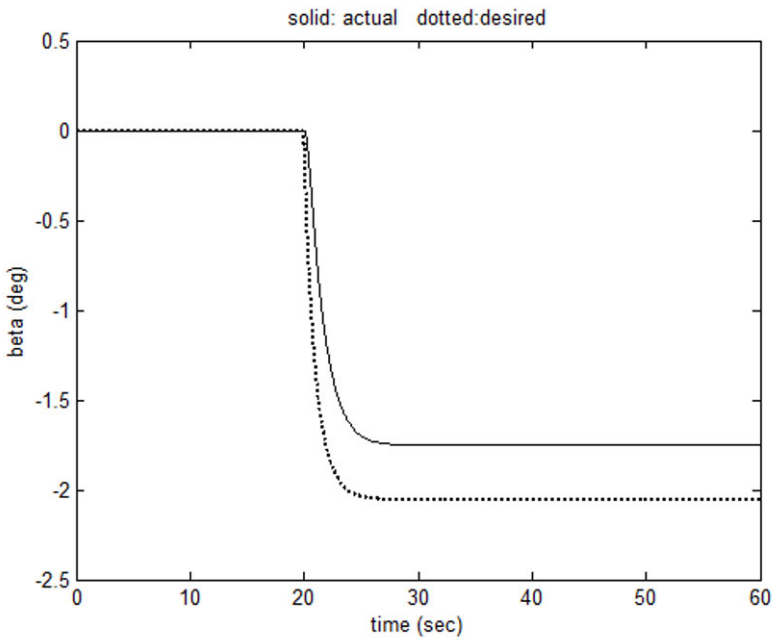
Figure 8-14. Slip angle with controller 1

solid: actual   dotted:desired

Y (m)

X (m)
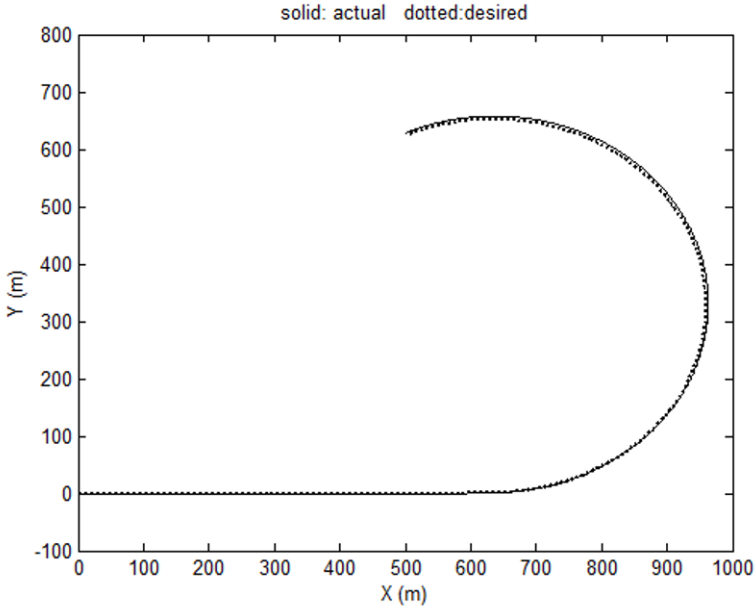
Figure 8-15. Vehicle trajectory with controller 2 on a road with friction coefficient 0.8

solid: actual   dotted:desired

beta (deg)

time (sec)
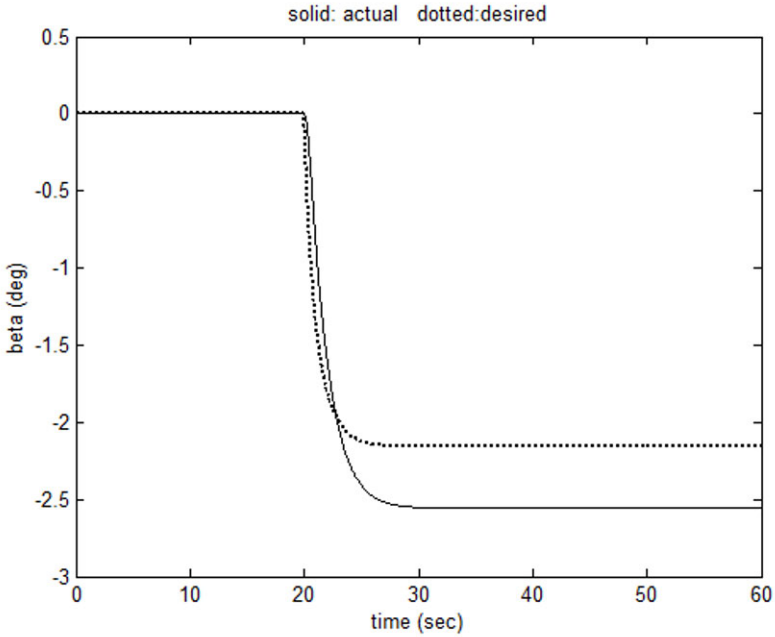
Figure 8-16. Slip angle with controller 2

Figure 8-15 shows the trajectory of the vehicle using controller 2 on the same road and Figure 8-16 shows the corresponding slip angle of the vehicle. As seen in Figure 8-15, the vehicle is able to track the desired trajectory when controller 2 is used. In this case, the slip angle is only slightly larger than the desired slip angle, as seen in Figure 8-16.

8.6   CHAPTER SUMMARY

This chapter reviewed three types of yaw stability control systems: differential braking based systems, steer-by-wire systems and independent drive torque control systems.

A major portion of the chapter focused on differential braking based systems. A hierarchical control architecture in which an upper controller determines desired yaw torque and a lower controller provides the desired yaw torque was presented. The driver's steering angle input together with a measure of tire-road friction conditions was used to determine a target yaw rate and a target slip angle for the vehicle. A sliding surface based control system was designed to ensure tracking of the target yaw rate and slip angle.

A design of a steer-by-wire system for yaw stability control was presented based on the work of Ackerman (1997). The front wheel steering angle was determined as a sum of the driver's input and an additional steer-by-wire control signal. The steer-by-wire control signal was designed so as to make the yaw rate of the vehicle unobservable from the lateral acceleration of the vehicle. This ensured that the driver could concentrate on the task of path following while the steer-by-wire controller compensated for disturbances that affected the yaw rate of the vehicle.

The design of an independent drive torque control system was discussed. A twin-clutch torque transfer differential together with a transfer case can be used to control the proportion of drive torque provided to the 4 wheels. This can be used as a control mechanism for yaw stability control. Compared to a differential braking based system, the use of a drive torque control system would ensure that the vehicle does not decelerate during yaw stability control.

Finally, simulation results were presented to demonstrate the benefits of combined yaw rate and slip angle control compared to purely yaw rate control.

NOMENCLATURE

F_y lateral tire force

F_x longitudinal tire force

$F_{yf\ell}$	lateral tire force on front left tire
F_{yfr}	lateral tire force on front right tire
$F_{yr\ell}$	lateral tire force on rear left tire
F_{yrr}	lateral tire force on rear right tire
$F_{xf\ell}$	longitudinal tire force on front left tire
F_{xfr}	longitudinal tire force on front right tire
$F_{xr\ell}$	longitudinal tire force on rear left tire
F_{xrr}	longitudinal tire force on rear right tire
$\dot{x}$	longitudinal velocity at c.g. of vehicle
$\dot{y}$	lateral velocity at c.g. of vehicle
δ	steering wheel angle
δ_{ss}	steady state value of steering angle on a circular road
m	total mass of vehicle
I_z	yaw moment of inertia of vehicle
ℓ_w	distance between left and right wheels (track length)
ℓ_f	longitudinal distance from c.g. to front tires
ℓ_r	longitudinal distance from c.g. to rear tires
L	total wheel base ($\ell_f + \ell_r$)
$\dot{\psi}$	yaw rate of vehicle
α_f	slip angle at front tires
α_r	slip angle at rear tires
σ_x	slip ratio
$\sigma_{f\ell}$	slip ratio at front left wheel
σ_{fr}	slip ratio at front right wheel
$\sigma_{r\ell}$	slip ratio at rear left wheel
σ_{rr}	slip ratio at rear right wheel

ω_w	angular speed of a wheel
$\omega_{f\ell}$	angular speed of front left wheel
ω_{fr}	angular speed of front right wheel
$\omega_{r\ell}$	angular speed of rear left wheel
ω_{rr}	angular speed of rear right wheel
r_{eff}	effective tire radius
C_α	cornering stiffness of tire
C_σ	longitudinal stiffness of tire
F_z	normal force on tire
μ	tire-road friction coefficient
J_w	rotational moment of inertia of each wheel
$T_{bf\ell}$	brake torque on front left wheel
T_{bfr}	brake torque on front right wheel
$T_{br\ell}$	brake torque on rear left wheel
T_{brr}	brake torque on rear right wheel
$P_{bf\ell}$	brake pressure on front left wheel
P_{bfr}	brake pressure on front right wheel
$P_{br\ell}$	brake pressure on rear left wheel
P_{brr}	brake pressure on rear right wheel
P_0	measured brake pressure at a wheel
$\dot{\psi}_{des}$	desired yaw rate of driver
$\dot{\psi}_{target}$	target yaw rate for yaw control system
$\dot{\psi}_{upper\_bound}$	upper bound on desired yaw rate
β	slip angle of vehicle
β_{des}	desired slip angle of vehicle
β_{target}	target slip angle for yaw control system

β_{upper_bound}	upper bound on desired slip angle
δ_{driver}	driver steering angle input in steer-by-wire system
δ_{sbw}	steer by wire steering angle correction
a_{yP}	lateral acceleration at decoupling point P
a_x	longitudinal acceleration
a_{y_cg}	lateral acceleration at c.g. of vehicle
ℓ_P	longitudinal distance of point P from vehicle c.g.
$T_{df\ell}$	drive torque on front left wheel
T_{dfr}	drive torque on front right wheel
$T_{dr\ell}$	drive torque on rear left wheel
T_{drr}	drive torque on rear right wheel
T_d	drive torque on any axle
T_{clutch}	clutch torque in an active differential
$M_{\psi b}$	yaw torque due to differential braking
ΔF_{xf}	extra differential longitudinal tire force required to provide desired yaw torque
η	constant used in sliding surface control system design
ξ	constant used in definition of sliding surface for differential braking based controller
ρ	front-to-back brake proportioning ratio
λ	variable used in Dugoff tire model
$f(\lambda)$	function used in Dugoff tire model
A_w	brake area of the wheel
μ_b	the brake friction coefficient
R_b	brake radius
q	constant determined by gear ratios in active differential

REFERENCES

Ackermann, "Robust Control Prevents Car Skidding," 1996 Bode Lecture Prize Article, *IEEE Control Systems Magazine*, pp. 23-31, June 1997.

Ackermann, J., "Robust Decoupling, Ideal Steering Dynamics and Yaw Stabilization of 4WS Cars," *Automatica*, Vol. 30, No. 11, pp. 1761-1768, 1994.

Bevly, D.M., Sheridan, R. and Gerdes, J.C., "Integrating INS Sensors with GPS Velocity Measurements for Continuous Estimation of Vehicle Sideslip and Cornering Stiffness," *Proceedings of the American Control Conference*, Vol. 1, pp. 25-30, 2001.

Daily, R. and Bevly, D.M., "The Use of GPS for Vehicle Stability Control Systems," *IEEE Transactions on Industrial Electronics*, Vol. 51, No. 2, April 2004.

Drakunov, S.V., Ashrafi, B. and Rosiglioni, A., "Yaw Control Algorithm via Sliding Mode Control," *Proceedings of the American Control Conference*, pp. 580 - 583, June 2000.

Dugoff, H., Fancher, P.S. and Segal, L., "Tyre Performance Charecteristics Affecting Vehicle Response to Steering and Braking Control Inputs," *Final Report, Contract CST-460*, Office of Vehicle Systems Research, US National Bureau of Standards, 1969.

Forster, H.J., "Der Fahrzeugfuhrer als Bindeglied Zwischen Reifen," Fharwerk und Fahrbahn, *VDI Berichte*, No. 916, 1991.

Fukada, Y., "Slip Angle Estimation for Vehicle Stability Control," *Vehicle System Dynamics*, Vol. 32, pp. 375-388, 1999.

Ghoneim, Y.A., Lin, W.C., Sidlosky, D.M., Chen, H.H., Chin, Y.K. and Tedrake, M.J., "Integrated Chassis Control System to Enhance Vehicle Stability," *International Journal of Vehicle Design*, Vol. 23, No. 1/2, pp. 124-144, 2000.

Gillespie, T.D., *Fundamentals of Vehicle Dynamics*, SAE, ISBN 1-56091-199-9, 1992.

Hahn, J.O., Rajamani, R. and Alexander, L., "GPS-Based Real-Time Identification of Tire-Road Friction Coefficient", *IEEE Transactions on Control Systems Technology*, Vol. 10, No. 3, pp. 331-343, May 2002.

Hoffman, D. and Rizzo, M., "Chevrolet C5 Corvette Vehicle Dynamic Control System," *SAE Technical Paper Series*, SAE-980233, 1998.

Jost, K., "Cadillac Stability Enhancement," *Automotive Engineering*, October, 1996.

Koibuchi, K., Yamamoto, M., Fukada, Y. and Inagaki, S., "Vehicle Stability Control in Limit Corenering by Active Brake," *SAE Technical Paper Series*, 960487, 1996.

Leffler, H., Auffhammer, R., Heyken, R. and Roth, H., "New Driving Stability Control System with Reduced Technical Effort for Compact and Medium Class Passenger Cars," *SAE Technical Paper Series*, SAE-980234, 1998.

Liebemann, E.K., Meder, K., Schuh, J. and Nenninger, G., "Safety and Performance Enhancement: The Bosch Electronic Stability Control (ESP)," *SAE Paper,* Paper No. 2004-21-0060, 2004.

Osborn, R.P. and Shim, T., "Independent Control of All-Wheel Drive Torque Distribution," *SAE Technical Paper Series*, 2004-01-2052, 2004.

Piyabongkarn, D., Rajamani, R., Lew, J.Y. and Grogg, J.A., "Active Driveline Torque Management Systems – Individual Wheel Torque Control for Active Automotive Safety Applications," *IEEE Control Systems Magazine*, Vol. 30, No. 4, pp. 86-102, August 2010.

Piyabongkarn, D., Rajamani, R., Grogg, J.A. and Lew, J.Y., "Development and Experimental Evaluation of a Slip Angle Estimator for Vehicle Stability Control," *IEEE Transactions on Control Systems Technology*, Vol. 17, No. 1, pp. 78-88, January 2009.

Piyabongkarn, D., Lew, J.Y., Rajamani, R., Grogg, J.A. and Yuan, Q., "On the Use of Torque Biasing Systems for Electronic Stability Control: Limitations and Possibilities," *IEEE Transactions on Control Systems Technology*, Vol. 15, No. 3, pp. 581-589, May 2007.

Sawase, K. and Sano, Y., "Application of Active Yaw Control to Vehicle Dynamics by Utilizing Driving/ Braking Force", *JSAE Review*, Vol. 20, pp. 289-295, 1999.

Shim, T. and Margolis, D., "Using μ Feedforward for Vehicle Stability Enhancement, " *Vehicle System Dynamics*, Vol. 35, No. 2, pp. 103-119, 2001.

Slotine, J.J.E. and Li, W., *Applied Nonlinear Control*, Prentice Hall, 1991.

Tseng, H.E., Ashrafi, B., Madau, D., Brown, T.A. and Recker, D., "The Development of Vehicle Stability Control at Ford," *IEEE/ASME Transactions on Mechatronics*, Vol. 4, No. 3, pp. 223-234, September, 1999.

Uematsu, K. and Gerdes, J.C., "A Comparison of Several Sliding Surfaces for Stability Control," *Proceedings of the International Symposium on Advanced Vehicle Control* (AVEC), 2002.

Van Zanten, A. T., Erhardt, R., Pfaff, G., Kost, F., Uwe, H. and Ehret, T., "Control Aspects of the Bosch-VDC," *Proceedings of the International Symposium on Advanced Vehicle Control*, Vol. 1, pp. 573-608, 1996.

J. Wang, L. Alexander and R. Rajamani "Friction Estimation on Highway Vehicles Using Longitudinal Measurements", *ASME Journal of Dynamic Systems, Measurement and Control,* Special Issue on Sensors, Vol. 126, No. 2, pp. 265-275, June 2004.

Yi, K., Chung, T., Kim, J. and Yi, S., "An Investigation into Differential Braking Strategies for Vehicle Stability Control," *Proceedings of the Institution of Mechanical Engineers*, Part D: Journal of Automobile Engineering, Vol. 217, pp. 1081-1093, 2003.

Yoshioka, T., Adachi, T., Butsuen, T., Okazaki, H. and Mochizuki, H., "Application of Sliding Mode Control to Control Vehicle Stability," *Proceedings of the International Symposium on Advanced Vehicle Control* (AVEC), pp. 455-459, 1998.

Chapter 9

MEAN VALUE MODELING OF SI AND DIESEL ENGINES

The engine models presented in this chapter are useful in the development of control systems for cruise control, adaptive cruise control and other longitudinal vehicle control applications.

The type of engine models we will study in this chapter are called mean value models (Cho and Hedrick, 1989, Hendricks and Vesterholm, 1992, Hendricks and Sorenson, 1990). A mean value model is a mathematical engine model which is intermediate between large cyclic simulation models and simplistic transfer function models. It predicts the mean values of major external engine variables like crank shaft speed and manifold pressure dynamically in time. The time scale for this mean value description is much longer than that required for a single engine cycle but sufficiently shorter than that required for describing longitudinal vehicle motion. Hence such models can be well utilized for longitudinal vehicle control applications.

The outline of this chapter is as follows. Sections 9.1 and 9.2 focus on mean value models for spark ignition (SI) engines. Section 9.1 describes a parametric mean value model while section 9.2 presents a mean value model based on the use of engine maps. Section 9.3 provides an introduction to turbocharged diesel engines. Section 9.4 describes a mean value model for diesel engines equipped with a variable geometry turbocharger and a exhaust gas recirculation valve. Section 9.5 presents an engine control system for SI engines designed to provide real-time commanded vehicle acceleration.

9.1   SI ENGINE MODEL USING PARAMETRIC EQUATIONS

The major elements of the SI (gasoline) engine considered in a mean value model of the engine rotational dynamics are

1) the air flow model for the intake manifold and
2) the rotational dynamics of the crankshaft.

The intake manifold of the engine is the volume between the throttle plate and the intake valves of the cylinder (see Figure 9-1). The throttle controls the air flow into the intake manifold. The rate of outflow from the intake manifold into the engine cylinders depends to a large degree on the operating engine speed and the pressure in the intake manifold.
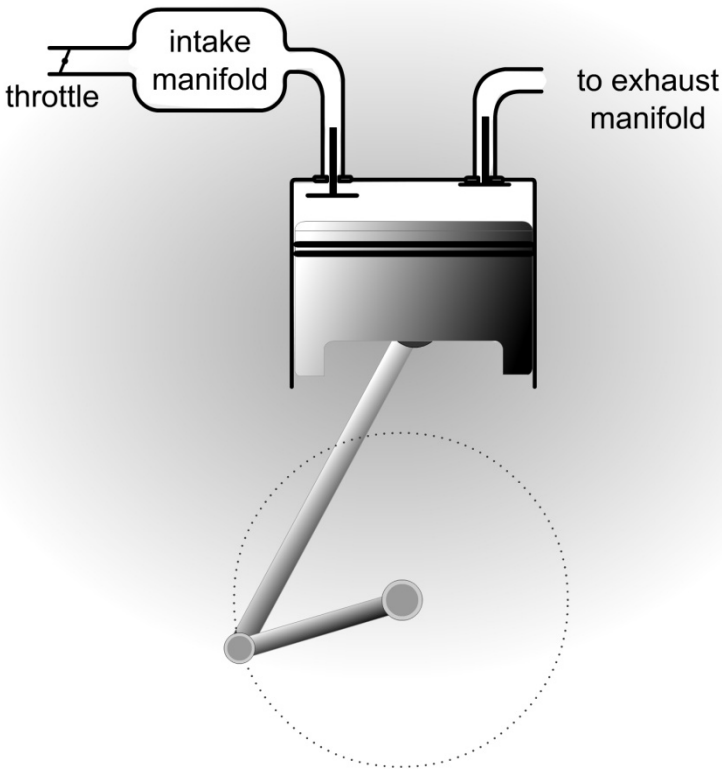

Figure 9-1.   Line Diagram of Internal Combustion Engine

Air from the intake manifold flows into the engine cylinders during the intake stroke of the piston. Drops of gasoline are mixed into the air. Then the piston moves back up to compress the air-fuel mixture during the compression

stroke. At the top of the compression stroke, the spark plug releases a spark to ignite gasoline and cause combustion. Combustion in the engine cylinders releases energy which is responsible for the torque generated at the crankshaft of the engine. As we shall see later, the net torque generated by the engine is primarily a function of the operating engine speed, the rate of air flow from the intake manifold into the cylinders, the fueling rate and the losses in the engine cylinders. The expansion caused by combustion drives the piston down for the expansion or power stroke. Finally, the piston goes up again for the exhaust stroke and the outlet valve opens to allow the used air to leave the piston.

9.1.1 Engine rotational dynamics

The crankshaft rotational dynamics can be represented by

$$I_e \dot{\omega}_e = T_{ind} - T_{load} + T_f \tag{9.1}$$

where T_{ind} is the indicated combustion torque, T_{load} is the external load torque on the crankshaft, T_f represents the pumping and friction losses in the engine and I_e is the rotational moment of inertia of the engine.

The load on the engine T_{load} is typically provided by a torque converter which couples the engine to the transmission. Torque converter models have been discussed in Chapter 4 of this book. The transmission in turn is coupled to the driving wheels of the vehicle through the differential. The load torque on the engine T_{load} can be calculated as described in section 4.2 and section 5.5.1 of this book.

The calculation of indicated torque T_{ind} and friction torque T_f is discussed in the following sub-sections (sections 9.1.2 and 9.1.3) that follow.

9.1.2 Indicated combustion torque

The indicated torque, T_{ind}, is generated by combustion and can be represented by (Hendricks and Sorenson, 1990):

$$T_{ind} = \frac{H_u \eta_i \dot{m}_f}{\omega_e} \tag{9.2}$$

where H_u is the fuel energy constant, η_i is the thermal efficiency multiplier

and accounts for the cooling and the exhaust system losses, and $\dot{m}_f$ represents

the fuel mass flow rate into the cylinders. The fuel mass flow rate $\dot{m}_f$ is

typically determined by a fuel injection control system which attempts to maintain a stoichiometric air to fuel ratio in the cylinders. If it is assumed that a stoichiometric air fuel ratio is successfully maintained in the cylinders,

then the fuel mass flow rate $\dot{m}_f$ is related to the outflow from the intake

manifold into the cylinders of the engine as follows (Ganguli and Rajamani, 2004):

$$\dot{m}_f = \frac{\dot{m}_{ao}}{\lambda \cdot L_{th}} \tag{9.3}$$

where $\dot{m}_{ao}$ is air mass flow rate out of the intake manifold and into the cylinder, L_{th} is the stoichiometric air/fuel mass ratio for gasoline (fuel) and λ is the air/fuel equivalence ratio. Here, $\lambda = 1$ and $L_{th} = 14.67$.

In reality, the indicated and friction torques vary as the engine rotates through the thermodynamic cycle. In a mean value engine model however, the dynamics of rotation are averaged over time.

9.1.3   Friction and pumping losses

The term T_f in the rotational engine dynamic equation (9.1) represents the

hydrodynamic and pumping friction losses represented in terms of a loss torque.

Hydrodynamic or fluid-film friction is the principal component of mechanical friction losses in an engine. A reasonable choice of polynomial expression for these friction losses in terms of engine speed ω_e rad/s is (Heywood, 1988):

$$F_{loss} = a_0\omega_e^2 + a_1\omega_e + a_2 \tag{9.4}$$

In this expression, the constant term a_2 represents boundary friction, the linear term $a_1\omega_e$ accounts for hydrodynamic or viscous friction and the

$a_0\omega_e^2$ accounts for turbulent dissipation. Turbulent dissipation is found to

be proportional to ω_e^2 and the constant of proportionality depends on the geometry of the flow-path. Sections 13.3.1 and 13.3.2 in Heywood (1998) describe hydrodynamic friction and turbulent dissipation and provide a detailed explanation for the choice of polynomial expression in equation (9.4).

The pumping losses are found to be proportional to the pumping mean effective pressure and the operating speed (Hendricks and Sorenson, 1990). The pumping mean effective pressure is defined to be the difference between exhaust pressure and manifold pressure, $p_{exh} - p_{man}$. Therefore the pumping losses can be modeled as:

$$P_{loss} = b_0 \omega_e . p_{man} + b_1 p_{man} \tag{9.5}$$

since the exhaust pressure is nearly constant and is equal to the atmospheric pressure.

Total friction and pumping losses in an engine can thus be expressed as polynomials in the engine speed and the manifold pressure as follows (Hendricks and Sorenson, 1990, Ganguli and Rajamani, 2004):

$$T_f = a_0 \omega_e^2 + a_1 \omega_e + a_2 + b_0 \omega_e . p_{man} + b_1 p_{man} \tag{9.6}$$

where a_0, a_1, a_2, b_0, b_1 are parameters dependent on the specific engine.

9.1.4 Manifold pressure equation

The intake manifold is the volume between the throttle plate and the intake valves of the cylinder. The state equation for the intake manifold is obtained by applying conservation of mass to the intake manifold volume.

$$\dot{m}_{man} = \dot{m}_{ai} - \dot{m}_{ao} \tag{9.7}$$

where $\dot{m}_{ai}$ and $\dot{m}_{ao}$ represent mass flow rate in and out of the intake manifold i.e. through the throttle valve and into the cylinder respectively.

The pressure in the intake manifold p_{man} can be related to the mass of air in the manifold m_{man} using the ideal gas equation:

$$p_{man} V_{man} = m_{man} R T_{man} \tag{9.8}$$

where R is the ideal gas constant, T_{man} is the intake manifold temperature and V_{man} is the intake manifold volume.

Taking derivatives of equation (9.8) and substituting from equation (9.7), the intake manifold pressure equation is obtained as

$$\dot{p}_{man} = \frac{RT_{man}}{V_{man}}\left(\dot{m}_{ai} - \dot{m}_{ao}\right) \tag{9.9}$$

The calculation of $\dot{m}_{ai}$ and $\dot{m}_{ao}$ is described in the following sub-sections.

9.1.5   Outflow rate $\dot{m}_{ao}$ from intake manifold

The mass flow rate out of the intake manifold $\dot{m}_{ao}$ is the rate at which the air-fuel mass is 'swept' out of the cylinder by the piston. It is easy to see that $\dot{m}_{ao}$ can be expressed as (Hendricks and Sorenson, 1990)

$$\dot{m}_{ao} = \eta_{vol} \frac{\omega_e}{4\pi} V_d \frac{p_{man}}{RT_{man}} \tag{9.10}$$

where η_{vol} is the volumetric efficiency (which is a complex function of many engine parameters and the variables p_{man} and ω_e), V_d is the displacement volume of the engine cylinders and $\frac{p_{man}}{RT_{man}}$ is the density of air in the intake manifold. The expression in equation (9.10) accounts for the fact that in a four-stroke engine, the charge is swept out of the intake manifold into the cylinders only every alternate rotation cycle of the crankshaft.

9.1.6   Inflow rate $\dot{m}_{ai}$ into intake manifold

The mass flow rate through the throttle body into the intake manifold can be calculated from the standard orifice equation for compressible fluid flow. A detailed analysis can be found in (Cho and Hedrick, 1989 and Hendricks and Sorenson, 1990). A summary of the final equation for $\dot{m}_{ai}$ is presented here from Ganguli and Rajamani (2004). $\dot{m}_{ai}$ can be represented as a product of three variables:

$$\dot{m}_{ai} = MAX \cdot TC(\alpha) \cdot PRI \tag{9.11}$$

where

1. *MAX* is a constant dependent on the size of the throttle body and is equal to the maximum possible intake airflow rate.
2. *TC(α)* is the throttle characteristic which is the projected area the flow sees as a function of the throttle angle α. It can be modeled as (Hendricks and Sorenson, 1990, Cho and Hedrick, 1989):

$$TC(\alpha) = 1 - \cos(\alpha + \alpha')\qquad(9.12)$$

   where α' is the minimum throttle angle seen by the engine. There is a minimum leakage area even when the throttle plate is closed against the throttle bore and this is represented by α'. This leakage area can be significant in calculations when operating at small throttle openings.
3. *PRI* is the pressure ratio influence function, which describes the choked/sonic flow that occurs through the throttle valve. The sonic velocity is the velocity of propagation of a sound wave in the gas. This is the maximum velocity that a compressible fluid flowing through a pipe can rise to. At this velocity the effect of lower downstream pressure can no longer be transmitted upstream to increase the flow rate. The flow is then said to be choked. The downstream to upstream pressure ratio at which the sonic velocity is reached is called the critical pressure ratio ρ_c. For air $p_c \approx 0.5283$.

In case of SI engines, the intake manifold pressure is always less than the atmospheric pressure leading air from the surrounding environment (upstream) into the intake manifold (downstream). Considering the throttle valve to be an orifice, based on standard theory of flow through orifice, the following relationship can be obtained for *PRI* (Hendricks and Sorenson, 1990):

$$PRI = \begin{cases} \sqrt{1 - \left(\dfrac{p_r - p_c}{1 - p_c}\right)^2} & p_r > p_c \quad (choked) \\ 1 & p_r \le p_c \quad (sonic) \end{cases}\qquad(9.13)$$

where $p_r = \dfrac{p_{man}}{p_{amb}}$ and p_c is the critical pressure ratio. p_c can be assumed to be approximately 0.5283.

Substituting the above relations into equation (9.9), we get the manifold pressure equation:

$$\dot{p}_{man} = \frac{RT_{man}}{V_{man}} \left\{ MAX \cdot TC(\alpha) \cdot PRI(\frac{p_{man}}{p_{amb}}) - \frac{\omega_e}{4\pi} \frac{V_d \eta_{vol}}{RT_{man}} \, p_{man} \right\}$$

i.e.,

$$\dot{p}_{man} = \frac{RT_{man}}{V_{man}} \cdot MAX \cdot TC(\alpha) \cdot PRI(\frac{p_{man}}{p_{amb}}) - \frac{\omega_e}{4\pi} \frac{V_d}{V_{man}} \eta_{vol} p_{man} \quad (9.14)$$

Example values of parameters for the mean value model discussed in section 9.1 can be found on the web site http://www.iau.dtu.dk/~eh/index.html and in Cho and Hedrick, 1989.

9.2   SI ENGINE MODEL USING LOOK-UP MAPS

An often used alternative to the parametric engine model described in sections 9.1.1 – 9.1.6 is one in which engine maps from experimental data are used to replace several parametric functions. For example, the functions T_{ind} and T_f in equation (9.1) were defined as functions of various engine parameters and the dynamic variables ω_e and p_{man} (see equations (9.2) and (9.6)). In an engine map based model, the function $T_{net} = T_{ind} - T_f$ is obtained experimentally from dynamometer tests in the form of tabular data. Similarly the functions $\dot{m}_{ao}(\omega_e, p_m)$ and $\dot{m}_{ai}(\alpha, p_m)$ are obtained from dynamometer tests in the form of tabular data. Such tabular data is then used directly in the engine model (Cho and Hedrick, 1989).

9.2.1   Introduction to engine maps

An example of the engine map $T_{net}(\omega_e, p_{man})$ in the form of tabular data is shown in Table 9-1. Data is presented for engine speed ω_e varying from 52 rad/s to 586 rad/s (496.6 rpm to 5596 rpm) and manifold pressure p_{man} varying from 10 kPa to 100 kPa (the table presented in Table 9-1 only contains partial data for p_{man} varying up to 42.14 kPa).

For each pair (ω_e, p_{man}), a corresponding value of $T_{net}(\omega_e, p_{man})$ is available in the table. Such data is obtained by dynamometer testing for each pair of values (ω_e, p_{man}). It should be noted that for constructing an engine map for a particular engine, such tabular data must be obtained for that specific type of engine.

Table 9-1. Partial tabular data representing an engine map $T_{net}(\omega_e, p_{man})$

ω_e (rad/s)	p_{man} (kPa)		
	10	16.43	22.86
52	-63.58	-51.62	-28.53
85.38	-64.91	-54.7	-25.76
118.75	-64.28	-51.81	-23.09
152.13	-61.53	-47.24	-20.3
185.5	-59.58	-42.64	-15.45
218.88	-58.2	-38.65	-8.01
252.25	-55.53	-33.77	-1.97
285.63	-52.56	-28.72	1.67
319	-50.82	-25.65	3.94
352.38	-50.7	-24.05	4.79
385.75	-51.34	-25.23	4.31
419.13	-54.35	-27.44	2.08
452.5	-58.31	-31.38	-2.05
485.88	-63.53	-36.33	-8.09
519.25	-70.03	-43.71	-15.57
552.63	-77.99	-51.9	-24.75
586	-86.96	-61.75	-34.98

$T_{net}(\omega_e, p_{man})$ is shown graphically as a function of ω_e and p_{man} in Figure 9-2, Figure 9-3 and Figure 9-4. In Figure 9-2, T_{net} on the y axis is shown as a function of p_{man} on the x axis for various values of ω_e. From the figure, it can be seen that T_{net} increases monotonically with p_{man}. In Figure 9-3 T_{net} is shown as a function of ω_e for one fixed value of p_{man} (p_{man} equal to 74.29 kPa). It can be seen that $T_{net}(\omega_e, p_{man})$ increases with ω_e, reaches a maximum and then decreases. Figure 9-4 shows $T_{net}(\omega_e, p_{man})$ on the y axis as a function of ω_e on the x axis for various values of p_{man} ranging from 10 kPa to 100 kPa.

The function $\dot{m}_{ao} = \dot{m}_{ao}(\omega_e, p_m)$ is similarly provided in the form of tabular data as a function of p_m and ω_e. The graphical nature of this relationship is shown through an example engine map in Figure 9-5. The characteristics of the function shown in Figure 9-5 above can be compared with that of equation (9.8) reproduced below:

$$\dot{m}_{ao} = \eta_{vol} \frac{\omega_e}{4\pi} V_d \frac{p_{man}}{RT_{man}}$$

(9.15)

By comparing equation (9.8) with the characteristic from Figure 9-5, it is clear that η_{vol} is not a constant but a function of ω_e and p_m. Hence, in Figure 9-5, for constant ω_e, $\dot{m}_{ao}$ is not linearly proportional to p_m but is a nonlinear function of p_{man}.
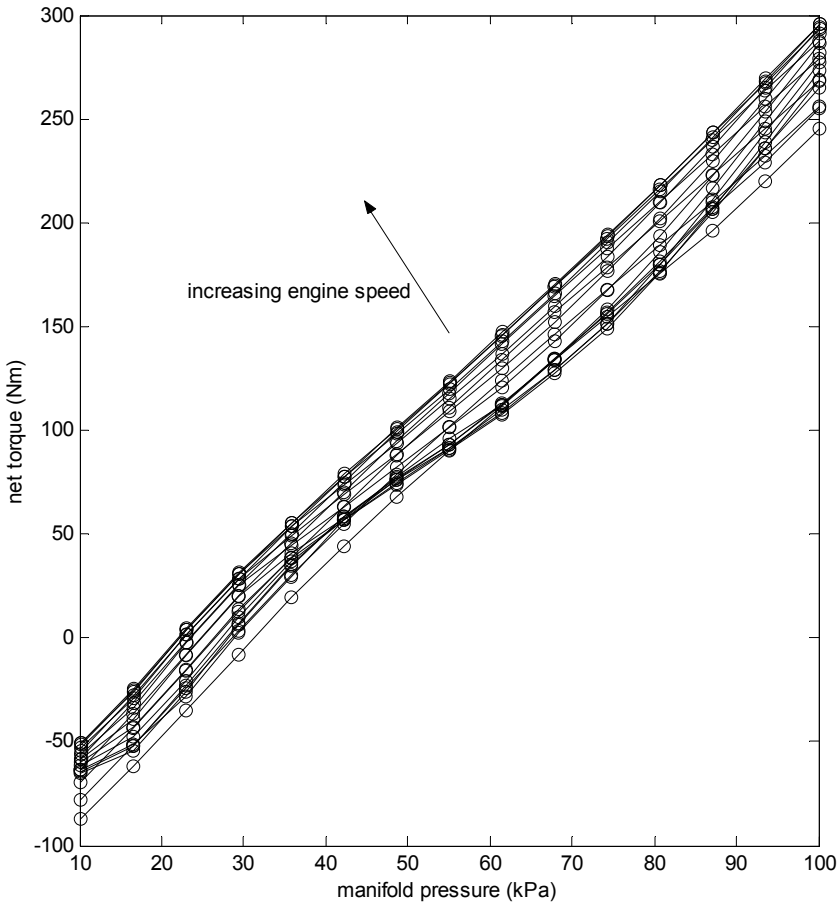

Figure 9-2. $T_{net}(\omega_e, p_{man})$ as a function of p_{man} for various fixed values of ω_e

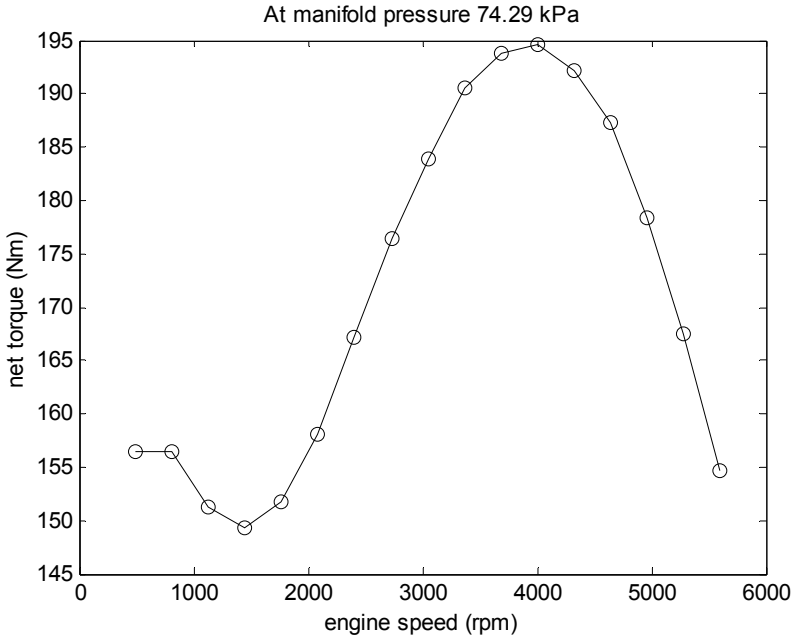At manifold pressure 74.29 kPa

Figure 9-3. $T_{net}(\omega_e, p_{man})$ as a function of ω_e for p_{man} = 74.29 kPa

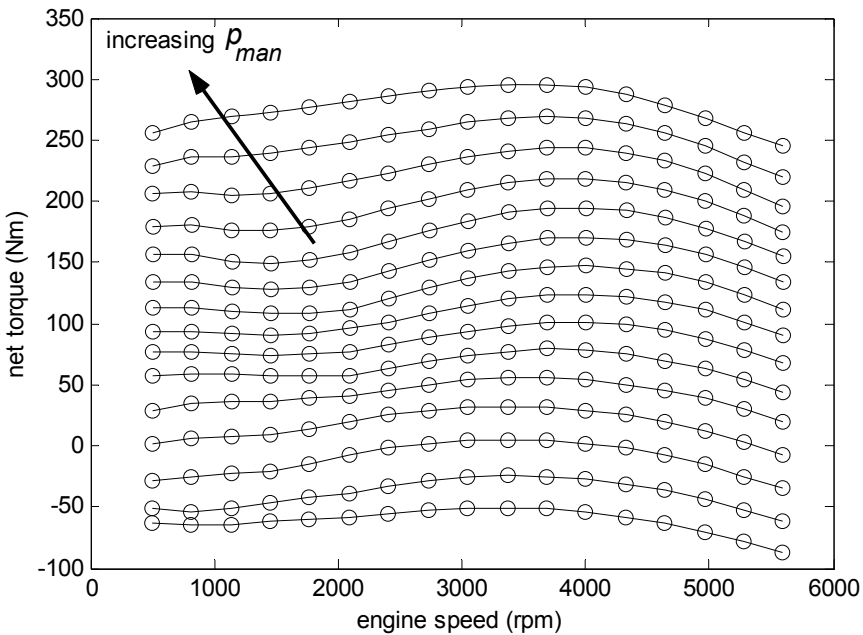increasing p_{man}

Figure 9-4. $T_{net}(\omega_e, p_{man})$ as a function of ω_e for various fixed values of p_{man}
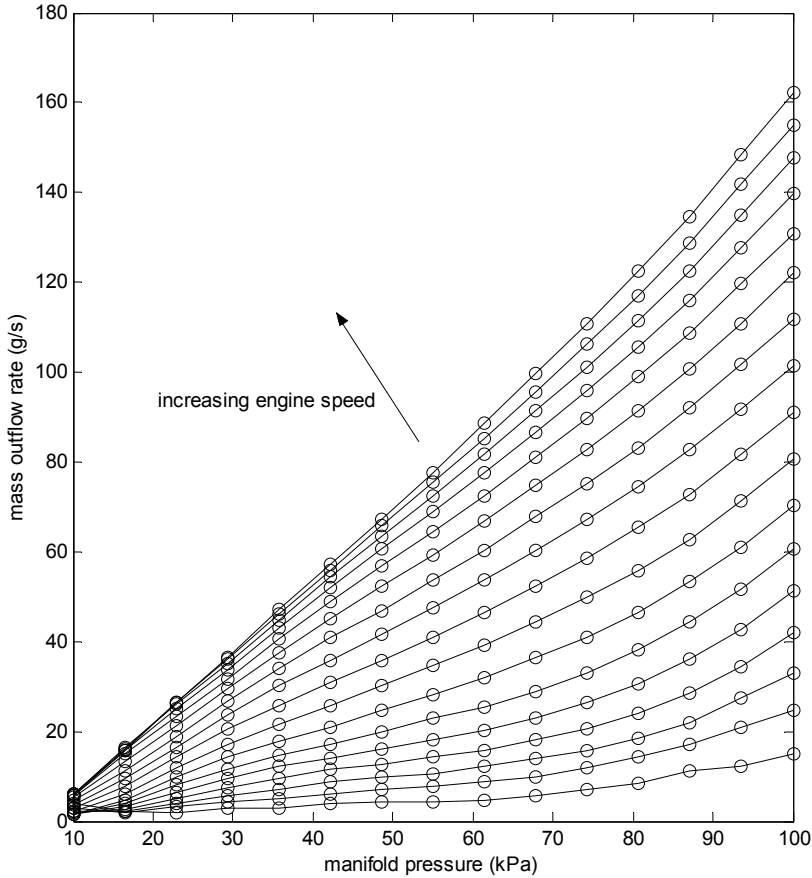
Figure 9-5. $\dot{m}_{ao}(\omega_e, p_{man})$ as a function of p_{man} for various fixed values of ω_e

9.2.2 Second order engine model using engine maps

Engine-map based engine models can be second order consisting of two states (ω_e and p_{man}) or first order consisting of only one state ω_e. The second order model is analogous to the parametric model described in section 9.1 of this chapter. The only difference is that the functions $T_{net}(\omega_e, p_{man})$, $\dot{m}_{ao}(\omega_e, p_{man})$ and $\dot{m}_{ai}(\alpha, p_{man})$ are now experimentally derived as engine maps instead of the parametric equations described in section 9.1.

The two equations of the second order engine model are summarized as follows:

Manifold equation

$$\dot{p}_{man} = \frac{RT_{man}}{V_{man}}\left(\dot{m}_{ai} - \dot{m}_{ao}\right) \tag{9.16}$$

where

$$\dot{m}_{ai} = MAX \cdot TC(\alpha) \cdot PRI \tag{9.17}$$

$TC(\alpha)$ and PRI are both obtained from engine maps and $\dot{m}_{ao}(\omega_e, p_m)$ is obtained directly from an engine map.

Engine rotational dynamics equation

$$I_e\dot{\omega}_e = T_{net} - T_{load} \tag{9.18}$$

where $T_{net}(\omega_e, p_m)$ is obtained from an engine map and is the net torque after losses $(T_{net} = T_{ind} - T_f)$. T_{load} is the load torque as before (typically from a torque converter).

9.2.3   First order engine model using engine maps

A first order engine model can be used if the intake manifold filling dynamics are ignored. This type of model is still valid for some longitudinal vehicle control applications, if the bandwidth of the control system to be designed is low.

In the case of the first order model, the engine dynamics consist of just one state ω_e. The dynamics of ω_e are given by

$$I_e\dot{\omega}_e = T_{net} - T_{load} \tag{9.19}$$

where T_{load} is the load torque as before (typically from a torque converter) and $T_{net}(\alpha, \omega_e)$ is obtained from a map and is the net torque after losses. $T_{net}(\alpha, \omega_e)$ is provided as a steady state function of the throttle angle α and the engine speed ω_e. The transient values of T_{net} as p_m in the intake manifold varies and reaches steady state (for each value of α and ω_e) are ignored.

An example of an engine map for the net torque $T_{net}(\alpha, \omega_e)$ as a function of throttle angle α and engine sped ω_e is shown in Figure 9-6. It can be seen that T_{net} increases with throttle angle nonlinearly but monotonically. For each throttle angle, T_{net} initially increases with engine speed ω_e, reaches a maximum and then decreases. Thus for each α, there is a engine speed ω_e at which maximum torque is achieved.
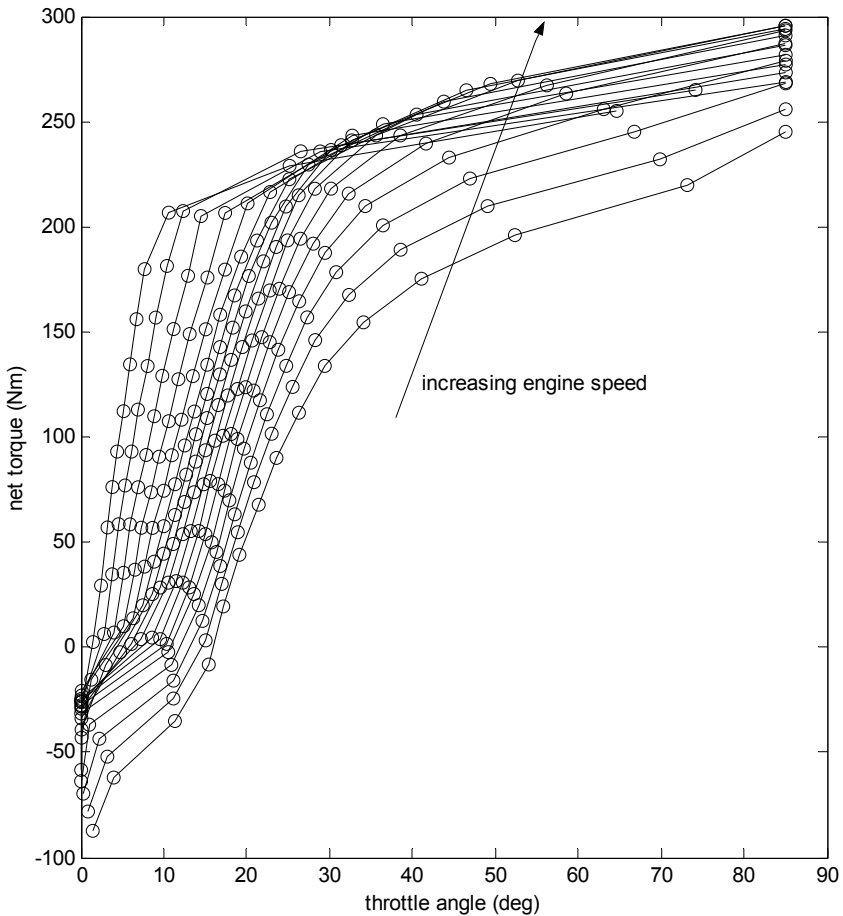

Figure 9-6. $T_{net}(\alpha, \omega_e)$ as a function of α for various values of ω_e

9.3 INTRODUCTION TO TURBOCHARGED DIESEL ENGINES

Compared to a gasoline engine, a diesel engine has the inherent advantages of lower fuel consumption and lower CO_2, CO and hydrocarbon emissions. NO_x and particulate matter emissions, however, are lower in gasoline engines (Heywood, 1988).

This section considers a diesel engine equipped with a controlled turbocharger and a controlled exhaust gas recirculation (EGR) valve. The use of a controlled turbocharger and EGR is done to minimize NO_x and particulate matter (smoke) emissions from a diesel engine. A turbocharger consists of a compressor and a turbine coupled by a common shaft. The engine exhaust is used to drive the turbine, which in turn drives the compressor. The compressor, in turn, takes air from the ambient and directs it into the intake manifold. Because of the increased quantity of air due to compression, a larger quantity of fuel than in a non-turbocharged engine can be efficiently burned (Watson and Janota, 1982).

Turbocharging increases air-fuel ratio, air charge density and temperature and reduces particulate emissions. However, it increases NO_x emissions. NO_x emissions can be reduced by using exhaust gas recirculation (EGR). The EGR system is used to divert a portion of the exhaust gas back to the engine intake manifold to dilute the air coming from the compressor. The recirculated exhaust gas acts as an inert gas in the intake manifold and increases the specific heat capacity of the charge, reducing the burn rate and hence decreasing the formation of NO_x. A high level of EGR, however, lowers the air-to-fuel ratio in the engine and causes unacceptable smoke generation (Kolmanovsky, et. al., 1997).

Traditionally, turbocharging and EGR were used at fixed settings (without real-time control). Real-time control of the turbocharger and the EGR flow rate can be used to ensure that both smoke and NO_x emissions are reduced. This can be done without a major sacrifice in fuel economy or drivability (response to driver torque demand). Real-time control of the turbo-charging process can be obtained through a variable geometry turbocharger (VGT) (Kolmanovsky, et. al., 1997). A VGT is equipped with a system of pivoted guide vanes that changes the turbine flow area and the angle at which the exhaust gas is directed at the turbine motor. This controls the power transferred to the compressor and hence the amount of air flow into the intake manifold of the engine.

For a more comprehensive review of diesel engine control, including VGT control, see (Kolmanovsky, et. al., 1997) and the references therein.

9.4   MEAN VALUE MODELING OF TURBOCHARGED DIESEL ENGINES

A schematic of the simulation model for turbocharged diesel engines is shown in Figure 9-7. The simulation model incorporates mean-value dynamics and has six states, viz $p_1, m_1, p_2, m_2, \omega_e$ and P_c where p and m represent the pressure and mass respectively, P_c represents the compressor power and ω_e represents the engine crankshaft speed. The subscripts 1 and 2 refer to the intake and exhaust manifolds respectively. The model equations described below are a slightly modified version of the equations described in Kolmanovsky, et. al., 1997 and Jankovic and Kolmanovsky, 1998. They are based on laws of mass and energy conservation and on the ideal gas law for the intake and exhaust manifolds. The control inputs in this model are the mass flow rate through the exhaust gas recirculation value W_{egr}, and that through the turbine, W_t. Other external inputs include the fueling rate W_f (kg/hour), which is determined from the driver's accelerator pedal input .
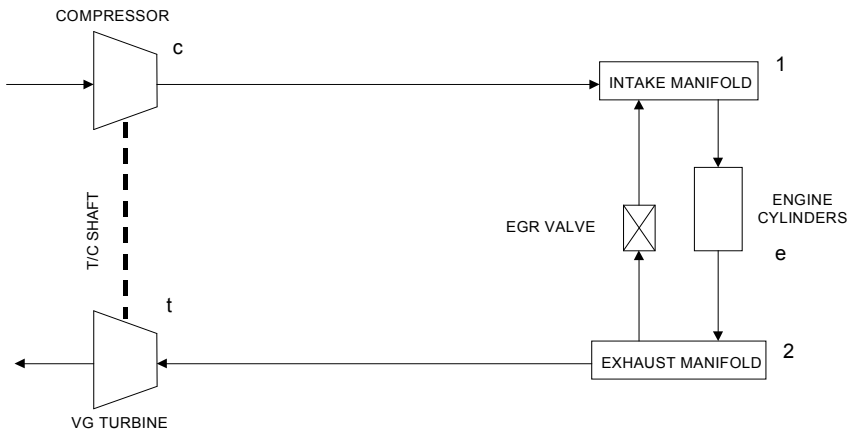

Figure 9-7. Components of a Simple Simulation Model

9.4.1 Intake manifold dynamics

As opposed to the intake manifold dynamics for the SI engine, the manifold dynamics here cannot be considered to be isothermal. This is because the significant exhaust gas recirculation (EGR) that can happen in a diesel engine implies that the temperature inside the intake manifold cannot be assumed to be constant but depends on EGR.

The dynamics in the intake manifold are assumed to be adiabatic, with no heat exchange occurring. The mass flow rate balance in the intake manifold leads to

$$\dot{m}_1 = W_{c1} + W_{egr} - W_{1e} \qquad (9.20)$$

The adiabatic process assumption leads to the equation

$$\dot{p}_1 = \frac{\gamma R}{V_1}(W_{c1}T_a + W_{egr}T_2 - W_{1e}T_1) \qquad (9.21)$$

9.4.2 Exhaust manifold dynamics

The exhaust manifold dynamics are also assumed to be adiabatic, leading to the following equations:

$$\dot{m}_2 = W_{e2} + W_f - W_{egr} - W_t \qquad (9.22)$$

$$\dot{p}_2 = \frac{\gamma R}{V_2}(W_{e2}T_2 + W_f T_2 - W_{egr}T_2 - W_t T_2) \qquad (9.23)$$

9.4.3 Turbocharger dynamics

The turbocharger shaft dynamics are modeled by

$$\dot{\omega}_{tc} = \frac{1}{I_{tc}\omega_{tc}}(P_t - P_c) \qquad (9.24)$$

where P_t and P_c are the turbine power and compressor power respectively.

The turbine power depends on the control input W_t and is defined by

$$P_t = \eta_t c_p T_2 \left[1 - \left(\frac{p_a}{p_2} \right)^{\mu} \right] W_t \tag{9.25}$$

with $\mu = \dfrac{\gamma - 1}{\gamma}$.

The power transfer between the turbine and the compressor is modeled by

$$\tau \dot{P}_c + P_c = \eta_m P_t \tag{9.26}$$

where η_m and τ are the turbo efficiency and the turbo-lag time constants respectively.

The air flow into the intake manifold from the compressor is determined from the compressor power equation

$$W_{c1} = \frac{\eta_c}{T_a c_p} \frac{P_c}{\left(\dfrac{p_1}{p_a} \right)^{\mu} - 1} \tag{9.27}$$

where η_c is the compressor isentropic efficiency and T_a is the ambient air temperature.

9.4.4   Engine crankshaft dynamics

The engine dynamics are obtained from a torque balance on the engine crankshaft

$$\dot{\omega}_e = \frac{1}{I_e} \left(T_e - T_f - T_{load} \right) \tag{9.28}$$

where T_e is the indicated combustion torque, T_f is the friction and pumping losses expressed in terms of a loss torque and T_{load} is the load torque (typically from the torque converter).

The indicated engine torque is given by

$$T_e = \eta_{ind} Q_{LHV} m_f \tag{9.29}$$

where η_{ind} is the indicated efficiency

$$\eta_{ind} = \left(a_1 + a_2\omega_e + a_3\omega_e^2\right)\left(1 - k_1\Phi_2^{\ k}\right) \tag{9.30}$$

and Φ is the theoretical air ratio which is given by $\Phi = \dfrac{(F/A)_{actual}}{f_s}$

where $(F/A)_{actual} = \dfrac{\dot{m}_f}{\dot{m}_a}$.

The variables in the right hand sides of all of the above equations are either constant parameters or external inputs or can be expressed as non-linear functions of the five states and inputs. The parameters are defined in the Nomenclature section. The subscript 1 stands for the intake manifold, subscript 2 for the exhaust manifold and subscript e for the engine cylinders.

The flow from the intake manifold to the engine cylinders is given by

$$W_{1e} = \eta_{vol}\rho_1 V_d \frac{N_e}{120} = -k_e p_1 \tag{9.31}$$

with k_e being defined as

$$k_e = \frac{\eta_{vol} V_d N_e}{120 k_1 V_1} \tag{9.32}$$

The flow into the exhaust manifold from the engine cylinders is

$$W_{e2} = W_{1e} + W_f \tag{9.33}$$

9.4.5   Control system objectives

In addition to using the engine crankshaft dynamics of equation (9.28) together with the drivetrain dynamics to control the longitudinal speed or acceleration of the vehicle, additional control system objectives include:

1) To maintain air-fuel ratio at a desired value
2) To maintain a desired level of burnt gas fraction in the intake manifold

The model equations presented above can be used to design a control system that attempts to meet all of the above objectives (Stefanopoulou, et.al., 1998, van Nieuwstadt , et. al., 1998).

9.5   LOWER LEVEL CONTROLLER WITH SI ENGINES

This section discusses lower level controller design for SI engines. In the lower controller, the throttle and brake actuator inputs are determined so as to track a desired acceleration command from the upper controller (see Chapter 5). A simplified model of vehicle dynamics can be used for the development of the lower level controller. The simplified model used is based on the assumptions that the torque converter in the vehicle is locked and that there is zero-slip between the tires and the road (Rajamani, et. al., 2000). These assumptions relate the vehicle speed directly to the engine speed (see Nomenclature for explanation of symbols)

$$\dot{x} = V_x = (Rr_{eff}\omega_e) \tag{9.34}$$

As seen in Chapter 5 (section 5.5.1), the dynamics relating engine speed ω_e to the pseudo-inputs 'net combustion torque' T_{net} and brake torque T_{br} can be modeled under these assumptions by

$$\dot{\omega}_e = \frac{T_{net} - c_a R^3 r_{eff}^3 \omega_e^2 - R(r_{eff}R_x + T_{br})}{J_e} \tag{9.35}$$

where $J_e = I_e + (mr_{eff}^2 + I_\omega)R^2$ is the effective inertia reflected on the engine side, R is the gear ratio and r_{eff} the effective tire radius.

$T_{net}(\omega_e, m_a)$ is a nonlinear function of engine speed and mass of air in the intake manifold (and can be obtained from steady state engine maps available from the vehicle manufacturer, as ssen in section 9.2.1). The dynamics relating m_a to the throttle angle α can be modeled as

$$\dot{m}_{man} = MAX \ TC(\alpha) \ PRI(m_{man}) - \dot{m}_{ao} \tag{9.36}$$

where MAX is a constant dependent on the size of the throttle body, $TC(\alpha)$ is a nonlinear invertible function of the throttle angle, PRI is the pressure influence function that describes the choked flow relationship which occurs through the throttle valve and $\dot{m}_{ao}$ is the mass flow rate into the combustion chamber (again available as a nonlinear function of P_m and

ω_e from the engine manufacturer). The ideal gas law is assumed to hold in the intake manifold

$$P_{man}V_{man} = m_{man}RT_{man} \tag{9.37}$$

The control design for the lower level controller is based on a modification of the standard sliding surface control technique (Hedrick, et. al, 1991). If the net combustion torque is chosen as

$$(T_{net}) = \frac{J_e}{R\,r_{eff}}\ddot{x}_{des} + [c_aR^3r_{eff}^{\;3}\omega_e^{\;2} + R(r_{eff}R_x + T_{br})] \tag{9.38}$$

then, from equation (9.35), the acceleration of the car is equal to the desired acceleration defined by the upper level controller: $\ddot{x}_i = \ddot{x}_{ides}$.

Once the required combustion torque is obtained from equation (9.38), the throttle angle required to provide this torque is calculated by the following procedure. The pressure of air in the manifold P_{man} and temperature T_{man} are measured and m_{man} is then calculated using the ideal gas law (9.37). Next the map $T_{net}(\omega_e, m_{man})$ is inverted using the desired value of net torque to obtain the desired value for mass of air in the intake manifold m_{man_des}.

A sliding surface controller (Slotine and Li, 1991) is then used to calculate the throttle angle α necessary to make m_{man} track m_{man_des}. Define the surface

$$s_2 = m_{man} - m_{man\_des} \tag{9.39}$$

Setting $\dot{s}_2 = -\eta_2 s_2$, we obtain

$$MAX\ \ TC(\alpha)\ \ PRI(m_{man}) = \dot{m}_{ao} + \dot{m}_{man\_des} - \eta_2 s_2 \tag{9.40}$$

Since $TC(\alpha)$ is invertible, the desired throttle angle can be calculated from equation (9.40).

If the desired net torque defined by equation (9.38) is negative, the brake actuator is used to provide the desired torque. An algorithm for smooth switching between the throttle and brake actuators is designed in Choi and Devlin (1995) and can be used by the longitudinal control system.

9.6   CHAPTER SUMMARY

This chapter discussed dynamic models for SI and diesel engines. The type of engine models studied are called mean value models and are adequate for developing control systems for longitudinal vehicle motion control applications.

In SI engines, the two major elements considered in the dynamic model were the air flow model for the intake manifold and the rotational dynamics of the crankshaft. The two states used in the model were the intake manifold pressure p_{man} and the engine crankshaft speed ω_e.

For diesel engines, a turbocharged diesel engine equipped with a variable geometry turbocharger and an exhaust gas recirculation valve was considered. Five states consisting of the mass and pressure in the intake manifold (m_1 and p_1) and exhaust manifold (m_2 and p_2) and the engine crankshaft speed (ω_e) were used in the dynamic model. A complete set of model equations was provided.

The design of a lower level controller for SI engines was discussed. The controller was designed to ensure that a desired longitudinal acceleration for the vehicle could be obtained. This controller will be used in Chapters 5, 6 and 7 for longitudinal vehicle control applications. Nonlinear control synthesis techniques were utilized in the control system design.

NOMENCLATURE

For SI Engines

I_e	rotational moment of inertia for engine
ω_e	rotational engine crankshaft speed
T_{ind}	indicated combustion torque
T_f	friction losses expressed as a torque
T_{load}	load torque on engine
$\dot{m}_f$	fuelling rate
η_i	indicated thermal efficiency
H_u	fuel energy constant
L_{th}	stoichiometric air fuel mass ratio
λ	air/fuel equivalence ratio

$\dot{m}_{ao}$	air flow rate from intake manifold into engine cylinders
$\dot{m}_{ai}$	air flow rate into intake manifold
p_{man}	pressure of air in intake manifold
m_{man}	mass of air in the intake manifold
m_{man_des}	desired value for mass of air in intake manifold used in lower controller
V_{man}	volume of intake manifold
T_{man}	temperature of air in intake manifold
R	constant used in ideal gas law for intake manifold
V_d	displacement volume of engine cylinders
η_{vol}	volumetric efficiency
α	throttle angle input
α'	minimum throttle angle
$TC(\alpha)$	throttle characteristic representing the projected area of flow
PRI	pressure ratio influence function
MAX	constant that represents the maximum possible intake air flow rate
R_x	rolling resistance

For Diesel Engines

m_1	mass of air in intake manifold
m_2	mass of air in exhaust manifold
p_1	pressure of air in intake manifold
p_2	pressure of air in exhaust manifold
T_1	temperature of air in intake manifold
T_2	temperature of air in exhaust manifold
V_1	volume of intake manifold
V_2	volume of exhaust manifold

T_a	temperature of ambient air
W_{egr}	flow rate for exhaust gas recirculation
W_{1e}	flow rate from intake manifold into engine cylinders
W_{c1}	flow rate from compressor into intake manifold
W_t	flow through the variable geometry turbine
W_{e2}	flow rate from engine cylinders into exhaust manifold
P_c	compressor power
P_t	turbine power
η_m	turbo efficiency
τ	turbo lag time constant
γ	ratio of specific heats
p_a	pressure of ambient air

REFERENCES

Acquino, C.F., 'Transient A/F Control Characteristics of the 5 Liter Central Fuel Injected Engine,' SAE Technical Paper Series, Paper No. 810494, 1981.

Amstutz, A. and Del Re, L.R., 'EGO sensor based robust output control of EGR in diesel engines,' *IEEE Transactions on Control Systems Technology*, vol. 3, No. 1, 1995.

Arsie, I., Pianese, C. and Rizzo, G, 'A Computer Code for S.I. Engine Control and Powertrain Simulation', *SAE Technical Paper Series*, PaperNo. 2000-01-0938.

Arsie, Ivan. Pianese, Cesare. Rizzo, Gianfranco, 'Models for the prediction of performance and emissions in a spark ignition engine - a sequentially structured approach,' *Modeling of SI and Diesel Engines, SAE Special Publications*, Vol. 1330, SAE, Warrendale, PA, USA. p 59-73 980779, February 1998.

Cho, D. and Hedrick, J.K. 'Automotive Powertrain Modeling for Control,' *ASME Journal of Dynamic Systems, Measurement and Control*, v 111, No. 4, pp. 568-576, 1989.

Choi, S.B. and Devlin, P., 'Throttle and Brake Combined Control for Intelligent Vehicle Highway Systems', *SAE Technical Paper Series*, Paper No. 951897, 1995.

Coates, F.E., and Fruechte, R.D., 'Dynamic Engine Models for Control Development. Part II: Application to Idle Speed Control,' *International Journal of Vehicle Design*, SP4, 1983.

Ganguli, A. and Rajamani, R., 'Tractable Model Development and System Identification for Longitudinal Vehicle Dynamics,' *Journal of Automobile Engineering*, Proceedings of the Institution of Mechanical Engineers, Part D, Vol. 218, No. 10, pp. 1077-1084, October, 2004.

Guzzella, L. and Amstutz, A., 'Control of diesel engines', *IEEE Control Systems Magazine*, vol. 18, No. 5, pp. 53-71, 1998.

Hedrick, J.K., McMahon, D., Narendran, V.K. and Swaroop, D., 'Longitudinal Vehicle Controller Design for IVHS Systems', *Proceedings of the 1991 American Control Conference*, Vol. 3, pp. 3107-3112, June 1991.

Hendricks, E. and Sorenson, S.C. 'Mean Value Modeling of Spark Ignition Engines' *SAE Technical Paper Series*, Paper No. 900616, 1990.

Hendricks, Elbert. Vesterholm, Thomas, 'Analysis of mean value SI engine models,' *SAE Technical Paper Series*, Published by SAE, Warrendale, PA, USA., pp 1-19 920682, 1992.

Huang, Rong W. Velinsky, Steven A., 'Spark ignition engine modeling for vehicle dynamic simulation,' Advanced Automotive Technologies, *American Society of Mechanical Engineers, Dynamic Systems and Control Division (Publication) DSC*, Published by ASME, New York, NY, USA. v 52, pp. 369-378, 1993.

Heywood, J.B., *Internal Combustion Engine Fundamentals*, Mc-Graw Hill, Inc., 1988.

Jankovic, M. and Kolmanovsky, I., 'Robust Nonlinear Controller for Turbocharged Diesel Engines,' *Proceedings of the 1998 American Control Conference*, pp. 1389-1394, 1998.

Kao, M. and Moskwa, J.J., 'Turbocharged diesel engine modeling for nonlinear engine control and estimation', *ASME Journal of Dynamic Systems, Measurement and Control*, vol. 117, pp. 21-30, March 1995.

Kolmanovsky, I., Moraal, P., van Nieuwstadt, M. and Stefanopoulou, A., 'Issues in modelling and control of intake flow in variable geometry turbocharged diesel engines', *Proceedings of the 18th IFIP Conference on System Modeling and Optimization*, Detroit, July 1997.

Moody, J.F., 'Variable geometry turbocharging with electronic control', *SAE Technical Paper Series*, Paper No. 860107, 1986.

Moskwa, J.J. and Hedrick, J.K., 'Modelling and Validation of Automotive Engines for Control Algorithm Development', *ASME J. of Dynamic Systems, Mesurement and Control*, Vol. 114, No. 2, Pages 278-285, June 1992.

Powell, B.K. and Cook, J.A., 'Nonlinear Low Frequency Phenomenological Engine Modelling and Analysis', *Proceedings of American Controls Conference*, Pages 332-340, Minneapolis, MN, June 1987.

Rajamani, R., Tan, H.S., Law, B. and Zhang, W.B., 'Demonstration of Integrated Lateral and Longitudinal Control for the Operation of Automated Vehicles in Platoons,' *IEEE Transactions on Control Systems Technology*, Vol. 8, No. 4, pp. 695-708, July 2000.

Slotine, J.J.E. and Li, W., *Applied Nonlinear Control*, Prentice Hall, 1991.

Stefanopoulou, A.G., Kolmanovsky, I. And Freudenberg, J.S., 'Control of variable geometry turbocharged diesel engines for reduced emissions', *Proceedings of the 1998 American Control Conference*, pp. 1383-1388, Philadelphia, June 1998.

Taylor, C.F., *The Internal-Combustion Engine in Theory and Practice*, Volume I, The M.I.T. Press, Second Edition, 1976.

van Nieuwstadt, M., Moraal, P. , Kolmanovsky, I. and Stefanopoulou, A.G., 'A comparison of SISO and MIMO designs for EGR-VNT control of a light duty diesel engine', *Proceedings of the IFAC Workshop on Advances in Automotive Control*, Mohican State Park, Ohio, pp. 191-196, February 1998.

Watson, N. and Janota, M.S., *Turbocharging the Internal Combustion Engine*, Wiley Interscience, New York, 1982.

SI Engine Model on website: http://www.iau.dtu.dk/~eh/index.html

Chapter 10

DESIGN AND ANALYSIS OF PASSIVE AUTOMOTIVE SUSPENSIONS

10.1 INTRODUCTION TO AUTOMOTIVE SUSPENSIONS

10.1.1 Full, half and quarter car suspension models

An automotive suspension supports the vehicle body on the axles. A "full car" model of a suspension with 7 rigid body degrees of freedom is shown in Figure 10-1. The vehicle body is represented by the "sprung mass" m while the mass due to the axles and tires are represented by the "unsprung" masses m_{u1}, m_{u2}, m_{u3} and m_{u4}. The springs and dampers between the sprung and unsprung mass represent the vehicle suspension. The vertical stiffness of each of the 4 tires are represented by the springs k_{t1}, k_{t2}, k_{t3} and k_{t4}.

The seven degrees of freedom of the full car model are the heave z, pitch θ and roll ϕ of the vehicle body and the vertical motions of each of the four unsprung masses. The variables z_{r1}, z_{r2}, z_{r3} and z_{r4} are the road profile inputs that excite the system.
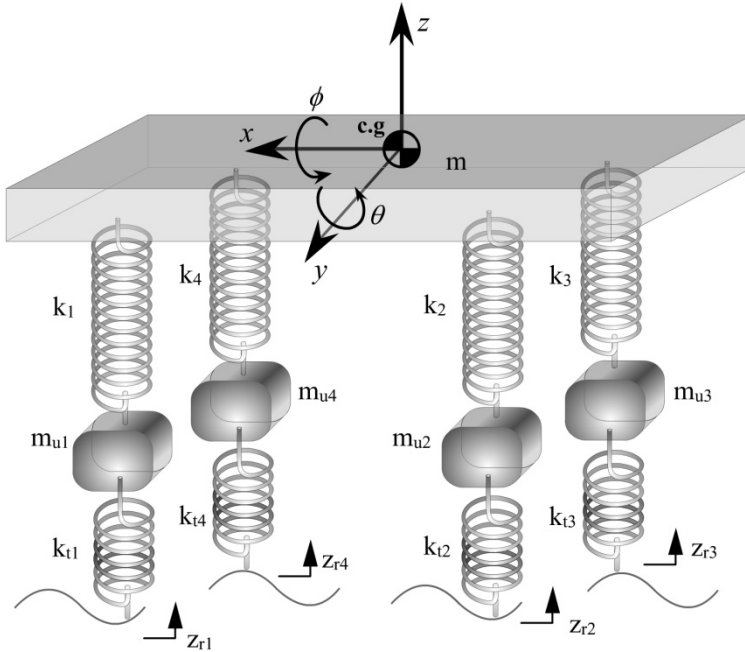
Figure 10-1. Full car automotive suspension model

A "half car" model with four degrees of freedom is shown in Figure 10-2. In the half car model, the pitch and heave motions of the vehicle body (θ and z) and the vertical translation of the front and rear axles (z_{u1} and z_{u2}) are represented.

A two-degree-of-freedom "quarter-car" automotive suspension system is shown in Figure 10-3. It represents the automotive system at each wheel i.e. the motion of the axle and of the vehicle body at any one of the four wheels of the vehicle. The suspension itself is shown to consist of a spring k_s, a damper b_s and an active force actuator F_a. The active force F_a can be set to zero in a passive suspension. The sprung mass m_s represents the quarter-car equivalent of the vehicle body mass. The unsprung mass m_u represents the equivalent mass due to the axle and tire. The vertical stiffness of the tire is represented by the spring k_t. The variables z_s, z_u and z_r represent the vertical displacements from static equilibrium of the sprung mass, unsprung mass and the road respectively.
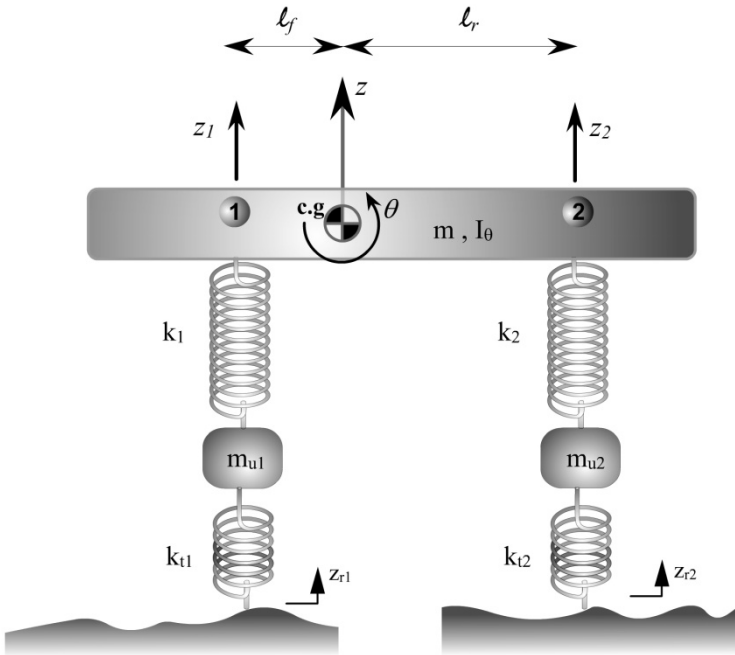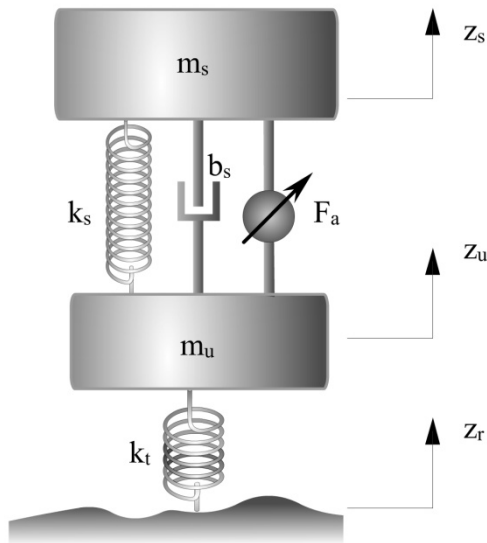
Figure 10-2. Half car automotive suspension model

Figure 10-3. Quarter-car active automotive suspension

10.1.2   Suspension functions

The automotive suspension on a vehicle typically has the following basic tasks (D. Bastow, 1987):

1) <u>To isolate a car body from road disturbances in order to provide good ride quality</u>
   Ride quality in general can be quantified by the vertical acceleration of the passenger locations. The presence of a well-designed suspension provides isolation by reducing the vibratory forces transmitted from the axle to the vehicle body. This in turn reduces vehicle body acceleration. In the case of the quarter car suspension, sprung mass acceleration $\ddot{z}_s$ can be used to quantify ride quality.

2) <u>To keep good road holding</u>
   The road holding performance of a vehicle can be characterized in terms of its cornering, braking and traction abilities. Improved cornering, braking and traction are obtained if the variations in normal tire loads are minimized. This is because the lateral and longitudinal forces generated by a tire depend directly on the normal tire load. Since a tire roughly behaves like a spring in response to vertical forces, variations in normal tire load can be directly related to vertical tire deflection $(z_u - z_r)$. The road holding performance of a suspension can therefore be quantified in terms of the tire deflection performance.

3) <u>To provide good handling</u>
   The roll and pitch accelerations of a vehicle during cornering, braking and traction are measures of good handling. Half-car and full-car models can be used to study the pitch and roll performance of a vehicle. A good suspension system should ensure that roll and pitch motion are minimized.

4) <u>To support the vehicle static weight</u>
   This task is performed well if the rattle space requirements in the vehicle are kept small. In the case of the quarter car model, it can be quantified in terms of the maximum suspension deflection $(z_s - z_u)$ undergone by the suspension.

The outline of the rest of this chapter is as follows. In section 10.2 of the chapter, we will review standard results on modal decoupling. In sections 10.3-10.7, the use of modal decoupling and its approximation for the design and analysis of quarter car suspension systems will be studied. Section 10.8 verifies the results of the decoupled approximation using the accurate complete model. Section 10.9 of the chapter will study the decoupling of half car models and the extension of the result to full car models.

10.1.3 Dependent and independent suspensions

In the case of dependent suspensions, the vertical motions of one wheel of an axle are directly linked to that of the other wheel of that axle. Some cars are still designed and built with dependent rear suspension systems. Figure 10-4 shows a solid-axle leaf-spring dependent rear suspension system. The advantages of such a suspension are that it is simple and inexpensive. The drive axle is clamped to the leaf springs. The shock absorbers are also attached to the clamps. The ends of the leaf springs are attached directly to the chassis (vehicle body), as are the shock absorbers. Since the axle couples both the rear wheels, the vertical motion of one is transferred to the other.

In the case of dependent suspensions, the axle cannot be represented by 2 independent unsprung masses.

In all of the suspension system models considered in section 10.1.1 (full, half and quarter-car models), both the front and rear wheels were assumed to have *independent* suspensions.
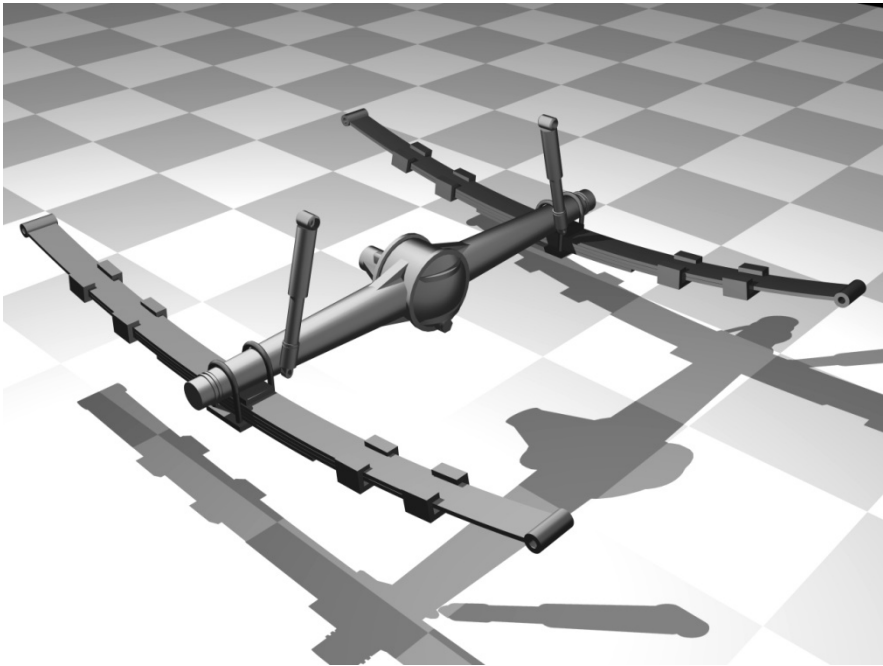
Figure 10-4. Solid-axle leaf-spring rear suspension[1]

---

[1] Figure provided by The Suspension Bible, http://www.chris-longhurst.com/carbibles/

Figure 10-5. Double-A arm independent suspension[2]

The front wheel's suspension systems are always designed to be independent (except for the presence of an antiroll bar). In an independent suspension, the vertical motions of the two wheels are not directly linked to each other. This was the implicit assumption in the full, half and quarter-car models introduced in section 10.1.1.

Figure 10-5 shows a *double-A arm* type of independent suspension. The wheel spindle is supported by an upper and lower 'A' shaped arm. The A-shaped arms constitute a basic lever system that allows the wheel spindle to travel vertically up and down, independent of the other wheel. When the wheel moves vertically, it will also have a slight side-to-side motion caused by the arc which the levers scribe around their pivot point. This side-to-side motion is known as scrub. Unless the links are infinitely long the scrub motion is always present. The springs and shocks in this figure are in a so-called 'coil over oil' arrangement whereby the shock absorbers sit inside the springs. This type of suspension is also commonly referred to as a "double wishbone" suspension as the A shaped arms resemble a wishbone. In an unequal-length A-arm suspension, the upper control arm is often designed to

---

[2] Figure provided by The Suspension Bible, http://www.chris-longhurst.com/carbibles/

be shorter than the lower A-arm. This causes the upper arm to swing through a shorter arc than the lower and pulls in the top of the tire as the wheel travels upwards. Thus the wheel tips in and gains negative camber. During cornering, as the vehicle body rolls against the wheels, the increasing negative camber on the outside allows the tire to generate increased cornering force. By adjusting the length of the arms and their respective angles to the ground, the roll center height and swing arm length of the vehicle can be adjusted.

10.2 MODAL DECOUPLING

This section contains a brief summary of modal decoupling. Modal decoupling will be used later in this chapter to study the influence of different suspension parameters on the properties of the automotive suspension.

Consider an undamped finite degree of freedom system represented by the matrix equation

$$M\ddot{x} + Kx = F \tag{10.1}$$

where M and K are the mass and stiffness matrix respectively and F is the excitation vector. Let ω_i, $i = 1, 2, \cdots, n$ represent the natural frequencies of the system and $\tilde{\phi}_i$ represent the corresponding mass-normalized mode shapes (Thompson and Dahleh, 2001). Then the natural frequencies ω_i are given by

$$\det(-\omega_i^2 M + K) = 0 \tag{10.2}$$

and the mode shapes $\tilde{\phi}_i$ are given by

$$\left[-\omega_i^2 M + K\right]\tilde{\phi}_i = 0 \tag{10.3}$$

Let $\tilde{P} = \begin{bmatrix} \tilde{\phi}_1 & \tilde{\phi}_2 & \cdots & \tilde{\phi}_n \end{bmatrix}$ and $\Lambda = \begin{bmatrix} \omega_1^2 & 0 & \cdots & 0 \\ 0 & \omega_2^2 & 0 & 0 \\ \vdots & 0 & \ddots & \\ 0 & 0 & \cdots & \omega_n^2 \end{bmatrix}$. Since

$\tilde{\phi}_i$ is mass normalized, we have

$$\widetilde{P}^T M \widetilde{P} = I \tag{10.4}$$

and

$$\widetilde{P}^T K \widetilde{P} = \Lambda \tag{10.5}$$

The following change of coordinates

$$r = \widetilde{P}^T M x \tag{10.6}$$

results in decoupled equations of motion in the new coordinates (Thompson and Dahleh, 2001)

$$\ddot{r} + \Lambda r = \widetilde{P}^T F \tag{10.7}$$

Here the matrix Λ is diagonal, consisting of the squares of the natural frequencies ω_i^2 as the diagonal elements.

10.3   PERFORMANCE VARIABLES FOR A QUARTER CAR SUSPENSION

The equations of motion of the two-degree-of-freedom quarter-car suspension shown in Figure 10-3 are

$$m_s \ddot{z}_s + b_s (\dot{z}_s - \dot{z}_u) + k_s (z_s - z_u) = F_a \tag{10.8}$$

$$m_u \ddot{z}_u + b_t (\dot{z}_u - \dot{z}_r) + k_t (z_u - z_r) - b_s (\dot{z}_s - \dot{z}_u) - k_s (z_s - z_u) = -F_a \tag{10.9}$$

In standard second-order matrix form, the system can be represented as

$$M\ddot{z} + C\dot{z} + Kz = H_1 z_r + H_2 \dot{z}_r + H_3 F_a \tag{10.10}$$

or

$$\begin{bmatrix} m_s & 0 \\ 0 & m_u \end{bmatrix} \begin{Bmatrix} \ddot{z}_s \\ \ddot{z}_u \end{Bmatrix} + \begin{bmatrix} k_s & -k_s \\ -k_s & k_s + k_t \end{bmatrix} \begin{Bmatrix} z_s \\ z_u \end{Bmatrix} + $$

$$\begin{bmatrix} b_s & -b_s \\ -b_s & b_s + b_t \end{bmatrix} \begin{Bmatrix} \dot{z}_s \\ \dot{z}_u \end{Bmatrix} = \begin{Bmatrix} 0 \\ k_t \end{Bmatrix} z_r + \begin{Bmatrix} 0 \\ b_t \end{Bmatrix} \dot{z}_r + \begin{Bmatrix} 1 \\ -1 \end{Bmatrix} F_a \qquad (10.11)$$

where $M = \begin{bmatrix} m_s & 0 \\ 0 & m_u \end{bmatrix}$, $K = \begin{bmatrix} k_s & -k_s \\ -k_s & k_s + k_t \end{bmatrix}$ and the other matrices are as defined in equation (10.11).

The state space model of the quarter-car active automotive suspension system can be written as (Yue, et. al., 1988)

$$\dot{x} = Ax + BF_a + L\dot{z}_r \qquad (10.12)$$

where

$x_1 = z_s - z_u$ is the suspension deflection (rattle space)

$x_2 = \dot{z}_s$ is the absolute velocity of sprung mass

$x_3 = z_u - z_r$ tire deflection

$x_4 = \dot{z}_u$ absolute velocity of unsprung mass

$$A = \begin{bmatrix} 0 & 1 & 0 & -1 \\ -\dfrac{k_s}{m_s} & -\dfrac{b_s}{m_s} & 0 & \dfrac{b_s}{m_s} \\ 0 & 0 & 0 & 1 \\ \dfrac{k_s}{m_u} & \dfrac{b_s}{m_u} & -\dfrac{k_t}{m_u} & -\dfrac{(b_s + b_t)}{m_u} \end{bmatrix}, \quad B = \begin{Bmatrix} 0 \\ 1/m_s \\ 0 \\ -1/m_u \end{Bmatrix} \quad \text{and}$$

$$L = \begin{Bmatrix} 0 \\ 0 \\ -1 \\ \dfrac{b_t}{m_u} \end{Bmatrix}$$

In the case of a passive suspension, the active force F_a is set to zero.

The following three transfer functions are of interest and their attenuation will be used to judge the effectiveness of the suspension system :

a) Acceleration transfer function

$$H_A(s) = \frac{\ddot{z}_s(s)}{\dot{z}_r(s)} \tag{10.13}$$

b) Rattle space transfer function

$$H_{RS}(s) = \frac{z_s(s) - z_u(s)}{\dot{z}_r(s)} \tag{10.14}$$

c) Tire deflection transfer function

$$H_{TD}(s) = \frac{z_u(s) - z_r(s)}{\dot{z}_r(s)} \tag{10.15}$$

Note that pitch and roll transfer functions cannot be studied using the quarter car model.

The following values of parameters are typical for a passenger sedan: $k_s = 16000$, $b_s = 1000$, $m_s = 250$, $m_u = 45$, $k_t = 160000$, $b_t = 0$. The tire damping b_t is assumed to be negligible. We will assume that the active force F_A is zero. For now, we are only analyzing a passive suspension system.

10.4   NATURAL FREQUENCIES AND MODE SHAPES FOR THE QUARTER CAR

In order to study the effects of specific suspension parameters on the suspension performance, we calculate the natural frequencies and mode shapes of the suspension system and then transform to a new set of coordinates in which the two equations of motion are approximately decoupled.

The two undamped natural frequencies of the quarter-car suspension system ω_1 and ω_2 are determined by solving

$$\det(-\omega^2 M + K) = 0 \tag{10.16}$$

where the matrices M and K are as defined in equation (10.11). Hence

$$\det\begin{bmatrix} k_s - m_s\omega^2 & -k_s \\ -k_s & k_s + k_t - m_u\omega^2 \end{bmatrix} = 0$$

i.e.

$$\omega^2 = \frac{k_t m_s + k_s m_s + m_u k_s \pm \sqrt{(k_t m_s + k_s m_s + m_u k_s)^2 - 4k_s k_t m_u m_s}}{2m_u m_s}$$

$$= \frac{k_t + k_s}{2m_u} + \frac{k_s}{2m_s} \pm \frac{\sqrt{(k_t + k_s)^2 m_s^2 + m_u^2 k_s^2 - 2(k_t - k_s)k_s m_u m_s}}{2m_u m_s} \tag{10.17}$$

For the particular case where the tire stiffness is much higher than the suspension stiffness, we make the approximations

$$k_s + k_t \approx k_t - k_s \approx k_t \tag{10.18}$$

which then results in the natural frequencies

$$\omega_1 = \sqrt{\frac{k_s}{m_s}} \tag{10.19}$$

and

$$\omega_2 = \sqrt{\frac{k_t}{m_u}} \tag{10.20}$$

For the typical parameters discussed earlier, the approximate natural frequencies turn out to be

$$f_1 = \frac{\omega_1}{2\pi} = 1.27 \text{ Hz and } f_2 = \frac{\omega_2}{2\pi} = 9.49 \text{ Hz.}$$

The exact natural frequencies solved using Matlab (without making the approximations of equation (10.18)) are found to be 1.21 Hz and 9.96 Hz.

The mode shapes ϕ_1 and ϕ_2 corresponding to the two natural frequencies can be obtained using $\left[-\omega_1^2 M + K\right]\phi_1 = 0$ and $\left[-\omega_2^2 M + K\right]\phi_2 = 0$. Let the modal matrix be $\widetilde{P} = \begin{bmatrix} \phi_1 & \phi_2 \end{bmatrix}$.

The mode shapes ϕ_1 and ϕ_2 can be mass-normalized so that the mass-normalized modal matrix $\widetilde{P} = \begin{bmatrix} \phi_1 & \phi_2 \end{bmatrix}$ satisfies

$$\widetilde{P}^T M \widetilde{P} = \begin{bmatrix} 1 & 0 \\ 0 & 1 \end{bmatrix} = I \tag{10.21}$$

The mass-normalized modal matrix for the quarter-car suspension system is found to be

$$\widetilde{P} = \begin{bmatrix} -0.0632 & 0.002 \\ -0.006 & -0.149 \end{bmatrix} \tag{10.22}$$

From the mode shapes in equation (10.22), one can see that the mode corresponding to the first natural frequency predominantly consists of sprung mass motion. This mode is therefore called ***the sprung mass mode***. The mode corresponding to the second natural frequency is called ***the unsprung mass mode***.

We also find

$$\widetilde{P}^T K \widetilde{P} = \begin{bmatrix} \omega_1^2 & 0 \\ 0 & \omega_2^2 \end{bmatrix} = 4\pi^2 \begin{bmatrix} (1.21)^2 & 0 \\ 0 & (9.96)^2 \end{bmatrix} \tag{10.23}$$

10.5   APPROXIMATE TRANSFER FUNCTIONS USING DECOUPLING

Let

$$r = \widetilde{P}^T M z \tag{10.24}$$

Note that the inverse transformation matrix is

$$\left(\tilde{P}^T M\right)^{-1} = \tilde{P} \tag{10.25}$$

The equations of motion in terms of r are then given by

$$\ddot{r} = \tilde{P}^T M \ddot{z} \quad \text{or}$$

$$\ddot{r} = -\tilde{P}^T K P \, r - \tilde{P}^T C \tilde{P} \, \dot{r} + \tilde{P}^T H_1 z_r + \tilde{P}^T H_2 \dot{z}_r \quad \text{or}$$

$$\ddot{r} + \Lambda r + \tilde{P}^T C \tilde{P} \, \dot{r} = \tilde{P}^T H_1 z_r + \tilde{P}^T H_2 \dot{z}_r \tag{10.26}$$

where $\Lambda = \begin{bmatrix} \omega_1^2 & 0 \\ 0 & \omega_2^2 \end{bmatrix}$ is diagonal. In this case the damping term $\tilde{P}^T C \tilde{P}$ also turns out to be diagonal. This happens because the damping matrix C can be expressed in this case as a linear combination of the matrices M and K.

In the case of the automotive suspension system

$$\tilde{P}^T M = \begin{bmatrix} -15.8 & -0.26 \\ 0.62 & -6.7 \end{bmatrix} \tag{10.27}$$

and $\tilde{P}^T H_1 = \begin{bmatrix} -960 \\ -23840 \end{bmatrix}$

The two new decoupled coordinates can therefore be approximated by

$$r_1 = -15.8 z_s \quad \text{if } |z_s| \geq |z_u| \tag{10.28}$$

and

$$r_2 = -6.7 z_u \quad \text{if } |z_u| \geq |z_s| \tag{10.29}$$

The two approximate decoupled equations turn out to be

$$m_s \ddot{z}_s + b_s \dot{z}_s + k_s z_s = b_s \dot{z}_r + k_s z_r \quad \text{when } |z_s| \gg |z_u| \tag{10.30}$$

and

$$m_u \ddot{z}_u + b_s \dot{z}_u + k_t z_u = k_t z_r \qquad \text{when } |z_u| >> |z_s| \tag{10.31}$$

The following figures show the decoupled 1 dof approximations to the quarter car suspension system:

Sprung mass mode approximation:

Valid when $|z_s| >> |z_u|$
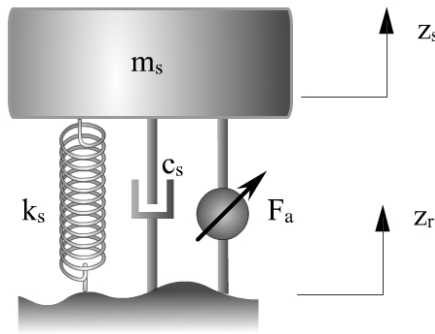
Figure 10-6. Sprung mass mode

Unsprung mass mode approximation:
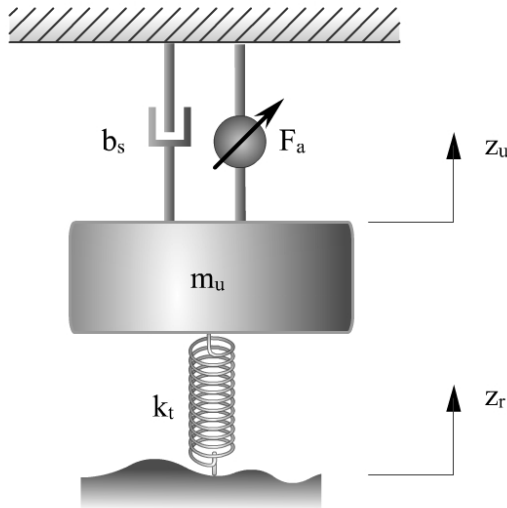
Valid when $|z_u| >> |z_s|$

Figure 10-7. Unsprung Mass Mode

The following approximate transfer functions can then be obtained:

From the sprung mass mode

The equation of motion of the 1dof system shown in Figure 10-6 is

$$m_s \ddot{z}_s + b_s \dot{z}_s + k_s z_s = k_s z_r + b_s \dot{z}_r$$

This approximation leads to the transfer function

$$H_A(s) \approx \frac{(b_s s + k_s)s}{\left(m_s s^2 + b_s s + k_s\right)} \quad \text{if } |z_s| \geq |z_u| \tag{10.32}$$

From the unsprung mass mode

The equation of motion of the 1dof system shown in Figure 10-7 is

$$m_u \ddot{z}_u + k_t (z_u - z_r) + b_s \dot{z}_u + k_s z_u = 0$$

This leads to the relations

$$Z_u(s) = \frac{k_t}{m_u s^2 + b_s s + k_s + k_t} Z_r(s) \quad \text{if } |z_u| \geq |z_s| \tag{10.33}$$

and

$$H_{TD}(s) \approx \frac{-m_u s^2 - b_s s - k_s}{m_u s^3 + b_s s^2 + (k_s + k_t)s} \quad \text{if } |z_u| \geq |z_s| \tag{10.34}$$

To evaluate the acuracy of the approximate transfer functions of equations (10.32) and (10.34), Figures 10-8 and 10-9 show a comparison between the actual and approximate transfer functions. It is clear that the approximate transfer function (10.32) matches the actual transfer function $H_A(s)$ well for the frequency range $\omega \leq 2\omega_1$. Similarly the approximate transfer function (10.34) matches the actual transfer function $H_{TD}(s)$ well for the frequency range $\omega \geq 0.5\omega_2$.
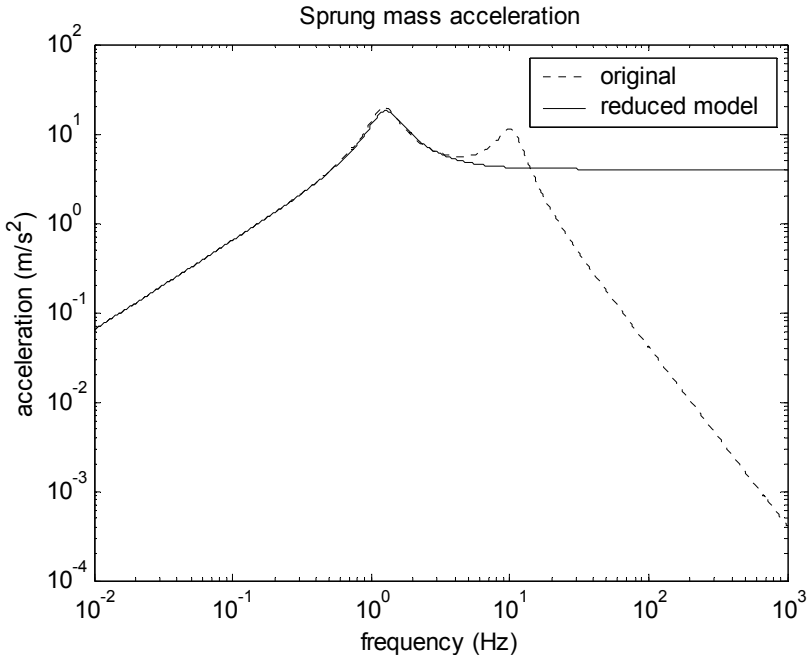
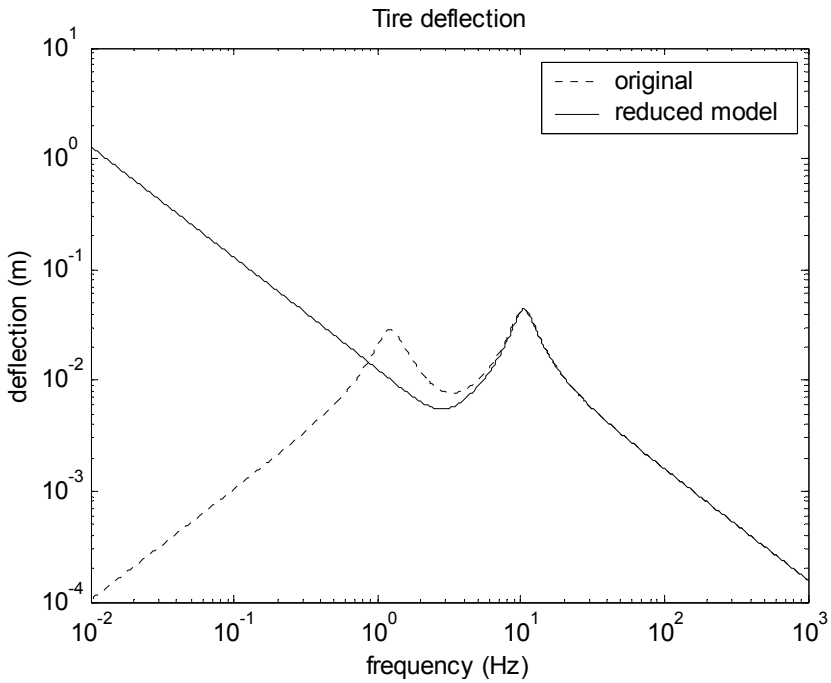*Figure 10-8.* Actual and approximate $H_A(s)$

Figure 10-9. Actual and approximate $H_{TD}(s)$

The suspension deflection transfer function can be approximated by

$$H_{RS}(s) \approx \frac{Z_s - Z_r}{\dot{Z}_r} = \frac{-m_s s^2}{\left(m_s s^2 + b_s s + k_s\right)s} \quad \text{if } \omega \leq 2\omega_1 \qquad (10.35)$$

and

$$H_{RS}(s) \approx \frac{Z_u}{\dot{Z}_r} = \frac{k_t}{\left(m_u s^2 + b_s s + k_s + k_t\right)s} \quad \text{if } \omega \geq 0.5\omega_2 \qquad (10.36)$$

Armed with the above knowledge on the decoupled motions of the sprung and unsprung mass, one can now study the effects of specific system parameters on the performance of the suspension system.

10.6   ANALYSIS OF VIBRATIONS IN THE SPRUNG MASS MODE

As discussed in the previous section, the approximate transfer functions for vibrations in the sprung mass mode are

$$\frac{1}{s}H_A(s) = \frac{z_s}{z_r} = \frac{k_s + b_s s}{m_s s^2 + b_s s + k_s} \qquad (10.37)$$

and

$$sH_{RS}(s) = \frac{z_s - z_r}{z_r} \approx -\frac{m_s s^2}{m_s s^2 + b_s s + k_s} \qquad (10.38)$$

By inspection of the simple second order transfer functions in equations (10.37) and (10.38) above, it is clear that changes in the suspension stiffness k_s and in the suspension damping b_s will lead to the changes in the transfer function $H_A(s)$ and $H_{RS}(s)$ as shown in Table 10.1.

From the Table, it can be seen that a softer suspension (lower k_s) leads to an improvement in ride quality by reducing the first resonant frequency and hence causing the roll-off in the transfer function $H_A(s)$ to start at a lower frequency. However, a softer suspension leads to increased suspension deflection at low frequencies, thus increasing rattle space requirements.

An increase in suspension damping b_s reduces or eliminates the resonant peak corresponding to the sprung mass natural frequency. Thus the ride quality transfer function $H_A(s)$ will be significantly improved at the sprung mass frequency. However, due to the impact of b_s on the numerator in equation (10.37), the higher damping introduces high frequency harshness in $H_A(s)$ by causing a slower roll-off.

Table 10-1. Influence of Suspension Parameters on Sprung Mass Vibrations

Suspension Change	Influence	Impact on Ride Quality	Impact on Rattle Space
Reduced suspension stiffness k_s	Decrease in the value of the first natural frequency ω_1	**GOOD** Improved sprung mass acceleration transfer function at high frequencies	**BAD** Increased suspension deflection at low frequencies
Increased suspension damping b_s	Better damping at the first natural frequency ω_1	**GOOD** Reduces or eliminates the first resonant peak resulting in highly improved ride quality at the first resonant frequency. **BAD** Deteriorates ride quality at high frequencies by causing a slower roll-off and resulting in high frequency "harshness"	**GOOD** Reduces or eliminates the first resonant peak in the suspension deflection transfer function resulting in improved suspension deflection performance at the first resonant frequency. **BAD** This change has no detrimental effects on the suspension deflection transfer function

The increase in suspension damping will have no detrimental effects on the suspension deflection transfer function $H_{RS}(s)$. It reduces or eliminates the resonant peak in $H_{RS}(s)$.

Consider again the decoupled sprung mass mode model of Figure 10-6. If the damping b_s were placed between the sprung mass and inertial ground, instead of being placed between the sprung mass and the road, the resonant peak in the ride quality transfer function would be damped without causing the slower roll off at high frequencies. Thus significant ride quality improvement at the sprung mass frequency could be obtained without any high frequency harshness. Such a damper placed between the sprung mass and inertial ground is called a "sky-hook" damper. While the benefits of a sky-hook damper are clear, it is obviously not directly realizable in a passive suspension system. In the case of an active suspension system, the equivalent effect of a sky-hook damper can be obtained by controlling a hydraulic actuator placed between the sprung and unsprung masses (Redfield and Karnopp, 1989).

10.7   ANALYSIS OF VIBRATIONS IN THE UNSPRUNG MASS MODE

For the case where $|z_u| >> |z_s|$ (in the unsprung mass mode), the quarter car system can be replaced by the 1 dof system shown in Figure 10-7 earlier. As seen earlier, the tire deflection transfer function in this case can be approximated by

$$\frac{z_u - z_r}{z_r} = \frac{-m_u s^2}{m_u s^2 + b_s s + k_t} \tag{10.39}$$

Influence of tire stiffnes on road holding

By examining the simple second order transfer function in equation (10.39), it is clear that an increase in tire stiffness reduces tire deflection by reducing the low frequency asymptotte of $H_{TD}(s)$. Table 10.2 summarizes the influence of an increase in tire stiffness.

Table 10-2. Influence of Suspension Parameters on Unsprung Mass Vibrations

Suspension Change	Influence	Impact on Road Holding
Increased tire stiffness k_t	Increase in the value of the second natural frequency ω_2. Reduction in the low frequency asymptote of the tire deflection transfer function.	**GOOD** Improves tire deflection transfer function by reducing its low frequency asymptote

10.8   VERIFICATION USING THE COMPLETE QUARTER CAR MODEL

10.8.1   Verification of the influence of suspension stiffness

The effects of decreasing suspension stiffness k_s are studied in Figures 10-10, 10-11 and 10-12 by reducing k_s by a factor of 10. The suspension damping is correspondingly reduced so that the damping ratio remains 0.25.

As seen in Figure 10-10, the softer suspension is seen to provide better vibration isolation (reduced sprung mass acceleration). However, as seen in Figure 10-11, rattle space requirements are higher. The tire deflection performance with the softer suspension is shown in Figure 10-12. Tire deflection is significantly reduced at the sprung mass natural frequency. However, it appears to have a higher peak at the unsprung mass resonant frequency due to the reduced suspension damping, since the tire by itself has very little damping.
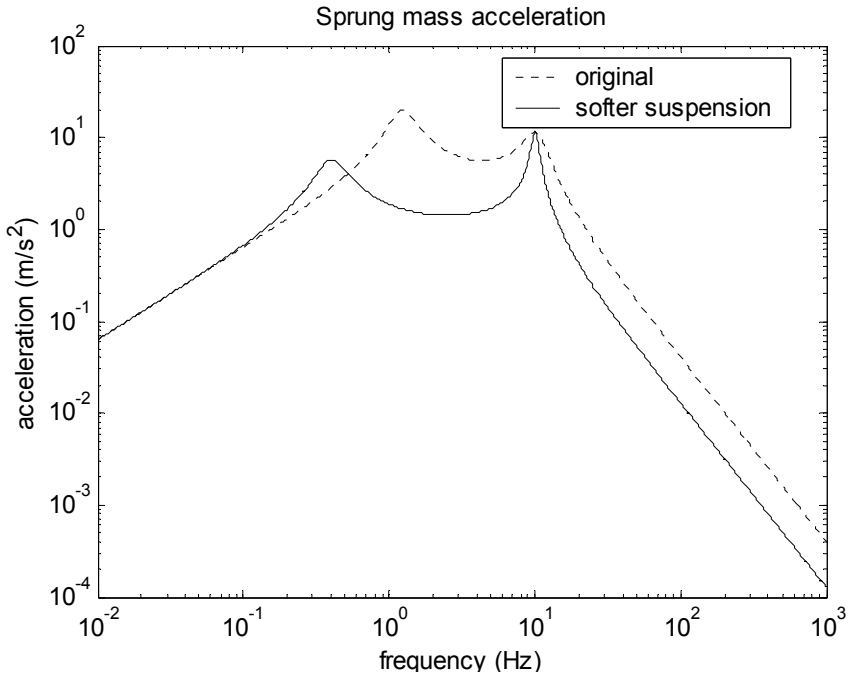
Figure 10-10. $\left| H_A(j\omega) \right|$ with reduced suspension stiffness
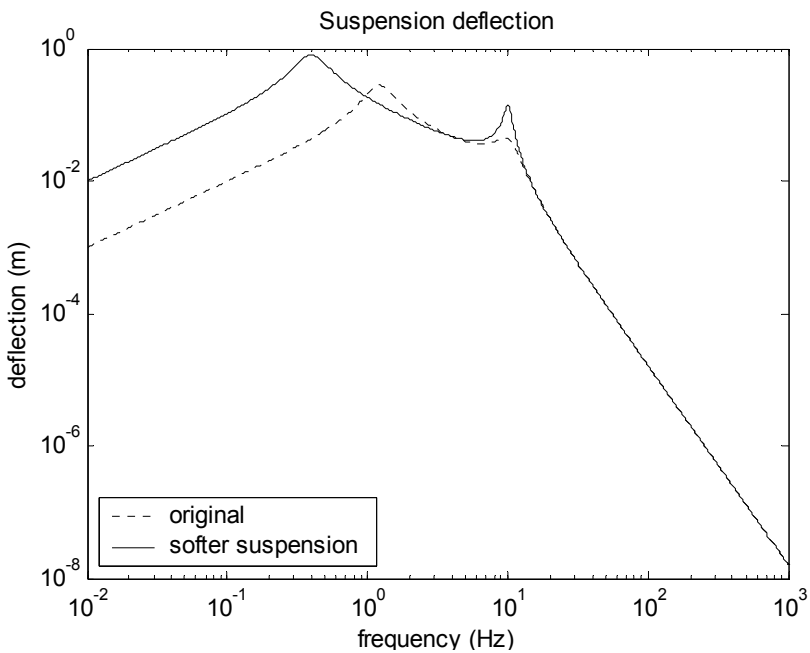
Figure 10-11. $\left| H_{RS}(j\omega) \right|$ with reduced suspension stiffness
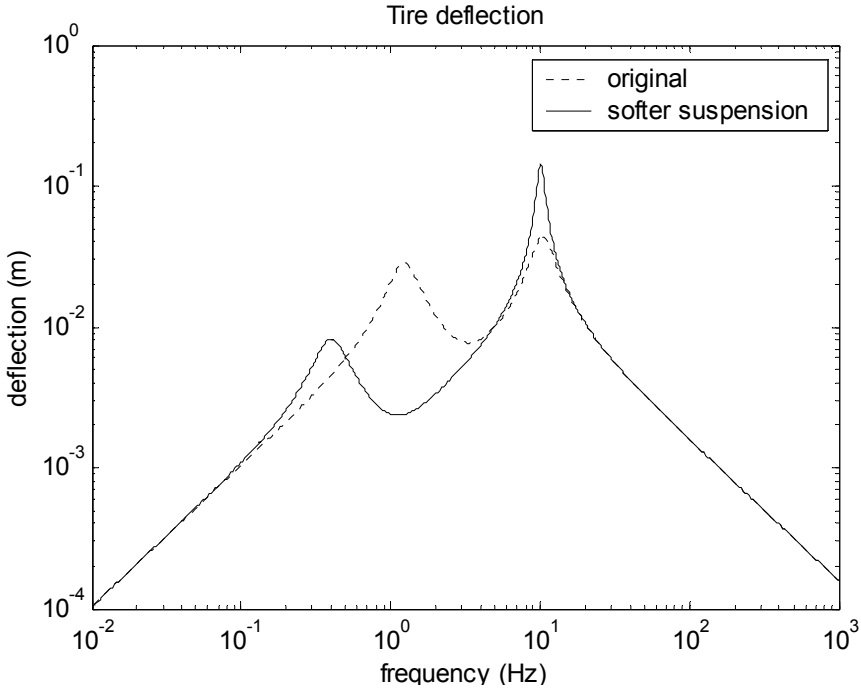
Figure 10-12. $\left| H_{TD}(j\omega) \right|$ with reduced suspension stiffness

10.8.2   Verification of the influence of suspension damping

Next, the effects of increasing suspension damping only are studied by increasing damping coefficient b_s by a factor of 2. The new damping ratio becomes 0.5 (originally the damping ratio was 0.25).

   In Figure 10-13, the higher damping is seen to reduce the sprung mass resonant peak of the acceleration transfer function but at the cost of high frequency harshness (slower roll-off in sprung mass acceleration at high frequencies). Higher damping reduces both resonant peaks in the suspension deflection transfer function, as seen in Figure 10-14, leading to significant overall improvement in suspension deflection performance. Similarly, higher suspension damping also lead to increased damping ratios for both resonant peaks in the tire deflection transfer function, as seen in Figure 10-15.
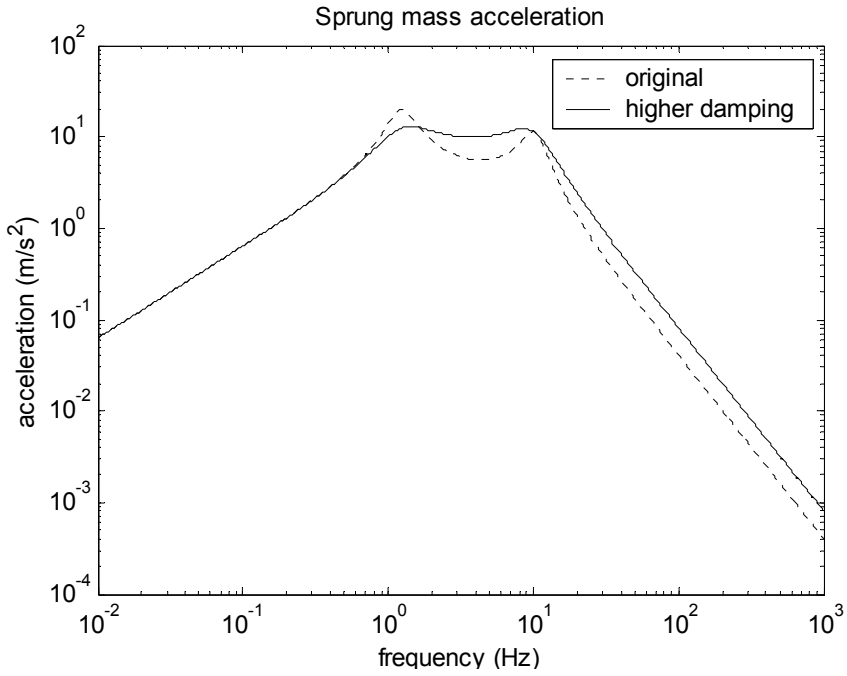
Figure 10-13. $\left| H_A(j\omega) \right|$ with increased suspension damping
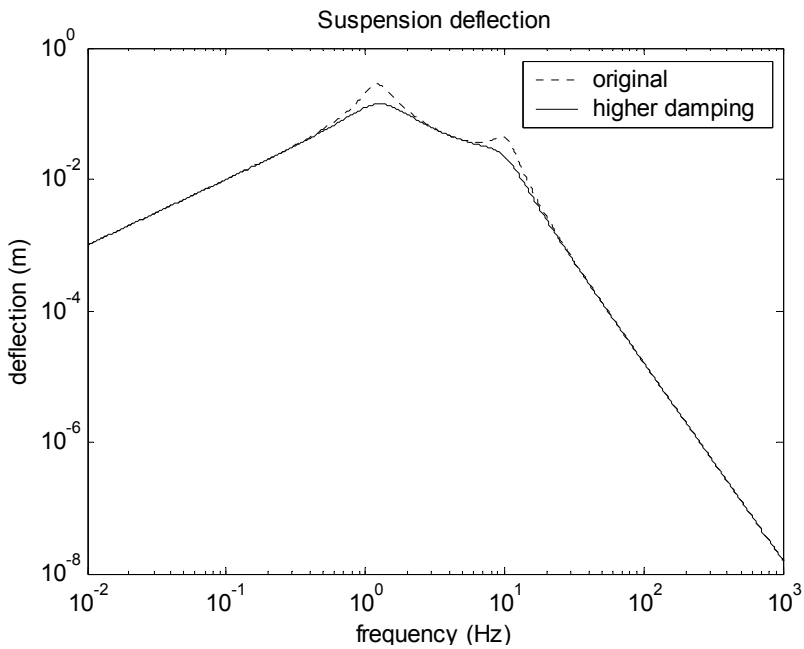
Figure 10-14. $\left| H_{RS}(j\omega) \right|$ with increased suspension damping
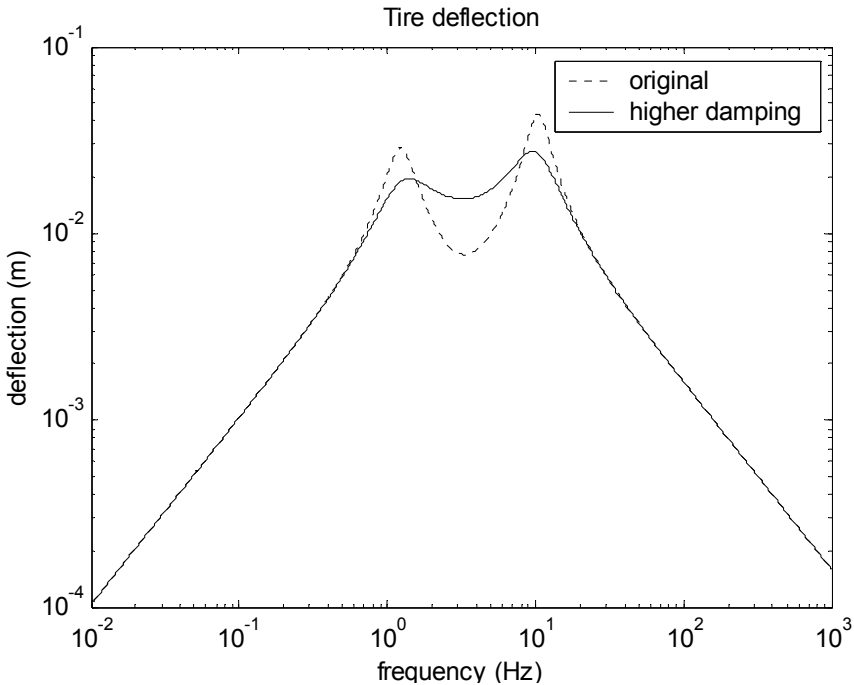
Figure 10-15. $\left| H_{TD}(j\omega) \right|$ with increased suspension damping

10.8.3   Verification of the influence of tire stiffness

Next the tire stifness is increased by a factor of 10.

As seen in Figure 10-18, the resulting suspension is seen to provide significantly reduced tire deflections and hence better road holding and cornering performance. However, as seen in Figure 10-16, this is obtained at the cost of increased sprung mass accelerations due to roll-off of the sprung mass acceleration transfer function occuring at a higher frequency. The suspension deflection performance is similarly worsened at high frequencies (Figure 10-17) due to the increase in unsprung mass resonant frequency.
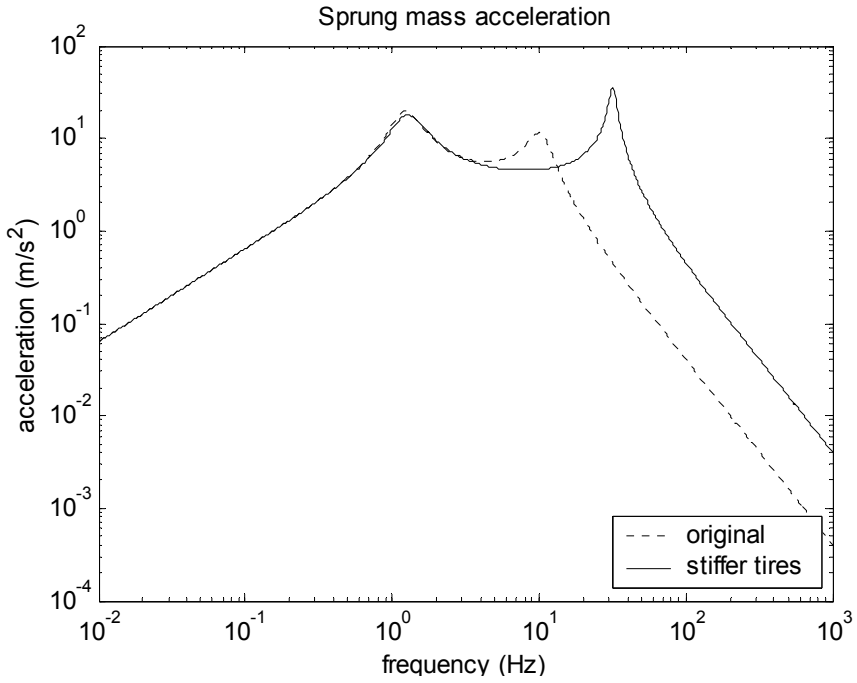
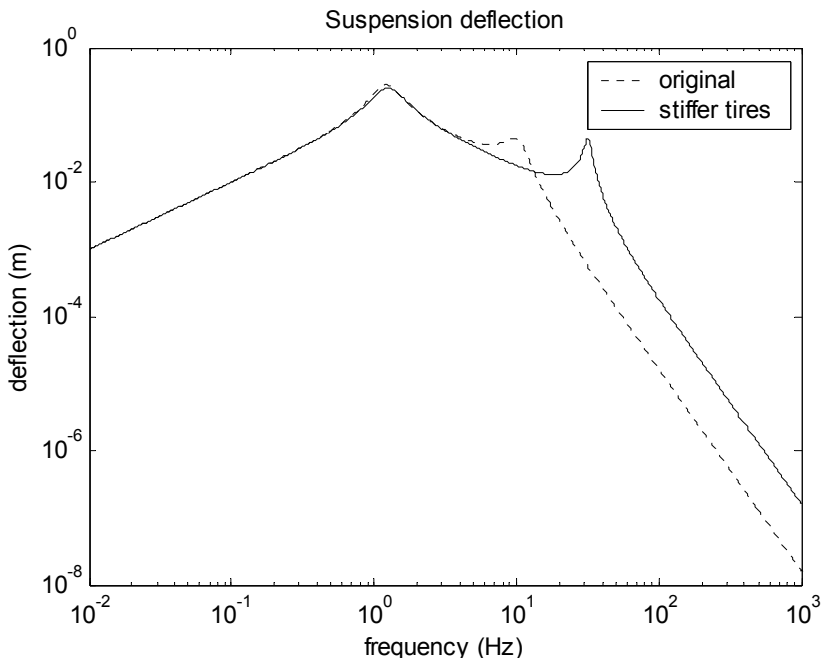*Figure 10-16.* $\left| H_A(j\omega) \right|$ with increased tire stiffness

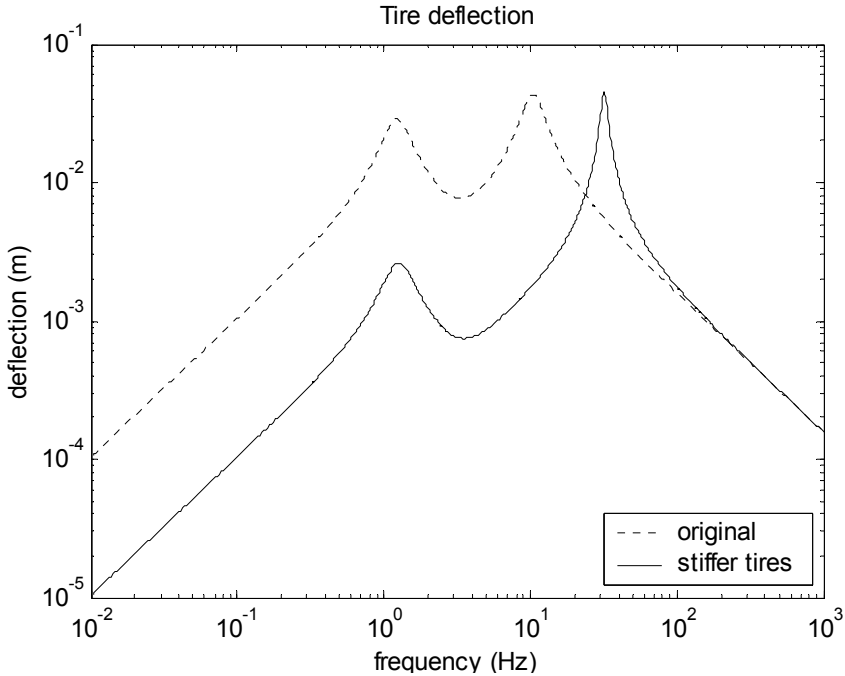*Figure 10-17.* $\left| H_{RS}(j\omega) \right|$ with increased tire stiffness

Figure 10-18. $\left| H_{TD}(j\omega) \right|$ with increased tire stiffness

Let us briefly consider the case where the tire stiffness is kept the same, but significant tire damping is introduced. The increased tire damping will reduce the resonant peak of the sprung mass acceleration transfer function at the unsprung mass resonant frequency. The suspension deflection and tire deflection transfer functions will also be improved at the unsprung mass resonant frequency. While these are all desirable, increasing the tire damping is non-trivial. Hence these beneficial effects cannot be physically realized.

10.9   HALF-CAR AND FULL-CAR SUSPENSION MODELS

Consider a two degree of freedom half-car model of an automotive suspension system, as shown in Figure 10-19 below. The two degrees of freedom are the pitch θ and the heave (vertical translation) z.
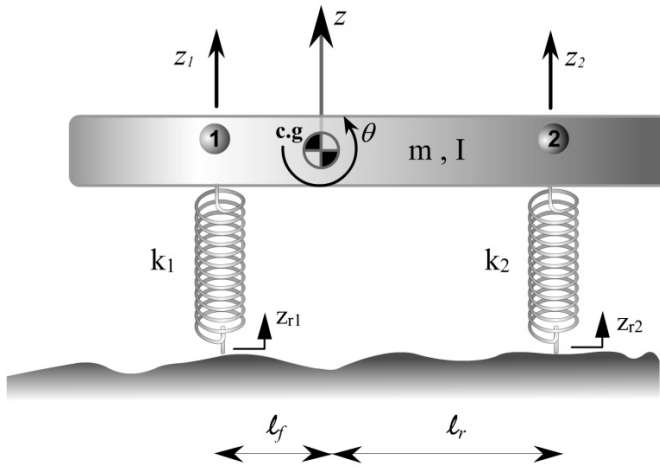
Figure 10-19. Two-degree of freedom half car model

The displacements of the car body at the two suspension locations are related to z and θ by

$$z_1 = z - \ell_f \theta \tag{10.40}$$

and

$$z_2 = z + \ell_r \theta \tag{10.41}$$

Using Newton's laws, we have

$$m\ddot{z} + k_1(z_1 - z_{r1}) + k_2(z_2 - z_{r2}) = 0 \tag{10.42}$$

and

$$I\ddot{\theta} - k_1(z_1 - z_{r1})\ell_f + k_2(z_2 - z_{r2})\ell_r = 0 \tag{10.43}$$

Substituting for z_1 and z_2 from equations (10.40) and (10.41), the equations of motion turn out to be:

$$\begin{bmatrix} m & 0 \\ 0 & I \end{bmatrix}\begin{bmatrix} \ddot{z} \\ \ddot{\theta} \end{bmatrix} + \begin{bmatrix} k_1 + k_2 & k_2\ell_r - k_1\ell_f \\ k_2\ell_r - k_1\ell_f & k_1\ell_f^{\,2} + k_2\ell_r^{\,2} \end{bmatrix}\begin{bmatrix} z \\ \theta \end{bmatrix}$$
$$= \begin{bmatrix} k_1 & k_2 \\ -k_1\ell_f & k_2\ell_r \end{bmatrix}\begin{bmatrix} z_{r1} \\ z_{r2} \end{bmatrix} \tag{10.44}$$

The standard procedure for decoupling the equations of motion can be followed by calculating the natural frequencies and mode shapes.

First consider the special case where the moment of inertia is given by

$$I = m\ell_f\ell_r \tag{10.45}$$

In this special case, the natural frequencies (obtained by using $\det(-\omega_i^{\,2} M + K) = 0$) turn out to be

$$\omega_1^{\,2} = \frac{k_1}{m\dfrac{\ell_r}{\ell_f + \ell_r}} \quad \text{and} \quad \omega_2^{\,2} = \frac{k_2}{m\dfrac{\ell_f}{\ell_f + \ell_r}} \tag{10.46}$$

The mass-normalized mode shapes are

$$\tilde{\phi}_1 = \frac{1}{\sqrt{m(\ell_f + \ell_r)}}\begin{bmatrix} \sqrt{\ell_r} \\ -\dfrac{1}{\sqrt{\ell_r}} \end{bmatrix} \quad \text{and} \quad \tilde{\phi}_2 = \frac{1}{\sqrt{m(\ell_f + \ell_r)}}\begin{bmatrix} \sqrt{\ell_f} \\ \dfrac{1}{\sqrt{\ell_f}} \end{bmatrix} \tag{10.47}$$

and $\tilde{P} = \begin{bmatrix} \tilde{\phi}_1 & \tilde{\phi}_2 \end{bmatrix}$.

The decoupled coordinates are found using $\begin{bmatrix} r_1 \\ r_2 \end{bmatrix} = \tilde{P}^T M \begin{bmatrix} z \\ \phi \end{bmatrix}$ to be

$$r_1 = z - \ell_f\theta = z_1 \text{ and } r_2 = z + \ell_r\theta = z_2 \tag{10.48}$$

Thus, the decoupled coordinates turn out to be the vertical motion of the points 1 and 2 i.e. of the front and rear of the suspension respectively. *In this special case the front and rear suspensions can be designed independently!*

Let us interpret this special case $I = m\ell_f \ell_r$. Consider two masses m_f and m_r on a link of length $\ell_f + \ell_r$, as shown in Figure 10-20 below.

If the system shown in Figure 10-20 were to represent the coupled two-dof system shown in Figure 10-19, then the two masses m_f and m_r must satisfy
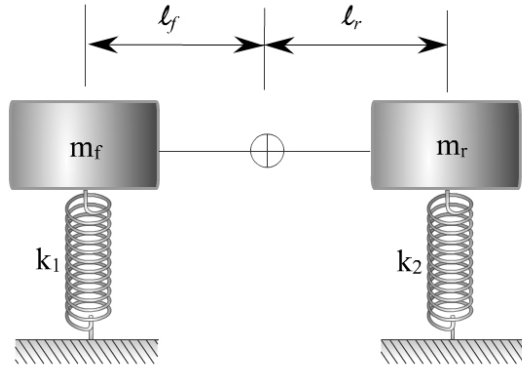

Figure 10-20. Decoupled front and rear suspension systems

$$m_f + m_r = m \tag{10.49}$$

$$m_f \ell_f = m_r \ell_r \tag{10.50}$$

Equation (10.49) states that the total sum of the masses must be m while equation (10.50) states that the two masses must be located at distances of ℓ_f and ℓ_r respectively from the c.g.

Solving equations (10.49) and (10.50) for m_f and m_r, we obtain

$$m_f = m \frac{\ell_r}{\ell_f + \ell_r} \tag{10.51}$$

$$m_r = m \frac{\ell_f}{\ell_f + \ell_r} \tag{10.52}$$

Using the above defintions of m_f and m_r, the moment of inertia can be calculated as

$$I = m_f \ell_f{}^2 + m_r \ell_r{}^2$$

$$= m \left[\frac{\ell_f{}^2 \ell_r}{\ell_f + \ell_r} + \frac{\ell_f \ell_r{}^2}{\ell_f + \ell_r} \right]$$

$$= m \ell_f \ell_r$$

Thus, the special case $I = m \ell_f \ell_r$ corresponds to a system where the coupled 2-dof system of Figure 10-19 can be exactly represented by the decoupled masses at the front and rear of the system. In this case the front and rear suspensions can be designed independently.

It turns out that for a typical passenger sedan, the relationship $I = m \ell_f \ell_r$ is approximately satisfied. Some typical values of parameters for a passenger sedan are

$m = 1460$

$\ell_f = 1.4$ meters

$\ell_r = 1.4$ meters

$I_\theta = 2460 \ kg \ m^2$

$m \ell_f \ell_r = 2862 \ kg \ m^2$

Thus $m \ell_f \ell_r \approx I_\theta$.

Since the motions at the front and rear are decoupled, independent design of the front and rear suspensions is adequate to control both heave and pitch motions due to road irregularities.

Similarly, the roll and heave vibrations of the automotive suspension can also be analyzed using a half car model. The corresponding roll-heave parameters for a typical passenger sedan are

$I_\phi = 660 \ kg \ m^2$
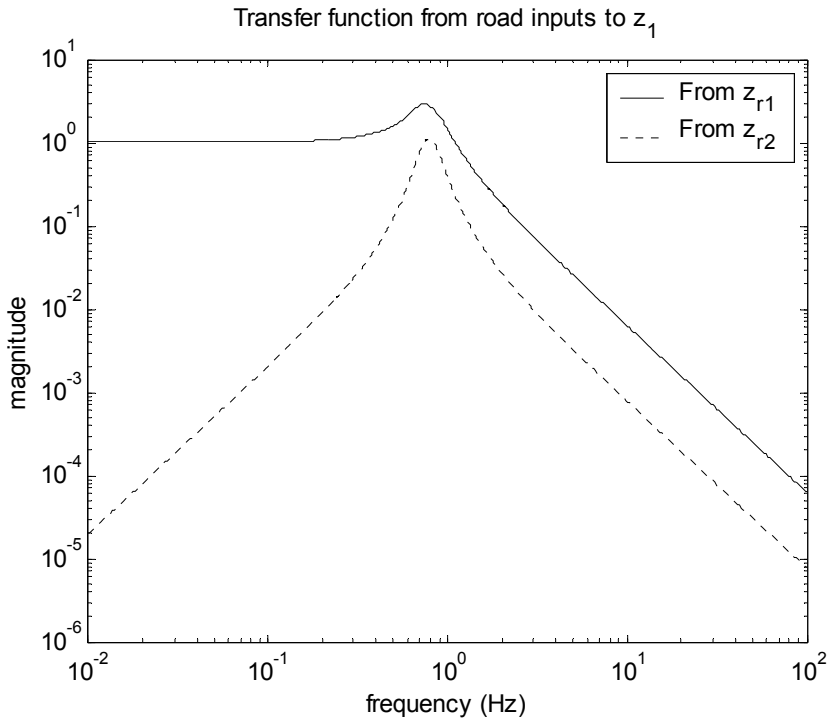
$\ell_f = 0.761$ meters

$\ell_r = 0.761$

Figure 10-21. Transfer function from the two road inputs to z_1

Calculations show that $m\ell_f\ell_r = 845.5\ kg\ m^2$ which is to be compared with $I_\phi = 660\ kg\ m^2$.

The approximation $I \approx m\ell_f\ell_r$ does not seem to be very accurate in this case. However, as can be seen in , the transfer function from z_{r2} to z_1 has a significantly smaller magnitude that the transfer function from z_{r1} to z_1. Thus, the vertical motion of points z_1 and z_2 continue to be decoupled. The vertical motion of the sprung mass at each wheel is significantly influenced by the road input at that wheel. In summary, quarter car models are adequate to design suspensions when the influence of road irregularities is being considered. However, it must here be noted that, full car models are needed when the influence of cornering on vehicle roll and the influence of braking and longitudinal acceleration on vehicle pitch are to be considered. When only the influence of road irregularities is being considered, a quarter car model is adequate.

10.10   CHAPTER SUMMARY

In addition to providing vibration isolation for the vehicle body, an auto-motive suspension strongly influences the cornering, traction and handling properties as well as the rattle space requirements of the vehicle. An improve-ment in the performance of any one function is often obtained at the expense of another. A high order multi-degree-of-freedom model involving many suspension parameters is typically required in order to analyze the influence of suspension design on all the performance functions. This chapter utilized approximate decoupling to obtain simple single degree of freedom models from a high order automotive suspension model. Each simple model involved a small number of parameters and enabled easy analysis of the performance of some suspension functions. Using the approximately decoupled models, the following conclusions on suspension design were obtained

a) Decreasing suspension stiffness improves ride quality and road holding. However, it increases rattle space requirements.
b) Increased suspension damping reduces resonant vibrations at the sprung mass frequency. However, it also results in increased high frequency harshness.
c) Increased tire stiffness provides better road holding but leads to harsher ride at frequencies above the unsprung mass frequency.
d) An analysis of the full car and half car models' response to road irregularities indicated that the suspensions can be designed independently at each wheel. The quarter car suspension model is therefore adequate to study and design automotive suspension systems for optimizing response to road irregularities.
e) To study the influence of cornering on vehicle roll and the influence of braking and longitudinal acceleration on vehicle pitch, half car and/or full car models must be used.

NOMENCLATURE

z_s	sprung mass displacement
z_u	unsprung mass displacement
z_r	road profile input
m_s	sprung mass
m_u	unsprung mass
k_s	suspension stiffness

b_s	suspension damping
k_t	tire stiffness
b_t	tire damping
F_a	active suspension actuator force
ϕ	roll motion of sprung mass
θ	pitch motion of sprung mass
I_ϕ	roll moment of inertia of sprung mass
I_θ	pitch moment of inertia of sprung mass
ℓ_f	longitudinal distance from vehicle c.g. to front axle
ℓ_r	longitudinal distance from vehicle c.g. to rear axle
s	Laplace transform variable
$H_A(s)$	sprung mass acceleration transfer function
$H_{RS}(s)$	suspension deflection transfer function
$H_{TD}(s)$	tire deflection transfer function
A, B, L	matrices used in state space model of quarter car suspension
x	state space vector
ω_1	sprung mass resonant frequency
ω_2	unsprung mass resonant frequency
ϕ_1	modal vector corresponding to sprung mass resonant frequency
ϕ_2	modal vector corresponding to unsprung mass resonant frequency
r	decoupled coordinates for suspension system
$\widetilde{P}$	mass normalized modal matrix
M, K, C	matrices used in the mass-stiffness-damping suspension model
H_1, H_2, H_3	matrices used in the mass-stiffness-damping suspension model

REFERENCES

Bastow, D., *Car Suspension and Handling*, Pentech Press Limited, 2nd Edition, 072730318X, 1987.

Rajamani, R. and Hedrick, J.K., "Performance of Active Automotive Suspensions with Hydraulic Actuators : Theory and Experiment", *Proceedings of the 1994 American Control Conference (ACC),* Baltimore, Maryland, June 29-July 1, 94CH3390-2, Vol 2, pp. 1214-1218, 1994,

Redfield, R.C. and Karnopp, D.C., "Performance sensitivity of an actively damped vehicle suspension to feedback variation," *Journal of Dynamic Systems, Measurement and Control, Transactions ASME*, Vol. 111, No. 1, p 51-60, March, 1989.

Sharp, R.S. and Hassan, S.A., "Evaluation of Passive Automotive Suspension Systems with Variable Stiffness and Damping Parameters," *Vehicle System* Dynamics, Vol. 15, No. 6, pp. 335-350, 1986.

Thompson and Dahleh, *Theory of Vibration with Applications*, Prentice-Hall, 5th Edition, 2001.

Yue, C., Butsuen, T. and Hedrick, J.K., "Alternative Control Laws for Automotive Suspensions," *Proceedings of the American Control Conference*, pp. 2373-2378, 1988.

Chapter 11

ACTIVE AUTOMOTIVE SUSPENSIONS

The analysis of passive automotive suspensions in the last chapter showed that there are significant trade-offs in performance between the ride quality, rattle space and tire deflection transfer functions. Improvements in any one of the three transfer functions in the case of passive suspensions is often obtained at the expense of deterioration in the other two transfer functions. In this chapter, we look at the use of active suspensions in which electronically controlled actuators placed in the suspension are used to provide significantly superior performance. Alternate control laws are analyzed and the performance that active suspensions can provide is studied and compared with that of passive suspensions. The factors that limit the performance of active suspensions are studied. The analysis of "invariant points" is used to understand these performance limitations. A simple control law called sky-hook damping which needs only a few sensor measurements and can provide most of the benefits of full state feedback control laws is discussed. Finally, the chapter looks at actual experimental implementation issues, including the dynamics of hydraulic actuators used to provide the active force.

11.1   INTRODUCTION

A two-degree-of-freedom "quarter-car" automotive suspension system is shown in Figure 11-1 below. It represents the automotive system at each wheel i.e. the motion of the axle and of the vehicle body at any one of the four wheels of the vehicle. The suspension itself is shown to consist of a spring k_s, a damper b_s and an active force actuator F_a. The sprung mass m_s represents the quarter-car equivalent of the vehicle body mass. The

unsprung mass m_u represents the equivalent mass due to the axle and tire. The vertical stiffness of the tire is represented by the spring k_t. The variables z_s, z_u and z_r represent the vertical displacements from static equilibrium of the sprung mass, unsprung mass and the road respectively.
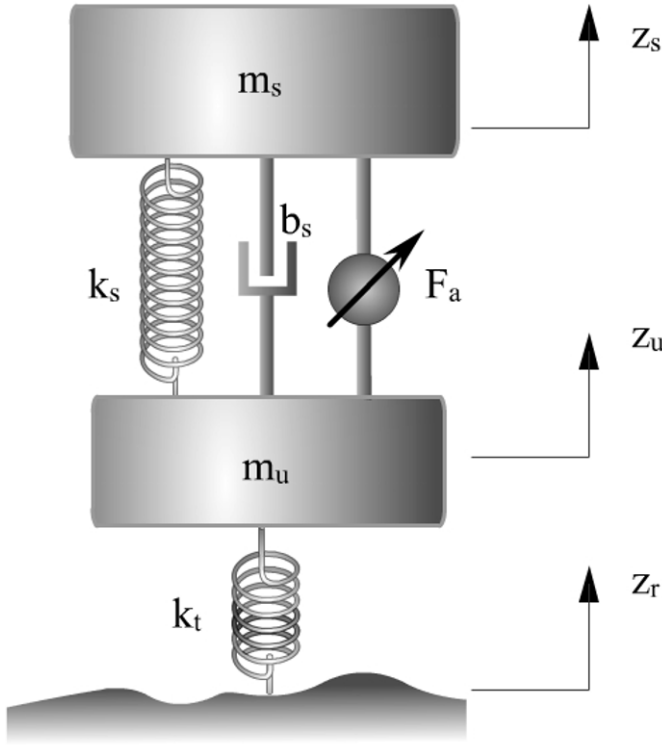

Figure 11-1. Quarter-car active automotive suspension

The equations of motion of the two-degree-of-freedom quarter-car suspension shown in Figure 11-1 are

$$m_s \ddot{z}_s + b_s (\dot{z}_s - \dot{z}_u) + k_s (z_s - z_u) = F_a \tag{11.1}$$

$$m_u \ddot{z}_u + k_t (z_u - z_r) - b_s (\dot{z}_s - \dot{z}_u) - k_s (z_s - z_u) = -F_a \tag{11.2}$$

The state space model of the quarter-car active automotive suspension system can be written as (Yue, et. Al., 1988)

$$\dot{x} = Ax + BF_a + L\dot{z}_r \tag{11.3}$$

where

$$x = \begin{bmatrix} x_1 & x_2 & x_3 & x_4 \end{bmatrix}^T$$

$x_1 = z_s - z_u$ is suspension deflection (rattle space)
$x_2 = \dot{z}_s$ is the absolute velocity of sprung mass
$x_3 = z_u - z_r$ is tire deflection
$x_4 = \dot{z}_u$ is the absolute velocity of unsprung mass

$$A = \begin{bmatrix} 0 & 1 & 0 & -1 \\ -\dfrac{k_s}{m_s} & -\dfrac{b_s}{m_s} & 0 & \dfrac{b_s}{m_s} \\ 0 & 0 & 0 & 1 \\ \dfrac{k_s}{m_u} & \dfrac{b_s}{m_u} & -\dfrac{k_t}{m_u} & -\dfrac{(b_s + b_t)}{m_u} \end{bmatrix}, \quad B = \begin{Bmatrix} 0 \\ 1/m_s \\ 0 \\ -1/m_u \end{Bmatrix} \quad \text{and}$$

$$L = \begin{Bmatrix} 0 \\ 0 \\ -1 \\ 0 \end{Bmatrix} \tag{11.4}$$

In general, there are two different approaches towards developing an active vibration control system for any application – the feedforward approach and the feedback approach (Hansen and Snyder, 1997). Feedforward control involves feeding a signal related to the disturbance input into the controller which then generates a signal to drive a control actuator in such a way as to cancel the disturbance. On the other hand, feedback control uses signals measured from the system response to a disturbance to drive a control actuator so as to attenuate the response. Theoretically, a feedforward control system can provide superior performance than feedback control. However, a major limitation with feedforward control is that a signal that is well correlated with the distrubance input needs to be available to the controller. Since this is often impractical, feedback controllers have a much larger range of applications. In this chapter, only feedback control strategies will be considered, since obtaining a reference signal related to the road disturbance still remains impractical.

11.2   ACTIVE CONTROL : TRADE-OFFS AND LIMITATIONS

11.2.1   Transfer functions of interest

The following three transfer functions are of interest and their attenuation will be used to judge the effectiveness of the suspension system:

a) Acceleration transfer function

$$H_A(s) = \frac{\ddot{z}_s(s)}{\dot{z}_r(s)} \tag{11.5}$$

b) Rattle Space transfer function

$$H_{RS}(s) = \frac{z_s(s) - z_u(s)}{\dot{z}_r(s)} \tag{11.6}$$

c) Tire deflection transfer function

$$H_{TD}(s) = \frac{z_u(s) - z_r(s)}{\dot{z}_r(s)} \tag{11.7}$$

11.2.2   Use of the LQR formulation and its Relation to H_2-optimal control

Consider the following plant

$$\dot{x} = Ax + B_1 d + B_2 u \quad A \in R^{n \times n}, B_1 \in R^n, B_2 \in R^n \tag{11.8}$$

$$z = C_1 x + D_{12} u \quad C_1 \in R^{m \times n}, D_{12} \in R^{m \times 1} \tag{11.9}$$

where $d \in R$ is a disturbance input, assumed to be zero-mean white noise of unit intensity, $u \in R$ is the control input and the variables in $z \in R^m$ constitute the ones to be minimized. In the case of the active suspension problem, the variables in z consist of the sprung mass acceleration, the

suspension deflection and the tire deflection. Assume that the pair (A, C_1) is detectable, the pair (A, B_2) is stabilizable and that $D_{12}{}^T D_{12} > 0$.

If the control design problem for the above system is posed as that of minimizing the variance of the output z, for the input d being white noise, then this control design problem is called the H_2 optimal control problem (Levine, 1996).

It turns out that the solution to the H_2 optimal control problem is the same as the solution to the linear quadratic regulator (LQR) problem (Levine, 1996). In the LQR problem, the controller is to be designed so that the following performance index is minimized:

$$J = \int_0^\infty z^T z\, dt = \int_0^\infty \left[x^T C_1{}^T C_1 x + 2 x^T C_1{}^T D_{12} u + u^T D_{12}{}^T D_{12} u \right] dt \qquad (11.10)$$

for all initial conditions $x_0 = x(0)$.

The solution to the LQR problem is

$$
\begin{aligned}
u &= -\left(D_{12}{}^T D_{12} \right)^{-1} B_2{}^T P x - \left(D_{12}{}^T D_{12} \right)^{-1} \left(C_1{}^T D_{12} \right)^T x \\
&= -\left(D_{12}{}^T D_{12} \right)^{-1} \left[B_2{}^T P + \left(C_1{}^T D_{12} \right)^T \right] x
\end{aligned} \qquad (11.11)
$$

with the matrix P being given by the positive semi-definite solution to the Riccati equation

$$A^T P + PA + C_1{}^T C_1 - (B_2{}^T P + D_{12}{}^T C_1)^T \left(D_{12}{}^T D_{12} \right)^{-1} (B_2{}^T P + D_{12}{}^T C_1) = 0 \qquad (11.12)$$

The optimal value of the performance index with the above control input is

$$J_{opt} = x_0{}^T P x_0 \qquad (11.13)$$

In this chapter, the LQR solution of equation (11.11) will be used as the solution to the H_2 optimal control problem of minimizing the variance of the variables z in the presence of the white noise disturbance d.

11.2.3   LQR formulation for active suspension design

The original research on which the results presented in sections 11.2 – 11.7 of this chapter are largely based are credited to the doctoral dissertation of Tetsuro Butsuen (Butsuen, 1989).

Define the following quadratic performance index.

$$J = \left[\int_0^\infty \ddot{z}_s^{\,2} + \rho_1(z_s - z_u)^2 + \rho_2\dot{z}_s^{\,2} + \rho_3(z_u - z_r)^2 + \rho_4\dot{z}_u^{\,2}\,dt \right] \quad (11.14)$$

where the weighting factors ρ_1, ρ_2, ρ_3 and ρ_4 can be chosen so as to emphasize appropriate variables of interest.

The performance index J can be put into the standard matrix form of equation (11.10) as follows (Butsuen, 1989). We have

$$\ddot{z}_s^{\,2} = \frac{1}{m_s^{\,2}}[k_s^{\,2}x_1^{\,2} + b_s^{\,2}x_2^{\,2} + b_s^{\,2}x_4^{\,2} + F_a^{\,2} + 2k_sb_sx_1x_2 - 2k_sb_sx_1x_4$$
$$- 2b_s^{\,2}x_2x_4 - 2k_sx_1F_a - 2b_sx_2F_a + 2b_sx_4F_a]$$

Hence

$$\ddot{z}_s^{\,2} + \rho_1(z_s - z_u)^2 + \rho_2\dot{z}_s^{\,2} + \rho_3(z_u - z_r)^2 + \rho_4\dot{z}_u^{\,2} =$$
$$x^T Q x + 2x^T N F_a + F_a^T R F_a$$

where

$$Q = \begin{bmatrix} \dfrac{k_s^{\,2}}{m_s^{\,2}} + \rho_1 & \dfrac{b_sk_s}{m_s^{\,2}} & 0 & -\dfrac{b_sk_s}{m_s^{\,2}} \\[2mm] \dfrac{b_sk_s}{m_s^{\,2}} & \dfrac{b_s^{\,2}}{m_s^{\,2}} + \rho_2 & 0 & -\dfrac{b_s^{\,2}}{m_s^{\,2}} \\[2mm] 0 & 0 & \rho_3 & 0 \\[2mm] -\dfrac{b_sk_s}{m_s^{\,2}} & -\dfrac{b_s^{\,2}}{m_s^{\,2}} & 0 & \dfrac{b_s^{\,2}}{m_s^{\,2}} + \rho_4 \end{bmatrix}, \quad N = \begin{Bmatrix} -\dfrac{k_s}{m_s^{\,2}} \\[2mm] -\dfrac{b_s}{m_s^{\,2}} \\[2mm] 0 \\[2mm] \dfrac{b_s}{m_s^{\,2}} \end{Bmatrix} \quad \text{and}$$

$$R = \frac{1}{m_s^{\,2}}.$$

The performance index is then written as

$$J = \left[\int_0^\infty \left(x^T Q x + 2 x^T N u + u^T R u \right) dt \right] \tag{11.15}$$

Along the lines of the solution discussed in equation (11.11), the solution to the optimal control problem that minimizes this performance index is a state feedback law $F_a = -Gx$ where the feedback gain G is determined by solving the following Riccati equation

$$\left(A - B R^{-1} N \right)^T P + P \left(A - B R^{-1} N \right) + \left(Q - N^T R^{-1} N \right) - P B R^{-1} B^T P = 0 \tag{11.16}$$

$$G = R^{-1} \left(B^T P + N \right) \tag{11.17}$$

The gain matrix G in equation (11.17) consists of two parts: $R^{-1} B^T P$ and $R^{-1} N$. Note that $R^{-1} N$ does not depend on the solution to the Riccati equation (11.16). It also does not depend on the weights ρ_1, ρ_2, ρ_3 and ρ_4 used in the performance index. It turns out that (Butsuen, 1989)

a) the first term $R^{-1} B^T P$ depends on the choice of the weights ρ_1, ρ_2, ρ_3 and ρ_4 used in the performance index

b) the second term $R^{-1} N$ exactly cancels out the passive force $k_s x_1 + b_s (x_2 - x_4)$ due to the passive spring and damper.

Hence the total force that acts on the sprung and unsprung masses in the case of this control system is independent of the passive elements k_s and b_s. Even if the passive elements were changed in value, the optimal feedback gains would not change since the force due to the passive elements is canceled out by the $R^{-1} N$ part of the control law.

11.2.4   Performance studies of the LQR controller

The performance of the LQR controller has been studied for different values of the weights ρ_1, ρ_2, ρ_3 and ρ_4 (Butsuen, 1989). The sprung mass acceleration can be heavily penalized without penalizing any of the other variables in the performance index by choosing the weights on the other
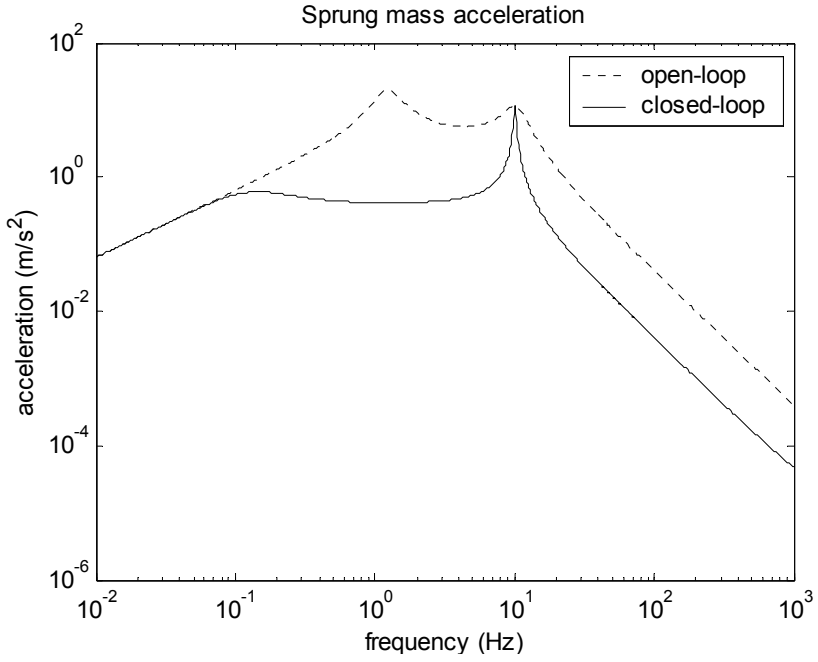
Figure 11-2. Sprung mass acceleration with heavily weighted ride quality
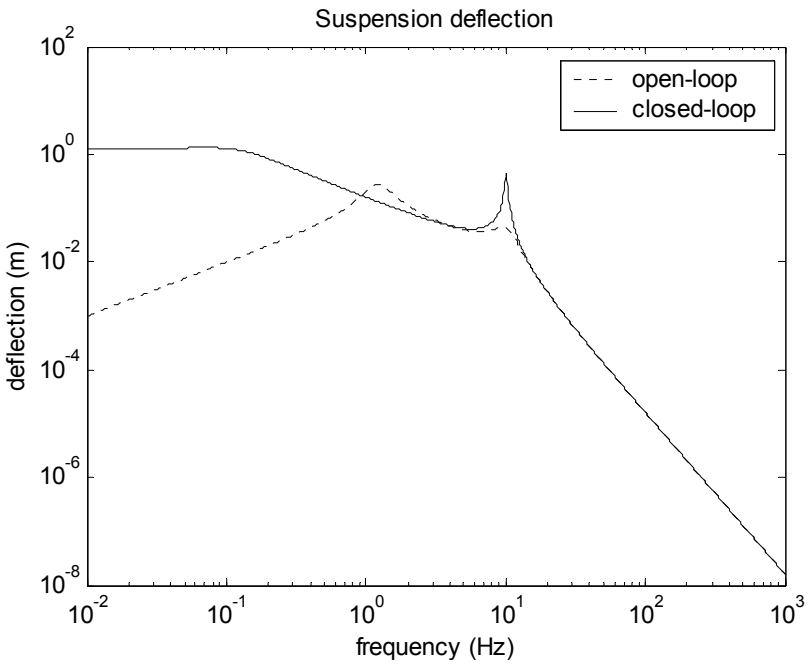

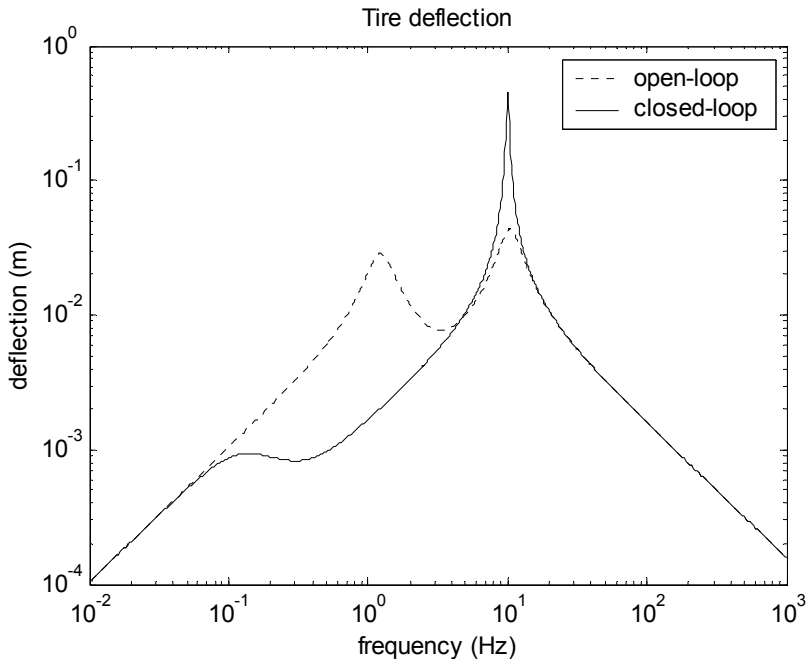*Figure 11-3.* Suspension deflection with heavily weighted ride quality

Figure 11-4. Tire deflection with heavily weighted ride quality

variables to be very small: ρ_1=0.4, ρ_2=0.16, ρ_3=0.4 and ρ_4 = 0.16. The performance of the corresponding controller can be seen in the following figures (Figures 11-2, 11-3 and 11-4). One can see that the sprung mass acceleration is reduced considerably over a broad frequency range. However, its value is unchanged compared to the passive suspension at one particular frequency - the unpsrung mass resonant frequency of 10 Hz. No matter how heavily the sprung mass acceleration is weighted, its performance cannot be improved at that frequency.

For these weights the suspension deflection and tire deflection transfer functions are considerably worse than that of the passive suspension at the unsprung resonant frequency. Also, the suspension deflection transfer function has a constant asymptote at low frequencies which is considerably worse than that of the passive suspension.

The following plots (Figures 11-5, 11-6 and 11-7) show performance using a LQR controller in which the sprung mass acceleration (ride quality) was more heavily weighted and the other states were less weighted. The weights used were ρ_1=400, ρ_2=16, ρ_3=400 and ρ_4 = 16 (Butsuen, 1989).

One can see that the sprung mass acceleration is considerably reduced at the sprung mass resonant frequency of 1 Hz. However, no improvement in
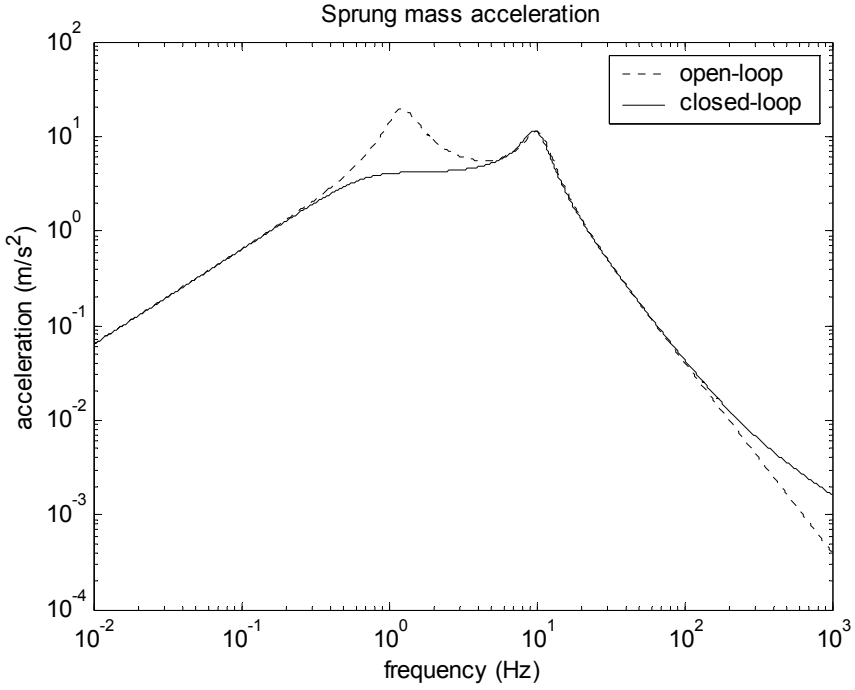
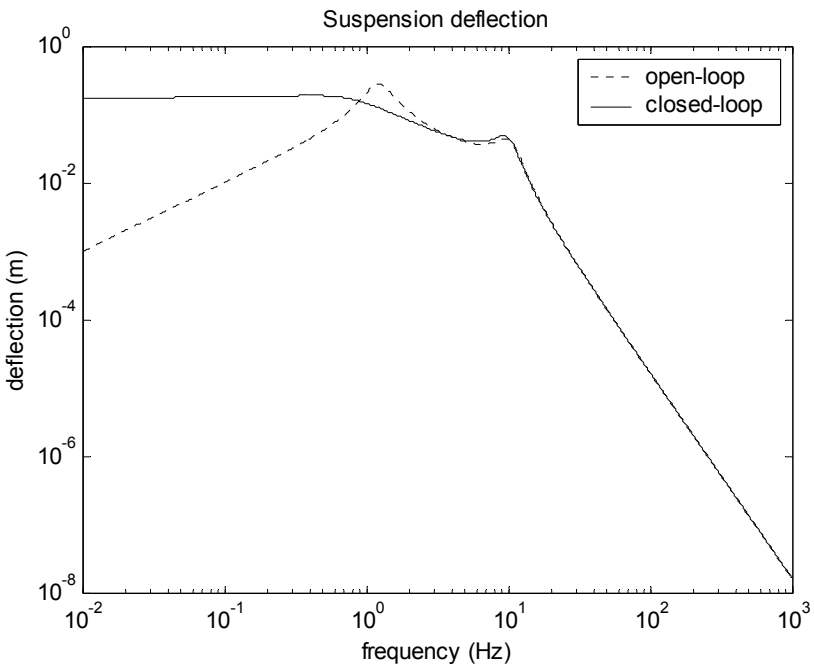*Figure 11-5.* Sprung mass acceleration with moderately weighted ride quality

Figure 11-6. Suspension deflection with moderately weighted ride quality
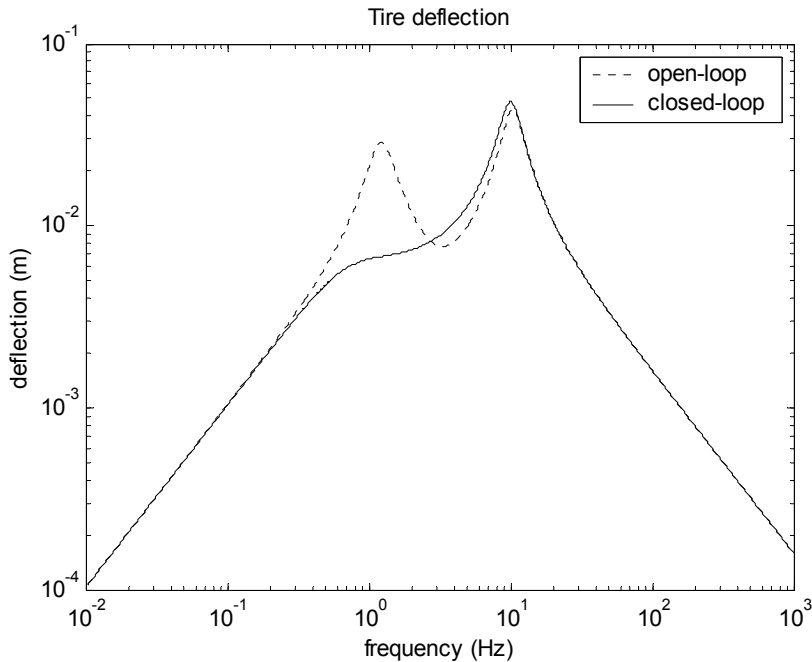
Figure 11-7. Tire deflection with moderately weighted ride quality

ride quality is obtained at the unsprung mass resonant frequency compared to the passive suspension. Further, at high frequencies, the above LQR controller results in a roll off at 20 dB/dec instead of 40 dB/dec in the sprung mass acceleration transfer function. This high frequency "harshness" can potentially be eliminated by introducing a low-pass filter into the controller transfer function. The suspension deflection is considerably *increased* at low frequencies compared to the passive suspension. The tire deflection is reduced at the sprung mass frequency but unchanged at the unsprung mass frequency.

The following plots (Figures 11-8, 11-9 and 11-10) show performance using a controller designed with LQR in which suspension deflection and tire deflection were heavily weighted while sprung mass acceleration (ride quality) was less weighted. The weights used were $\rho_1 = 10,000$, $\rho_2 = 100$, $\rho_3 = 100,000$ and $\rho_4 = 100$.

We see that the mid and high frequency performance of the sprung mass acceleration transfer function is considerably worse than that of the passive suspension. The high frequency roll off is slower. Some improvement is obtained, however, at the sprung mass frequency. The suspension deflection transfer function is improved at both the sprung and unsprung mass natural frequencies. However, its performance at low frequencies is poor. The tire deflection transfer function is improved at both resonant frequencies.
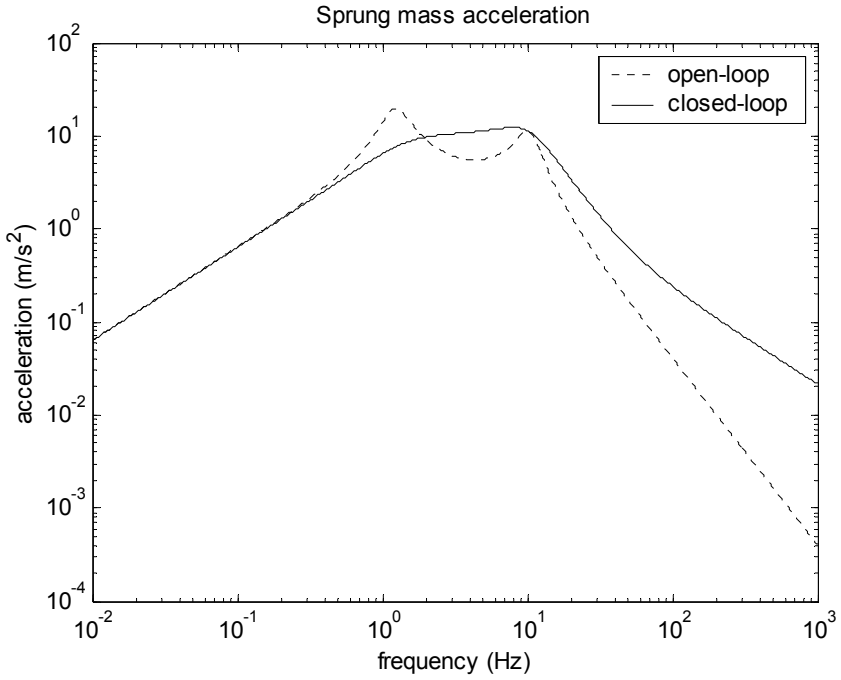
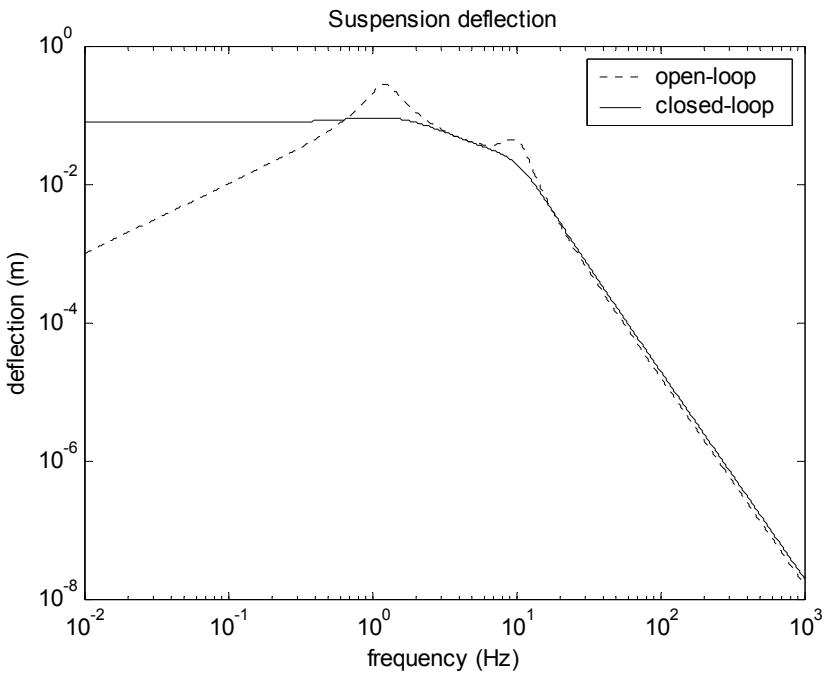*Figure 11-8.* Sprung mass acceleration with heavily weighted suspension and tire deflections

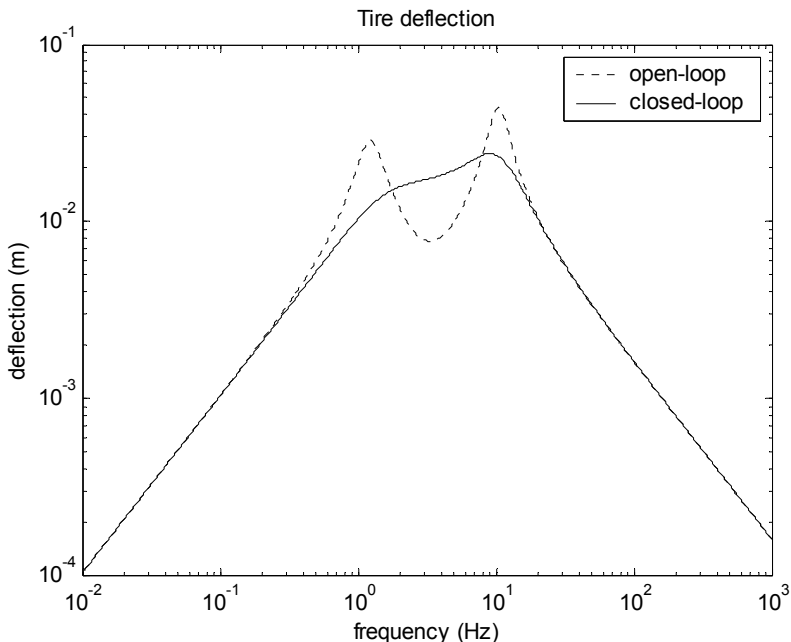*Figure 11-9.* Suspension deflection with heavily weighted suspension and tire deflections

Figure 11-10. Tire deflection with heavily weighted suspension and tire deflections

The performance results obtained from the LQR controller can be understood from an analysis of the active system asymptotes (section 11.3 of this book) and from an analysis of the "invariant points" of the system (section 11.4).

11.3   ACTIVE SYSTEM ASYMPTOTES

Consider the full-state feedback law written in the following form:

$$F_a = -g_1(z_s - z_u) - g_2\dot{z}_s - g_3(z_u - z_r) - g_4\dot{z}_u \qquad (11.18)$$

By substituting equation (11.18) in equations (11.1) and (11.2), taking Laplace transforms and solving, the following closed-loop transfer functions can be derived in terms of the feedback gains g_1, g_2, g_3 and g_4 (Butsuen, 1989):

$$H_A(s) = \frac{s\left\{ m_u g_3 s^2 + (b_s - g_4)k_t s + (k_s + g_1)k_t \right\}}{d(s)} \qquad (11.19)$$

$$H_{RS}(s) = \frac{s\{g_3 m_u - (k_t - g_3)m_s\} - (g_2 + g_4)k_t}{d(s)} \qquad (11.20)$$

$$H_{TD}(s) =$$
$$\frac{m_u m_s s^3 + \{(b_s - g_4)m_s + (b_s + g_2)m_u\}s^2 + (k_s + g_1)(m_u + m_s)s}{d(s)} \qquad (11.21)$$

where

$$\begin{aligned}
d(s) = {} & m_s m_u s^4 + \{(b_s + g_2)m_u + (b_s - g_4)m_s\}s^3 \\
& + \{(k_s + g_1)m_u + (k_t + k_s + g_1 - g_3)m_s\}s^2 \\
& + \{(b_s + g_2)k_t\}s + \{(k_s + g_1)k_t\}
\end{aligned}$$

The following asymptotic properties can then be shown (Butsuen, 1989):

Sprung mass acceleration transfer function:

$$\text{Active: } \lim_{s \to 0} H_A(s) = s, \quad \lim_{s \to \infty} H_A(s) = \left(\frac{g_3}{m_s}\right)\frac{1}{s} \qquad (11.22)$$

$$\text{Passive: } \lim_{s \to 0} H_A(s) = s, \quad \lim_{s \to \infty} H_A(s) = \left(\frac{k_t b_s}{m_u m_s}\right)\frac{1}{s^2} \qquad (11.23)$$

The low frequency asymptote is thus independent of both the passive and active suspension parameters. In the case of the active suspension system, the high frequency asymptote depends on the tire deflection feedback gain g_3 and rolls off at 20 dB/decade while in the case of the passive suspension, the high frequency asymptote rolls off at 40 dB/decade. The use of tire deflection feedback thus results in high frequency "harshness" in the ride.

Suspension deflection transfer function:

Active:

$$\lim_{s \to 0} H_{RS}(s) = -\frac{g_2 + g_4}{k_s + g_1}$$

$$\lim_{s \to \infty} H_{RS}(s) = \left(\frac{g_3 m_u - (k_t - g_3)m_s}{m_u m_s} \right) \frac{1}{s^3} \tag{11.24}$$

Passive:

$$\lim_{s \to 0} H_{RS}(s) = -\frac{m_s s}{k_s}, \quad \lim_{s \to \infty} H_{RS}(s) = -\left(\frac{k_t}{m_u} \right) \frac{1}{s^3} \tag{11.25}$$

The high frequency asymptotes for the passive and active suspensions have the same roll-off rate but the low frequency roll-off characteristics are entirely different. Equation (11.24) shows a general property that full state feedback and absolute velocity feedback laws have, that of a constant low frequency asymptote whereas the passive system decreases at low frequencies.

Tire deflection transfer function:

$$\text{Active}: \lim_{s \to 0} H_{TD}(s) = -\frac{(m_s + m_u)s}{k_t}, \quad \lim_{s \to \infty} H_{TD}(s) = -\frac{1}{s} \tag{11.26}$$

$$\text{Passive}: \lim_{s \to 0} H_{TD}(s) = -\frac{(m_s + m_u)s}{k_t}, \quad \lim_{s \to \infty} H_{TD}(s) = -\frac{1}{s} \tag{11.27}$$

It can be seen that both the low and high frequency asymptotes are independent of the active suspension force.

11.4 INVARIANT POINTS AND THEIR INFLUENCE ON THE SUSPENSION PROBLEM

Adding equations (11.1) and (11.2), one obtains

$$m_s \ddot{z}_s + m_u \ddot{z}_u + k_t(z_u - z_r) = 0 \tag{11.28}$$

Equation(11.28) is independent of both the passive and active suspension forces! This is the basic invariant equation for this vibration isolation problem and many interesting conclusions can be drawn from it (Butsuen, 1989). The Laplace transform of equation (11.28), assuming zero initial conditions, is

$$m_s \ddot{z}_s(s) + (k_t + m_u s^2) z_u(s) = k_t z_r(s) \tag{11.29}$$

In terms of the acceleration, suspension deflection and tire deflection transfer functions defined in equations (11.5), (11.6) and (11.7), the following relations can be obtained on setting $s = j\omega$

$$m_s H_A(j\omega) + \left(k_t - m_u \omega^2\right) H_{TD}(j\omega) = -jm_u \omega \tag{11.30}$$

$$-m_s \omega^2 H_{RS}(j\omega) - \left(k_t - (m_s + m_u)\omega^2\right) H_{TD}(j\omega) = -j\left(m_s + m_u\right)\omega \tag{11.31}$$

$$\omega^2\left(k_t - m_u \omega^2\right) H_{RS}(j\omega) + \left(k_t - (m_s + m_u)\omega^2\right) H_A(j\omega) = j\omega k_t \tag{11.32}$$

Equations (11.30), (11.31) and (11.32) point out the fact that once one of the three transfer functions is determined, then the other two are determined by the constraint equations. This is true, irrespective of what the passive and active suspension forces are. This sheds light on why the LQR solution can be used to significantly improve any one of the three transfer functions over a broad frequency band, but typically at the cost of deterioration in the other two transfer functions.

Equations (11.30), (11.31) and (11.32) can also be used to understand why the acceleration and suspension deflection transfer functions contain "invariant points" i.e. frequencies at which the closed-loop transfer function is the same as the open-loop passive transfer function, no matter how the active suspension forces are chosen. From equation (11.30), we see that the acceleration transfer function $H_A(s)$ has an invariant point at

$$\omega_{inv\_1} = \sqrt{\frac{k_t}{m_u}} \tag{11.33}$$

and

$$H_A(j\omega_{inv\_1}) = j\frac{\sqrt{m_u k_t}}{m_s} \tag{11.34}$$

From equation (11.31), it can be seen that the rattle space transfer function has an invariant point at

$$\omega_{inv\_2} = \sqrt{\frac{k_t}{m_s + m_u}} \tag{11.35}$$

and

$$H_{RS}(j\omega_{inv\_2}) = j\frac{m_s + m_u}{m_u}\sqrt{\frac{m_s + m_u}{k_t}} \tag{11.36}$$

From equations (11.30) and (11.31), it can be seen that the tire deflection transfer function does not possess any invariant points, except at $\omega = 0$ $\left(H_{TD}(0) = 0\right)$.

Since the invariant point ω_{inv_1} occurs at a frequency approximately equal to the unsprung mass natural frequency, this explains why the acceleration cannot be improved at unsprung mass frequency (The unsprung mass frequency is approximately given by $\sqrt{\dfrac{k_t}{m_u}}$). No matter how the value of the suspension stiffness k_s is chosen or how the active suspension control law is chosen, the acceleration transfer function will not change at the unsprung mass frequency.

11.5   ANALYSIS OF TRADE-OFFS USING INVARIANT POINTS

The constraint equations (11.28), (11.29) and (11.30) can be used to shed light on why the LQR solution can significantly improve any one of the three transfer functions over a broad frequency band, but typically only at the cost of deterioration in the other two transfer functions. This is because once one of the three transfer functions is determined, then the other two are determined by the constraint equations.

The results presented in this section were initially obtained by Tetsuro Butsuen (Butsuen, 1989).

11.5.1   Ride quality/ road holding trade-offs

Equation (11.30) can be re-written as (Butsuen, 1989)

$$H_A(j\omega) = \alpha_1(\omega)H_{TD}(j\omega) - jr_1\omega \tag{11.37}$$

where

$$\alpha_1(\omega) = r_1\left(\omega^2 - {\omega_{inv\_1}}^2\right) \tag{11.38}$$

$$\omega_{inv\_1} = \sqrt{\frac{k_t}{m_u}} \text{ and } r_1 = \frac{m_u}{m_s} \tag{11.39}$$

Any change $\delta H_A(j\omega)$ to the ride quality transfer function results in a change $\delta H_{TD}(j\omega)$ in the tire deflection transfer function. From equation (11.37), the relation between $\delta H_A(j\omega)$ and $\delta H_{TD}(j\omega)$ can be written as

$$H_A(j\omega) + \delta H_A(j\omega) = \alpha_1(\omega)H_{TD}(j\omega) + \alpha_1(\omega)\delta H_{TD}(j\omega) - jr_1\omega \tag{11.40}$$

Hence

$$\delta H_A(j\omega) = \alpha_1(\omega)\delta H_{TD}(j\omega) \tag{11.41}$$

If

$$\delta H_A(j\omega) = -\varepsilon H_A(j\omega) \tag{11.42}$$

then (Butsuen, 1989)

$$\delta H_{TD}(j\omega) = -\frac{\varepsilon H_A(j\omega)}{\alpha_1(\omega)} = -\frac{\varepsilon}{\alpha_1(\omega)}\left[\alpha_1(\omega)H_{TD}(j\omega) - jr_1\omega\right] \text{ or}$$

$$\delta H_{TD}(j\omega) = -\varepsilon H_{TD}(j\omega) + \frac{\varepsilon}{\alpha_1(\omega)}jr_1\omega \tag{11.43}$$

At low frequencies ($\omega << \omega_{inv\_1}$), the second term in equation (11.43) is negligible. $\frac{\varepsilon jr_1\omega}{r_1(\omega^2 - {\omega_{inv\_1}}^2)} \approx \frac{\varepsilon j\omega}{-{\omega_{inv\_1}}^2} \approx 0$. The first term dominates.

Hence, at low frequencies, tire deflection can be improved while the sprung mass acceleration is being improved. Thus both tire deflection and sprung

mass acceleration can be improved at low frequencies. (e.g. by choosing ε equal to 0.9).

At high frequencies $\dfrac{\varepsilon_1\omega}{\omega^2 - \omega_{inv\_1}^2}$ becomes very big at frequencies close

to ω_{inv_1}. Acceleration is impossible to improve at $\omega = \omega_{inv\_1}$. At frequencies ω just above ω_{inv_1}, acceleration can be improved (for example, by penalizing acceleration only in LQR). However, this will result in a dramatic deterioration in tire deflection.

11.5.2   Ride quality/ rattle space trade-offs

As shown in Butsuen (1989), equation (11.32) can be re-written as

$$H_A(j\omega) = -\frac{\omega^2\left(k_t - m_u\omega^2\right)}{k_t - (m_s + m_u)\omega^2} H_{RS}(s) + \frac{j\omega k_t}{k_t - (m_s + m_u)\omega^2} \quad (11.44)$$

Hence

$$H_A(j\omega) = \alpha_2(\omega)H_{RS}(s) + \frac{j\omega\omega_{inv\_2}^2}{\omega_{inv\_2}^2 - \omega^2} \quad (11.45)$$

where

$$\alpha_2(\omega) = -\frac{m_u}{m_s + m_u}\frac{\omega^2(\omega^2 - \omega_{inv\_1}^2)}{\omega^2 - \omega_{inv\_2}^2} \quad (11.46)$$

Hence

$$\delta H_A(j\omega) = \alpha_2(\omega)\delta H_{RS}(j\omega) \quad (11.47)$$

Let

$$\delta H_A(j\omega) = -\varepsilon H_A(j\omega) \quad (11.48)$$

Then

$$\delta H_{RS}(j\omega) = -\varepsilon H_{RS}(j\omega) - \varepsilon\left(\frac{m_s}{m_u}+1\right)\frac{j\omega_{inv\_2}{}^2}{\omega\left(\omega^2 - \omega_{inv\_1}{}^2\right)} \qquad (11.49)$$

Thus as $\omega \to 0$ and as $\omega \to \omega_{inv\_1}$ $(\omega > \omega_{inv\_1})$, $\delta H_{RS}(j\omega)$ is dominated by the second term. Hence improvements in acceleration at low frequencies and at frequencies above the unsprung mass resonant frequency $(\omega > \omega_{inv\_1})$ can only be obtained with deterioration in rattle space.

11.6   CONCLUSIONS ON ACHIEVABLE ACTIVE SYSTEM PERFORMANCE

From the results in the previous sections, we see that the following perform-ance limitations will exist for state feedback control, irrespective of the values of the state feedback gains used :

1) The acceleration transfer function has an invariant point at the unsprung mass frequency $\omega_{inv\_1} = \sqrt{\dfrac{k_t}{m_u}}$. The ride quality cannot be improved by state feedback at this frequency. High weights on the sprung mass acceleration in the performance index result in deterioration of tire and suspension deflection performances at the unsprung mass frequency without any corresponding improvement in ride quality.
2) The use of tire deflection feedback results in the acceleration transfer function rolling off at 20 dB/decade unlike the passive system which rolls off at 40 dB/decade. This results in high requency harshness in the ride.
3) The active suspension deflection transfer function will have a constant low frequency asymptote which results in higher suspension deflection values compared to the passive system at very low frequencies. This constant low frequency asymptote will exist as long as the feedback gains on sprung and unsprung mass velocity are non-zero.
4) The suspension deflection transfer function has an invariant point at about 4 Hz $\omega_{inv\_2} = \sqrt{\dfrac{k_t}{(m_s + m_u)}}$. The suspension deflection cannot be improved at this frequency by active control.

5) Improvements in tire deflection at the unsprung mass natural frequency can only be obtained at the expense of increased sprung mass acceleration.

In order to improve ride quality without deterioration in the suspension deflection and tire deflection transfer functions, the best one can do is

1) Achieve significant reduction in sprung mass acceleration at the sprung mass frequency.
2) Simultaneously achieve significant reduction in suspension deflection and tire deflection at the sprung mass natural frequency.
3) Avoid any deterioration in all three transfer functions at the unsprung mass natural frequency.
4) Avoid high frequency harshness by ensuring that the sprung mass acceleration rolls off at 40 dB/decade at high frequencies.
5) If possible, ensure that the suspension deflection transfer function does not have a constant low frequency asymptote.

11.7 PERFORMANCE OF A SIMPLE VELOCITY FEEDBACK CONTROLLER

Since very little performance improvement can be obtained at the unsprung mass resonant frequency (10 Hz), it might be best to concentrate on improving performance at the sprung mass resonant frequency (1.2 Hz). Almost all of the performance improvement at the sprung mass resonant frequency can be obtained by using a simple velocity feedback control law, also known as "sky-hook" damping, defined as follows (Karnopp, 1986):

$$F_a = -k_2 \dot{z}_s \tag{11.50}$$

This control law is simpler, does not require full-state feedback and provides almost all the performance improvement that the earlier full state feedback LQR control law could provide. Note that the absolute (i.e. inertial) sprung mass velocity is being used in the skyhook damping control law.

The figures (Figures 11-11, 11-12 and 11-13) show the performance of this sky-hook damping control law. A feedback gain of $k_2 = 4000$ was used. Note that the slower roll-off at high frequencies in the ride quality transfer function is eliminated by the sky-hook damping controller.
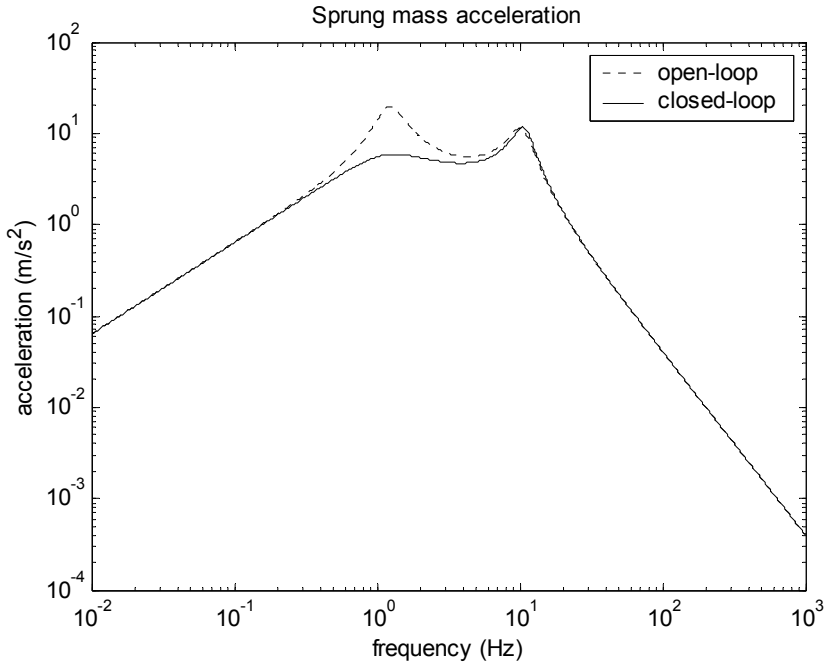
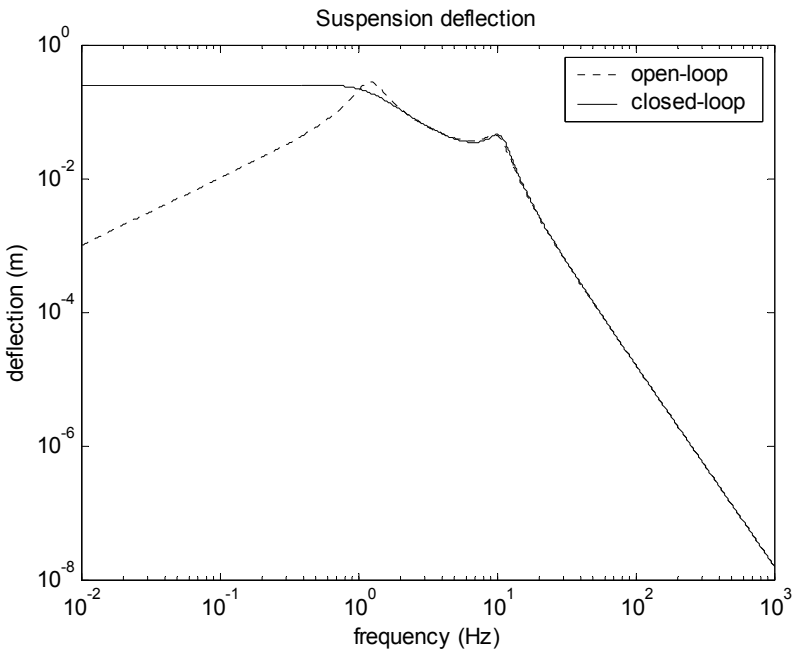*Figure 11-11*. Sprung mass acceleration with sky-hook damping

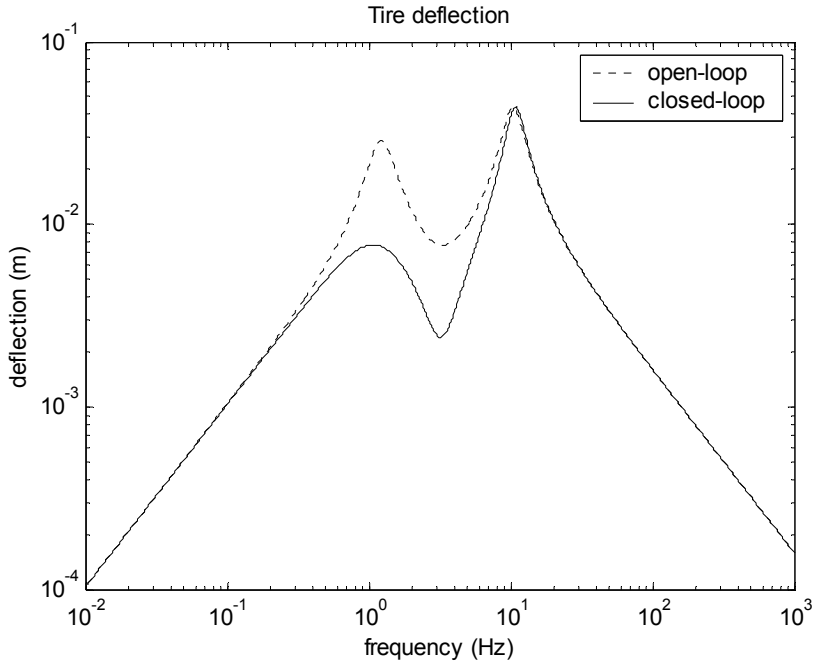*Figure 11-12*. Suspension deflection with sky-hook damping

Figure 11-13. Tire deflection with sky-hook damping

11.8 HYDRAULIC ACTUATORS FOR ACTIVE SUSPENSIONS

In all of the analysis so far, the active suspension control system has been designed assuming that the force F_a is the control input. Spool valve controlled electro-hydraulic actuators are often used to provide the force F_a.

Several papers in literature have focused on the control of a electro-hydraulic actuator to track a desired force specified by an active suspension controller of the type discussed in sections 11.2 – 11.7 (Rajamani and Hedrick, 1994, Rajamani and Hedrick, 1995, Chantranuwathanl and Peng, 1999, Liu and Alleyne, 2000, Zhang and Alleyne, 2001).

The dynamics of a spool valve controlled hydraulic actuator can be approximated by (Rajamani and Hedrick, 1994)

$$\dot{F}_a = \alpha A_p C_d w u \sqrt{\frac{P_s - \text{sgn}(u)\dfrac{F_a}{A_p}}{\rho}} - \alpha A_p{}^2 \left(\dot{z}_s - \dot{z}_u \right) \tag{11.51}$$

Here F_a is the suspension force provided by the actuator while u is the spool valve movement from equilibrium and constitutes the control input for controlling the hydraulic actuator. The other parameters in the equation are as follows –

a) the parameter α is defined as $\alpha = \dfrac{4\beta}{V_t}$ where V_t is the total

hydraulic cylinder volume and is equal to $2V_0$ where V_0 is the equilibrium volume of each chamber of the cylinder.
b) β is the bulk modulus of the hydraulic fluid.
c) C_d discharge coefficient of the spool valve.
d) w is the spool valve width.
e) A_p is the piston area.

Assume that the desired suspension force is denoted by F_{des}. This is typically a force determined by an LQR controller or by a sky-hook damping controller of the type discussed in sections 11.2 – 11.7. The goal then is to determine a control law for the spool valve input u that ensures that the desired suspension force is tracked.

The sliding surface control methodology or other nonlinear control design methods can be used to ensure tracking of the desired suspension force (Rajamani and Hedrick, 1994, Liu and Alleyne, 2000).

Define the surface

$$s = F_a - F_{a\_des} \tag{11.52}$$

Differentiate equation (11.52) to obtain

$$\dot{s} = \alpha A_p C_d wu \sqrt{\frac{P_s - \operatorname{sgn}(u)\dfrac{F_a}{A_p}}{\rho}} - \alpha A_p{}^2 (\dot{z}_s - \dot{z}_u) - \dot{F}_{a\_des} \tag{11.53}$$

Convergence to the surface $s = 0$ can be ensured if the closed-loop dynamics for the surface are $\dot{s} = -\eta s$. Set $\dot{s} = -\eta s$ to get

$$\alpha A_p C_d wu \sqrt{\frac{P_s - \operatorname{sgn}(u)\dfrac{F_a}{A_p}}{\rho}} = -\eta s + \alpha A_p{}^2 (\dot{z}_s - \dot{z}_u) + \dot{F}_{a\_des}$$

Hence, the following control law can be used to ensure convergence to the surface $s = 0$

$$u = = \frac{\left(-\eta s + \alpha A_p^{\;2}\left(\dot{z}_s - \dot{z}_u\right) + \dot{F}_{a\_des}\right)}{\alpha A_p C_d w \sqrt{\dfrac{P_s - \text{sgn}(u)\dfrac{F_a}{A_p}}{\rho}}} \tag{11.54}$$

Note that $\text{sgn}(u)$ appears in the denominator of equation (11.54). Thus u appears both on the left hand side and the right hand side of this equation. The value of $\text{sgn}(u)$ is determined by the sign of the numerator in equation (11.54). Hence the value of the numerator is calculated first. If this value is negative, then $\text{sgn}(u)$ takes on a value of -1. If the value of the numerator is positive then $\text{sgn}(u)$ takes on a value of +1. The denominator of equation (11.54) is then calculated using the correct value of $\text{sgn}(u)$.

Considerable literature can be found on the dynamics and control of hydraulic actuators for active automotive suspensions. The reader is referred to Rajamani and Hedrick (1994), Rajamani and Hedrick (1995), Chantranuwathanl and Peng (1999), Liu and Alleyne (2000), Zhang and Alleyne (2001) and the references found therein.

11.9   CHAPTER SUMMARY

This chapter discussed control system design for active suspension systems using quarter car suspension models. The LQR formulation was used for control design. The relation between LQR and H_2-optimal control for disturbance rejection was also discussed.

The three transfer functions of interest for the quarter car system were the ride quality, suspension deflection and tire deflection transfer functions. The influence of a variety of different weighting factors in the LQR performance index on these three transfer functions under closed-loop active control was studied.

The suspension system was shown to have two invariant points – one each for the ride quality and the suspension deflection transfer functions. The analysis of these invariant points helped understand the limitations of achievable performance with any active suspension control system. It was found that in order to improve ride quality without deterioration in the

suspension deflection and tire deflection transfer functions, the best that could be achieved is as follows:

1) Achieve significant reduction in sprung mass acceleration at the sprung mass frequency.
2) Simultaneously achieve significant reduction in suspension deflection and tire deflection at the sprung mass natural frequency.
3) Avoid any deterioration in all three transfer functions at the unsprung mass natural frequency.
4) Avoid high frequency harshness by ensuring that the sprung mass acceleration rolls off at 20 dB/decade at high frequencies.
5) If possible, ensure that the suspension deflection transfer function does not have a constant low frequency asymptote.

Section 11.7 showed that the "sky-hook damping" controller provides almost all of the achievable performance described above. The sky-hook damping controller can therefore be effectively used in place of a full state feedback controller.

NOMENCLATURE

z_s	sprung mass displacement
z_u	unsprung mass displacement
z_r	road profile input
m_s	sprung mass
m_u	unsprung mass
k_s	suspension stiffness
b_s	suspension damping
k_t	tire stiffness
F_a	active suspension actuator force
s	Laplace transform variable
$H_A(s)$	sprung mass acceleration transfer function
$H_{RS}(s)$	suspension deflection transfer function
$H_{TD}(s)$	tire deflection transfer function
A, B, L	matrices used in state space model of quarter car suspension

x	state space vector
A, B_1, B_2	matrices used in explanation of H_2-optimal control
C_1, D_{12}	matrices used in explanation of H_2-optimal control
J	LQR performance index
Q, R, N	matrices used in LQR performance index
ρ_1, ρ_2, ρ_3, ρ_4	weights used in LQR performance index for active suspension system
G	feedback gain matrix from LQR solution
g_1, g_2, g_3, g_4	feedback gains from LQr solution
ω_{inv_1}	invariant point for sprung mass acceleration transfer function
ω_{inv_2}	invariant point for suspension deflection transfer function
$\alpha_1(\omega)$, $\alpha_2(\omega)$, r_1	functions used in the analysis of invariant points

REFERENCES

Butsuen, T., "The Design of Semi-Active Suspensions for Automotive Vehicles," *Ph.D. Dissertation*, M.I.T., 1989.

Chantranuwathanal, S. and Peng, H., "Force Tracking Control for Active Suspensions – Theory and Experiments," Proceedings of the 1999 IEEE International Conference on Control Applications, Kohala Coast-Island of Hawaii, Hawaii, USA, August 22-27, 1999.

Haddad, W.M.R., Hyland, A. and David, C., "Active vibration isolation of multi-degree of freedom systems," *Proceedings of the American Control Conference,* Vol. 6, pp. 3537-3541, 1997.

Hansen, C.H. and Snyder, S.D., *Active Control of Noise and Vibration*, Chapter 12, Chapman and Hall, ISBN 0 419 19390 1, 1997.

Hedrick, J.K. and Butsuen, T., "Invariant properties of automotive suspensions," *Proceedings of the Institution of Mechanical Engineers*, Part D: Transport Engineering. v 204 n 1 1990 p 21-27

Hyde, T.T. and Anderson, E.H., "Actuator with built-in viscous damping for isolation and structural control," *AIAA Journal*, Vol. 34, No. 1, pp. 129-135, Jan 1996.

Karnopp, D., "Theoretical Limitations in Active Vehicle Suspenions," *Vehicle System Dynamics*, Vol. 15, No. 1, pp. 41-54, 1986.

Levine, W.S., Editor, *The Control Handbook*, CRC Press, ISBN 0-8493-8570-9, 1996.

Liu, R. and Alleyne, A., "Nonlinear Force/Pressure Tracking of an Electro-Hydraulic Actuator," ASME Journal of Dynamic Systems, Measurement and Control, Vol. 122, pp. 232-237, March 2000.

Prasad, J.V.R., "Active vibration control using fixed order dynamic compensation with frequency shaped cost functionals," *IEEE Control Systems Magazine*, Vol. 11, pp. 71-78, 1991.

Rajamani, R. and Hedrick, J.K., "Performance of Active Automotive Suspensions with Hydraulic Actuators : Theory and Experiment", *Proceedings of the 1994 American Control Conference*, Baltimore, Maryland, June 29-July 1, 1994, 94CH3390-2, Vol 2, pp. 1214-1218.

Rajamani, R. and Hedrick, J.K., "Adaptive Observers for Active Automotive Suspensions - Theory and Experiment", *IEEE Transactions on Control Systems Technology*, Vol. 3, No.1, pp. 86-93, March 1995.

D. Sciulli, and D.J. Inman, "Isolation design for fully flexible systems," *Journal of Intelligent Material Systems and Structures*," Vol. 10, No. 10, pp. 813-824, October, 2000.

Wilson, D.A., Sharp, R.S. and Hassan, S.A., "Application of Linear Optimal Control Theory to the Design of Active Automotive Suspensions," *Vehicle System Dynamics*, Vol. 15, No. 2, pp. 105-118, 1986.

Yue, C., Butsuen, T. and Hedrick, J.K., "Alternative Control Laws for Automotive Suspensions," *Proceedings of the American Control Conference*, pp. 2373-2378, 1988.

Zhang, Y. and Alleyne, A., "A Novel Approach to Active Vibration Isolation with Electro-hydraulic Actuators," *Proceedings of the ASME International Mechanical Engineering Congress and Exposition*, Paper FPST-25010, New York, 2001.

Chapter 12

SEMI-ACTIVE SUSPENSIONS

12.1   INTRODUCTION

A semi-active suspension system utilizes a variable damper or other variable dissipation component in the automotive suspension. An example of a variable dissipator is a twin tube viscous damper in which the damping coefficient can be varied by changing the diameter of the orifice in a piston.

Figure 12-1 shows the schematic of a twin tube variable orifice damper in which the orifice diameter can be varied with electronic control. As the piston moves inside the cylinder, it causes fluid flow through the orifice. A larger orifice provides less dissipative resistance while a smaller orifice provides increased dissipative resistance.

To use the variable orifice damper as a semi-active actuator, the opening of the orifice is determined in real time by feedback control laws. Thus the damping provided by the device is varied in real time by feedback control.

Another example of a semi-active dissipator is a magneto rheological (MR) damper which uses MR fluid. A MR damper is shown in Figure 12-2. Magnetorheological (MR) fluids are materials that respond to an applied magnetic field with a change in rheological behavior. Typically, this change is manifested by the development of a yield stress that monotonically increases with applied magnetic field. The dissipative force provided by the damper can be controlled by controlling the electromagnetic field.

The dissipative force as a function of velocity across the piston of the MR damper is shown in Figure 12-3 for different values of current in the electromagnetic coil. Thus, with different levels of current, different levels of dissipative force can be obtained.
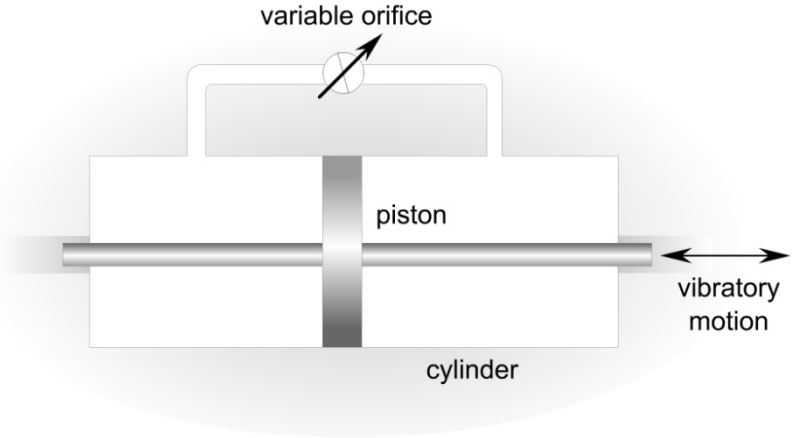
Figure 12-1. Schematic of a variable orifice damper
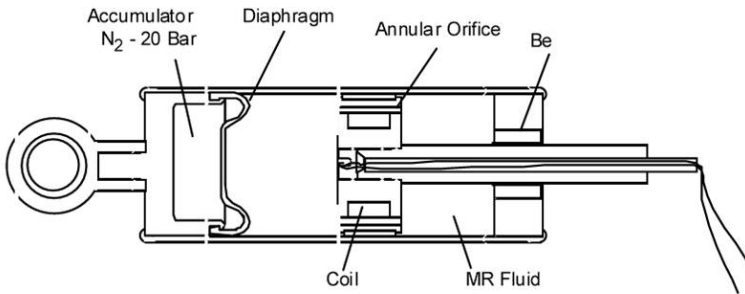
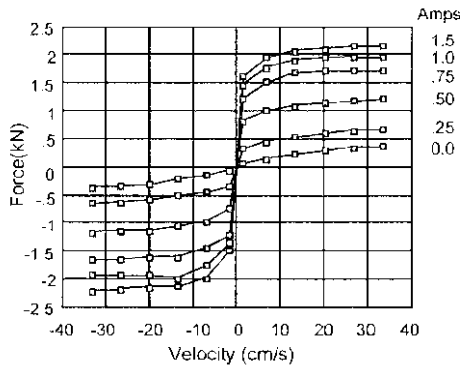*Figure 12-2.* Commercial Linear MR Fluid-based Damper[1]

Figure 12-3. Performance curves for the linear MR damper[2]

---

[1] Figure printed with permission from Jolly, Bender and Carlson (1998)
[2] Figure printed with permission from Jolly, Bender and Carlson (1998)

This chapter focuses on the development of control systems that utilize variable dissipators in the suspension system to improve the performance of the automotive suspension. Such a suspension system that utilizes a variable dissipator which is controlled in real-time is called a semi-active suspension.

Advantages of a Semi-Active Suspension System

Compared to fully active suspension systems, semi-active systems consume significantly less power. The power consumption in a semi-active system is only for purposes of changing the real-time dissipative force characteristics of the semi-active device. For example, power is used to change the area of the piston orifice in a variable opening damper or to change the current in the elecromagnetic coil of a MR damper. External power is not directly used to counter vibratory forces. Another advantage of semi-active systems over active systems is that they cannot cause the suspension system to become unstable. This is due to the fact that they do not actively supply energy to the vibratory suspension system but only dissipate energy from it.

12.2   SEMI-ACTIVE SUSPENSION MODEL

A quarter car semi-active suspension system is shown in Figure 12-4. The variable damper $b_{semi}(t)$ is constrained to be between the following values:

$$0 \leq b_{semi}(t) \leq b_{\max} \tag{12.1}$$

The equations of motion of the two-degree-of-freedom quarter-car suspension shown in Figure 12-4 are

$$m_s \ddot{z}_s + b_s(\dot{z}_s - \dot{z}_u) + k_s(z_s - z_u) = -b_{semi}(t)(\dot{z}_s - \dot{z}_u) \tag{12.2}$$

$$m_u \ddot{z}_u + k_t(z_u - z_r) - b_s(\dot{z}_s - \dot{z}_u) - k_s(z_s - z_u) = b_{semi}(t)(\dot{z}_s - \dot{z}_u) \tag{12.3}$$

The state space model of the quarter-car active automotive suspension system can be written as (Yue, et. al., 1988)

$$\dot{x} = A_0 x + B F_{semi} + L \dot{z}_r \tag{12.4}$$

$$= A_0 x + N x b_{semi} + L \dot{z}_r \tag{12.5}$$

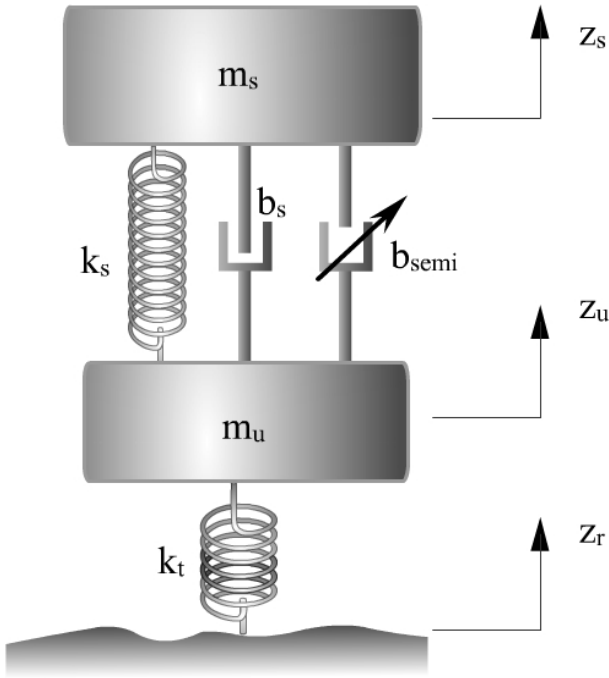$$= A_0 x - B b_{semi}(x_2 - x_4) + L \dot{z}_r \tag{12.6}$$

Figure 12-4. Quarter car semi-active automotive suspension

where the variables are as follows

$x_1 = z_s - z_u$ suspension deflection (rattle space)

$x_2 = \dot{z}_s$ absolute velocity of sprung mass

$x_3 = z_u - z_r$ tire deflection

$x_4 = \dot{z}_u$ absolute velocity of unsprung mass

F_{semi} semi-active force $(= -b_{semi}(\dot{z}_s - \dot{z}_u))$

$x_2 - x_4$ relative suspension velocity

$$A_0 = \begin{bmatrix} 0 & 1 & 0 & -1 \\ -\dfrac{k_s}{m_s} & -\dfrac{b_s}{m_s} & 0 & \dfrac{b_s}{m_s} \\ 0 & 0 & 0 & 1 \\ \dfrac{k_s}{m_u} & \dfrac{b_s}{m_u} & -\dfrac{k_t}{m_u} & -\dfrac{b_s}{m_u} \end{bmatrix}, \qquad B = \begin{Bmatrix} 0 \\ 1/m_s \\ 0 \\ -1/m_u \end{Bmatrix}$$

$$, N = \begin{bmatrix} 0 & 0 & 0 & 0 \\ 0 & -\dfrac{1}{m_s} & 0 & \dfrac{1}{m_s} \\ 0 & 0 & 0 & 0 \\ 0 & \dfrac{1}{m_u} & 0 & -\dfrac{1}{m_u} \end{bmatrix} \text{ and } L = \begin{Bmatrix} 0 \\ 0 \\ -1 \\ 0 \end{Bmatrix}$$

Equations (12.4), (12.5) and (12.6) are different representations that have been used in literature for the same semiactive suspension system. In this chapter, we will primarily use the representation (12.5).

Note that the term Nxb_{semi} involves a product of the states Nx and the control input b_{semi}. Hence the semi-active suspension system is not linear, but is a *bilinear* system.

12.3   THEORETICAL RESULTS: OPTIMAL SEMI-ACTIVE SUSPENSIONS

This section presents theoretical results on how the semi-active control system design problem is formulated and solved mathematically.

This section can be skipped during a first time reading of this chapter. The reader who is more interested in the final control law (rather than its derivation) can skip to section 12.4. The theoretical results in this section are largely based on the original work of Tetsuro Butsuen (Butsuen, 1989).

12.3.1   Problem formulation

For the plant given by equation (12.5), assume that the road input $\dot{z}_r$ is white noise with intensity γ. Assume that the passive system is by itself stable i.e.

$$\text{Re}\{\lambda(A_0)\} < 0 \tag{12.7}$$

The performance index of this system is the same as that of the active system in the previous chapter and is given by

$$
J = \lim_{T \to \infty} \frac{1}{T} E\left[\int_0^T \ddot{z}_s^2 + \rho_1(z_s - z_u)^2 + \rho_2 \dot{z}_s^2 + \rho_3(z_u - z_r)^2 + \rho_4 \dot{z}_u^2 \right]
$$

(12.8)

where $\rho_1, \rho_2, \rho_3, \rho_4$ are weighting factors as before.

The integrand in the performance index in equation (12.8) can be separated into two terms – one with b_{semi} and one without b_{semi}. With this separation, equation (12.8) can be re-written as (Butsuen, 1989)

$$
J = \lim_{T \to \infty} \frac{1}{T} E\left[\int_0^T x^T (Q_0 + Q_{semi})x \ dt \right]
$$

(12.9)

where Q_0 is the same as Q in the active chapter and is given by

$$
Q_0 = \begin{bmatrix}
\dfrac{k_s^2}{m_s^2} + \rho_1 & \dfrac{b_s k_s}{m_s^2} & 0 & -\dfrac{b_s k_s}{m_s^2} \\[3mm]
\dfrac{b_s k_s}{m_s^2} & \dfrac{b_s^2}{m_s^2} + \rho_2 & 0 & -\dfrac{b_s^2}{m_s^2} \\[3mm]
0 & 0 & \rho_3 & 0 \\[3mm]
-\dfrac{b_s k_s}{m_s^2} & -\dfrac{b_s^2}{m_s^2} & 0 & \dfrac{b_s^2}{m_s^2} + \rho_4
\end{bmatrix}
$$

(12.10)

and where $Q_{semi}(b_{semi})$ is a function of the control input b_{semi} and is given by

$$
Q_{semi} = \begin{bmatrix}
0 & \dfrac{k_s b_{semi}}{m_s^2} & 0 & -\dfrac{k_s b_{semi}}{m_s^2} \\[3mm]
\dfrac{k_s b_{semi}}{m_s^2} & \dfrac{(2b_s + b_{semi})b_{semi}}{m_s^2} & 0 & -\dfrac{(2b_s + b_{semi})b_{semi}}{m_s^2} \\[3mm]
0 & 0 & 0 & 0 \\[3mm]
-\dfrac{k_s b_{semi}}{m_s^2} & -\dfrac{(2b_s + b_{semi})b_{semi}}{m_s^2} & 0 & \dfrac{(2b_s + b_{semi})b_{semi}}{m_s^2}
\end{bmatrix}
$$

(12.11)

The performance index can also be rewritten as

$$J = \int_0^\infty \left(x^T Q_0 x + 2 b_{semi}{}^T S(x) x + b_{semi}{}^T R(x) b_{semi} \right) dt \qquad (12.12)$$

where

$$R(x) = \frac{1}{m_s{}^2} (x_2 - x_4)^2 = R(x_2 - x_4)^2 \qquad (12.13)$$

$$S(x) = \left[-\frac{k_s}{m_s{}^2} \quad -\frac{b_s}{m_s{}^2} \quad 0 \quad \frac{b_s}{m_s{}^2} \right] (x_2 - x_4) = -S_0(x_2 - x_4) \qquad (12.14)$$

Thus, $R = \dfrac{1}{m_s{}^2}$ and $S_0 = \left[-\dfrac{k_s}{m_s{}^2} \quad -\dfrac{b_s}{m_s{}^2} \quad 0 \quad \dfrac{b_s}{m_s{}^2} \right].$

Note that, as in section 11.2.2, minimizing the variance of the output for a white noise road input profile is an H_2-optimal control problem. The output vector contains the variables of interest and would include suspension deflection, tire deflection and sprung mass acceleration. Again, as in section 11.2.2, this H_2-optimal control problem has the same solution as the quadratic regulator problem in which one attempts to minimize the performance index of equation (12.12) for all initial conditions.

12.3.2   Problem definition

The semi-active control design problem is defined mathematically as follows:

Find the optimal control input $b_{semi}{}^*(t)$ so as to minimize the performance index (12.12) subject to the following constraints (12.15) and (12.16) and the initial condition (12.17).

$$\dot{x} = A_0 x + Nx b_{semi} \qquad (12.15)$$

$$0 \le b_{semi} \le b_{max} \tag{12.16}$$

$$x(0) = x_0 \tag{12.17}$$

Before solving the above problem directly, we would like to consider the problem which has no constraint on b_{semi} i.e. $-\infty < b_{semi} < \infty$. This is the result in Theorem 12.1.

12.3.3   Optimal solution with no constraints on damping

THEOREM 12.1

If there is no constraint on $b_{semi}(t)$, the optimal control $b_{semi}^{*}(t)$ can be expressed as (Butsuen, 1989)

$$b_{semi}^{*} = -R(x)^{-1}\Big[(Nx)^{T} P + S(x)\Big]x \quad \text{if} \ \ x_2 \neq x_4 \tag{12.18}$$

$$b_{semi}^{*} = 0 \ \ \text{if} \ \ x_2 = x_4 \tag{12.19}$$

where

$$R(x) = \frac{1}{m_s^{2}}(x_2 - x_4)^2 = R(x_2 - x_4)^2$$

$$S(x) = -\left[-\frac{k_s}{m_s^{2}} \quad -\frac{b_s}{m_s^{2}} \quad 0 \quad \frac{b_s}{m_s^{2}}\right](x_2 - x_4) \ = -S_0(x_2 - x_4)$$

and where P is determined by the following Riccati equation

$$P\overline{A} + \overline{A}^{T} P + \overline{Q} - PBR^{-1}B^{T} P = 0 \tag{12.20}$$

with

$$\overline{A} = A_0 - BR^{-1}S_0 \tag{12.21}$$

$$\overline{Q} = Q_0 - S_0^{T} R^{-1} S_0 \tag{12.22}$$

Furthermore, the optimal cost J^* is

$$J^* = x^T(0)Px(0) \tag{12.23}$$

Equation (12.23) shows that the minimum cost of this system is exactly the same as that of a fully active suspension system.

Proof: The statement of this theorem is taken from Butsuen, 1989. The proof of the theorem is available in Butsuen, 1989.

Interpretation:
First, note that

$$-R(x)^{-1}S(x)x = \frac{m_s^2 S_0}{x_2 - x_4}x = \frac{[k_s x_1 + b_s(x_2 - x_4)]}{x_2 - x_4}. \text{ Thus, the } -R(x)^{-1}S(x)x$$

term serves to cancel both the passive spring force and the passive damper force.

Next, note that the $-R(x)^{-1}(Nx)^T Px$ term is equal to a state feedback term of the type $-Kx$. In fact, this term is exactly equal to the state feedback term of $F_{a1} = -R^{-1}B^T Px$ obtained in the fully active suspension control law of equation (11.17).

Hence

$$F_{semi} = \left\{ -R(x)^{-1}\left[(Nx)^T P + S(x)\right]x \right\}(x_2 - x_4) = F_{s1} + F_{s2}$$

where

a) $F_{s1} = -\left\{R(x)^{-1}(Nx)^T Px\right\}(x_2 - x_4) = -Kx$ is the state feedback force and

b) $F_{s2} = -\left\{R(x)^{-1}S(x)x\right\}(x_2 - x_4) = k_s x_1 + b_s(x_2 - x_4)$ is the component that cancels the passive spring and damper forces.

Thus Theorem 12.1 says that the two systems shown in Figure 12-5 below (the force control and the modulated damper control systems) are equivalent if the modulated damper rate , $b_{semi}(t)$, takes all real values.
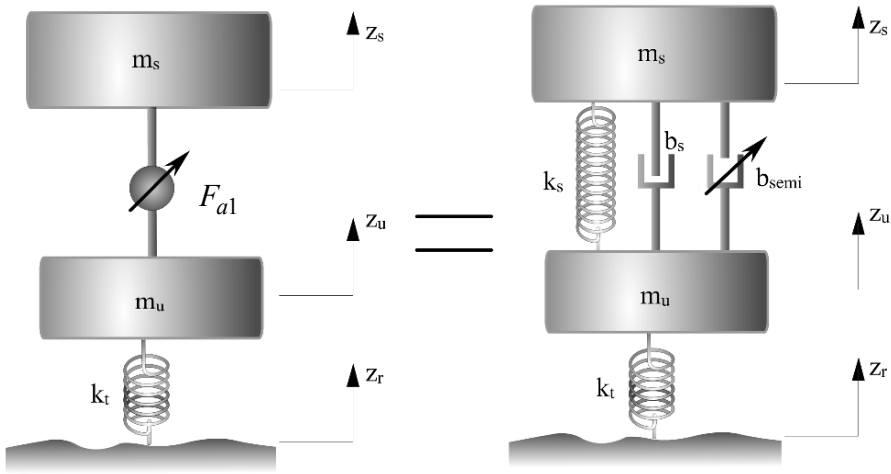
Figure 12-5. Equivalence of force control and unconstrained modulated damper control systems

The force between the sprung mass and the unsprung mass for a fully active suspension is equal to the total suspension force in the case of a semiactive suspension if the modulated damper b_{semi}^{*} is allowed to take all real values. If the state feedback component of the fully active suspension after cancellation of the passive terms is given by

$$F_{a1} = -Kx = -R^{-1}B^{T}Px \qquad (12.24)$$

then the total force that acts between the sprung mass and the unsprung mass in the case of the optimal semi-active suspension is given by

$$F_{semi} = -k_s x_1 - b_s(x_2 - x_4) - b_{semi}^{*}(x_2 - x_4) = -R^{-1}(B^{T}P)x = F_{a1} \qquad (12.25)$$

Thus, if there were no constraints on the semi-active damping coefficient $b_{semi}(t)$, then the performance of the optimal semi-active suspension would be completely equal to that of the fully active suspension system.

The next result takes the constraints $0 \leq b_{semi} \leq b_{max}$ into consideration. Again, this result was originally obtained by Tetsuro Butsuen (Butsuen, 1989).

12.3.4 Optimal solution in the presence of constraints

THEOREM 12.2

In the presence of the constraints $0 \leq b_{semi} \leq b_{max}$, the optimal control b^* can be obtained as (Butsuen, 1989)

$$b^* = 0 \ \text{if} \ \left\{ (Nx)^T P + S(x) \right\} \geq 0 \tag{12.26}$$

$$b^* = -R(x)^{-1} \left\{ (Nx)^T P + S(x) \right\} x < 0$$
$$\text{if} \ -R(x)b_{max} < \left\{ (Nx)^T P + S(x) \right\} < 0 \tag{12.27}$$

$$b^* = b_{max} \ \text{if} \ \left\{ (Nx)^T P + S(x) \right\} < -R(x)b_{max} \tag{12.28}$$

where the matrix P is determined by the same Riccati equation (12.20) as before.

The optimal cost J^* is

$$J^* = x^T(0)Px(0) + \int_{\lambda_1 > 0} R(x)^{-1} \lambda_1^2 dt + \int_{\lambda_2 > 0} R(x)^{-1} \lambda_2^2 dt \tag{12.29}$$

where λ_1 and λ_2 are Lagrange multipliers for constraint equations (12.11) and (12.12) such that

$$\lambda_1 = \left\{ (Nx)^T P + S(x) \right\} x \ , \ \lambda_2 = 0 \ \text{if} \ \left\{ (Nx)^T P + S(x) \right\} \geq 0 \tag{12.30}$$

$$\lambda_1 = 0, \ \lambda_2 = 0 \ \text{if} \ -R(x)b_{max} < \left\{ (Nx)^T P + S(x) \right\} < 0 \tag{12.31}$$

$$\lambda_1 = 0, \lambda_2 = -\left\{ (Nx)^T P + S(x) \right\} x - R(x)b_{max}$$
$$\text{if} \ \left\{ (Nx)^T P + S(x) \right\} < -R(x)b_{max} \tag{12.32}$$

Proof: The statement of this theorem is taken from Butsuen, 1989. The proof of the theorem is available in Butsuen, 1989.

12.4   INTERPRETATION OF THE OPTIMAL SEMI-ACTIVE CONTROL LAW

Let the optimal active control force be given as

$$F_a = -Kx + k_s x_1 + b_s (x_2 - x_4) \tag{12.33}$$

or

$$F_a = -R^{-1}\left(B^T P + S_0\right)x$$

where

$$k_s x_1 + b_s (x_2 - x_4) = -R^{-1} S_0 x \tag{12.34}$$

is the passive suspension force and

$$- Kx = R^{-1} B^T Px \tag{12.35}$$

is the optimal state feedback force component obtained from the LQR solution for the fully active system (see chapter 11, equation (11.17)).

Thus the total active force is $F_a = -R^{-1}\left(B^T P + S_0\right)x$.

Note that the term $(Nx)^T P + S(x)$ appearing on the right hand side of equations (12.26), (12.27) and (12.28) is equivalent to $\dfrac{F_a}{x_2 - x_4}$

The optimal semi-active control law derived in section 12.3 can therefore be written in terms of the suspension variables as

$$b_{semi}{}^* = 0 \quad \text{if } -F_a(x_2 - x_4) \le 0 \tag{12.36}$$

$$b_{semi}{}^* = -\frac{F_a}{x_2 - x_4} \quad \text{if } 0 < -\frac{F_a}{x_2 - x_4} \le b_{max} \tag{12.37}$$

$$b_{semi}{}^* = b_{max} \quad \text{if } -\frac{F_a}{x_2 - x_4} > b_{max} \tag{12.38}$$

and the corresponding semi-active force is given by

$$F_{semi} = -b_{semi}{}^{*}(x_2 - x_4) \qquad (12.39)$$

$$b_{semi} = -\frac{F_a}{x_2 - x_4}$$

$$b_{semi} \le b_{max}$$

$$b_{semi} = 0$$

$$b_{semi} = 0$$

$$b_{semi} = -\frac{F_a}{x_2 - x_4}$$

$$b_{semi} \le b_{max}$$
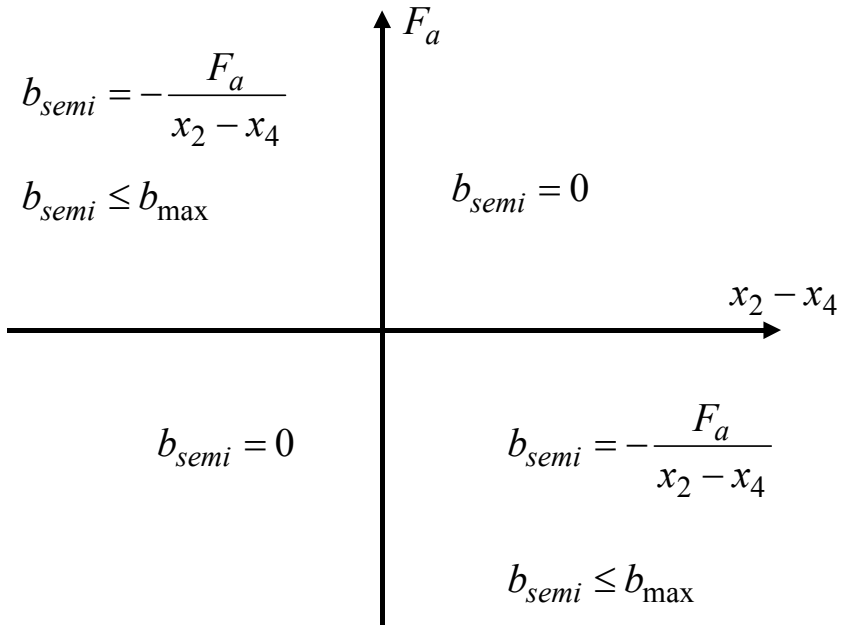
Figure 12-6. Semi-active control law shown schematically as a function of F_a and relative velocity

Figure 12-6 shows the semi-active control law schematically. When the fully active force F_a and the relative suspension velocity $x_2 - x_4$ have the same sign, then the required active force is in the same direction as the relative velocity. Such an active force cannot be provided by a dissipative device, since a dissipative device can only provide a force which is opposite to the relative velocity. In this case the value of damping b_{semi} in the semi-active device is chosen to be zero. When the fully active force F_a and the relative velocity $x_2 - x_4$ have the opposite sign, then a dissipative device can indeed provide the desired force. In this case the value of the semi-active damping coefficient b_{semi} is chosen to be $b_{semi} = -\dfrac{F_a}{x_2 - x_4}$. If this value

exceeds the maximum available damping coefficient b_{max}, then b_{semi} is set to be equal to b_{max}.

The semi-active control law is also summarized in Table 12-1 of this chapter.

Table 12-1. Summary of Semi-Active Control Law

SUMMARY OF SEMI-ACTIVE CONTROL LAW		
Symbol	**Nomenclature**	**Equation**
F_a	Optimal fully-active force	$F_a = -Kx + k_s \dot{z}_s + b_s(\dot{z}_s - \dot{z}_u)$ See equations (11.16) and (11.17) in Chapter 11
b_{semi}	Semi-active (variable) damping coefficient	$b_{semi}^{\ *} = 0 \qquad\qquad \text{if } -F_a(\dot{z}_s - \dot{z}_u) \leq 0$ $b_{semi}^{\ *} = -\dfrac{F_a}{x_2 - x_4} \quad \text{if } 0 < -\dfrac{F_a}{\dot{z}_s - \dot{z}_u} \leq b_{max}$ $b_{semi}^{\ *} = b_{max} \qquad \text{if } -\dfrac{F_a}{x_2 - x_4} > b_{max}$ and $F_{semi} = -b_{semi}^{\ *}(x_2 - x_4)$

12.5   SIMULATION RESULTS

The performance of the semi-active control laws of equations (12.36), (12.37) and (12.38) is shown in Figures 12-7, 12-8 and 12-9. A road input frequency of 1 Hz was used in the time simulations. As shown in these figures, ride quality, suspension deflection and tire deflection are all improved significantly at 1 Hz compared to the passive system.

In the case of the passive suspension system, in Figures 12-7, 12-8 and 12-9, the time response of the system is purely at 1 Hz due to the road input being at this frequency. In the case of the semi-active suspension system, however, the response contains higher frequencies in addition to the 1 Hz
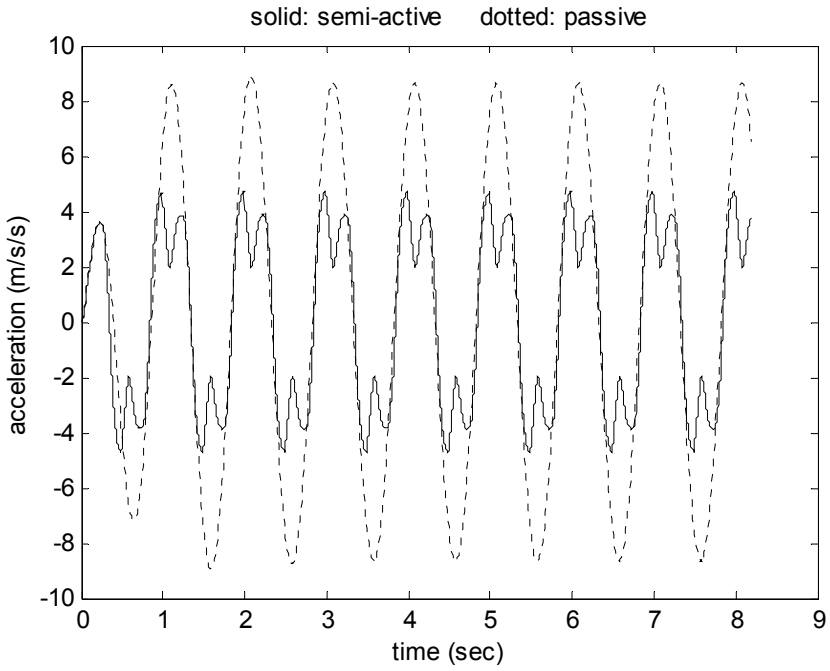
Figure 12-7. Acceleration at 1 Hz
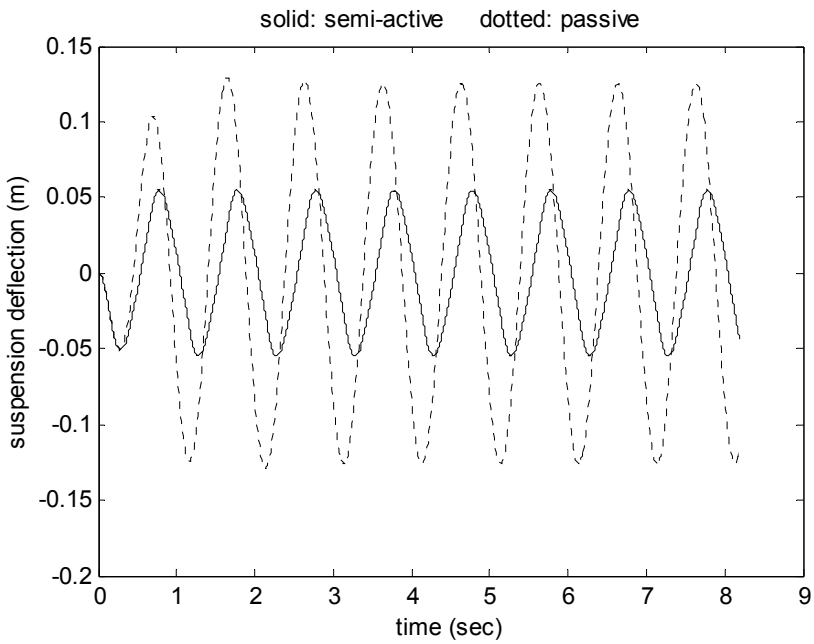
Figure 12-8. Suspension deflection at 1 Hz

solid: semi-active   dotted: passive
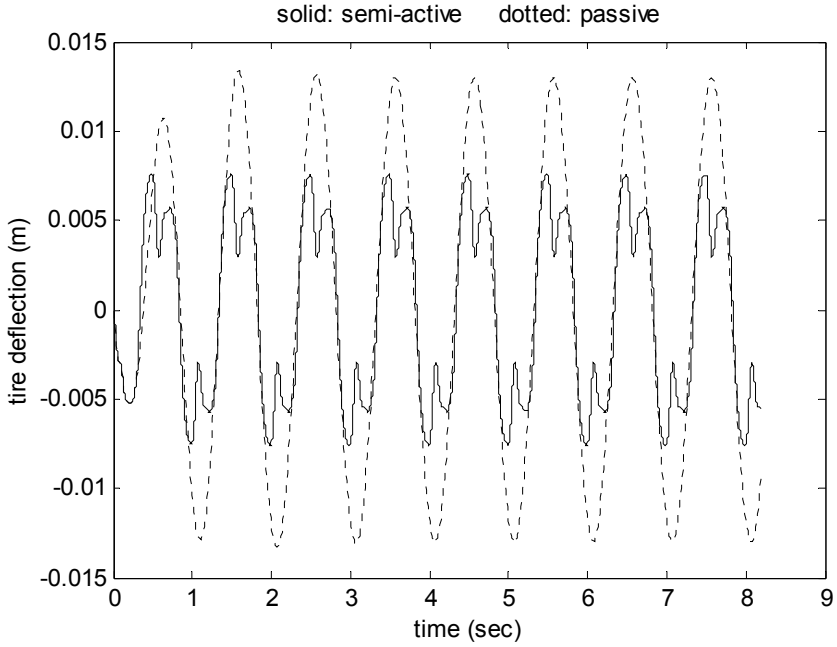
Figure 12-9. Tire deflection at 1 Hz

solid: acceleration   dotted: scaled semi-active damping coefficient
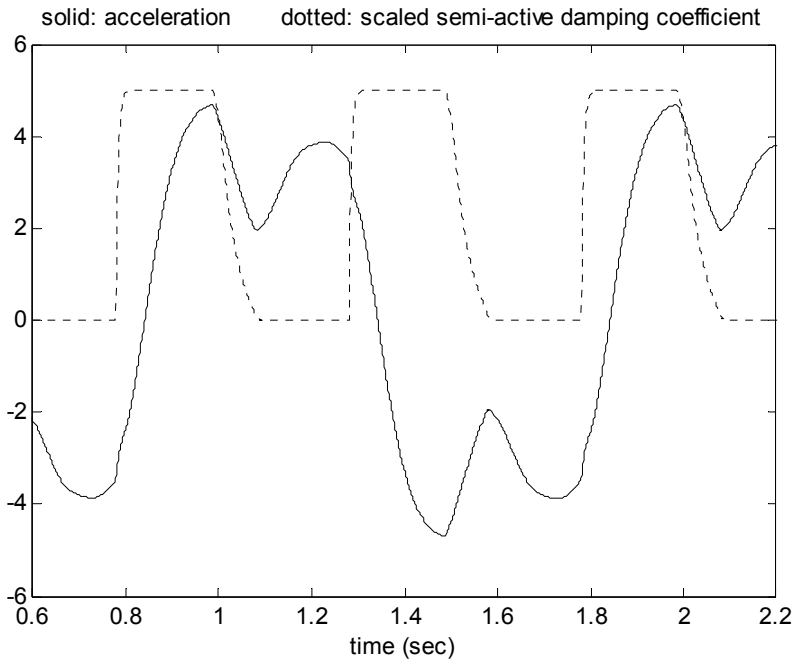
Figure 12-10. Acceleration and semi-active damping coefficient

frequency. This is because of the switching nature of the nonlinear semi-active control law. The semi-active damping coefficient b_s switches between zero and the equivalent active force value as the relative suspension velocity changes sign with respect to the active force. Figure 12-10 shows the scaled semi-active damping coefficient and the sprung mass acceleration on the same plot. It can be clearly seen from this figure that the higher frequency in the sprung mass acceleration is caused by the periodic switching in the semi-active damping coefficient from active force value to zero or maximum value and vice-versa.

12.6 CALCULATION OF TRANSFER FUNCTION PLOTS WITH SEMI-ACTIVE SYSTEMS

Since the semi-active system is nonlinear, with the control law being the switched nonlinear laws of equations (12.36) – (12.38), it is not obvious how closed-loop transfer function plots can be calculated for this system. The transfer function calculation is done in two steps (Butsuen, 1989):

1) The external road input excitation problem is represented as an equivalent initial condition problem and the time response of the semi-active system to the equivalent initial condition is obtained by simulation.
2) A Fast Fourier Transform of the output signal from the simulation is obtained and appropriately scaled to obtain the transfer functions for sprung mass acceleration, suspension deflection and tire deflection.

To see how the road input excitation problem can be represented as an equivalent initial condition problem note that the closed-loop system is given by

$$\dot{x} = (A - BK)x + L\dot{z}_r \tag{12.40}$$

In the absence of initial conditions, the transfer function is

$$x = (sI - A + BK)^{-1} L\dot{z}_r \tag{12.41}$$

If $\dot{z}_r$ is white noise of intensity α, its Laplace transform is α. Hence

$$x = (sI - A + BK)^{-1} L\alpha \tag{12.42}$$

This is equivalent to the response of the closed-loop system to the initial condition

$$x_0 = L = \alpha \begin{bmatrix} 0 \\ 0 \\ -1 \\ 0 \end{bmatrix} \qquad (12.43)$$

with there being no road input.

In Butsuen (1989), it has been shown that the output-input amplitude ratio for the transfer function in equation (12.42) is independent of the input amplitude α, in spite of the fact that the semi-active system is nonlinear. Hence the response of the closed-loop system to the white noise input $\dot{z}_r$ can be represented by an equivalent initial condition problem in which $\dot{z}_r$ is assumed to be zero.

The time response of the semi-active system can be obtained to the initial condition given in equation (12.43) and its Fast Fourier transform can then yield the closed-loop transfer function.

Figure 12-11 shows the sprung mass acceleration time-response of the semi-active system. The initial condition was assumed to be $x_0 = \begin{bmatrix} 0 & 0 & -0.01 & 0 \end{bmatrix}^T$ and the road input was taken to be zero. The transfer function from road input to sprung mass acceleration obtained by
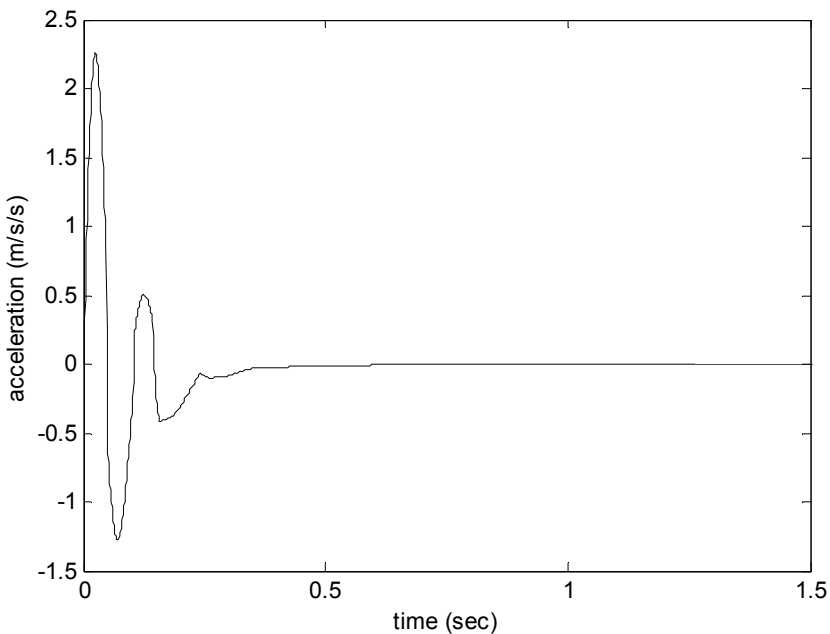
Figure 12-11. Initial condition response of the semi-active system

taking the Fast Fourier Transform of this time response is shown in Figure 12-12. A detailed study of the performance of the semi-active system and comparison of the performance with passive systems is presented in the next section.
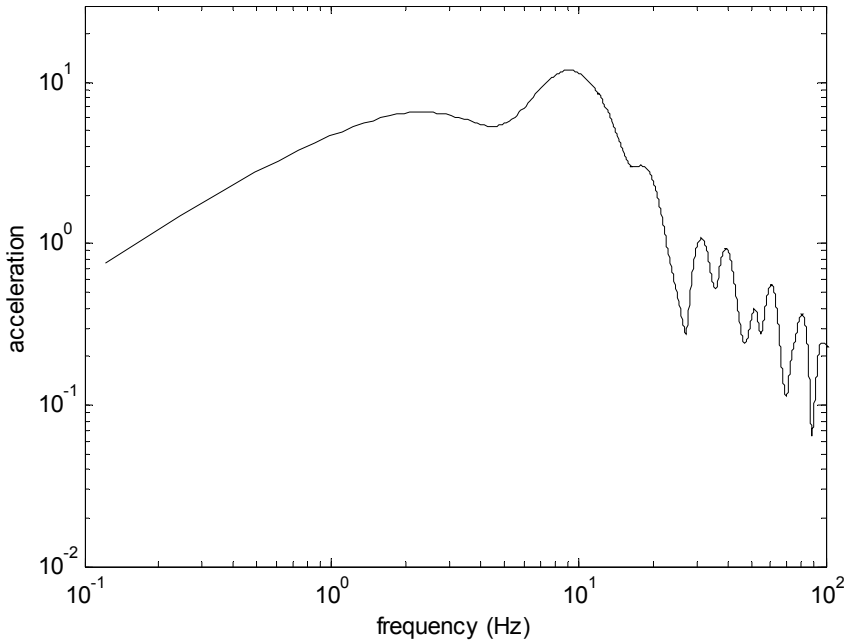
Figure 12-12. FFT of the initial condition response of the semi-active system

12.7   PERFORMANCE OF SEMI-ACTIVE SYSTEMS

12.7.1   Moderately weighted ride quality

The following plots (Figures 12-13, 12-14 and 12-15) show performance of the semi-active system using the following weights in the performance index: ρ_1=400, ρ_2=16, ρ_3=400 and ρ_4 = 16. As explained in the previous chapter on fully active suspension systems, these weights are such that the sprung mass acceleration (ride quality) is more heavily weighted and the other states are less weighted.

   The performance of the semi-active system with the above weights and its comparison with the standard passive system is shown in Figures 12-13, 12-14 and 12-15. The sprung mass acceleration, suspension deflection and tire deflection are all significantly improved at the first natural frequency.
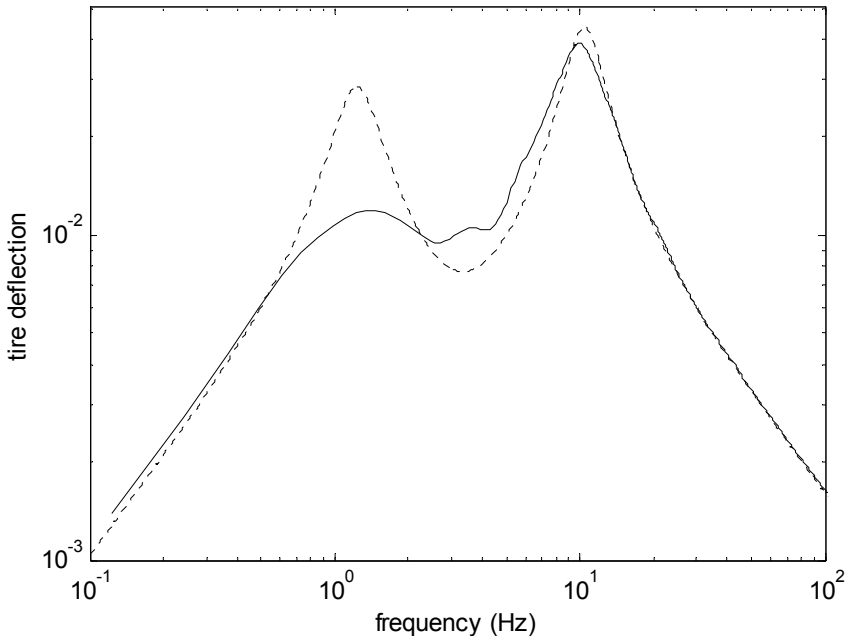
Figure 12-13. Tire deflection transfer functions for a performance index with moderate weights
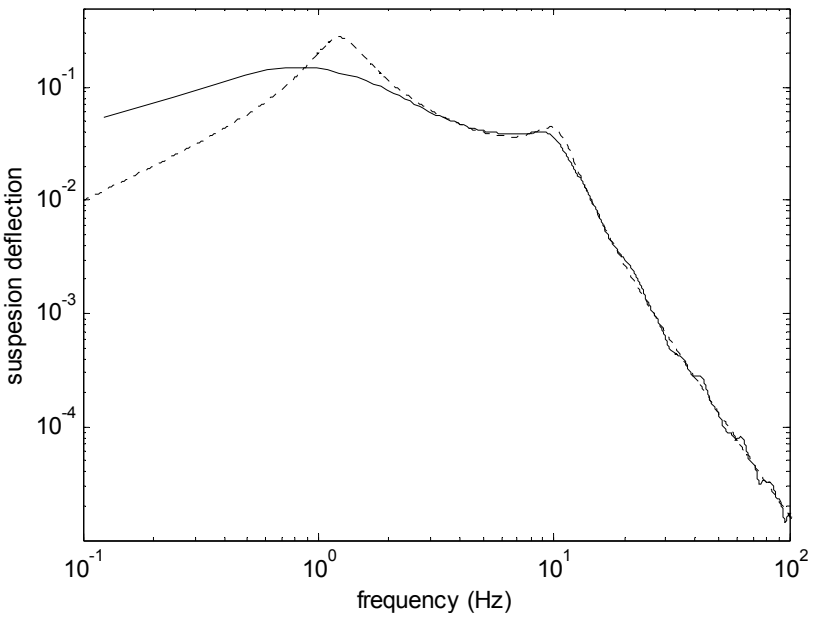
Figure 12-14. Suspension deflection transfer function for a performance index with moderate weights

However, there is no difference in performance in any of these transfer functions at the second natural frequency. It can also be seen from Figure 12-15 that the switching nature of the semi-active system introduces some high frequency variations in the sprung mass acceleration transfer function.
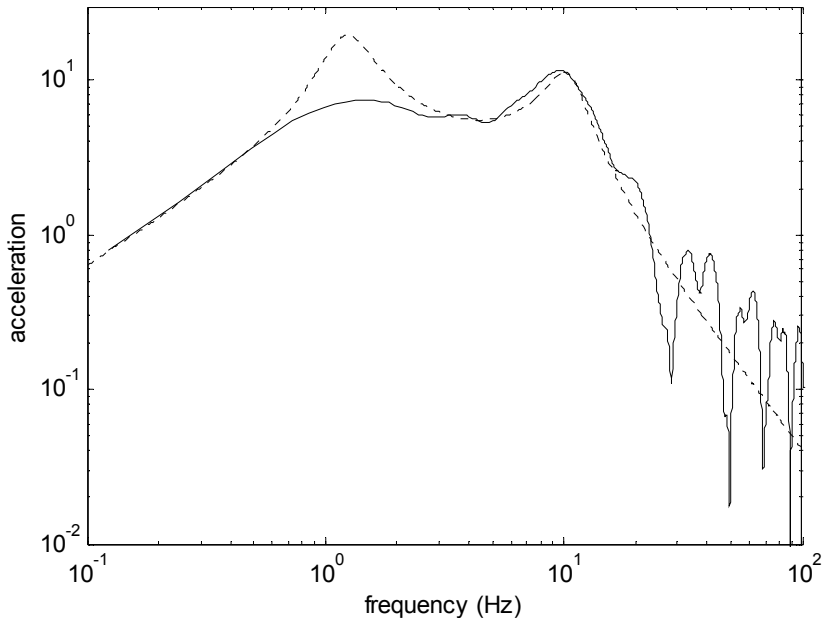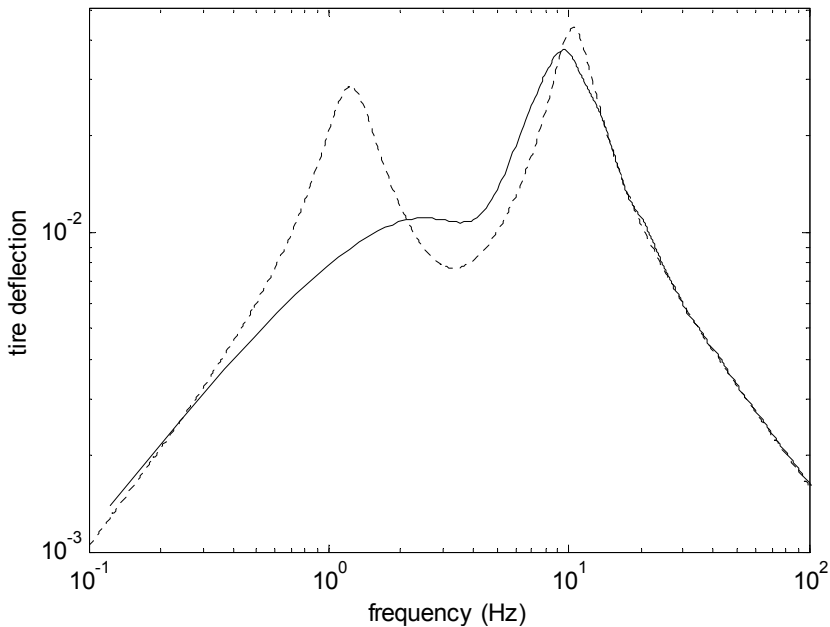

Figure 12-15. 15 Acceleration transfer functions for a performance index with moderate weights

12.7.2 Sky hook damping

This section demonstrates the performance of a semi-active system which attempts to provide the equivalent of sky-hook damping. The desired semi-active force is defined as

$$F_a = -4000\dot{z}_s \qquad (12.44)$$

The semi-active damping coefficient is determined as before, using

$$b^* = 0 \quad \text{if} \quad -F_a(x_2 - x_4) \le 0 \qquad (12.45)$$

$$b^* = -\frac{F_a}{x_2 - x_4} \quad \text{if} \quad 0 < -\frac{F_a}{x_2 - x_4} \leq b_{\max} \tag{12.46}$$

$$b^* = b_{\max} \quad \text{if} \quad -\frac{F_a}{x_2 - x_4} > b_{\max} \tag{12.47}$$

The performance of this system and its comparison with the standard passive system is shown in Figures 12-16, 12-17 and 12-18. One can see that the sprung mass acceleration, suspension deflection and tire deflection are all significantly improved at the first natural frequency. There is no difference in performance at the second natural frequency. The performance achieved in sky-hook damping is similar to that achieved in section 12.7.1. It is also clear from Figure 12-18 that the switching nature of the semi-active system introduces some high frequency variations in the sprung mass acceleration transfer function.

Figure 12-16. Tire deflection transfer functions for semi-active control with sky hook damping
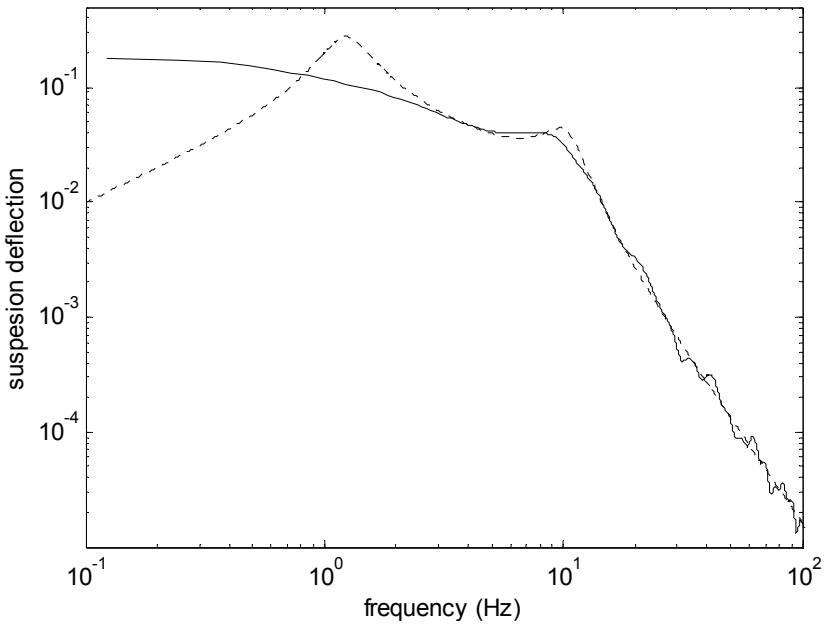
Figure 12-17. Suspension deflection transfer functions for semi-active control with sky hook damping
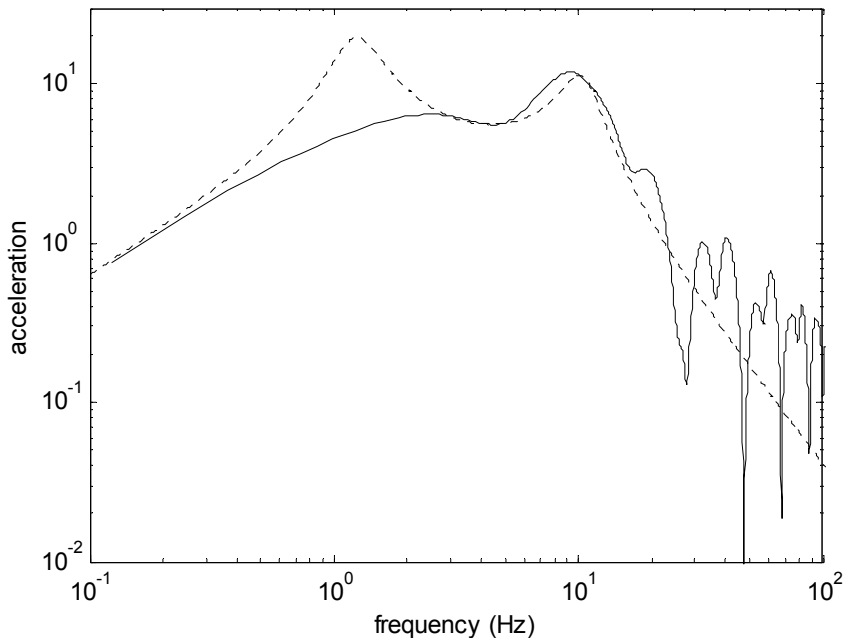
Figure 12-18. Acceleration transfer functions for semi-active control with sky hook damping

12.8   CHAPTER SUMMARY

This chapter focused on the development of semiactive control systems for automotive suspensions. Compared to fully active suspension systems, semi-active systems consume significantly less power. The power consumption in a semi-active system is only for purposes of changing the real-time dissipative force characteristics of the semi-active device. External power is not directly used to counter vibratory forces. Another advantage of semi-active systems over active systems is that since they only use energy dissipation, they cannot cause the suspension system to become unstable.

The rigorous development of a control system that utilizes a variable damper as the control input for the semi-active suspension is a challenging problem. It was found that if there were no constraints on allowable damping (i.e. it is allowed to take any positive or negative value), then the perform-ance obtained with a semiactive suspension is the same as that obtained with a fully active suspension. With constraints on damping, the optimal control system provided the same semi-active force as the fully active force as long as the required damping coefficient for doing so was in the allowable range. If the required damping coefficient was out of the allowable range, then the optimal control system required the use of the constrained limit values of damping.

Simulation results showed that the semi-active system could provide significant improvements in the ride quality, suspension deflection and tire deflection transfer functions at the sprung mass resonant frequency. The ride quality has high frequency harshness due to the switching that occurs in the semi-active control system. However, this high frequency harshness can be reduced by reducing the switching bandwidth of the semi-active damper.

NOMENCLATURE

z_s	sprung mass displacement
z_u	unsprung mass displacement
z_r	road profile input
m_s	sprung mass
m_u	unsprung mass
k_s	suspension stiffness

b_s	suspension damping
k_t	tire stiffness
F_a	active suspension actuator force
F_{semi}	semiactive force
b_{semi}	variable damping coefficient of semi-active damper
b_{max}	maximum allowable damping coefficient
s	Laplace transform variable
$H_A(s)$	sprung mass acceleration transfer function
$H_{RS}(s)$	suspension deflection transfer function
$H_{TD}(s)$	tire deflection transfer function
A, B, L	matrices used in state space model of quarter car suspension
x	state space vector
J	optimal control performance index
Q_0, Q_{semi}, R, N	matrices used in the optimal control performance index
ρ_1, ρ_2, ρ_3, ρ_4	weights used in the optimal control performance index
$S(x)$, $R(x)$	functions used in the optimal control performance index
S_0, R	matrices used in the optimal control performance index
G	feedback gain matrix from LQR solution
g_1, g_2, g_3, g_4	feedback gains from LQr solution
λ_1, λ_2	Lagrange multipliers

REFERENCES

Butsuen, T., "The Design of Semi-Active Suspensions for Automotive Vehicles," *Ph.D. Dissertation*, M.I.T., 1989.

Jolly, M.R., Bender, J.W. and Carlson, J.D., "Properties and Applications of Commercial Magnetorheological fluids," *SPIE 5th Annual Int Symposium on Smart Structures and Materials*, San Diego, CA, March 15, 1998.

Karnopp, D., "Force Generation in Semi-Active Suspensions Using Modulated Dissipative Elements," *Vehicle System Dynamics*, v 16, n 5-6, p 333-343, 1987.

Rajamani, R. and Hedrick, J.K., "Semi-active Suspensions - A Comparison Between Theory and Experiments", *Vehicle System Dynamics*, International Journal of Vehicle Mechanics and Mobility, Supplement to Vol. 20, pp.504-518; Proceedings of the 12th IAVSD Symposium on The Dynamics Of Vehicles on Roads and on Tracks, Lyon, France, Aug 26-30, 1991.

Sharp, R.S. and Hassan, S.A., "Performance and Design Considerations for Dissipative Semi-Active Suspensions Systems for Automobiles," *Proceedings of the Institution of Mechanical Engineers*, Part D: Transport Engineering, Vol. 201, No. D2, pp. 149-153, 1987.

Tseng, H.E. and Hedrick, J.K., "Semi-Active Control Laws: Optimal and Sub-Optimal," *Vehicle System Dynamics*, Vol. 23, No. 7, pp. 545-569, October 1994.

Yue, C., Butsuen, T. and Hedrick, J.K. "Alternative Control Laws for Automotive Suspensions," *Proceedings of the American Control Conference*, pp. 2373-2378, 1988.

Chapter 13

LATERAL AND LONGITUDINAL TIRE FORCES

13.1   TIRE FORCES

Forces and moments from the road act on each tire of the vehicle and highly
influence the dynamics of the vehicle. This chapter focuses on mathematical
models for describing these tire forces and moments.

side view

top view
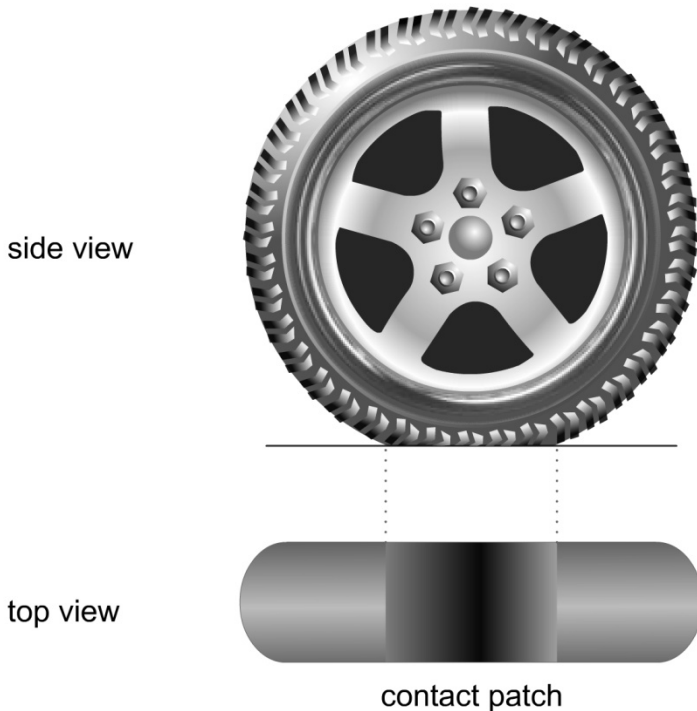
contact patch

Figure 13-1. The contact patch of a tire

Unlike a rigid undeformable wheel, the tire does not make contact with the road at just one point. Instead, as shown in Figure 13-1, the tire on a vehicle deforms due to the vertical load on it and makes contact with the road over a non-zero footprint area called the contact patch.

Figure 13-2 shows the sign convention adopted in this book for the major forces and moments that act on the tire. The origin of the reference axes is at the center of the contact patch. The X axis is defined by the intersection of the ground plane with the mean plane of the wheel. Axis Z is perpendicular to the ground and points upwards. To ensure a right handed axes, the Y axes points rightwards.

The force the tire receives from the road is assumed to be at the center of the contact patch and can be decomposed along the three axes. The lateral force F_y is the force along the Y axis, the longitudinal force F_x is the force along the X axis and the normal or vertical force F_z is the force along the Z axis. Similarly, the moment the tire receives from the road can be
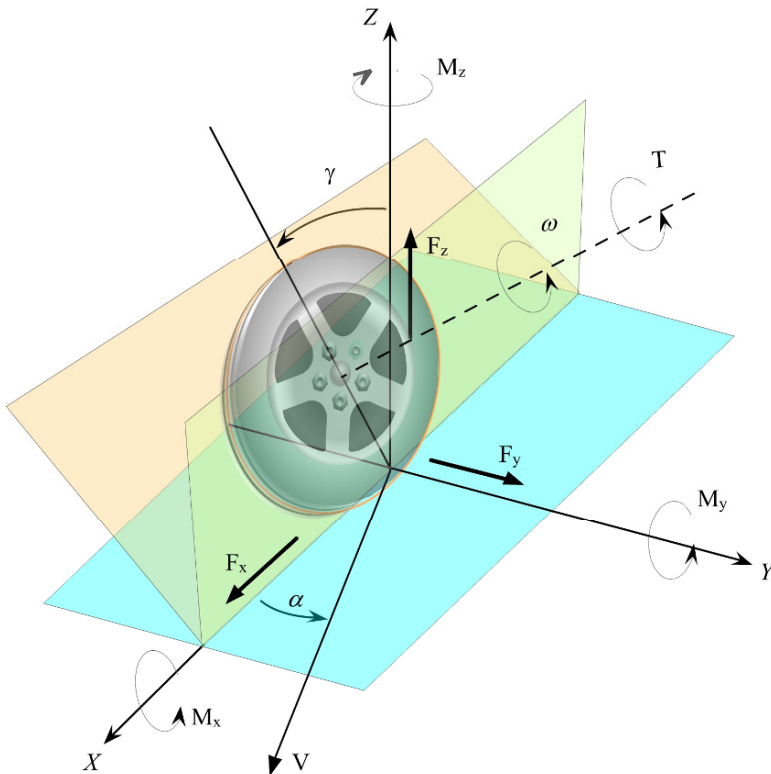
Figure 13-2. Tire forces and moments
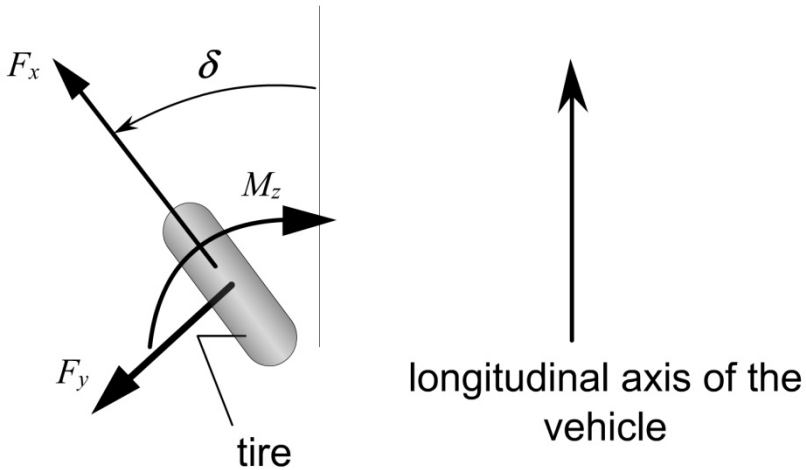
Figure 13-3. Lateral and longitudinal forces and restoring moment

decomposed along the three axes. The moment along the Z axes M_z is called the aligning moment. The moment along the X axes M_x is called the overturning moment and the moment along the Y axis M_y is called the rolling resistance moment.

In this chapter we shall be primarily concerned with the lateral force F_y, the longitudinal force F_x and the aligning moment M_z. These are shown in Figure 13-3.

13.2   TIRE STRUCTURE

The "carcass" of the tire is made up of a number of layers of flexible cords of high modulus of elasticity encased in a matrix of low modulus rubber compounds. The geometric disposition of the layers of rubber coated cords, particularly their directions, play a significant role in the behavior of the tire. Tires are commonly *bias-ply* or *radial-ply* (Wong, 2001).

In bias ply tires, the cords in the carcass have an angle (or bias) of approximately 40 degrees with respect to the circumference. The cords in adjacent plies run in opposite directions. A bias ply tire usually has 2 or more plies (up to 20 plies for heavy-load tires).
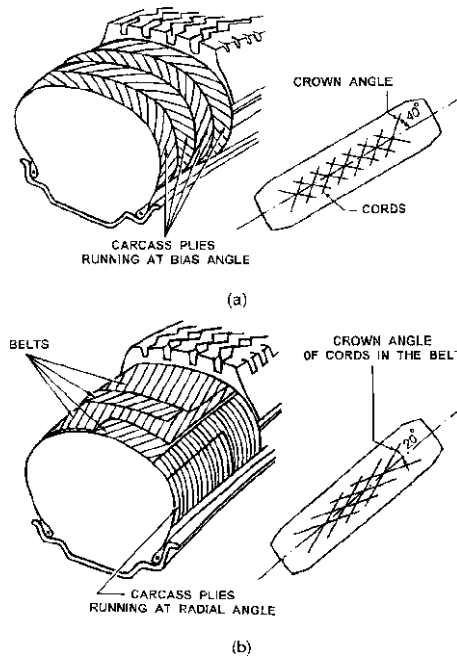
Figure 13-4. Tire construction: a) Bias-ply tire and b) Radial-ply tire[1]

The radial ply tire is a belted tire and has one or more belts, in addition to plies. A *belt* is a steel mesh placed between the body and the tread. Each belt adds an additional layer in the tread area but leaves the sidewall area untouched. Besides the belt, a radial tire also has plies just like the bias-ply tire, but the cords in these plies are made of a softer material like polyester instead of nylon. The cords in the plies run perpendicular to the circumference of the tire. On the side walls of the tire, the direction of these cords is radial and hence the name "radial" tires.

The use of radial ply tires has now become dominant for passenger cars and trucks. The radial ply tire has low sidewall stiffness and provides a smoother ride. The contact patch is also larger and more stable with radial tires, hence providing better handling. The power dissipation of the radial ply tire could be as low as 60% of that of the bias ply tire under similar conditions and the life of the radial ply tire could be as long as twice that of the equivalent bias-ply tire (Wong, 2001).

---

[1] Reprinted from "Ground Vehicles," by Wong (2001), with permission from John Wiley and Sons, Inc.

13.3   LONGITUDINAL TIRE FORCE AT SMALL SLIP RATIOS

Experimental results have shown that the longitudinal tire force at small "slip ratio" is proportional to the slip ratio.

Slip ratio

The difference between the actual longitudinal velocity at the axle of the wheel V_x and the equivalent rotational velocity $r_{eff}\omega_w$ of the tire is called longitudinal slip. In other words, longitudinal slip is equal to $\left(r_{eff}\omega_w - V_x\right)$. *Longitudinal slip ratio* is defined as

$$\sigma_x = \frac{r_{eff}\omega_w - V_x}{V_x} \quad \text{during braking} \tag{13.1}$$

$$\sigma_x = \frac{r_{eff}\omega_w - V_x}{r_{eff}\omega_w} \quad \text{during acceleration} \tag{13.2}$$
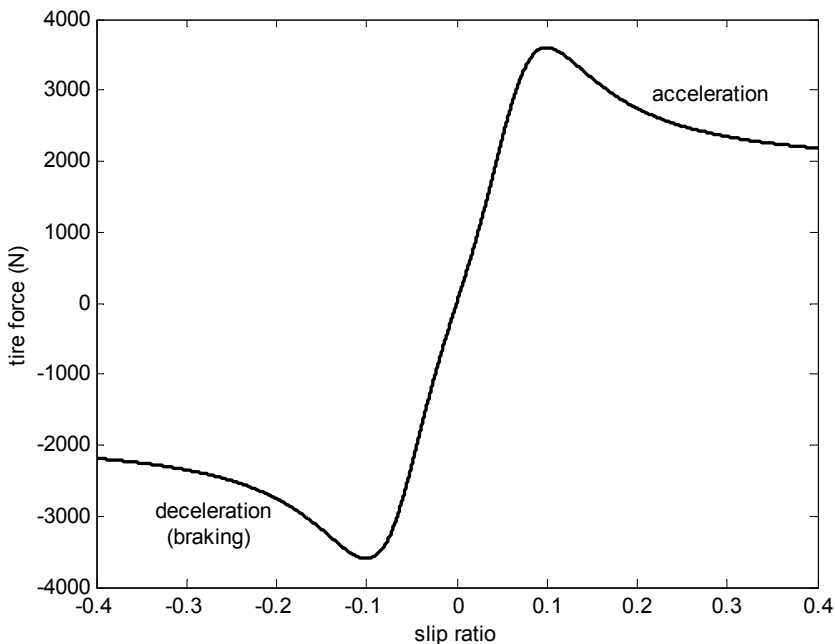
Figure 13-5. Longitudinal tire force as a function of slip ratio

Experimental results have established that the longitudinal tire force generated by each tire depends on the slip ratio, the normal (vertical) force on the tire and the friction coefficient of the road surface.

If the friction coefficient of the tire-road interface is assumed to be 1 and the normal force is assumed to be a constant, the typical variation of longitudinal tire force as a function of the slip ratio is shown in Figure 13-5.

From Figure 13-5, it is clear that in the case where longitudinal slip is small (less than 0.1 on dry surface), the longitudinal tire force is directly proportional to the slip ratio. The tire force in this case can thefore be modeled as

$$F_{xf} = C_{\sigma f} \sigma_{xf} \tag{13.3}$$

$$F_{xr} = C_{\sigma r} \sigma_{xr} \tag{13.4}$$
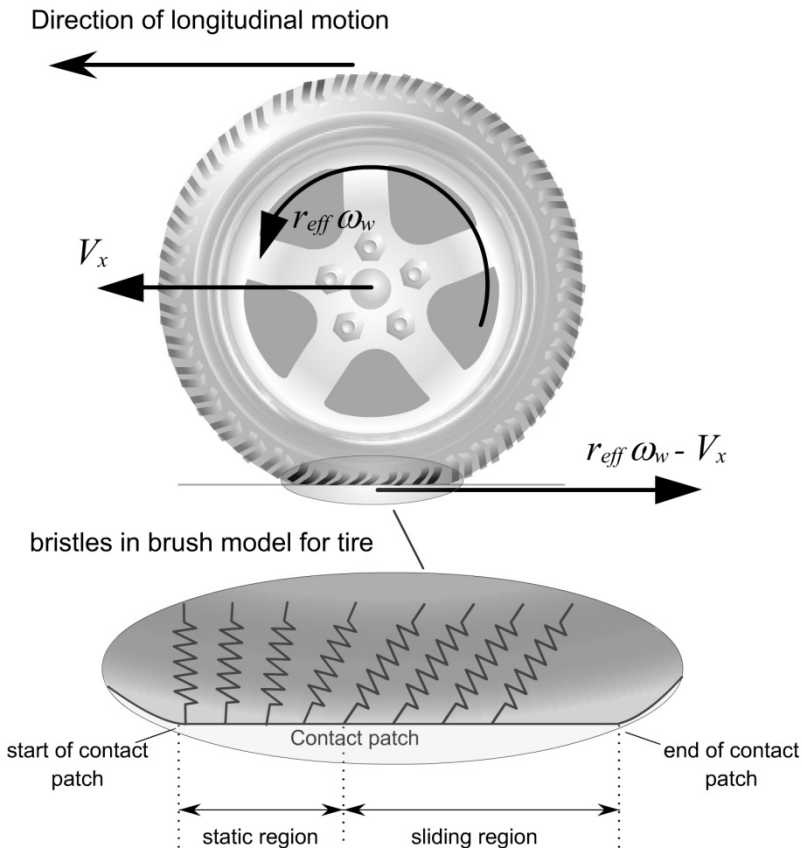
Figure 13-6. Longitudinal force in a driving wheel

where $C_{\sigma f}$ and $C_{\sigma r}$ are called the longitudinal tire stiffness parameters of the front and rear tire respectively. It should be noted that longitudinal slip ratio is typically small during normal (gentle) driving on a dry surface road.

A rough explanation of why the longitudinal force is proportional to slip ratio can be seen from Figure 13-6.

The lower portion of Figure 13-6 shows a schematic representation of deformation of the tread elements of the tire. The tread elements are modeled as a series of independent springs that undergo longitudinal deformation and resist with a constant longitudinal stiffness. Such a model of the tire is called a "brush" model or an "elastic foundation" model (Pacejka, 1991, Dixon, 1991).

Let the longitudinal velocity of the wheel be V_x and its rotational velocity be ω_w. Then the net velocity at the treads, as shown in Figure 13-6, is $r_{eff}\omega_w - V_x$.

First, consider the case where the wheel is a driving wheel, for example, the front wheels in a front-wheel drive vehicle. In this case, since the wheel is a driving wheel, $r_{eff}\omega_w > V_x$. Hence the net velocity of the treads is in a direction opposite to that of the longitudinal velocity of the vehicle. Assume that the slip $r_{eff}\omega_w - V_x$ is small. Then there is a region of the contact patch where the tread elements do not slide with respect to the ground (called the "static region" in Figure 13-6). As the tire rotates and a tread element enters the static region of the contact patch, its tip which is in contact with the ground must have zero velocity. This is because there is no sliding in the static region of the contact patch. The upper part of the tread element moves with a velocity of $r_{eff}\omega_w - V_x$. Hence the tread element will bend forward as shown in Figure 13-6 and the bending will be in the direction of the longitudinal direction of motion of the vehicle. The maximum bending deflection of the tread is proportional to the slip velocity $r_{eff}\omega_w - V_x$ and to the time duration for which the tread element remains in the contact patch. The time duration in the contact patch is inversely proportional to the rotational velocity $r_{eff}\omega_w$. Hence the maximum deflection of the tread element is proportional to the ratio of slip to absolute velocity i.e. proportional to the slip ratio $\dfrac{r_{eff}\omega_w - V_x}{r_{eff}\omega_w}$.

Thus the net longitudinal force on the tires from the ground is in the forward direction in the case of a driving wheel and is proportional to the slip ratio of the wheel.

In the case where the tire is on a driven wheel, the longitudinal velocity is greater than the rotational velocity $(V_x > r_{eff}\omega_w)$. In this case the net velocity at the treads is in the forward direction and hence the bristles on the tire will bend backwards. Hence the tire force on the driven wheel is in a direction opposite to that of the vehicle's longitudinal velocity. Again, for small slip ratio, the tire force will be proportional to slip ratio.

13.4   LATERAL TIRE FORCE AT SMALL SLIP ANGLES

Experimental results show that for small "slip angle", the lateral force on a tire is proportional to the slip angle at the tire.
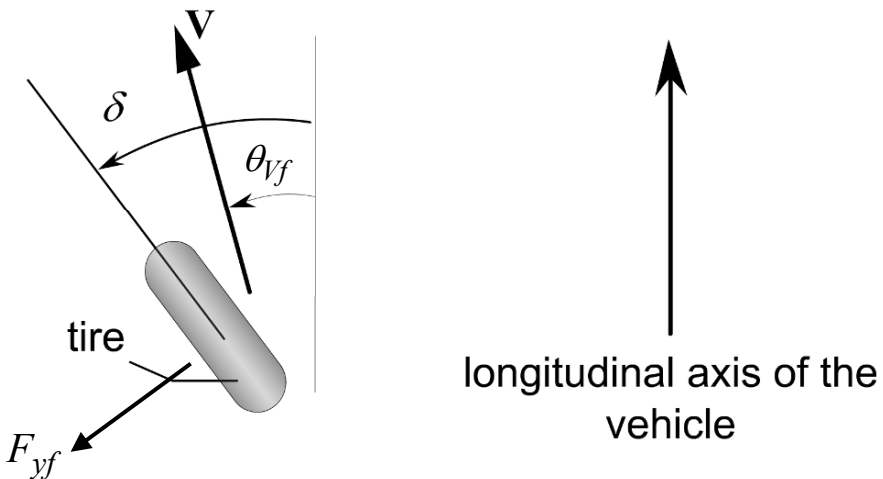
Figure 13-7. Tire slip angle and lateral force at front tire

Slip Angle

The slip angle of a tire is defined as the angle between the orientation of the tire and the orientation of the velocity vector of the wheel (see Figure 13-7). In Figure 13-7, the slip angle of the front wheel is

$$\alpha_f = \delta - \theta_{Vf} \tag{13.5}$$

where θ_{Vf} is the angle that the velocity vector at the front wheel makes with the longitudinal axis of the vehicle and δ is the front wheel steering angle. The rear wheel slip angle is similarly given by

$$\alpha_r = -\theta_{Vr} \qquad (13.6)$$

where θ_{Vr} is the angle that the velocity vector at the rear wheel makes with the longitudinal axis of the vehicle.

Note that if a vehicle is not being steered and is traveling straight ahead, then the velocity angle at the tire and the steering angle are both zero, resulting in zero slip angle.

A rough physical explanation of why the lateral tire force is proportional to slip angle is as follows. In the static region of the contact patch, the tip of each tread is in contact with the ground and remains stationary. The top of the tread therefore moves with respect to the tip of the tread resulting in tread deformation. As seen in Figure 13-7, if the velocity at the wheel is V_w, the lateral component of the velocity is $V_w \sin(\alpha)$. The magnitude of lateral deflection of the tread is proportional both to the lateral velocity and to the magnitude of time spent by the tread in the contact patch. Since the lateral velocity is proportional to velocity and slip angle while the amount of time in the contact patch is inversely proportional to the rotational velocity, the lateral tread deflection is effectively proportional only to the slip angle.

The lateral force on the tire depends on the magnitude of lateral deflection of the treads in the contact patch. Hence, for small slip angles, the lateral force is proportional to slip angle.

A more detailed explanation of the relationship between lateral force and slip angle can be found in section 13.6.

The lateral tire force for the front wheels of the vehicle can therefore be written as

$$F_{yf} = C_\alpha(\delta - \theta_{Vf}) \qquad (13.7)$$

where the proportionality constant C_α is called the cornering stiffness, δ is the front wheel steering angle and θ_{Vf} is the front tire velocity angle.

Similarly, the lateral tire force for the rear wheels of the vehicle can be written as

$$F_{yr} = C_\alpha(-\theta_{Vr}) \qquad (13.8)$$

where C_α is the cornering stiffness and $\theta_{V\,r}$ is the rear tire velocity angle.

The ratio of the lateral velocity to the longitudinal velocity at each wheel can be used to calculate the velocity angle at that wheel. Hence the following relations can be used to calculate θ_{vf} and θ_{vr}:

$$\tan\left(\theta_{V\,f}\right) = \frac{V_y + \ell_f \dot\psi}{V_x} \tag{13.9}$$

$$\tan\left(\theta_{V\,r}\right) = \frac{V_y - \ell_r \dot\psi}{V_x} \tag{13.10}$$

where V_y is the lateral velocity at the c.g. of the vehicle, V_x is the longitudinal velocity at the c.g. of the vehicle, $\dot\psi$ is the yaw rate of the vehicle and ℓ_f and ℓ_r are the longitudinal distances from the c.g. to the front and rear wheels respectively.

Using small angle approximations,

$$\theta_{V\,f} = \frac{V_y + \ell_f \dot\psi}{V_x} \tag{13.11}$$

$$\theta_{V\,r} = \frac{V_y - \ell_r \dot\psi}{V_x} \tag{13.12}$$

Hence

$$F_{yf} = C_\alpha\left(\delta - \frac{V_y + \ell_f \dot\psi}{V_x}\right) \tag{13.13}$$

$$F_{yr} = C_\alpha\left(-\frac{V_y - \ell_r \dot\psi}{V_x}\right) \tag{13.14}$$

13.5 INTRODUCTION TO THE MAGIC FORMULA TIRE MODEL

The linear tire force models discussed in sections 13.3 and 13.4 are good approximations when the slip ratio and slip angle are small respectively. A more sophisticated model is required for large slip angles and large slip ratios. The Magic Formula tire model (Pacejka and Bakker, 1993) provides a method to calculate lateral and longitudinal tire forces F_y and F_x and aligning moment M_z for a wide range of operating conditions including large slip angle and slip ratios as well as combined lateral and longitudinal force generation.

In the simpler case where only either lateral or longitudinal force is being generated, the force generated Y can be expressed as a function of the input variable X as follows:

$$Y(X) = y(x) + S_v \tag{13.15}$$

with

$$y(x) = D\sin\left[C\arctan\{Bx - E(Bx - \arctan Bx)\}\right] \tag{13.16}$$

$$x = X - S_h \tag{13.17}$$

where

Y is the output variable: longitudinal force F_x or lateral force F_y or aligning moment M_z

X is the input variable: slip angle α or slip ratio σ_x.

The model parameters B, C, D, E, S_v and S_h have the following nomenclature:

B stiffness factor
C shape factor
D peak value
E curvature factor
S_h horizontal shift
S_v vertical shift
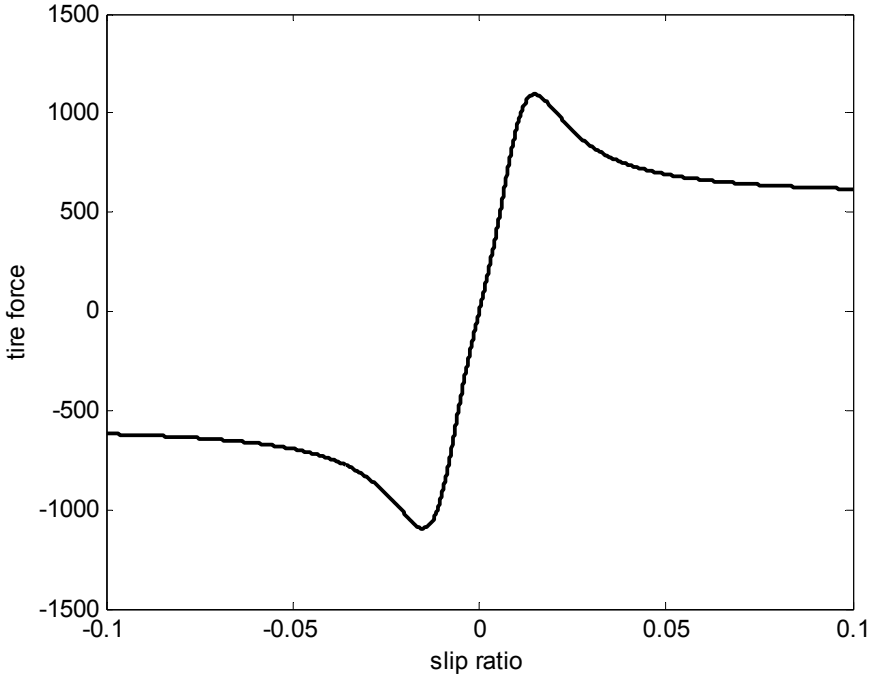
Figure 13-8. Magic Formula tire force curve

This empirical formula is capable of producing characteristics (see Figure 13-8) that closely match measured curves for the side force F_y and the longitudinal force F_x as functions of their respective slip quantities: slip angle α and longitudinal slip ratio σ_x.

To learn more about the Magic Formula tire model and how the parameters B, C, D, E, S_h and S_v are chosen, see section 13.9 of this chapter.

For small slip angles and small slip ratio values, the linear tire force relation between Y and X can be approximated by

$$Y = (BCD)\, X \tag{13.18}$$

The quantity BCD in equation (13.18) represents the cornering stiffness C_α or the longitudinal tire stiffness C_σ.

13.6 DEVELOPMENT OF LATERAL TIRE MODEL FOR UNIFORM NORMAL FORCE DISTRIBUTION

This section develops an analytical model for the relation between lateral tire force and the variables slip angle, normal force, tire-road friction coefficient and elastic tire properties. Section 13.6.1 deals with small slip angles while section 13.6.2 deals with a general formulation where the slip angle is allowed to be large.
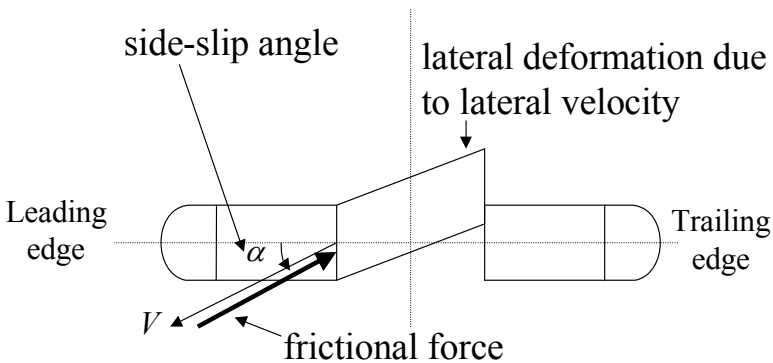
Figure 13-9. Lateral tire deflection and force generation

Lateral forces on the tire from the road occur primarily due to the presence of side-slip angle i.e. due to the presence of non-zero lateral velocity. Friction forces act in a direction opposite to that of the velocity (see Figure 13-9). The tire force can take any value between $+\mu F_z$ and $-\mu F_z$ where μ is the value of the friction coefficient between the road and the tire and F_z is the value of the normal (vertical) load on the tire. The actual value taken by the force depends on the slip angle and on the stiffness and elastic properties of the tire.

As we have seen, the material of a tire is a multi-layered, non-uniform, anisotropic, cord-rubber composite. In order to develop a tractable model for the tire, significant simplification in the representation of the tire is necessary.

The elastic foundation model is a simplification in which each small element of the contact patch surface is considered to act independently; if forced by the ground it can be displaced from its null position relative to the foundation and resists with a given stiffness (Fiala, 1954, Dixon, 1991).

Figure 13-10 shows a plan view of a tire during cornering, showing the lateral deflection of the tire center-line in the contact patch. Each element is constrained by a foundation stiffness spring, attempting to restore the element to its central position. The elastic foundation model for lateral force generation was developed by Fiala (Fiala, 1954).
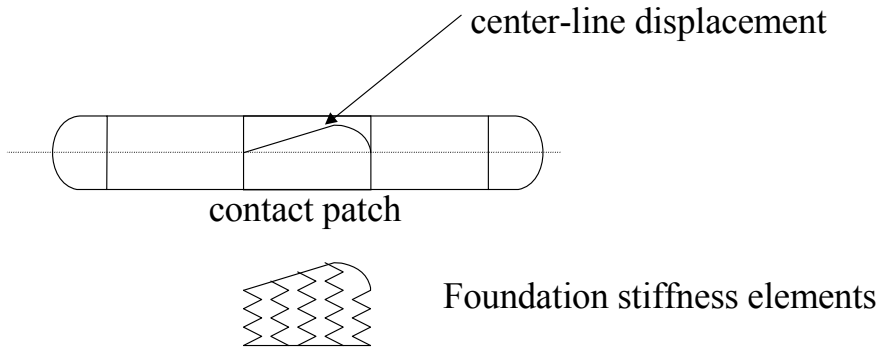

Figure 13-10. Lateral tire deflection and foundation stiffness elements

The elastic foundation model is the simplest model - it allows a discontinuous distribution of displacement and a discontinuous slope of the center-line. A more sophisticated model is the so-called "string model" which allows discontinuous change of slope, but not of deflection. The "beam model" does not allow discontinuities of either. None of these models reflect directly, in a physical sense, the true complexity of a real tire. However, even the simplest model, the elastic foundation alone, produces many of the interesting characteristics of a real tire, and this model will be used in this chapter to predict various properties of tires and to illustrate force generation behavior in the contact patch.

13.6.1   Lateral forces at small slip angles

Let α be the slip angle at the tire i.e. the angle between the orientation of the wheel and the velocity of the wheel, as shown in Figure 13-11. Due to friction forces, as explained in section 13.4, the treads of the tire bend in a direction opposite to that of the velocity. Hence the deformation of the tire caused by friction is as shown in Figure 13-11.

The maximum value that the lateral friction force can reach is μF_z where μ is the tire-road friction coefficient and F_z is the vertical (normal) force on the tire. The actual value of the friction force depends on the force

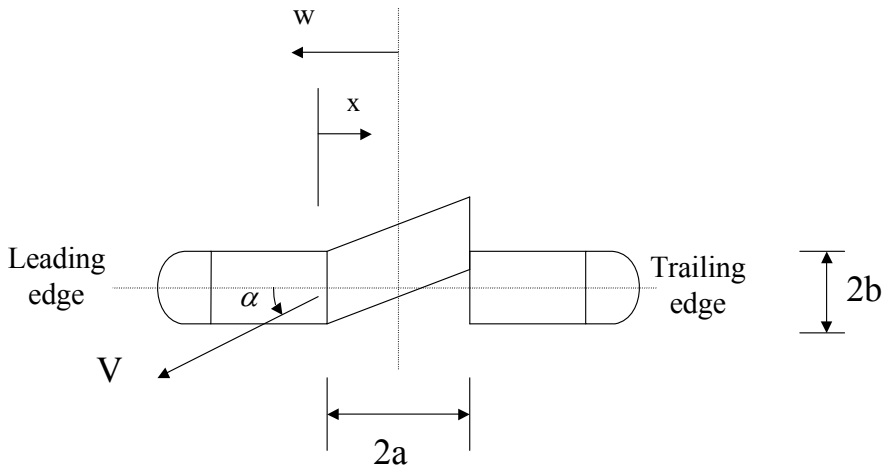required to produce the deflection shown in Figure 13-11 but is limited to a maximum of μF_z.

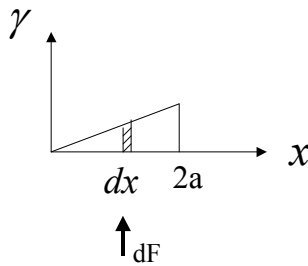*Figure 13-11.* Tire deformation at small slip angle

Figure 13-12. Tire deformation notation

Let c be the lateral stiffness per unit length of the tire and $\gamma(x)$ be the lateral displacement of the tire as a function of x. Then

$$dF = c(\gamma)(dx) \tag{13.19}$$

The total lateral force is given by

$$F_y = \int_0^{2a} c\gamma(x)\, dx \tag{13.20}$$

Self-aligning moment is the moment about the contact patch center-point and is given by

$$M_z = \int_0^{2a} c\gamma(x)(x-a)\,dx \qquad (13.21)$$

As slip angle increases, tire deflection increases and hence tire force increases, up to the maximum allowable value of μF_z.

In this section, we consider the case where

a) the vertical (normal) pressure distribution is uniform over the contact patch
b) the slip angle is small, so that tire road forces are less than μF_z over the entire contact patch.

For the small slip angle regime with no sliding

$$\gamma(x) = Sx$$

where $S = \tan\alpha \approx \alpha$ for small slip angles.

Hence

$$F_y = \int_0^{2a} c\gamma(x)\,dx = cS\left.\frac{x^2}{2}\right|_0^{2a} = 2ca^2 S \approx 2ca^2\alpha$$

The force acts through the triangle centroid, a distance $\dfrac{2}{3}(2a)$ from the point of initial contact and hence $\dfrac{1}{6}(2a)$ behind the patch center-point. Hence the self-aligning moment is

$$M_z = \frac{F_y(2a)}{6}$$

Table 13-1. Summary of Lateral Tire Model for Small Side Slip Angle

SUMMARY OF LATERAL TIRE MODEL FOR SMALL SLIP ANGLE		
Symbol	Nomenclature	Equation
F_y	Lateral force	$F_y = C_\alpha \alpha$
M_z	Self-aligning moment	$M_z = \dfrac{a}{3} F_y$
C_α	Cornering stiffness	$C_\alpha = 2ca^2$

13.6.2   Lateral forces at large slip angles

Next we allow slip angle to be large and allow sliding between the road and the tire.

Under the uniform contact pressure assumption, the pressure as a function of x is given by
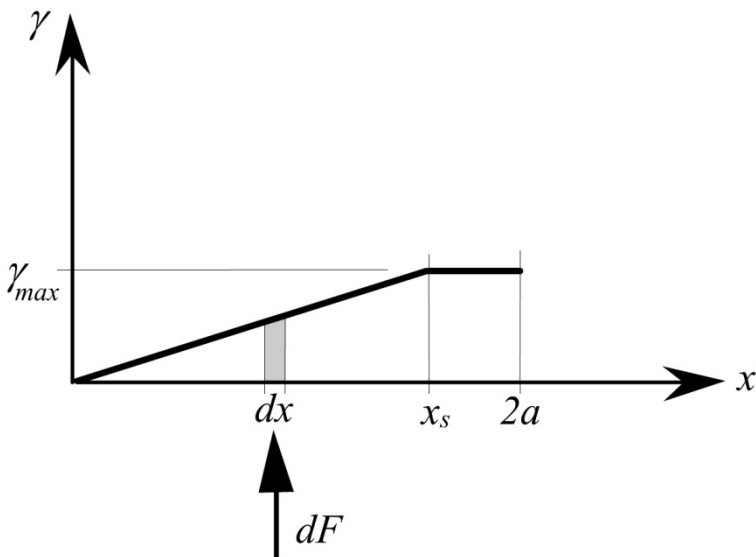
Figure 13-13. Tire deformation for large slip angle and uniform normal force distribution

$$p(x) = p = \frac{\mu F_z}{(2a)(2b)} \tag{13.22}$$

In this case the lateral deflection in the contact patch will be of the profile shown in Figure 13-13.

Consider the case where the slip angle α and hence the lateral deflection $\gamma(x)$ are positive. There will be no sliding at all in the contact patch if the following condition is satisfied along the entire contact patch

$$2ac\gamma(x) \le \mu F_z \tag{13.23}$$

Hence the maximum possible lateral tire displacement with no sliding is

$$\gamma_{max} = \frac{\mu F_z}{c(2a)} \tag{13.24}$$

Now consider the case where the slip angle is larger so that sliding occurs in a portion of the contact patch. In the presence of sliding, the lateral displacement is given by

$$\gamma(x) = \frac{\gamma_{max}}{x_s}x \quad 0 \le x \le x_s \tag{13.25}$$

$$\gamma(x) = \gamma_{max} \quad x_s \le x \le 2a \tag{13.26}$$

where x_s is the value of x at which sliding begins to occur.

The lateral force in this case is given by

$$F_y = \int_0^{2a} c\gamma(x)\, dx$$

$$= \int_0^{x_s} c\frac{x}{x_s}\gamma_{max}\, dx + \int_{x_s}^{2a} c\gamma_{max}\, dx$$

$$= \frac{1}{2}c\gamma_{max}x_s + c\gamma_{max}(2a - x_s) \tag{13.27}$$

Define lateral slip as follows

$$S = \tan(\alpha) \tag{13.28}$$

The initiation point for sliding x_s can be calculated as follows:

$$\tan\alpha = S = \frac{\gamma_{max}}{x_s}$$

Hence

$$x_s = \frac{\gamma_{max}}{S} = \frac{\mu F_z}{2acS} \tag{13.29}$$

Substituting $x_s = \dfrac{\mu F_z}{c(2a)S}$ and $\gamma_{max} = \dfrac{\mu F_z}{c(2a)}$, we get a quadratic relation for the lateral force F_y.

$$F_y = \mu F_z - \frac{\mu^2 F_z^{\,2}}{8ca^2 S} \tag{13.30}$$

As an illustrative example, if the contact patch length is 180 mm, the normal load is 5kN, the friction coefficient is 1.0, and effective foundation stiffness is 3 Mpa, then this gives $\alpha_{sliding}$ = 2.95 degrees, S = 0.051, γ_{max} = 9.3 mm.

The self-aligning moment is given by

$$M_z = \int_0^\ell c\gamma(x)\left(x - \frac{1}{2}\ell\right)dx = \frac{ca\gamma_{max}x_s}{2} - \frac{c\gamma_{max}x_s^{\,2}}{6}$$

or

$$M_z = \frac{\mu^2 F_z^{\,2}}{8caS} - \frac{\mu^3 F_z^{\,3}}{48c^2 a^3 S^2} \tag{13.31}$$

The *pneumatic trail* is defined as the ratio of the aligning moment to the total lateral force on the tire. It can be interpreted as the distance behind the center of the contact patch at which the equivalent lateral force vector acts. The pneumatic trail in this case can be calculated to be

$$t = \frac{M_z}{F_y} = \frac{12\mu F_z ca^2 S - 2\mu^2 F_z^2}{96c^2 a^3 S^2 - 12\mu F_z caS} = \frac{6\mu F_z ca^2 S - \mu^2 F_z^2}{48c^2 a^3 S^2 - 6\mu F_z caS}$$

(13.32)

Hence the self-aligning torque reduces as the slip angle increases, even though the force increases. This is because the pneumatic trail goes to zero due to the increasing value of the term $S = \tan(\alpha)$.

The reduction of self-aligning moment and hence of steering wheel torque as the lateral force approaches its limit is a valuable form of feedback to the driver. It is especially important in giving warning of a poor friction surface.

It is more realistic to consider the contact pressure to have a parabolic distribution. This will be considered in the next section.

Table 13-2. Summary of Lateral Tire Model for Uniform Normal Force Distribution

SUMMARY OF LATERAL TIRE MODEL FOR UNIFORM NORMAL FORCE DISTRIBUTION		
Symbol	Nomenclature	Equation
x_s	Initiation point in the contact patch for sliding	$x_s = \dfrac{\gamma_{max}}{S} = \dfrac{\mu F_z}{2acS}$
F_y	Lateral force	$F_y = \mu F_z - \dfrac{\mu F_z^2}{8ca^2 S}$
M_z	Self-aligning moment	$M_z = \dfrac{\mu^2 F_z^2}{8caS} - \dfrac{\mu^3 F_z^3}{48c^2 a^3 S^2}$
S	Lateral slip	$S = \tan(\alpha)$

13.7 DEVELOPMENT OF LATERAL TIRE MODEL FOR PARABOLIC NORMAL PRESSURE DISTRIBUTION

It is much more accurate to consider the normal force (pressure) distribution on the contact patch to be parabolic. In this case the pressure distribution in the contact patch is given by

$$p = p_0 \left\{ 1 - \frac{w^2}{a^2} \right\} \tag{13.33}$$

where $w = a - x$, as shown in Figure 13-14. Again, $2a$ is the length of the contact patch and $2b$ is the width of the contact patch.
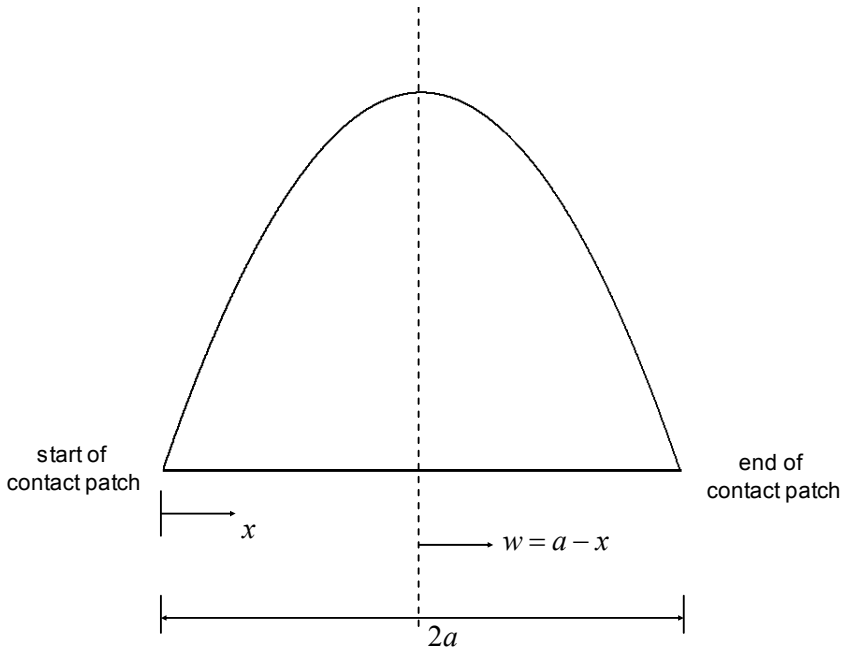

Figure 13-14. Parabolic normal pressure distribution on contact patch

The constant p_0 can be calculated as follows. Vertical force equilibrium requires $\int_{-a}^{a} 2bp(w)\, dw = F_z$ and hence

$$p_0 = \frac{3F_z}{8ab} \tag{13.34}$$

Hence , the normal pressure is

$$p(x) = \frac{3F_z}{8ab}\left[1 - \frac{(a-x)^2}{a^2}\right] \tag{13.35}$$

which can be rewritten as

$$p(x) = \frac{3F_z}{8a^3b}\left[x(2a-x)\right] \tag{13.36}$$

In the case of parabolic normal force distribution, as we shall see, there will always be a region of sliding in the contact patch, unless the slip angle is zero. The overall lateral deflection in the contact patch will have a profile as shown in Figure 13-15.
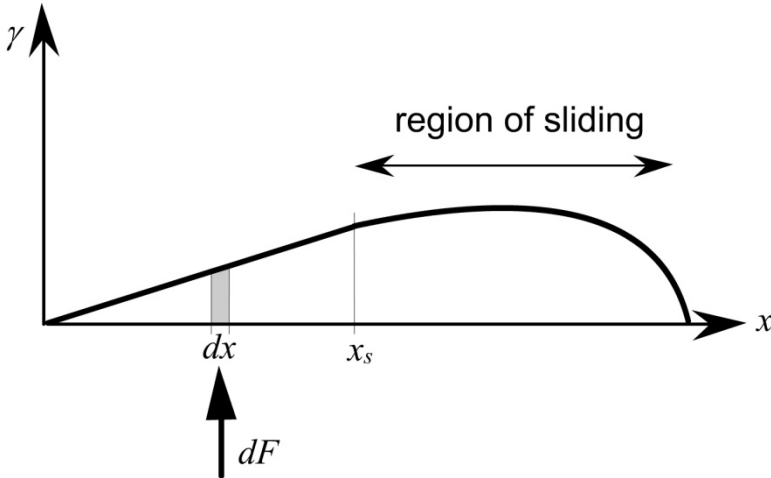

Figure 13-15. Lateral deformation with parabolic normal force distribution

Let the lateral stiffness of the tire per unit area be k N/m^3. Note that k is related to the lateral stiffness per unit length c by

$$k = \frac{c}{2b} \tag{13.37}$$

Consider the case where the slip angle is positive (i.e. $S = \tan(\alpha) > 0$). The deflection profile in the region of sliding can be calculated from lateral force equilibrium as follows:

$$k\gamma_{sliding}(x) = \mu\, p(x)$$

or

$$k\gamma_{sliding}(x) = \frac{3\mu F_z}{8a^3 b}\, \{x(2a - x)\} \tag{13.38}$$

Define

$$\theta = \frac{4a^2 bk}{3\mu F_z} \tag{13.39}$$

Then the lateral deflection profile in the region of sliding is

$$\gamma_{sliding} = \frac{1}{2a\theta}\{x(2a - x)\} \tag{13.40}$$

Initiation of sliding

The point $x = x_s$ in the contact patch at which sliding begins can be calculated from

$$\gamma(x_s) = Sx_s = \frac{1}{2a\theta} x_s(2a - x_s)$$

where $S = \tan(\alpha)$. Hence $2a\theta S = 2a - x_s$, or

$$x_s = 2a(1 - \theta S) \tag{13.41}$$

Note tht if $S < 0$ then equation (13.41) becomes

$$x_s = 2a(1 + \theta S) \tag{13.42}$$

From equation (13.41), it is clear that $x_s \leq 2a$. In fact x_s can be equal to $2a$, only if $S = 0$. Hence, there will always be sliding, unless the slip angle is zero, i.e. $S = 0$. In all other cases, $x_s < 2a$, and there will be a region of sliding in the contact patch.

Total lateral force

Again, first consider the case $S > 0$. The total lateral tire force can be obtained from the equation

$$F_y = 2b \int_0^{x_s} kx \frac{\gamma(x_s)}{x_s} \, dx + 2b \int_{x_s}^{2a} \frac{k}{2a\theta} x(2a - x) \, dx$$

where the first term is the force from the region with no sliding and the second term is the force from the region of sliding. Hence

$$F_y = 2bk \frac{\gamma(x_s)}{x_s} \frac{x_s^2}{2} + \frac{2bk}{2a\theta} \left[\frac{2ax^2}{2} - \frac{x^3}{3} \right]_{x_s}^{2a}$$

$$= \frac{2bk}{2a\theta} \frac{x_s(2a - x_s)}{x_s} \frac{x_s^2}{2} + \frac{2bk}{2a\theta} \left[4a^3 - \frac{8a^3}{3} - ax_s^2 + \frac{x_s^3}{3} \right]$$

$$= \frac{bk}{a\theta} \left[\frac{4a^3}{3} - \frac{x_s^3}{6} \right]$$

$$= \frac{8bka^3}{6a\theta} \left[1 - \left(\frac{x_s}{2a} \right)^3 \right]$$

or

$$F_y = \mu F_z \left[1 - \left(\frac{x_s}{2a} \right)^3 \right] \qquad (13.43)$$

Replacing x_s from equation (13.41), the lateral force is obtained as

$$F_y = \mu F_z \left[1 - \frac{1}{8a^3} 8a^3 (1 - \theta S)^3 \right]$$

$$F_y = \mu F_z \left[1 - (1 - \theta S)^3 \right]$$

$$F_y = \mu F_z \left[3\theta S - 3\theta^2 S^2 + \theta^3 S^3 \right] \qquad (13.44)$$

Note that since $0 \leq x_s \leq 2a$, it follows from equations (13.41) and (13.42) that $|S| \leq \frac{1}{\theta}$. Hence the total lateral force F_y cannot exceed μF_z.

Note that when $S = \frac{1}{\theta}$, then equation (13.44) yields $F_y = \mu F_z$. If $|S| \geq \frac{1}{\theta}$, then $F = \mu F_z \, \text{sgn}(S)$. $|S| = \frac{1}{\theta}$ is the limit of slip and represents the value of slip at which a situation of complete sliding is reached.

Hence, the complete expression for the lateral force can be more explicitly written as

$$F_y = \mu F_z \left[3\theta |S| - 3\theta^2 |S|^2 + \theta^3 |S|^3 \right] \text{sgn}(S) \quad |S| \leq \frac{1}{\theta} \qquad (13.45)$$

$$F_y = \mu F_z \, \text{sgn}(S) \qquad |S| > \frac{1}{\theta} \qquad (13.46)$$

with $\theta = \dfrac{4a^2bk}{3\mu F_z}$

Self-aligning moment

For $S \geq 0$, the self-aligning moment can be obtained from

$$M_z = -2b \int_{-a}^{a} F_y w \, dw \quad \text{or}$$

$$M_z = -2b \int_{0}^{2a} F_y (a - x) \, dx \quad \text{or}$$

$$M_z = \mu F_z a \left(\frac{x_s}{2a}\right)^3 \left(1 - \frac{x_s}{2a}\right) \text{ if } F_y \leq \mu F_z.$$

Hence, for both positive and negative values of S,

$$M_z = \mu F_z a \left[\theta|S| - 3\theta^2|S|^2 + 3\theta^3|S|^3 - \theta^4|S|^4\right]\text{sgn}(S) \quad |S| \leq \frac{1}{\theta} \quad (13.47)$$

$$M_z = 0 \qquad\qquad |S| > \frac{1}{\theta} \qquad\qquad\qquad\qquad\qquad (13.48)$$

The pneumatic trail is obtained by dividing M_z by F_y which yields

$$t(S) = \frac{M_z}{F_y} = \frac{1}{3} a \frac{1 - 3\theta|S| + 3\theta^2|S|^2 - \theta^3|S|^3}{1 - \theta|S| + \frac{1}{3}\theta^2|S|^2} \quad |S| \leq \frac{1}{\theta} \qquad (13.49)$$

$$t(S) = 0 \qquad\qquad |S| > \frac{1}{\theta} \qquad\qquad\qquad\qquad\qquad (13.50)$$

Hence $M_z = t(S)F_y$.

Table 13-3. Summary of Lateral Tire Model for Parabolic Normal Force Distribution

SUMMARY OF LATERAL TIRE MODEL FOR PARABOLIC NORMAL FORCE DISTRIBUTION		
Symbol	Nomenclature	Equation
S	Tangent of slip angle	$S = \tan(\alpha)$
θ	Constant related to tire parameters and normal force	$\theta = \dfrac{4a^2bk}{3\mu F_z}$
F_y	Lateral force	$F_y = \mu F_z\left[3\theta\lvert S\rvert - 3\theta^2\lvert S\rvert^2 + \theta^3\lvert S\rvert^3\right]\mathrm{sgn}(S)$ $\quad\text{if } \lvert S\rvert \le \dfrac{1}{\theta}$ $F_y = \mu F_z\,\mathrm{sgn}(S) \quad \text{if } \lvert S\rvert > \dfrac{1}{\theta}$
M_z	Self-aligning moment	$M_z = \mu F_z a\left[\theta\lvert S\rvert - 3\theta^2\lvert S\rvert^2 + 3\theta^3\lvert S\rvert^3 - \theta^4\lvert S\rvert^4\right]$ $\mathrm{sgn}(S) \ \text{if } \lvert S\rvert \le \dfrac{1}{\theta}$ $M_z = 0 \quad \text{if} \quad \lvert S\rvert > \dfrac{1}{\theta}$

13.8 COMBINED LATERAL AND LONGITUDINAL TIRE FORCE GENERATION

The previous sections discussed generation of lateral or longitudinal tire forces in the presence of pure lateral side slip angle or pure longitudinal slip ratio respectively. In the presence of both side-slip angle and slip ratio, the tire force equations have to be modified to account for the fact that the total vector sum of the force generated cannot exceed μF_z.
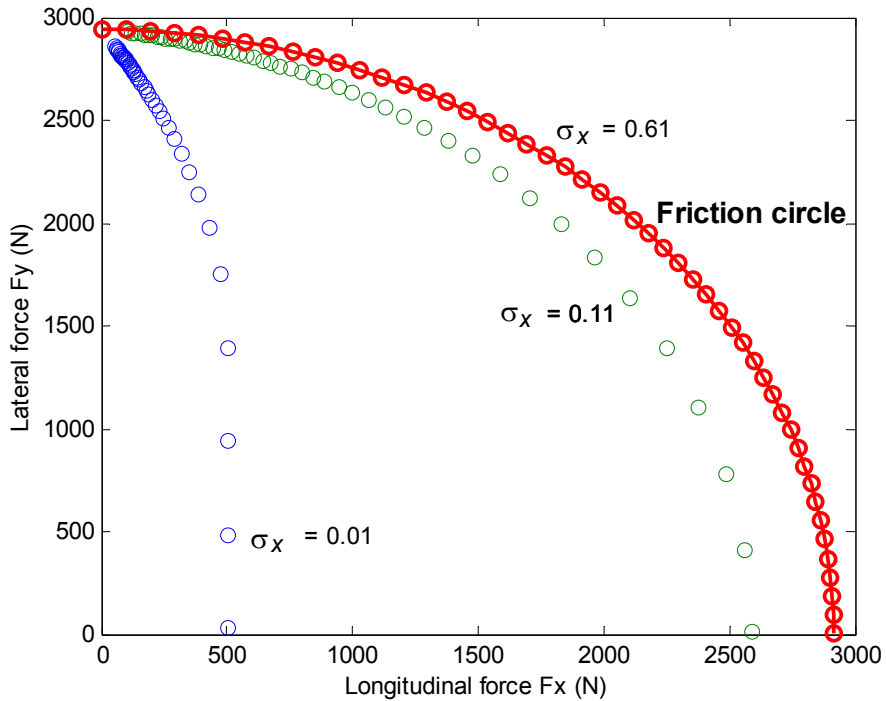
Figure 13-16. Friction circle for tire forces

Figure 13-16 shows the friction circle diagram obtained from an analytical model for combined lateral and longitudinal tire forces. The inner circles represent different combinations of lateral and longitudinal tire forces corresponding to various levels of slip ratio and slip angle. The innermost circle is the curve corresponding to a longitudinal slip ratio of $\sigma_x = 0.01$ and various values of lateral slip angle increasing from 0.001 radians to 0.78 radians. It can be seen that for the same value of longitudinal slip ratio, the magnitude of longitudinal tire force produced decreases as the lateral slip angle (and hence the lateral tire force) increase. Thus, the magnitude of longitudinal tire force that can be produced decreases with increase in the lateral tire force, and vice-versa. The second circle is a curve corresponding to a longitudinal slip ratio of $\sigma_x = 0.11$ and the outermost circle is a curve corresponding to a longitudinal slip ratio of $\sigma_x = 0.61$. As the longitudinal slip ratio increases, the longitudinal tire force that can be produced saturates. The outermost circle shows that the total vector sum of lateral and longitudinal forces generated cannot lie outside the circle of radius μF_z.

In the presence of both significant side slip angle and longitudinal slip ratio, the combined tire force model for a parabolic normal force distribution

is described mathematically as follows. The magnitude of the total force is (Pacejka and Sharp, 1991)

$$F = \mu F_z \left\{ 3\theta\sigma - \frac{1}{3}(3\theta\sigma)^2 + \frac{1}{27}(3\theta\sigma)^3 \right\} \text{ if } \sigma \leq \sigma_m \qquad (13.51)$$

$$F = \mu F_z \qquad \text{if } \sigma > \sigma_m \qquad (13.52)$$

In the above equations, σ is total slip, and σ_m is the value of the slip where complete sliding is reached, and it is given by the following:

$$\sigma_m = \frac{1}{\theta} \qquad (13.53)$$

where

$$\theta = \frac{4a^2 bk}{3\mu F_z} \qquad (13.54)$$

The total slip σ is composed of the longitudinal and the lateral slip:

$$\sigma = \sqrt{\sigma_x^2 + \sigma_y^2} \qquad (13.55)$$

Note that σ as defined by equation (13.55) is always positive. Likewise, the force F defined by equations (13.51) and (13.52) is also positive.

The longitudinal and the lateral forces are given by:

$$F_x = \frac{\sigma_x}{\sigma} F \qquad (13.56)$$

$$F_y = \frac{\sigma_y}{\sigma} F \qquad (13.57)$$

where σ_x and σ_y are defined as follows:

$$\sigma_x = \frac{r_{eff}\omega_w - V_x}{r_{eff}\omega_w}, \text{ during acceleration} \qquad (13.58)$$

Table 13-4. Summary of Tire Model for Combined Force Generation

	SUMMARY OF TIRE MODEL FOR COMBINED FORCE GENERATION (Adapted from results in Pacejka and Sharp, 1991)	
Symbol	Nomenclature	Equation
σ_x	Longitudinal slip ratio	$\sigma_x = \dfrac{r_{eff}\omega_w - V_x}{r_{eff}\omega_w}$ during acceleration $\sigma_x = \dfrac{r_{eff}\omega_w - V_x}{V_x}$ during braking
σ_y	Lateral side slip	$\sigma_y = \dfrac{V_x}{r_{eff}\omega_w}\tan\alpha$
σ	Total slip	$\sigma = \sqrt{\sigma_x{}^2 + \sigma_y{}^2}$
$\sigma_m =$	Value of slip for complete sliding	$\theta = \dfrac{4a^2 bk}{3\mu F_z}$
F	Total force	$F = \mu F_z\left\{3\theta\sigma - \dfrac{1}{3}(3\theta\sigma)^2 + \dfrac{1}{27}(3\theta\sigma)^3\right\}$ if $\sigma \le \sigma_m$ $F = \mu F_z$ if $\sigma \ge \sigma_m$
F_y	Lateral force	$F_y = \dfrac{\sigma_y}{\sigma} F$
F_x	Longitudinal force	$F_x = \dfrac{\sigma_x}{\sigma} F$
M_z	Self-aligning moment	$M_z = \dfrac{\sigma_y}{\sigma}\mu F_z a\left[\theta\sigma - 3\theta^2\sigma^2 + 3\theta^3\sigma^3 - \theta^4\sigma^4\right]$ if $\sigma \le \sigma_m$ $M_z = 0$ if $\sigma > \sigma_m$

$$\sigma_x = \frac{r_{eff}\omega_w - V_x}{V_x} \text{ , during braking} \tag{13.59}$$

and

$$\sigma_y = \frac{V_x}{r_{eff}\omega_w}\tan\alpha \tag{13.60}$$

where ω_w is the wheel speed of revolution, r_{eff} is the effective tire radius and V_x is the longitudinal vehicle speed. F_x and F_y have the same sign as σ_x and σ_y respectively.

The following table (Table 13-4) summarizes the force and self aligning moment equations for the combined tire model.

The above equations for combined force generation can be reduced to the equations for pure lateral or longitudinal force generation as follows.

In the case of pure lateral slip, set $\sigma_y = \tan(\alpha)$ and $\sigma_x = 0$ in equations (13.55) and (13.51). In the case of pure longitudinal slip, set $\sigma_y = 0$, calculate σ_x from equation (13.58)-(13.59) and use equations (13.55) and (13.51).

13.9   THE MAGIC FORMULA TIRE MODEL

The analytical elastic foundation models or brush models developed in sections 13.6, 13.7 and 13.8 are physically intuitive and appear quite realistic. Results from these models can match experimental data well for cases of pure lateral or pure longitudinal force generation. However, the analytical models do not always lead to quantitatively accurate results (Pacejka and Sharp, 1991). Differences from experimental data are observed, especially at large slip and at combined slip. The following important features which are not included in the simple brush model may be responsible for these differences:

1) unequal stiffness in x and y directions,
2) non-symmetric and non-constant pressure distribution.
3) non-constant friction coefficient, including a difference between static and kinetic friction coefficients

While these factors could be accounted for by introducing them into the physical model, that would highly increase model complexity. An alternate

way to obtain a more accurate mathematical model is to use empirical expressions. A widely used empirical tire model is the so-called Magic Formula (Pacejka and Bakker, 1993) presented below.

In the simpler case where either lateral or longitudinal force only is being generated, the force generated Y can be expressed as a function of the input variable X as follows:

$$y = D\sin\left[C\arctan\{Bx - E(Bx - \arctan Bx)\}\right] \tag{13.61}$$

with

$$Y(X) = y(x) + S_v \tag{13.62}$$

$$x = X - S_h \tag{13.63}$$

where

Y is the output variable: longitudinal force F_x or lateral force F_y or aligning moment M_z

X is the input variable: slip angle α or slip ratio σ_x.

The model parameters B, C, D, E, S_v and S_h have the following nomenclature:

B stiffness factor
C shape factor
D peak value
E curvature factor
S_h horizontal shift
S_v vertical shift

For given values of the coefficients B, C, D and E the curve shows an anti-symmetric shape with respect to the origin. Without the horizontal and vertical shifts S_h and S_v, the Magic Formula $y(x)$ typically produces a curve that passes through the origin $x = y = 0$, reaches a maximum and subsequently tends to a horizontal asymptote. To allow the curve to have an offset with respect to the origin, the two shifts S_h and S_v are introduced (Pacejka and Bakker, 1993) and a new function $Y(X)$ is obtained as shown in . The formula is capable of producing characteristics that closely match measured experimental curves for the lateral force F_y and the

longitudinal force F_x as functions of their respective slip variables: slip angle α and longitudinal slip σ_x.

Figure 13-17 illustrates the meaning of some of the factors with the help of a typical lateral tire force characteristic:

1) The coefficient D represents the peak value of the tire force (or moment)
2) The product BCD corresponds to the slope at the origin $(x = y = 0)$.
3) The value y_s is the asymptotic value of the output y at large values of x.
4) The shape factor C controls the limits of the range of the sine function appearing in the formula (13.61) and thereby determines the shape of the resulting curve.

$$C = \frac{2}{\pi} \sin^{-1}\left(\frac{y_s}{D}\right) \tag{13.64}$$

5) The factor B is left to determine the slope at the origin and is called the stiffness factor.
6) The offsets S_h and S_v account for ply-steer and conicity effects and possibly the rolling resistance which can cause the F_y and F_x curves to not pass through the origin (Pacejka and Bakker, 1993).
7) E is called the curvature factor. It does not change the value of stiffness (slope at zero slip or zero slip angle). E also does not change the value of the peak. But E can be used to change the shape of the curve i.e. the curvature near the peak of the curve. E also controls the value of the slip x_m at which the peak of the curve occurs (if present):

$$E = \frac{Bx_m - \tan\left(\dfrac{\pi}{2C}\right)}{Bx_m - \tan^{-1}(Bx_m)} \tag{13.65}$$

8) Wheel camber can give rise to a considerable offset of the F_y versus α curves. Such a shift may be accompanied by a significant deviation from the pure anti-symmetric shape of the original curve (Pacejka and Bakker, 1993). To accommodate such an asymmetry, the curvature factor E is made dependent on the sign of the abscissa (x).

$$E = E_o + \Delta E \operatorname{sgn}(x) \tag{13.66}$$

Also the difference in shape that is expected to occur in the F_x vs σ characteristic between the driving and braking ranges can be taken care of by this modification (Pacejka and Bakker, 1993).

9)   The asymptotic value which y approaches at large slip values equals
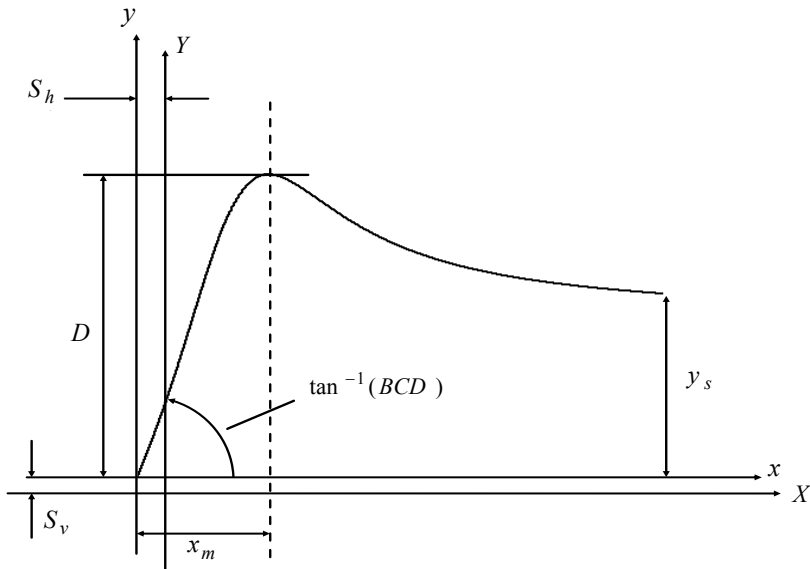
$$y_s = D \sin\left(\frac{\pi}{2}C\right) \tag{13.67}$$

Figure 13-17. Explanation of magic formula parameters

Functions of friction coefficient and normal tire load

The various parameters in the Magic Formula are functions of normal load and wheel camber angle. The parameters B, C, D and E can be expressed as functions of the normal load F_z and friction coefficient μ as follows (Pacejka and Bakker, 1993):

$$D = a_1 F_z^{\,2} + a_2 F_z \tag{13.68}$$

$$BCD = a_3 \sin\!\left(a_4 \arctan\!\left(a_5 F_z\right)\right) \text{ (lateral force)} \tag{13.69}$$

$$BCD = \frac{a_3 F_z{}^2 + a_4 F_z}{e^{a_5 F_z}} \text{ (longitudinal force)} \tag{13.70}$$

$$E = a_6 F_z{}^2 + a_7 F_z + a_8 \tag{13.71}$$

The variables a_1, $a_2, \cdots, a_8$ are constants that have to be determined for each tire.

13.10   DUGOFF'S TIRE MODEL

13.10.1 Introduction

Dugoff's tire model (Dugoff, et. al., 1969) is an alternative to the elastic foundation analytical tire model developed by Fiala (1954) for lateral force generation and by Pacejka and Sharp (1991) for combined lateral-longitudinal force generation.

Dugoff's model provides for calculation of forces under combined lateral and longitudinal tire force generation. It assumes a uniform vertical pressure distribution on the tire contact patch. This is a simplification compared to the more realistic parabolic pressure distribution assumed in Pacejka and Sharp (1991). However, the model offers one significant advantage – it allows for independent values of tire stiffness in the lateral and longitudinal directions. This is a major advantage, since the longitudinal stiffness in a tire could be quite different from the lateral stiffness.

Compared to the Magic Formula Tire Model (Pacejka and Bakker, 1993), Dugoff's model has the advantage of being an analytically derived model developed from force balance calculations. Further, the lateral and longitudinal forces are directly related to the tire road friction coefficient in more transparent equations.

The development of the Dugoff model is similar to the derivation developed in section 13.6 of this book for pure lateral force generation under the assumption of uniform vertical pressure distribution. The model development is not presented in this book, only the final model equations and their interpretation are presented.

13.10.2 Model equations

Let σ_x be the longitudinal slip ratio of the tire under consideration and α be the side slip angle. Let the cornering stiffness of the tire be given by C_α and the longitudinal tire stiffness by C_σ. Then the longitudinal tire force is given by (Guntur and Sankar, 1980, Dugoff, 1969)

$$F_x = C_\sigma \frac{\sigma_x}{1 + \sigma_x} f(\lambda) \tag{13.72}$$

and the lateral tire force is given by

$$F_y = C_\alpha \frac{\tan(\alpha)}{1 + \sigma_x} f(\lambda) \tag{13.73}$$

where λ is given by

$$\lambda = \frac{\mu F_z (1 + \sigma_x)}{2 \left\{ (C_\sigma \sigma_x)^2 + (C_\alpha \tan(\alpha))^2 \right\}^{1/2}} \tag{13.74}$$

and

$$f(\lambda) = (2 - \lambda)\lambda \text{ if } \lambda < 1 \tag{13.75}$$

$$f(\lambda) = 1 \text{ if } \lambda \geq 1 \tag{13.76}$$

F_z is the vertical force on the tire while μ is the tire-road friction coefficient.

13.10.3 Friction circle interpretation of Dugoff's model

A friction circle interpretation of the Dugoff model was developed by Guntur and Sankar (1980). Let

$$F_{x\_u\ell} = C_\sigma \frac{\sigma_x}{1 + \sigma_x} \tag{13.77}$$

and

$$F_{y\_u\ell} = C_\alpha \frac{\tan(\alpha)}{1+\sigma_x} \tag{13.78}$$

where $F_{x\_u\ell}$ and $F_{y\_u\ell}$ are the lateral and longitudinal tire forces that would be generated if the friction coefficient μ were unlimited.

Define

$$\mu_{u\ell} = \frac{\left(F_{x\_u\ell}{}^2 + F_{y\_u\ell}{}^2\right)^{1/2}}{F_z} \tag{13.79}$$

If $\lambda > 1$, then it follows from the definition of λ in equation (13.74) that the resultant of the lateral and longitudinal forces is less than half the maximum available friction force ($\mu F_z / 2$). In this case the lateral and longitudinal tire forces generated are equal to the values $F_{x\_u\ell}$ and $F_{y\_u\ell}$:

$$F_x = F_{x\_u\ell} \tag{13.80}$$

$$F_y = F_{y\_u\ell} \tag{13.81}$$

This is equivalent to the operating point being inside the friction circle.

If $\lambda < 1$, this is equivalent to the operating point being outside the friction circle. In this case, the lateral and longitudinal forces are given by (Guntur and Sankar, 1980)

$$F_x = \mu F_z \frac{C_\sigma \sigma_x}{\left\{(C_\sigma \sigma_x)^2 + (C_\alpha \tan(\alpha))^2\right\}^{1/2}} \left(1 - \frac{\mu}{4\mu_{u\ell}}\right) \tag{13.82}$$

$$F_y = \mu F_z \frac{C_\alpha \tan(\alpha)}{\left\{(C_\sigma \sigma_x)^2 + (C_\alpha \tan(\alpha))^2\right\}^{1/2}} \left(1 - \frac{\mu}{4\mu_{u\ell}}\right) \tag{13.83}$$

Equivalently, if $\mu < \dfrac{\mu_{u\ell}}{2}$, then the operating point is outside the friction circle and the lateral and longitudinal tire forces are given by

$$F_x = F_{x\_u\ell} \frac{\mu}{\mu_{u\ell}} \left(1 - \frac{\mu}{4\mu_{u\ell}} \right) \tag{13.84}$$

$$F_y = F_{y\_u\ell} \frac{\mu}{\mu_{u\ell}} \left(1 - \frac{\mu}{4\mu_{u\ell}} \right) \tag{13.85}$$

13.11   DYNAMIC TIRE MODEL

A typical dynamic model that can be used for lateral tire force dynamics is first order and represented by

$$\tau_{lag} \dot{F}_{y\_lag} + F_{y\_lag} = F_y \tag{13.86}$$

where F_y is the tire lateral force from any of the quasi-static models described in the previous sections of this chapter and F_{y_lag} is the dynamic or lagged lateral force (Guenther, et. al., 1990, Heydinger, et. al., 1991). The time constant τ_{lag} is the relaxation time constant and can be approximated by

$$\tau_{lag} = \frac{C_\alpha}{KV_x} \tag{13.87}$$

where V_x is the longitudinal velocity, $C_\alpha = \left. \dfrac{\partial F_y}{\partial \alpha} \right|_{\alpha=0}$ is the cornering stiffness and $K = \left. \dfrac{\partial F_y}{\partial y} \right|_{y=0}$ is the equivalent tire lateral stiffness. Multiplying relaxation time constant by vehicle speed gives tire relaxation length

$$L = \frac{C_\alpha}{K} \tag{13.88}$$

The relaxation length is the approximate distance needed to build up tire forces.

This model is not valid for low velocities (note the presence of longitudinal velocity in the denominator in equation (13.87)).

It has also been shown that experimentally measured lateral tire forces have under-damped characteristics at high speeds (Heydinger, et. al., 1991). Changing the tire dynamic model from first-order lateral tire force dynamics to second-order slip angle dynamics helps capture the under-damped tire dynamics accurately (Heydinger, et. al., 1991).

13.12 CHAPTER SUMMARY

This chapter discussed models for lateral and longitudinal tire force generation. In addition to tire parameters, the primary variables these tire forces depend on are slip angle, slip ratio, normal tire load and tire-road friction coefficient. At small slip angles, the lateral tire force is proportional to slip angle. At small slip ratios, the longitudinal tire force is proportional to slip ratio. The reasons for this linear dependence were explained physically by analyzing the tire tread deformations in the contact patch.

An analytical elastic foundation model was developed which could be used to describe tire force at larger slip angles and slip ratios. The analytical elastic foundation model has been found to be accurate and convenient to use when either longitudinal or lateral force only is generated. For combined force generation, the Pacejka Magic Formula tire model which is an empirical model can be utilized. The Magic Formula model was presented and the parameters used in the model were explained. The Magic Formula model, with appropriate choice of parameters, can be very effective in representing both lateral, longitudinal and combined tire force generation. An alternative model for combined force generation is the Dugoff tire model which has the advantage of being an analytically developed model.

NOMENCLATURE

Tire related variables

α	slip angle at a tire
S	lateral slip ($= \tan(\alpha)$)
σ_x	longitudinal slip ratio

σ_y lateral slip $= \dfrac{V_x}{r_{eff}\,\omega_w}\tan(\alpha)$

σ total slip $= \sqrt{\sigma_x^{\,2} + \sigma_y^{\,2}}$

x_S distance from leading edge of the tire at which sliding initiates

a half-length of contact patch

b half-width of contact patch

k isotropic stiffness of tire elements per unit area of the belt surface

$c = 2bk$ lateral stiffness of tire defined per unit length

F_y lateral force on a tire

M_z self-aligning moment of a tire

ω_w rotational velocity of tire

r_{eff} effective tire radius

μ tire-road friction coefficient

F_z normal (vertical) load

θ Inverse of the limiting value of slip $= \dfrac{4a^2bk}{3\mu F_z}$

σ_m limiting value of slip $= \dfrac{1}{\theta}$

μ tire-road friction coefficient

λ variable used in Dugoff tire model

$f(\lambda)$ function used in Dugoff tire model

$F_{y\_u\ell},\; F_{x\_u\ell}$ variables used in Dugoff tire model

$\mu_{u\ell}$ variable used in Dugoff tire model

τ_{lag} relaxation time constant used in dynamic tire model

L tire relaxation length

B, C, D, E, S_v, S_h Magic Formula factors

Vehicle related variables

F_{yf}, F_{yr}	lateral forces at front and rear tires respectively
α_f, α_r	slip angles at the front and rear tires respectively
$C_{\alpha f}, C_{\alpha r}$	cornering stiffness of each front and rear tire respectively
$C_{\sigma f}, C_{\sigma r}$	longitudinal stiffness of each front and rear tire respectively
V_x	longitudinal velocity
V_y	lateral velocity at the c.g. of the vehicle
I_z	yaw-moment of inertia of the vehicle
m	mass of the vehicle
ℓ_f, ℓ_r	distances from c.g. to the front and rear tires respectively

REFERENCES

Bakker, E., Nyborg, L. and Pacejka, H.B., "Tyre Modelling for Use in Vehicle Dynamics Studies," *SAE Technical Paper Series*, Paper No. 870421, pp. 1-15, 1987

Dixon, J.C., *Tyres, Suspension and Handling*, Cambridge University Press, ISBN 0 521 40194 1, 1991.

Dugoff, H., Fancher, P.S. and Segal, L., "Tyre performance charecteristics affecting vehicle response to steering and braking control inputs, " *Final Report, Contract CST-460*, Office of Vehicle Systems Research, US National Bureau of Standards, 1969.

Fiala, E., "Lateral Forces on Rolling Pneumatic Tires, " *Zeitschrift V.D.I.* 96, No. 29, October 1954 (in German).

Guenther, D.A., Loeb, J.S., Ellis, J.R., and Chen, F.H., "Lateral Stiffness, Cornering Stiffness and Relaxation Length of the Pneumatic Tire," *SAE Technical Paper Series*, Paper No. 900129, SAE Congress and Exposition, 1990.

Guntur, R. and Sankar, S., "A friction circle concept for Dugoff's tyre friction model," *International Journal of Vehicle Design*, vol. 1, no. 4, pp. 373 – 377, 1980.

Heydinger, G.J., Riley, G.W. and Chrstos, J.P., "Importance of Tire Lag on Simulated Vehicle Response, " *SAE Technical Paper Series*, Paper No. 910235, 13 pages, 1991.

Pacejka, H.B. and Sharp, R.S., "Shear force development by pneumatic tyres in steady state conditions. A review of modelling aspects," *Vehicle System Dynamics*, Vol. 20, No. 3-4, pp. 121-176, 1991.

Pacejka, H.B. and Bakker, E., "The Magic Formula Tyre Model," *Vehicle System Dynamics*, v 21, Supplement, Tyre Models for Vehicle Dynamics Analysis, p 1-18, 1993

Pacejka, H.B. and Besselink, I.J.M., "Magic Formula Tyre Model with Transient Properties," *Vehicle System Dynamics*, Supplement 27, pp. 234-249, 1997.

Wong, J.Y., *Theory of Ground Vehicles*, Wiley-Interscience, ISBN 0-471-35461-9, Third Edition, 2001

Zegelaar, P.W.A., Gong, S. and Pacejka, H.B., "Tyre models for the study of in-plane dynamics," *Vehicle System Dynamics*, Vol. 23, Supplement, p 578-590, 1994.

Chapter 14

TIRE-ROAD FRICTION MEASUREMENT ON HIGHWAY VEHICLES

This chapter focuses on real-time tire-road friction coefficient measurement systems that are aimed at estimating friction coefficient and detecting abrupt changes in its value. The main type of friction estimation systems presented here are systems that utilize longitudinal vehicle dynamics and longitudinal motion measurements. The algorithms and experimental results presented in this chapter are largely adapted from the paper published by Wang, et. al. (2004).

14.1   INTRODUCTION

14.1.1   Definition of tire-road friction coefficient

Let F_x, F_y, and F_z be the longitudinal, lateral, and normal (vertical) forces acting on a tire. The normalized traction force for the tire, ρ, is defined as:

$$\rho := \frac{\sqrt{F_x^2 + F_y^2}}{F_z} \tag{14.1}$$

If we consider only longitudinal motion, and assume that the lateral force F_y can be neglected, then

$$\rho := \frac{F_x}{F_z} \tag{14.2}$$

From the discussions on longitudinal tire forces in Chapter 13, it is clear that ρ must be a function of both slip ratio σ_x and the tire-road friction coefficient μ. The tire road-friction coefficient μ on any given road surface is defined as the maximum value that ρ can achieve on that surface for any slip ratio value.

For a given normal force F_z, the longitudinal tire force F_x initially increases as slip ratio is increased and at an optimum value of slip ratio can reach a maximum value equal to μF_z. If μ is equal to 1, the maximum longitudinal force generated can be as much as the normal force F_z and this happens at an optimum value of slip ratio that depends on the particular tire under consideration. If μ is less than 1, then the maximum longitudinal force that can be generated will only be a fraction of the normal force F_z.

Some researchers refer to the normalized traction force ρ itself as the friction coefficient and refer to μ as the "maximum" friction coefficient. This book will, however, refer to ρ as the normalized traction force and to μ simply as the tire-road friction coefficient.

14.1.2   Benefits of tire-road friction estimation

Many vehicle control systems, especially active safety control systems such as ABS, traction control, vehicle stability control, collision warning, collision avoidance, adaptive cruise control (ACC) and four-wheel-steering can greatly profit from being made "road-adaptive," i.e., the control algorithms can be modified to account for the external road conditions if the actual tire-road friction coefficient information is available in real time. For example, in an ACC system, road condition information from friction coefficient estimation can be used to adjust the longitudinal spacing headway from the preceding vehicle that the ACC vehicle should maintain. In the case of vehicle stability control systems, as discussed in Chapter 8, the value of tire-road friction coefficient is needed for estimating the target value of yaw rate for the vehicle.

The estimation of tire-road friction coefficient is also useful for winter maintenance vehicles like snowplows. In the case of such vehicles, which have to operate in a harsh winter road environment, the knowledge of friction coefficient can help to improve the safety of operation. Further, the vehicle operator can use this information to adjust the amount and kind of deicing material to be applied to the roadway. It can also be used to automate the application of deicing material.

14.1.3 Review of results on tire-road friction coefficient estimation

Several different approaches have been proposed in literature for the real-time estimation of tire-road friction coefficient. These include the use of an acoustic microphone to listen to the tire (Eichorn, et. al., 1992, Breuer, et. al., 1992) and the use of optical sensors to investigate road reflections (Eichorn and Roth, 1992).

Researchers have also tried to utilize the measurement of the vehicle motion itself to obtain an estimate of the tire-road friction coefficient. Two types of friction estimation systems have been studied in this area:

a) Systems that utilize longitudinal vehicle dynamics and longitudinal motion measurements
b) Systems that utilize lateral vehicle dynamics and lateral motion measurements

The lateral system can be utilized primarily while the vehicle is being steered. A recently published paper by Hahn et al. (2002) discusses a lateral dynamics approach in which differential GPS signals are used to estimate the tire-road friction coefficient. Lateral systems are not studied in this chapter. The reader is referred to Hahn, et. al. (2002) for a discussion of lateral vehicle motion based systems.

A major portion of this chapter discusses longitudinal motion based systems which are applicable during vehicle acceleration and deceleration. The most well known research in this area is on the use of "slip-slope" for friction coefficient identification (Gustaffson, 1997, Yi, et. al., 1999, Hwang and Song, 2000, Muller, et. al., 2001, Wang, et. al., 2004). Results on the slip-slope based approach are discussed in a separate sub-section (section 14.1.4) below. In addition to the slip-slope based approaches, a Kalman filter based approach to tire-road friction coefficient identification has been studied by Ray (1997).

14.1.4 Review of results on slip-slope based approach to friction estimation

Let the longitudinal velocity at the tire under consideration be V_x and the equivalent rotational velocity of the tire be $r_{eff}\omega_w$ where r_{eff} is the effective radius of the tire and ω_w is the angular velocity of the wheel. Then the longitudinal slip ratio of the tire is defined as

$$\sigma_x = \frac{r_{eff}\omega_w - V_x}{V_x} \text{ during braking} \tag{14.3}$$

$$\sigma_x = \frac{r_{eff}\omega_w - V_x}{r_{eff}\omega_w} \quad \text{during acceleration} \qquad (14.4)$$

At low values of slip ratio, as discussed in Chapter 13, the normalized longitudinal force $\rho = \dfrac{F_x}{F_z}$ is proportional to the slip ratio σ_x. The slope of the relation between ρ and σ_x at low values of σ_x is called the "slip slope." The basic idea behind the use of slip-slope for friction coefficient estimation is that at low slip ratios the tire-road friction coefficient is proportional to the slip-slope. Thus by estimating slip-slope, the tire road friction coefficient can be estimated.

Gustafsson first proposed the slip-slope based friction coefficient estimation method in 1997. In Gustafsson (1997) a Kalman filter was designed to estimate slip-slope and the friction coefficient was then obtained from a stored map that related slip-slope to friction coefficient based on test data in the low-slip regions. The system worked in acceleration (traction) on a front wheel drive passenger car, with the rear wheel ABS sensor providing the absolute velocity reference and front wheels serving as the slipping wheels. The traction contribution of rear wheels was assumed to be zero. The slip was calculated directly from the difference between the speed of front wheels and rear wheels. The normalized traction force, ρ, was calculated from the estimated engine torque (based on measured injection time and engine speed) and the normal force. A Kalman filter recursively calculated the slip-slope during acceleration. Extensive testing on icy, snowy, gravel, wet, and dry surfaces with four different types of tires indicated that the estimated slip-slope could be used to reliably classify the friction levels of different road surfaces when the vehicle longitudinal slip ratio was adequate.

Yi et al. (1999) and Hwang and Song (2000) also provide more experimental evidence that the slip-slope could be used to classify the road surface during normal acceleration. However, a common disadvantage for all the approaches described above is that they need to use the driven wheel speed as an estimate of the absolute speed. This will not be accurate for an all-wheel drive vehicle and/or during braking (in which all wheels will slip and contribute forces). Another shortcoming of the results was that the estimator could work only at low slip ratios during acceleration in order to accurately estimate the friction coefficient.

In 2001, Müller, et.al. broadened the slip-slope friction coefficient estimation to braking situations. The rear wheel brakes of an experimental vehicle were turned off and served as the absolute velocity reference. Hence only the front wheels were considered as the source of the braking force and these were measured using brake pressure sensors. However, in practice, all

of the wheels would contribute tire forces and hence this approach cannot be directly used in the real world.

The results by Wang, et al. (2004) addressed the above shortcomings of the previous slip-slope based friction coefficient estimators. Their friction estimation utilized differential GPS in addition to wheel speed measurements and an accelerometer for longitudinal motion measurements. The estimation system was also extended to work during both low-slip (linear model) and high-slip (nonlinear model) maneuvers. Further, both front/rear-wheel drive and all-wheel drive vehicle acceleration and braking situations were accommodated. The experimental performance of their friction coefficient estimation system was demonstrated on an instrumented winter highway maintenance vehicle called the SAFEPLOW for a variety of different road surfaces under different operating maneuvers. The experimental results described in this chapter are taken from Wang, et. al., 2004.

14.2 LONGITUDINAL VEHICLE DYNAMICS AND TIRE MODEL FOR FRICTION ESTIMATION

14.2.1 Vehicle longitudinal dynamics
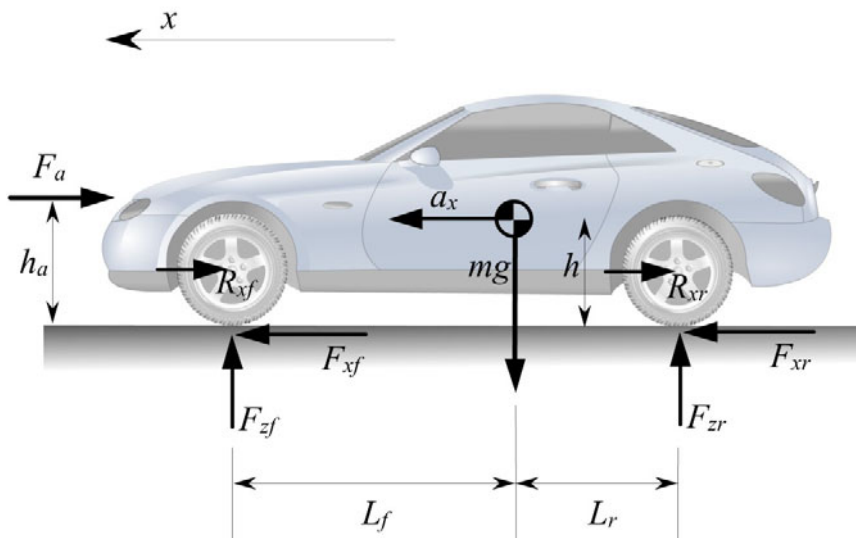
Figure 14-1. Vehicle longitudinal dynamics schematic diagram

Consider a bicycle type model (the difference between right and left tires is ignored) shown in Figure 14-1. Ignoring the road gradient and wind speed, the longitudinal dynamics can be represented as:

$$ma_x = F_{xf} + F_{xr} - R_x - D_a V_x^2 \qquad (14.5)$$

where m is the total mass of the vehicle., a_x is the longitudinal acceleration/ deceleration, F_{xf} and F_{xr} are the front and rear wheel traction/braking forces, $R_x = R_{xf} + R_{xr} = C_{roll} mg$ is the rolling resistance force with C_{roll} being the rolling resistance coefficient, D_a is the aerodynamic drag force constant and V_x is the longitudinal velocity. Let L_f be the distance from c.g. to the front axle; L_r the distance from c.g. to the rear axle and $L = L_f + L_r$ be the wheelbase of the vehicle.

The total longitudinal tire force F_x therefore can be calculated as follows:

$$F_x = F_{xf} + F_{xr} = m|a_x| + |R_x| + \left|D_a V_x^2\right|, \text{ if } a_x \geq 0 \text{ (acceleration)} \quad (14.6)$$

$$F_x = F_{xf} + F_{xr} = m|a_x| - |R_x| - \left|D_a V_x^2\right|, \text{ if } a_x < 0 \text{ (deceleration)} \quad (14.7)$$

Thus, once the vehicle longitudinal acceleration/deceleration, a_x, is measured by using an accelerometer and corrected for bias, the total vehicle longitudinal force, F_x, can be obtained based on equations (14.6) and (14.7).

14.2.2   Determination of the normal force

It is important to calculate the value of the normal force F_z for each tire as accurately as possible for the friction estimation algorithm. The weight of the vehicle contributes the major part of the normal forces on the tires. Longitudinal acceleration and deceleration forces acting on the vehicle redistribute the normal forces between the tires. If the vehicle is traveling in a straight line on level road, the normal forces at the front and rear tires can be calculated using a static force model of the vehicle as described in (Gillespie, 1992):

$$F_{zf} = \frac{mgL_r - ma_x h - D_a V^2 h_a}{L}$$

$$F_{zr} = \frac{mgL_f + ma_x h + D_a V^2 h_a}{L} \tag{14.8}$$

Thus an acceleration of the vehicle causes the normal forces on the front tires to decrease and the normal forces on the rear tires to increase.

The above normal force calculation method is based on a static force model and ignores the influence of the vibrations of the suspension. This method gives a fairly reasonable estimate of the normal force, especially when the road surface is fairly paved and not bumpy. However, if the road surface is very bumpy, a dynamic normal force estimation method incorporating the suspension dynamics will provide a more accurate calculation of the normal force. Such a method was proposed by Hahn, Rajamani, et. al in (2002). However, in practice, it requires vertical acceleration and suspension deflection sensors which are expensive.

Note also that during cornering, the normal forces of the right and left tires on both front and rear axle are different due to vehicle roll moment. However, since we are using a bicycle model, the differences in the left and right tires cannot be considered in this formulation.

14.2.3   Tire model

The longitudinal force generated at each tire is known to depend on the longitudinal slip ratio, the tire-road friction coefficient, and the normal force applied at the tire. As discussed in Chapter 13, the Magic Formula tire model with appropriate choice of model parameters can be used to represent the influence of these variables on the tire force for any tire. The explicit influence of the normal force F_z and the friction coefficient μ on the Magic Formula tire parameters A, B, C, D and E was also discussed. Unfortunately, due to the large number of parameters involved in the Magic Formula, it cannot be directly used conveniently for tire-road friction coefficient identification. In place of the Magic Formula, the tire model can instead be described using slip slope for purposes of tire-road friction coefficient identification.

Figure 14-2 shows the traction and braking force vs. slip ratio relationship for a variety of road surfaces computed using the Magic Formula model. As the figure shows, $\rho = \dfrac{F_x}{F_z}$ is an increasing function of

slip ratio σ_x until a critical slip value, where ρ reaches a value equal to μ and then starts decreasing slowly.
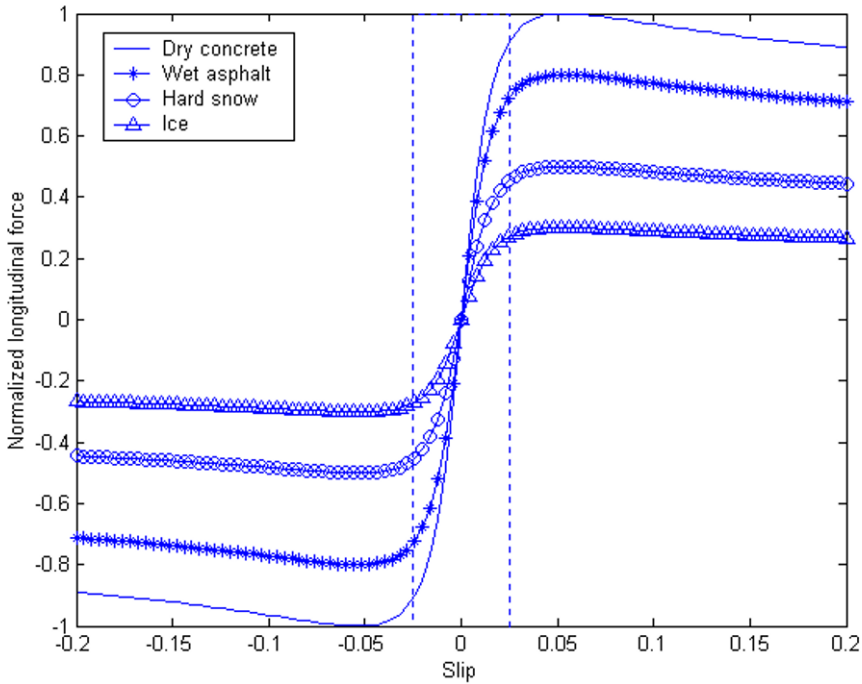
Figure 14-2. Longitudinal force vs. slip computed using Magic Formula model

In the slip-slope model used for tire road friction coefficient identification, we merely assume that the slip-slope is proportional to the tire road friction coefficient at small slip ratios. In other words the force ratio ρ is modeled as being proportional to the slip ratio, with the proportionality constant being a function of the tire road friction coefficient. At high values of slip ratio, the force ratio is constant and independent of the slip ratio. The constant value of the force ratio is a function of the friction coefficient. Hence the tire is modeled at high slip ratios with a constant ρ, with the value of the constant being dependent on the tire-road friction coefficient.

14.2.4   Friction coefficient estimation for both traction and braking

This section develops a unified slip-slope based friction coefficient estimation method for front or rear-wheel drive as well as all-wheel drive vehicles in

both traction and braking situations. Knowledge of the traction and braking force distribution ratios between front and rear axles is not required.

As described in the previous section, the normalized longitudinal force generated at an individual tire is proportional to its slip ratio in the low-slip region (or the linear part of the friction curve) for any given road surface and normal force. This relationship can be described as:

$$\rho = \frac{F_x}{F_z} = K\sigma_x \tag{14.9}$$

where K is the slip-slope, whose value changes with road surface conditions and could be used to predict the tire-road friction coefficient μ. However, the above equation holds only for an individual tire, which means that the longitudinal force F_x, normal force F_z, and the slip σ_x in the equation have to be the values for the same single tire. For the longitudinal vehicle bicycle model, we can consider the right and left tires together, but there are still two sets (front and rear) of tires that will contribute longitudinal force during all-wheel driving and braking. Thus, in order to apply the slip-slope estimation method, the forces and slip ratios for the front and rear tires need to be calculated separately.

For an all-wheel drive vehicle, the linear relationships between slip and normalized longitudinal force for the front and rear tires can be written as:

$$\rho_f = \frac{F_{x_f}}{F_{z_f}} = K_f\sigma_{xf} \tag{14.10}$$

$$\rho_r = \frac{F_{xr}}{F_{zr}} = K_r\sigma_{xr} \tag{14.11}$$

$$F_x = F_{xf} + F_{xr} \tag{14.12}$$

where, F_x is the total vehicle longitudinal tire force, which can be calculated as described in section 14.2.1. K_f and K_r are the slip-slopes of the front and rear tires whose values are determined by the front and rear tire properties and road surface characteristics. Combining the above three equations, we get

$$F_x = F_{xf} + F_{xr} = K_f F_{zf}\sigma_{xf} + K_r F_{zr}\sigma_{xr} \tag{14.13}$$

If we assume that the front and rear tires are on the same road surface condition, which is true for many driving situations, then the difference between the values of K_f and K_r is mainly dominated by the tire properties (including the tire type and number of tires for front and rear axles), which are independent of the road surface condition. Therefore, K_f and K_r can be related as:

$$K_f = \alpha K_r \tag{14.14}$$

where, α is a ratio coefficient determined by the front and rear tire properties and independent of road surface condition. Thus, the relationship between total force and slip ratios can be written as:

$$F_x = F_{xf} + F_{xr} = K_f F_{zf} \sigma_{xf} + K_r F_{zr} \sigma_{xr} = K_r (\alpha F_{zf} \sigma_{xf} + F_{zr} \sigma_{xr}) \tag{14.15}$$

where, F_x, F_{zf}, F_{zr}, σ_{xf} and σ_{xr} can be measured or calculated in real-time, and α can be determined experimentally for each vehicle. For example, if the vehicle chassis configuration is as shown in Figure 14-3, with two tires on the front axle and four tires on the rear axle (which is the configuration of the SAFEPLOW used in Wang, et. al., 2004), and all tires are exactly the same, then $\alpha = \frac{1}{2}$. If the front tires are different from the
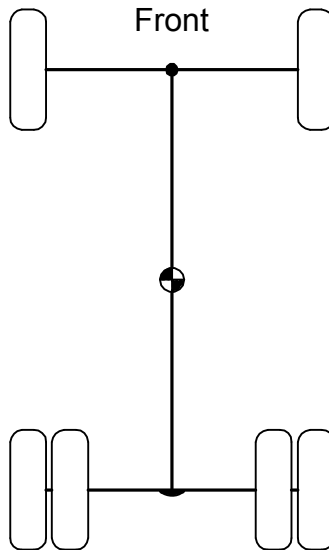
Figure 14-3. Chassis tire configuration example

rear tires in terms of wear level and tread pattern, then the value of α could be experimentally determined as some value less than 0.5. But, its value will stay constant for a considerably long time once it is determined and will not change with road surface friction coefficient. Adaptation for α can potentially be used also.

If the vehicle is rear-wheel drive instead of all-wheel drive, then $\alpha = 0$ during acceleration by ignoring the traction force of the front tires. During braking α can be chosen as a specific value determined by the chassis configuration. If the vehicle is front-wheel drive, the equations for K_f can be derived similarly as:

$$F_x = F_{xf} + F_{xr} = K_f F_{zf} s_{xf} + K_r F_{zr} s_{xr} = K_f (F_{zf} s_{xf} + \frac{1}{\alpha} F_{zr} s_{xr}) \quad (14.16)$$

where $\dfrac{1}{\alpha} = 0$ or $\alpha = \infty$ during acceleration and α is a different specific value determined by the chassis configuration during braking.

Along the lines of Wang, et. al. (2004), we present the rear-wheel drive case for the friction coefficient identification in the estimation algorithm derivation in the following section. However, the same algorithm can also be used for front-wheel drive and all-wheel drive vehicles.

The equation (14.15) can be rewritten into a standard parameter identification format as:

$$y(t) = \varphi^T(t)\theta(t) \quad\quad\quad\quad (14.17)$$

where, $y(t) = F_x$ is the system output, $\theta(t) = K_r$ is the unknown parameter, and $\varphi(t) = \alpha F_{zf} s_{xf} + F_{zr} s_{xr}$ is the measured regression vector. The only unknown parameter K_r can be identified in real-time using a parameter identification approach as will be described in the next section. Once the slip-slope K_r is identified, it can be related to the road surface condition or the maximum friction coefficient μ by a classification function.

Since the above method incorporates both front and rear tire forces and slip ratios, it can be used to identify the friction coefficient for both traction and braking situations on rear or front-wheel drive as well as all-wheel drive vehicles.

Note that the above slip-slope based approach is for operation in the low slip ratio region (linear part of the friction-slip curves) only. If the slip ratio is high, as in hard braking situations, the tire will work outside the region of

linear relationship between normalized force and slip ratio. The slip-slope based method will fail in this region. Fortunately, in the high slip ratio region, the magnitude of the normalized longitudinal force is different for different road surfaces and this difference can be used to classify the road surfaces. Thus, for the high slip ratio region, the normalized force $\rho = F_x / F_z$ is directly used to classify the road surface friction level. Similar to the earlier slip-slope method, it can be written in standard parameter identification form as:

$$y(t) = \varphi^T(t)\theta(t) \tag{14.18}$$

with $y(t) = F_x$ as the measured longitudinal force, $\theta(t) = \mu$ as the unknown parameter, and $\varphi^T(t) = F_z^T = F_z$ as the regressor variable.

14.3   SUMMARY OF LONGITUDINAL FRICTION IDENTIFICATION APPROACH

The following flow chart (Figure 14-4) summarizes the overall approach to tire-road friction coefficient estimation discussed in this chapter. Note that at
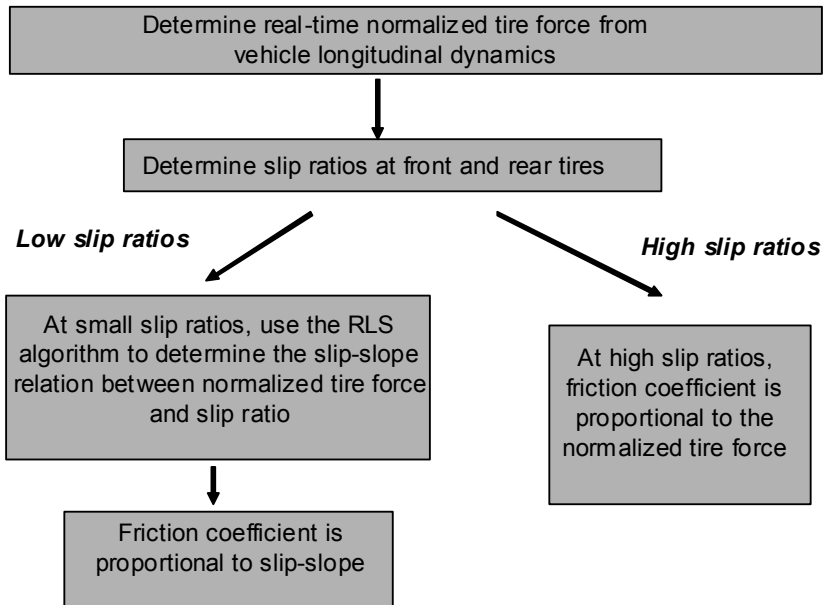
Figure 14-4. Summary of algorithm for tire-road friction estimation

low slip ratios, the slip-slope is used to identify the friction coefficient while at high slip ratios, the magnitude of the normalized longitudinal force itself is used to identify the friction coefficient.

14.4   IDENTIFICATION ALGORITHM DESIGN

14.4.1   Recursive least-squares (RLS) identification

The slip-slope model described in the previous chapter can be formulated in the parameter identification form as:

$$y(t) = \varphi^T(t)\theta(t) + e(t) \tag{14.19}$$

where $\theta(t)$ is the vector of estimated parameters, $\varphi(t)$ is the input regression vector, $e(t)$ is the identification error between the measured output $y(t)$ and estimated value $\varphi^T(t)\theta(t)$.

In the case of the tire-road friction estimation problem at small slip ratios, $y(t) = F_x$ is the measured output, $\theta(t) = K_r$ is the unknown parameter, and $\varphi(t) = \alpha F_{zf} s_{xf} + F_{zr} s_{xr}$ is the measured regression vector. At high slip ratios, $y(t) = F_x$ is the measured longitudinal force, $\theta(t) = \mu$ is the unknown parameter and $\varphi^T(t) = F_z^T = F_z$ is the normal force.

The RLS (recursive least squares) algorithm (Sastry and Bodson, 1989, Gustaffson, 2000 and Kailath, et. al., 2000) provides a method to iteratively update the unknown parameter vector, $\theta(t)$, at each sampling time, using the past data contained within the regression vector, $\varphi(t)$. The RLS algorithm updates the unknown parameters so as to minimize the sum of the squares of the modeling errors. The calculations in the RLS algorithm at each step t are as follows:

Step 1: Measure the system output, $y(t)$, and calculate the regression vector $\varphi(t)$.

Step 2: Calculate the identification error, $e(t)$, which is the difference between system actual output at this sample and the predicted model output obtained from the estimated parameters in previous sample, $\theta(t-1)$, i.e.

$$e(t) = y(t) - \varphi^T(t)\theta(t-1) \tag{14.20}$$

Step 3: Calculate the updated gain vector, $K(t)$, as

$$K(t) = \frac{P(t-1)\varphi(t)}{\lambda + \varphi^T(t)P(t-1)\varphi(t)}$$ (14.21)

and calculate the covariance matrix, $P(t)$, using

$$P(t) = \frac{1}{\lambda}[P(t-1) - \frac{P(t-1)\varphi(t)\varphi^T(t)P(t-1)}{\lambda + \varphi^T(t)P(t-1)\varphi(t)}]$$ (14.22)

Step 4: Update the parameter estimate vector, $\theta(t)$, as

$$\theta(t) = \theta(t-1) + K(t)e(t)$$ (14.23)

The parameter, λ, in the above equations is called the *forgetting factor*, which is used to effectively reduce the influence of old data which may no longer be relevant to the model, and therefore prevent a covariance wind-up problem. This allows the parameter estimates to track changes in the process quickly. A typical value for λ is in the interval [0.9, 1]. The size of the forgetting factor can be intuitively understood as follows: the RLS algorithm uses a batch of $N = \frac{2}{1-\lambda}$ data to update the current estimation (Gustaffson, 2000). When $\lambda = 1$, the RLS uses all the previous data from the starting time to update the current estimation. The smaller the value of λ chosen the faster the parameters converge. However, decreasing λ will increase the sensitivity of the estimation procedure to noise, causing parameter estimates to become oscillatory. This brings about a trade-off between the ability to track changes in parameter values quickly and high immunity to noise for the RLS algorithm. This trade-off will be addressed in the next sub-section.

14.4.2   RLS with gain switching

In a traditional RLS with a constant forgetting factor, there is a trade-off between fast convergence and sensitivity to noise. If a relatively big forgetting factor (such as $\lambda = 0.995$) is used then the convergence rate is slow but the estimated parameter is stable and does not have significant oscillations after convergence. On the other hand, if a relatively small value of forgetting factor (such as $\lambda = 0.9$) were used then the estimated parameter converges quickly. This high convergence rate makes the system more perceptive and able to promptly respond to sharp changes in road condition, which is very desirable for vehicle control systems. However, this

high convergence rate is achieved at the expense of decreased immunity to noise. The estimated parameter value will oscillate around its true value. For illustrative details, the reader is referred to Wang, et. al., 2004.

In Gustaffson (2000), a change detection algorithm running in parallel with a Kalman filter was used to trigger the amplification of the covariance matrix entries of the Kalman filter and thus to increase the tracking ability of the filter during parameter transition.

Similarly, in Wang, et. al. (2004), an approach that combines the change detection algorithm in parallel with the ordinary RLS estimator was proposed to solve the convergence rate vs. noise immunity trade-off mentioned above.

There are several change detection algorithms available in literature. The CUSUM (Page, 1954) change detection algorithm was chosen in Wang, et. al. (2004) to monitor the identification error $e(t) = y(t) - \varphi^T(t)\theta(t-1)$. An alarm signal is generated if the absolute value of identification errors have been bigger than a specific threshold value for a specified time duration. The recursive formulae of this algorithm are as follows:

$$a_t = \max(a_{t-1} + |e_t| - d, 0) \qquad (14.24)$$

$$a_0 = 0 \qquad (14.25)$$

The input of the change detector is the ordinary RLS identification error e_t, and the output is the alarm signal a_t. If the output of the change detector $a_t > h$, the entries of the matrix $P(t)$ will be increased by a constant factor to track the sudden change of friction coefficient quickly. This increase in the entries of $P(t)$ will remain until the absolute value of the identification error drops below a certain level and a_t becomes 0. Here, the drift parameter d is used to high-pass bigger identification errors and ignore small errors. The threshold value h is used to determine when the alarm signal should trigger the gain amplification.

A relatively big forgetting factor $\lambda = 0.995$ can now be used, since quick convergence during parameter transition can now be obtained even with a large value of λ. During parameter transition, the change detector catches the large identification error and generates an alarm signal, which triggers the gain amplification and makes the estimated slip-slope converge quickly to the true value. After the estimated slip-slope converges to the true value, the identification error becomes small enough to be high-passed by the change detector, and the alarm signal disappears correspondingly. Then, the covariance matrix resumes its normal value and quells the influence of noise.

Illustrative examples of the use of the change detection algorithm can be found in Wang, et. al. (2004).

14.4.3   Conditions for parameter updates

The precision of the estimate of the friction coefficient value depends on the qualities of the estimator input signals, the longitudinal force (traction/braking) and slip. If the longitudinal force or the slip is very small, the experimental data obtained is then around the origin of the tire force-slip curve, where the estimate will be stochastically uncertain. Besides, since the longitudinal force is calculated from the output signal of an accelerometer, if the acceleration/deceleration is small, then the signal-to-noise ratio (SNR) of the acceleration/deceleration will be small, which may lead to overestimation of the friction coefficient. Therefore, to ensure good estimator performance, the friction coefficient is not updated when the absolute value of the measured acceleration is less than 0.3 m/s^2 and the absolute value of the slip is less than 0.005. The experimental results in Wang, et. al., 2004, verified that these threshold values could ensure reliable updates for the friction coefficient estimation.

14.5   ESTIMATION OF ACCELEROMETER BIAS

In the friction identification algorithm described in this chapter, the accelerometer plays a key role in obtaining a real-time estimate of the longitudinal tire force using equations (14.6) and (14.7). An accelerometer typically suffers from bias errors due to changes in temperature, supply voltage, and orientation of the device. Therefore, to calculate the acceleration/deceleration of the vehicle accurately, the bias needs to be estimated and removed from the accelerometer output signal. A sensor fusion method that incorporates both accelerometer and GPS signals through a Kalman filter can be used to estimate the accelerometer bias in real-time. This is described below and was used in Wang, et. al., 2004.

Note that the longitudinal velocity of the vehicle can be obtained from differential GPS (DGPS) signals as:

$$V_{x\_GPS} = \dot{x} \tag{14.26}$$

The $\dot{x}$ in equation (14.26) can be obtained by numerical differentiation of the DGPS position signal, which is quite accurate but very slow, usually with an update rate around 10Hz. On the other hand, the longitudinal velocity can also be obtained by integrating the measured longitudinal

acceleration $\dot{V}_{x\_acc}$. Due to bias present in the acceleration signal, the velocity obtained by integration of the accelerometer output signal usually drifts. However, a combination of these two signals (GPS and accelerometer) provides a way to estimate the accelerometer bias. This methodology is adapted from the gyro bias estimation method suggested in Bevly, et. al., 2000. In the following state space system, the accelerometer measurement $\dot{V}_{x\_acc}$ is used as input and the GPS signal V_{x_GPS} as output. The states of the system include both the estimated longitudinal velocity, $\hat{V}_x$, and the estimated accelerometer bias, $\hat{\dot{V}}_{x\_acc\_b}$.

$$\begin{pmatrix} \dot{\hat{V}}_x \\ \ddot{\hat{V}}_{x\_acc\_b} \end{pmatrix} = \begin{pmatrix} 0 & -1 \\ 0 & 0 \end{pmatrix} \begin{pmatrix} \hat{V}_x \\ \hat{\dot{V}}_{x\_acc\_b} \end{pmatrix} + \begin{pmatrix} 1 \\ 0 \end{pmatrix} \dot{V}_{x\_acc} + w$$

$$V_{x\_GPS} = \begin{pmatrix} 1 & 0 \end{pmatrix} \begin{pmatrix} \hat{V}_x \\ \hat{\dot{V}}_{x\_acc\_b} \end{pmatrix} + e$$

(14.27)

where, w and e are unknown process noise and measurement noise, respectively.

The time updates and measurement updates in the Kalman filter are:

$$\hat{x}_{t+1|t} = A\hat{x}_{t|t} + Bu_t \tag{14.28}$$

$$P_{t+1|t} = AP_{t|t}A^T + Q \tag{14.29}$$

$$\hat{x}_{t|t} = \hat{x}_{t|t-1} + K_t(y_t - C\hat{x}_{t|t-1}) \tag{14.30}$$

$$P_{t|t} = P_{t|t-1} - K_tCP_{t|t-1} \tag{14.31}$$

where $Q_t = Cov(w)$ is the covariance matrix of the stochastic noise w. $K_t = P_{t|t-1}C^T(CP_{t|t-1}C^T + R_t)^{-1}$ is the Kalman gain. $P_{t|t}$ is the covariance

matrix for the state estimate. $A = \begin{bmatrix} 0 & -1 \\ 0 & 0 \end{bmatrix}$, $B = \begin{bmatrix} 1 & 0 \end{bmatrix}^T$, $C = \begin{bmatrix} 1 & 0 \end{bmatrix}$, and

$\hat{x}_{t|t} = \begin{pmatrix} \hat{V}_x \\ \hat{V}_{x\_acc\_b} \end{pmatrix}$ is the system state.

Figure 14-5 shows one of the experimental results from Wang, et. al., 2004, in which the SAFEPLOW performs both acceleration and deceleration. The Kalman filter is used to estimate the accelerometer bias and a 4th order Elliptic digital low-pass filter is designed to attenuate the high frequency noise in the accelerometer signal. As the figure indicates, both the Kalman filter and low-pass filter work well in estimating the accelerometer bias and hence the acceleration.
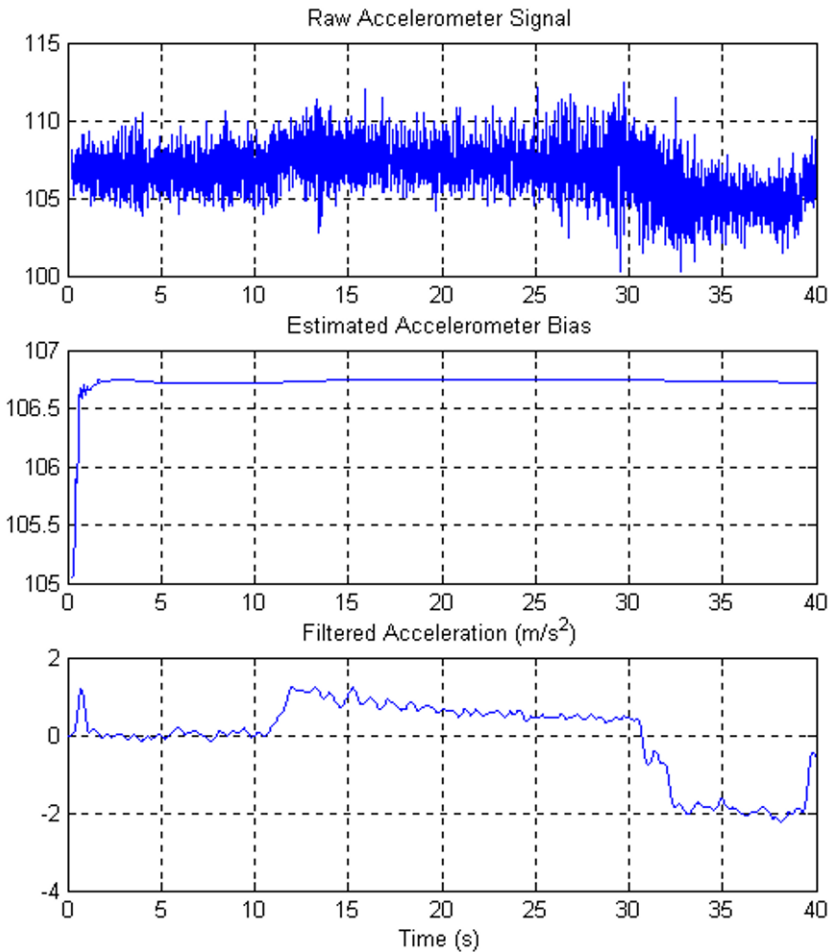
Figure 14-5. Experimental results for accelerometer bias and acceleration estimation

14.6   EXPERIMENTAL RESULTS

This section summarizes some of the experimental results on tire road friction identification obtained in Wang, et. al., 2004. For a description of the complete set of experimental results, the reader is referred to the original paper.

14.6.1   System hardware and software

The vehicle used to conduct the experiments was a full sized snowplow (referred to as SAFEPLOW) manufactured by Navistar International Truck Company as shown in Figure 14-6.

The main parameters of the SAFEPLOW related to the friction coefficient identification algorithm are listed in Table 14.1.

Figure 14-6. The SAFEPLOW used for the experiments

Table 14-1. SAFEPLOW main parameters

Parameter	Total Mass (Kg)	L_f (m)	L_r (m)	Height of C.G. (m)	Vehicle Front Area (m²)
Value	9834	2.339	2.716	1.2	6.0

In order to experimentally implement the designed friction coefficient estimator in real-time, the SAFEPLOW was equipped with a differential GPS system, an accelerometer, and ABS wheel speed sensors. The Mathworks xPC system was used to serve as the real-time system and included a host PC (TOSHIBA 4200 laptop) and a target PC (DELL GX110). Details of the experimental hardware can be found in Wang, Alexander and Rajamani (2004).

After designing the estimation algorithm, extensive experimental tests were carried out to improve and verify the estimation system performance. This section presents some of the experimental results.

14.6.2   Tests on dry concrete road surface

The experiments for this part were carried out on the dry concrete testing track at the MnRoad Research Facility on sunny days. The track was a well-paved concrete surface and completely dry. So, the friction level of the surface was very good.

Acceleration (Traction) Test

The slip-slope based friction coefficient estimation method was evaluated for acceleration with different starting speeds. At the beginning of the test, the speed of the vehicle was kept constant for about 6 seconds to allow the
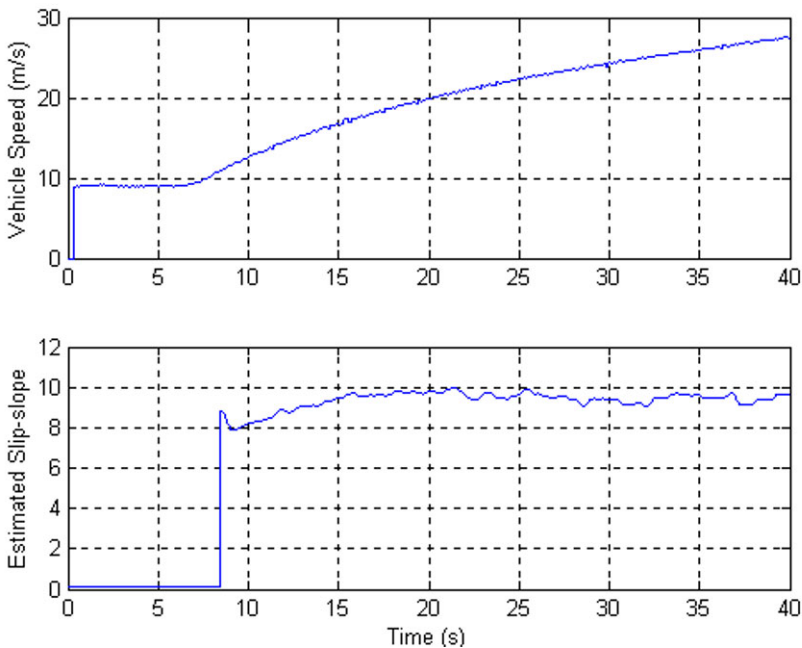
Figure 14-7. Acceleration starting at 20mph on dry concrete surface
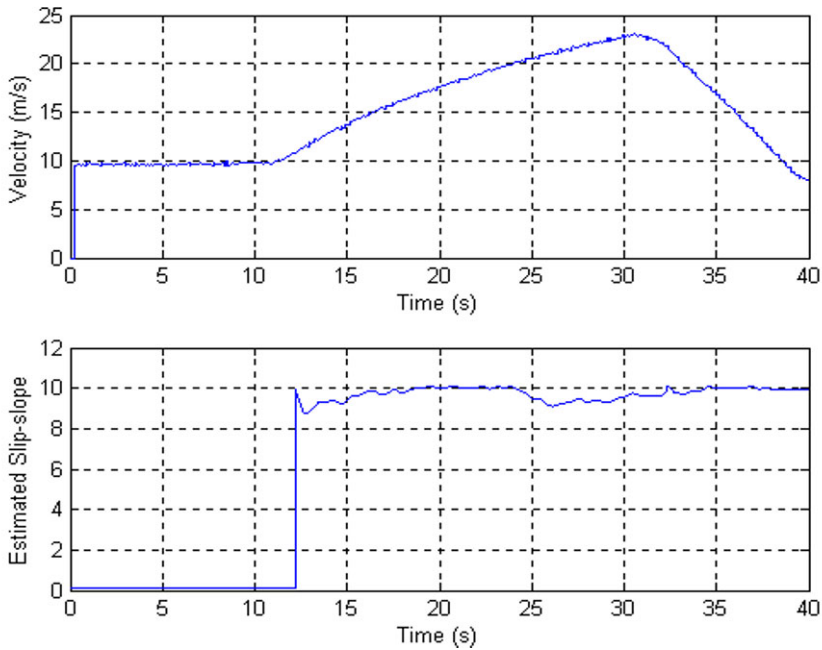
Figure 14-8. Slip-slope estimation during acceleration and braking

low-pass filters to initialize and the Kalman filter to estimate the accelerometer bias. After that, the vehicle starts accelerating. Figure 14-7 shows the slip-slope estimation results for acceleration with the starting speed at 20 mph (9 m/s). As the results indicate, the slip-slope for the acceleration on dry concrete converges to a value of about 9.8.

Combination of Acceleration and Braking Test

Experiments for a situation of sequential acceleration and braking were also studied on the same dry concrete surface. Figure 14-8 shows one of the test results. The SAFEPLOW first stays at a constant speed for a while to let the filters initialize and estimate the accelerometer bias, then it starts accelerating for about 20 seconds and then gently brakes for about 10 seconds. As the result indicates, the slip-slope consistently converges to about the same value around 9.8.

From the experimental results, it was observed that for acceleration and braking in the small slip region, the slip-slope consistently converges to some value around 9.8 on this surface. Therefore, we can use this slip-slope value to classify the road surface as dry concrete, dry concrete like surface or to classify the friction coefficient μ as being close to 1.

14.6.3   Tests on concrete surface with loose snow covering

The experiments for this part were carried out also on the concrete test track at the MnRoad Research Facility, but on a day after a heavy snow day. The track had already been plowed, but since no salt and sand were put on it, it was still lightly covered by loose snow brought on by wind. Figure 14-9 shows a photograph of the exact road surface condition for the experiments presented in this section. The right side lane in the figure was used for the testing. Since the road surface is slightly slippery, the friction coefficient μ is expected to be noticeably less than 1.

Figure 14-9. The road surface used to conduct the experiments for this section

Combination of Acceleration and Braking Test

Similar to the tests described earlier, experiments for the situation of sequential acceleration and braking were also conducted on the same concrete surface. Figure 14-10 shows one of the test results. The SAFEPLOW first stays at a constant speed for a while to let the filters initialize and estimate the accelerometer bias, then it starts accelerating for about 16 seconds and then gently brakes for about 16 seconds. As the result indicates, the slip-slope consistently converges to about the same value around 7.0. Note that the estimator stops updating the slip-slope at about 32 seconds because the wheel speeds are below a threshold value. Thus, the system just keeps the last estimated value before stopping the updating.

From the experimental results, we can see that for acceleration and braking in the small slip region, the slip-slope consistently converges to some value around 7.0, which is quite different from the slip-slope value (9.8) obtained on dry concrete surface. Therefore, we can use this slip-slope value to classify the road surface as a slightly slippery surface or to classify the friction coefficient μ as being about 0.7.
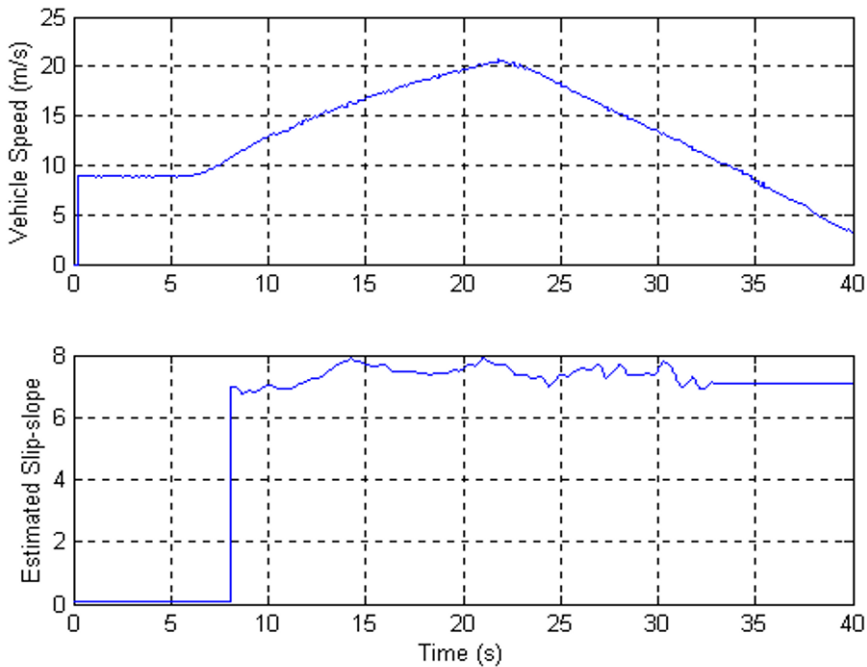
Figure 14-10. Acceleration and braking on surface with light covering snow

14.6.4   Tests on surface consisting of two different friction levels

The purpose of the experiments in this section is to test the system's transient response performance and its ability to detect a sudden change of the road friction level. The tests were conducted on a track at Minnesota Highway Safety and Research Center (St. Cloud, Minnesota). The test track consists of two surfaces with different friction levels — dry asphalt surface and icy surface. Figure 14-11 shows a photograph of the transitional part of the track.

Figure 14-11. The track used to conduct the experiments for this section
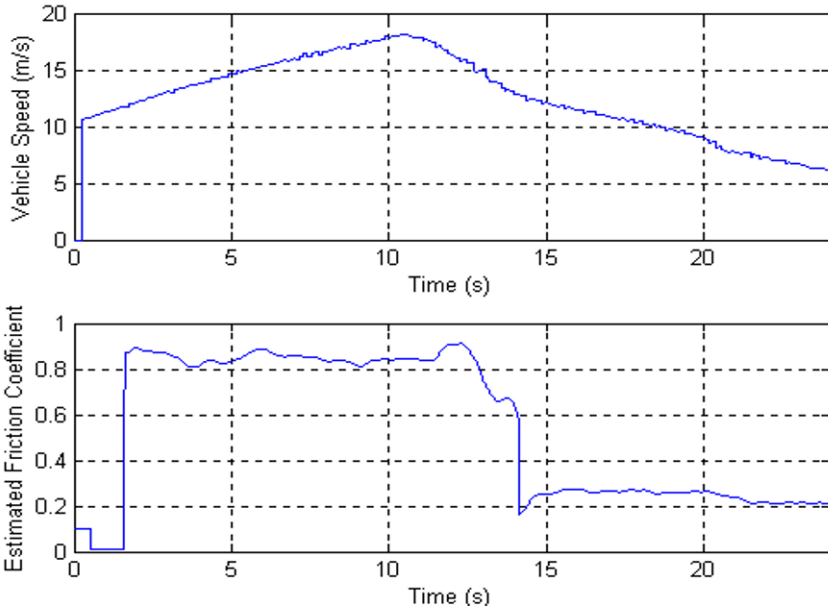
Figure 14-12. System response when braking through the transitional part

Combination of Acceleration and Braking Test

Figure 14-12 shows experimental results from a test in which the SAFEPLOW accelerates on the dry asphalt surface and brakes through the transitional part of the track. As before, on the dry asphalt surface, tires work in the low-slip linear region and the slip-slope is used to classify the surface friction level for both acceleration and braking. However, the wheels lock up once the vehicle reaches the icy surface when performing braking. Thus, the slip ratio will be almost as high as 100% and the tires are working in the nonlinear region of the tire force characteristics. Therefore, the normalized force is used to classify the surface friction level. As the result indicates, the friction coefficient estimate promptly converges to a value of about 0.22 once the vehicle reaches the icy surface.

14.6.5 Hard braking test

This section is used to further verify the system performance in high-slip region (nonlinear part of the force-slip curves). The SAFEPLOW performs hard braking on a dry concrete surface at MnROAD Research Facility. Figure 14-13
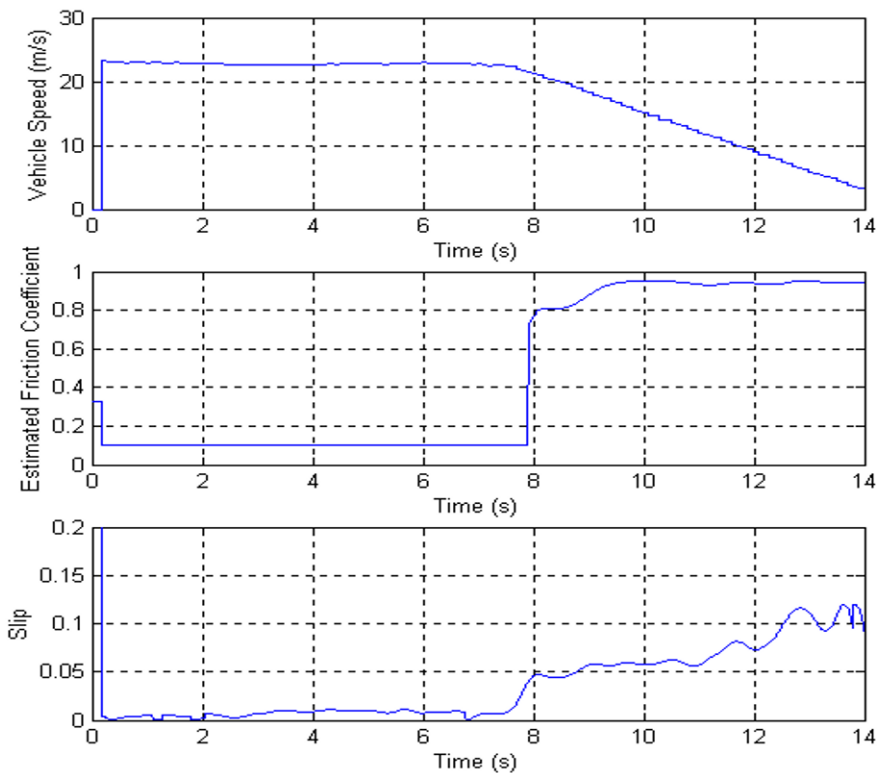
Figure 14-13. Test results for hard braking

shows a test result. Since the tires are working outside the linear region, the normalized force is directly used to classify the surface friction level. As the result indicates, the system behaves well even in the nonlinear region. The estimated friction coefficient converges to about 0.96 once the vehicle starts hard braking.

14.7   CHAPTER SUMMARY

This chapter discussed real-time tire-road friction coefficient measurement systems aimed at estimating road surface friction levels and quickly detect abrupt changes in friction coefficient. Vehicle based friction estimation systems of two types have been studied in literature:

a) Systems that utilize longitudinal vehicle dynamics and longitudinal motion measurements
b) Systems that utilize lateral vehicle dynamics and lateral motion measurements

This chapter only discussed longitudinal motion based systems which are applicable during vehicle acceleration and deceleration. The friction coefficient at small slip ratios can be estimated in real-time by estimating the "slip-slope" of the normalized longitudinal force versus slip ratio data. At large slip ratios, the magnitude of the normalized longitudinal force itself provides an estimate of the tire-road friction coefficient.

A real-time estimation algorithm from Wang, et. al. (2004) was presented which was applicable during both vehicle acceleration and braking and worked reliably for a wide range of slip ratios, including high slip conditions. The developed system can be utilized on front or rear-wheel drive as well as all-wheel drive vehicles. A summary of experimental results from Wang, et. al. (2004) was presented and discussed and included data from various different types of road surfaces. The experimental tests were done with a winter maintenance vehicle called the "SAFEPLOW." The experimental results showed that the system performed quite reliably and quickly in estimating friction coefficient on different road surfaces during various vehicle maneuvers.

A limitation of the developed system is that it requires sufficient tire slip in order to estimate the friction coefficient accurately. If the slip is extremely small, (as can happen during vehicle coasting) the system will not be able to update the friction coefficient information at that time. Limitations of utilizing differential GPS include the slow update rates and the lack of wide availability of differential correction. Limitations involved with using an accelerometer to estimate longitudinal tire force include its sensitivity to vertical vibrations as well as road grade inputs and bias errors.

NOMENCLATURE

F_x	longitudinal force
F_{xf}	longitudinal force from front tires
F_{xr}	longitudinal force from rear tires
F_y	lateral force
F_z	normal force
F_{zf}	normal force of front tires
F_{zr}	normal force of rear tires
ρ	normalized traction force
μ	tire-road friction coefficient
σ_x	slip ratio
σ_{xf}	slip ratio of front tires
σ_{xr}	slip ratio of rear tires
r_{eff}	effective tire radius
V_x	longitudinal speed
ω_w	wheel speed
D_a	aerodynamic drag force constant
R_x	rolling resistance
R_{xf}	rolling resistance of front tires
R_{xr}	rolling resistance of rear tires
h	height of application of aerodynamic drag forces
L_f	longitudinal distance from c.g. to front axle
L_r	longitudinal distance from c.g. to rear axle
L	wheel base $(= L_f + L_r)$
K	slip slope
α	coefficient relating front and rear slip-slopes
K_f	slip slope of front tires

K_r	slip slope of rear tires
$e(t)$	error in RLS algorithm
$\theta(t)$	parameter estimates in RLS algorithm
$\varphi(t)$	regression variables in RLS algorithm
λ	forgetting factor in RLS algorithm
$P(t)$	covariance matrix in RLS algorithm
$K(t)$	gain vector in RLS algorithm
a_t , a_0	parameters used in change detection algorithm
V_{x_GPS}	longitudinal velocity from GPS
$\dot{V}_{x\_acc}$	longitudinal acceleration from accelerometer
$\hat{V}_x$	estimate of longitudinal velocity
$\dot{\hat{V}}_{x\_acc\_b}$	estimate of bias value in accelerometer

REFERENCES

Breuer, B., Eichhorn, U. and Roth, J., "Measurement of tyre/road friction ahead of the car and inside the tyre," *Proceedings of AVEC'92 (International Symposium on Advanced Vehicle Control)*, pp. 347–353, 1992.

Bevly, D., Gerdes, J.C., Wilson, J. and Zhang, G., "The Use of GPS Based Velocity Measurements for Improved Vehicle State Estimation," *Proceedings of the American Control Conference*, Chicago, Illinois, pp. 2538-2542, June 2000.

Eichhorn, U. and Roth, J., "Prediction and Monitoring of Tyre/Road Friction," *Proceedings of FISITA*, London, 1992, pp. 67-74.

Pasterkamp, W.R. and Pacejka, H.B., "The Tyre as a Sensor to Estimate Friction," *Vehicle System Dynamics*, vol. 27, 1997, pp.409-422.

Gustaffson, F., "Slip-Based Tire-Road Friction Estimation," *Automatica* Vol. 33 (6), pp1087-1099, 1997.

Fancher, P.S., Ervin, R.D., Winkler, C.B. and Gillespie, T.D., "A Factbook of the Mechanical Properties of the Components for Single-Unit and Articulated heavy Trucks," *The University of Michigan Transportation Research Institute Report*, Dec. 1986.

Gillespie, T.D., *Fundamentals of Vehicle Dynamics*, Society of Automotive Engineers, Inc., 1992.

Germann, S., Würtenberger, M. and Daiß, A., "Monitoring of the Friction Coefficient Between Tyre and Road Surface," *Proceedings of the third IEEE Conference on Control Applications*, pp. 613-618, 1994.

Gustafsson, F., *Adaptive Filtering and Change Detection*, John Wiley & Sons, Ltd. Chichester, England, 2000.

Hahn, J.O., Rajamani, R. and Alexander, L., "GPS-Based Real-Time Identification of Tire-Road Friction Coefficient," *IEEE Transactions on Control Systems Technology*, Vol 10, No. 3, May 2002.

Hwang, W. and Song, B.S., "Road Condition Monitoring System Using Tire-road Friction Estimation," *Proceedings of AVEC 2000*, Ann Arbor, Michigan, pp 437-442, Aug. 2000.

Kailath, T., Sayed, A.H. and Hassibi, B., *Linear Estimation*, Prentice Hall, 2000.

Müller, S., Uchanski, M. and Hedrick, J.K., "Slip-Based Tire-Road Friction Estimation During Braking," *Proceedings of 2001 ASME International Mechanical Engineering Congress and Exposition*, New York, 2001, pp. 213-220.

Pacejka, H.B. and Bakker, E., "The Magic Formula Tyre Model," *Vehicle System Dynamics*, v 21, Supplement, Tyre Models for Vehicle Dynamics Analysis, p 1-18, 1993

Page, E.S., Continuous Inspection Schemes, *Biometrika*, Vol. 41, pp. 100-115, 1954.

Rajamani, R., "Radar Health Monitoring for Highway Vehicle Applications," *Vehicle System Dynamics*, Vol. 38, No. 1, pp. 23-54, 2002.

Ray, L.R., "Nonlinear Tire Force Estimation and Road Friction Identification: Simulation and Experiments", *Automatica*, Vol. 33, No. 10, pp. 1819-1833, 1997.

SAE, "Vehicle Dynamics Terminology," SAE J670e, *Society of Automotive Engineers Handbook*, 2000.

Sastry, S. and Bodson, M., *Adaptive Control: Stability, Convergence, and Robustness*, Englewood Cliffs, NJ: Prentice-Hall, 1989.

Uno, T., Sakai, Y., Takagi, J. and Yamashita, T., "Road Surface Recognition Method Using Optical Spatial Filtering," *Proceedings of AVEC*, pp. 509-515, 1994.

Wang, J., Alexander, L. and Rajamani, R., "Friction Estimation on Highway Vehicles Using Longitudinal Measurements", *ASME Journal of Dynamic Systems, Measurement and Control*, Special Issue on Sensors, Vol. 126, No. 2, pp. 265-275, June 2004.

Yi, K., Hedrick, J.K. and Lee, S.C., "Estimation of Tire-Road Friction Using Observer Based Identifiers," *Vehicle System Dynamics*, Vol. 31, p. 233-261, 1999.

Chapter 15

ROLL DYNAMICS AND ROLLOVER PREVENTION

Vehicle rollovers account for a significant fraction of highway traffic fatalities. While only 3% of vehicle accidents result in rollovers, 33% of all fatalities have vehicle rollover as a contributing factor (NHTSA, 2011). Hence there is significant research being conducted on development of rollover prevention technologies (Liu, et.al., 1997, Odenthal, et.al., 1999, Chen and Peng, 2001, Carlson and Gerdes, 2003, Liebemann, et.al., 2004, Yoon, et.al., 2007, Piyabongkarn, et. al., 2010).

15.1   ROLLOVER RESISTANCE RATING FOR VEHICLES

The National Highway Traffic Safety Administration (NHTSA) provides rollover resistance ratings for all new vehicles, as part of its new car assessment program (NCAP) for consumer information. The rollover rating system ranges from one star (40% or greater risk of rollover) to five stars (10% or less risk of rollover). Initially, the NCAP rollover resistance ratings were provided during 2001-2003 purely on the basis of the static stability factor of a vehicle (Boyd, 2005, TRB, 2002). The static stability factor of a vehicle is defined as

$$SSF = \frac{\ell_w}{2h} \tag{15.1}$$

where ℓ_w and h are the track width and the height of the c.g. of the vehicle measured from the ground respectively, as shown in Figure 15-1.
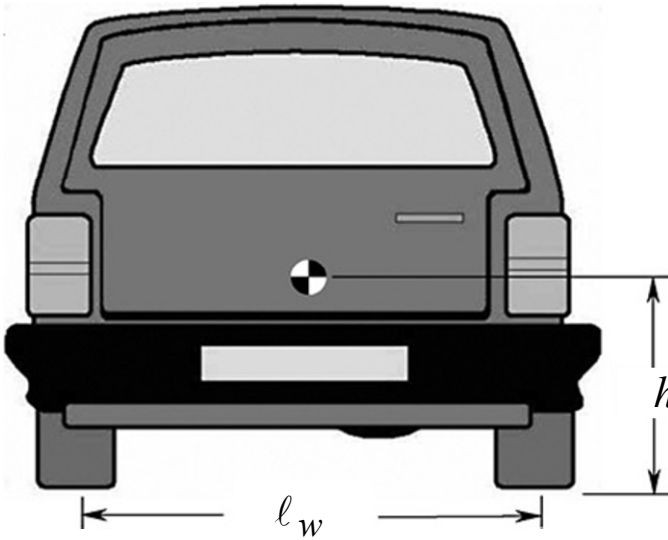
Figure 15-1. Parameters for vehicle static stability factor (TRB, 2002)
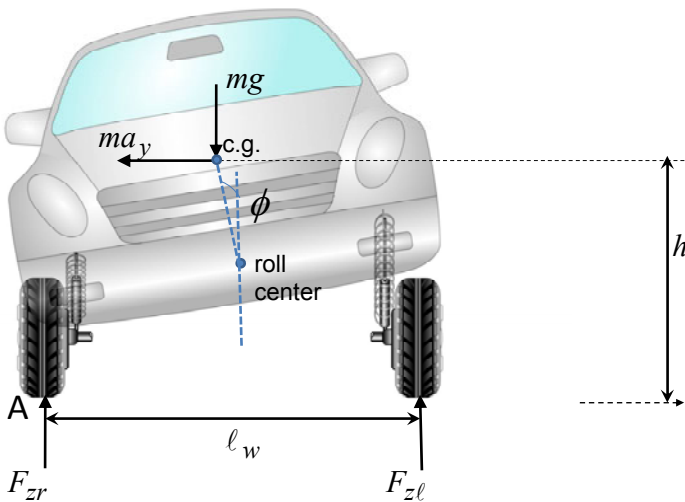
Figure 15-2. Roll moment balance in steady state cornering

The motivation behind the SSF definition of equation (15.1) can be understood from the moment balance shown in Figure 15-2. This figure shows a vehicle under steady state cornering with a lateral acceleration a_y. The normal (vertical) load on the left or inner tires is denoted by $F_{z\ell}$ and on the right (or outer) tires is denoted by F_{zr}. The weight of the vehicle is denoted by mg. The bank angle of the road is assumed to be zero. The force ma_y shown in the figure is the d Alembert's force that makes the system a quasi-static system. Taking moments about the right (or outer) wheel contact point A, assuming the roll angle ϕ is small,

$$ma_y h + F_{z\ell} \ell_w - mg \frac{\ell_w}{2} = 0 \qquad (15.2)$$

Hence the force on the left (or inner) wheels is given by

$$F_{z\ell} = \frac{mg \dfrac{\ell_w}{2} - ma_y h}{\ell_w} \qquad (15.3)$$

When the lateral acceleration of the vehicle is zero, the normal force on the inner wheels is $\dfrac{mg}{2}$, as seen from equation (15.3). As the lateral acceleration of the vehicle increases, the normal force decreases until it becomes zero at a high enough lateral acceleration. This is the point at which the inner wheels lift off the ground and this could be considered the initiation of a rollover. The lateral acceleration at which the inner wheels lift off is therefore given by setting $F_{z\ell} = 0$ in equation (15.3) to obtain

$$a_{y\_lift-off} = \frac{\ell_w}{2h} g \qquad (15.4)$$

The factor $\dfrac{\ell_w}{2h}$ in equation (15.4) is called the static stability factor (SSF). The lower the SSF, the lower the lateral acceleration level at which a rollover occurs.

Since 2003, NHTSA has added dynamic maneuver tests, in addition to use of the SSF, in calculating rollover resistance ratings for vehicles.

Rollovers, in general, can be either *tripped* or *untripped* rollovers. The vast majority of rollovers are tripped rollovers and occur due to the influence of an external mechanical force input on the vehicle, for example, due to impact of the vehicle with a curb, with guard rails, due to wheel rims digging into a pavement, pot holes, soft soil, etc. Untripped rollovers, on the other hand, occur due to sharp steering, for example going around a curved road at high speed or undertaking a quick lane change. The resulting lateral forces generated at the tires cause the vehicle to rollover.

Since 2004, the J-turn maneuver test and the fishhook test are used by NHTSA as dynamic maneuver tests to evaluate the transient properties of vehicles. Dynamic maneuver tests evaluate the ability of a vehicle to avoid untripped rollovers during driving maneuvers. However, since untripped rollovers constitute only a small fraction of all rollovers, it is necessary to also use the SSF in rating the overall rollover resistance of a vehicle.

It should be noted that the SSF represents rollover resistance to both tripped and untripped rollovers. The shortcomings of SSF come from the fact that it includes only geometric properties. It does not include the effect of suspension properties or electronic stability control (ESC), both of which can reduce the rollover propensity of a vehicle.

The results from the dynamic maneuver tests complement the SSF and help determine the overall rollover resistance rating of a vehicle. The SSF still plays a larger role than the dynamic maneuver tests in calculation of the rollover rating.

J-Turn Maneuver

The NHTSA J-Turn maneuver represents an avoidance maneuver in which a vehicle is steered away from an obstacle using a ramp steering input (Forkenbrock, et.al., 2003). This is a common maneuver in test programs conducted by vehicle manufacturers and others. Since the differences between various vehicles in steering ratio, wheelbase and linear range understeer properties (Forkenbrock, et.al., 2002, Boyd, 2005) need to be taken into account, equivalent steering wheel angles have to be defined for all vehicles. Hence the handwheel angle that would produce a steady-state lateral acceleration of 0.3 g at 50 mph on a level paved surface is first measured for a particular vehicle. The 0.3 g lateral acceleration value is used because

   a) the steering angle variability in achieving this lateral acceleration is quite low for any given vehicle, and
   b) stability control intervention cannot influence the test results at this low acceleration.

A: SS* handwheel position at 0.3g

SS: Steering scalar

T_1 : 4 second pause

T_2 : 2 seconds

Initial steering rate: 1000 deg/sec
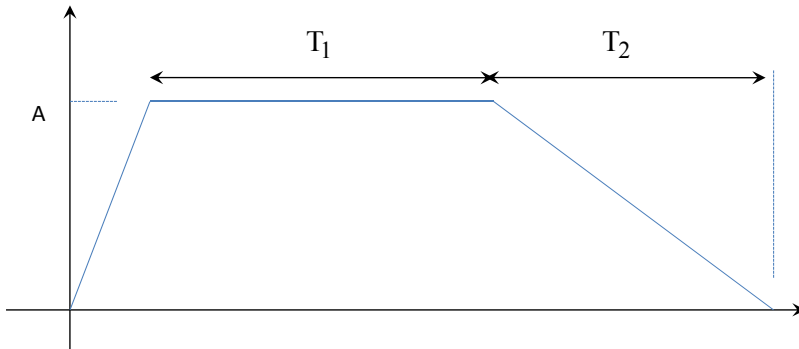
Figure 15-3. NHSTA J-turn maneuver

Since the magnitude of the handwheel position at 0.3 g is small, it is multiplied by a scalar value of 8 to provide a maneuver of adequate roll-inducing severity. This typically results in a handwheel angle of approximately 330 degrees (Forkenbrock, 2002). The ramp rate used for the handwheel is 1000 degrees per second. Figure 15-3 illustrates the J-Turn maneuver in terms of the automated steering inputs commanded by the programmable steering machine during the test.

To begin the maneuver, the vehicle is driven in a straight line at a speed slightly greater than the desired entrance speed. The driver releases the throttle, coasts to the test speed, and then triggers the commanded handwheel input. The nominal maneuver entrance speeds used in the J-Turn maneuver range from 35 to 60 mph, increased in 5 mph increments until a termination condition is achieved. Termination conditions are simultaneous two inch or greater lift of a vehicle's inside tires or completion of a test performed at the maximum entrance speed without two wheel lift. If two-wheel lift is observed, a downward iteration of vehicle speed is used in 1 mph increments until such lift is no longer detected. Once the lowest speed for which two wheel lift could be detected is isolated, two additional tests are performed at that speed to verify two-wheel lift repeatability.

Fishhook Maneuver

The original version of the fishhook maneuver test was developed by Toyota, and variations of it were suggested by Nissan and Honda (Forkenbrock,

et.al., 2003). Figure 15-4 describes the Fishhook maneuver in terms of the automated steering inputs commanded by the programmable steering machine. NHTSA has experimented with several versions since 1997, and the present test includes roll rate feedback in order to time the counter-steer to coincide with the maximum roll angle of each vehicle in response to the first steer. The initial steering magnitude and countersteer magnitudes are symmetric, and are calculated by multiplying the handwheel angle that would produce a steady state lateral acceleration of 0.3 g at 50 mph on level pavement by 6.5. When this scalar is multiplied by handwheel angles commonly observed at 0.3 g, the result is approximately 270 degrees (Forkenbrock, 2002, Boyd, 2005). As in the case of the J-Turn, the procedure above is an objective way of compensating for differences in steering gear ratio, wheelbase and understeer properties between vehicles. The fishhook maneuver dwell times (the time between completion of the initial steering ramp and the initiation of the countersteer) are defined by the roll rate achieved by the vehicle being evaluated, and can vary on a test-to-test basis. Roll rate is monitored in real-time. The counter steer begins when the roll rate reaches ±1.5 deg/sec. The handwheel rates of the initial steer and countersteer ramps are 720 degrees per second.

As in the case of the J maneuver, the fishhook maneuver begins by driving the vehicle in a straight line at a speed slightly greater than the desired entrance speed (Boyd, 2005). The driver releases the throttle, coasts to the target speed, and then triggers the commanded handwheel input described in Figure 15-4. The nominal maneuver entrance speeds used in the fishhook maneuver range from 35 to 50 mph, increased in 5 mph increments until a termination condition is achieved. Termination conditions include simultaneous two inch or greater lift of a vehicle's inside tires or completion of a test performed at the maximum maneuver entrance speed without two-wheel lift. If two-wheel lift is observed, a downward iteration of vehicle speed is used in 1 mph increments until such lift is no longer detected. Once the lowest speed for which two-wheel lift could be detected is isolated, two additional tests are performed at that speed to verify two-wheel lift repeatability. NHTSA observed that during the Fishhook tests, excessive steering caused some vehicles to reach their maximum roll angle response to the initial steering input before it had been fully completed (this is essentially equivalent to a "negative" T1 in Figure 15-4). Since dwell time duration can have a significant effect on the Fishhook maneuver's ability to produce two-wheel lift, excessive steering may stifle the most severe timing of the counter steer for some vehicles. In an attempt to better insure high maneuver severity, a number of vehicles that did not produce two-wheel lift with steering inputs calculated with the 6.5 multiplier were also tested with lesser steering angles by reducing the multiplier to 5.5. This change

increased the dwell times observed during the respective maneuvers. Some vehicles tipped up in Fishhook maneuvers conducted at the lower steering angle (5.5 multiplier) but not at the higher steering angle (6.5 multiplier). NHTSA adopted the practice of performing Fishhook maneuvers at both steering angles for NCAP (Boyd, 2005, Forkenbrock, et.al., 2002).

A : SS * handwheel position at 0.3g

SS : Steering scalar

T_1 : Time from completion of first handwheel ramp to ± 1.5deg/sec roll velocity

T_2 : 3 second pause

T_3 : 2 seconds

Initial steer and counter steer performed at 720 deg/sec
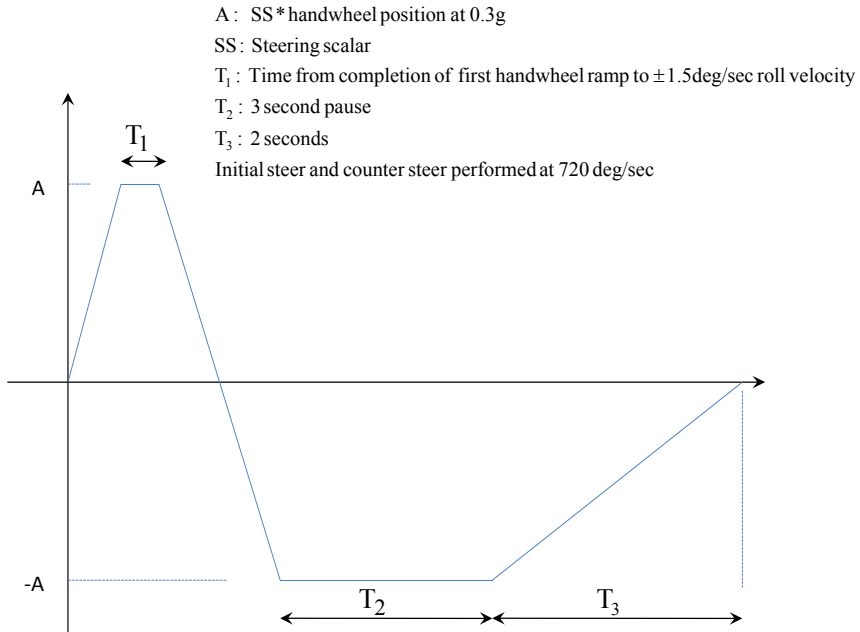
Figure 15-4. NHSTA fishhook maneuver

15.2 ONE DEGREE OF FREEDOM ROLL DYNAMICS MODEL

The simplest roll dynamics model for a vehicle can consist of just one-degree-of-freedom motion, as shown in Figure 15-5. To begin with, assume that the axles and tires have negligible mass compared to the vehicle chassis. In other words the vehicle is modeled as consisting of just a sprung mass, with the unsprung mass assumed to be zero. Also, assume that the vehicle is on a flat road with zero bank angle. These simplifying assumptions will be later removed to obtain more accurate equations. The single degree of freedom considered is the roll angle ϕ, as shown in Figure 15-5.
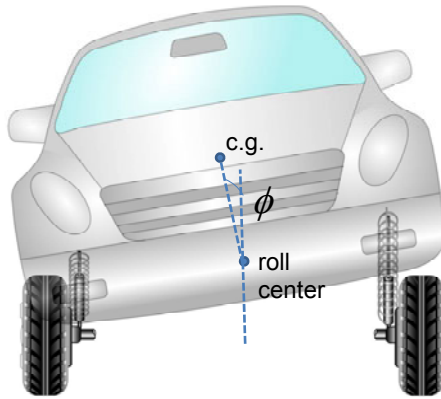
(a) Schematic for vehicle roll dynamics, 1 dof model
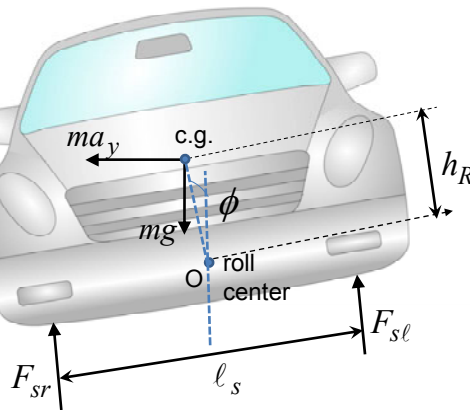
(b)   Free body diagram for 1 dof roll model

Figure 15-5. Roll dynamics and free body diagram

Assume that the total vehicle mass is m, the roll moment of inertia about the c.g. is I_{xx}, the distance between left and right suspension locations is ℓ_s, and the height of the c.g. of the sprung mass from the roll center is h_R. Let a_y be the lateral acceleration experienced by the vehicle. Let the left and right dynamic suspension forces be denoted by $F_{s\ell}$ and F_{sr} respectively and the total lateral tire force be denoted by F_{lat}. From the lateral dynamics of the vehicle, we have $F_{lat} = ma_y$. It should be noted that the d'Alembert's

force $F_{lat} = ma_y$ has been applied at the c.g. of the vehicle in Figure 15-5 in order to make it a quasi-static system.

Taking moments about the roll center O, the roll dynamics equation can be written as

$$(I_{xx} + mh_R{}^2)\ddot{\phi} = \sum M_x$$

$$= F_{lat}h_R \cos\phi + mgh_R \sin\phi + F_{s\ell}\frac{\ell_s}{2} - F_{sr}\frac{\ell_s}{2} \tag{15.5}$$

or

$$\left(I_{xx} + mh_R{}^2\right)\ddot{\phi} = F_{lat}h_R \cos\phi + mgh_R \sin\phi + \frac{\ell_s}{2}\left(F_{s\ell} - F_{sr}\right) \tag{15.6}$$

The suspension forces $F_{s\ell}$ and F_{sr} act on both sides of each of the suspension springs (Figure 15-6). The sprung mass deflection on the left side due to roll is as follows:

$$z_{s\ell} = \frac{\ell_s}{2}\sin\phi \tag{15.7}$$

and on the right side is

$$z_{sr} = -\frac{\ell_s}{2}\sin\phi \tag{15.8}$$

Hence, the dynamic suspension forces are

$$F_{s\ell} = -k_s\frac{\ell_s}{2}\sin(\phi) \tag{15.9}$$

$$F_{sr} = k_s\frac{\ell_s}{2}\sin(\phi) \tag{15.10}$$

or

$$F_{s\ell} - F_{sr} = -k_s \ell_s \sin\phi \qquad (15.11)$$
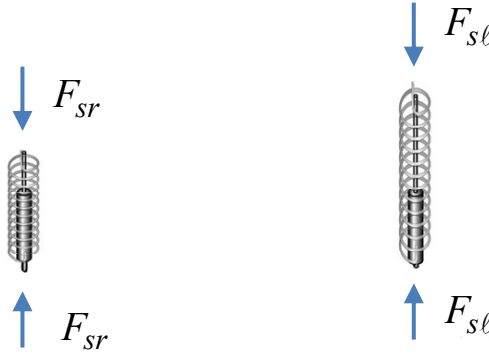
Figure 15-6. Suspension forces

Substituting from equation (15.11) into (15.6)

$$\left(I_{xx} + mh_R^2\right)\ddot{\phi} = F_{lat}h_R \cos\phi + mg\, h_R \sin\phi - \frac{1}{2}k_s\ell_s^2 \sin\phi \qquad (15.12)$$

The equation of motion (15.12) does not have any damping forces. Including suspension damping in addition to stiffness, the roll dynamics can finally be written down as

$$\left(I_{xx} + mh_R^2\right)\ddot{\phi} = ma_y h_R \cos\phi + mg\, h_R \sin\phi$$
$$-\frac{1}{2}k_s\ell_s^2 \sin\phi - \frac{1}{2}b_s\ell_s^2 \dot{\phi}\cos\phi \qquad (15.13)$$

It should be noted that the roll dynamics depend on the lateral dynamics through the lateral acceleration term a_y. By avoiding further expansion of this term in terms of lateral tire forces and lateral dynamic states, a complicated coupled set of equations between roll and lateral dynamics is avoided. Instead, the variable a_y is assumed to be measured and is assumed to be a known input.

The static tire forces on the ground, in the absence of roll angle, are $\dfrac{mg}{2}$ on the left tires and on the right tires. The total tire forces on the ground (including both dynamic and static forces) are

$$F_{z\ell} = \frac{mg}{2} + F_{s\ell} = \frac{mg}{2} - k_s \frac{\ell_s}{2} \sin(\phi) - b_s \frac{\ell_s}{2} \dot{\phi} \cos(\phi) \tag{15.14}$$

and

$$F_{zr} = \frac{mg}{2} + F_{sr} = \frac{mg}{2} + k_s \frac{\ell_s}{2} \sin(\phi) + b_s \frac{\ell_s}{2} \dot{\phi} \cos(\phi) \tag{15.15}$$

Direction of Suspension Forces

In the derivation of the one-degree of freedom model, it was assumed that the suspension forces always act perpendicular to the sprung mass in Figure 15-5. This leads to the sprung mass roll motion given by equation (15.16).

$$\left(I_{xx} + mh_R^2\right)\ddot{\phi} = F_{lat}h_R \cos\phi + mgh_R \sin\phi + \frac{\ell_s}{2}\left(F_{s\ell} - F_{sr}\right) \tag{15.16}$$

Consider the case where the suspension forces always act in the vertical direction, as shown in Figure 15-7 (a).

The sprung mass roll dynamics in this case are given by equation (15.17).

$$\begin{aligned}
\left(I_{xx} + mh_R^2\right)\ddot{\phi} &= F_{lat}h_R \cos\phi + mgh_R \sin\phi \\
&\quad + \frac{\ell_s}{2}\left(F_{s\ell} - F_{sr}\right)\cos\phi \\
&\quad - \left(F_{sr} + F_{s\ell}\right)\left(h_R - h_s\right)\sin\phi
\end{aligned} \tag{15.17}$$

Since $F_{s\ell} + F_{sr} = mg$, this leads to

$$\left(I_{xx} + mh_R^2\right)\ddot{\phi} = F_{lat}h_R \cos\phi + mgh_s \sin\phi + \frac{\ell_s}{2}\left(F_{s\ell} - F_{sr}\right)\cos\phi$$

$$\tag{15.18}$$
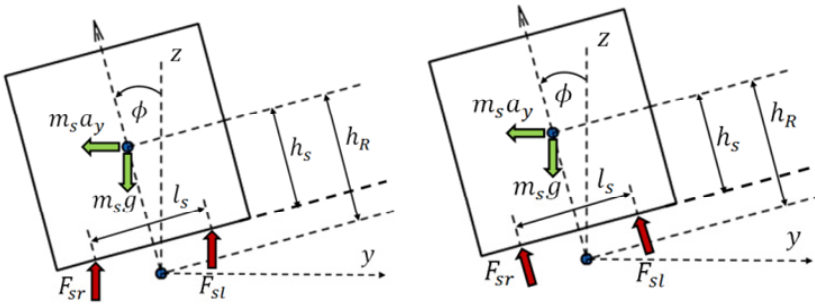
a) Suspension forces are always vertical.   b) Suspension forces are perpendicular to
                                                  the sprung mass.

Figure 15-7. Different directions for suspension forces

Thus the major difference between equations (15.16) and (15.18) is the presence of the coefficient h_s instead of h_R in the gravity term. Both models are quite similar. Since the parameters h_s and h_R will be never be perfectly known, the difference between the two models is not of great importance. To keep the presentation consistent and simple, the sprung mass roll dynamics as described by equation (15.16) will be used in the rest of this chapter.

Inclusion of road bank angle

Next, let us consider the presence of road bank angle. In Figure 15-8, the road bank angle is shown as ϕ_r and is assumed to be positive in the direction opposite to that of the roll angle ϕ.

Moment balance about the roll center yields

$$\left(I_{xx} + mh_R^{\,2}\right)\ddot{\phi} = F_{lat}h_R \cos\phi + mg\, h_R \sin(\phi - \phi_r) - F_{sr}\frac{\ell_s}{2} + F_{s\ell}\frac{\ell_s}{2}$$

$$(15.19)$$

In order to see how the lateral tire force F_{lat} is related to the measured lateral acceleration of the vehicle in this case, consider the lateral dynamics of the vehicle. From the lateral dynamics, the translational equation gets modified due to the bank angle as follows:

$$m\left(\ddot{y} + V_x\dot{\psi}\right) = F_{yf} + F_{yr} - mg\sin\phi_r$$

$$(15.20)$$
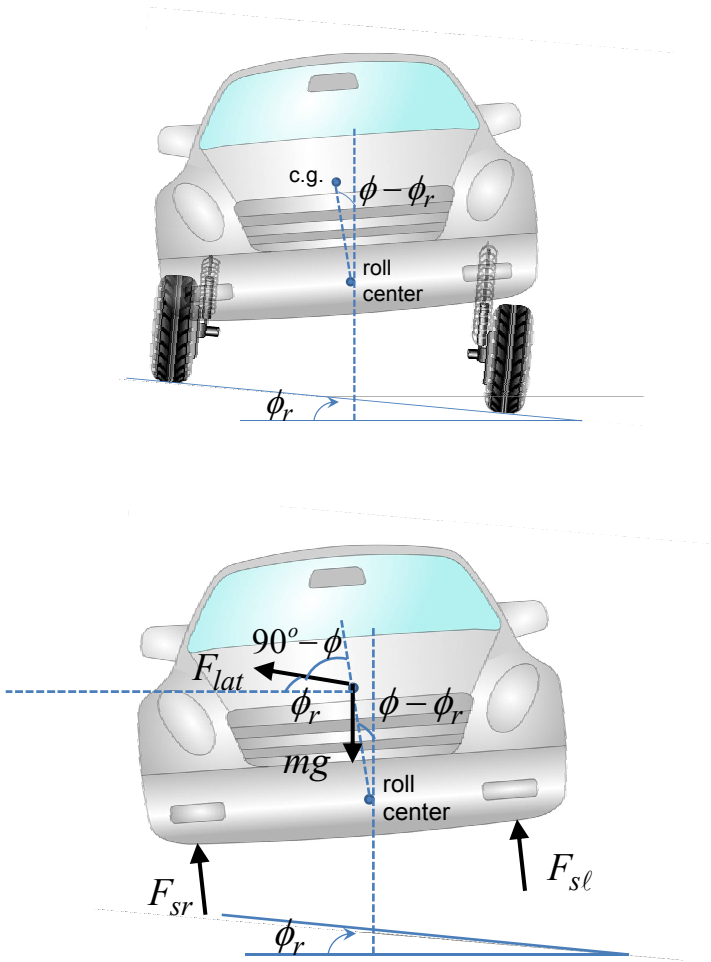
Figure 15-8. Roll dynamics and free body diagram

Hence

$$F_{lat} = F_{yf} + F_{yr} = m(\ddot{y} + V_x\dot{\psi} - g\sin\phi_r) \qquad (15.21)$$

An accelerometer placed on the unsprung mass in the lateral direction reads the total lateral acceleration plus the component of gravity in the lateral direction (with appropriate sign). Hence, the lateral acceleration measured with a lateral accelerometer is (Piyabongkarn, et.al., 2009)

$$a_{y,meas} = \ddot{y} + V_x\dot{\psi} - g\sin\phi_r \qquad (15.22)$$

Hence $F_{lat} = ma_{y,meas}$ includes the effect of both lateral forces as well as the component of gravity due to the road bank angle. Substituting $F_{lat} = ma_{y,meas}$ into equation (15.19)

$$\left(I_{xx} + mh_R^2\right)\ddot{\phi} = ma_{y,meas}h_R\cos\phi + mg\,h_R\sin(\phi - \phi_r)$$
$$- F_{sr}\frac{\ell_s}{2} + F_{s\ell}\frac{\ell_s}{2} \tag{15.23}$$

Next substituting for the dynamic suspension forces F_{sr} and $F_{s\ell}$, the final roll dynamics equation in the presence of road bank angle is written down as

$$\left(I_{xx} + mh_R^2\right)\ddot{\phi} = ma_{y,meas}h_R\cos\phi + mg\,h_R\sin(\phi - \phi_r)$$
$$- \frac{1}{2}k_s\ell_s^2\sin\phi - \frac{1}{2}b_s\ell_s^2(\cos\phi)\dot{\phi} \tag{15.24}$$

It should be noted that this equation differs from the case with zero bank angle only in the term due to the gravity moment $mgh_R\sin(\phi - \phi_r)$. The $mgh_R\sin\phi$ term is replaced with the term $mgh_R\sin(\phi - \phi_r)$.

15.3   FOUR DEGREES OF FREEDOM ROLL DYNAMICS MODEL

The four degrees of freedom considered in this model are

   a) vertical translation of the sprung mass, called heave, and denoted by z_s
   b) roll motion of the sprung mass denoted by ϕ
   c) vertical translation of the left unsprung mass, denoted by $z_{u\ell}$
   d) vertical translation of the right unsprung mass, denoted by z_{ur}

The four degrees of freedom $z_{u\ell}$, z_{ur}, z_s and ϕ are shown in Figure 15-9. The variables $z_{r\ell}$ and z_{rr} are road inputs that act on the system. Inclusion of the influence of the road inputs implies that roll motion induced by road bumps and road potholes can also be analyzed by this model in addition to roll motion induced by lateral acceleration.

Assume that the motions $z_{u\ell}$, z_{ur}, and z_s are measured from the position of static equilibrium. Let the dynamic suspension forces on the left

and right sides be denoted by $F_{s\ell}$ and F_{sr} respectively and the dynamic tire forces on the left and right tires be denoted by $F_{t\ell}$ and F_{tr} respectively, as shown in Figure 15-10.
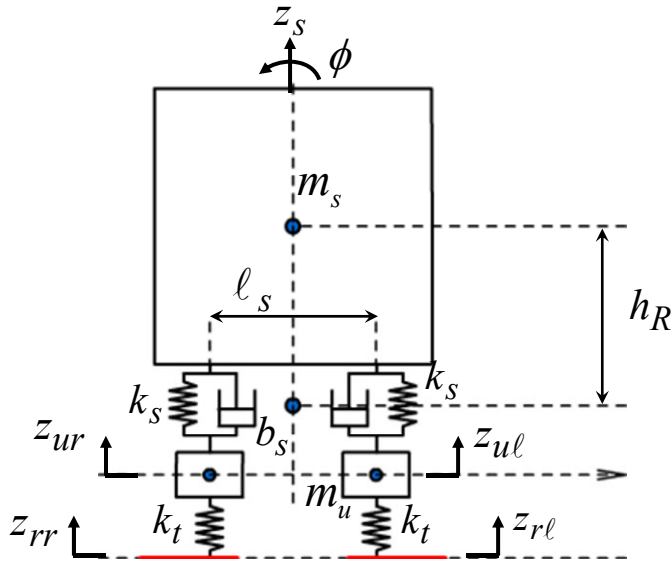
Figure 15-9. Four degree-of-freedom roll dynamics model
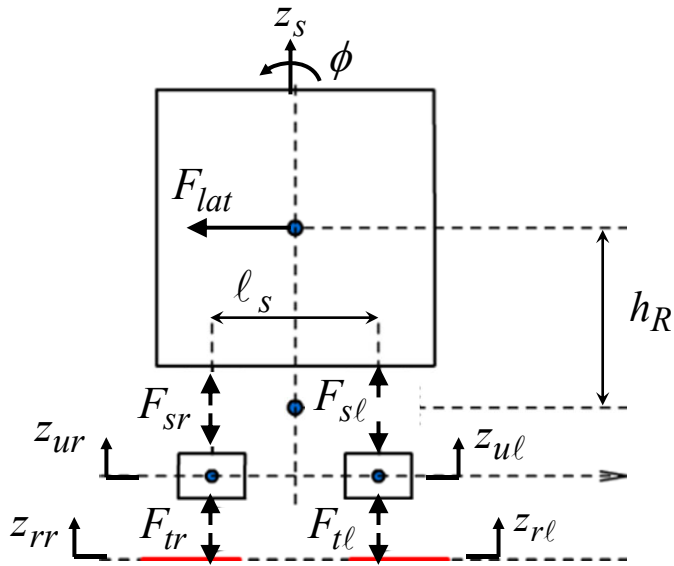
Figure 15-10. Four degree-of-freedom model with suspension and tire dynamic forces

Vertical force balance on the sprung mass and the two unsprung masses yield the following equations

$$m_s \ddot{z}_s = F_{s\ell} + F_{sr} \tag{15.25}$$

$$m_u \ddot{z}_{u\ell} = -F_{s\ell} + F_{t\ell} \tag{15.26}$$

$$m_u \ddot{z}_{ur} = -F_{sr} + F_{tr} \tag{15.27}$$

The roll dynamics of the sprung mass are given by the following equation as developed in section 15.2:

$$\left(I_{xx} + m_s h_R^2\right)\ddot{\phi} = m_s a_y h_R \cos\phi + m_s g\, h_R \sin\phi + \frac{\ell_s}{2}\left(F_{s\ell} - F_{sr}\right) \tag{15.28}$$

The dynamic suspension forces are given by

$$F_{s\ell} = -k_s\left(z_{s\ell} - z_{u\ell}\right) - b_s\left(\dot{z}_{s\ell} - \dot{z}_{u\ell}\right)$$

$$= -k_s\left(z_s + \frac{\ell_s}{2}\sin\phi - z_{u\ell}\right) - b_s\left(\dot{z}_s + \frac{\ell_s}{2}\dot{\phi}\cos\phi - \dot{z}_{u\ell}\right) \tag{15.29}$$

$$F_{sr} = -k_s\left(z_{sr} - z_{ur}\right) - b_s\left(\dot{z}_{sr} - \dot{z}_{ur}\right)$$

$$= -k_s\left(z_s - \frac{\ell_s}{2}\sin\phi - z_{ur}\right) - b_s\left(\dot{z}_s - \frac{\ell_s}{2}\dot{\phi}\cos\phi - \dot{z}_{ur}\right) \tag{15.30}$$

and the dynamic tire forces are given by

$$F_{t\ell} = -k_t\left(z_{u\ell} - z_{r\ell}\right) \tag{15.31}$$

$$F_{tr} = -k_t\left(z_{ur} - z_{rr}\right) \tag{15.32}$$

From equations (15.29) and (15.30)

$$F_{s\ell} - F_{sr} = -k_s\ell_s \sin\phi - b_s\ell_s\dot{\phi}\cos\phi + k_s(z_{u\ell} - z_{ur}) + b_s(\dot{z}_{u\ell} - \dot{z}_{ur}) \tag{15.33}$$

Substituting from equation (15.33) into (15.28)

$$\left(I_{xx} + m_s h_R{}^2\right)\ddot{\phi} = m_s a_y h_R \cos\phi + m_s g\, h_R \sin\phi$$
$$- \frac{k_s \ell_s{}^2}{2} \sin\phi - \frac{b_s \ell_s{}^2}{2} \dot{\phi}\cos\phi \qquad (15.34)$$
$$+ \frac{k_s \ell_s}{2}(z_{u\ell} - z_{ur}) + \frac{b_s \ell_s}{2}(\dot{z}_{u\ell} - \dot{z}_{ur})$$

Hence the overall equations of motion are

$$m_s \ddot{z}_s = -k_s\left(z_s + \frac{\ell_s}{2}\sin\phi - z_{u\ell}\right) - b_s\left(\dot{z}_s + \frac{\ell_s}{2}\dot{\phi}\cos\phi - \dot{z}_{u\ell}\right)$$
$$- k_s\left(z_s - \frac{\ell_s}{2}\sin\phi - z_{ur}\right) - b_s\left(\dot{z}_s - \frac{\ell_s}{2}\dot{\phi}\cos\phi - \dot{z}_{ur}\right)$$
$$(15.35)$$

$$m_u \ddot{z}_{u\ell} = k_s\left(z_s + \frac{\ell_s}{2}\sin\phi - z_{u\ell}\right) + b_s\left(\dot{z}_s + \frac{\ell_s}{2}\dot{\phi}\cos\phi - \dot{z}_{u\ell}\right) \qquad (15.36)$$
$$- k_t\left(z_{u\ell} - z_{r\ell}\right)$$

$$m_u \ddot{z}_{ur} = k_s\left(z_s - \frac{\ell_s}{2}\sin\phi - z_{ur}\right) + b_s\left(\dot{z}_s - \frac{\ell_s}{2}\dot{\phi}\cos\phi - \dot{z}_{ur}\right) \qquad (15.37)$$
$$- k_t\left(z_{ur} - z_{rr}\right)$$

and

$$\left(I_{xx} + m_s h_R{}^2\right)\ddot{\phi} = m_s a_y h_R \cos\phi + m_s g\, h_R \sin\phi$$
$$- \frac{k_s \ell_s{}^2}{2} \sin\phi - \frac{b_s \ell_s{}^2}{2} \dot{\phi}\cos\phi \qquad (15.38)$$
$$+ \frac{k_s \ell_s}{2}(z_{u\ell} - z_{ur}) + \frac{b_s \ell_s}{2}(\dot{z}_{u\ell} - \dot{z}_{ur})$$

The total tire forces on the ground include both static forces due to weight and dynamic forces. Including both static and dynamic forces, the total tire forces on the ground are given by

$$F_{z\ell} = F_{t\ell} + \frac{m_s}{2} g + m_u g \qquad\qquad (15.39)$$

$$F_{zr} = F_{tr} + \frac{m_s}{2} g + m_u g \qquad\qquad (15.40)$$

where m_u is the total unsprung mass on each of the left and right sides of the vehicle and m_s is the vehicle sprung mass.

15.4   ROLLOVER INDEX

A rollover index is a real-time variable that indicates the likelihood of the vehicle to rollover and is computed in active rollover prevention systems in order to trigger differential braking to prevent rollover. Accurate calculation of the rollover index is important in order to ensure that rollovers can be prevented in time while at the same ensuring that active rollover prevention is not triggered unnecessarily.
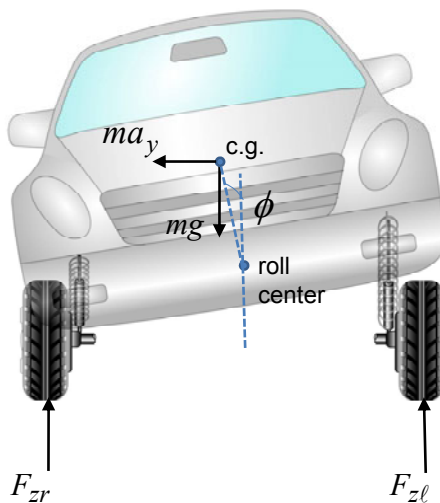
Figure 15-11. Rollover index using lateral load transfer

A common method of defining the rollover index is based on the use of the real-time difference in normal (or vertical) tire loads between left and right sides of the vehicle. Figure 15-11 shows a schematic of a vehicle with a sprung mass that undergoes roll motion. The difference between the vertical tire forces $F_{z\ell}$ and F_{zr} caused by the roll motion of the vehicle is used to define the rollover index R (Liu, et.al., 1997):

$$R = \frac{F_{zr} - F_{z\ell}}{F_{zr} + F_{z\ell}} \tag{15.41}$$

As the sprung mass experiences a positive roll angle, as shown in Figure 15-11, the vertical tire force on the right (or outer) tires increase while the vertical tires forces on the left (or inner) tires decrease. At a sufficiently large roll angle, the vertical tire forces on the inner tires can reach zero, leading to the inner wheels lifting off from the ground. In this case, $F_{z\ell} = 0$.
Hence, at left wheel lift off, $R = \dfrac{F_{zr} - 0}{F_{zr} + 0} = 1$. Likewise, for a sufficiently large negative roll angle, right wheel lift off occurs at $F_{zr} = 0$ and $R = -1$.

Thus wheel lift-off occurs when $R = 1$ or $R = -1$. When the vehicle is being driven straight with zero steering, so that $F_{zr} = F_{z\ell}$, the value of the rollover index is $R = 0$.

Other names for the rollover index in literature include load transfer ratio and lateral load transfer ratio.

The rollover index in equation (15.41) cannot be directly computed in real-time because the tire forces $F_{z\ell}$ and F_{zr} cannot be easily measured. Hence, an estimate of the rollover index has to be obtained by using roll dynamic models to relate the values of $F_{zr} - F_{z\ell}$ and $F_{zr} + F_{z\ell}$ to other easily measured variables.

From equations (15.14) and (15.15) for the one degree-of-freedom roll dynamics model, we have the total tire forces as

$$F_{z\ell} + F_{zr} = mg \tag{15.42}$$

$$F_{zr} - F_{z\ell} = k_s \ell_s \sin\phi + b_s \ell_s \dot{\phi} \cos\phi \tag{15.43}$$

Then the rollover index is

$$R = \frac{F_{zr} - F_{z\ell}}{F_{zr} + F_{z\ell}} = \frac{k_s \ell_s \sin\phi + b_s \ell_s \dot{\phi}\cos\phi}{mg} \tag{15.44}$$

Equation (15.44) requires measurement of the roll angle and roll rate of the sprung mass. Unfortunately, the roll angle is also not a measurement that is typically available on most vehicles. Measurement of roll angle requires use of LVDTs or other relative deflection sensors to measure left and right suspension deflections and hence compute the roll angle. Such sensors are expensive and typically not available on most passenger vehicles. Furthermore, equation (15.44) also assumes linear spring and damper behavior for the suspension and requires knowledge of suspension parameters.

The term $k\ell_s \sin\phi + b\ell_s \dot{\phi}\cos\phi$ can be further estimated from the one degree roll dynamic model under certain assumptions.

In the roll dynamics equation of motion (15.13), set $\ddot{\phi} = 0$, for ignoring transient dynamics. Then

$$\frac{1}{2}k\ell_s^{\,2}\sin\phi + \frac{1}{2}b\ell_s^{\,2}\dot{\phi}\cos\phi = ma_y h_R \cos\phi + mg\, h_R \sin\phi$$

or

$$k\ell_s \sin\phi + b\ell_s \dot{\phi}\,\cos\phi = \frac{2ma_y h_R \cos\phi + 2mg\, h_R \sin\phi}{\ell_s} \tag{15.45}$$

Assume $\ell_s = \ell_w$. Hence the rollover index can be estimated as

$$R = \frac{2h_R a_y \cos\phi + 2gh_R \sin\phi}{\ell_w g} = \frac{2h_R}{\ell_w g}a_y \cos\phi + \frac{2h_R}{\ell_w}\sin\phi \tag{15.46}$$

Rollover index (15.46) involves the lateral acceleration of the vehicle a_y measured on the unsprung mass, and the roll angle of the vehicle ϕ. The unsprung mass does not undergo any roll motion and a lateral accelerometer placed on the unsprung mass therefore retains its direction and measures vehicle lateral acceleration. The parameters in the equation that need to be known are the height of the center-of-gravity (c.g.) h_R and the track width ℓ_w.

At small roll angles, the requirement to measure roll angle can be removed. Assuming $\sin\phi \approx 0$ and $\cos\phi \approx 1$, the rollover index of equation (15.46) can be approximated for small roll angles by

$$R_{approx} = \frac{2h_R a_y}{\ell_w g} \tag{15.47}$$

The index of equation (15.47) requires measurement of lateral acceleration only, a measurement which is typically available on all cars equipped with electronic stability control systems.
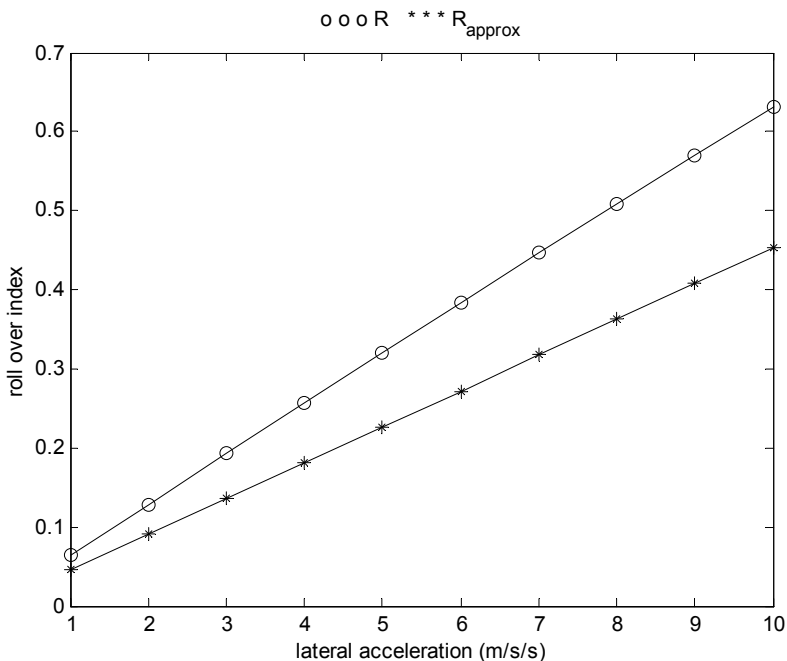
Figure 15-12. Rollover indices R and R_{approx} as a function of lateral acceleration

Figure 15-12 shows the original rollover index R of equation (15.46) and its approximation R_{approx} for a typical SUV as a function of lateral acceleration during steady state cornering around a circular track. It can be seen that the difference between the two curves increases as lateral acceleration increases, resulting in higher error during tight cornering maneuvers. Further, the error increases with increase in height of the c.g. Hence, if the roll angle can be estimated, a more accurate computation of the rollover index can be obtained from equation (15.46) compared to (15.47).

It should be noted that the height of the c.g. is a constant parameter. However, it changes with change in the passenger and freight load on the vehicle.

Results on estimation of roll angle and c.g. height can be found in Rajamani, et.al., 2009, and other recent publications.

15.5   ROLLOVER PREVENTION

Once it has been determined that the vehicle is close to rollover from the computed real-time rollover index, an effective rollover prevention action needs to be initiated. Rollovers, in the case of untripped rollovers, can be prevented by stiffening the suspension in the vehicle, by braking to reduce the vehicle speed and by differential braking to reduce both yaw rate and vehicle speed. Rollover prevention is often incorporated as an additional function of the electronic stability control system of the vehicle (Piyabongkarn, et.al. 2010, Liebemann, et.al., 2004). In this case, differential braking or differential drive torque is the mechanism utilized for rollover prevention.
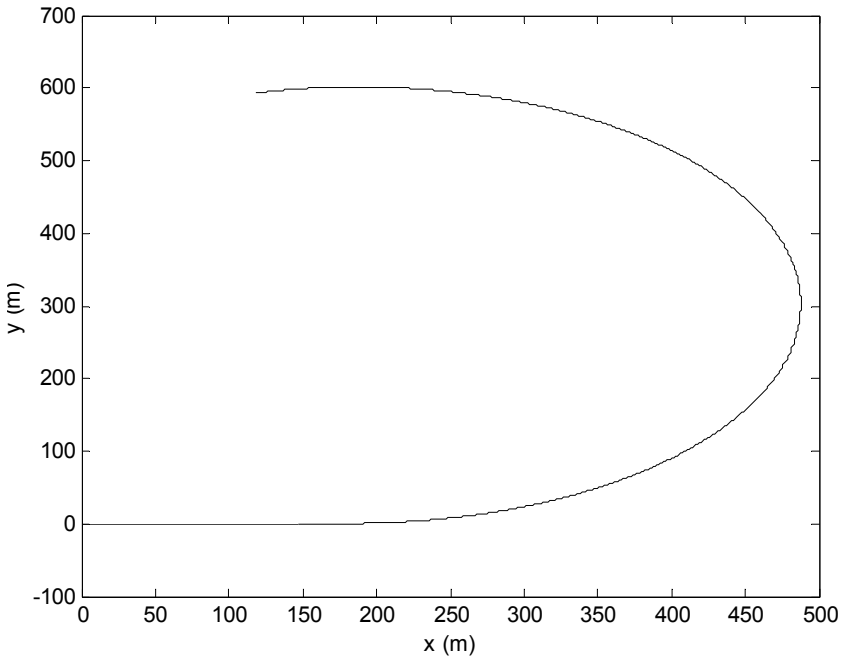
Figure 15-13. Circular trajectory executed by vehicle
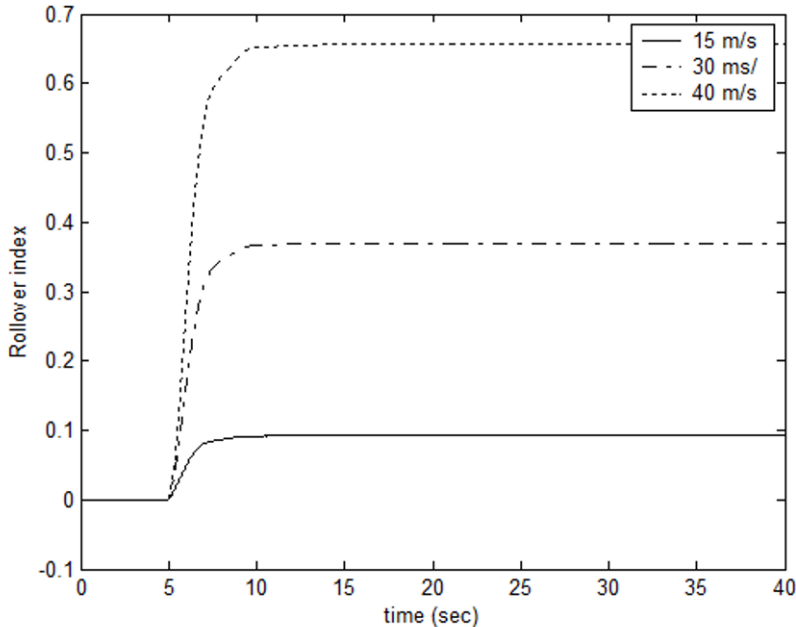
Figure 15-14. Rollover index at different speeds

Consider a vehicle navigating a circular segment of a road. Figure 15-13 shows the trajectory executed by the vehicle and consists of a straight road travel segment followed by travel on a circular segment of radius 300 meters. Figure 15-14 shows the rollover index for three different speeds of 15, 30 and 40 m/s (33.75 mph, 67.5 mph and 90 mph respectively). As seen in Figure 15-14, R is only 0.1 at 15 m/s, but is 0.38 at 30 m/s and 0.66 at 40 m/s. Since the exact same trajectory is being executed at all 3 speeds, the radius of the circular portion of the trajectory R is the same, but the yaw rate $\dot{\psi} = \dfrac{V_x}{R}$ is lower at smaller speeds. Hence the steady state lateral acceleration given by $a_{y\_ss} = V_x\dot{\psi} = \dfrac{V_x^2}{R}$ is significantly lower at smaller speeds. This explains why lowering the speed reduces rollover propensity.

The reduction of yaw rate without reducing vehicle speed also reduces rollover propensity. In the case of the dynamic rollover assessment tests conducted by NHTSA, the rollover performance of the vehicle is tested at various speeds. For example, the fishhook maneuver performance is evaluated at a range of speeds from 35 to 50 mph. Cruise control can be used to maintain constant speed during the fishhook maneuver. Without reducing speed, an ESC system can reduce yaw rate using differential braking. The cruise control system controls throttle in this case to provide a constant speed.

Consider the simulation results shown in Figures 15-15 – 15-18 for execution of a fishhook maneuver. The steering angle input is of the form shown in Figure 15-4. An ESC system with bounds on the desired yaw rate is implemented. The desired yaw rate is first computed from the driver's steering input, as described in chapter 8. However, the desired yaw rate is subsequently bounded so that the rollover index remains less than a maximum threshold. Use the rollover index definition

$$R = \frac{2h_R a_y}{\ell_w g} \tag{15.48}$$

If the rollover index needs to remain below a threshold value $R_{threshold}$, then the corresponding maximum allowable lateral acceleration is given by

$$a_y \leq \frac{R_{threshold} \ell_w g}{2h_R} \tag{15.49}$$

Set the lateral acceleration term to be equal to the centripetal acceleration $a_y = V\dot{\psi}$. In doing this, the translational sliding term $\ddot{y}$ is being ignored.

$$V\dot{\psi}_{des} \leq \frac{R_{threshold} \ell_w g}{2h_R} \tag{15.50}$$

By doing yaw stability control with this bound on the desired yaw rate, rollover prevention is naturally incorporated as a part of electronic stability control.

Since the translational sliding term and the roll angle term in the rollover index were both ignored, a bound of ± 0.3 rad/s was conservatively used for the simulation results shown in the following figures. The simulations involved a SUV with a c.g. height of 0.8 meters. Cruise control is used in these simulations so that the longitudinal speed stays approximately at 15 m/s (33mph) throughout the simulation. Differential braking is used for ESC with bounded desired yaw rate, as described above. The dotted curves in all the simulation results describe open-loop execution of a fishhook maneuver, while the solid curves describe execution of the same fish-hook maneuver under the use of electronic stability control (ESC). As seen in Figure 15-15, the yaw rate obtained is bounded by 0.3 rad/sec due to the use of bounded-yaw-rate ESC.
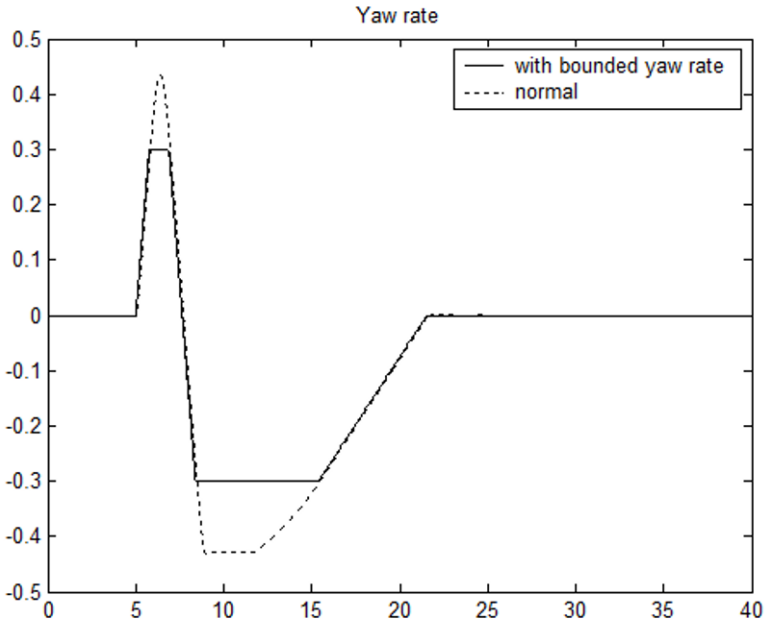
Figure 15-15. Yaw rate – nominal and bounded
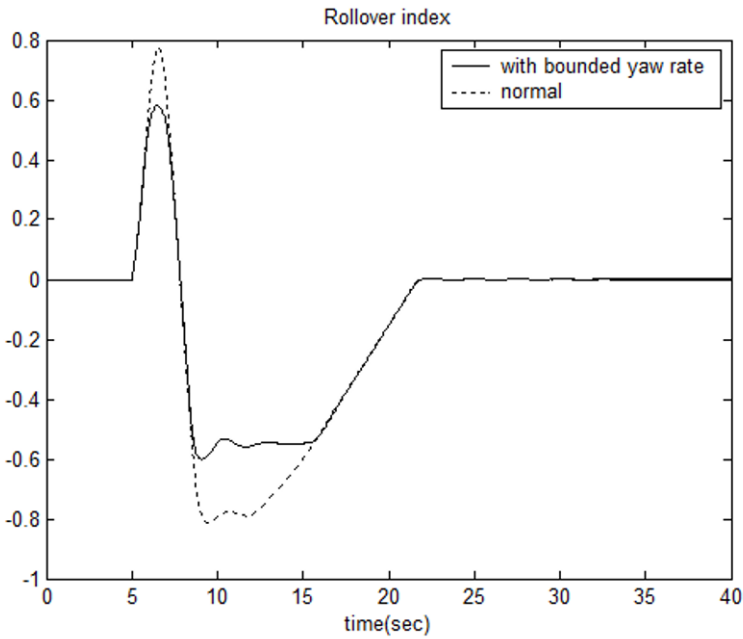
Figure 15-16. Rollover index – nominal and bounded yaw rate
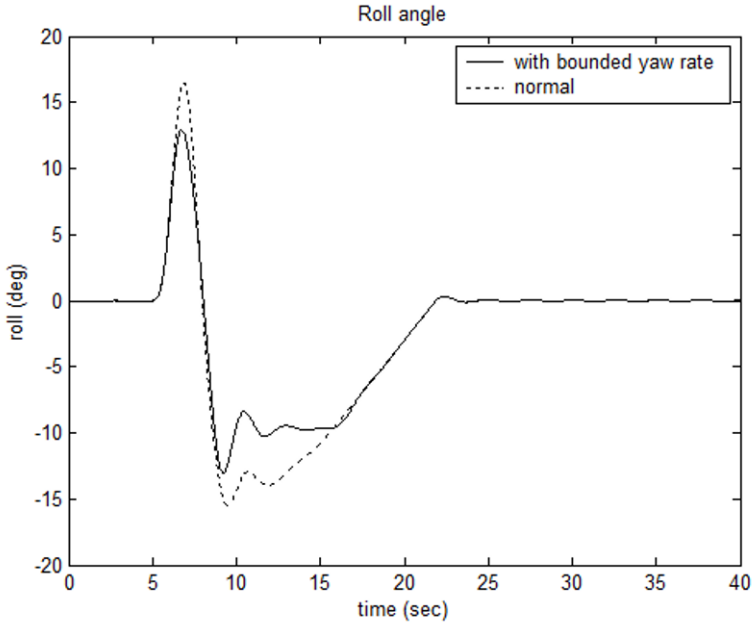
Figure 15-17. Roll angle – nominal and bounded yaw rate
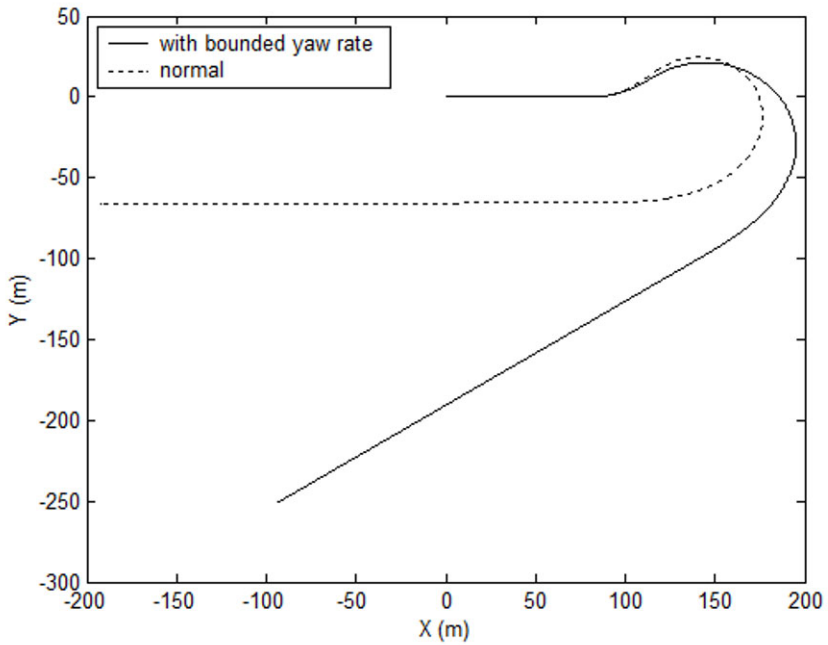
Figure 15-18. Vehicle trajectory - nominal and bounded yaw rate

The rollover index is as high as 0.8 for the system without ESC, while the ESC system with bounded yaw rate has a rollover index with a maximum value of only 0.55, as shown in Figure 15-16. Likewise, the roll angle is much smaller for the ESC system, as shown in Figure 15-17. Thus the rollover propensity is significantly reduced with the bounded-yaw-rate ESC system. However, due to the yaw rate being different, the planar trajectory executed by the ESC based system is different from the trajectory executed by the non-ESC system, as shown in Figure 15-18. If the same trajectory is desired with a lower yaw rate, then a lower longitudinal speed should be used.

15.6   CHAPTER SUMMARY

This chapter described the static stability factor (SSF) and the dynamic maneuver tests used in the rollover resistance ratings for vehicles by NHTSA. Models for roll dynamics of a vehicle were presented. A one degree of freedom model was presented that provides roll dynamic response of a vehicle to lateral acceleration maneuvers. A 4-degree of freedom model was presented that provides roll dynamic response to both lateral acceleration and road vertical inputs.

A rollover index is a real-time variable that indicates the likelihood of the vehicle to rollover. A fundamental way to calculate the rollover index is based on detection of wheel lift and utilizes the difference between inner and outer tire normal forces. The rollover index can be approximated by a formula that uses lateral acceleration and roll angle.

If the rollover index exceeds a threshold indicating a high danger of rollover, rollover prevention can be triggered. Rollover prevention implemented as an accessory to an electronic stability control typically uses differential braking to reduce both vehicle speed and yaw rate for prevention of rollover.

NOMENCLATURE

SSF	static stability factor
ℓ_w	track width
ℓ_s	lateral distance between left and right suspensions
h	height of vehicle c.g. from grounnd
h_R	height of vehicle c.g. from roll center

h_s	height of vehicle c.g. from suspension location
a_y	lateral acceleration of vehicle
a_{y_meas}	signal measured by lateral accelerometer
$a_{y\_lift-off}$	lateral acceleration for wheel lift off
a_{y_ss}	steady state lateral acceleration on a circular curve
m	vehicle mass
m_s	vehicle sprung mass
m_u	unsprung mass on either left or right side of vehicle
I_{xx}	roll moment of inertia about c.g.
g	acceleration due to gravity
F_{lat}	total lateral tire force (from front and rear tires)
$F_{s\ell}$	left suspension dynamic force
F_{sr}	right suspension dynamic force
$F_{t\ell}$	left tire dynamic force
F_{tr}	right tire dynamic force
$F_{z\ell}$	total left tire force
F_{zr}	total right tire force
ϕ	roll angle
ϕ_r	road bank angle
z_s	vertical deflection of c.g. of vehicle
$z_{s\ell}$	vertical deflection of left side of sprung mass
z_{sr}	vertical deflection of right side of sprung mass
$z_{u\ell}$	vertical deflection of left unsprung mass
z_{ur}	vertical deflection of right unsprung mass
$z_{r\ell}$	left road displacement input
z_{rr}	right road displacement input

V_x vehicle longitudinal velocity

$\dot{\psi}$ yaw rate of vehicle

$\dot{\psi}_{des}$ desired yaw rate

$\dot{y}$ translational lateral velocity

k_s suspension stiffness

b_s suspension damping coefficient

k_t tire stiffness

R rollover index

R_{approx} approximate rollover index

$R_{threshold}$ threshold on rollover index for rollover prevention initiation

REFERENCES

Boyd, P.L., "NHTSA's NCAP Rollover Resistance Rating System," Paper # 05-0450, Proceedings - *19th International Technical Conference on the Enhanced Safety of Vehicles*, Washington, D.C., June 6-9, 2005, Available on NHTSA web site, http://www-nrd.nhtsa.gov/pdf/esv/esv19/05-0450-O.pdf.

Chen, B. and Peng, H., "Differential braking based rollover prevention for sport utility vehicles with human-in-the-loop evaluations," *Vehicle System Dynamics*, Vol. 36, No. 4-5, pp. 359-389, 2001.

Carlson, C.R. and Gerdes, J.C., "Optimal Rollover Prevention with Steer by Wire and Differential Braking," *Proceedings of the ASME International Mechanical Engineering Congress and Exposition*, pp. 345-355, November, 2003.

Forkenbrock, G.J., Garrott, W.R., Heitz, M. and O'Harra, B.C., "Experimental Examination of J-Turn and Fishhook Maneuver that may Induce On-Road Untripped Light Vehicle Rollover," *SAE Paper,* No. 2003-01-1008, 2003.

Forkenbrock, G.J., Garrott, W.R., Heitz, M. and O'Harra, B.C., "A Comprehensive Experimental Examination of Test Maneuvers that May Induce On-Road, Untripped Light Vehicle Rollover – Phase IV of NHTSA's Light Vehicle Rollover Research Program," *NHTSA Technical Report*, DOT HS 809 513, October 2002.

Hac, A., Brown, T. and Martens, J., "Detection of Vehicle Rollover," *SAE Technical Paper Series*, 2004-01-1757, SAE World Congress, 2004.

Lew, J.Y., Piyabongkarn, D. and Grogg, J.A., "Minimizing Dynamic Rollover Propensity with Electronic Limited Slip Differentials," *SAE Transactions Journal of Passenger Cars: Mechanical Systems*, pp. 1183-1190, SAE book number V115-6, 2006.

Liebemann, E.K., Meder, K., Schuh, J. and Nenninger, G., "Safety and Performance Enhancement: The Bosch Electronic Stability Control (ESP)," *SAE Paper*, No. 2004-21-0060, 2004.

Liu, P.J., Rakheja, S. and Ahmed, A.K.W., "Detection of Dynamic Roll Instability of Heavy vehicles for Open-Loop Rollover Control," *SAE Paper*, No. 973263.

NHTSA, USDOT, *Fatality Analysis Reporting System* (FARS),
    http://www-fars.nhtsa.dot.gov/Main/index.aspx, accessed June 2011.
Odenthal, D., Bunte, T. and Ackermann, J., "Nonlinear Steering and Braking Control for
    Vehicle Rollover Avoidance," *Proceedings of the European Control Conference*, 1999.
Piyabongkarn, D. Rajamani, R., Grogg, J. and Lew, J., "Development and Experimental
    Evaluation of a Slip Angle Estimator for Vehicle Stability Control," *IEEE Transactions on
    Control Systems Technology,* Vol. 17, No. 1, pp. 78-88, January 2009.
Piyabongkarn, D., Rajamani, R. and Lew, J.Y., "Active Driveline Torque Management
    Systems – Individual Wheel Torque Control for Active Automotive Safety Applications,"
    IEEE Control Systems Magazine, Vol. 30, Issue 4, pp. 86-102, August 2010.
Rajamani, R., Piyabongkarn, D., Tsourapas, V. and Lew, J.Y., "Real-Time Estimation of Roll
    Angle CG Height for Active Rollover Prevention Applications," *Proceedings of the
    American Control Conference*, 2009.
Takano, S. and Nagai, M., "Dynamic Control of Large Vehicles for Rollover Prevention," pp.
    85-89, *Proceedings of IEEE IVEC*, 2001.
Transportation Research Board (TRB), *the National Academies*, Special Report 265, "The
    National Highway Traffic Safety Administration's Rating System for Rollover Resistance:
    An Assessment," 2002.
Yoon, J., Kim, D. and Yi, K., "Design of a Rollover Index Based Vehicle Stability Control
    Scheme," *Vehicle System Dynamics*, Vol. 45, No. 5, pp. 459-475, May 2007.

Chapter 16

DYNAMICS AND CONTROL OF HYBRID GAS ELECTRIC VEHICLES

A hybrid automobile is one that has two or more major sources of propulsion power. Most hybrid vehicles currently available to consumers are gas-electric hybrids. They have both gasoline engines and electric motors and can be powered by either power source or both sources at the same time.

Compared to a conventional engine-only vehicle, a hybrid gas-electric vehicle can offer significantly reduced fuel consumption and can also help reduce polluting emissions. The improvement in fuel consumption comes due to the following reasons:

a) In some hybrid vehicles, both the engine and the motor can simultaneously power the wheels of the vehicle. This allows the engine size to be downsized and allows the choice of an engine designed for average torque demands during driving. The peak torque demand can be met using additional torque from the electric motor.

b) In other hybrid vehicles, the engine is not directly connected to the wheels and is instead used as a generator to charge a battery. The battery powers a motor that drives the wheels of the vehicle. Since the engine is not directly connected to the wheels, it can operate at its optimum speed-torque points, allowing for significantly more efficient operation and lower fuel consumption.

c) In all hybrid vehicles, the electric motor is used in reverse as a generator during deceleration. This is called regenerative braking and is used instead of friction brakes to achieve deceleration of the vehicle. Regenerative braking allows recapture of the kinetic energy of the

vehicle to a re-usable form. In a regular vehicle, friction brakes would waste the kinetic energy of the vehicle as heat.

d) Other means to reduce fuel consumption include the ability to completely stop the engine when the vehicle is stopped at a traffic light or stop sign. This saves fuel and cuts the significant emissions that would otherwise occur during idling of the engine.

The engine in a regular car is sized for peak power (when the driver floors the accelerator pedal for fast acceleration). Most drivers, however, only use peak power less than 1% of the time, if at all. A typical engine with 150 hp might be able to accelerate from 0-60 mph in 10 seconds. A hybrid vehicle like the Toyota Prius is able to achieve the same level of acceleration using only a 76 hp engine. Due to the smaller size of the engine, significantly higher fuel economy can be achieved.

16.1   TYPES OF HYBRID POWERTRAINS

The types of common powertrains seen in gas-electric hybrid automobiles are as follows.

Parallel Hybrid

As the name implies, in a parallel hybrid vehicle, both the engine and the motor can simultaneously drive the wheels of the vehicle. This is enabled by use of an appropriate transmission system, as shown in Figure 16-1. The battery in a parallel hybrid is charged during regenerative braking and during other times from the engine when the power demand of the vehicle is very low.
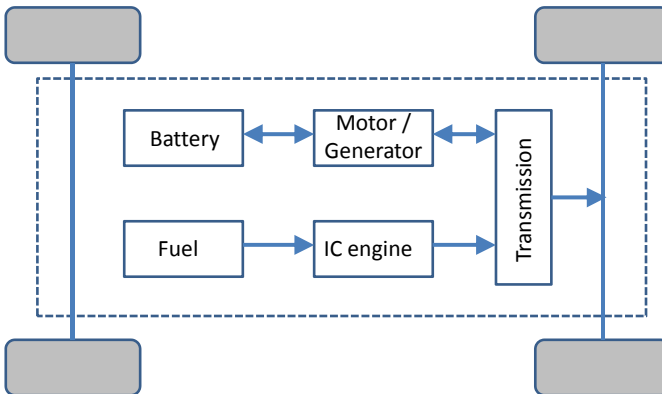
Figure 16-1. Schematic of powertrain for a parallel hybrid vehicle

The parallel hybrid obviates the need for conversion of the engine power to electric power before its use at the wheels. This eliminates the inefficiency associated with mechanical-to-electrical energy conversion. However, unlike the series hybrid, the engine cannot operate at its most efficient speed-torque conditions and must operate over a wide range of speeds and torque demands.

The Honda Insight, Civic and Accord cars use the parallel type of hybrid propulsion system.

Series Hybrid

In a series hybrid, only the electric motor drives the wheels of the vehicle. The motor receives power either from a battery pack or from an engine-generator set, as shown in Figure 16-2. The control system determines in real-time what fractions of the power come from the battery-pack and from the engine-generator. The battery pack can be recharged both from the engine-generator and from the motor-generator during regenerative braking (deceleration).

The engine in a conventional vehicle is forced to operate over a wide range of operating conditions, while in a series hybrid it can operate at its most efficient operating conditions. This is because the engine is used in a series hybrid purely to recharge the battery and does not have to change its operating conditions to meet the power, torque and speed demands of the vehicle. This also eliminates the need for a multi-speed transmission system.

A series hybrid needs a larger battery and motor than a parallel hybrid, since these are used to entirely meet the driving demands of the vehicle. The engine is typically smaller than in a conventional vehicle. The engine has to
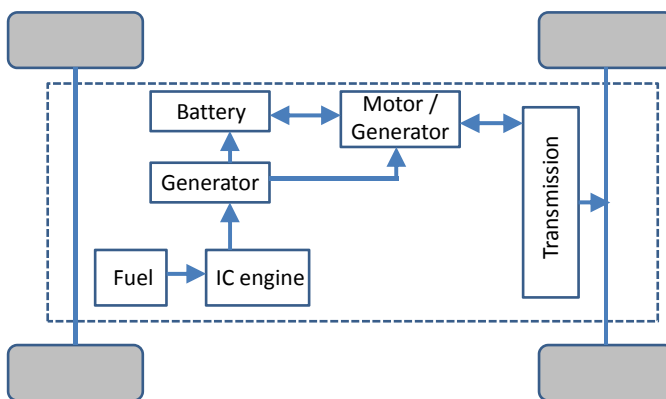
Figure 16-2. Schematic of powertrain for a series hybrid vehicle

meet the average power demand while the peak power demands can be met by the battery and motor. A series hybrid is likely to be more expensive than a parallel hybrid, due to the larger motor and battery and due to the need for a separate generator. However, a series hybrid is also likely to have a simpler drivetrain due to elimination of the transmission.

A series hybrid is a good powertrain for buses and other urban vehicles involved in a lot of stop-and-go driving.

Power-split or Series-Parallel Hybrid

The power-split hybrid combines the advantages and the hardware of the parallel and series drivetrains. By combining the two designs, the engine can be used to drive the wheels directly (as in the parallel drivetrain) and also be effectively disconnected from the wheels so that only the electric motor powers the wheels (as in the series drivetrain). As a result of this combination, the engine operates at near optimum efficiency more often. At lower speeds where efficient engine operation is more important to achieve due to the stop-and-go nature of driving, the power-split drivetrain operates more as a series vehicle. At high speeds, where the series drivetrain is less efficient, the engine connects directly to the wheels and energy loss in going from mechanical operation to electricity generation is minimized. This system is more expensive due to the more complex hardware and also requires a sophisticated control system. However, the power-split hybrid has the potential to perform better than either of the series or parallel systems alone. The schematic of a power-split hybrid powertrain is shown in Figure 16-3.
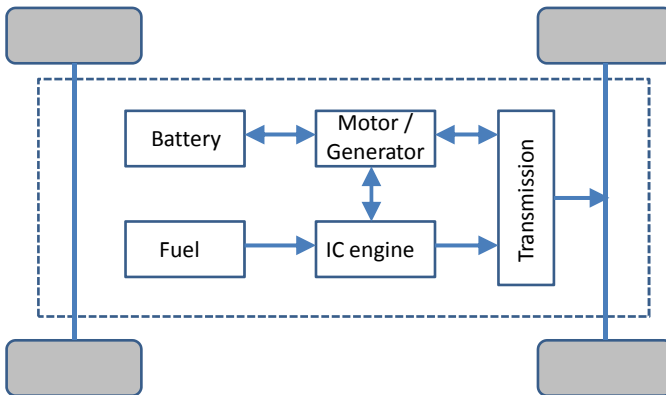
Figure 16-3. Schematic of powertrain for a power-split hybrid vehicle

The Toyota Prius is one of the most well known vehicles with a power-split hybrid powertrain.

Other Power Sources

In addition to gasoline engines and electric motors, other types of power sources that have been used in hybrid vehicles include hydraulic systems, fuel cells and pneumatic actuator systems (Wu, et. al., 2002, Rodatz, et. al., 2005, and Vahidi, et. al., 2006). The U.S. Environmental Protection Agency (EPA) and its industry partners have developed a delivery van with a series hydraulic hybrid drivetrain in a UPS vehicle (US EPA, 2006). This hydraulic hybrid demonstration vehicle has been shown to achieve 60-70% better fuel economy in laboratory tests and 40% or more reduction in carbon dioxide emissions. UPS has purchased 7 such vehicles from EPA for deployment by 2010.

16.2 POWERTRAIN DYNAMIC MODEL

16.2.1 Dynamic Model for Simulation of a Parallel Gas-Electric Hybrid Vehicle

Inertial Dynamics:
The longitudinal vehicle dynamics remain the same as that for any other automobile and can be represented by

$$m\dot{V}_x = F_x - C_a V_x^2 - R_x - mg\sin(\theta) \qquad (16.1)$$

where V_x represents the longitudinal vehicle velocity, F_x is the total longitudinal tire traction force, R_x is the force due to rolling resistance, θ is the road grade angle, m is vehicle mass and C_a is the aerodynamic drag coefficient.

For purposes of determining the total drive torque at the wheels, the dynamics of the wheels can be represented using one virtual wheel. The dynamics of the wheels of the vehicle (lumped into one virtual wheel) are given by

$$I_w \dot{\omega}_w = T_d - T_{fbrake} - r_{eff} F_x \qquad (16.2)$$

where I_w is the moment of inertia of the wheels, T_d is the drive torque supplied to the drive wheels, T_{fbrake} is the total frictional brake torque and r_{eff} is the effective tire radius.

Power Split Ratio:
Driver throttle command, speed, desired speed, desired inter-vehicle spacing, or other longitudinal control criteria are used to determine the required total drive torque T_d. This wheel drive torque T_d needs to be provided by a parallel combination of the engine and the motor through a transmission. Hence

$$T_d = \frac{1}{R}\left(T_{ICE} + T_{EM}\right) \tag{16.3}$$

where R is the transmission gear ratio, T_{EM} is the torque from the electric motor and T_{ICE} is the torque from the IC engine. Note that $R < 1$ and is the ratio of the wheel speed to the engine/motor speed.

The variable $u = \dfrac{T_{EM}}{RT_d}$ is chosen as the control input. This is the ratio of torque provided by the electrical motor to the total torque from the motor and the engine and is called the power split ratio.

The required torque from the engine T_{ICE} is determined based on knowledge of desired total drive torque and the value of the control input. A discussion of how the desired total drive torque is determined is presented in section 16.6.

Engine Fuel Consumption:
The motor and engine rotational speeds are given by

$$\omega_{EM} = \omega_{ICE} = \frac{1}{R}\omega_w \tag{16.4}$$

The fuel consumption rate of the engine can be modeled as an algebraic function of the engine torque and engine angular speed:

$$\dot{m}_f = f(T_{ICE}, \omega_{ICE}) \tag{16.5}$$

Often the fuel consumption for a given vehicle is calculated using a map. The map provides $\dot{m}_f$ for various values of T_{ICE} and ω_{ICE}. An example of a fuel consumption map from the Toyota hybrid Prius vehicle is provided in section 16.2.2.

Motor and SOC dynamics:
Power discharge from the battery to the motor is given by

$$P_{batt} = \eta^k T_{EM} \omega_{EM} \tag{16.6}$$

where η is the electrical-mechanical conversion efficiency and

$$k = -1 \ \text{ if } \ T_{EM} \geq 0 \tag{16.7a}$$

$$k = 1 \ \text{ if } T_{EM} < 0 \tag{16.7b}$$

Note that the power discharge from the battery is positive when $T_{EM} \geq 0$ and negative when $T_{EM} < 0$ (during braking , when regenerative action occurs).

The state of charge dynamics of the battery is given by

$$\frac{d}{dt} SOC = -\frac{I_{batt}}{Q_{batt\_o}} \tag{16.8}$$

where SOC represents the state-of-charge of the battery, I_{batt} represents the current flowing from the battery and Q_{batt_o} represents the total or maximum charge at full charge for the battery.

The power discharge dynamics of the battery system are given by

$$P_{batt} = V_{oc} I_{batt} - R_{batt} I_{batt}{}^2 \tag{16.9}$$

where V_{oc} is the open circuit battery voltage and R_{batt} includes the internal and terminal resistance of the battery. I_{batt} is obtained by solving the quadratic equation (16.9) as

$$I_{batt} = \frac{V_{oc} \pm \sqrt{V_{oc}{}^2 - 4 P_{batt} R_{batt}}}{2 R_{batt}} \tag{16.10}$$

Of the two possible solutions in equation (16.10), only 1 solution is viable. The viable solution is given by

$$I_{batt} = \frac{V_{oc} - \sqrt{V_{oc}{}^2 - 4\eta^k T_{EM} \omega_{EM} R_{batt}}}{2 R_{batt}} \tag{16.11}$$

The battery resistance R_{batt} is a function of the SOC of the battery and of temperature.

Hence the state of charge dynamics are given by

$$\frac{d}{dt} SOC = -\frac{V_{oc} - \sqrt{V_{oc}^2 - 4\eta^k T_{EM} \omega_{EM} R_{batt}}}{2R_{batt} Q_{batt\_o}} \tag{16.12}$$

16.2.2 Dynamic Model for Simulation of a Power-Split Hybrid Vehicle

The Toyota Prius utilizes a power-split or series-parallel hybrid powertrain system that combines the advantages and the hardware of the series and parallel hybrid powertrains. A planetary gear system enables the engine to both drive the wheels directly when desired and also to be disconnected from the wheels so as to only charge the battery.

Planetary Gear System
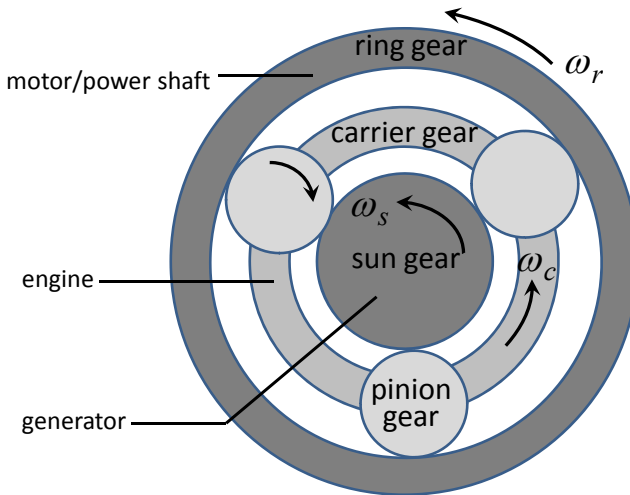
Figure 16-4. Planetary gear based power split system

The power split device in the Toyota Prius THS-II system uses a planetary gear to transmit torque from the engine to both the generator as well as the wheels. As shown in Figure 16-4, the engine is connected to the

carrier gear in the planetary system. By using appropriate pinion gears on the carrier, it is possible for the engine to connect to the motor, the generator, or both. Thus the carrier gear can transmit torque both to the ring gear and the sun gear. The sun gear is linked to the generator which charges a battery. The ring gear is on a common shaft with a motor and drives the front axle through a reduction gear. The torque that drives the wheels is the sum of the ring gear torque and the torque produced by the electric motor.

The rotational speeds of the ring gear, sun gear and carrier gear satisfy the following relationship

$$\omega_s R_s + \omega_r R_r = \omega_c (R_s + R_r) \tag{16.13}$$

where R_r and R_s are the radii of the ring gear and sun gear respectively, and ω_s, ω_r and ω_c are rotational speeds of the sun, ring and carrier gears.

Since the generator is connected to the sun gear, the motor is on a common shaft with the ring gear, the wheels are connected to the ring gear through a reduction gear, and the IC engine is connected to the carrier gear, we have $\omega_s = \omega_G$, $\omega_c = \omega_{ICE}$, and

$$\omega_r = \frac{1}{r_{final}} \omega_w \tag{16.14}$$

where r_{final} is the final reduction gear ratio. Hence

$$\omega_G R_s + \omega_w \frac{R_r}{r_{final}} = \omega_{ICE}(R_s + R_r) \tag{16.15}$$

This means only 2 independent variables exist between ω_G, ω_w and ω_{ICE}.

According to equation (16.15), the relation between the engine speed and the wheel speed is determined not only by a gear ratio, but also by the generator speed ω_G. There are two independent variables in equation (16.15) which could be chosen to be ω_{ICE} and ω_w. The power split device is therefore a type of continuously variable transmission (CVT). The gear ratio in this CVT is determined by the value of ω_G. The power-split transmission system is therefore sometimes called an electronic variable transmission (Liu and Peng, 2008, Kimura, et. al., 1999).

Let the gear ratio between the sun gear and the ring gear be denoted by ρ:

$$\rho = \frac{R_s}{R_r} \qquad (16.16)$$

Then dividing equation (16.15) by R_r, it follows that

$$\omega_G \rho + \omega_w \frac{1}{r_{final}} = \omega_{ICE}(1+\rho) \qquad (16.17)$$

or

$$\omega_G \frac{\rho}{1+\rho} + \left(\frac{\omega_w}{r_{final}}\right)\frac{1}{(1+\rho)} = \omega_{ICE} \qquad (16.18)$$

Torque transferred from the IC engine to the ring gear is given by

$$T_r = \frac{1}{1+\rho}T_{ICE} \qquad (16.19)$$

and from the IC engine to the generator is

$$T_G = \frac{\rho}{1+\rho}T_{ICE} \qquad (16.20)$$

The drive shaft is connected to the ring gear through a final reduction gear with gear ratio r_{final}. Hence the total drive torque at the wheels is

$$T_d = \frac{1}{r_{final}}(T_r + T_{EM}) = \frac{1}{r_{final}}\left(T_{EM} + \frac{1}{1+\rho}T_{ICE}\right) \qquad (16.21)$$

Motor speed and wheel speed are proportional:

$$\omega_{EM} = \frac{1}{r_{final}}\omega_w \qquad (16.22)$$

Vehicle Dynamics:
The longitudinal vehicle dynamics remain the same as that for any other automobile and can be represented by

$$m\dot{V}_x = F_x - C_a V_x^2 - R_x - mg\sin(\theta) \qquad (16.23)$$

Wheel Dynamics:
The dynamics of the wheels of the vehicle (lumped into one virtual wheel) are given by

$$I_w \dot{\omega}_w = T_d - T_{fbrake} - r_{eff} F_x \qquad (16.24)$$

SOC dynamics:
Power discharge from the battery to the motor and charging from the generator to the battery is given by

$$P_{batt} = \eta^k T_G \omega_G + \eta^k T_{EM} \omega_{EM} \qquad (16.25)$$

where η is the electrical-mechanical conversion efficiency and

$k = -1$ during discharging
$k = 1$ during charging.

The state of charge dynamics is given by

$$\frac{d}{dt}SOC = -\frac{I_{batt}}{Q_{batt\_o}} \qquad (16.26)$$

The electrical dynamics of the battery system are given by

$$P_{batt} = V_{oc} I_{batt} - R_{batt} I_{batt}^2 \qquad (16.27)$$

I_{batt} is obtained by solving the quadratic equation (16.27) as

$$I_{batt} = \frac{V_{oc} \pm \sqrt{V_{oc}^2 - 4P_{batt} R_{batt}}}{2R_{batt}} \qquad (16.28)$$

Of the two possible solutions in equation (16.28), only 1 is viable. Hence

$$I_{batt} = \frac{V_{oc} - \sqrt{V_{oc}^2 - 4\left(\eta^k T_G \omega_G + \eta^k T_{EM} \omega_{EM}\right) R_{batt}}}{2R_{batt}} \qquad (16.29)$$

R_{batt} is a function of the SOC and of temperature.

Hence the state of charge dynamics are given by

$$\frac{d}{dt} SOC = -\frac{V_{oc} - \sqrt{V_{oc}^2 - 4\left(\eta^k T_G \omega_G + \eta^k T_{EM} \omega_{EM}\right) R_{batt}}}{2R_{batt} Q_{batt\_0}} \qquad (16.30)$$

Engine Fuel Consumption
Since a major objective in hybrid vehicle system design is to lower the fuel consumption, an engine map that provides fuel consumption rates for different operating conditions is necessary in the engine dynamics model for
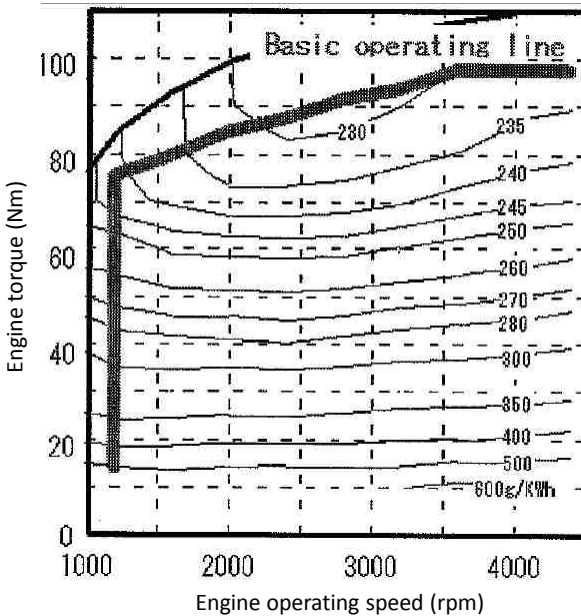
Figure 16-5. Engine map for the 1.5L engine in the THS-II powertrain system (Meisel, 2006)[1]

---

[1] Reprinted with permission from SAE paper 2004-01-0064 © 2004 SAE International

analysis. From the reference (Meisel, 2006), the engine map for the THS-II powertrain system in the Toyota Prius is shown in Figure 16-5. Each contour on the map represents a constant fuel consumption contour for a range of torque and engine speed conditions. The "basic operating line" shown on the map is the locus of the minimum BSFC (brake specific fuel consumption, g/kW-hr) for a given engine power level. This operating line represents the best engine torque-speed combinations for a given engine power level.

A 2-D lookup table model can be chosen to represent the engine map. For the engine map shown in Fig. 16-5, the engine speed and engine torque can be chosen as the column and row vectors, respectively.

For example, the engine torque vector could be

Engine torque in Nm (row): [0 10 20 30 40 50 60 70 80 90 100]; and the engine speed vector could be

Engine speed in rpm (column): [1000; 1500; 2000; 2500; 3000; 3500; 4000; 4500].

The brake specific fuel consumption in grams/kW-hr would then be a matrix with each element of the matrix corresponding to an engine speed-torque combination. Such a matrix could be constructed from the data shown in Figure 16-5.

The values of fuel consumption at operating points between the grid points in the matrix can be obtained by interpolation.

In the case of the power-split hybrid powertrain, there are two independent control inputs – these could be chosen as the generator speed and the ratio of power to be provided by the IC engine. For each candidate value of the power to be provided by the IC engine, the corresponding engine speed that offers optimum efficiency can be chosen. The engine speed is not proportional to wheel speed and can be determined independently by adjusting the generator speed. The generator torque is determined so as to provide the desired generator and engine speeds, according to equation (16.18). The engine torque is then determined from equation (16.20). Once engine torque and engine speed are known, the fuel consumption rate can be determined from the map.

16.3   BACKGROUND ON CONTROL DESIGN TECHNIQUES FOR ENERGY MANAGEMENT

16.3.1 Dynamic Programming Overview

Dynamic programming is a numerical method of finding the optimal solution to a many-stage decision making problem. It is based on Bellman's principle of optimality, which can be described as follows (How, 2008):

   If the optimal solution for a problem passes through an intermediate state (x,t), then the optimal solution to the same problem starting at (x,t) must be the continuation of the same path.

   To understand how Bellman's principle is useful in determining the optimal solution, consider the following illustrative example shown in Figure 16-6. In this problem, one desires to go from point A to point Z. The cost of each section of all possible paths is shown in the Figure. The objective is to find the path of least cost.
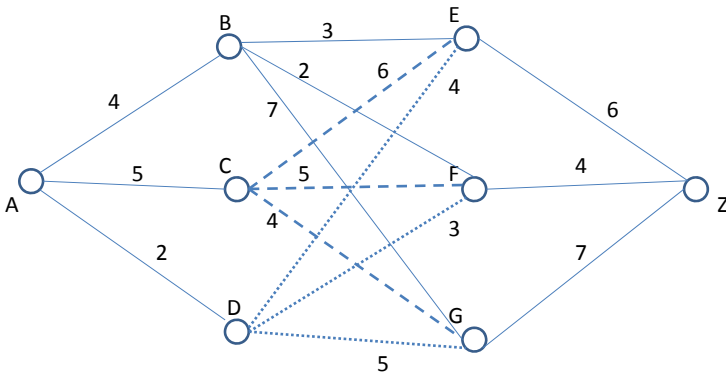
Figure 16-6. Illustration of dynamic programming

   It can be seen that there are nine possible paths to go from point A to point Z, and they are as follows:
   ABEZ, ABFZ, ABGZ
   ACEZ, ACFZ, ACGZ
   ADEZ, ADFZ, ADGZ
   At point B, the costs associated with different paths from B to Z are
   BEZ: 3+6 = 9
   BFZ: 2+4 = 6
   BGZ: 7+7 = 14
Hence the best choice of path to go from B to Z is BFZ. The associated cost is 6.
   At C, the costs associated with different paths from C to Z are
   CEZ: 6+6 = 12
   CFZ: 5+4 = 9
   CGZ: 4+7 = 11
Hence the best choice of path to go from C to Z is CFZ. The associated cost is 9.
   At D, the costs associated with different paths from D to Z are
   DEZ: 4+6 = 10
   DFZ: 3+4 = 7
   DGZ: 5+7 = 12

Hence the best choice of path to go from D to Z is DFZ. The associated cost is 7.

In order to go from A to Z, the optimal path can go through either B, C or D. From Bellman's principle of optimality, it follows that if the optimal path goes through B, then the optimal path must include BFC (the best choice to go from B to Z). Likewise, if the optimal path goes through C, it must include CFZ and if it goes through D, it must include DFZ. The optimal path can therefore be determined by comparing ABFZ, ACFZ and ADFZ.

Cost of ABFZ= Cost of AB + optimal cost from B = 4 + 6 = 10
Cost of ACFZ= AC + optimal cost from C = 5 + 9 =14
Cost of ADFZ= AD + optimal cost from D = 2 + 7 = 9

Hence the optimal solution is ADFZ.

How is dynamic programming applied for control system design in a hybrid electric vehicle? Consider the schematic shown in Figure 16-7 for the control decisions to be made in a parallel hybrid electric vehicle. The choice of power split ratios at each time step is illustrated in the figure. At time
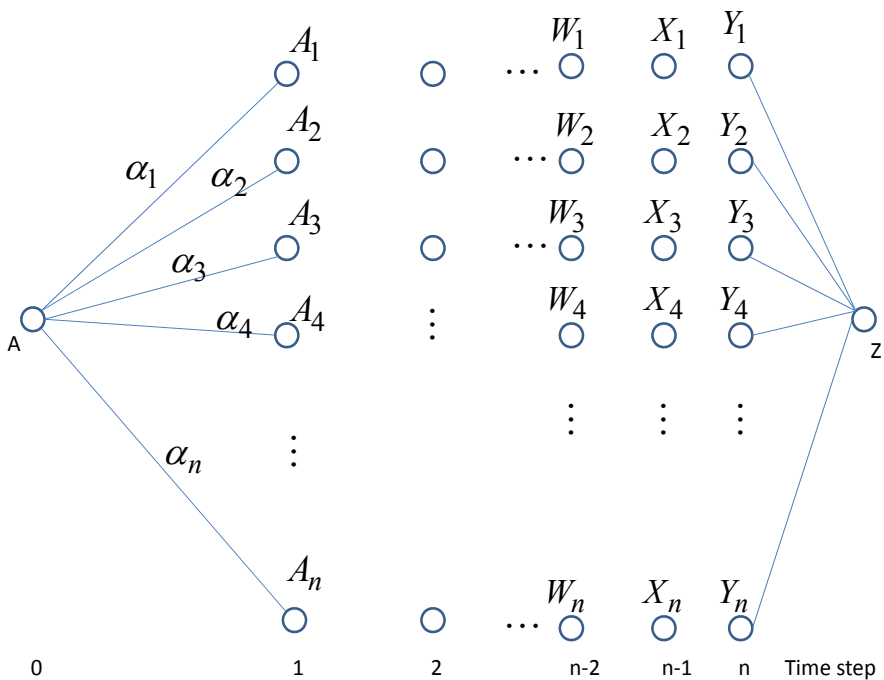
Figure 16-7. Dynamic programming for hybrid vehicle control system design

step1, the choice is between A_1, A_2, A_3, …. and A_n. Here A_1, A_2, A_3, …. and A_n represent the fraction of torque provided by the electrical motor, for example, $A_1 = 0.1$, $A_2 = 0.2$, $A_3 = 0.3$, etc. The initial condition could consist of purely electric start, for which the power split ratio is $A = 1.0$.

The costs α_1, α_2, α_3, …. and α_n in going from one time step to the next are determined from operating conditions and vehicle models. Assume that the desired vehicle speed and desired acceleration as well as road grade are known for the entire duration of the optimal control problem. From the desired speed and acceleration, the total desired torque at each time instant can be computed. Given the total desired torque, the required IC engine torque is determined for each candidate value of the control input. This engine torque value together with engine speed determines fuel consumption rates. The fuel consumption rates typically make up the costs α_1, α_2, α_3, …. and α_n in the choice of power split ratios at each time step. The SOC of the battery also needs to be determined for each choice of power split ratio, in order to ensure that upper and lower constraints on SOC are not violated.

For each X_i, compute the optimal cost to reach Z. If the optimal path passes through X_i, then the optimal path will include the optimal path from X_i to Z. Use this information to find the optimal path from W_i to Z. Proceed backwards in the same way to find the optimal path from V_i to Z. Keep proceeding backward in the same manner all the way to initial state A to find the complete optimal path solution.

Of course, the question that arises at this stage is how can the operating conditions (speed, acceleration, road grade) be known in advance? Since the solution must be obtained by iterating backwards from the final state in the case of dynamic programming, how will the operating conditions for the entire trip be known? This problem is addressed through one of the following methods:

a) Different energy management algorithms for hybrid electric vehicles are often compared based on their performance for standard duty cycles such as the EPA Urban Driving Cycle or the EPA Highway Driving Cycle. In this case the entire trip, consisting of the driving cycle, is known in advance. These driving cycles are discussed in more detail in section 16.4.
b) From GPS navigation guidance systems wherein the destination is entered by the driver, the operating conditions of the trip can be approximately known in advance. Of course traffic congestion conditions can significantly affect operating conditions, even if the route and speed limits are known. In this case wireless traffic updates would be useful in order to determine optimum energy management control inputs for the trip.

c) When no trip information is available, assumptions such as constant speed for an assumed finite time horizon can be used.

The dynamic programming problem can be solved numerically after discretization of the state and control variables with finite grids. At each step of the optimization search, the cost function is evaluated at the grid points of the state variables. Linear interpolation is used to evaluate the cost function at other intermediate points. Kang, et. al. (2001) provides a numerical algorithm for dynamic programming that can be implemented in Matlab.

16.3.2 Model Predictive Control Overview

Model predictive control (MPC) or receding horizon control is a control design technique that utilizes a model of the plant to find the numerical solution to a constrained optimal control problem over a finite time horizon (Camacho and Bordons, 2007).

To illustrate model predictive control design, consider a linear discrete-time plant model described by

$$x(k+1) = Ax(k) + B_1 u(k) + B_2 w(k) \tag{16.31}$$

$$y = Cx(k) \tag{16.32}$$

The linear system (16.31)-(16.32) is considered here for purposes of illustration for the first-time reader. Of the two inputs in equation (16.31), $w(k)$ is assumed to be a known external input while $u(k)$ is the control input that needs to be determined by model predictive control. In the case of the parallel hybrid vehicle system, $w(k)$ could be the wheel speed or motor speed in the vehicle at each time step while the state $x(k)$ could be the SOC of the battery.

The objective of the control design is to minimize a performance index. For instance, a quadratic performance index that penalizes tracking error and control energy could be described by

$$J = y(N)^T Sy(N) + \sum_{j=0}^{N-1} y(j)^T Qy(j) + u(j)^T Ru(j) \tag{16.33}$$

The performance index is defined over a time horizon N. The function $y(N)^T Sy(N)$ represents the terminal cost and could be used to penalize deviation from a final desired state. In the case of a hybrid vehicle, the

terminal cost could be a constraint on the final SOC, for example a constraint that the final SOC should be equal to the initial SOC.

Constraints on the state and the control input could be added, for example,

$$u_{\min} \leq |u| \leq u_{\max} \tag{16.34}$$

on each control input, and

$$g(x,u) = 0 \tag{16.35}$$

as a constraint on the states. The constraints on the states are used to ensure that highly undesired events are not allowed to occur. For example, in the use of MPC for adaptive cruise control (Bageshwar, et. al., 2004), the hard constraint on the states can be used to ensure that a collision is not allowed to occur, as far as possible.

Without the constraints on the inputs and the states, without the disturbance $w(k)$, and with the time horizon N allowed to go to infinity, the above problem is the same as the LQR problem and has an analytical solution.

With constraints added and with future unknown disturbances that can act on the system, a finite time horizon problem is solved numerically. The procedure is as follows.

The evolution of the state as predicted by the model is described by

$$x(k) = A^k x(0) + \sum_{i=0}^{k-1} A^i B_1 u(k-1-i) + \sum_{i=0}^{k-1} A^i B_2 w(k-1-i) \tag{16.36}$$

Hence, the output $y(k)$ is given by

$$y(k) = CA^k x(0) + \sum_{i=0}^{k-1} CA^i B_1 u(k-1-i) + \sum_{i=0}^{k-1} CA^i B_2 w(k-1-i) \tag{16.37}$$

Equation (16.37) can be rewritten in matrix form as

$$Y = \overline{A}x(0) + \overline{B}_1 U + \overline{B}_2 W \tag{16.38}$$

where

$$Y = \begin{bmatrix} y(1) \\ y(2) \\ y(3) \\ \vdots \\ y(N) \end{bmatrix} \tag{16.39}$$

$$U = \begin{bmatrix} u(0) \\ u(1) \\ u(2) \\ \vdots \\ u(N-1) \end{bmatrix}, W = \begin{bmatrix} w(0) \\ w(1) \\ w(2) \\ \vdots \\ w(N-1) \end{bmatrix} \tag{16.40}$$

$$\overline{A} = \begin{bmatrix} CA \\ CA^2 \\ CA^3 \\ \vdots \\ CA^N \end{bmatrix} \tag{16.41}$$

$$\overline{B}_1 = \begin{bmatrix} CB_1 & 0 & 0 & \cdots & 0 \\ CAB_1 & CB_1 & 0 & \cdots & 0 \\ CA^2B_1 & CAB_1 & CB_1 & \cdots & 0 \\ \vdots & \cdots & \vdots & \cdots & \vdots \\ CA^{N-1}B_1 & CA^{N-2}B_1 & \cdots & \cdots & CB_1 \end{bmatrix},$$

and

$$\overline{B}_2 = \begin{bmatrix} CB_2 & 0 & 0 & \cdots & 0 \\ CAB_2 & CB_2 & 0 & \cdots & 0 \\ CA^2B_2 & CAB_2 & CB_2 & \cdots & 0 \\ \vdots & \cdots & \vdots & \cdots & \vdots \\ CA^{N-1}B_2 & CA^{N-2}B_2 & \cdots & \cdots & CB_2 \end{bmatrix} \tag{16.42}$$

The performance index can be rewritten as

$$J = y(N)^T Sy(N) + y(0)^T Qy(0) + \cdots + y(N-1)^T Qy(N-1)$$
$$+ u(0)^T Ru(0) + \cdots + u(N-1)^T Ru(N-1)$$
(16.43)

or

$$J = y(0)^T Qy(0) + Y^T \overline{Q} Y + U^T \overline{R} U$$
(16.44)

where

$$\overline{Q} = \begin{bmatrix} Q & 0 & 0 & \cdots & 0 \\ 0 & Q & 0 & \cdots & 0 \\ 0 & 0 & \ddots & \cdots & 0 \\ \vdots & \vdots & & Q & 0 \\ 0 & 0 & \cdots & 0 & S \end{bmatrix}$$
(16.45)

$$\overline{R} = \begin{bmatrix} R & 0 & 0 & \cdots & 0 \\ 0 & R & 0 & \cdots & 0 \\ 0 & 0 & \ddots & \cdots & 0 \\ \vdots & \vdots & & R & 0 \\ 0 & 0 & \cdots & 0 & R \end{bmatrix}$$
(16.46)

Substituting from equation (16.38) into (16.44)

$$J(U, y(0)) = y(0)^T Qy(0)$$
$$+ \{\overline{A}x(0) + \overline{B}_1 U + \overline{B}_2 W\}^T \overline{Q} \{\overline{A}x(0) + \overline{B}_1 U + \overline{B}_2 W\} + U^T \overline{R} U$$
(16.47)

$$J(U, x(0)) = x(0)^T \{C^T QC + \overline{A}^T \overline{Q} \overline{A}\} x(0) + U^T HU + 2GU$$
$$+ W^T \overline{B}_2{}^T \overline{Q} \overline{B}_2 W + 2G_2 W + 2U^T \overline{B}_1{}^T \overline{Q} \overline{B}_2 W$$
(16.48)

where

$$H = \overline{R} + \overline{B}_1{}^T \overline{Q} \overline{B}_1$$
(16.49)

$$G = x(0)^T \overline{A}^T \overline{Q} \overline{B}_1$$
(16.50)

$$G_2 = x(0)^T \overline{A}^T \overline{Q} \overline{B}_2 \tag{16.51}$$

The term $x(0)^T \left\{ C^T Q C + \overline{A}^T \overline{Q} \overline{A} \right\} x(0)$ is constant and independent of the control input. Also, $W^T \overline{B}_2^{\,T} \overline{Q} \overline{B}_2 W$ and $2G_2 W$ are independent of the control input. Hence the term to be minimized is

$$\min_U U^T H U + 2G(x(0))U + 2W^T \overline{B}_2^{\,T} \overline{Q} \overline{B}_1 U \tag{16.52}$$

subject to inequality constraints on the input

$$L_{IN} U \le M_{IN}(x(0)) \tag{16.53}$$

and equality constraints on the input given by

$$L_{EQ} U = M_{EQ}(x(0)) \tag{16.54}$$

Note that the disturbance input $w(k)$ for the entire time horizon needs to be known.

An optimal control sequence $U = \begin{bmatrix} u(0) \\ u(1) \\ u(2) \\ \vdots \\ u(N-1) \end{bmatrix}$ is obtained for the given

initial condition $x(0)$ by solving the optimal minimization problem in equation (16.52). However, only the first control input in this sequence $u(0)$ is actually applied to the plant. Subsequently, the state measurement is updated and a new control optimal sequence is generated

$U_j = \begin{bmatrix} u(j) \\ u(j+1) \\ u(j+2) \\ \vdots \\ u(j+N-1) \end{bmatrix}$ corresponding to each time j for $j = 1, 2, \cdots, N$. At

each time, only the first control input $u(j)$ is actually applied to the plant.

Implementation in Matlab

The function *quadprog* in Matlab can be used to obtain the optimal control sequence to the model predictive control problem described above. The function *quadprog* finds a minimum for a problem specified by

$$\min_{u} \frac{1}{2} u^T H u + f^T u \text{ such that } Lu \le b, \; L_{eq} u = b_{eq} \text{ and } lb \le u \le ub$$

where H, L, and L_{eq} are matrices, and f, b, beq, lb, ub, and u are vectors.

u = quadprog(H,f,A,b) returns a vector u that minimizes 1/2*u'*H*u + f'*x subject to A*$u \le$ b.

u = quadprog(H,f,A,b,Aeq,beq) solves the preceding problem while additionally satisfying the equality constraints Aeq*u = beq. If no inequalities exist, the following settings can be used: A = [] and b = [].

u = quadprog(H,f,A,b,Aeq,beq,lb,ub) defines a set of lower and upper bounds on the design variables, u, so that the solution is in the range $lb \le u \le ub$. If no equalities exist, the following settings can be used: Aeq = [] and beq = [].

16.3.3 Equivalent Consumption Minimization Strategy

The equivalent consumption minimization strategy (ECMS) reduces the global-time performance index minimization problem to that of an instantaneous minimization problem that can be solved at each instant in time. Unlike the model predictive and dynamic programming techniques described in the previous two sections, the ECMS technique does not require any knowledge of future operating conditions for the hybrid vehicle system.

The performance index is defined based on the instantaneous equivalent fuel consumption as

$$J(t,u) = \Delta E_f(t,u) + s(t) \Delta E_e(t,u) \tag{16.55}$$

where the variables $\Delta E_f(t,u)$ and $\Delta E_e(t,u)$ are the fuel energy use and the electrical energy use in the time interval Δt. The equivalence factor $s(t)$ determines the relative weighting between the fuel energy use and electrical energy utilization.

The performance index can be equivalently rewritten as

$$J(t,u) = \dot{m}_f(t,u) + s(t) \frac{P_{elec}}{Q_{lhv}}(t,u) \tag{16.56}$$

where $\dot{m}_f(t,u)$ is the instantaneous rate of fuel consumption, P_{elec} is the instantaneous power consumption of the electrical system, and Q_{lhv} is the energy content per unit mass of the fuel (fuel lower heating value).

The range of acceptable values of the control input is determined. This range is discretized into a set of candidate values for the control input. For example, the candidate values could be 0.1, 0.2, …. 1.0 for the power split ratio. For each candidate value, the value of the performance index in equation (16.56) is calculated. The candidate that yields the lowest value of the performance index is then chosen as the optimal control input.

It should be noted that the electrical energy term in the performance index can be positive or negative (during regenerative braking), depending on the value of the candidate control input.

The choice of the equivalence factor $s(t)$ plays an important role in determining how well the ECMS technique performs for optimizing fuel economy. At any given time t, if $s(t)$ is too large, then the use of electrical energy can be highly penalized and consequently the fuel consumption of the vehicle can increase. On the other hand, if $s(t)$ is too small, then fuel consumption is more highly penalized and consequently fuel consumption decreases while electrical energy consumption increases by decreasing the SOC of the battery.

In order to ensure charge sustainability, the equivalence factor $s(t)$ needs to be chosen such that the use of electrical energy is more strongly penalized as the SOC becomes low, and is lightly penalized when the SOC is high. This requires that the control system incorporate a SOC sensor or a real-time estimator to estimate the SOC of the battery.

Researchers (Sciarretta, et. al., 2004) have demonstrated that performance comparable to that obtained with dynamic programming can also be obtained by the ECMS technique, if the equivalence factor $s(t)$ is chosen so that it switches between two constant values s_{ch} and s_{disch}, during charging and discharging of the battery respectively. The exact values of s_{ch} and s_{disch} are chosen optimally depending on the drive cycle, so that the performance matches that of the performance from a control system designed by dynamic programming. This, in effect, requires that the drive cycle be known, since the values of the constants s_{ch} and s_{disch} depend on the specific drive cycle under consideration.

Potential techniques to overcome the requirement on the knowledge of the drive cycle have been proposed by Pisu and Rizzoni, Gu and Rizzoni, and others. In the method proposed by Pisu and Rizzoni (2007), autoregressive models are used to predict future driving conditions using data on driving conditions from the recent past. In the method proposed by

Gu and Rizzoni (2006), a pattern recognition algorithm is used to identify the drive cycle from a set of drive cycles pre-stored in the system (city, highway, etc).

16.4   DRIVING CYCLES

A driving cycle is a standardized driving pattern described by means of a table showing velocity as a function of time. Examples of a city or urban driving cycle and a highway driving cycle are shown in Figure 16-8 and Figure 16-9 respectively.
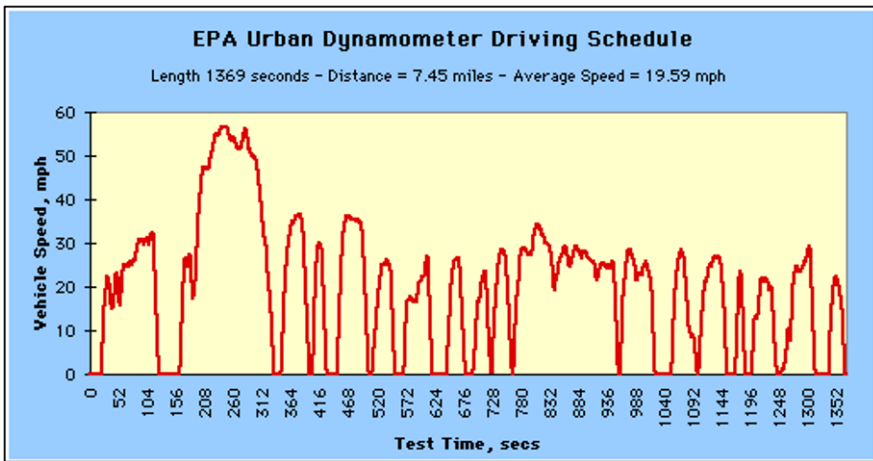
Figure 16-8. EPA Urban Driving Cycle (EPA, 2011)
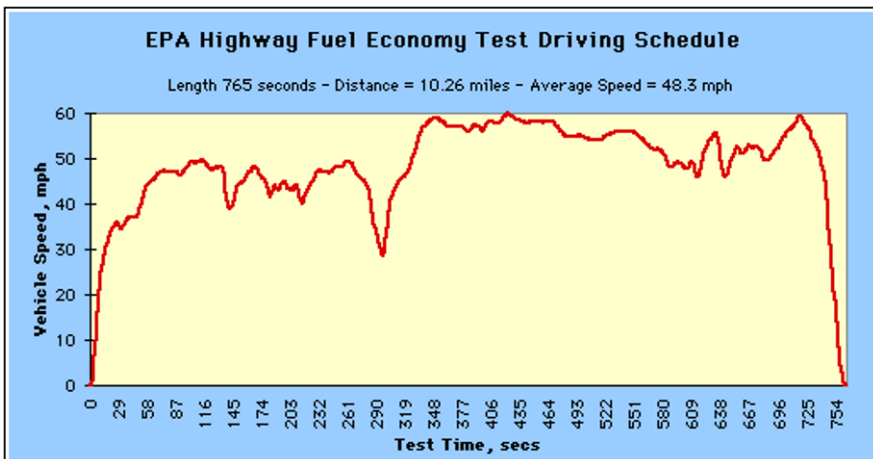
Figure 16-9. EPA Highway Driving Cycle (EPA, 2011)

The EPA city driving cycle shown in Figure 16-8 represents urban driving, in which a vehicle is started with the engine cold and driven in stop-and-go rush hour traffic.

The EPA highway driving cycle shown in Figure 16-9 represents a mixture of rural and Interstate highway driving with a warmed-up engine, typical of longer trips in free-flowing traffic.

The fuel economy of each brand of vehicle is determined by the EPA by measuring it under controlled conditions in a laboratory using a series of driving cycles. For 2007 and earlier model year vehicles, only the *city* and *highway* schedules were used for determining fuel economy. Beginning with 2008 models, three additional tests are used to adjust the city and highway

Table 16-1. Summary of Driving Cycles
(obtained from EPA web site, May 2011)

Driving Schedule Attributes	Test Schedule				
	City	Highway	High Speed	AC	Cold Temp
Trip Type	Low speeds in stop-and-go urban traffic	Free-flow traffic at highway speeds	Higher speeds; harder acceleration & braking	AC use under hot ambient conditions	City test w/ colder outside temperature
Top Speed	56 mph	60 mph	80 mph	54.8 mph	56 mph
Average Speed	21.2 mph	48.3 mph	48.4 mph	21.2 mph	21.2 mph
Max. Acceleration	3.3 mph/sec	3.2 mph/sec	8.46 mph/sec	5.1 mph/sec	3.3 mph/sec
Simulated Distance	11 mi.	10.3 mi.	8 mi.	3.6 mi.	11 mi.
Time	31.2 min.	12.75 min.	9.9 min.	9.9 min.	31.2 min.
Stops	23	None	4	5	23
Idling time	18% of time	None	7% of time	19% of time	18% of time
Engine Startup*	Cold	Warm	Warm	Warm	Cold
Lab temperature	68–86ºF	68–86ºF	68–86ºF	95ºF	20ºF
Vehicle air conditioning	Off	Off	Off	On	Off

* A vehicle's engine doesn't reach maximum fuel efficiency until it is warm.

estimates to account for higher speeds, air conditioning use, and colder temperatures. Manufacturers test their own vehicles—usually pre-production prototypes—and report the results to EPA. EPA reviews the results and confirms about 10-15 percent of them through their own tests at the National Vehicles and Fuel Emissions Laboratory.

In the laboratory, the vehicle's drive wheels are placed on a dynamometer that simulates the driving environment. The energy required to move the rollers can be adjusted to account for wind resistance and the vehicle's weight. A professional driver then runs the vehicle through standardized driving cycles. For vehicles using carbon-based fuels (e.g., gasoline, diesel, natural gas, etc.), a hose is connected to the tailpipe to collect the engine exhaust during the tests. The carbon in the exhaust is measured to calculate the amount of fuel burned during the test. This is more accurate than using a fuel gauge. This method does not work for vehicles using non-carbon-based fuels, such as fuel cell vehicles and electric vehicles.

The EPA Urban Dynamometer Driving Schedule (UDDS) shown in Figure 16-8 is commonly called the "LA4" or "the city test" and represents city driving conditions. It is used for light duty vehicle testing. The Highway Fuel Economy Driving Schedule (HWFET) represents highway driving conditions under 60 mph. The EPA Heavy Duty Urban Dynamometer Driving Schedule is for heavy duty vehicle testing. Detailed velocity-time tables of the driving cycles are available at the following web site:
http://www.epa.gov/nvfel/testing/dynamometer.htm

16.5   PERFORMANCE INDEX, CONSTRAINTS AND SYSTEM MODEL DETAILS FOR CONTROL DESIGN

Performance Index:

In general, a performance index that can be used in dynamic programming or model predictive control design for a hybrid vehicle energy management system is given by

$$J = \int_0^{t_f} L[t, u(t)]dt + \phi[SOC(t_f)] \qquad (16.57)$$

where $L[t, u(t)]$ is used to penalize fuel consumption while $\phi[SOC(t_f)]$ is used to penalize low SOC of the battery at the end of the trip or the driving cycle.

For example, the function

$$L[t, u(t)] = \dot{m}_f[t, u(t)] \tag{16.58}$$

leads to the simplest performance index J equal to the total fuel mass consumed over a time duration of t_f. In order to account for pollutant emission performance, the emission rates of specific pollutants can be included in the performance index using weighting factors for each pollutant species (see, for example, Johnson, et. al., 2000). For SI engines, only the mass fuel rate is often used in the performance index.

The function

$$\phi[SOC(t_f)] = \alpha[SOC(t_f) - SOC(0)]^2 \tag{16.59}$$

can be used to penalize the deviation of the final state-of-charge of the battery from the initial state-of-charge. However, a quadratic cost function penalizes not only a decrease in the state-of-charge of the battery, but also an increase in the state-of-charge. Since an increase in the state-of-charge is available to the vehicle for later use, an increase should not be penalized. Hence, the terminal cost function can be changed to the linear function

$$\phi[SOC(t_f)] = -\alpha[SOC(t_f) - SOC(0)] \tag{16.60}$$

This can be rewritten in integral form as

$$\phi[SOC(t_f)] = -\alpha \int_0^{t_f} \frac{d}{dt} SOC(t) dt \tag{16.61}$$

Hence the performance index becomes

$$J = \int_0^{t_f} \left\{ \dot{m}_f[t, u(t)] - \alpha \frac{d}{dt} SOC(t) \right\} dt \tag{16.62}$$

with

$$\alpha = \frac{E_{batt,\max}}{Q_{lhv}} \frac{C_{elec}}{C_{fuel}} \tag{16.63}$$

where C_{fuel} is the cost of fuel in dollars per unit of energy, C_{elec} is the cost of electricity in dollars per unit of energy (\$/kWh), Q_{lhv} is the fuel energy content per unit of mass, and $E_{batt,\max}$ is the amount of energy that the battery can hold when it is fully charged. The terminal cost in this case has units of mass (the mass of fuel and its equivalent in cost to the amount of charge spent from the battery). Alternately, the weighting factor α can be derived from the regulatory standard SAE J1711 of 38 kWh per gallon of gasoline.

Constraints:

The constraints imposed on the optimal problem formulation include the following:

The state of charge must remain within an allowable range

$$SOC_{\min} \le SOC(t) \le SOC_{\max} \tag{16.64}$$

The control variable (power split ratio) must remain within an allowable range

$$u_{\min} \le u(t) \le u_{\max} \tag{16.65}$$

If the hybrid is NOT a plug-in hybrid, so that the total charge must be substantially unchanged at the end of the trip, a terminal constraint on the state-of-charge could be added. For example,

$$SOC(t_f) = SOC(0) \tag{16.66}$$

States

In the case of dynamic programming algorithms, the computational burden increases linearly with the final time t_f but increases exponentially with the number of state variables (Sciaretta and Guzzella, 2007). Hence long trips can be analyzed and optimal control laws determined even for very long trips. However, the number of state variables is required to be small.

Hence only a single state model is often used for purposes of finding the solution to the optimal control problem. The full model, as described in section 16.2 (16.2.1 and 16.2.2) is used for simulation and evaluation of the designed controller.

In the case of a parallel hybrid electric vehicle, the following equation describing the SOC dynamics is used as the state equation.

$$\frac{d}{dt} SOC = -\frac{V_{oc} - \sqrt{V_{oc}^2 - 4\eta^k T_{EM} \omega_{EM} R_{batt}}}{2R_{batt} Q_{batt\_o}} \tag{16.67}$$

In the case of the power split hybrid electric vehicle, the following equation describing the SOC dynamics is used as the plant model for controller design:

$$\frac{d}{dt} SOC = -\frac{V_{oc} - \sqrt{V_{oc}^2 - 4\left(\eta^k T_G \omega_G + \eta^k T_{EM} \omega_{EM}\right) R_{batt}}}{2R_{batt} Q_{batt\_0}} \tag{16.68}$$

The plant model can be linearized and discretized in time to obtain a discrete time model suitable for dynamic programming or model predictive control design.

For the parallel hybrid electric vehicle, the power split ratio is the sole control input.

In the case of the power split hybrid vehicle, the generator speed and the ratio of power to be provided by the IC engine are both control inputs. The generator speed can be determined so that the engine speed is optimum for the required IC engine power. This subsequently determines the engine torque. To achieve a desired engine speed, equation (16.18) is used to calculate the corresponding generator speed. The generator torque is controlled to provide the desired generator speed. The corresponding IC engine torque is then obtained from equation (16.20). Thus, for each candidate value of IC engine power, a corresponding generator speed is automatically obtained to achieve efficient IC engine operation. The ratio of power to be provided by the IC engine is then the only remaining control input to be determined by dynamic programming, model predictive control or the equivalent consumption minimization strategy.

16.6   ILLUSTRATION OF CONTROL SYSTEM DESIGN FOR A PARALLEL HYBRID VEHICLE

Control system design for a parallel hybrid vehicle can be typically done using the following step-by-step procedure:

a) First calculate the desired torque and speed at the wheels.

If the desired longitudinal speed of the vehicle is V_x and the desired longitudinal acceleration is a_x, then the desired traction (longitudinal tire force) is

$$F_x = ma_x + CV_x^2 + R_x + mg\sin\theta \tag{16.69}$$

where θ is the road grade angle and R_x is the rolling resistance.

The rolling equations for the 4 wheels lumped together as one equivalent wheel can be represented as

$$I\dot{\omega}_w = T_d - T_{fbrake} - r_{eff}F_x \tag{16.70}$$

Hence, the desired drive torque at the wheels is obtained as

$$T_d = I\dot{\omega}_w + r_{eff}\left(ma_x + CV_x^2 + R_x + mg\sin\theta\right) \tag{16.71}$$

The desired speed at the wheels is

$$\omega_w = \frac{V_x}{r_{eff}} \tag{16.72}$$

b) Assume a candidate value for the power split ratio between the electric motor and the IC engine. This candidate value is the candidate control input and is defined as

$$u = \frac{T_{EM}}{RT_d} \tag{16.73}$$

where T_{EM} is the torque provided by the electrical motor, T_{ICE} is the torque provided by the IC engine and T_d is the total torque at the wheels.

Calculate the engine torque and engine speed and the motor torque and motor speed for this candidate power split ratio. For a candidate control input value u, the torque provided by the motor is given by

$$T_{EM} = uT_d R \tag{16.74}$$

and the torque provided by the IC engine is

$$T_{ICE} = (1-u)T_d R \tag{16.75}$$

where R is the gear ratio (typically smaller than 1).

The engine speed is given by

$$\omega_{ICE} = \frac{V_x}{Rr_{eff}} \tag{16.76}$$

and, likewise, the motor speed is given by

$$\omega_{EM} = \frac{V_x}{Rr_{eff}} \tag{16.77}$$

c) For the computed candidate values of engine torque and speed, calculate the fuel consumption rate. The fuel consumption rate of the IC engine is available as a look-up table or a map, as discussed in section 16.2.2.

$$\dot{m}_f = f(T_{ICE}, \omega_{ICE}) \tag{16.78}$$

d) For the computed candidate values of motor torque and speed, calculate the state of charge as given by equation (16.12).

e) Use the above calculations to compute the performance index for the assumed candidate value of the control input. In the case of the equivalent fuel consumption based control design technique, calculate the performance index based on the value of the instantaneous equivalent fuel consumption as

$$J = \int_0^{t_f} \left\{ \dot{m}_f[t, u(t)] - \alpha \frac{d}{dt} SOC(t) \right\} dt \tag{16.79}$$

f) Repeat the entire procedure for all the candidate values of control input.
g) Then determine the optimum control input that minimizes the performance index and meets the system's constraints.

The candidate control input that provides the lowest value of the performance index (lowest value of equivalent fuel consumption) is selected as the optimal control input at each time step.

In the case of the dynamic programming technique, start from the final state and compute the performance index for each candidate control input. Proceed backwards one step at a time to the present time, computing the performance indices and optimal control inputs at each time step. Follow the procedure described in section 16.3.1.

In model predictive control, the SOC dynamics equation is used as the plant model. This equation is linearized at the operating point at each time step during calculation of the optimal control input. For the parallel hybrid, the power split ratio or the motor torque input T_{EM} serves as the control input and the motor speed ω_{EM} serves as the known external input. The linearized matrices H, L, and L_{eq}, and the vectors f, b, beq, lb, and ub are computed. Then follow the procedure described in section 16.3.2 to compute the optimal power split ratio.

16.7   CHAPTER SUMMARY

This chapter presented the types of powertrains typically used in hybrid gas electric vehicles. Dynamic models used for control system design and for simulation were presented for parallel hybrid powertrains and for power-split hybrid powertrains. A review of the techniques used for energy management system design in hybrid vehicles was presented. The techniques included dynamic programming, model predictive control and the instantaneous consumption minimization strategy. Finally, the steps in control system design for the energy management system in a parallel hybrid electric vehicle were illustrated.

NOMENCLATURE

V_x longitudinal velocity at c.g. of vehicle

m total mass of vehicle

F_x total longitudinal tire force (sum of longitudinal tire forces)

C_a	aerodynamic drag parameter
R_x	longitudinal force due to rolling resistance
g	acceleration due to gravity
θ	road gradient angle
I_w	moment of inertia of wheels
ω_w	rotational speed of wheel
ω_{EM}	rotational speed of electric motor
T_d	total drive torque supplied to wheels
T_{fbrake}	frictional brake torque at wheels
T_{ICE}	torque from IC engine
T_{EM}	torque from electrical motor
T_G	torque supplied to generator
T_r	torque supplied to ring gear
r_{eff}	effective tire radius
u	control input, typically the control input is the power split ratio
R	gear ratio
r_{final}	final reduction gear ratio
ρ	gear ratio between sun gear and ring gear in planetary system
$\dot{m}_f$	fuel consumption rate
P_{batt}	battery power discharge
I_{batt}	current flowing from the battery
V_{oc}	open circuit battery voltage
R_{batt}	internal and terminal resistance of battery
η	electromechanical conversion efficiency
Q_{batt_o}	total charge at full charge for battery
Q_{lhv}	energy content per unit mass of fuel (fuel lower heating value)
ω_r	rotational speed of ring gear

ω_c rotational speed of carrier gear

ω_G rotational speed of generator

J performance index used in various control design techniques

$s(t)$ equivalence factor

s_{ch} equivalence factor during charging of battery

s_{disch} equivalence factor during discharging of battery

SOC state of charge of battery

REFERENCES

Ambuhl, D. and Guzzella, L., "Predictive Reference Signal Generator for Hybrid Electric Vehicles," *IEEE Transactions on Vehicular Technology*, Vol. 58, No. 9, pp. 4730-4740, November 2009.

Bageshwar, V.L., Garrard, W.L. and Rajamani, R., "Model Predictive Control of Transitional Maneuvers for Adaptive Cruise Control Vehicles," *IEEE Transactions on Vehicular Technology*, Vol. 53, No. 5, pp. 1573-1585, September 2004.

Camacho, E.F. and Bordons, C., *Model Predictive Control*, 2nd edition, p. 405, Springer, 2007.

Gu, B. and Rizzoni, G., "An Adaptive Algorithm for Hybrid Electrical Vehicle Energy Management Based on Driving Pattern Recognition," *Proceedings of the 2006 ASME International Mechanical Engineering Congress and Exposition*, 2006.

How, J., *Principles of Optimal Control*, Class Notes, Open Courseware, MIT, 2008. Available online at:
http://ocw.mit.edu/courses/aeronautics-and-astronautics/16-323-principles-of-optimal-control-spring-2008/

Johnson, V.H., Wipke, K.B. and Rausen, D.J., "HEV Control Strategy for Real-Time Optimization of Fuel Economy and Emissions," *Proceedings of the SAE*, Paper 2000-01-1543, 2000.

Kang, J.M., Kolmanovsky, I. and Grizzle, J.W., "Dynamic Optimization of Lean Burn Engine Aftertreatment," *ASME Journal of Dynamic Systems, Measurement and Control*, Vol. 123, No. 2, pp. 153-160, June 2001.

Kimura, A., Abe, T. and Sasaki, S., "Drive Force Control of a Parallel-Series Hybrid System," *JSAE Review*, Vol. 20, No.3, pp. 337-341, July 1999.

Lin, C.C., Peng, H., Grizzle, J.W. and Kang, J.M., "Power Management Strategy for a Parallel Hybrid Electric Truck," *IEEE Transactions on Control Systems Technology*, Vol. 11, No. 6, pp. 839-849, 2003.

Liu, J. and Peng, H., "Modeling and Control of a Power-Split Hybrid Vehicle," *IEEE Transactions on Control Systems Technology*," Vol. 16, No. 6, pp. 1242-1251, 2008.

Meisel, J., "An Analytic Foundation for the Toyota Prius THS-II Powertrain with a Comparison to a Strong Parallel Hybrid-Electric Powertrain," *2006 SAE World Congress, Publication* 2006-01-0666, 2006.

Musardo, C., Rizzoni, G., Guezennec, Y. and Stacia, B., "A-ECMS: An Adaptive Algorithm for Hybrid Electric Vehicle Energy Manegement," *European Journal of Control*, Vo. 11, No. 4-5, pp. 509-524, 2005.

Pisu, P. and Rizzoni, G., "A Comparative Study of Supervisory Control Strategies for Hybrid Electric Vehicles," *IEEE Transactions on Control Systems Technology*, Vol. 15, No. 3, pp. 506-518, 2007.

Rodatz, P., Paganelli, G., Sciarretta, A. and Guzzella, L., "Optimal Power Management of an Experimental Fuel Cell/ Supercapacitor-Powered Hybrid Vehicle," *Control Engineering Practice*, Vol. 13, No. 1, pp. 41-53, January 2005.

Sciarretta, A., Back, M. and Guzzella, L., "Optimal Control of Parallel Hybrid Electric Vehicles," *IEEE Transactions on Control Systems Technology*, Vol. 12, No. 3, pp. 352-363, 2004.

Sciarretta, A. and Guzzella, L., "Control of Hybrid Electric Vehicles," *IEEE Control Systems Magazine*, pp. 60-70, April 2007.

Toyota, "Toyota Hybrid System THS-II," Brochure available on Toyota's web site, Accessed on June 22, 2010, web site:
http://www.toyota.co.jp/en/tech/environment/ths2/SpecialReports_12.pdf, May 2003.

US Environmental Protection Agency, "World's First Full Hydraulic Hybrid in a Delivery Truck," EPA420-F-06-054, available at
http://www.epa.gov/otaq/technology/420f06054.htm, June 2006

Vahidi, A., Stefanopoulou, A. and Peng, H., "Current Management in a Hybrid Fuel Cell Power System: A Model-Predictive Control Approach," *IEEE Transactions on Control Systems Technology*, Vol. 14, No. 6, pp. 1047-1057, November 2006.

Wu, B., Lin, C-C., Filipi, Z., Peng, H. and Assanis, D., "Optimization of Power Management Strategies for a Hydraulic Hybrid Medium Truck," *Proceedings of the 2002 Advanced Vehicle Control Conference*, Hiroshima, Japan, September 2002.

EPA, Driving Cycles: http://www.fueleconomy.gov/feg/fe_test_schedules.shtml, 2011.

Index